ICANS-XIV

The Fourteenth Meeting of the International Collaboration on Advanced Neutron Sources

June 14-19, 1998
Starved Rock Lodge
Utica, Illinois

Volume 2

ANL-98/33
ISSN 1560-859X

Argonne National Laboratory, with facilities in the states of Illinois and Idaho, is owned by the United States government, and operated by The University of Chicago under the provisions of a contract with the Department of Energy.

DISCLAIMER

This report was prepared as an account of work sponsored by an agency of the United States Government. Neither the United States Government nor any agency thereof, nor any of their employees, makes any warranty, express or implied, or assumes any legal liability or responsibility for the accuracy, completeness, or usefulness of any information, apparatus, product, or process disclosed, or represents that its use would not infringe privately owned rights. Reference herein to any specific commercial product, process, or service by trade name, trademark, manufacturer, or otherwise, does not necessarily constitute or imply its endorsement, recommendation, or favoring by the United States Government or any agency thereof. The views and opinions of authors expressed herein do not necessarily state or reflect those of the United States Government or any agency thereof.

Reproduced from the best available copy.

Available to DOE and DOE contractors from the
Office of Scientific and Technical Information
P.O. Box 62
Oak Ridge, TN 37831
Prices available from (423) 576-8401

Available to the public from the
National Technical Information Service
U.S. Department of Commerce
5285 Port Royal Road
Springfield, VA 22161

ICANS XIV

Proceedings of the 14th Meeting of the International Collaboration on Advanced Neutron Sources

Starved Rock Lodge
Utica, Illinois
U.S.A.

June 14-19, 1998

Volume II

Editors
J.M. Carpenter
C.A. Tobin

Intense Pulsed Neutron Source
Argonne National Laboratory
9700 South Cass Avenue
Argonne, IL 60439
U.S.A.

ICANS XIV
Volume II
ISSN 1560-859X
ANL-98/33

Cover Design by:
Argonne National Laboratory
Information and Publishing Division

This publication is available from:
Argonne National Laboratory
Intense Pulsed Neutron Source
J.M. Carpenter
9700 South Cass Avenue
Argonne, Illinois, USA 60439
Phone: 630-252-5519
FAX: 630-252-4163
E-mail: jmcarpenter@anl.gov

TABLE OF CONTENTS

VOLUME I

FOREWARD ..... *i*

IN MEMORIAM MOTOHARU KIMURA ..... *iii*

ICANS XIV AGENDA ..... *vii*

STATUS REPORTS 1

Status of IPNS
B. S. Brown, J. Carpenter, R. Kent Crawford, G. McMichael and W. Ruzicka 3

SINQ as of 1998 (Status Report)
G. S. Bauer 10

News from Moscow Meson Factory
S.F Sidorkin 19

Status of Neutron Scattering Facility in JAERI Neutron Science Project
Y. Oyama, R. Hino, N. Watanabe, M. Mizumoto and T. Mukaiyama 22

A Progress Report on the Spallation Neutron Source
B.R. Appleton 32

The IBR-2 Fast Pulsed Reactor: Present and Future
V.L. Aksenov, V.D. Ananiev, A.V. Belushkin and A.V. Vinogradov 41

Status Report of KENS
H. Ikeda 46

Progress at ISIS
A.D. Taylor and W.G. Williams 51

Current Status of JHF N-arena Development
M. Furusaka and H. Ikeda 56

BNL Activities in Advanced Neutron Source Development: Past and Present
J.B. Hastings, H. Ludewig, P. Montanez, M. Todosow, G.C. Smith and J.Z. Larese 57

AUSTRON Progress Report
E. Jericha, H. Rauch, M. Regler and H. Weber 61

SPECIAL TOPICS PRESENTATIONS 69

Front End and Linac Developments for the Spallation Neutron Source
J.R. Alonso 71

Ring Developments Relevant to Short-Pulse Spallation Neutron Sources
R.J. Macek 84

Report on the International Workshop on Cold Moderators for Pulsed Neutron Sources
J. M. Carpenter 98

The ACoM Collaboration: An International Effort to Develop Advanced Cold Moderators
G. S. Bauer 101

Neutron Scattering Instruments

INSTRUMENTATION AND TECHNIQUES 111

Backscattering Spectroscopy with 2 μeV Resolution at Pulsed Spallation Sources
F. Mezei and G. Zsigmond 113

Experimental Test of Constant q Single Crystal Spectroscopy on a Time-of-Flight Spectrometer
S. Schorr and F. Mezei 119

INSTRUMENTATION AND TECHNIQUES (cont'd)
Experimental Studies on Cold Neutron Beam Focusing by Magnetic Field
Y. Kiyanagi, Y. Suda, H. Nakagawa, T. Kamiyama, Y. Ogawa, H. Iwasa, H.M. Shimizu, H. Kato, T. Oku and T. Wakabayashi 125
Enhancement of Reflectivity of Short D-Spacing Multilayer Mirrors by Ion Polishing in Combination with Ion Beam Sputtering Deposition
K. Soyama, W. Ishiyama and K. Murakami 132
General Time-Focusing of the Pulsed Source Crystal Analyzer Spectrometer
J. M. Carpenter 144
Extending the Domain of Time-of-Flight Powder Diffraction Techniques
P.G. Radaelli 159
Polarisation Modulated Crosscorrelation Neutron Spectroscopy Using ^{3}He Polarising Filters on a Pulsed Source
W.G. Williams 169
New Horizons with Position Sensitive ^{3}He Detectors
C.D. Frost, R.S. Eccleston, J. Norris, N.J. Rhodes and D.J. White 184

COMPUTER SOFTWARE 193
Remote Data Collection and Analysis
T.G. Worlton 195
Report on the Workshop on Monte Carlo Simulation of Neutron Scattering Instruments
R. K. Crawford 201
The Neutron Instrument Monte Carlo Library MCLIB: Recent Developments
P. A. Seeger, L.L. Daemen, R.P. Hjelm, Jr. and T.G. Thelliez 202

INSTRUMENT SUITES 219
Neutron Scattering Instruments for the Spallation Neutron Source (SNS)
R. K. Crawford, K.W. Herwig and T. Fornek 221

LIQUID TARGET SYSTEMS 227
Heat Deposition in Mercury by 24 GeV Protons
G. S. Bauer, H. Spitzer, G. von Holzen, L. Ni and J. Hastings 229
Measurement of Pressure Wave in Mercury Target
M. Futakawa, K. Kikuchi, H. Conrad and H. Stechemesser and ASTE Collaboration 244
Spallation Target Development at JAERI
R. Hino, M. Kaminaga, T. Aso, H. Kogawa, S. Ishikura, A. Susuki, A. Terada, H. Kinoshita and K. Haga 252
Thermal and Hydraulic Design of Mercury Target -Cross Flow Type-
M. Kaminaga, R. Hino, A. Susuki, M. Sakashita, F. Nakamura and H. Tagawa 269
Preliminary Design of Mercury Target -Return Flow Type-
R. Hino, M. Kaminaga, S. Ishikura, I. Yanagisawa, M. Uzawa, K. Kurosawa, K. Ikeda and S. Uchida 278
Analyses on Pressure Wave Propagation and Dynamic Stress in Mercury Targets
S. Ishikura, M. Kaminaga, A. Susuki, R. Hino, I. Harada, K. Kamba and M. Sakashita 288
Opportunities for Irradiation Studies of Structural Materials for Neutron Sources at the Proton Beam-Stop of Moscow Meson Factory
S.F. Sidorkin, G. S. Bauer, Y. Dai, M.I. Grachev, L.V. Kravchuk and Y.I. Orlov 301
Flow Study of JHF N-arena Liquid Target
J. Sakakibara, T. Ino and Y. Takeda 320

LIQUID TARGET SYSTEMS (cont'd)
Flow Measurement in a SINQ Mockup Target Using Mercury
Y. Takeda, H. Kikura and G. Bauer 321
Flow Study on the ESS Target Water Model
K. Haga, Y. Takeda, G. Bauer and B. Guttek 329

SOLID TARGET SYSTEMS 343
Engineering Design of the Lujan Center Target
N.K. Bultman 345
Target Materials Development for SINQ and Out of Beam Testing
A. Malik, G. Bauer and G. Heidenreich 361
Lessons Learned From the First 500 mAh of Beam on SINQ
H. Heyck, B. Amrein, G.S. Bauer and K. Geissmann 374
Measurements of Heat Transfer at the Beam Window in a Mockup Target for SINQ Using Mercury
I. Platnieks, G.S. Bauer, O. Lielausis and Y. Takeda 382
Heat Transfer and Thermomechanic Analyses on the Test Rods in the SINQ-Target Mark 2 for SINQ Using Mercury
L. Ni and G.S. Bauer 396
Thermal Hydraulic Design Concept of the N-Arena Solid Target System
K. Mishima, Y. Saito and T. Hibiki 411
Discussion on the Thickness Optimization of the Water Cooled Solid Target for N-arena
N. Takenaka, Y. Hayashida, R. Yasumura, T. Fujii, N. Hata,
Y. Ogawa and Y. Kiyanagi 424

AUTHOR INDEX

VOLUME II

TABLE OF CONTENTS

Neutron Scattering Instruments (cont'd)

NEUTRON PRODUCTION AND TARGET PHYSICS 439
Radiation Physics Experiments to Develop the Target-Moderator-Reflector System for ESS (European Spallation Neutron Source)
R.-D. Neef 441
Measurement and Analysis of Reaction Rate Distributions in a Lead Assembly Containing Tungsten Target with 500 MeV Proton Bombardment
H. Takada, S. Meigo, T. Sasa and K. Tsujimoto 448
Measurement of Incident Proton Beam Characteristics for AGS Spallation Target Experiment
H. Nakashima, H. Takada, S. Meigo, Y. Kasugai, Y. Ikeda, Y. Oyama,
N. Watanabe and ASTE Collaboration 457
Measurements of Reaction Rate Distributions on a Mercury Target Bombarded with High Energy Protons
H. Takada, Y. Kasugai, H. Nakashima, Y. Ikeda, Y. Oyama,
N. Watanabe, M. Arai, Y. Kiyanagi and ASTE Collaboration 468
Proton Energy Dependence of Reflector Effect on a Beam Intensity from a Decoupled Water Moderator
R. Takagi and Y. Kiyanagi 478

MODERATOR PHYSICS AND PERFORMANCE 487
A Ring Moderator Concept for a Long-Pulse Source
E.J. Pitcher, G.J. Russell and P.D. Ferguson 489
On Radiation Effects in Water Ice at Low Temperatures
E.P. Shabalin 497
Cryogenic Moderator Simulations: Confronting Reality
E.B. Iverson and J.M. Carpenter 507
Use of a Cold Beryllium Reflector-Filter to Enhance Cold Source Brightness at Long Wavelengths
E.J. Pitcher, G.J. Russell and P.D. Ferguson 524
Thermal Neutron Scattering Kernels for Moderator Materials: Comparison of NJoy Results from a Synthetic Model and Its Standard Library
M.M. Sbaffoni, V.H. Gillette, M.E. Pepe and J.R. Granada 533
Development of a Cold Methane Pellet Moderator for ESS
H. Barnert-Wiemer, K. Döring and H. Stechemesser 557
Comparison of Decoupled Cryogenic Moderators for High Resolution Experiments
Y. Ogawa, M. Konno, H. Iwasa, T. Kamiyama, Y. Kiyanagi, M. Furusaka and N. Watanabe 569

NEW INSTRUMENTS AND EQUIPMENT 579
HET II: A Proposed Upgrade for HET, the High Energy Chopper Spectrometer at ISIS
R.S. Eccleston, S. Foster and R.I. Bewley 581
The Backscattering Spectrometer HERMES: Design Issues
J.Z. Larese, L. Daemen, P.A. Seeger, J. Eckert and T.O. Brun 586
HELIOS: A High Intensity Chopper Spectrometer at LANSCE
T.E. Mason, C. Broholm, B. Fult, R. Osborn, R.A. Robinson, G. Aeppli, H.A. Mook, S.E. Nagler, B. Keimer and S. Kern 598
A Design for a High Resolution Very-Low-Q Time-of-Flight Diffractometer
R.P. Hjelm, P.A. Seeger, P. Thiyagarajan, L. Assoufid, L.R. Bertolini and B. Heuser 628
Optimisation of PRISMA at ISIS for Cold Neutron Single Crystal Spectroscopy
M. Bull, M. Harris, M. Hagen, U. Steigenberger, C. Petrillo, F. Sacchetti and K. McEwen 642
Recent Developments of Neutron Diffraction Instruments at the IBR-2 Pulsed Reactor
A.M. Balagurov 650
Design and Placement Considerations for Propeller-Type T-Zero Choppers
R.A. Robinson 657

Targets and Moderators

TARGET AND MODERATOR NEUTRONICS 668
Comparisons of MCNP Thermal Scattering Kernels in a Calculation of the Spectrum from the RAL Liquid Hydrogen Moderator
D.J. Picton, T.D. Beynon and T.A. Broome 669
Progress Report: SNS Neutronics Studies
L.A. Charlton, J.M. Barnes, J.O. Johnson and T.A. Gabriel 678
A Modular Approach to the Design of Cold Moderators
A.T. Lucas 687
Target Options for SINQ-A Neutronic Assessment
G. S. Bauer, A. Dementyev and E. Lehmann 703

TARGET AND MODERATOR NEUTRONICS (cont'd)

Neutronic Aspects of the SINQ Mark 2 Target with Irradiation Test Samples
A. Dementyev, G. S. Bauer, Y. Dai and E. Lehmann 717
A Conceptual Design Study of Target-Moderator-Reflector System for JAERI 5 MW Spallation Source
N. Watanabe, M. Teshigawara, H. Takada, H. Nakashima, Y. Oyama, T. Nagao, T. Kai, Y. Ikeda and K. Kosako 728
Towards a High-Efficiency Pulsed Cold Neutron Source
N. Watanabe, M. Teshigawara, H. Takada, H. Nakashima, Y. Oyama, T. Kai, T. Nagao and K. Kosako 743
Neutron Production Enhancements for the Intense Pulsed Neutron Source
E.B. Iverson, J.M. Carpenter, T.L. Scott, M.E. Miller, L.D. Peters and M.W. Schlueter 751

POSTERS 759
The Iris 4.2 K Cold Graphite Analyser Design
M. Adams, J. Balchin, T. Broome, C. Carlile, D. Cragg, J. Tomkinson, C. Uden, ISIS ... 761
Membrane Windows with Get-Lost Tubes for Use at Small Scattering Angles in Neutron Spectrometers
H. Belch, R. Kleb, J. Carpenter, and K. Crawford, ANL 764
Development and Modernization of the System for the Diagnostics of the State of the Pulsed Neutron Source IBR-2
Yu.N Pepyolyshev, A.V. Belushkin and A.V. Vinogradov, JINR 768
Sample Environments at the Intense Pulsed Neutron Source (IPNS)
D. E. Bohringer and K. J. Volin, ANL 773
A "Hot Stage" Displex®: 20 - 800K in a Neutron Scattering Environment
K. J. Volin and D. E. Bohringer, ANL 783
The New Drive System for ISIS Disc Choppers
Z. Bowden, M. Fischer, P. Chorley; ISIS
B. Halls, Spectral Drives & Controls, Ltd. 791
A New Scintillator for Neutron Scattering Instruments
J.B. Czirr, Mission Support, Inc. 792
Structural and Hydraulic Study on Cold Source Moderator
T. Aso, S. Ishikura, A. Terada, T. Kai, M. Teshigawara, M. Kaminaga, R. Hino, N. Watanabe, JAERI 804
Incident Spectrum Determination for Time-of-Flight Powder Neutron Diffraction Data Analysis
J. Hodges, J. Jorgensen, S. Short, D. Argyriou and J. Richardson Jr., ANL 813
Behavior of ^{7}Be in the Moderator Cooling System at the Pulsed Neutron Source, KENS
S. Itoh, T. Miura, M. Furusaka, S. Yasui, Y. Ogawa, Y. Kiyanagi, S. Sasaki, K. Iijima .. 823
The High-Resolution Medium-Energy Chopper Spectrometer (HRMECS): Instrumentation Upgrade and Future Scientific Opportunities
C. Loong, J. Hammonds, D. Yocum, J. Nipko, K. Takeuchi, D. Chen, L. Donley, G. Ostrowski, R. Crawford, H. Belch and R. Kleb, ANL 829
Material Development for Spallation Target at JAERI
K. Kikuchi, H. Kogawa, M. Futakawa, I. Ioka and R. Hino 830
Preliminary Design Studies for an Iridium Rod Target at the BNL-AGS
H. Ludewig, J. Hastings, P. Montanez, and M. Todosow 836
A Foil-less Charge Exchange Injection (LUCE) for the Intense Proton Storage Ring
Y. Suzuki (JAERI) (Presented by Y. Oyama) 847

POSTERS (cont'd)
Adjustable Collimation for the General Materials Diffractometer (GEM)
L.C. Perrott, S.A. Temple, and G. Thomas, ISIS 852
A New Polarized Neutron Reflectometer at KENS
M. Takeda, N. Toyoshima and Y. Endoh 855
Performance of the Small-Angle Diffractometer SAND at IPNS
P. Thiyagarajan, V. Urban, K. Littrell, C. Ku, D. G. Wozniak, H. Belch, R. Vitt, J. Toeller, D. Leach, J.R. Haumann, G.E. Ostrowski, L.I. Donley, J. Hammonds, J.M. Carpenter and R. K. Crawford, ANL 864

WORKING GROUP REPORTS 879
Working Group on Monte Carlo Simulation of Neutron Scattering Instruments
R.K. Crawford, Chair 881
Report on the Workshop Group Meeting on: Next Generation Powder Diffractometers
P. G. Radaelli, Chair 884
Report of the Workshop on Small-Angle and Reflectometry Instruments on Future Spallation Sources
P.A. Seeger, Chair 887
Working Group Report: Critical Heat Flux: Limitation to Solid Target?
Y. Takeda, Chair 889
Summary of the Objective Discussion of Solid and Liquid Targets for High-Power Sources
N. Watanabe and P. Ferguson, Co-Chairs 890
Summary Report for the Working Group "Needs for Target Systems and Instrument Materials, Beamline Components, Detectors, and Beamline Technology"
M. Furusaka, Chair 891
Working Group: Spectroscopy in Future Neutron Sources
C. Loong, Chair 894
Moderator Performance Enhancement and Development Activities: Progress and Needs
G. Russell, Chair and E. Pitcher, Co-Chairman 895

VENDOR PAPER
Equipment and Software for Research with Neutrons
H. Betzold 907

GROUP PHOTO

LIST OF ATTENDEES

VENDOR LIST

AUTHOR INDEX

Neutron Scattering Instruments (cont'd)

NEUTRON PRODUCTION AND TARGET PHYSICS

ICANS-XIV
14th Meeting of the International Collaboration on
Advanced Neutron Sources
June 14-19, 1998
Starved Rock Lodge Utica, Illinois U.S.A.

RADIATION PHYSICS EXPERIMENTS TO DEVELOP THE TARGET-MODERATOR-REFLECTOR SYSTEM FOR ESS (EUROPEAN SPALLATION NEUTRON SOURCE)

R.-D. Neef
(For the NESSI-, ASTE-, JESSICA- and RECOIL Collaboration)
Forschungszentrum Juelich GmbH, Institut fuer Kernphysik
D-52425 Juelich, Germany
+49-2461-61-5232

ABSTRACT

To develop high power spallation targets the calculational methods have to be applied to demonstrate feasibility, to optimize the design configuration and to support the engineering layout. The requirements of the calculational methods in spallation technology are the predictions for the following interesting questions, which have to be answered for all high current accelerators and their target stations: - neutron, gamma and charged particle production and fluxes; - energy deposition and heating; - radioactivity and after heat; - materials damage by radiation; - high energy source shielding.

The ability to predict, on a theoretical or computational basis, all aspects of radiation physics is crucial for the performance optimization of the whole system by advising engineers in their decisions with respect to the effect on the source characteristics. While the standard of computational models for neutronics and nucleonics calculations is generally quite high, there are still some areas where more research is urgently needed.

Manifold experiments have been performed to proof and validate the physical models of secondary particle production and transport of particles through matter applied in Monte Carlo simulations. Several basic nuclear experiments are underway to validate important parameters for the ESS target station design and will be discussed.

1. Introduction

In the ESS study report[1] we identified several areas where further spallation physics research and code validation is urgently needed: Neutron and charged particle production and multiplicities above one GeV incident protons, energy deposition and heating, material damage

parameters, radioactivity and after heat, and high energy source shielding. All simulation calculations will be done using the Jülich HERMES code system[2]. For this purpose and the various aspects four collaborations were organized: NESSI (Neutron Scintillator Silicon Detector), ASTE (AGS Spallation Target Experiment), JESSICA (Jülich Experimental Spallation Target Setup in COSY Area) and RECOIL.

The NESSI Experiment[3]

Within the NESSI collaboration at COSY-Jülich (Cooler Synchrotron) neutron and charged particles multiplicities are measured up to 2.5 GeV incident proton energy for "thin"and "thick" targets for various structure and target materials from Al to Pb (and U). For thin targets (only one nuclear interaction in the target) the number of evaporative neutrons is a good measure of the distribution of the thermal excitation energy induced in the nucleus. In this sense the neutron multiplicity distribution is a sensitive test of the primary spallation process, i.e., the intranuclear cascade part of the theoretical model. At high excitation energies above about 2-3 MeV/nucleon in heavy nuclei additional information on light charged particles (evaporative protons and He) improves the excitation energy resolution by about a factor 2-3. For thick targets (multiple reactions) the alteration of the neutron multiplicity distribution reflects the production of additional neutrons produced in secondary reactions and thus it is a sensitive test to both the intra- and internuclear cascade part of theoretical models.

In summary, one can show the advantage of measuring the whole neutron multiplicity distributions instead of single average values. This brings much more constraint to the INCE (intra nuclear cascade evaporation) model. Also the measurements in both thin and thick targets appear quite complementary since, in thick targets, compensation effects between the first reaction and secondary reactions can mask deficiencies in reproducing the primary reaction by the INCE model. The thick target measurement brings an additional, although indirect, test of the thin target measurement insofar as it allows one to follow the fate of the products of the primary interaction in generating extra neutrons.

The experimental equipment consists of two 4π-detectors, namely the large spherical neutron tank (BNB) with 1500 litres of scintillating liquid and 24 photomultipliers on the surface, and, inside the tank and around the target, the silicon detector (BSIB). BNB uses the old principle of slowing down the neutrons and detecting them by their capture in Gadolinium. BSIB is a spherical shell of 20 cm diameter, assembled in a selfsupporting way from 162 silicon detectors, 12 pentagons and the "magic" number of 150 hexagons. They all have the same size (7.5 cm^2) and thickness (500 μm). BSIB detects and to some degree identifies all charged nuclear particles by energy, or energy loss, and time-of-flight over the 10 cm from the target.

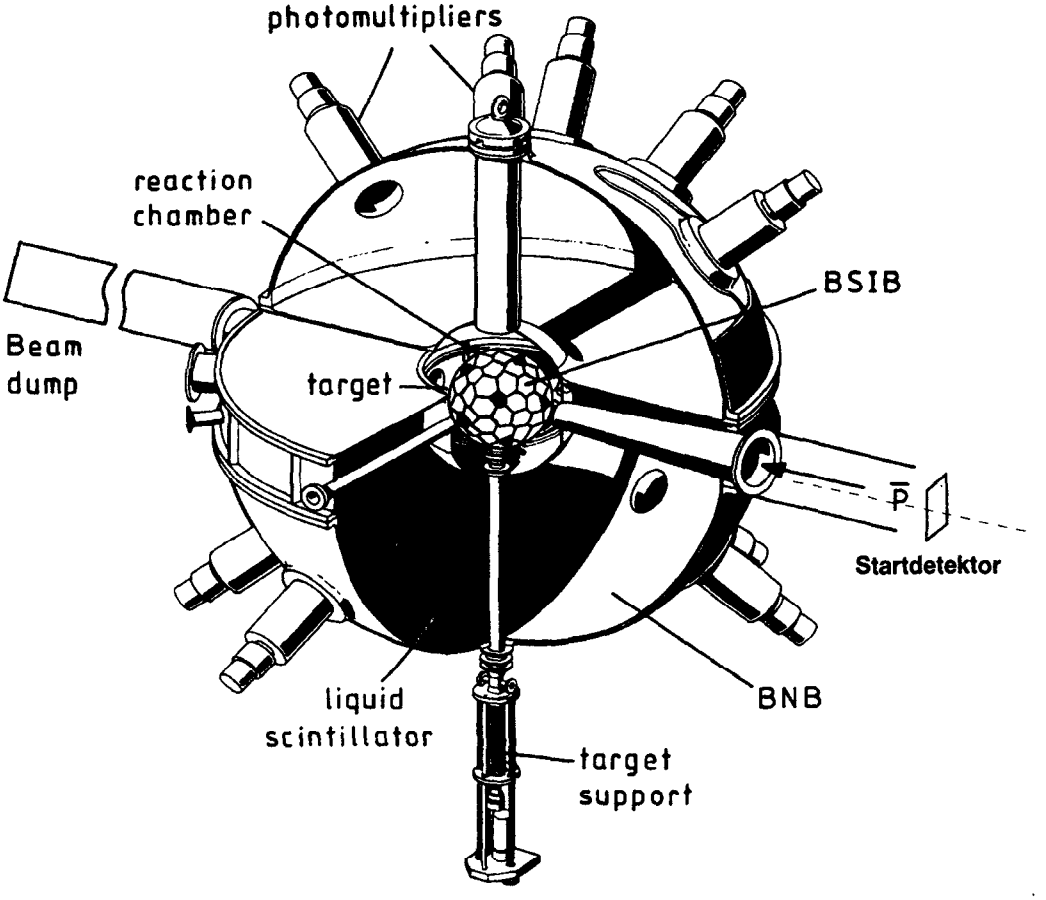

Fig. 1: The NESSI detector

During the first experiment at COSY in April 1997 we measured the neutron multiplicity of a thin Hg target (5 mm thick, diameter 20 mm, stainless steel 0,3 mm container). This is very important because mercury is the favourite target material for ESS (European Spallation Source) and there exist no experimentally estimated cross sections.

For comparison with the experiment the simulated result of the neutron multiplicity of the thin mercury target setup is shown in figure 2.

Measured and simulated neutron multiplicities are distributed very differently. Whereas the experimental multiplicity shows its maximum at 15 neutrons the simulation shows the maximum at 23 neutrons. The detector system has an energy dependent detection efficiency which has to be taken into account . If we fold the simulated neutrons with this energy depend detector efficiency we receive a simulated neutron multiplicity distribution which should be comparable to the measured distribution. In fact we find a simulated distribution which tends to have a higher multiplicity by 1 neutron at both sides of the maximum. It is not possible to evaluate the real neutron multiplicity by experiment only, even not with the knowledge of the energy dependent detector efficiency. Therefore, the simulation is absolutely necessary for the interpretation of the experiment.

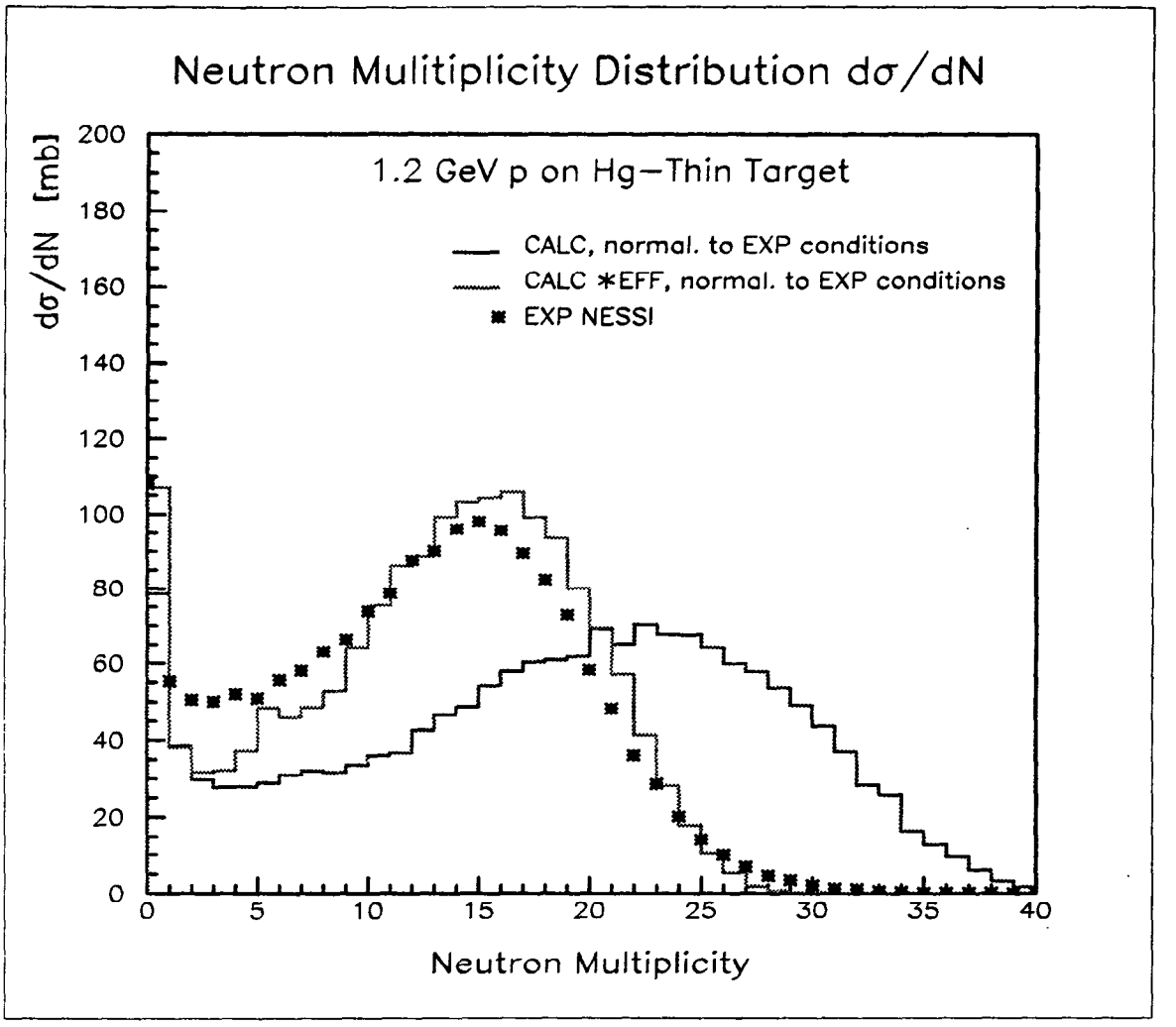

Fig. 2: Measured and simulated neutron multiplicity for 1.2 GeV protons on a thin mercury target.

For thick targets (multiple reactions) the alteration of the neutron multiplicity distribution reflects the production of additional neutrons produced in secondary reactions and thus it is a sensitive test to both the intra- and internuclear cascade part of theoretical models. We have prepared target blocks (15 cm in diameter and 40 cm length) from three materials, tungsten, mercury and lead, which are all suited for spallation neutron sources, with Hg beeing favoured for the European Spallation Source. These blocks are highly segmented in length and diameter, so that the neutron production at some selected proton energies can be simultaneously studied as a function of target geometry, thereby adding constraints also to the transport part of the models. The idea is to provide bench-mark data for the high energy transport codes.

In figure 3 a comparison of INCE and low energy neutron transport calculations with first experimental results for thick mercury targets are given. The open circles represent the calculated values. The stars represent the efficiency corrected values, which can be compared with experimental ones.

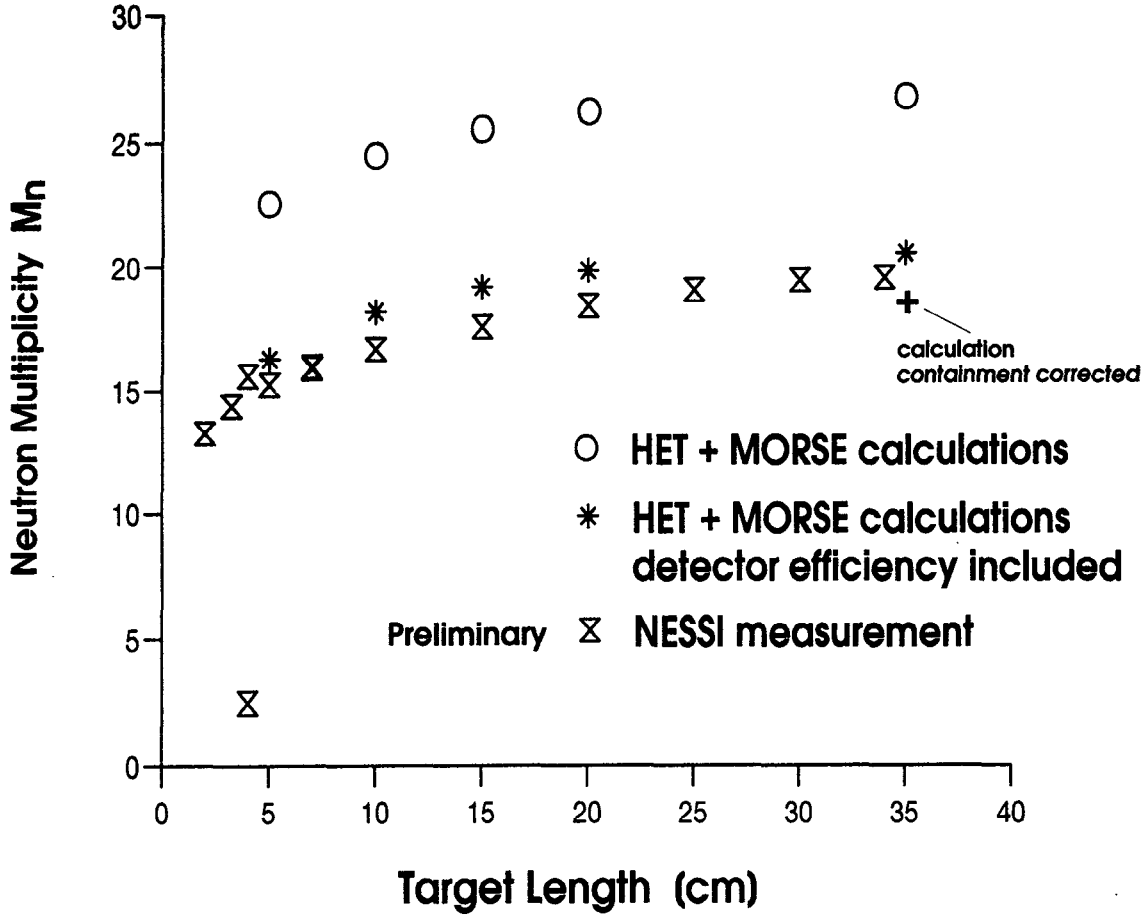

Fig. 3: Mean neutron multiplicity for 1.2 GeV incident protons on thick mercury targets of 15 cm diameter

The ASTE Experiment

The purpose of the ASTE-Collaboration is to perform experiments to verify experimentally a number of predictions from theoretical calculations on the neutronic and thermo-mechanical behaviour of spallation targets designed for pulsed operation in the megawatt power regime. The experiments started in 1997 with a first test run with a bare cylindrical (diameter 20 cm, length = 130 cm) mercury target and will continue with reflected target systems.

The main goals of the experiment are to verify experimentally a number of theoretical predictions:
distribution of neutron leckage reaction rates, energy deposition distribution from 1.5 to 24 GeV incident proton beam energy, pressure waves in mercury, stress wave monitoring of the target container, spallation product measurements, reaction rate distributions in reflected target systems and neutron spectra time of flight measurements.

Of major interest of the experiment is the estimation of energy deposition distribution in the target. A pulse with all protons of the AGS in two bunches, i.e. $2x4.0x10^{12}$ protons of 24 GeV

in less than ~ 30 ms introduced a maximum temperature jump of 3.4 K in the target. A comparison of the axial distribution of measured and simulated temperature jump is given in fig. 4. The calculation was performed using the measured incident proton beam density profile.

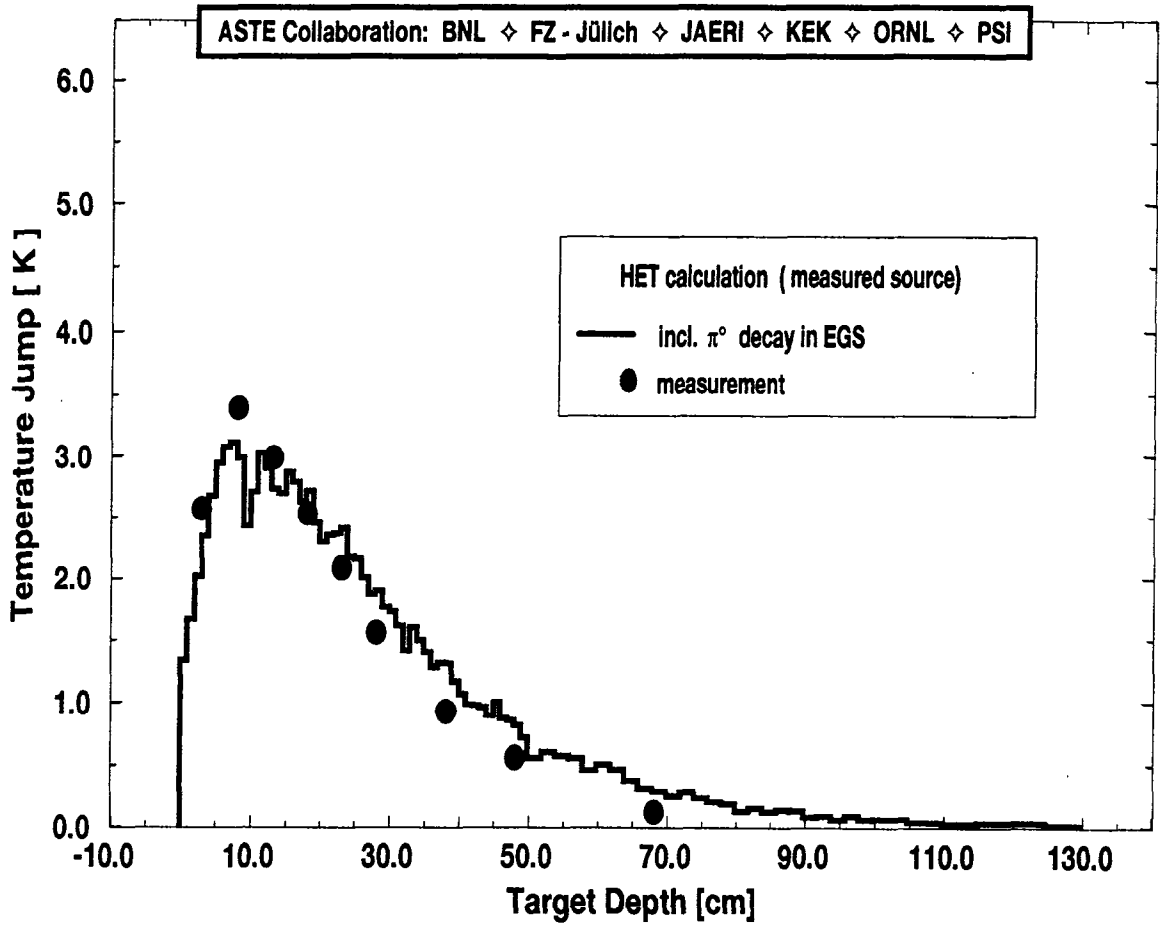

Fig. 4: Measured and calculated temperature jump in the mercury target during a 30 kJ incident proton pulse

A first comparison of calculated and measured temperature jump distribution indicates that the calculations are in good agreement with the measurements.

Two further experiments are in preparation at COSY-Jülich:

- JESSICA

JESSICA is planned as a ESS Target-Moderator-Reflector station mockup with in axial direction movable ESS mercury target. The experiments will be performed with bare and reflected target systems including beam tubes, cooling systems for reflector and moderators. Reflector and moderator materials and geometries can be changed easily for comparable measurements. This mockup will be an advanced cold moderator test facility for ESS.

- RECOIL

The recently found RECOIL collaboration will study the various aspects of proton induced reactions with nuclei by spallation physics experiments. The main part of the experimental installation is the large magnetic spectrometer THETYS from CERN with field strength of 1.2 Tesla and wide gap of 1.0x1.0x0.4 m^3 with a very homogeneous electromagnetic field. The planned experimental program consists of the measurement of spallation cross sections of recoiling nuclei over a proton energy range of 0.1-2.5 GeV on different target materials; inclusive and exclusive high energy charged particle spectra from 50 MeV to beam energy. The energy spectra of the recoiling nuclei are important to evaluate damage energy cross sections. The high energy charged particle spectra are important to validate the distribution of the excitation energy E^*, which is the transition energy from the intranuclear cascade to the evaporation phase of the de-exciting residual nucleus.

References

1. The European Spallation Source Study, Vol. III, ESS-96-53-M, ISBN 090 237 6 659, Nov. 1996

2. P. Cloth et al., HERMES, A Monte Carlo Program System for Beam Materials Interaction Studies, Report JUEL-2203, May 1988

3. F. Goldenbaum et al., Phys. Rev. Lett. 77 (1996), 12330 and
   D. Hilscher et al., Proc. of the Int. Workshop on Nuclear Methods for Transmutation of Nuclear Waste, Dubna 1997

ICANS-XIV
14th Meeting of the International Collaboration on
Advanced Neutron Sources
June 14-19, 1998
Argonne National Laboratory, 9700 S. Cass Avenue, Argonne, IL 60439, USA

Measurement and Analysis of Reaction Rate Distributions in A Lead Assembly Containing Tungsten Target with 500 MeV Proton Bombardment

H.Takada, S.Meigo, T.Sasa and K.Tsujimoto

Center for Neutron Science
Japan Atomic Energy Research Institute
Tokai-mura, Naka-gun, Ibaraki-ken, 319-1195, JAPAN

Abstract

In order to study the production and transport of spallation neutrons in a thick medium for the 500 MeV proton bombardment, an integral experiment was carried out using a lead assembly in which a tungsten target is placed in the center. The reaction rate distributions were measured with various activation detectors by the γ-ray spectrometry in the experiment. The analytical study was also performed using the NMTC/JAERI-MCNP4A code system with the nuclide production cross section values combining JENDL Dosimetry File and the ALICE-F calculation. The calculations using this code system reproduce the measured reaction rates with an accuracy of 20 to 30%.

1. Introduction

The Monte Carlo simulation code system NMTC/JAERI (1) combining MCNP4A (2) has been employed for the analysis of spallation experiments in JAERI. The code system is considered as a tool for neutronics design of the facilities proposed for the neutron science project (3). Experimental benchmark is required to validate the code system for estimating the source term as accurate as possible in the neutronic design study. The MCNP4A code itself and associated evaluated nuclear data below 20 MeV have been validated very well through the activities related to the fusion neutronics. Thus, the major interest is focused on the validation of the NMTC/JAERI code which simulates the production and transport of spallation neutrons in a thick medium.

As experimental data available for benchmark are very limited, we have started the thick target experiments (4,5) together with a thin target one (6). In the previous work (5), the transport of spallation neutrons in a lead assembly were studied using the activation detectors for 500 MeV proton bombardment at the beam dump room of the booster synchrotron utilization facility of High Energy Accelerator Research Organization (KEK). In this work, the reaction rate distribution of the activation detectors were measured in the lead assembly in which tungsten target was placed in the center aiming at studying the neutron production and transport dependent upon the target material. Tungsten was chosen because it was one of promising materials for an intense spallation target driven by a proton accelerator with power of MW. For

Keywords: lead assembly installing tungsten target, 500 MeV proton, activation detector, NMTC/JAERI

convenience, the lead assembly containing the tungsten target is denoted as 'tungsten/lead assembly' in this paper.

2. Experimental Procedure

The experimental procedure was essentially the same as for the previous work [5]. Figure 1 shows the cross sectional view of the tungsten/lead assembly. The size of the assembly was 60 cm in outer diameter and 100 cm in length. A 16 cm outer diameter and 30 cm long tungsten alloy target with weight fractions of 97 % W, 1% Ni and 2% Cu was embedded in the lead assembly. The tungsten target and the lead assembly was covered with 2.5 mm thick stainless steel (SS) plates, respectively. The protons were transported through a beam entrance hole of 10 cm in diameter and were injected perpendicular to the tungsten target surface.

The high purity metal pellets of Al, Ni, Au and Nb were used as the activation detectors. The diameter of pellets was 8 mm. The thickness was 1 mm for Au and 5 mm for Al and Nb. For Ni, both of 2.5 and 5.0 mm thick pellets were used. These pellets were packed in the Aluminum capsules having outer diameter of 9.4 mm with thickness of 0.5 mm, and then were inserted in the irradiation holes. W and Pb pellets were also filled in the capsules to prevent the perturbation of neutron flux. The surface of the irradiation hole was covered with 1.3 mm thick SS plate.

The number of incident protons were measured with a calibrated pick up coil [7] installed in the beam line and a Faraday cup using the lead assembly itself. The number of incident protons were estimated with accuracy of 3%. The shape of the beam was about 2.5 and 1.5 cm in FWHM in the horizontal and vertical directions, respectively.

The γ-ray spectrum of irradiated pellets were measured repeatedly from one day after irradiation to a few months. The peak efficiency of Ge-detector was determined using standard radionuclide sources with accuracies ranged from 1.5 to 2.0%. The errors of the efficiency was estimated as 5% through this calibration. The reaction rate of each activation detector was obtained from the peak counts of γ-ray spectrum by correcting the decay, peak efficiency, self absorption of γ-rays in a pellet and the coincidence sum effect in counting.

3. Calculation

The tungsten/lead assembly was modelled in a two-dimensional cylinder as shown in Fig. 2. The SS liner in the assembly was also taken into account in the two-dimensional geometry model. The reaction rates were obtained in the cells with 2 cm width along the longitudinal direction.

The neutron flux in the tungsten/lead assembly was calculated with NMTC/JAERI in combination with MCNP4A. NMTC/JAERI simulates the nuclear reactions and particle transport in the energy region above 20 MeV by the use of the intranuclear cascade model of Bertini [8] and a particle evaporation model taking account of the high energy fission process. The level density parameter derived by a formulae of Ignatyuk [9] was used in the evaporation calculation. The cut-off energies for particle transport were set to be 20 MeV for neutron and 2 MeV for charged particles. The energy group structure defined in the HILO-86R library [10] was employed up to 400 MeV in this calculation. For neutrons above 400 MeV, the energy group structure was extended with an interval of 50 MeV. The reaction rate was obtained with the nuclide production cross sections calculated by the ALICE-F code [11]. Here, some of calculated cross sections were adjusted to connect smoothly with the ones compiled in JENDL Dosimetry file [12] at 20 MeV. These cross sections are shown in Fig. 3.

MCNP4A calculates the transport of the neutrons in the energy region lower than 20 MeV using a continuous energy cross section library which has been processed from JENDL-Fusion File [13]. Transport of charged particles with energies below 2 MeV was not treated in

this calculation.

The histories of 2 millions of incident protons were calculated with the conditions that the incident beam shape was expressed by the Gaussian distribution with FWHMs of 2.5 and 1.5 cm in horizontal and vertical direction. The importance sampling technique was employed to obtain an enough statistics for estimating the neutron flux.

4. Results and Discussion

Figure 4 shows the reaction rate distribution of the $^{27}Al(n,x)^{24}Na$ reaction measured in the tungsten/lead assembly bombarded with 500 MeV protons. For comparison, the results of the previous experiment [5] are shown with the open marks in the Figure. It is observed that the reaction rate shows the maximum value around 25 cm from the front surface of the lead assembly and decreases with the distance. The width of longitudinal reaction rate distribution in tungsten target is narrower than that in lead one. This characteristics is attributed to the following physical aspects: The range of 500 MeV proton is about 12 cm for tungsten, while 20 cm for lead. The mean free path of fast neutron is shorter in tungsten than in lead because of large macroscopic total cross section of tungsten.

Figure 5 shows the measured and calculated reaction rates of the $^{nat}Ni(n,x)^{58}Co$ reaction in the tungsten/lead assembly. The calculation reproduces the shape of the measured reaction rate distribution well. Quantitatively, however, the calculation overestimates the measured reaction rates at the whole positions. The $^{nat}Ni(n,x)^{58}Co$ reaction is induced predominantly by the neutrons in the MeV region. Moreover, the cross section of this reaction is evaluated very well. Thus, this discrepancy indicates that the NMTC/JAERI-MCNP4A code system overestimates the neutron yield in the MeV region. This overestimation is attributable to the lack of the preequilibrium process in the nuclear reaction calculation in NMTC/JAERI. The excitation energy of a residual nucleus in the evaporation process is estimated somewhat higher so that the number of MeV neutrons emitted from the nucleus might be overestimated.

Figure 6 shows the measured and calculated reaction rates of the $^{197}Au(n,2n)^{196}Au$ reaction in the tungsten/lead assembly. The calculation is in good agreement with the experiments although slight discrepancies are observed at the longitudinal positions of 5, 55 and 65 cm from the front surface. The $^{197}Au(n,2n)^{196}Au$ reaction is sensitive to the neutrons from 10 to 20 MeV. As shown in Figs 7 and 8, good agreement is observed between the calculations and the experiments for the $^{27}Al(n,x)^{24}Na$ and $^{93}Nb(n,2n)^{92m}Nb$ reactions sensitive to the neutrons from 10 to 20 MeV, respectively. Consequently, it can be concluded that the NMTC/JAERI-MCNP4A code system estimates well the neutron yield in the energy region of 10 to 20 MeV for tungsten target.

Figures 9 and 10 show the reaction rate distributions of the $^{197}Au(n,4n)^{194}Au$ and $^{93}Nb(n,4n)^{90}Nb$ reactions in the tungsten/lead assembly, respectively. These reactions are sensitive to the neutrons in the energy region of 30 to 45 MeV where the production and transport of neutrons is treated by the NMTC/JAERI code. It is observed in Fig. 9 that the NMTC/JAERI calculation underestimates the measured reaction rates by 20 to 30% for the $^{197}Au(n,4n)^{194}Au$ reaction at almost all the positions. This result is similar with that of the previous experiment [5] using the pure lead assembly. On the other hand, good agreement is observed between the calculation and the experiment for the $^{93}Nb(n,4n)^{90}Nb$ reaction sensitive to neutrons with 30 to 40 MeV.

In Fig. 11, the total and the elastic neutron cross sections [14] for tungsten used in NMTC/JAERI are compared with those in an evaluated nuclear data file of Los Alamos National Laboratory [15]. Not only the total cross section but also the fraction of non-elastic one used in NMTC/JAERI is higher than the evaluated data. This suggests that the mean free path of neutrons in the energy region below 30 MeV might be estimated short in the NMTC

/JAERI calculation. However, this can be not confirmed in this integral experiment because of lack of available neutron spectrum data for thick tungsten target. It is noted that the nuclide production cross sections calculated by the ALICE-F code have not been evaluated yet. This is the other source of the discrepancy observed in the reactions sensitive to this energy range.

5. Conclusions

Reaction rate distributions of various activation detectors sensitive to 1 to 30 MeV were measured in the volume of 60 cm in diameter and 100 cm in length of the tungsten/lead assembly with 500 MeV proton bombardment. The reaction rate distributions were analyzed with the NMTC/JAERI-MCNP4A code system using the nuclide production cross section values combining JENDL Dosimetry File and the ALICE-F calculation.

It was found that the code system gave higher reaction rates than the experiment for the activation detector sensitive to the MeV region. Good agreement was obtained between the calculation and the experiment for the activation detectors sensitive to neutrons in the energy region from 10 to 20 MeV. For the activation detectors with threshold energies above 20 MeV, agreement between the calculations and the experiments was different among reactions because of ambiguity of reaction cross sections. Nevertheless, the calculation using the NMTC/JAERI-MCNP4A code system reproduced the measured reaction rate distributions with an accuracy of 20 to 30 %.

Acknowledgements

This experimental work was carried out under the contract on the facility utilizations of KEK. The authors would like to thank the staffs of neutron science laboratory for operation of booster synchrotron and are also indebted to those of radiation science center of KEK for kind instruction to treatment of irradiated samples.

References

(1) Y.Nakahara, T.Tsutsui: "NMTC/JAERI A Code System for High Energy Nuclear Reactions and Nucleon-Meson Transport Code", JAERI-M 82-198 (1982), [in Japanese].; H.Takada, et al.:"Au Upgraded Version of the Nucleon Meson Transport Code : NMTC/JAERI97", JAERI-Data/code 98-005 (1998).

(2) J.F.Briesmeister (Ed.) : "MCNP A General Monte Carlo N-Particle Transport Code, Version 4A", LA-12625, (1993).

(3) T.Mukaiyama, Y.Oyama, M.Mizumoto, T.Takizuka, R.Hino, : "Neutron Science Project at JAERI", Proc. of the Topical Mtg. on Nucl. Applications of Accel. Technol., Albuquerque, New Mexico, Nov. 16-20, 1997. pp. 398-404, (1997).

(4) S.Meigo, et al.: "Measurements of Spallation Neutrons from a Thick Lead Target Bombarded with 0.5 and 1.5 GeV Protons", Joint Proc. of the 13th Mtg. of the Int. Collaboration on Advanced Neutron Sources held at Paul Scherrer Institute, Oct. 11-14, 1995 and 4th Plenary Mtg. of the European Spallation Source Project, ESS, held at Weinfelden, Oct. 16-19, 1995, PSI-Proceedings 95-02, pp.442-453, (1995).

(5) H.Takada, et al.: "Measurement of Reaction Rate Distributions in A Lead Assembly Bombarded with 500 MeV Protons", Proc. of the 3rd Workshop on Simulating Accel. Radiat. Environments (SARE3), May 7-9, 1997, KEK, tsukuba, Japan, KEK Proceedings, 97-5, 284 (1997).

(6) T.Nakamoto, et al.: J. Nucl. Sci. Technol. **32** (1995) 827.; K.Ishibashi, et al.: J. Nucl. Sci. Technol. **34** (1997) 529

(7) Y.Irie, Y.Yano: Nucl. Instrm. Method Phys. Res. A **320**, (1992) 27.

(8) H.W.Bertini : Phys. Rev. **188**, (1969) 1711 .
(9) A.V.Ignatyuk, G.N.Smirenkin, A.S.Tishin : Sov. J. Nucl. Phys. **21**, (1975) 256 .
(10) H.Kotegawa, Y.Nakane, A.Hasegawa, Sh.Tanaka :"Neutron-photon Multigroup Cross Sections for Neutron Energies up to 400 MeV; HILO86R", JAERI-M 93-020, (1993).
(11) T.Fukahori :"ALICE-F Calculation of Nuclear Data up to 1 GeV", Proc. of the Specialists' Mtg. on High Energy Nucl. Data, Oct. 3-4, 1991, JAERI, Tokai, JAERI-M 92-039, pp. 114-122 (1992).
(12) M.Nakazawa, et al. : "JENDL Dosimetry File", JAERI-1325, (1992).
(13) S.Chiba, B.Yu, T.Fukahori : "Evaluation of JENDL Fusion File", Proc. of the 1991 Symp. on Nucl. Data, Nov. 28-29, 1991, JAERI, Tokai, Japan, JAERI-M 92-027, pp. 35-44 (1992).
(14) S.Pearlstein : Astrophys. J. **346**, (1989) 1049.
(15) M.B.Chadwick, et al.:"Cross Section Evaluations to 150 MeV for Accelerator-Driven Systems and Implementation in MCNPX", LA-UR-98-1825 (1998).

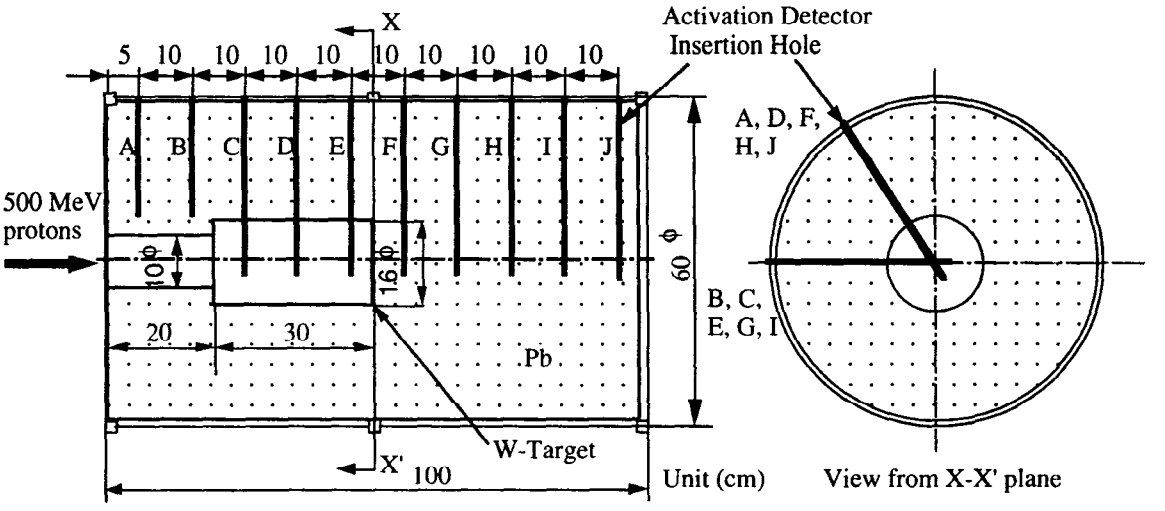

Fig. 1 Cross sectional view of the tungsten/lead assembly. The characters A to J indicate the irradiation hole for activation detectors.

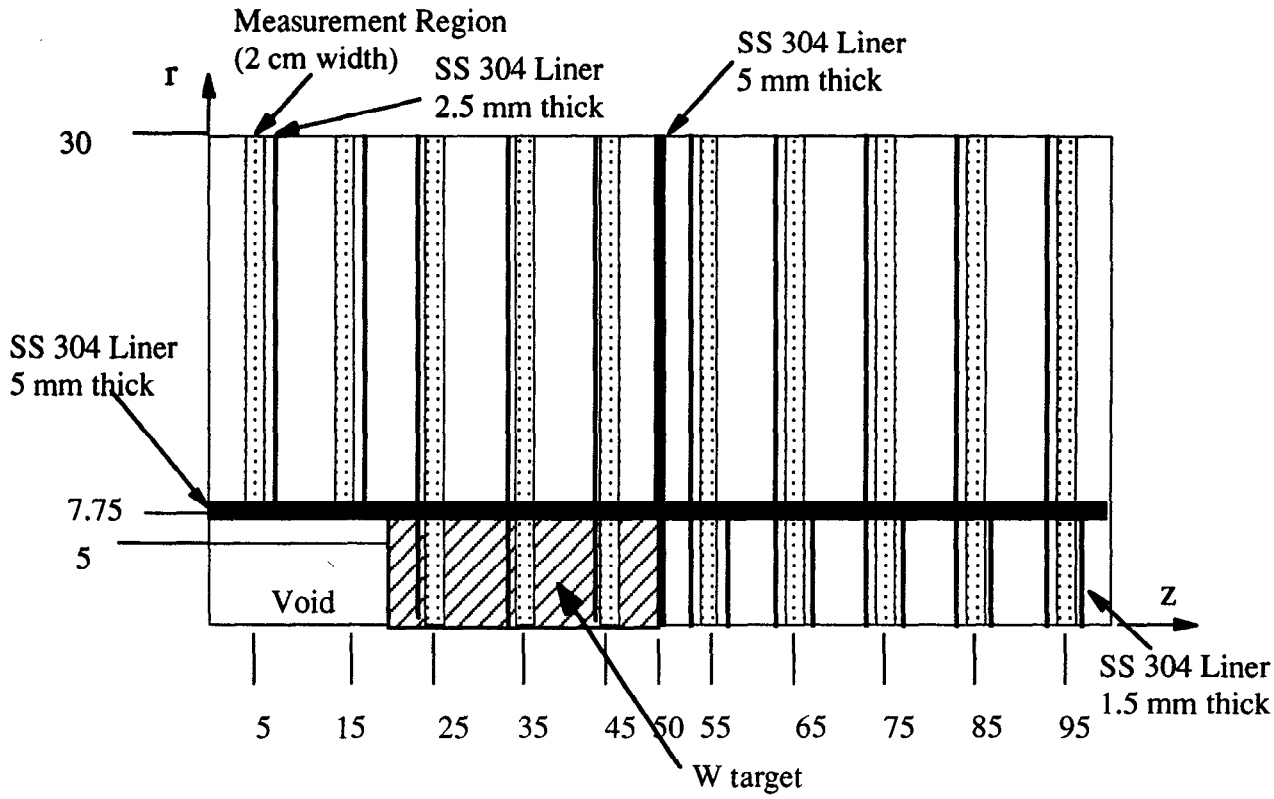

Fig. 2 Illustraion of the geometry model of the tungsten/lead assembly for analysis using the NMTC/MCNP4A code system.

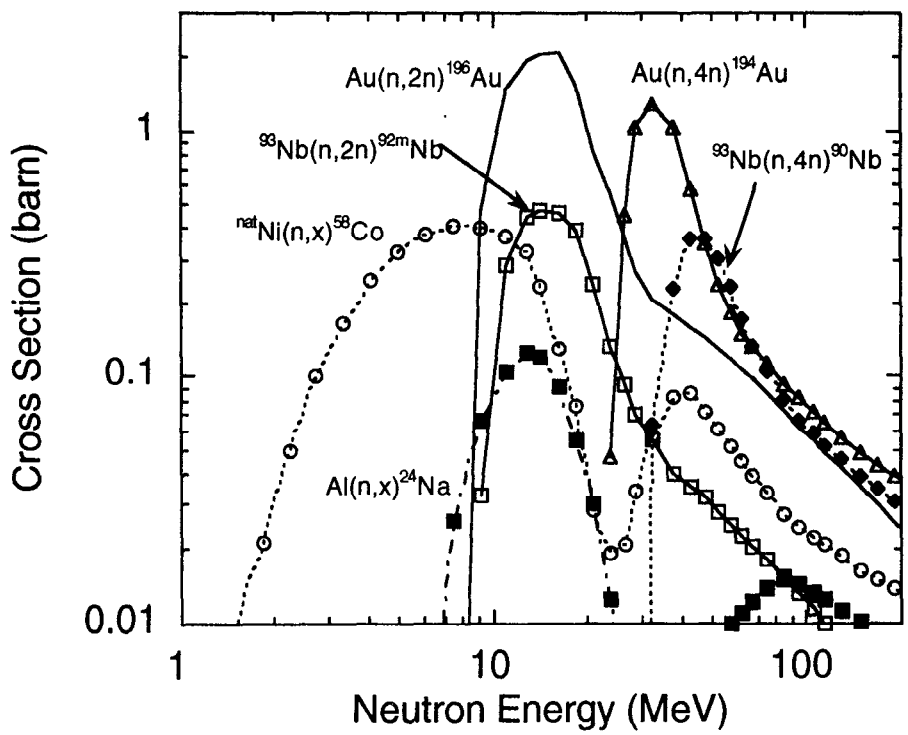

Fig. 3 Neutron cross sections of the reactions of $^{nat}Ni(n,x)^{58}Co$, $^{27}Al(n,x)^{24}Na$, $^{198}Au(n,2n)^{196}Au$, $^{93t}Nb(n,2n)^{92m}Nb$, $^{93t}Nb(n,4n)^{90}Nb$ and $^{198}Au(n,4n)^{194}Au$ employed in the calculation of reaction rate. The data below 20 MeV are taken from JENDL Dosimetry file[12]. Those above 20 MeV are calculated by ALICE-F[11].

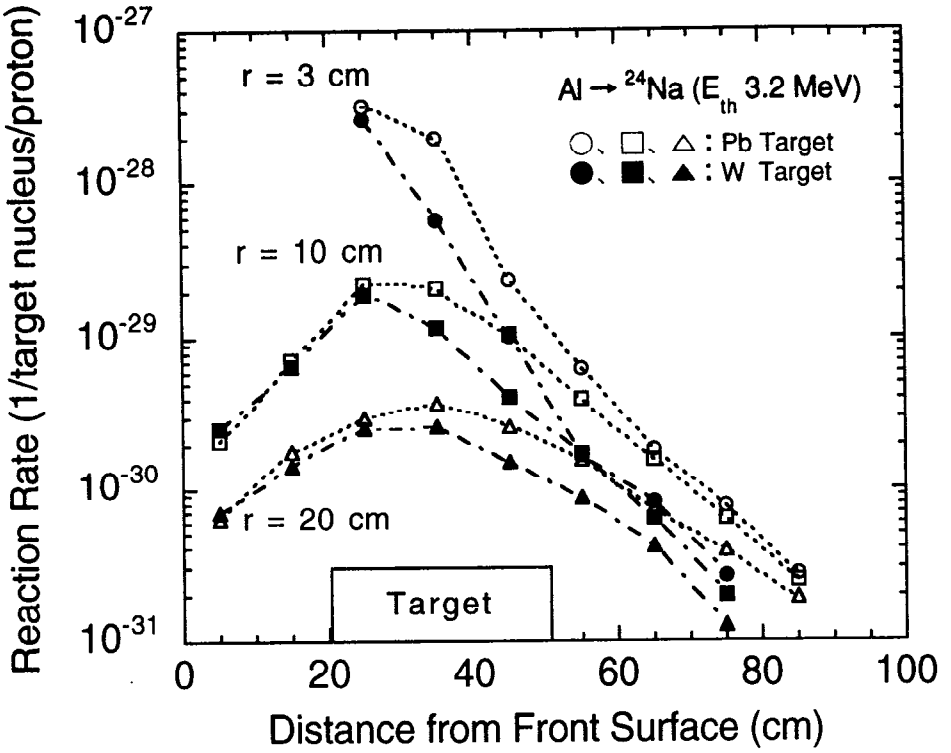

Fig. 4 Measured reaction rate distributions of the $^{27}Al(n,x)^{24}Na$ reaction in the lead assemblies bombarded with 500 MeV protons. The open and solid marks indicated the measured data for lead/lead assembly [5] and for tungsten/lead one, respectively.

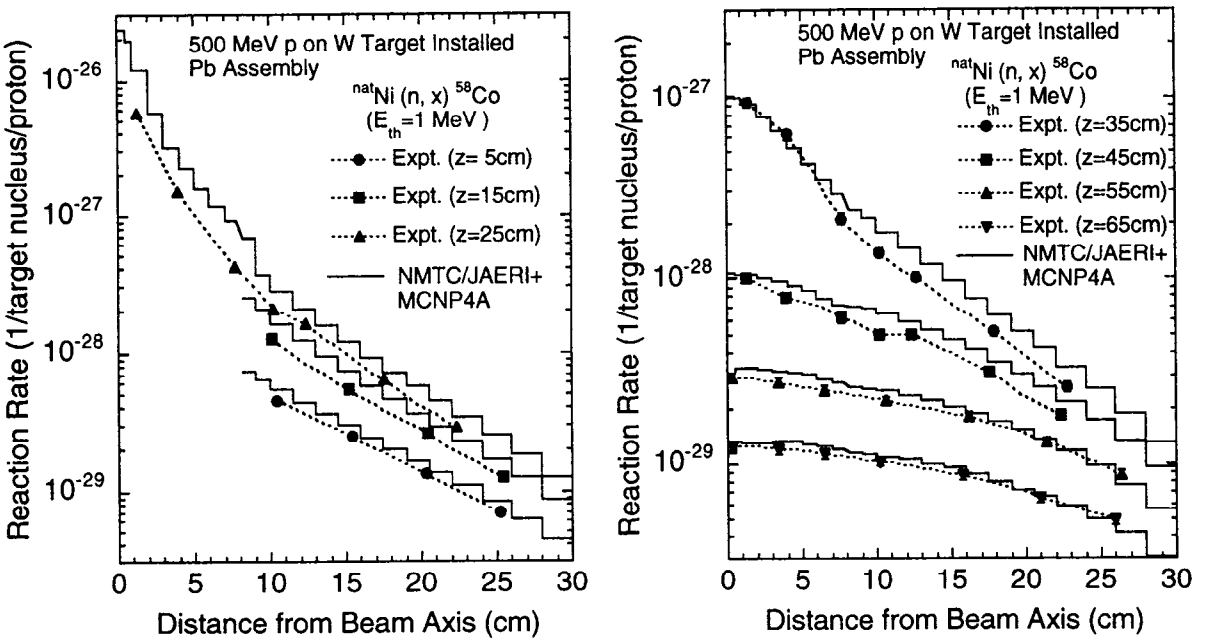

Fig. 5 Reaction rate distribution of the $^{nat}Ni(n,x)^{58}Co$ reaction in the tungsten/lead assembly bombarded with 500 MeV protons. The solid marks and lines indicate the experimental results and the calculation using the NMTC/JAERI-MCNP4A code system, respectively. The dotted lines are for eye guide. The character 'z' means the depth of the assembly where activation detectors were inserted.

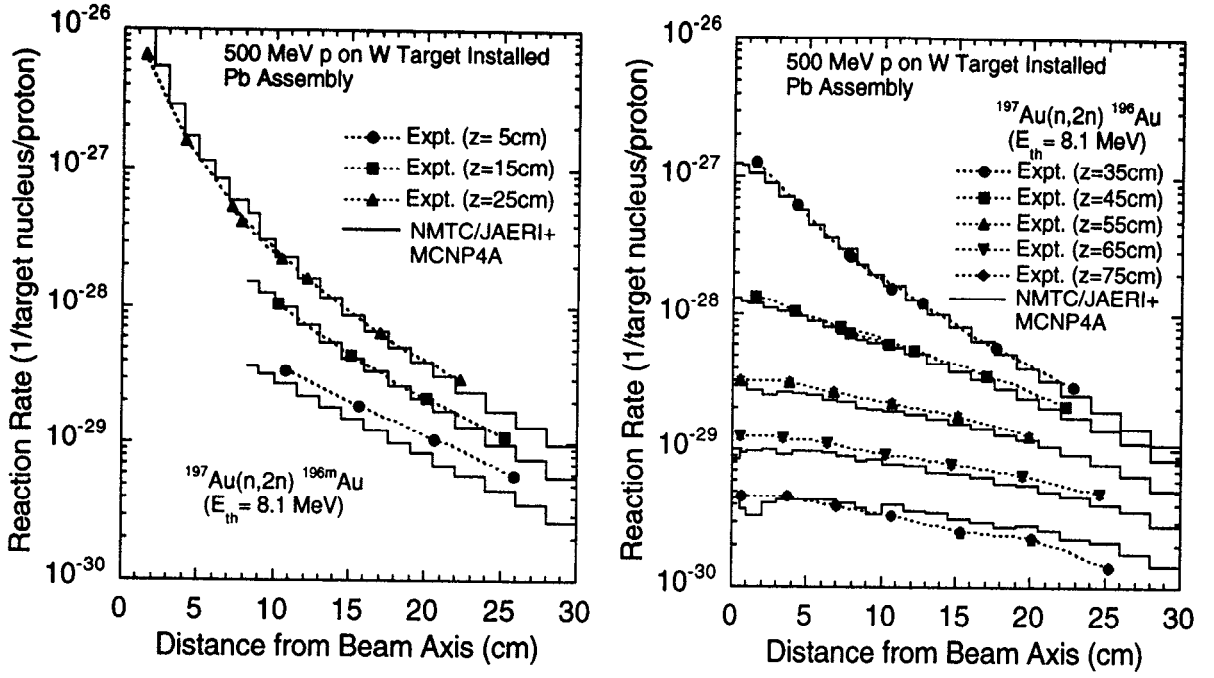

Fig. 6 Reaction rate distribution of the $^{197}Au(n,2n)^{196}Au$ reaction in the tungsten/lead assembly bombarded with 500 MeV protons. The notes to the marks and lines are the same as for Fig. 5.

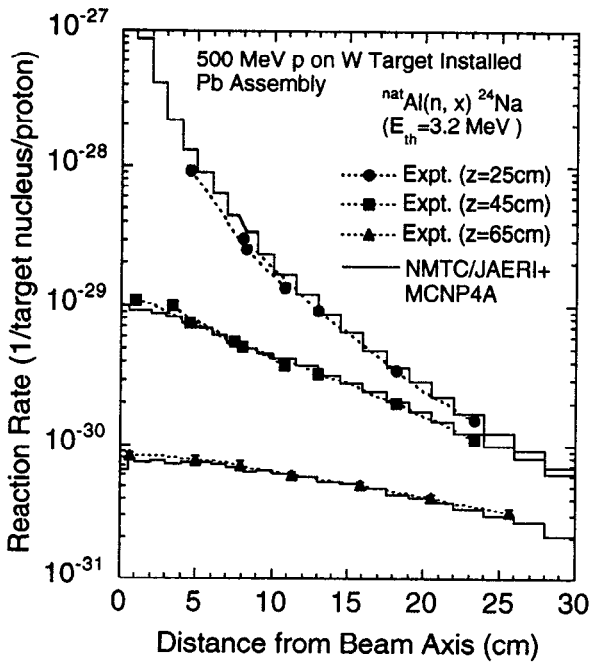

Fig. 7 Reaction rate distribution of the $^{27}Al(n,x)^{24}Na$ reaction in the tungsten/lead assembly bombarded with 500 MeV protons. The notes to the marks and the lines are the same as for Fig. 5.

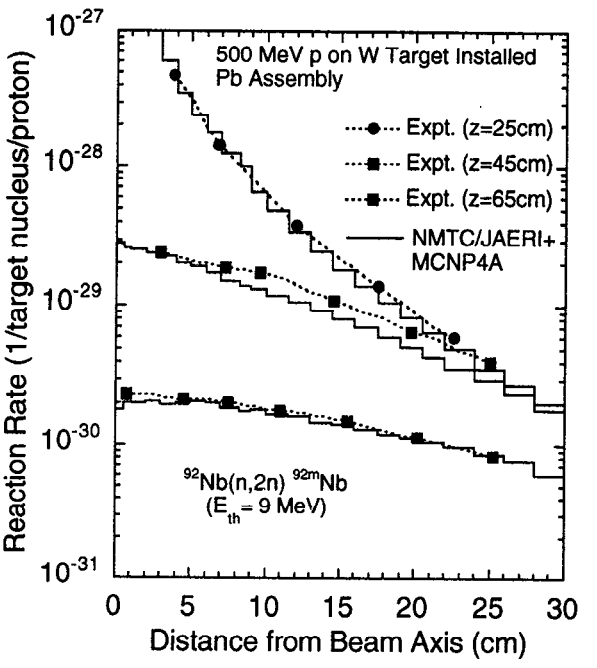

Fig. 8 Reaction rate distribution of the $^{93}Nb(n,2n)^{92m}Nb$ reaction in the tungsten/lead assembly bombarded with 500 MeV protons. The notes to the marks and the lines are the same as for Fig. 5.

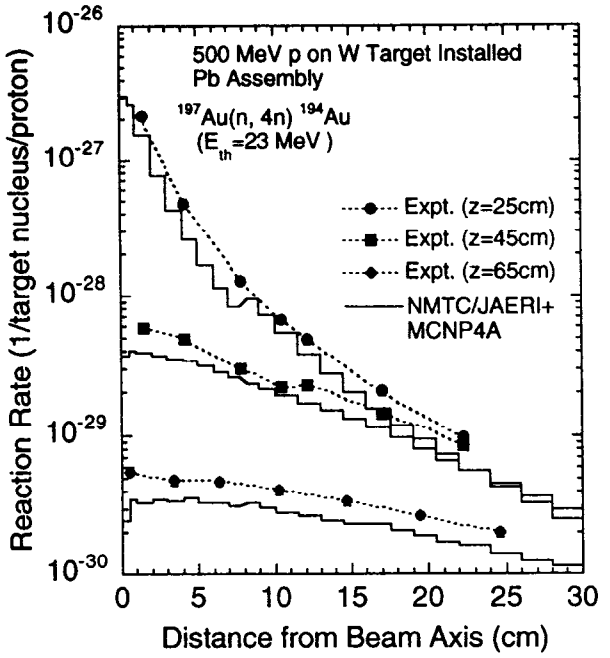

Fig. 9 Reaction rate distribution of the $^{197}Au(n,4n)^{194}Au$ reaction in the tungsten/lead assembly bombarded with 500 MeV protons. The notes to the marks and the lines are the same as for Fig. 5.

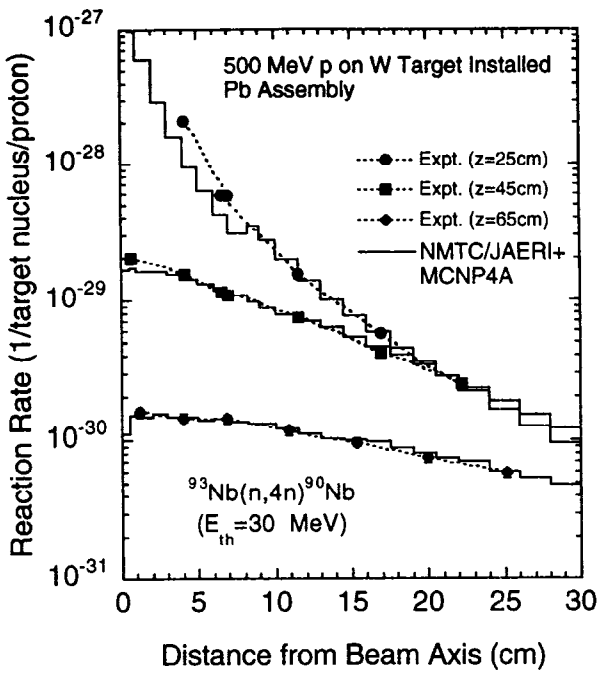

Fig. 10 Reaction rate distribution of the $^{93}Nb(n,4n)^{90}Nb$ reaction in the tungsten/lead assembly bombarded with 500 MeV protons. The notes to the marks and the lines are the same as for Fig. 5.

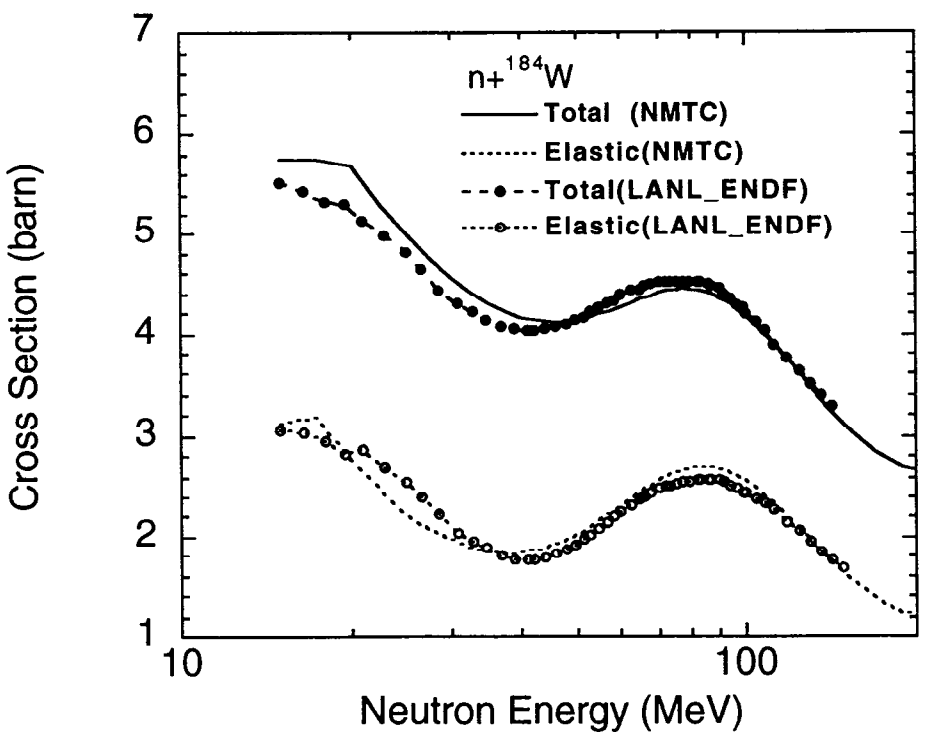

Fig. 11 Comaprison of neutron cross sections of ^{184}W. The solid and dotted lines indicate the total and elastic cross sections [14] emoployed in NMTC/JAERI. Those with marks stand for the cross sections evaluated by Chadwick et al. [15].

ICANS-XIV
14th Meeting of the International Collaboration on
Advanced Neutron Sources
June 14-19, 1998
Argonne National Laboratory, 9700 S. Cass Avenue, Argonne, IL 60439, USA

Measurement of Incident Proton Beam Characteristics for AGS Spallation Target Experiment

H. Nakashima, H. Takada, S. Meigo, Y. Kasugai, Y. Ikeda,
Y. Oyama, N. Watanabe and ASTE collaboration

Center for Neutron Science
Japan Atomic Energy Research Institute
Tokai-mura, Naka-gun, Ibaraki-ken, 319-1195, JAPAN

Abstract

In order to determine the initial conditions of the spallation integral experiments using a mercury target bombarded with high energy protons provided by the Alternating Gradient Synchrotron (AGS) accelerator at Brookhaven National Laboratory (BNL), the profile and the total number of incident protons were measured using an electrical method with multi-wire profile monitor, an imaging plate technique and an activation reaction of $Cu(p,x)^{24}Na$. The total number of incident protons was estimated $(6.61\pm0.74)\ x10^{13}$, $(3.57\pm0.40)\ x10^{13}$ and $(1.84\pm0.21)\ x10^{13}$ at the proton energies of 1.5, 7.0 and 24 GeV, respectively.

1. Introduction

In order to study the neutronic, thermal and mechanical characteristics of a mercury target as a spallation neutron source, a series of integral experiments has been started since 1997 using the short pulse, high energy proton beam of 1.5, 7.0 and 24.0 GeV from the Alternating Gradient Synchrotron (AGS) at Brookhaven National Laboratory (BNL). The profile and the number of incident protons are of interest as giving initial conditions for analyzing neutron flux, temperature distribution and pressure wave induced in the mercury target. From an analytical point of view, it is required to measure the profile with spatial resolution of a few mm.

The first experiment was performed under the following conditions : (1) No beam focusing magnet was installed on the beam line after the last switching magnet at the beam extraction point of AGS in spite that the mercury target was placed about 60 m downstream from the extraction point. Resultantly, it was expected that the horizontal and vertical widths including 95 % of the total beam were about 3 cm and 4.5 cm, respectively. (2) Beam diagnostics devices such as current transformer and secondary emission chamber was not settled in the beam line, though on-line measurement of the proton beam was required for temperature and pressure wave measurements. (3) Beam intensity was expected to be as high as $3.6x10^{12}$ to $5.7x10^{13}$ protons per bunch.

Considering the above experimental conditions and requirements, an electrical method using a multi-wire profile monitor (MWPM) and an imaging plate technique which measures the intensity distribution of an activated foil were employed for the beam profile measurement. The former provides us the profile pulse by pulse, though the profile is measured as the integrated charges along a wire. The latter gives us the beam intensity at an optional point of the imaging plate, so that more detailed profile information can be obtained in comparison with MWPM. For obtaining total number of incident protons, the activation method with the $Cu(p,x)^{24}Na$ reaction was used, because the reaction has threshold energy about 400 MeV and its cross sections have been well studied. It is noted that neutrons are emitted back to the activation foil from the mercury target when proton beam is injected on the target. However, the spectrum of the neutrons emitted backward generally have no high energy component. It

Keywords: Multi-wire profile monitor, Imaging plate, $Cu(p,x)^{24}Na$

is necessary, therefore, to select a certain threshold reaction which is insensitive to the neutron at least below a several hundreds of MeV.

2. Experimental Procedure

The set up of MWPM and monitor foils is illustrated in Fig. 1. Proton beam passing through the open air from the duct end of the beam line are incident to the mercury target settled 50 cm downstream of the duct end. The target is a cylinder of the mercury of 20 cm in diameter and 120 cm in length with the front surface of a hemisphere of 10 cm radius encapsulated by the stainless steel of 2.5 mm in thick. The MWPM was placed 44 cm upstream of the inside surface of the mercury target, while the monitor foils were placed 6 cm in front of the mercury target.

The MWPM is composed of 32 Au coated tungsten wires of 20 mm in diameter with intervals of 6 mm in both horizontal and vertical direction with respect to the beam axis. The induced charge by the emission of electrons was amplified wire by wire with an amplifier connected to the MWPM. The amplified signals were integrated by 30 msec interval and then converted its amplitude into proportional digits. The signal integration in the amplifier was triggered by a timing signal provided from the AGS accelerator. Time-integrated data during the irradiation were collected into a personal computer (PC), and each integrated signal for each shot was also taken into the PC as a list-mode data.

Two copper foils of 0.1 mm thickness with an area of 100 x 200 mm^2 were put on an aluminum frame together with a 0.025 mm thick aluminum one so as to cover the area of 200 x 200 mm^2. The purity of copper and aluminum foils was 99.99% and 99.5%, respectively. After irradiation, these foils were removed from the frame and intensity of induced activities in the foils were measured by two kind of techniques as followings.

The aluminum foil was attached on an imaging plate closely for 2 weeks in a low-background room after enough cooling time for short-lived nuclei such a ^{24}Na to decay out. As a result, the imaging plate was exposed by the γ and β rays from ^{22}Na and ^{7}Be. The relative exposure dose in each pixel having the area of 200 μm^2 were read out by an imaging plate reader manufactured by Fuji Film Co. Ltd.

The copper foils were cut to 100 pieces with a cross section of 20 x 20 mm^2. These pieces were stacked by every 10 pieces, and then the induced activity of ^{24}Na was measured by a Ge-detector(CANBERRA GC-5019/S) whose resolution was 1.8 keV for 1332 keV γ-peak and peak compton ratio over 64 in catalog value. The data was acquired by a multi-channel analyzer (CANBERRA Genie PC) with 8k channels. The position at the distance of 5 cm on the axis from the surface of Ge-detector was selected as the standard point for absolute γ-ray intensity measurement. The reaction rate of $Cu(p,x)^{24}Na$, Y_j, in j-th foil stack is obtained by correcting the decay through the irradiation, cooling and measuring period, detector efficiency, sum peak effect in counting and so on.

According to the beam operation data logged by the AGS control, the fluctuation of proton flux was as small as a few percent during irradiation period. Therefore, it is possible to assume that protons were supplied constantly as a function of time. Then, proton flux on j -th foil stack, ϕ_j, is represented as:

$$\phi_j = \frac{N_{p,j}}{S_j \cdot T_r}, \tag{1}$$

where, $N_{p,j}$, S_j and T_r indicate the total number of protons incident on the j -th foil stack, the area of the foil stack and irradiation period, respectively. Since the reaction rate, Y_j, is expressed as:

$$Y_j = N_A \frac{w_j}{M} \cdot \sigma \cdot \phi_j, \tag{2}$$

total incident number of protons is obtained from the above equations:

$$N_p = \sum_{j=1}^{10} \frac{M}{N_A \cdot w_j} \cdot \frac{Y_j}{\sigma} \cdot S_j \cdot T_r, \qquad (3)$$

where M indicates the atomic mass of copper, N_A the Avogadro's number, w_j the weight of j-th foil stack, σ the cross section of $Cu(p,x)^{24}Na$ reaction.

In order to estimate the number of protons injected on the mercury target, the fraction of intensity inside the circle with a diameter of 20 cm to that of whole copper sheet was estimated from the measured values by the imaging plate technique. The fractions for three incident energies of 1.5, 7.0 and 24.0 GeV are summarized in Table 1. The data used to obtain the total incident number of protons were listed in Table 2. The physical constants used in the γ-ray spectrometry were taken from Ref. 1. The detector efficiency was determined by a γ-ray measurement using calibrated radioactive standard sources. The cross sections of the $Cu(p,x)^{24}Na$ reaction at proton energies of 1.5, 7.0 and 24.0 GeV were estimated from the experimental data [2-5]. The measured cross sections of the $Cu(p,x)^{24}Na$ reaction are plotted as a function of proton energy in Fig. 2.

In this measurement, the sources of the error were attributed to the following items.

1) Statistical error of peak count
2) Detector efficiency error
3) Uncertainty of the cross section of $Cu(p,x)^{24}Na$
4) Error of weight of foil stack

The statistical error of peak count was in the range from 1.8% to 5.3%. The detector efficiency error was estimated as 5.0% at 1369 keV. The uncertainty of the cross section of $Cu(p,x)^{24}Na$ was estimated as 10.0% from the recent data [2-5] as shown in Fig. 2. The error of the weight of foil stack was less than 0.1%. The errors concerning to the decay constant, γ-ray branching ratio, irradiation time, measuring time, cooling time were negligible in the present work.

3. Results and Discussion

3.1 Beam Profile

The two-dimensional plots of beam profile measured by the imaging plate method are shown in Figs. 3 to 5 for the incident proton energies of 1.5, 7.0 and 24.0 GeV. It is note that these data are obtained by the integration in area of 2 mm x 2 mm for getting enough counting statistics. The projections to horizontal and vertical axes are shown in Figs. 6 and 7 for the proton energies of 1.5 and 24 GeV, respectively. It is observed that the beam profile differ from each other very much dependent upon incident energy and the beam center is not on the target center.

In Figs. 8 and 9, the integrated values along horizontal and vertical axes obtained by the imaging plate technique are compared with those measured with MWPM for 7.0 GeV proton incidence. It is observed that the results of imaging plate give almost the same full width half maximum (FWHM) as those of MWPM in both directions but the former is somewhat broader than the later. The reason of the broadening may be caused by the resolution of the imaging plate technique. It was found the effective spatial resolution of the profile measured by the imaging plate was estimated to be 3 mm from the measurement at the edge of the aluminum plate.

Since the aluminum foil was placed near the mercury target, it is possible that the foil is activated by the secondary particles emitted backward from the target. An analytical study was also performed to estimate the contribution of the secondary particles to the nuclide production in the aluminum foil. Figure 10 shows the secondary neutron energy spectra calculated by the HERMES code system [6] at the foil position where the measured beam profile was used as the input conditions. The reaction rates of $^{27}Al(p/n,x)^{22}Na$ were calculated using the cross section data evaluated by the ALICE-F code [7], while those of $^{27}Al(p/n,x)^{7}Be$ were obtained from the measured cross sections with protons [8-11], because the cross sections are not calculated by the ALICE-F code and neutron cross section is not measured. These reactions have the threshold energies of about 30 MeV. The calculated results are compared in Tables 3(a) and 3(b) with the measured data by means of γ -ray spectrometry.

It is found in these tables that the HERMES calculation gives 60% lower reaction rates

than the measured data for 1.5 GeV proton incidence, although the calculation includes the contribution of secondary particles. This indicates that ^{22}Na and ^{7}Be have been produced by the forward-scattered particles other than by the incident protons. The forward-scattered particles are seemed to be produced on the structure such as a beam tube. In fact, beam loss of about 30% has been observed in the beam intensity measurement using copper foil as described in the following sub-section. Though it is difficult to estimate the spatial distribution of the forward scattered particles, the distribution is assumed to be almost uniform. Thus, it is seemed that these particles do not distort the relative beam profile. For 7.0 GeV proton incidence, the calculated reaction rates agree with the measured ones within about 10%. According to the calculation, the backward-emitted neutrons produce ^{22}Na about 30% to the total amount, while they produce ^{7}Be only 3%. However, the contribution of the backward-emitted neutrons reduces from 30% to some extent because the activity of ^{7}Be was higher than that of ^{22}Na by a factor of 2 at the exposure period in the imaging plate measurement. For 24.0 GeV proton incidence, it is suggested that about half of ^{22}Na and 20% of ^{7}Be was produced in the aluminum foil by the backward-emitted neutrons. In the additional calculation it was found that the effect of the backward-emitted neutrons can be reduced to less than 10 % for 24 GeV by placing the aluminum foil to 50 cm upstream from the mercury target.

3.2 Total Number of Incident Protons

According to the procedure described in the previous section, the total number of protons was obtained as $(6.61 \pm 0.74)\ \times 10^{13}$, $(3.57 \pm 0.40)\ \times 10^{13}$ and $(1.84 \pm 0.21)\ \times 10^{13}$ for 1.5, 7.0 and 24.0 GeV proton incidence, respectively. In Table 4, these values are compared with those measured with a secondary emission chamber (SEC) and a current transformer (CT) installed in the AGS ring at 50 m upstream of the mercury target.

It is clear that total numbers of incident protons obtained at the secondary container surface are smaller than those measured at 50 m upstream except for 24 GeV proton incidence. This is due to the condition that any focusing magnet was not installed on the beam line, resulting that proton beam diverges and be lost after passing through the last focusing magnet. Furthermore, the arrangement of the magnets in the AGS ring is not well-designed for 1.5 GeV, although the beam profile at the target position is decided by the beam emittance at the extraction magnet under this condition. Therefore, the ratio of total number of incident protons measured by Cu-foil to that of CT becomes the lowest at 1.5 GeV among the three incident energies.

4. Concluding Remarks

In the AGS experiment using the mercury target, the profile and total number of incident protons were measured by using the MWPM, the imaging plate and the activation technique.

The relative beam profiles were obtained for 1.5 7.0 and 24.0 GeV protons using imaging plate technique. The FWHM obtained by the imaging plate technique was somewhat broader than that by MWPM in the beam profile integrated along horizontal and vertical axes. It seems that the data include the uncertainty of several tens of percent because neutrons emitted backward from the mercury target produced ^{22}Na and ^{7}Be in the aluminum foil. The uncertainty increases with increasing the incident proton energy, because of the contribution of backward-emitted neutrons. Since the contribution is as a function of the distance between the foil position and the target, it is necessary to optimize the foil position in the future experiment to improve the quality of data.

The total number of incident protons was measured by the activation reaction of $Cu(p,x)^{24}Na$. The resultant total number of incident protons was estimated as $(6.61 \pm 0.74)\ \times 10^{13}$, $(3.57 \pm 0.40)\ \times 10^{13}$ and $(1.84 \pm 0.21)\ \times 10^{13}$ for 1.5, 7.0 and 24.0 proton incidence, respectively. In comparison with the values measured with the secondary emission chamber and the current transformer in the AGS ring, the values measured by the activation technique were smaller by 73% to 95% than those obtained by the devices in the AGS ring because of lack of beam focusing magnets between the AGS ring and the target.

Acknowledgments

This work has been carried out in a frame of the ASTE collaboration. The authors would like to thank to all the staffs of BNL involved in the ASTE experiment for their help and support. The authors also thank to Prof. Y.Irie and Drs. Y.Yano and S.Muto of KEK for their valuable discussion about beam profile measurement.

References

(1) Lederer, C. M. and Shirley, V. S. (Ed.): "Table of Isotopes 7th Edition", Willey Interscience Publication, N.Y., (1978).
(2) Schopper H. (Ed.): "LANDORT-BÖRNSTEIN, Numerical Data and Functional Relation ships in Science and Technology, New Series, Group I: Nuclear and Particle Physics, Vol. 13, Production of Radionuclides at Intermediate Energies, Subvol. a, Interactions of Protons with Targets from He to Br", Springer-Verlag, Berlin Heidelberg, (1991).
(3) Schopper H. (Ed.): ibid., "subvol. d, Interactions of Protons with Nuclei (Supplement to I/13a. b, c)", Springer-Verlag, Berlin Heidelberg, (1994).
(4) Michel, R., et al.: Nucl. Instrm. Methods, B113, 183 (1995).
(5) Titarenko, Yu. E., et al.: "Experimental and Computer Simulation Study of Radionuclide Yields in the ADT Materials Irradiated with Intermediate Energy Protons", Proc. of 3rd Specialists' Mtg. on High Energy Nucl. Data, Mar. 30-31, 1998, JAERI, Tokai, JAERI-Conf, (to be published).
(6) Cloth, P., et al.: "HERMES A Monte Carlo Program System for Beam Materials Interaction Studies", Jül-2203, (1988).
(7) Fukahori, T.: "ALICE-F Calculation of Nuclear Data up to 1 GeV", Proc. of the Specialists' Mtg. on High Energy Nucl. Data, Oct. 3-4, 1991, JAERI, Tokai, JAERI-M 92-039, pp. 114-122 (1992).
(8) Cumming, J. B., et al.: Phys. Rev., **128**, 2392 (1962).
(9) Furukawa, M., et al.: Nucl., Phys., **69**, 362 (1965).
(10) Bogatin, V. I., et al.: Nucl. Phys, A, **260**, 446 (1976).
(11) Aleksandrov, V. N., et al.: At. Energi, **64**, 445 (1988).

Table 1. Fraction of intensity inside the circle of 20 cm diameter in the copper sheet

Proton Energy	Fraction
1.5 GeV	96 %
7.0 GeV	97 %
24.0 GeV	97 %

Table 2. Data used for obtaining the total incident number of protons

Item	Value
Avogadro's number	6.02×10^{23}
Atomic mass of copper	63.5
Cross section of $Cu(p,x)^{24}Na$	2.00 mb at 1.5 GeV 3.60 mb at 7.0 GeV 3.50 mb at 24.0 GeV
Decay Constant of ^{24}Na	1.29×10^{-5}
γ-ray energy of ^{24}Na	1368.9 keV
Detector efficiency at 5 cm	0.62 % at 1368.9 keV
Branching of 1368.9 keV γ-ray	100%

Table 3 (a). Measured and Calculated ^{22}Na production reaction rates in Al foil

Energy (GeV)	^{22}Na production in ^{27}Al ($x10^{-24}$/proton) Measurement	Calculation	Backward-Emitted Neutron Component in Calculation	Backward-Emitted Proton Component in Calculation	C/E
1.5	$1.79x10^{-2}$	$9.85x10^{-3}$	4%	0.4%	0.55
7.0	$1.50x10^{-2}$	$1.34x10^{-2}$	27%	2.6%	0.89
24.0	$1.61x10^{-2}$	$2.31x10^{-2}$	48%	9.5%	1.43

Table 3 (b). Measured and Calculated ^{7}Be production reaction rates in Al foil.

Energy (GeV)	^{7}Be production in ^{27}Al ($x10^{-24}$/proton) Measurement	Calculation	Backward-Emitted Neutron Component in Calculation	Backward-Emitted Proton Component in Calculation	C/E
1.5	$1.41x10^{-2}$	$8.52x10^{-3}$	2%	< 0.1%	0.60
7.0	$1.01x10^{-2}$	$8.91x10^{-3}$	3%	0.4%	0.88
24.0	$7.11x10^{-2}$	$1.03x10^{-2}$	19%	4.8%	1.45

Table 4. Comparison of total number of incident protons measured by different instruments.

Proton Energy (GeV)	Cu-foil ($x10^{13}$ protons)	S.E.C. ($x10^{13}$ protons)	C.T. ($x10^{13}$ protons)	Ratio of Cu-foil to C.T.
1.5	6.61±0.74	10.8	9.09	0.727
7.0	3.57±0.40	4.20	3.89	0.918
24.0	1.84±0.21	1.83	1.93	0.953

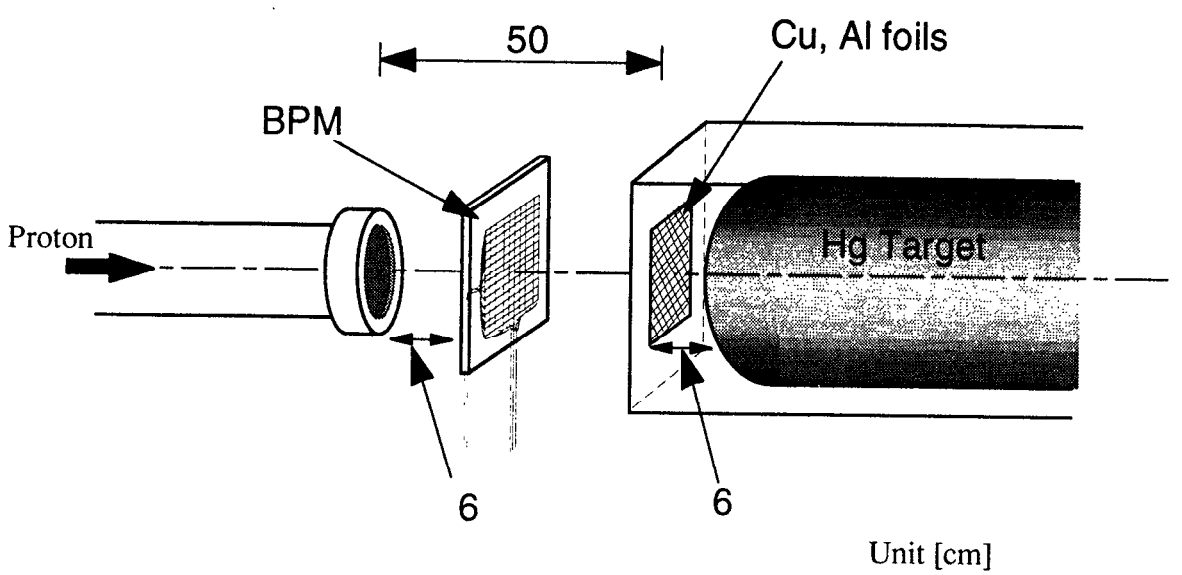

Fig.1 Experimental set up of a beam profile monitors and activation foils.

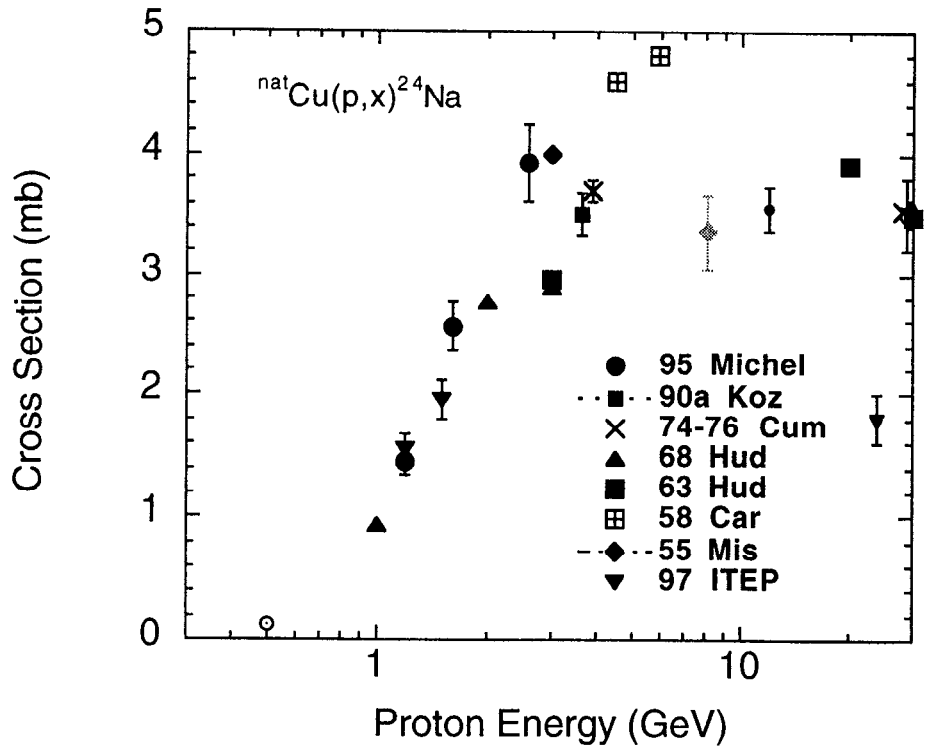

Fig. 2 Experimental neutron cross sections[2-5] of the Cu(n, x)^{24}Na reaction.

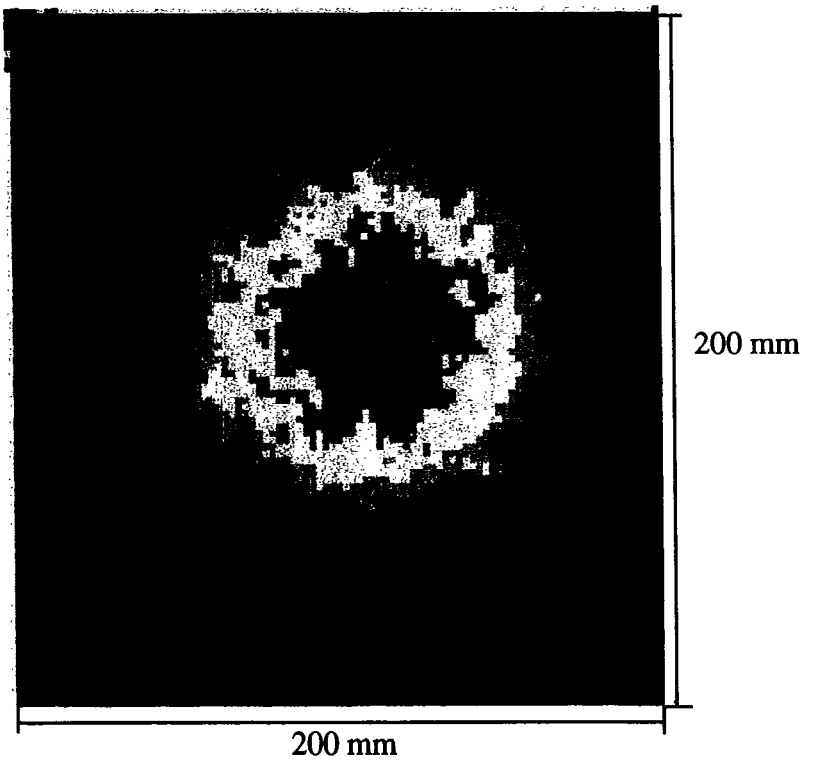

Fig. 3 Two-dimensional plots of beam profile measured with the imaging plate technique for 1.5 GeV proton incidence. The proton beam penetrates from the front surface of the foil to the back.

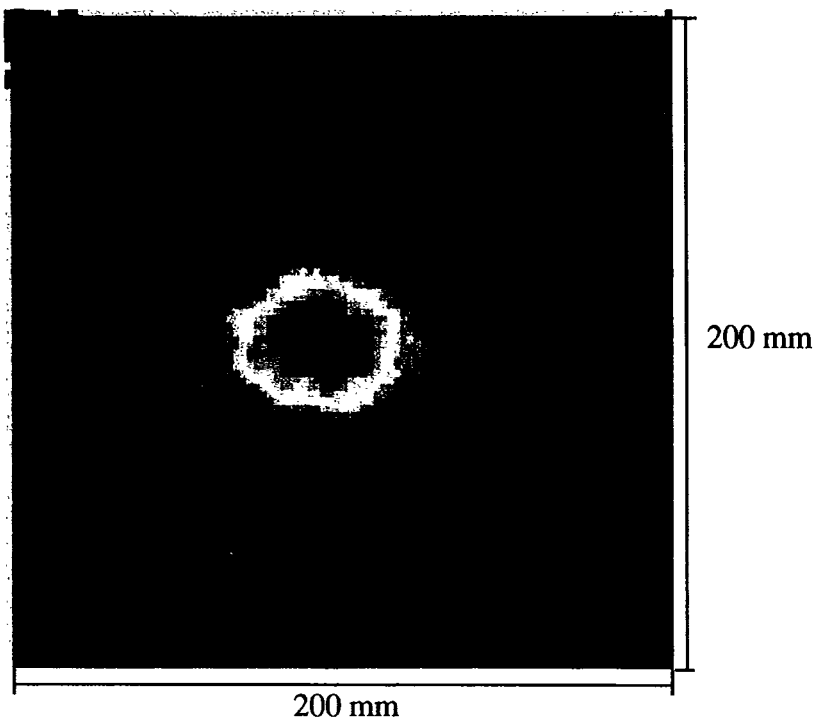

Fig. 4 Two-dimensional plots of beam profile measured with the imaging plate technique for 7.0 GeV proton incidence. The proton beam penetrates from the front surface of the foil to the back.

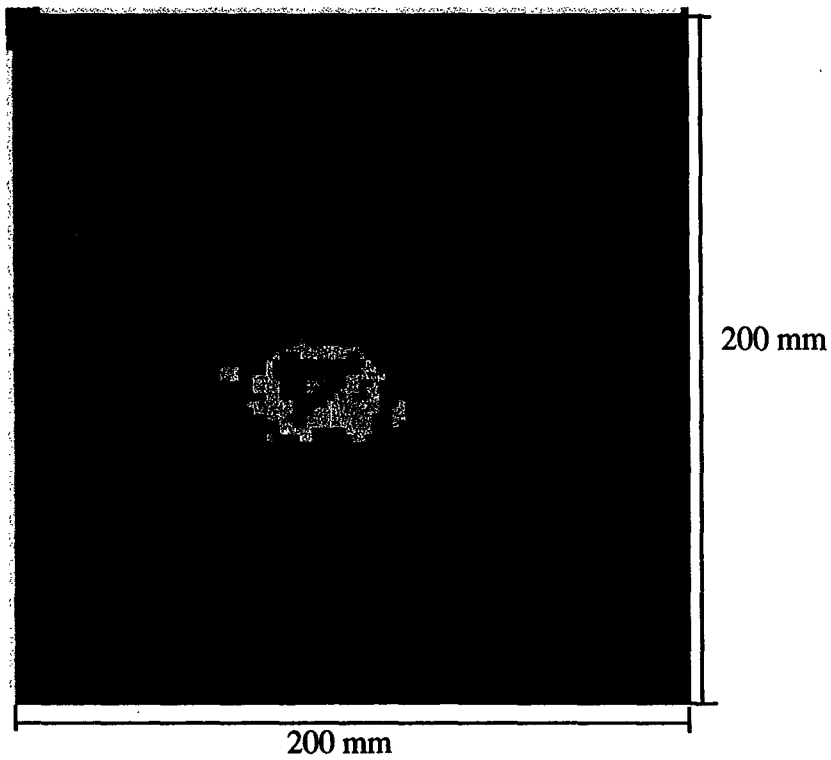

Fig. 5 Two-dimensional plots of beam profile measured with the imaging plate technique for 24.0 GeV proton incidence. The proton beam penetrated from the front surface of the foil to the back.

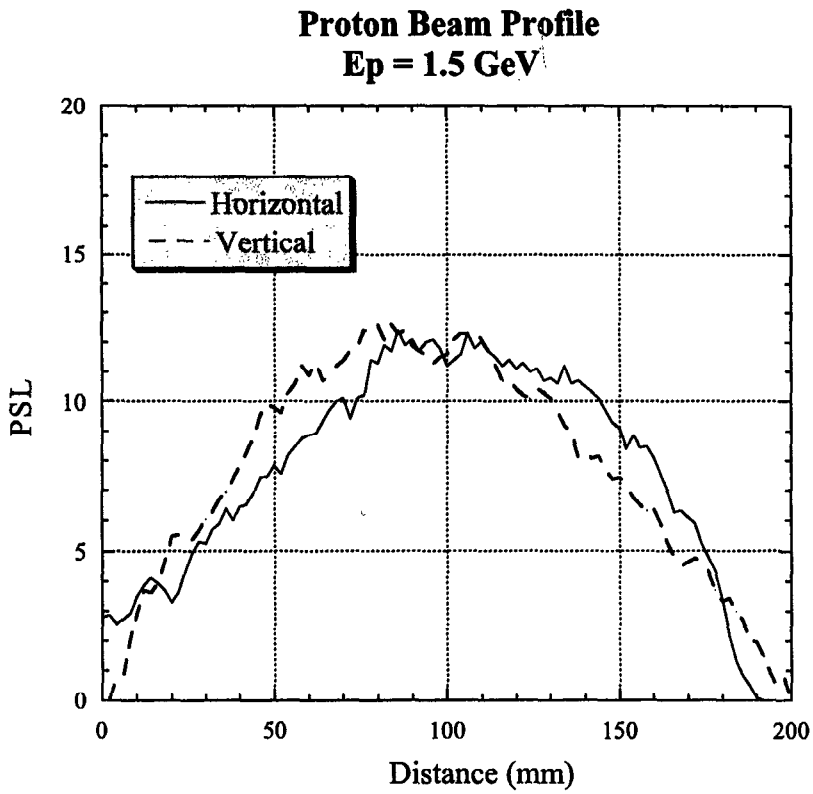

Fig. 6 Projection of beam profiles measured with the the imaging plate technique to horizontal and vertical axes for 1.5 GeV proton incidence.

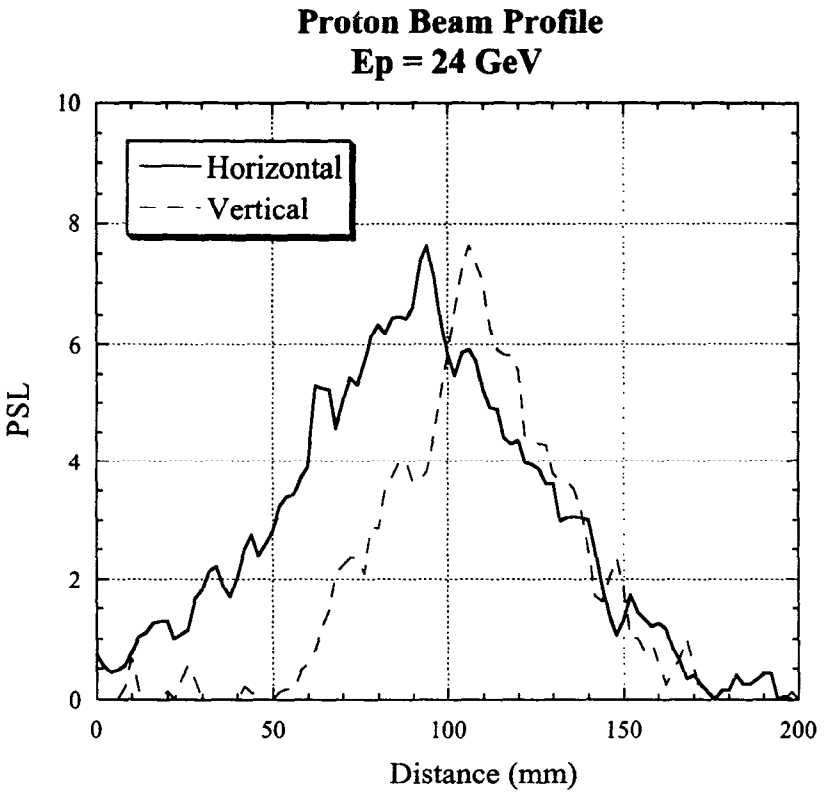

Fig. 7 Projection of beam profiles measured with the imaging plate technique to horizontal and vertical axes for 24.0 GeV proton incidence.

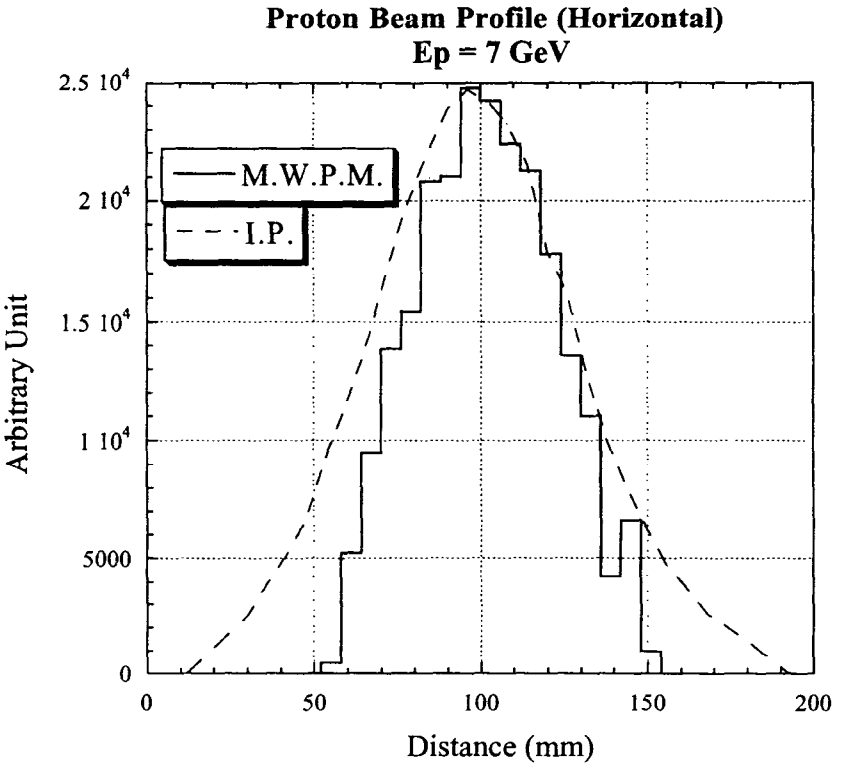

Fig. 8 Comparison of beam profile measured by the imaging plate technique with that obtained by MWPM for 7.0 GeV proton incidence. The profiles are integrated along the vertical axes at each position on horizontal axis.

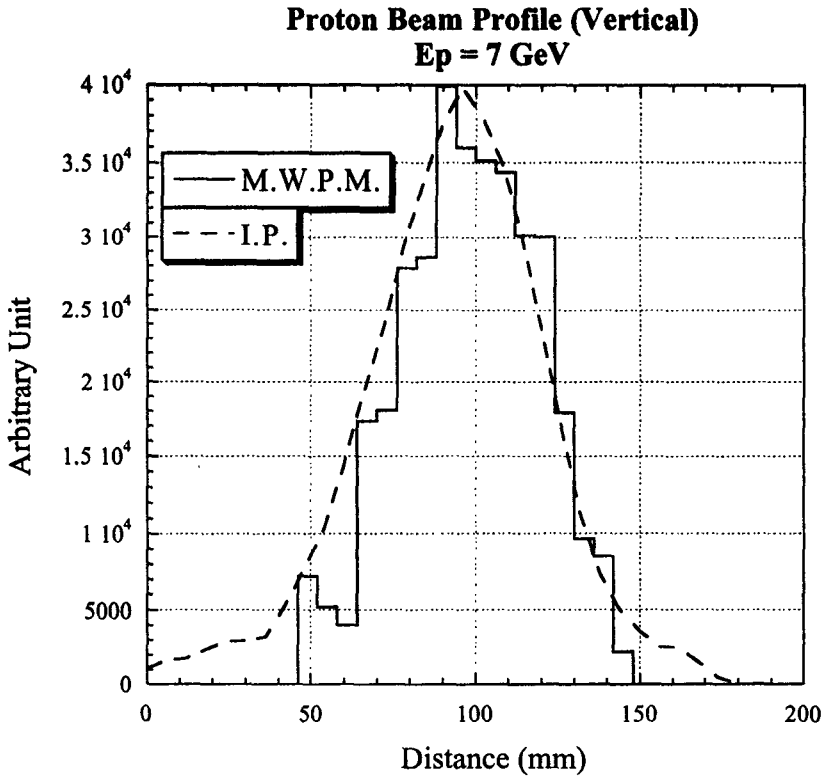

Fig. 9 Comparison of beam profile measured by the imaging plate technique with that obtained by MWPM for 7.0 GeV proton incidence. The profiles are integrated along the horizontal axes at each position on vertical axis.

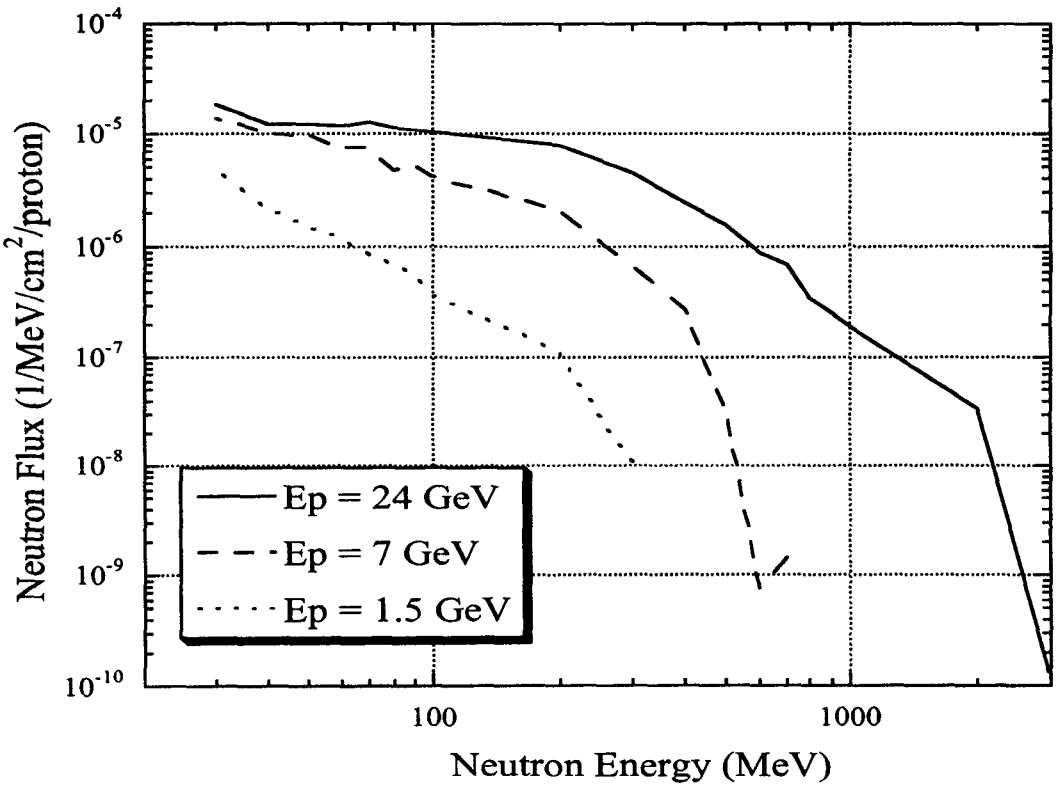

Fig. 10 Neutron fluxes emitted backward from the mercury target at the position where the aluminum foil was placed for 1.5, 7.0 and 24.0 GeV proton incidence. The fluxes were calculated by the HERMES code sysem.

ICANS-XIV
14th Meeting of the International Collaboration on
Advanced Neutron Sources
June 14-19, 1998
Argonne National Laboratory, 9700 S. Cass Avenue, Argonne, IL 60439, USA

Measurements of Reaction Rate Distributions on a Mercury Target Bombarded with High Energy Protons

H.Takada, Y.Kasugai, H.Nakashima, Y.Ikeda, Y.Oyama, N.Watanabe, M.Arai*, Y.Kiyanagi** and ASTE Collaboration

Center for Neutron Science
Japan Atomic Energy Research Institute,
Tokai-mura, Naka-gun, Ibaraki-ken, 319-1195, JAPAN

*: High Energy Accelerator Research Organization,
Oho, Tsukuba-shi, Ibaraki-ken, 305-8581, JAPAN

**: Faculty of Engineering, Hokkaido University,
Kita-13, Nishi-8, Kita-ku, Sapporo, 060-8628, JAPAN

Abstract

A spallation target experiment under the ASTE collaboration was carried out using a thick mercury target bombarded by 1.5 to 24 GeV protons. Reaction rate distributions on the target were measured using various activation detectors at incident proton energies of 1.5, 7.0 and 24.0 GeV. The intensity distribution of leakage neutrons was estimated from the measured reaction rate data of the ^{115}In(n,n')^{115m}In reaction. In consequence, the intensity distribution had a peak at 11.5 cm from the top of hemisphere of the mercury target for 1.5 GeV proton incidence and the peak position moved to 16.1 cm for 7.0 GeV and 19.6 cm for 24.0 GeV respectively. It was also found that the calculations using Monte Carlo code systems reproduced the measured reaction rate distributions qualitatively well.

1. Introduction

An international collaboration on a spallation target experiment at the Alternating Gradient Synchrotron (AGS) of Brookhaven National Laboratory (BNL), namely ASTE collaboration, was organized. Main missions are to study the neutronic, thermal and mechanical characteristics of a mercury target for estimating its feasibility as the spallation target because mercury has been proposed for one of the most promising target materials for an intense spallation neutron source driven by the proton accelerator with a power of 5 MW.

The experimental data related to the production and transport of spallation neutrons in the thick mercury target are important neutronics characteristics because of lack of experiments associated with the mercury target at incident energies above 1 GeV. They are also useful for the validation of calculation codes for the neutronic design study, such as HERMES[1], LAHET[2] and NMTC/JAERI[3].

Keywords : Mercury target, Reaction rate distribution, 1.5, 7.0 and 24.0 GeV protons

Under the ASTE collaboration, the reaction rate distributions on the mercury target have been measured using various activation detectors with different threshold energies. The three kind of incident energies of 1.5, 7.0 and 24.0 GeV were chosen as the incident proton energies according to the interest for the future plans of the spallation neutron source development.

2. Experimental

2.1 Activation Detector Arrangement

The mercury target was installed at a target room of the U-line of the AGS facility. The target configuration was 20 cm diameter and 130 cm long cylinder having the hemispherical top surface. Figure 1 shows the cross sectional view of the mercury target. The activation detectors were put on an acrylic bar and then installed on the four radial positions along the beam axis with an interval of 90° around the target. The position of 45° right-hand upward toward the downstream of the beam axis was indexed as "Main" and the others were labeled as "Sub-1", "Sub-2" and "Sub-3" according to the counter clockwise rotation direction around the target, respectively.

The following high purity metal foils were employed as activation detectors : In, Nb, Al, Au, Bi, Co, Ni, Fe and Cu. The size and purity of the foils are summarized in Table 1. The foils were classified into the following three groups: (A) In, (B) Nb, Al, Au and Bi, (C) Co, Ni, Fe and Cu. The foils classified into (B) and (C) were assembled to one foil stack, respectively, and then put on the acrylic bar. The In foils were set on the 17 positions from 0.5 to 95 cm on the "Main" position to obtain a neutron flux profile along the target, while the other foil stacks were mounted on 6 positions.

The physical characteristics of the activation detectors are listed in Table 2. The detectors cover from 0.5 to 54.0 MeV in threshold energy. The neutron cross sections of some detectors are shown in Fig. 2, where the cross section values below 20 MeV were taken from JENDL-Dosimetry file[4] and those above 20 MeV were calculated with the ALICE-F code[5].

2.2 γ-ray measurement

The γ-ray spectra of the activated foils were measured using the same Ge-detectors and data acquisition system for the beam characteristics measurement[6]. At each proton irradiation campaign, a series of γ-ray measurements for short-lived radioactivities was continued for 10 to 12 hours including the time needed to the foil sorting. Second measurements for modest long half-lived nuclides were performed a few days after irradiation.

The reaction rate of individual activation detector was obtained from the peak counts by correcting such as the decay, the detector efficiency, the coincidence sum effect in counting, the γ-ray self-absorption effect in foil and so on. The physical constants such as decay constant and branching ratio were taken from Ref. 7. The detector efficiency was determined by a γ-ray measurement using calibrated radioactive standard sources.

In this measurement, the sources of error in the data processing was attributed to the following items: 1) statistical error of peak count, 2) detector efficiency error, 3) uncertainty of the number of incident protons, 4) error of the weight of foil. The statistical error of peak count was better than 10 % in most cases for the activation detectors listed in Table 2. The detector efficiency error was estimated as 2.0 % from the calibration measurement with standard sources. The uncertainty of the number of incident protons was taken from the results[6] of the activation technique using the $Cu(p,x)^{24}Na$ reaction. The error of the weight of foil stack was less than 0.1 %. The errors concerning to the decay constant, γ-ray branching ratio, irradiation time, measuring time, cooling time were negligible small.

3. Calculations

The calculations were performed with the NMTC/JAERI-MCNP4A[8] code system. NMTC/JAERI simulates the nuclear reactions and particle transport in the energy region above 20 MeV by the use of the intranuclear cascade model of Bertini [9], the preequilibrium calculation model of Yoshizawa et al.[10] and a particle evaporation model taking account of the high energy fission process. The level density parameter derived by a formulae of Ignatyuk [11] was used in the evaporation calculation. The cut off energies for particle transport were set to be 20 MeV for neutron and 2 MeV for charged particles. The neutron flux on the cylindrical surface of the mercury target was estimated with the energy group structure defined in the HILO-86R library [12] up to 400 MeV. For neutrons above 400 MeV, For neutrons above 400 MeV, the energy group structure was extended up to 1.5 GeV. The reaction rate was obtained using the nuclide production cross section values calculated by the ALICE-F code. Here, some of calculated cross sections were adjusted to connect smoothly with the ones compiled in JENDL Dosimetry file at 20 MeV.

MCNP4A calculates the transport of the neutrons in the energy region lower than 20 MeV using a continuous energy cross section library which has been processed from JENDL-Fusion File [13].

The applicable energy range of the NMTC/JAERI code is limited up to 3.5 GeV for nucleons. The analyses for 7.0 and 24.0 GeV proton incidence have been carried out using the HERMES code system[1]. The nuclear data library and nuclide production cross sections used in the HERMES code system were the same as those for the NMTC/JAERI-MCNP4A calculation.

As reported in the incident proton beam characteristics measurement[6], the beam center was shifted from the target center. This condition was treated in the geometry model of the calculation as follows: The mercury target has the radius equal to the distance from the measured beam center position to the position of individual acrylic bar. The shape of incident beam was given by the fitting of the measured beam profile[6] with Gaussian distribution.

4. Results and Discussion

The reaction rate distribution of the ^{115}In(n,n')^{115m}In reaction measured on the "Main" position is shown in Fig 3 with those on the other positions for 1.5 GeV proton incidence on the mercury target. It is observed that the reaction rate values among the four positions differ from each other because the beam incident position shifted from the center axis of the target. The difference of about 50 % is observed in the reaction rates between the "Main" position and the "Sub-1" one at the distance range of 9 to 25 cm. The similar results were observed even in the cases of 7.0 and 24.0 GeV proton incidence, respectively, although they are not presented in this paper.

Figure 4 shows the reaction rate distributions of the ^{115}In(n,n')^{115m}In reaction on the cylindrical surface of the mercury target for 1.5, 7.0 and 24.0 GeV. In this case, the measured reaction rates were normalized to the values estimated by the NMTC/JAERI-MCNP4A calculation with the assumption that the proton beam was incident on the center of mercury target with radius of 10 cm. The peak position, full-width-half-maximum (FWHM) of peak and the attenuation constant were obtained from the normalized data by a curve fit. The results are summarized in Table 3. It is found that the peak position of reaction rate distribution moves to deeper positions along the mercury target with increase of incident proton energy. The peak position lies on 11.5 cm from the top of hemisphere of the mercury target for 1.5 GeV proton incidence, while it moves to 16.1 cm for 7.0 GeV and 19.6 cm for 24.0 GeV, respectively. In addition, the higher the incident energy becomes, the shorter the attenuation constant of the reaction rate distribution becomes. This is the evident that the number of neutrons transported

to the deeper position of the mercury target increases with incident proton energy. The measured data can be regarded as the neutron yield distribution along the mercury target because the $^{115}In(n,n')^{115m}In$ reaction has the threshold of 0.4 MeV enough to be sensitive to most of energetic neutrons.

The reaction rate distribution of the $^{92}Nb(n,2n)^{92m}Nb$ reaction measured along the mercury target is shown in Fig. 5. The reaction rate rises up from the front surface to the peak position, and then decreases with the distance. The peak position moves to deeper position from the front surface with increase of incident energy as well as the results of the $^{115}In(n, n')^{115m}In$ reaction.

In order to study the characteristics of the reaction rate distributions dependent on activation detectors and incident proton energy, the measured data of the different reactions of $^{115}In(n,n')^{115m}In$, $^{92}Nb(n,2n)^{92m}Nb$ and $^{209}Bi(n, 6n)^{204}Bi$ are compared in Fig. 6. For comparison, the measured data were normalized to those for 1.5 GeV proton incidence at all positions along the mercury target. It is observed that the reaction rate ratios among the three reactions increases with the distance from the front surface. In addition, the gradient of the reaction rate ratios for 24.0 GeV are steeper than those for 7.0 GeV. These results indicate that the spallation neutrons have been produced and transported in broader space in the mercury target with increase of the incident proton energy. On the other hand, there is little difference among the reaction rate ratios in case of the same incident energy. Thus, the shape of the reaction rate distribution is insensitive to the threshold energy of the activation detector.

The results of the NMTC/JAERI-MCNP4A calculations are compared with the experiments in Figs. 7(a) to 10 for 1.5 GeV proton incidence on the mercury target. Figures 8(a) and 8(b) show the results of the HERMES calculation with the experiments for 24.0 GeV proton incidence. For the $^{115}In(n,n')^{115m}In$ reaction, the NMTC/JAERI-MCNP4A calculation gives about 20% higher reaction rates than the experiments although the calculation reproduces the relative difference of reaction rates at different radial positions with respect to the "Main" position. As shown in Fig. 8(a), on the other hand, a large disagreement of about a factor of 2 is observed between the HERMES calculation and the experiment for 24 GeV. In HERMES, nuclear reaction is simulated with the physics models applicable below 3.5 GeV with an extrapolated nuclear data. The treatment of many other elemental interactions between intranuclear particles are missing in the code. This approximation may be too crude to reproduce the measured reaction rates. However, it is reported[14] that the code system could predicts well the total neutron yield of a thick lead target bombarded with protons below 12 GeV. This is a contradictory conclusion against the present result shown in Fig. 8(a). In the present calculation, the neutron yield in the energy region sensitive to the $^{115}In(n,n')^{115m}In$ reaction may be enhanced by some reason. The certain reason cannot be found in this work for the time being. More detailed investigation is required for both the data processing and analytical procedure to discuss about the source of disagreement.

As shown in Figs. 9 and 10, the NMTC/JAERI-MCNP4A calculations reproduce well the shape of reaction rate distributions of the activation detectors with higher threshold energies for 1.5 GeV proton incidence. However, significant disagreement is observed between the calculations and experiments at the positions near the beam incident surface. This is outstanding in the results of the $^{209}Bi(n,xn)$ reactions. The incident beam hits upon curving surface of the hemisphere part of the mercury target with broad profile. In the calcualtion, on the other hand, the proton beam was assumed to be injected on the top of the hemisphere part. The slight difference of target geometry between the calculation and the experiment may affect the neutron yield at the vicinity of the incident point so that the calculation estimates the neutron yield lower than the experiment. It is also noted that the calculated reaction rate values of the activation detectors with high threshold energies include the ambiguities because the neutron

cross sections calculated with ALICE-F code have not been evaluated. This is a subject to be solved to estimate the accuracy of the calculation code system in the analysis of thick target experiments.

5. Conclusions

The neutron intensity distribution along the cylindrical surface of the mercury target was estimated using the activation detector of the $^{115}In(n,n')^{115m}In$ reaction for 1.5, 7.0 and 24.0 GeV proton energies. It was found that the distribution of the leakage neutrons had a peak and the peak position moved to deeper position along the mercury target with increase of incident energy. The peak position lies on 11.5 cm from the top of hemisphere of the mercury target for 1.5 GeV proton incidence, while it is located on 16.1 and 19.6 cm for 7.0 and 24.0 GeV one, respectively.

The reaction rate distributions of various other activation detectors were also measured on the cylindrical surface of the mercury target. It was found that the distributions had relatively the same shape as that of the $^{115}In(n,n')^{115m}In$ reaction. These data would be useful for estimating the neutron flux distribution. Judging from the results analyzed up to now, the fine energy spectrum could be obtained by unfolding procedure in the energy range from 0.5 to 54 MeV.

The measured data were compared with the calculations uisng Monte Carlo code systems of NMTC/JAERI-MCNP4A and HERMES with the nuclide production cross section values combining the JENDL dosimetry file with the ALICE-F calculation. It was found that the calculations reproduce the measured reaction rate distributions qualitatively well. However, some disagreement appeared between the calculations and experiments for the activation detectors sensitive to neutrons above 20 MeV. The disagreement became more significant for 24.0 GeV proton incidence than for 1.5 GeV. This is attributable to the fact that the neutron cross section values in this energy range has not been verified. Further study is required from both of experimental and analytical point of view to remove the disagreement.

References

[1] P.Cloth, et al.: "HERMES A Monte Carlo Program System for Beam Materials Interaction Studies", Jül-2203, (1988).

[2] R.E.Prael, H.Lichtenstein : LA-UR-89-3014, "Users Guide to LCS: The LAHET Code System", (1989).

[3] Y.Nakahara, T.Tsutsui: "NMTC/JAERI A Code System for High Energy Nuclear Reactions and Nucleon-Meson Transport Code", JAERI-M 82-198 (1982), [in Japanese].; H.Takada, et al.: "An Upgraded Version of the Nucleon-Meson Transport Code NMTC/JAERI97", JAERI-Data/Code 98-005 (1998).

[4] M.Nakazawa, et al. : "JENDL Dosimetry File", JAERI-1325, (1992).

[5] T.Fukahori :"ALICE-F Calculation of Nuclear Data up to 1 GeV", Proc. of the Specialists' Mtg. on High Energy Nucl. Data, Oct. 3-4, 1991, JAERI, Tokai, JAERI-M 92-039, pp. 114-122 (1992).

[6] H.Nakashima, , et al. : "Measurement of Incident Proton Beam Characteristics for AGS Spallation Experiment", This Proceedings.

[7] C.M.Lederer and V.S.Shirley (Ed.): "Table of Isotopes 7th Edition", Willey Interscience Publication, N.Y., (1978).

[8] J.F.Briesmeister (Ed.) : "MCNP A General Monte Carlo N-Particle Transport Code, Version 4A", LA-12625, (1993).

[9] H.W.Bertini : Phys. Rev. **188**, (1969) 1711.

[10] N.Yoshizawa, K.Ishibashi, H.Takada : J. Nucl. Sci. Technol. **32**, (1995) 601.
[11] A.V.Ignatyuk, G.N.Smirenkin, A.S.Tishin : Sov. J. Nucl. Phys. **21** (1975) 256 .
[12] H.Kotegawa, Y.Nakane, A.Hasegawa, Sh.Tanaka :"Neutron-photon Multigroup Cross Sections for Neutron Energies up to 400 MeV; HILO86R", JAERI-M 93-020, (1993).
[13] S.Chiba, B.Yu, T.Fukahori : "Evaluation of JENDL Fusion File", Proc. of the 1991 Symp. on Nucl. Data, Nov. 28-29, 1991, JAERI, Tokai, Japan, JAERI-M 92-027, pp. 35-44 (1992).
[14] M.Arai, et al.: "Study on Neutron Yield for 12 GeV Protons", Proc. of the 3rd Workshop on Simulating Accel. Radiat. Environments (SARE3), May 7-9, 1997, KEK, tsukuba, Japan, KEK Proceedings 97-5, 293 (1997).

Table 1. Physical characteristics of foils employed as activation detectors.

Foil	Size	Purity
In	18 x 20 x 1.0 mm	99.99 %
	18 x 20 x 0.1 mm	
Al	20 x 20 x 1.0 mm	99.99 %
Nb	20 x 20 x 1.0 mm	99.95 %
Au	20 x 20 x 0.2 mm	99.95 %
Bi	20 ϕ x 2 mm	99.998 %
	15 ϕ x 1.5 mm	
Co	20 x 20 x 1 mm	99.9 %
Fe	20 x 20 x 1 mm	99.9 %
Ni	20 x 20 x 1 mm	99.9 %
Cu	20 x 20 x 1 mm	99.99 %

Table 2. Nuclear characteristics of activation detectors.

Activation Detector	Half Life	γ-ray Energy	Branching Ratio	Threshold
$^{115}In(n,n')^{115m}In$	4.3 hr	336.24 keV	46.7 %	0.5 MeV
$^{27}Al(n,x)^{24}Na$	15.02 hr	1368.9 keV	100%	4.9 MeV
$^{93}Nb(n,2n)^{92m}Nb$	10.12 day	934.46 keV	99.15 %	8.9 MeV
$^{93}Nb(n,4n)^{90}Nb$	14.7 hr	1129.2 keV	92.7 %	29.1 MeV
$^{197}Au(n,2n)^{196}Au$	6.183 day	355.65 keV	87.7 %	8.1 MeV
$^{197}Au(n,2n)^{196m}Au$	9.7 hr	147.77 keV	61.3%	8.7 MeV
$^{197}Au(n,4n)^{194}Au$	39.5 hr	328.47 keV	43.0%	23.2 MeV
$^{197}Au(n,\gamma)^{198}Au$	2.696 day	411.8 keV	95.5%	-
$^{209}Bi(n,4n)^{206}Bi$	6.243 day	803.1 keV	98.9%	22.6 MeV
$^{209}Bi(n,5n)^{205}Bi$	15.31 day	703.5 keV	31.0%	29.6 MeV
$^{209}Bi(n,6n)^{204}Bi$	11.3 hr	899.2 keV	99.2%	38.0 MeV
$^{209}Bi(n,7n)^{203}Bi$	11.76hr	820.3 keV	29.6%	45.3 MeV
$^{209}Bi(n,8n)^{202}Bi$	1.67 hr	422.2 keV	83.8%	54.0 MeV

Table 3. Characteristics of measured reaction rate distributions of the $^{115}In(n,n')^{115m}In$ reaction.

Incident Energy	Peak Position	FWHM of Peak	Attenuation constant after peak
1.5 GeV	11.5 cm	29.2 cm	0.0724
7.0 GeV	16.1 cm	38.2 cm	0.0498
24.0 GeV	19.6 cm	44.2 cm	0.0407

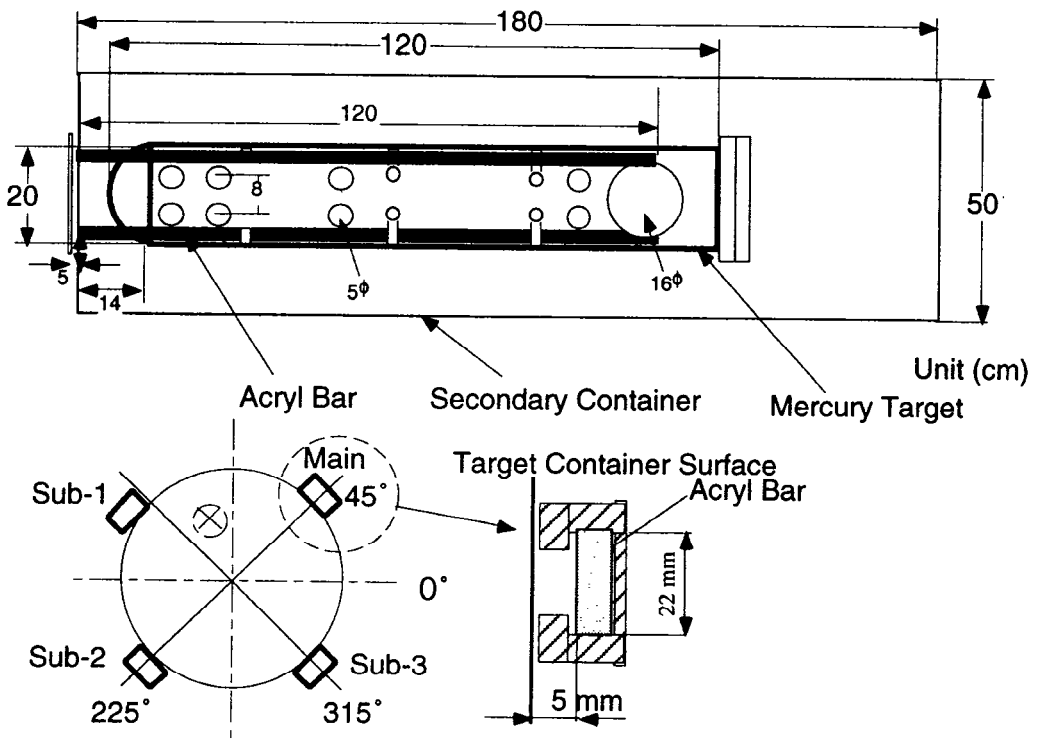

Fig.1 Cross sectional view of the mercury target.

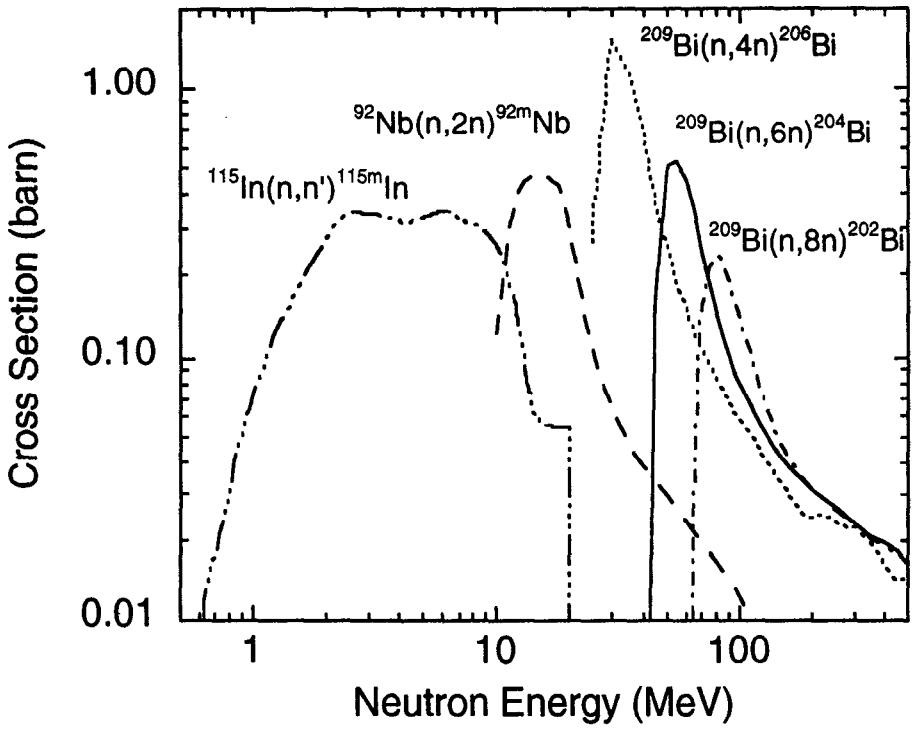

Fig. 2 Neutron cross sections of the reactions of ^{115}In(n,n')^{115m}In, ^{93}Nb(n,2n)^{92m}Nb, ^{209}Bi(n,4n)^{206}Bi, ^{209}Bi(n,6n)^{204}Bi and ^{209}Bi(n,8n)^{202}Bi.

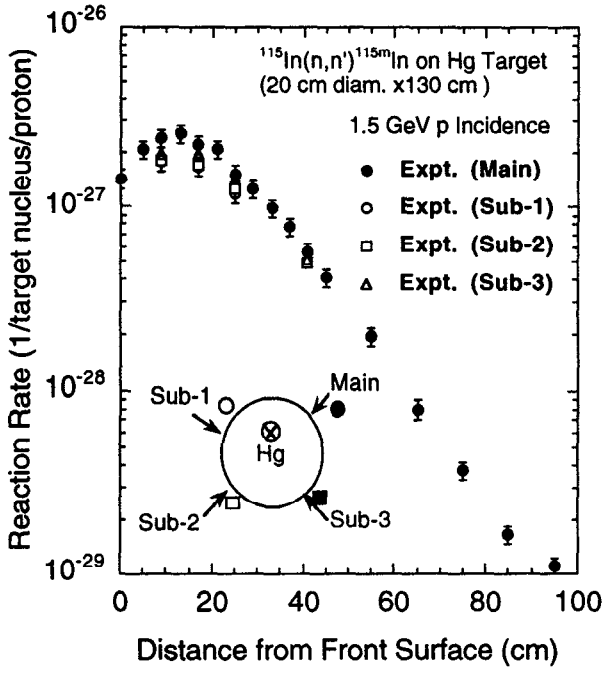

Fig. 3 Reaction rate distribution of the ^{115}In (n,n')^{115m}In reaction measured on the mercury target bombarded with 1.5 GeV proton incidence.

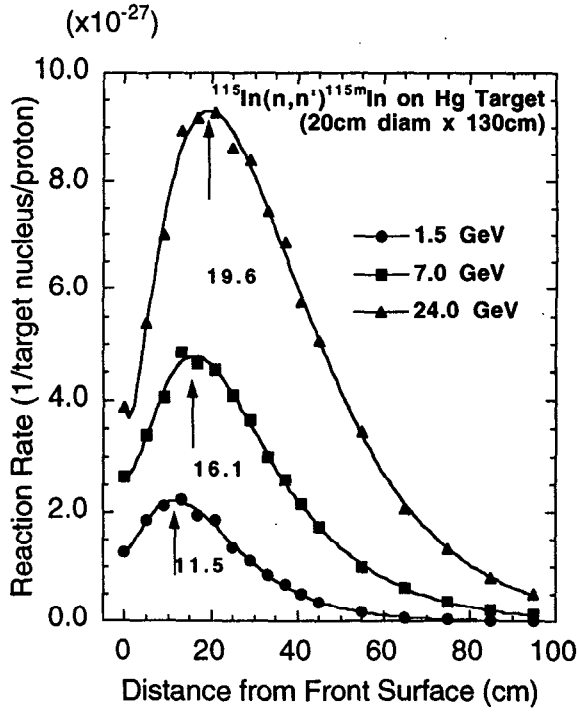

Fig. 4 Comparison of reaction rate distributions of the ^{115}In (n,n')^{115m}In reaction measured on the mercury target bombarded with protons of 1.5, 7.0 and 24.0 GeV.

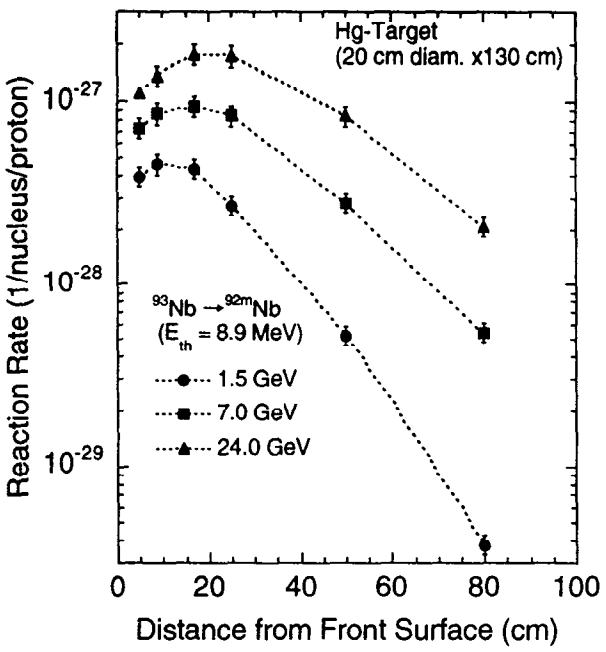

Fig. 5 Reaction rate distributions of the ^{92}Nb (n,2n)^{92m}Nb reaction measured on the mercury target bombarded with protons of 1.5, 7.0 and 24.0 GeV.

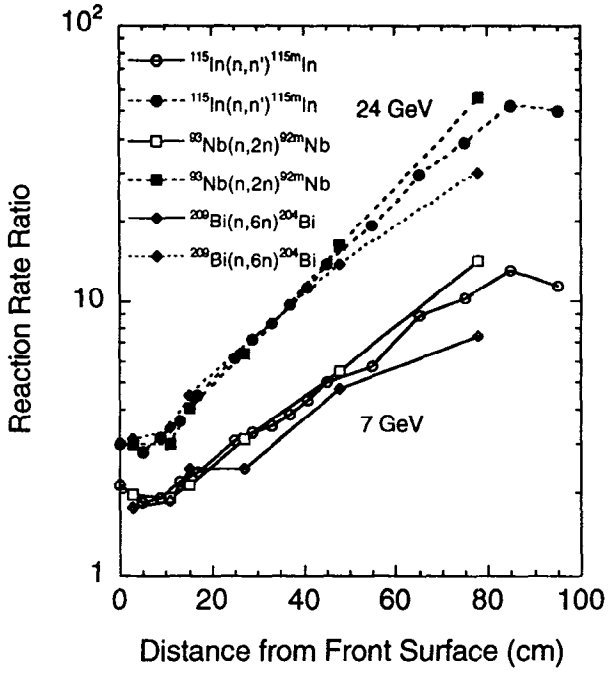

Fig. 6 Measured reaction rate ratios of the reactions of ^{115}In (n,n')^{115m}In, ^{92}Nb (n,2n)^{92m}Nb and ^{209}Bi (n,6n))^{204}Bi for 7.0 and 24.0 GeV proton incidence on the mercury target to those for 1.5 GeV one.

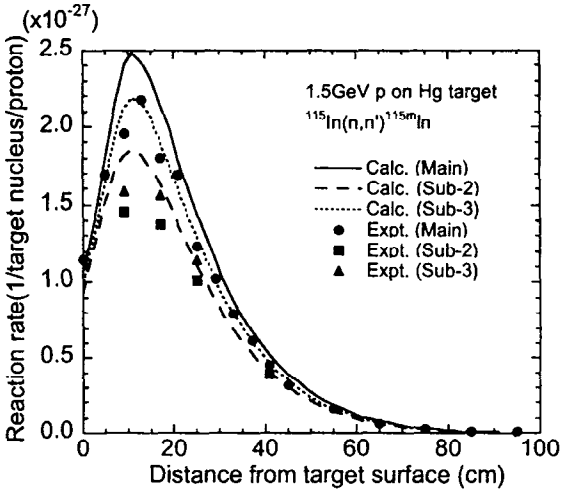

Fig. 7(a) Comparison of calculated and experimental reaction rates of the ^{115}In (n,n')^{115m}In reaction for 1.5 GeV proton incidence on the mercury target. The solid marks indicate the experimental results. The lines stand for the calculated results of NMTC/JAERI-MCNP4A.

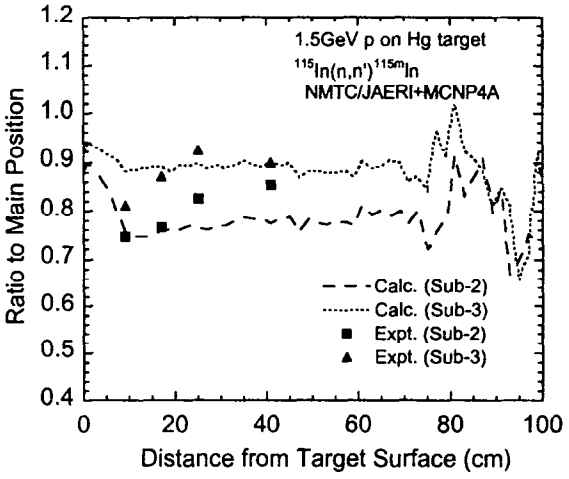

Fig. 7(b) Ratios of the reaction rates of ^{115}In (n,n')^{115m}In at different radial positions to those at the "Main" position. The notes to the marks and the lines are the same as for Fig. 7(a).

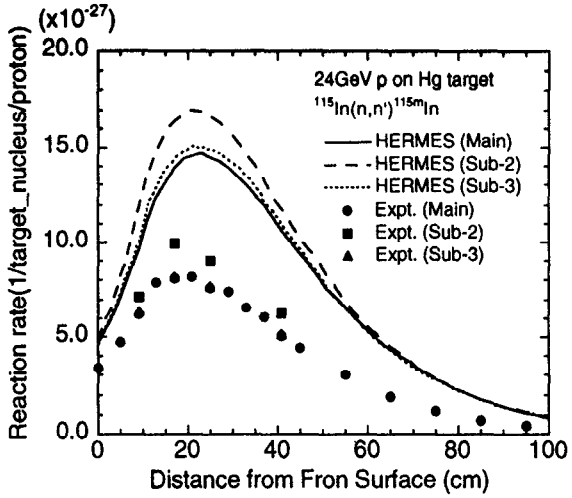

Fig. 8(a) Comparison of calculated and experimental reaction rates of the ^{115}In (n,n')^{115m}In reaction for 24.0 GeV proton incidence on the mercury target. The notes to the marks and the lines are the same as for Fig. 7(a).

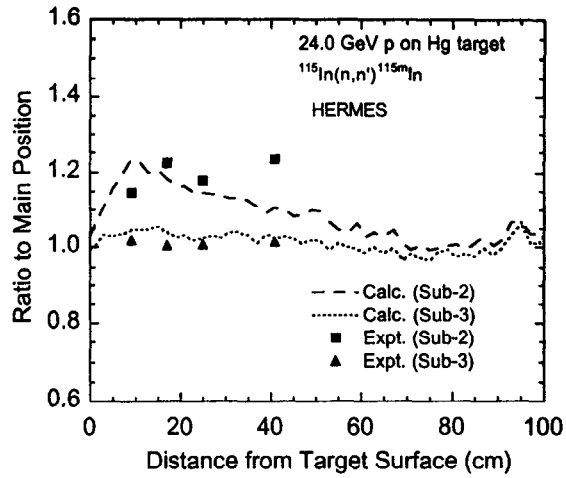

Fig. 8(b) Ratios of the reaction rates of the ^{115}In (n,n')^{115m}In reaction at the different radial positions to those at the "Main" position. The notes to the marks and the lines are the same as for Fig. 7(a).

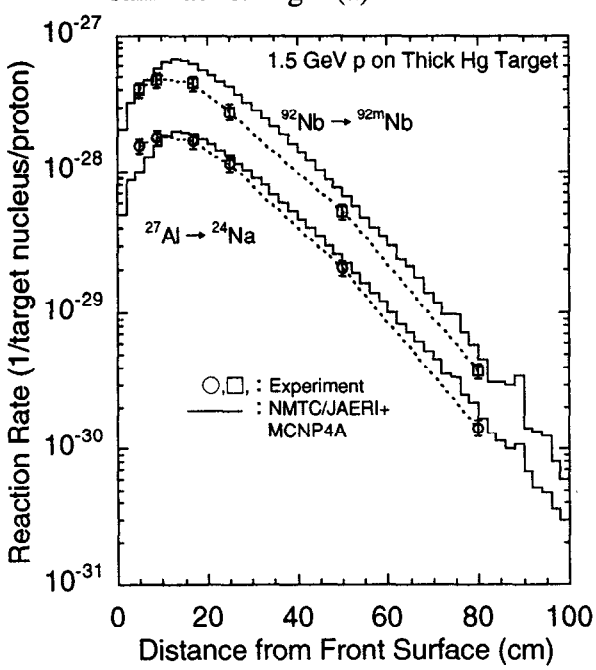

Fig. 9 Comparison of calculations with experiments for the reactions of ^{27}Al(n,x)^{24}Na and ^{93}Nb(n,2n)^{92m}Nb for 1.5 GeV proton incidence on the mercury target. The open marks indicate the experimental results. The solid lines stand for the calculated results of the NMTC/JAERI-MCNP4A code system. The dotted lines are for eye-guide.

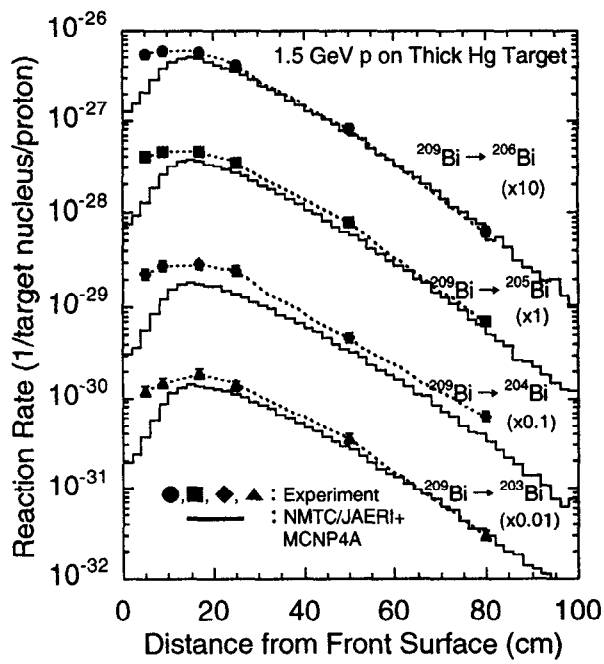

Fig. 10 Comparison of calculations with experiments for the reaction rates of ^{209}Bi(n,xn) for 1.5 GeV proton incidence on the mercury target. The notes to the marks and the lines are the same as for Fig. 9.

ICANS-XIV
The 14th Meeting of the International Collaboration on Advanced Neutron Sources
June 14-19, 1998
Starved Rock Lodge, Utica, Illinois

Proton Energy Dependence of Reflector Effect on a Beam Intensity from a Decoupled Water Moderator

R. Takagi and Y. Kiyanagi
Graduate School of Engineering, Hokkaido University, Sapporo 060-8628, Japan

Abstract

We studied change of relative beam intensities from a decoupled H_2O moderator with various reflector materials as a function of proton energy. We estimated the effect of secondary neutrons produced by spallation and (n,2n) reactions in the reflector, and found that the effect of the reflector changes depending on the proton energy. For proton energies below about 0.5 GeV beryllium was the best and above this energy lead was the best among the material studied.

1. Introduction

So for, beryllium have been used as a reflector in the existing pulsed spallation sources. However, the neutronic studies on reflector have been done[1]~[8], but proton energy dependence have not been studied. The result obtained by electron linac experiments indicated that Be (or BeO) was the best among graphite, lead and beryllium although the target-moderator-reflector assembly (TMRA) was very simple[9]. However, it was suggested that the effect of the reflector would depend on the spatial distribution of fast neutrons emitted from a target. Furthermore, in the case of the spallation neutron source the reflector works as a part of the target; namely, the reflector is another fast neutron source and the spatial distribution of the fast neutrons becomes wider with proton energy. On the other hand the fast neutrons produced by an electron linac is usually point like and there are no extra spallation neutrons. So, some difference will be expected between the electron source and the spallation source.

Recently, it is said that lead shows good neutronic performance from calculational results for spallation neutron sources. These results suggest that the proton energy dependence of the reflector effect is different between moderating and non-moderating reflectors.

Therefore, we intended to study the reflector effect as a function of the proton energy so as to understand the reflector effect systematically. We measured intensities and pulse

Keywords: Reflector, Energy dependence, Secondary neutron

shapes by using an electron linac and also calculated neutron intensities from moderators with several kinds of reflector materials at various proton energies by the LAHET Code System (LCS).

2. Experiments by using an electron linac

First, we measured the neutron intensities and the pulse shapes from a moderator with graphite or iron reflectors. We chose graphite as one of the moderating materials since beryllium is so expensive and chose iron since it has relatively large absorption cross section. Therefore, we expected that even in a coupled system the pulse may not be widened so much in the iron case. We also use the experimental results as a benchmark test of the calculations.

The experimental geometry is shown in Fig.1. We used the Hokkaido linac as a neutron generator. The target material was lead with a dimension of 7x7x7 cm^3. The size of H_2O moderator was 4.5x10x10 cm^3. The experiments were performed for the coupled and the decoupled H_2O moderators. For decoupler material we used B_4C (decoupling energy 2.5eV). Figure 2 shows energy spectra from the moderator. The shapes of the spectra are almost the same. The intensity from the decoupled moderator with the iron reflector is lowest but the intensity from the coupled moderator is higher than that from a decoupled moderator with graphite reflector. The intensity from a coupled moderator with graphite is much higher than the others. The relative intensities are summarized in Table 1.

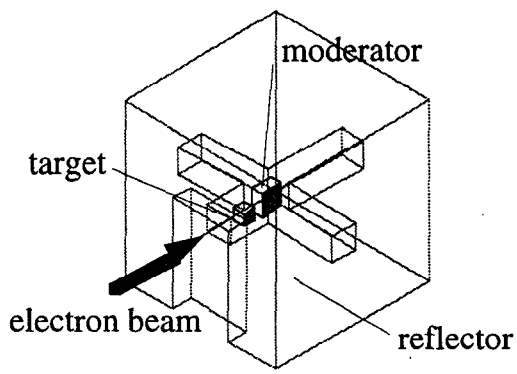

Fig.1 Experimental geometry

We also measured the pulse shapes from a moderator with the graphite and the iron reflectors in the case of the decoupled and the coupled systems. An example of the pulse shapes is shown in Fig.3. The pulse width of the coupled moderator with the iron reflector is not so broadened. Fig.4 shows pulse widths in full width at half maximum (FWHM). The FWHM's are slightly larger in the case of the coupled iron reflector than the decoupled graphite reflector. The difference is only about 20% in the thermal neutron region. The values of the iron coupled case approaches to the decoupled ones at higher energy. The FWHM's of the coupled graphite reflector are smaller than we expected but the pulse shape has long tail due to the slowing down in the graphite reflector as shown in Fig. 5. To estimate the effect of this tail we calculated the mean emission time by using

the experimental results. They are summarized in Table 2. The values of the coupled graphite case are one order of magnitude larger than those of the coupled iron reflector. These results suggest that a coupled iron reflector will be used in the spallation source. Therefore, we decided to include a coupled iron reflector in the following studies by simulation.

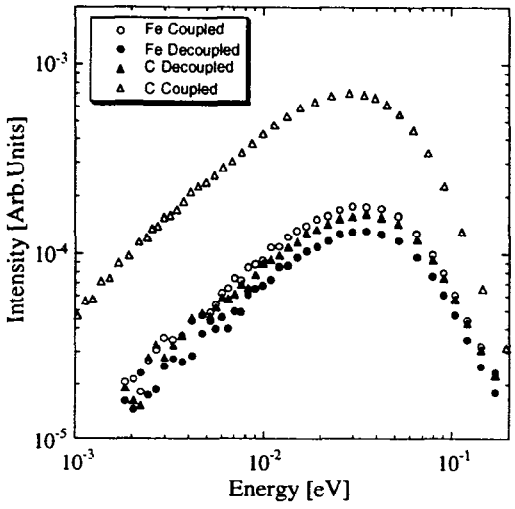

Fig.2 Energy spectra from a water moderator

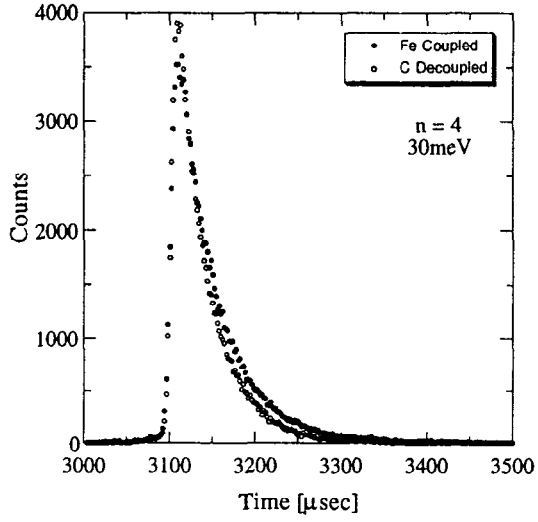

Fig.3 Pulse shapes in the case of coupled iron reflector and decoupled graphite reflector

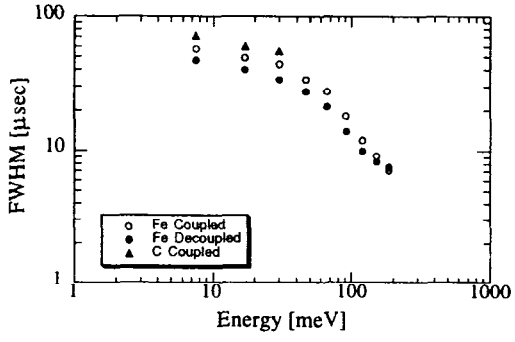

Fig.4 Pulse width in FWHM for a moderator with graphite and iron reflector

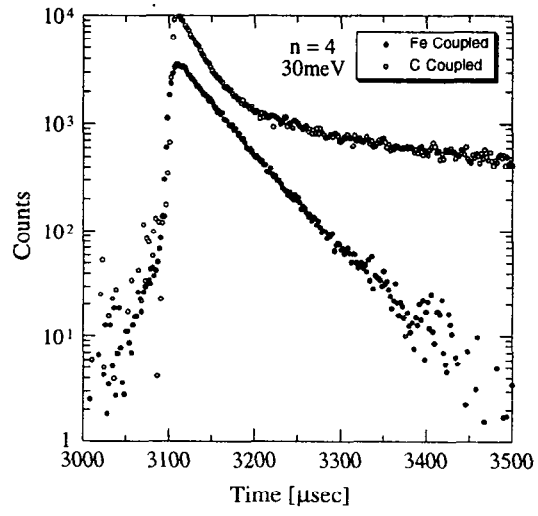

Fig.5 Pulse shapes from a coupled moderator with graphite and iron reflector

Table 1 Intensity ratios obtained by experiments and calculations

reflector type	experiment	calculation
Fe Coupled	1.000	1.000
Fe Decoupled	0.753	0.747
C Coupled	3.317	2.953
C Decoupled	0.921	0.935

Table 2 Mean emission time in the case of graphite and iron reflector

Energy [meV]	Fe Coupled	C Coupled
7.5	66.2	688
17	57.3	644
30	56.4	510

Then, calculations were performed on the same geometries by using LAHET Code System (LCS). For cross section data, ENDF/B-V was used. Relative intensities obtained by calculations are also shown in Table 1, these results were normalized by the intensity of the coupled H_2O moderator with iron reflector. It is found that the intensity ratios obtained by calculations agree very well with those by experiments. Therefore, it is said that LCS can simulate the experiment accurately.

Then, we performed the calculations in order to analyze the proton energy dependence of the neutron intensity from moderators with various reflector materials.

3. Proton energy dependence of neutron intensity from moderators

3-1. Calculations

In the spallation neutron sources, neutrons are not only produced in a target but also in a reflector. Therefore, we must also take into account the effect of reflector as neutron source when we consider TMRA. Main processes of neutron production in the reflector are spallation reaction and (n,2n) reaction. So, we estimated the effect of the neutrons produced in the reflector by spallation reaction and (n,2n) reaction by simulation using the LCS.

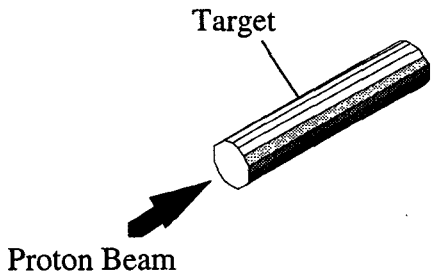

Fig.6(a) Geometry used for calculation (target)

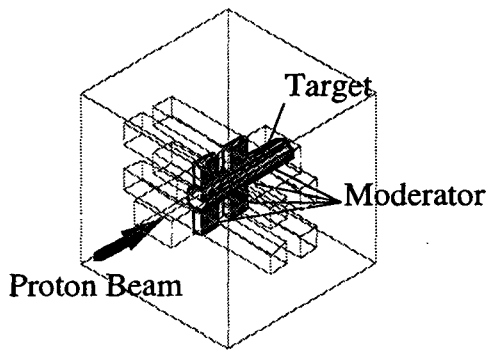

Fig 6(b) Geometry used for calculation (TMRA)

Geometries used in the calculations are shown in Fig.6(a) and Fig.6(b). Fig.6(a) is a geometry of a cylindrical target only. Target is a homogeneous mixture of tungsten and 10% D_2O coolant with the dimension of 10 cm (diam.) x 57.2 cm (length) at 3 GeV proton beam. The target length was adjusted depending on the proton energy. The profile of the proton beam is parabolic with a size of 3.5 cm in diameter on the incident surface of the target. Proton energies 0.12, 0.2, 0.5, 0.8, 1, 2 and 3 (GeV) are studied. Fig.6(b) is a geometry of TMRA. Target is surrounded by D_2O coolant. Four water moderators are located above and below the target. These are decoupled H_2O with the dimension of 5x10x10 cm^3. For decoupler material we chose B_4C (decoupling energy 2.5 eV). The distance between the target surface and moderator surface is 2 cm. As reflector materials, beryllium, graphite, iron and lead are studied.

LCS consists of two main codes, LAHET and HMCNP. The LAHET simulates the transport and interaction of high energy particles above cut off energy, and the HMCNP simulates them in the energy region below cut off[10]. We used a cut off energy of 15MeV.

We performed full system calculations by using the LCS. We also performed 2 step calculations to estimate contributions of neutrons produced by (n,2n) in the reflector. First we calculated sub 15MeV neutron production only in target by using the LAHET and second the sub 15MeV neutrons were transported to the full system of TMRA by using data obtained by the LAHET calculation. These calculations were done by the HMCNP code. From this calculation, we can estimate the number of neutrons produced by (n,2n) reaction in the reflector caused by sub 15 MeV neutrons. By comparing the results of these two type calculations we can obtain the neutrons produced in the process of high energy particle transportation, which are considered to be mainly due to the spallation.

3-2. Neutron numbers produced in TMRA

First we calculated the neutron yields in the TMRA. The results are shown in Table 3. The ratios of neutron yields of each process to that only in the target are also written in % in the parentheses. It is found that with increasing proton energy, contribution of the neutrons produced by the spallation reaction in the reflector increases especially in lead and the ratio of neutrons produced by (n,2n) reaction in reflector does not depend so much on the proton energies. The contribution of (n,2n) reaction is remarkable in beryllium.

Table 3 The number of neutrons produced in reflectors [n/p]
( ): ratio (%) to the yield in the target

Proton Energy	W Target	Be reflector		C reflector		Fe reflector		Pb reflector	
[GeV]	[n/p]	spallation	(n,2n)	spallation	(n,2n)	spallation	(n,2n)	spallation	(n,2n)
0.12	0.42	0.05 (10.9)	0.07 (16.3)	0.02 (5.4)	0.00 (0.0)	0.06 (14.1)	0.00 (1.0)	0.09 (22.3)	0.01 (3.5)
0.2	1.18	0.16 (13.4)	0.18 (15.4)	0.08 (6.4)	0.00 (0.0)	0.24 (20.1)	0.01 (1.0)	0.39 (32.9)	0.04 (3.4)
0.5	6.61	0.92 (14.0)	0.86 (13.1)	0.46 (7.0)	0.00 (0.0)	1.72 (26.1)	0.05 (0.8)	2.87 (43.5)	0.18 (2.7)
0.8	13.9	1.95 (14.1)	1.84 (13.3)	1.05 (7.6)	0.00 (0.0)	3.82 (27.5)	0.10 (0.7)	6.19 (44.6)	0.38 (2.7)
1	18.2	2.53 (14.0)	2.62 (14.5)	1.25 (6.9)	0.00 (0.0)	5.16 (28.5)	0.14 (0.8)	8.58 (47.3)	0.55 (3.0)
2	36.6	5.52 (15.1)	6.33 (17.3)	2.78 (7.6)	0.00 (0.0)	11.59 (31.7)	0.37 (1.0)	19.7 (53.8)	1.42 (3.9)
3	53.1	8.80 (16.6)	9.79 (18.5)	4.59 (8.7)	0.00 (0.0)	17.52 (33.0)	0.63 (1.2)	29.2 (54.9)	2.31 (4.4)

3-3. Comparison of Neutron intensities from moderators

In older to study the proton energy dependence of the efficiencies of various reflector materials, we compare the intensities from the moderators. Here we normalized the intensity by the one in the case of the decoupled lead reflector. Figure 7 shows relative neutron intensities from moderators in the case where contributions from the secondary neutrons are excluded. This indicates the pure efficiency as a neutron reflector. Figure

7(a) is the intensities only from upstream two moderators. The relative intensities in the cases of beryllium and graphite increase with decreasing the proton energy. These two are the moderating reflector. Therefore, they are efficient when neutrons are produced near the moderators due to the short slowing-down length. Figure 7(b) shows the relative total intensities from all four moderators. In this case graphite is better than beryllium since probably it has longer slowing-down length than beryllium. The results suggest that the spatial distribution of the fast neutrons from a target surface is important. Figure 8 shows the spatial distributions from target surface, which clearly shows broadening with the proton energy. We estimated the width of the distributions by the standard deviations and Fig.7(a) and Fig.7(b) were replotted as a function of the standard deviation. The result is shown in Fig.9(a) and 9(b). From these figures, it is found that the efficiency of beryllium and graphite become worse in the region of standard deviation greater than 4 cm.

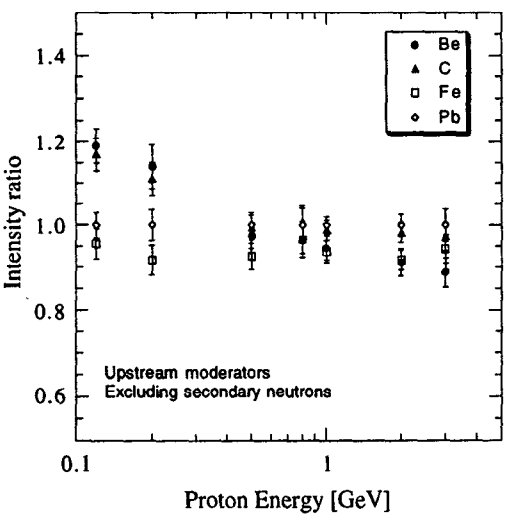

Fig.7(a) Relative neutron intensities from upstream moderators excluding secondary neutrons

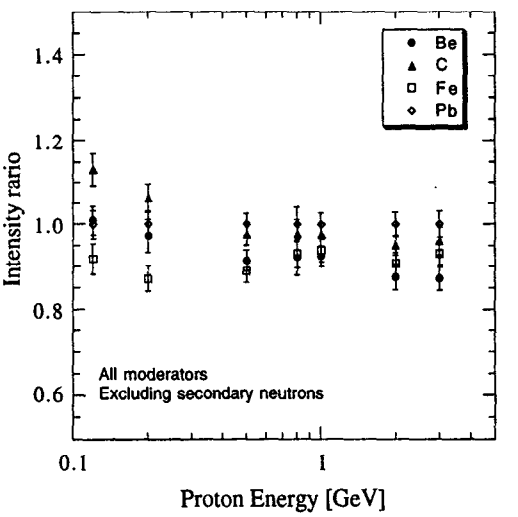

Fig.7(b) Relative neutron intensities from all moderators excluding secondary neutrons

Next, we studied effect of (n,2n) reaction. The results for upstream moderators and that for all moderators at various proton energies are shown in Fig.10(a) and Fig.10(b). When we compare Fig.10(a) with Fig.7(a), it is found that the neutron intensity in the case of beryllium reflector becomes relatively much higher over whole proton energies. The superiority of the beryllium reflector is weakened again when compared the total intensities as shown in Fig.10(b). It is due to the fact that the number of neutrons produced by (n,2n) reaction in reflector is much larger in beryllium than the others, as expected from the results indicated in Table 3.

The results obtained by the full system calculations including all produced neutrons are shown in Fig.11(a) for the upstream moderators and Fig.11(b) for all moderators,

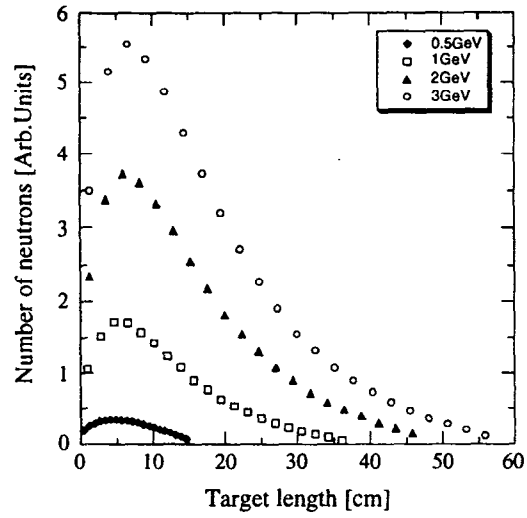

Fig.8 Neutron spatial distributions from a target surface

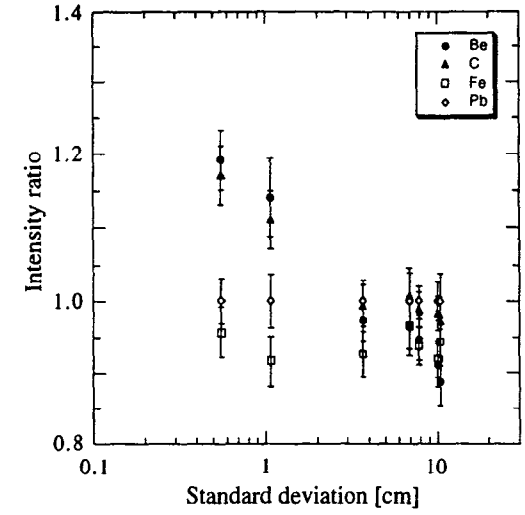

Fig.9(a) Relative neutron intensities from upstream moderators as a function of standard deviations in the case excluding secondary neutrons

respectively. The intensities in the lead reflector case increase compared with the intensities in other cases discussed before due to the contribution of the neutrons produced in the reflector especially in the higher proton energies since the contribution of the neutrons produced by spallation increases with the proton energy.

We also calculated the intensities in the case of the coupled lead and the iron reflectors as references. The intensity in the case of the coupled iron is much higher than that in the decoupled lead case. If it is still true that the pulse width is not broadened in a coupled iron case in the spallation source, iron will be one of the candidates. The intensity in the case of the coupled lead reflector is higher than that in the coupled iron. Lead moderate neutrons very slowly. Therefore, broadening of pulse width of neutrons from a moderator may not so large. To confirm this, it is necessary to measure the pulse shapes of these coupling systems. The intensity from the upstream moderators in the case of the lead reflector crosses with that in beryllium case around 0.5

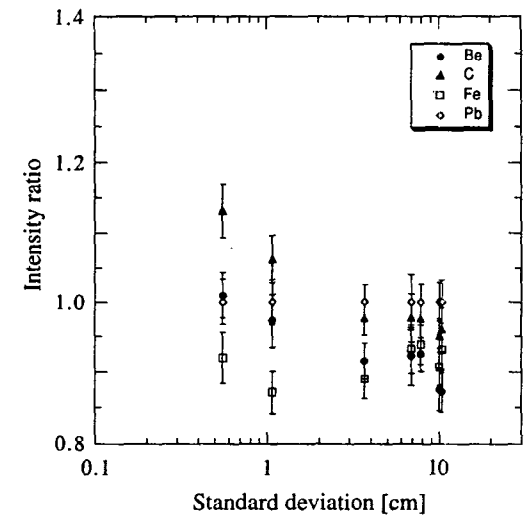

Fig.9(b) Relative neutron intensities from all moderators as a function of standard deviations in the case excluding secondary neutrons

GeV. this indicate the upper limit of the proton energy where the beryllium reflector is superior to the lead reflector.

Finally, we summarize the contributions of the secondary neutrons at 3 GeV protons in Fig.12. The efficiency as a reflector seems to be independent of atomic number above carbon. As expected the merits of beryllium at this proton energy is (n,2n) reaction and that of lead is spallation. The difference in intensities are mainly caused by the neutron production by these two reactions.

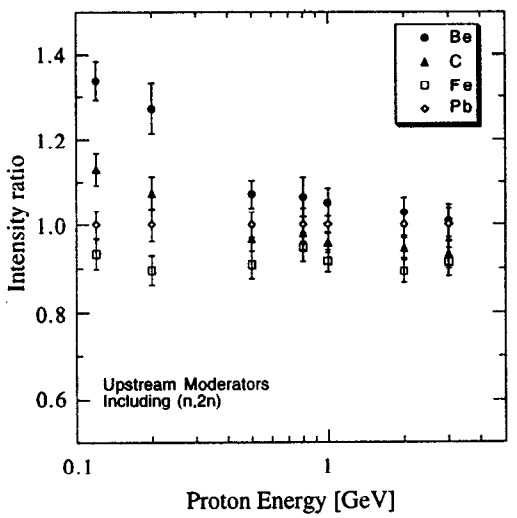

Fig.10(a) Relative neutron intensities from upstream moderators in the case including (n,2n) reaction

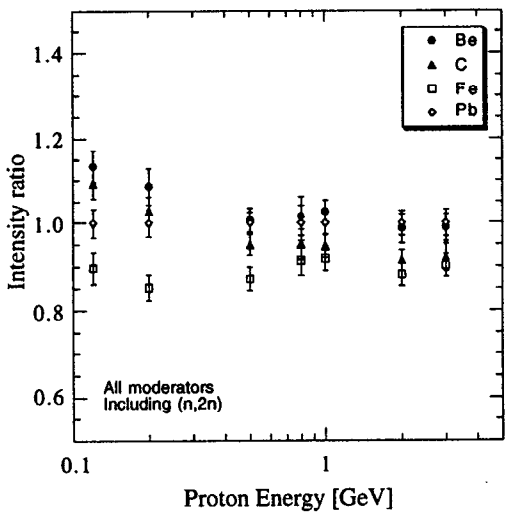

Fig.10(b) Relative neutron intensities from all moderators in the case including (n,2n) reaction

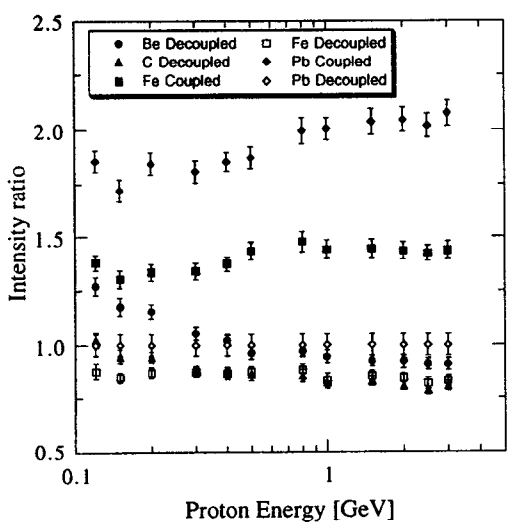

Fig.11(a) Relative neutron intensities from upstream moderators in the case including all neutrons produced

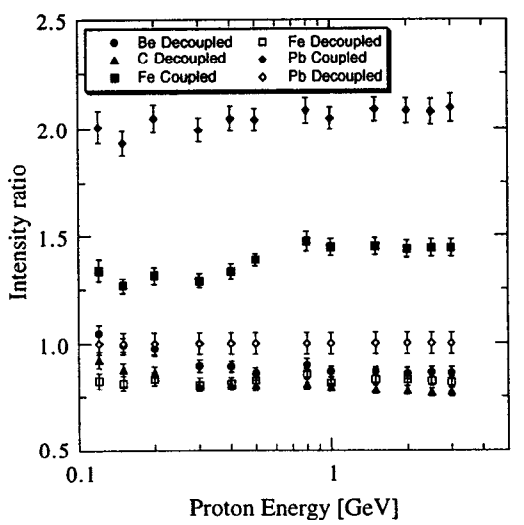

Fig.11(b) Relative neutron intensities from all moderators in the case including all neutrons produced

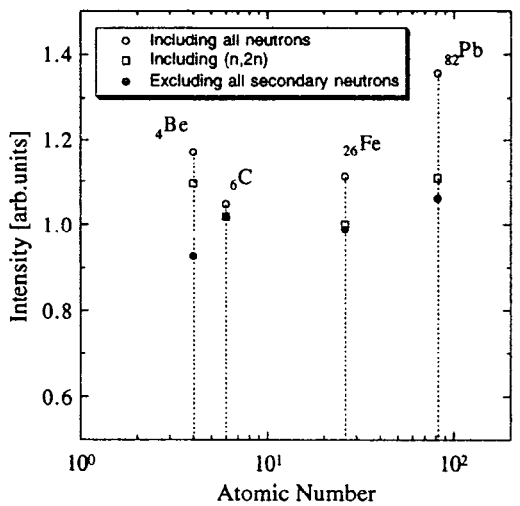

Fig.12 The effects of secondary neutrons on neutron intensities from moderators at 3 GeV

4. Conclusion

The contribution of the neutrons produced in a TMRA by spallation reaction increase with the proton energy and also with atomic number. It has become clear that a moderating type reflector is effective at lower proton energy since the spatial distribution of the emitted fast neutrons at a target surface is narrow. Beryllium is effective in the proton energy below about 0.5 GeV. Lead is the best among the materials studied here above this energy due to the contribution of the neutrons produced by spallation. A coupled reflector of iron should be studied in more detail since it may be able to remove the decoupler, cooling of which is not so easy.

5. References

[1] J.M. Carpenter: G.J. Marmer, ANL-sss-72-1 (1972).

[2] B.C. Boland et al.: RL-77-140/A (1977).

[3] A.D. Taylor: RL-81-057 (1981).

[4] K. Inoue et al.: J. At. Energy Soc. Jpn., (in Japanese), 21[11], 865 (1979).

[5] K. Inoue et al.: Nucl. Instrum. Methods, 192, 129 (1982).

[6] G.S. Bauer et al.: Proc. ICANS-V, p. 475 (1981).

[7] A.D. Taylor: ibid., p. 377.

[8] G.J. Russel et al.: ibid., p. 389.

[9] Y. Kiyanagi: J. Nucl. Sci. Tech., 24, 490 (1987).

[10] R.E. Prael and H. Lichtenstein, "User guide to LCS: The LAHET code system", LA-UR-89-3014 (1989).

Neutron Scattering Instruments

MODERATOR PHYSICS AND PERFORMANCE

ICANS XIV
14th Meeting of the International Collaboration
on Advanced Neutron Sources
June 14–19, 1998
Starved Rock Lodge, Utica, IL, USA

A RING MODERATOR CONCEPT FOR A LONG-PULSE SOURCE

Eric J. Pitcher, Gary J. Russell, and Phillip D. Ferguson

Manuel Lujan, Jr. Neutron Scattering Center, Los Alamos National Laboratory, USA

ABSTRACT

We propose a novel target-moderator configuration for use at a long-pulse spallation source in which a ring-shaped moderator is placed above a slab target. This single moderator could serve all flight paths of a long-pulse source, greatly simplifying the engineering of the target system over traditional four-moderator systems. It offers great flexibility in the number and layout of flight paths, with a total angular opening of 240°. Source brightness is nearly equivalent to that of a traditional wing moderator.

1 Introduction

We propose a novel target-moderator configuration for use at a long-pulse spallation source. The configuration consists of a single slab target with a single ring moderator in wing geometry, as depicted in Figure 1. This single moderator serves all flight paths. The curved neutron emission surface, which could potentially lead to broadening of the leading edge of the neutron pulse at a short-pulse source, is not a concern in long-pulse source applications, where the proton beam pulse width dominates the neutron pulse rise time.

This configuration provides several mechanical design and operation advantages. First, there is only one moderator serving all flight paths, which greatly simplifies the routing of supply lines as compared to conventional configurations with four or more moderators. In addition to mechanical simplification, this reduction in supply lines means a reduction in the displacement of reflector material, which should enhance neutronic performance. Second, this configuration is well adapted to the servicing concept of horizontal target extraction and vertical moderator extraction, as proposed for the LPSS target station (reference).[1] The target insert or the moderator insert may be extracted independently of one another, unlike configurations that have moderators placed below the target in which the target insert must be extracted prior to extraction of the moderator insert. Third, an

ultra-cold neutron source may be easily accommodated underneath the target or upstream of the moderator, both of which are high-flux regions. Finally, there is great flexibility in the number and placement of flight paths served by the moderator. Angular spacing between flight paths can be easily adjusted on an instrument-by-instrument basis, thereby optimizing instrument floor space and maximizing the number of flight paths.

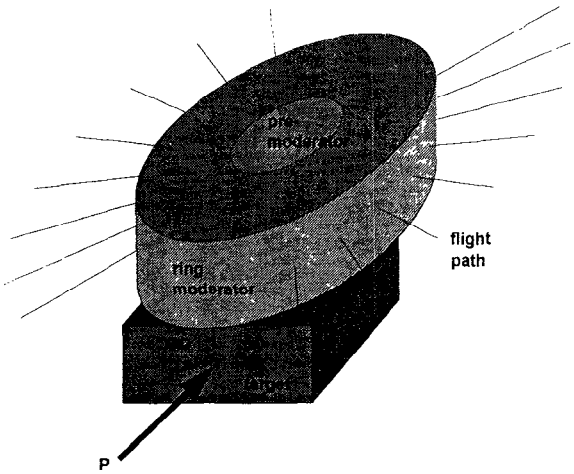

Figure 1. Slab target with a ring moderator in wing geometry.

The neutronic performance of such a ring moderator has been evaluated using the LAHET Code System.[2] Numerous material and geometrical optimizations were performed, and a reasonably well optimized geometry determined. The neutronic performance of the ring moderator has been found to compare favorably with that of a traditional wing moderator.

2 Material and Geometric Optimizations

Optimization studies performed included target aspect ratio, moderator position above the target, premoderator diameter, moderator thickness, inner reflector size, and reflector-filter thickness. Each of these is described below. Generally, our figure of merit is the time-averaged source brightness over the energy interval 0 to 5 meV, calculated using 12 point detectors, each viewing a 10x10 cm^2 area of the moderator surface and separated by 15° from one another. These 12 point detectors represent the central 12 of 16 presumed flight paths, shown in Figure 1, that could view the moderator through the two 120° angular openings in the reflector.

The starting point for the optimization studies is shown in Figure 2 in the form of vertical and horizontal cross-sectional slices through the MCNP geometry. Specifications of the "baseline" geometry are given here, although these varied depending on the particular optimization study. We used a partially coupled composite reflector. The inner reflector material is beryllium, the outer reflector material is lead, and there is a 0.081-cm-thick sheet of cadmium between them. The inner Be reflector diameter and height are both 70 cm; the total reflector diameter is 1.5 m and its height is 1.7 m. The slab target is 8.16 cm high by 12.25 cm wide for an aspect ratio of 1.5. The premoderator is beryllium cooled by 15 v% light water. Based on recent comparisons of calculated results to experiment,[3] we assumed a 90% para-, 10% ortho-hydrogen composition of liquid hydrogen for the ring moderator material. Each side of the moderator has a flight path angular opening of 120°. The moderator is 12 cm high.

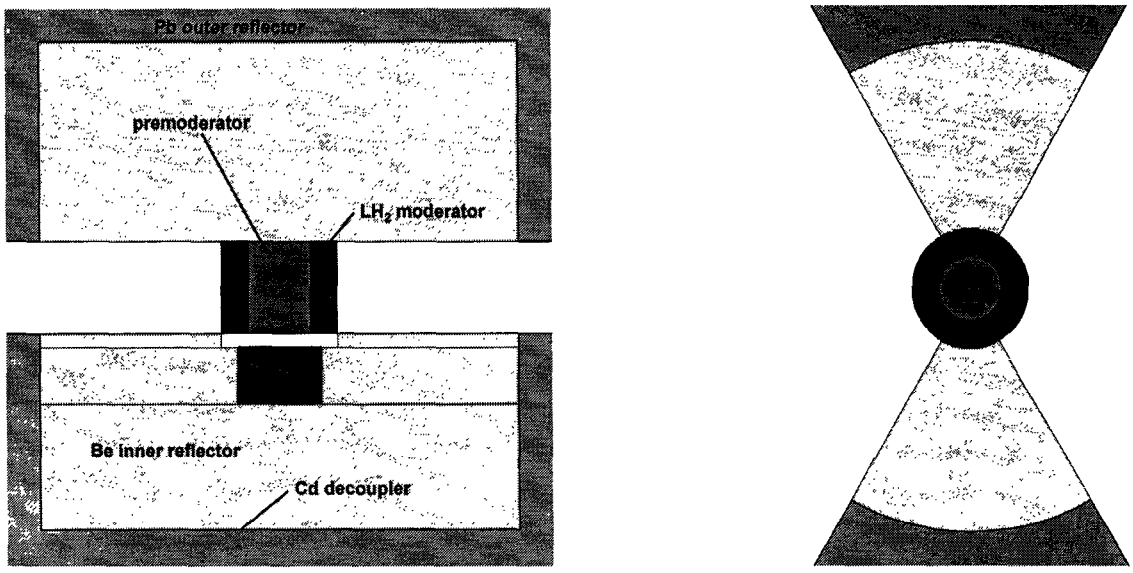

(a) (b)

Figure 2. LCS model of the ring moderator target station: (a) vertical, and (b) horizontal slices through the center of the ring moderator.

2.1 Target Aspect Ratio

The target aspect ratio is defined as the target width divided by the target height. A target with an aspect ratio greater than unity, that is, one that is wider than it is tall, is termed a "slab" target. Intuitively, a slab target should couple well with a ring moderator by positioning the neutron source closer to the moderator. We varied the target aspect ratio from 0.25 to 4. For each geometry, the beam aspect ratio was the same as the target aspect ratio, with the beam spot area fixed at 38.5 cm^2. The spatial profile was parabolic, and the peak current density was held constant for all aspect ratios such that the peak power density in the target did not vary with target aspect ratio. Thus we are justified in using the same coolant volume fraction in the target for all aspect ratios. The results of this study are plotted in Figure 3. It shows the source brightness to have a broad peak centered near an aspect ratio of 1.4. For an aspect ratio between 1 and 2, the source brightness varies by less than 2%, suggesting that factors other than neutronic performance, such as thermal-hydraulic performance or fabricability would probably guide the selection of target aspect ratio within the range 1 to 2.

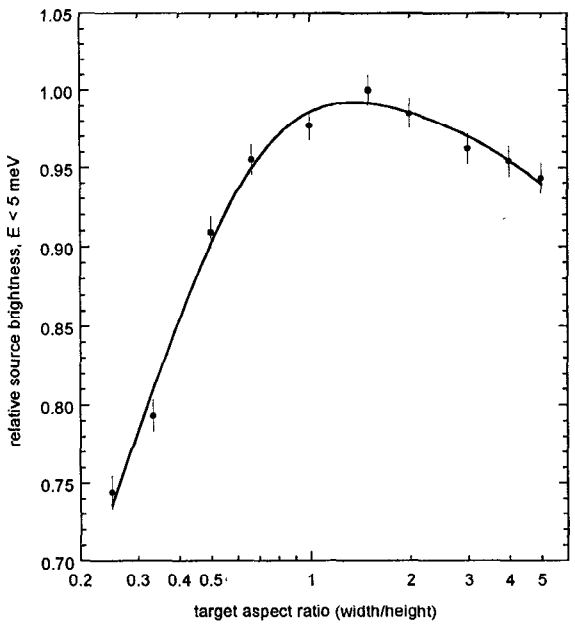

Figure 3. Dependence of source brightness on target aspect ratio.

2.2 *Moderator Position*

The distance *d* of the moderator central axis relative to the front face of the target (see Figure 4) can be adjusted to achieve various performance objectives. For example, flight paths viewing the upstream end of the ring moderator can be made brighter (at the sacrifice of brightness of flight paths viewing the downstream portion of the ring moderator) by simply moving the moderator downstream from its "optimal" position. Here, the optimal target position is defined as that which provides the highest brightness averaged over the central 12 of 16 flight paths. The variation of the average source brightness as a function of *d* is shown in Figure 4. It shows the optimal moderator position is that in which the central axis of the moderator is 5 cm upstream of the front face of the target. This position also provides the most uniform source brightness for all sixteen flight paths.

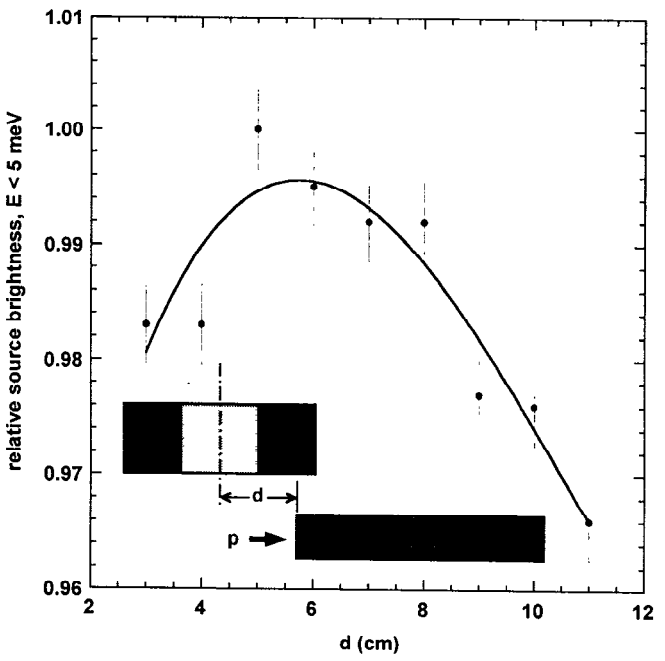

Figure 4. Dependence of source brightness on moderator position relative to the front face of the target.

2.3 *Premoderator Diameter and Moderator Thickness*

Source brightness has a moderate dependence on the premoderator diameter and moderator thickness. We performed a parametric study in which the Be premoderator diameter was varied from 0 to 7 cm and the hydrogen moderator thickness was varied from 6 to 10 cm. The results, plotted in Figure 5, show that, as the moderator becomes progressively thicker, the optimum premoderator diameter decreases until, at a moderator thickness of 9 cm, there is no longer any need for a premoderator. For a 90% para-hydrogen fraction, the moderator is somewhat transparent to low-energy neutrons and requires a relatively thick

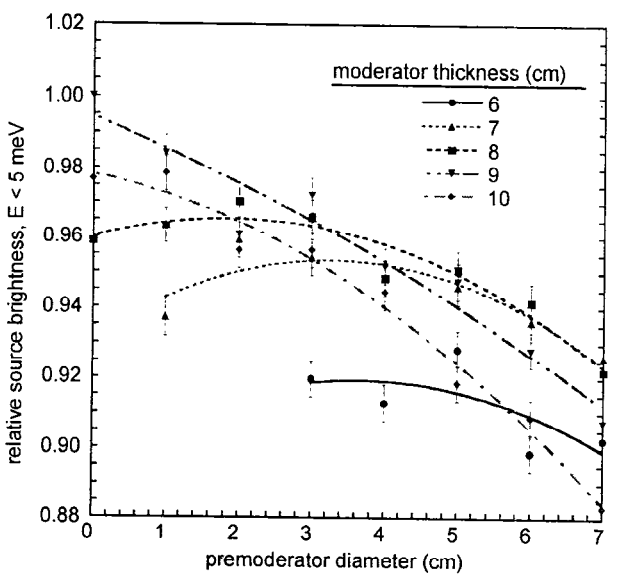

Figure 5. Source brightness dependence on ring moderator thickness and outside diameter.

moderator of 9 cm to achieve optimal source brightness. Beyond 9 cm thickness, the source brightness begins to decrease regardless of premoderator size.

2.4 Inner Reflector Size

As shown in previous studies of coupled moderator systems,[4] if the inner reflector is composed of a moderating medium such as beryllium or graphite, its size has a strong influence on time-averaged source brightness by changing the decay time constant of the neutron pulse. This phenomenon holds true for this target-moderator system as well, as shown in Figure 6, where the time-averaged source brightness and standard deviation of the neutron pulse are plotted as a function of the inner Be reflector size (both diameter and height). We see that both increase monotonically with inner reflector size. The pulse width is linearly proportional to the inner reflector size, while the time-averaged source brightness is slowly approaching a saturated value. For an inner reflector diameter and height equal to 140 cm, the time-averaged source brightness has increased by 45% over that of a 60-cm reflector size, whereas the standard deviation of the neutron pulse increases four-fold. As all flight paths share the same temporal characteristics, the instrument requiring the shortest decay constant will set the inner reflector size. This would be true for any target-moderator system in which all moderators are fully coupled to the reflector since, for coupled moderators, the reflector determines the decay constant of the neutron pulse.

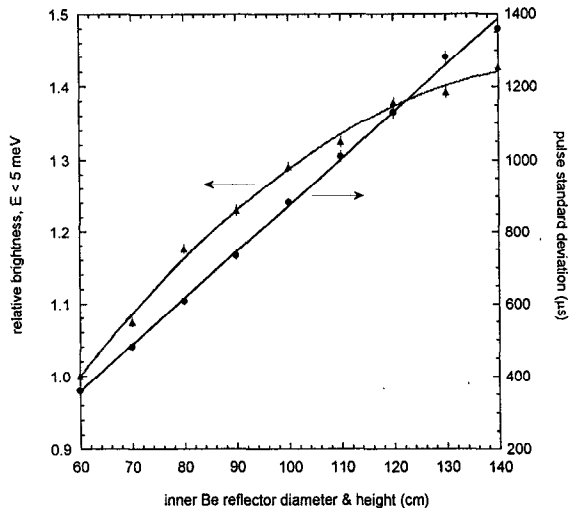

Figure 6. Variation of source brightness and pulse width standard deviation with inner Be reflector size.

3 Ring Moderator Performance Relative to that of a Traditional Wing Moderator

We have compared the performance of the optimized ring moderator-slab target geometry to that of a traditional wing moderator. The materials and geometries were matched as closely as possible between the two systems in order to obtain a meaningful comparison. The wing moderator is 12 cm wide by 12 cm high by 8 cm thick, while the ring moderator is 12 cm high by 16 cm diameter with no premoderator. Spectra for the two systems are plotted in Figure 7. The ratio of these two spectra (ring moderator source brightness to wing moderator source brightness) is plotted in Figure 8, which shows the ring moderator brightness varies from 75 to 91% of the brightness of a traditional wing moderator over the wavelength range 2 – 12 Å. For the integral brightness below 5 meV, the ring moderator has 90% of the brightness of a traditional wing moderator. The reason the ring moderator does not perform quite as well as a wing moderator is presumably due to the displacement of reflector resulting from the large angular openings that service the flight paths.

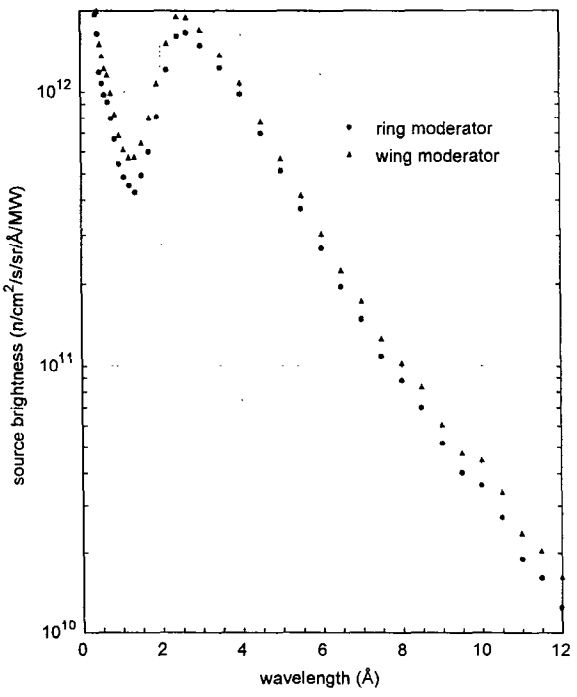

Figure 7. Wavelength-dependent source brightness for a ring moderator and a traditional coupled wing moderator.

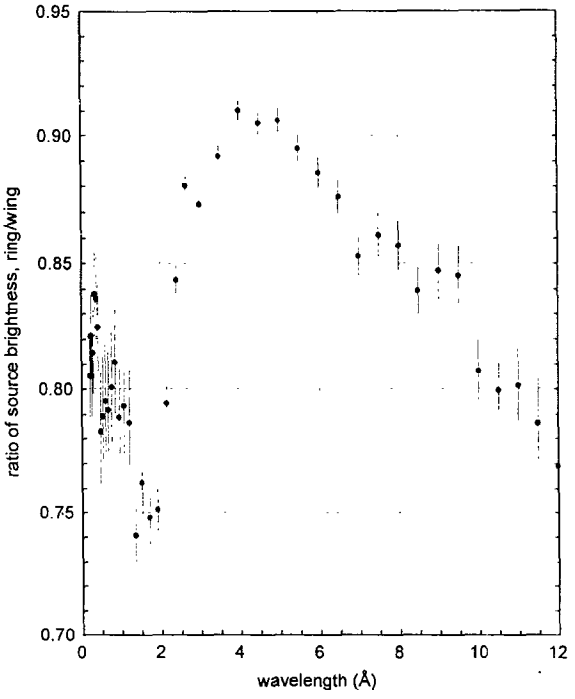

Figure 8. Wavelength-dependent source brightness of a ring moderator relative to that of a wing moderator.

4 Use of a Cold Be Reflector-Filter to Enhance Source Brightness

The large angular opening of 120° serving multiple flight paths on each side of the moderator causes a significant displacement of critical reflector material. As a solution to this problem, we considered using a cold (77 K) Be reflector-filter to reflect super-thermal neutrons leaking from the moderator emission surface back into the moderator. These neutrons are then given a second chance to downscatter into the thermal region and leak from the moderator as cold neutrons. Cold neutrons, on the other hand, are not reflected back into the moderator due to the precipitous drop in the Be cross section below 5 meV. We have investigated the use of a cold Be reflector-filter on the ring moderator system and found it to significantly enhance the brightness of neutrons with wavelengths greater than 4 Å. Shown in Figure 9 are the spectra for a standard ring moderator and one with a 13-cm-thick cold Be reflector-filter butted up against the moderator emission surface. Figure 10 shows the ratio (filtered to unfiltered) of the spectra. Beyond 4 Å, source brightness is enhanced by a factor of 1.6. This gain comes with virtually no increase in the pulse width, as shown in Figure 11. With the use of a cold Be reflector-filter, the time-averaged source brightness below 5 meV of a ring moderator-slab target system driven by a 1-MW, 800-MeV proton beam is 35% of the calculated source brightness of the CS-2 cold source at the Institut Laue-Langevin.[5] The efficacy of a cold Be reflector-filter on a long-pulse source, as well as other sources, is discussed in more detail elsewhere.[6]

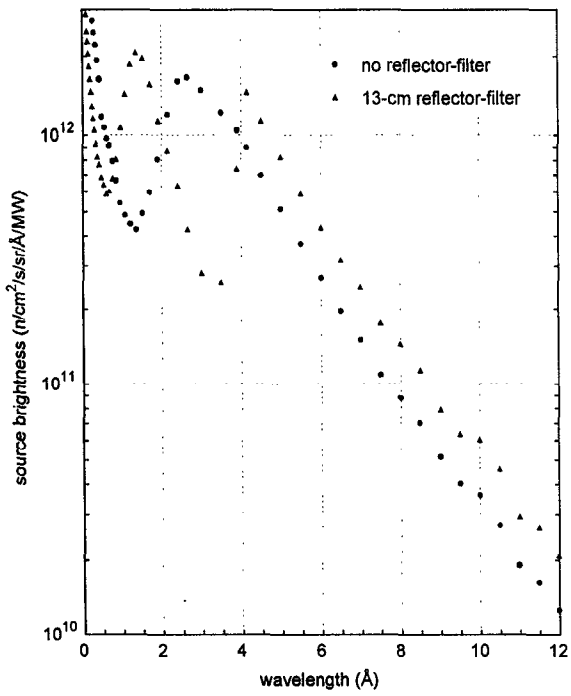

Figure 9. Wavelength-dependent source brightness for a ring moderator with and without a cold Be reflector-filter.

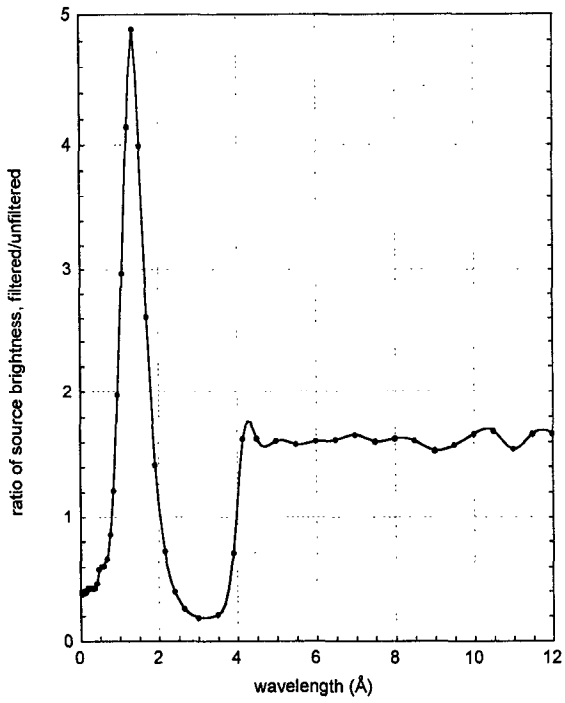

Figure 10. Wavelength-dependent source brightness of a filtered ring moderator relative to that of an unfiltered one.

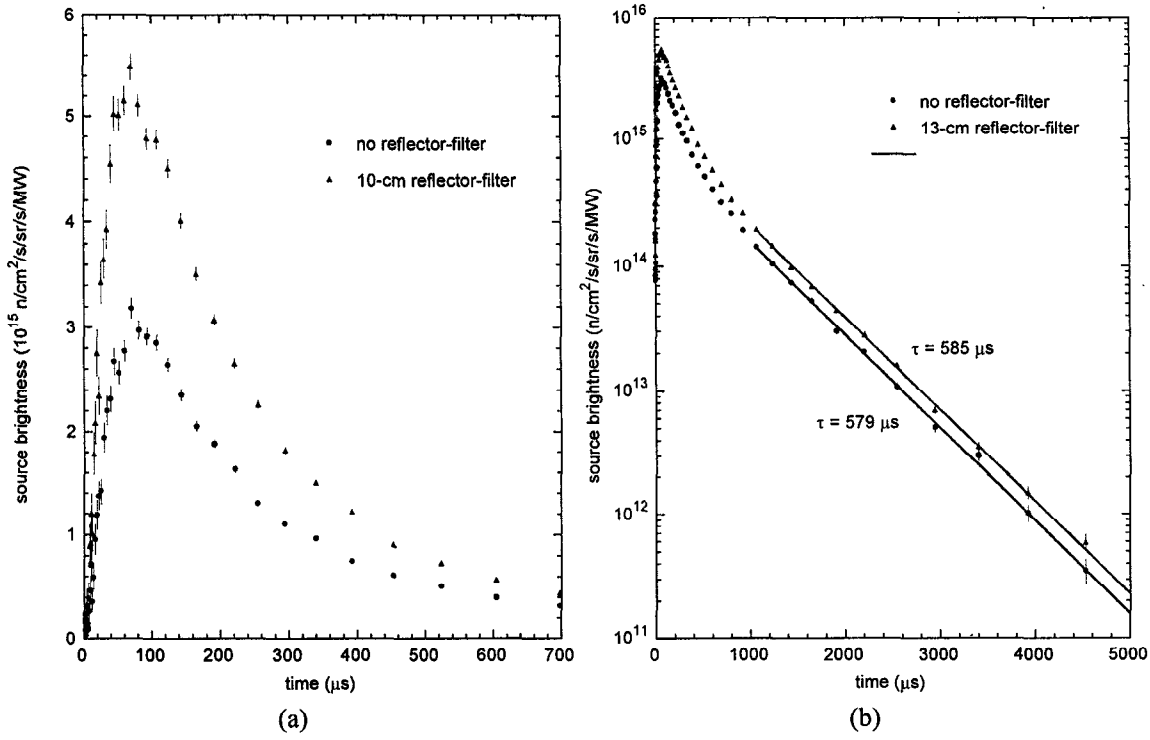

Figure 11. Time dependent source brightness (E < 5 meV) for an unreflected ring moderator and a ring moderator with a 10-cm-thick cold Be reflector-filter plotted on (a) linear, and (b) logarithmic scales.

5 Conclusion

We have proposed a novel target-moderator configuration in which a ring-shaped moderator is placed above a slab target. This single moderator could service all flight paths of a long-pulse source, greatly simplifying the engineering of the target system over traditional four-moderator systems. It offers great flexibility in the number and layout of flight paths, with a total angular opening of 240°. Its performance is nearly equivalent to that of a traditional wing moderator. With the use of a cold Be reflector-filter, a 1-MW long-pulse source utilizing a slab target-ring moderator geometry delivers a time-averaged cold source brightness ($E < 5$ meV) equivalent to 1/3 that of the world's most intense cold source.

6 References

1. G. J. Russell; P. D. Ferguson; E. J. Pitcher, and D. J. Weinacht, "A Long-Pulse Spallation Source at Los Alamos: Facility: Description and Preliminary Neutronic Performance for Cold Neutrons, Proceedings of the Symposium on Materials for Spallation Neutron Sources, February 10-12, 1997, Orlando, Florida.
2. R. E. Prael and H. Lichtenstein, "User Guide to LCS: The LAHET Code System," LA-UR–89-3014, September, 1989.
3. G. J. Russell, P. D. Ferguson, and E. J. Pitcher, "Sensitivity Studies of the Ortho/Para H_2 Concentration on the Neutronic Performance of the Lujan Center Liquid H_2 Moderator Using State-Of-The-Art Computational Tools," Proceedings of the International Workshop on Cold Moderators for Pulsed Neutron Sources, September 28 – October 2, 1997, Argonne, Illinois.
4. E. J. Pitcher, G. J. Russell, P. A. Seeger, and P. D. Ferguson, "Performance of Long-Pulse Source Reference Target-Moderator-Reflector Configurations," Proceedings of the 13th International Conference on Advanced Neutron Sources, September 11-14, 1995, Villigen, Switzerland.
5. P. Ageron, Nucl. Instr. Meth. **A284** (1989), 179-199. From Figure 2 of this paper, the integral brightness below 5 meV of the CS-2 cold source is calculated to be 7.25×10^{12} n/cm^2/s/sr.
6. E. J. Pitcher, G. J. Russell, and P. D. Ferguson, "Use of a Cold Be Reflector-Filter to Enhance Cold Source Brightness at Long Wavelengths," these proceedings.

ICANS-XIV
14th Meeting of the International Collaboration on
Advanced Neutron Sources
June 14-19, 1998
Argonne National Laboratory, Argonne, IL 60439-4814 USA

ON RADIATION EFFECTS IN WATER ICE AT LOW TEMPERATURES

E.P. Shabalin

Joint Institute for Nuclear Research, Dubna, 141980, Russia

ABSTRACT

In the paper an attempt is made to come to conclusion on possibility and conditions of fast release of stored energy in water ice irradiated with neutrons. In particular, the rough estimate of maximum allowable residence time of ice pellets in the supposed ESS moderator, before it suffers of sudden leap of temperature, is done having based on the scanty experimental data and some theoretical models of fast recombination.

1. Introduction

Recently, efforts have been started in various places to improve the performances of cold moderators in one way or the other. In particular, such combinations as of water ice and hydrogen, methane and water ice (clathrate) are considered to be effective for pulsed spallation neutron sources of the multi-megawatt range of beam power [1]. Being superior in neutronic performance to the currently used liquid or supercritical hydrogen, they would be "the hard nut to crack" because of their bad resistance to radiation.

Under radiation, free radicals are produced in many chemical compounds, and the candidates for the moderator material in question (methane clathrate, water ice, solid methane) are of no exception. At low temperatures, their accumulation gives rise to the stored chemical energy in an irradiated sample as recombination of radicals is an exothermic reaction. Usually, the process of fast recombination can be stimulated by heating of the sample but under specific condition, the stored energy may be released spontaneously, with no perturbation in cooling condition [2-10]. Naturally, sudden leap of temperature in the process has an ill effect on a yield of cold neutrons from a moderator.

This phenomenon is revealed by solid methane under fast neutron radiation in temperature range 15-25K; keeping up the tradition started by J. Carpenter, the author refer to this phenomenon as "a burp" or "burping.

Keywords: Cold moderator, radicals, stored energy

Unlike solid methane, only a little is known about burping of water ice under neutron radiation. Moreover, we lack a good deal of information about kinetics of radicals in ice which is necessary to make a conclusion on possibility and conditions of burping. Nevertheless, in the paper an attempt was made to have received at least the qualitative estimate, based on the scanty experimental data and some theoretical models of fast recombination.

As to the methane clathrate, there is no information about its radiation resistance properties. But, it is evident that radicals are expected to form faster than in pure water ice, due to higher opportunities for new radical producing reactions (such as $CH_4+H_2O^+ = CH_3+ H_3O^+$ that is exothermic with a very high cross-section) and a higher yield of H-atoms from methane. Therefore, methane clathrate seems to have to be prone to burping as well but no estimate can be made until irradiation experiment on it is performed.

2. Radiation yields of radiolysis products and kinetics of radicals

Radiation yield *G* is usually defined as the number of species per 100 eV absorbed energy of radiation. Main products of radiolysis of water ice are:

Molecules: H_2O, H_2O_2, H_2, O_2;

Radicals: H , OH, HO_2, H_3O;

Ions (intermediate products): H^-, H^+, H_2O^+, H_3O^+ etc.

Many factors affect *G*-values, such as LET (linear energy transfer), isotopes contents (heavy ice is damaged less than the light one), phase state and structure (for amorphous structure, the yields are several times higher, than for crystalline structure), impurities [11-24]. Temperature of irradiation has no effect upon the primary yield of radicals (that is, just after a track) but strongly determines their concentration in the course of irradiation.

The trapped hydrogen atoms in irradiated ice have been found to react over a large temperature range; there are stabilized atoms which react slowly at 60 K, as well as atoms which react rapidly at 15 K. No hydrogen atoms are stabilized at 77K. Decay of H-atoms shows a stepwise character instead of obeying a power law like $dH/dt = k (H)^n$; along a short temperature interval kinetics can be described in the usual way with the activation energy about 1 kcal/mol (500 K) at 30 K, and 1250 K at 40-50K, see in Fig.1 [19].

The rate of decay of H-atoms is relatively low, and at 20-30 K for short time interval (several minutes or an hour) we have final yield of H almost equal to the stabilized yield 0.33.

Following is a purely phenomenological model of the radicals behavior in cold ice by S.Siegel [20]. Highly energetic electrons formed by the interaction of primary particles with electrons in the ice matrix lose the energy in discrete bursts of approximately 60-100 eV per burst. This energy first exists as collective excitation involving the entire manifold of molecules. The collective excitation then degrades into the excitation of several H_2O molecules. In their turn H_2O molecules either degrade their extra energy into heat or dissociate to form OH radicals and H atoms. The distance between successive energy-transfer bursts from the primary electrons is of the order 4000 A°. Since diffusion is relatively slow at T<77K, it is possible to consider as independent the initial events in each energy transfer site, i.e., in each spur. If an H atom is going to recombine with an OH radical, it will do so within a relatively small volume

encompassing the point of formation. The probability of the reaction will depend only upon the number of OH radicals in the volume. OH radicals become mobile only at 110 K . Their activation energy is about 60 kcal/mol, 31000 K; the kinetics of OH is not quite clear. Anyway, OH radicals remains almost untouched to 80-90K, except some losses due to H+OH and $OH+H_2O^+$ reactions.

Radiation yields of some products of H_2O radiolysis under γ-radiation are in the Table 1.

Table 1. Yields of H_2O ice radiolysis products *G*, molecules/100 eV

Primary yields, $t < 10^{-6}$ sec *):

H	OH	H_2	H_2O_2
3.6	3.6	0.45	0.8

Stabilized yields, $10^2 > t > 10^{-6}$ sec:

0.9	0.8	0.45	0.8	T=4.2K
0.33	0.8			T=77K
(0.23)	(0.4)	(0.84)	(0.86)	water, 300K

Final yields of stabilized products, t >1 hour, low doses:

0.9	0.8			T=4.2 K
0.7-0.8	0.8			T=20 K
0.4-0.5	0.8			T=30 K
0.15-0.2				T=40 K
0.05	0.6-0.8			T=77 K
0	~0.6			T=110 K
0	~0	~0.8	~1	T>120 K

*)- *t* is the time after the primary ionization.

3. Experience on burping effects in water ice

Apart of solid methane, burping (that is, fast release of stored energy) of water ice is not yet studied except only casual experience.

3.1 Burping effects in H_2O-containing ices under UV-radiation.

A great number of experiments with mixtures of ices H_2O, CO, NH_3, CH_4 to confirm the hypothesis about the origin of organic life in grains of cosmic dust clouds have been performed by astrophisicists (Greenberg, Allamandola, Pironello, Strazzula, Schutte et al. [25-29].

Experimental condition :of the experiments:

Samples - thin layers of amorphous ice , 0.0001- 0.1 mm;

Irradiation temperature - 12 K;

Dose rates - much higher than expected at ESS .

Results of the experiments those of interest for cold moderator applications, are as follows:

- For samples of any size and composition, fast release of energy and flashes of light after warming to some temperature have been observed; for compounds with a high content of water, this temperature was 27 K.
- Energy released in water ice corresponds to 2.4 % of the saturated concentration of radicals.
- No sudden, spontaneous release of energy has been observed.

3.2 Sudden release of energy in the ice moderator of the NIST reactor.

Several years ago a cold moderator of the research reactor of the National Institute of Standards has been in operation [30-31]. Without annealing, it showed burps after 3-5 days of continuous operation with released energy >1 MJ. Conditions of irradiation and burps were as following:

- (93% heavy + 7% light) water ice moderator of 16 litres volume;

- dose rate 37.5 mW/g;

- temperature of irradiation 30-50K;

- excess of temperature at a burp 70K, released energy 60J/g;

- sudden releases of energy were initiated by any small perturbation, either an increase or decrease of temperature;

- most probably, it was OH+H reaction which took place during burps. It gives critical concentration of H-atoms 0.2-0.3%.

4. Analysis of the experience with irradiation of ice.

Making correlation between radiation effects in water ice and solid methane, one can see close similarity in burping. Really, in both cases there is an upper threshold of temperature above which no spontaneous burp can occur; it is 25K for methane, and about 50K for water ice. Moreover, there is a lower limit of temperature for spontaneous burping in both cases as well, not yet rigorously defined till now. It is somewhere between 10K and 15K for methane, and 27K, or a little bit less, for ice. There below, we are trying to analyze the situation.

First statement I'd like to stress at, is that , like the case of methane discussed in [32], the process of uncontrollable release of energy in water ice is properly a propagation of the front of recombination through a sample or propagation of soliton, not thermal instability of the slug irradiated. Critical condition for a burp is not governed by Frank-Kamenetski's equation as it is often referred to [33]:

$$\frac{Q \cdot T_{act} \cdot x^2 \cdot K(T) \cdot n^2}{\lambda \cdot T^2} = 0.88, \qquad (1),$$

where λ is the thermal conductivity, Q is the molar heat of recombination, $K(T)$ is the factor of recombination rate at temperature T usually obeying Arrhenius law with "activation energy" T_{act}. That can be proved by an analysis of the experiments with thin films of ice, mentioned above. Indeed, applying Eq.(1) with x (thickness of the film) equals to 0.01 cm (the largest value in the experiments) and with other values more or less defined, we receive $K(27K) \approx 0.1\text{-}1.0\ c^{-1}$. With such large value of the factor of recombination rate, it is impossible to understand why the saturated concentration of radicals at 40 K - 50 K amounts to 0.4-0.6% as it was in NIST case.

The same one can conclude calculating Eq.(1) for Greenberg's and NIST cases, i.e., burps at 27K and 40K. Parameters x and $K(T)$ in the NIST case are both 2-3 orders of magnitude greater, whereas other parameters in Eq.(1) are almost equal for both cases. So that, at least for one of two cases Eq.(1) does not work.

The weak dependence of critical concentration upon both temperature and a size of irradiated sample proves the conception of burping as a propagation of the front of recombination through the sample after the process was ignited at one small region of appropriate size. Moreover, we are urged to take into account the effect of nonuniformity of radicals on the critical concentration value as well. For the followiing consideration, let us use the critical conditions derived in Appendix A:

Being based on the conception of a burp as a propagation of recombination front , one seemingly jumps to the conclusion that spontaneous release of stored energy takes place elsewhere below some temperature at which critical density of radicals is equal to the saturated value of radical concentration. Indeed, the latter is the fast dropping function of temperature (see Appendix B) whereas the former is almost temperature independent in some temperature range, Eqs.(5) and (5a), see Fig.2. But in fact, at very low temperatures a spontaneous release of energy was observed neither for solid methane, nor for water ice. This phenomenon is still to have to be understood. Two options are open for discussion:

- 'Hot Point' version: at very low temperatures an irradiated sample is kept supercritical, instable, but probability for the rise of a 'hot point', the initiator of the chain recombination process, is too small for the period of expectation time. This explanation seems to be realistic as, regardless of the nature of hot points, their appearence should be strong temperature controlled.
- 'Crack Recombination'-version: if consider mechanical model of recombination, the critical concentration would have steep character at low temperatures, see (5a) in Appendix *A*. This could explain the existence of the lower limit of the critical density (probably, 27 K for water ice), as easily as it was done with the hypothesis of "hot point". Thus, in (5a) $n_{crit} \to \infty$ when $\delta \to \chi$.

There is no way to choose between two hypothesis except by experimental investigations.

5. Estimation of radiation effects in ESS moderator materials (burps)

Experience with irradiation of cold ices, together with up-to-date understanding of burp mechanism, enable us but roughly and not reliably, to have predicted possible radiation effects in water ice and solid methane subjected neutron radiation of ESS conditions which are:

- temperature of irradiation: 20-100K;
- dose rate : 1.3 W/g (water), 2 W/g (methane);
- samples: a batch of beads, 2-3 mm each, in contact with neighbours and with coolant.

Let's start consideration from low irradiation temperature 20-25K. In accordance with [19], G_H is about 0.7 at 20 K, if we take into account recombination of H atoms in a short time, about half an hour after formation. So that, rate of H-atoms production is 4-5 times faster than for NIST, at a given dose rate. Accounting for the real dose rate, we have radical production at ESS ice moderator equal to ≈ 140 of that of NIST, i.e. about 0.7% per hour. The critical concentration by HP version of ignition of a burp, Eq. (5), would be less than 0.6%, because the critical concentration in the case of neutron radiation is definitely lower than for NIST, where the most part of radiation was due to gamma. It means that a critical condition would be reached within one hour. It is very probable that occurrence of the hot points would be simplified by friction of pellets with each other and with walls of the chamber, in contrast to the case of Greenberg's experiments. So that, burping in ice pellets might be expected to occur faster than each hour at irradiation temperature 20K-25K.

If CC-version of criticality condition is true, then no burp occurs, no matter how long samples were being irradiated. Actually, saturated concentration does not depend on dose rate but temperature only (see Eq.6a in Appendix B), and therefore, would be less than 2.4%, Greenberg's value for 12 K, whereas the critical one would be higher, see Fig.2.

As to Table I, production rate of radicals at 40 K is 4-5 times lower which gives more time for building up of critical concentration, that is about 3 hours. Thus, we have a satisfactory data on burps at higher temperatures, but information is insufficient for lower temperatures <30 K. Also, it seems important to know whether friction of pellets takes an effect on initiation of a burp.

A rough notion on temperature dependence of the burp expectation time is given by Fig.3. The functions in the plot were calculated with the equation:

$$\tau_{res} \approx -\frac{n_{sat} \cdot ln(1 - n_{crit} / n_{sat})}{\dot{R}} \qquad (2),$$

which is based upon the time dependence of radical concentration given by Eq.(6):

$$n(t) = n_{sat} \cdot (1 - exp(-\dot{R} \cdot t / n_{sat}) \qquad (3),$$

where $R=1.3 \cdot D \cdot G$ is the radical production rate, mol.%/hour , D is the dose rate, W/g, and G is the radiation yield of radicals. In the case of water ice, the radical production rate R strongly depends upon temperature, see Table 1. The critical concentrations were calculated with Eq.(5a), with parameters of the equation satisfying two experimental points available and assuming the $T^{1/2}$-dependence of δ upon temperature.

For the solid methane, situation is quite similar except for more properly defined the temperature limits.

6. Summary

It was shown that water ice expected to display the same effect of burping under radiation at low temperature as solid methane does. Differences would be in a temperature range where the phenomenon takes place, and in a quantity of absorbed dose needed to cause it.

7. Acknowledgements

The author is very thankful to Dr. Guenter Bauer for formulation of the problem, and to Dr. E. Roumanov who has granted the result of his work not published yet.

8. References

1. G. S. Bauer. Pulsed Neutron Source Cold Moderators Concepts, Design and Engineering. In: Proc. of the International Workshop on Cold Moderators for Pulsed Neutron Sources, Argonne, Illinois, 28 Sep.-2 Oct. 1997. ANL-Report.
2. J.Carpenter. Thermally activated release of stored chemical energy in cryogenic media. Nature, 1987, n 330, n 6146, p.358-360.
3. S. Ikeda, N.Watanabe, S.Satoh et al, In : Proc. of International Collaboration on Advanced Neutron Sources (ICANS-IX). PSI, Willigen, 1986, v.II,p.18--227
4. J.Carpenter. Cold moderator for pulsed neutron sources. In: Proc. of Intern. Workshop on Cold Neutron Sources. LANCE, Los-Alamos, US, 1990, LA-12146C. p 131-153.
5. A.A.Beljakov, V.G.Ermilov, V.L.Lomidze et al. In: Proc. of ICANS--XII, RAL Report 94--025, v.II, p.144--155
6. E.P.Shabalin, A.A.Beljakov, V.G.Ermilov, V.V.Melikhov. In: "Advanced Pulsed Neutron Sources". Proc. of PANS II, Dubna, 14-17 June 1994. JINRCommunications, Dubna,1995.
7. J.L.Jackson. Dynamic Stability of Frozen Radicals. The Journal of Chemical Physics. V.31,1959, p.154-157,p.722-730
8. E.P.Shabalin. On the Phenomenon of the Fast Release of Energy in Irradiated Solid Methane. Part I and II. JINR Communications, 1995. E17-95-141 and E17-95-142.
9. A.A.Belyakov, V.V.Melikhov, Yu.N.Pepelyoshev,E.P.Shabalin. "Solid methane cold moderator at the IBR-2 reactor". Journal of Neutron Research, Vol.3, 1996, pp. 209-221.
10. E.P.Shabalin. Consideration of the "Burp" Phenomenon in Solid Methane Accounting for Nonuniform Distribution of Irradiation Defects. In: Proc. of the Workshop on Cold Moderators for Pulsed Neutron Sources, Argonne, Illinois, ANL, 28 Sep.-2 Oct. 1997. ANL-Report
11. J. Pucheault, R. Julien. "Radiolysis by protons: dose rate and LET effects". In: Radiation Chemistry, Proc. Of the Third Tihany Symposium on Radiation Chemistry. V.I, p.1191 (1972), Akademiai Kiado, Budapest.

12. R.H. Luebbe, Jr., and J.E. Willard, J. Am. Chem. Soc. 81, 761 (1959).

13. S.Siegel and R.Remnick. The Journal of Chemical Physics, V.45, 3712 (1966)

14. H.S. Judeikis, J.M. Flournoy, and S.Siegel . The Journal of Chemical Physics, V.37, 2272 (1962)

15. R.Livingston and A.J. Weinberger. Atomic and Molecular Hydrogen Yields from Irradiated Acids. The Journal of Chemical Physics, V.33, 499-508 (1960)

16. S.J.Rzad, P.P.Infelta, J.M.Warman, and R.H.Schuler. J.Chem.Phys. 52, 3971, (1970)]

17. Proc. of the Meeting on Tunneling Reaction and Low temperature Chemistry, 1995 July. Tokai, Japan. JAERI-Conf. 95-020.

18. .S.Siegel et al. The Journal of Chemical Physics, V.34, 1782-1788 (1961).

19. J.M. Fluornoy et al. Disappearance of Trapped Hydrogen Atoms in Gamma-Irradiated Ice. J.Chem.Phys., 36, 2229 (1962).

20. S.Siegel. The Journal of Chemical Physics, V. 39, 390 (1963)

21. L.H. Piette, R.C. Rempel, H.F. Weaver, J.M. Flournoy, J. Chem. Phys., V.30, 1623 (1959)

22. S.Siegel et al. The Journal of Chemical Physics, V.34, 339 (1961)

23. Knight L.B., Steadman J. J. Chem. Phys., 1983, V78, N 10, p.5840

24. "Pulse radiolysis of crystalline D_2O at 6 K. " J.Chem. Phys. V.78, N 5 , p.2449-2455.

25. W.A.Schutte and J.M. Greenberg. Explosive desorption of icy grain mantles in dense clouds, Astronomy and Astrophysics, 244, 190-204 (1991)

26. D'Hendecourt L.B., Allamandolla L.J., Baas F., and Greenberg J.M., Astronomy and Astrophysics, 109, L12 (1982)

27. G. Strazzula et al. Astronomy and Astrophysics, V. 321, N 2, p. 618-624 (1997).

28. V. Pironello. NATO 3th Conference of the Int. School on Space Chemistry, p. 505-521 (1996).

29. Int. Conf. on Chemistry and Phys. of Molecules and Grains in Space, London, 15-17 April 1998

30. Safety Analysis report on the D2O cold neutron source for the National Bureau of Standards Reactor . NBSR 13, 1984 (revised May 1987).

31. Journal of Research of the National Institute of Standards and Technology. Jan.-Feb. 1993, V.98, N 1, p.5-6. ISSN 1044-677x.

32. E.P.Shabalin. Consideration of the "Burp" Phenomenon in Solid Methane Accounting for Nonuniform Distribution of Irradiation Defects. In: [1].

33. D.A.Frank-Kamenetski. Diffusion & Heat Transfer in Chemical Kinetics (in Russian). Moscow, "Nauka", 1969.

Appendix *A*

Following is the simple deduction of a critical condition for propagation of recombination process through a bulk. Assumed approximations are:

- radicals are distributed in a clustering way with a density of clusters being uniform, and with a concentration in a cluster n_{cl} much more than averaged concentration n;
- all radicals in a cluster recombine quickly ('quickly' means a span of time less than r^2/χ, where r_0 is the size of a cluster, and χ is the temperature conductivity coefficient) if temperature exceeds some threshold value T_{cl}.

Propagation of recombination is provided if burning of one cluster gives rise to recombinations of at least one adjacent cluster. With the assumptions given above, it gives three equations to be solved:

$$(n/n_{cl})\cdot(R/r_0)^3 = 1 \qquad (4.1)$$

(this says that inside R around the burned cluster there is one adjacent cluster),

$$(T_{cl}.- T_0.) = T(R,t) \qquad (4.2),$$

$$\partial T(R,t)/\partial t = 0 \qquad (4.3).$$

Eqs. (4.2) and (4.3) follow from a condition that transient temperature $T(R,t)+T_0$ reaches T_{cl} just at the distance R from the centre of the burned cluster. Transient temperature function was used in the form of "prescribed diffusion":

$$T(r,t) = \frac{Q n_{cl} e r_0^3}{c_p \sqrt{(4\chi t + r_0^2)^3}} exp(-r^2/(4\chi t + r_0^2))$$

where Q is the molar heat of recombination, c_p is the molar heat capacity.

After calculations we have from (4.2) and (4.3):

$$R = r_0 \cdot \sqrt[3]{\frac{Q n_{cl}}{c_p (T_{cl} - T_0)}} \qquad (4.4).$$

Finally, from (4.1) and (4.4) a fairly evident equation follows:

$$n_{crit} = \frac{2 \cdot c_p \cdot (T_{cl} - T_0)}{Q} \qquad (5).$$

This value of the critical concentration is actually the upper estimate, as clusters have a finite size, and may be separated more distantly from one another to catch up the same temperature.

The rigorous critical condition seemingly needs the terms of both the temperature conductivity coefficient and the reaction rate at T_{cl} to account for the finite time of recombination inside a cluster. But it can be shown that the condition (5) is sufficient provided the origin statement of the "flammabillity" of a cluster at the temperature T_{cl} .

The latter means that the condition $r^2 > 4\chi\tau$ should be fulfilled, where τ is the time of recombination at T_{cl} .

Another probable model of fast recombination is thought to be one that accounts for acceleration of diffusion of radicals in cracks caused by a transient temperature gradient.

A theory of fast recombination, accounting for both thermal and mechanical nature of recombination, is currently under derivation by E. Roumanov (Institute of Macrokinetics, Moscow). This model seems to be the most applicable to our case. The expression for the critical concentration of radicals appeares to be in the form

$$n_{crit} = \frac{c_p \cdot const}{Q \cdot (1 - \chi / \delta)}. \tag{5a}$$

instead of (5), where δ is a value characterizing the extent to which crack formation affects the recombination process. By physical reasons, it should slightly depend on temperature being increased with a rise of temperature.

Appendix *B*.

As it was shown in [32], concentration of radicals during irradiation is ruled by the equation:

$$\partial n/\partial t = R - K(T)\cdot n^2 - R\cdot C_1 K(T^*)\cdot n \tag{6},$$

where R is the rate of production of radicals due to ionizing radiation, $K(T)$ is the factor of recombination rate at temperature T_0 (usually, Arrhenius factor $exp\,(-T_{act}/T)$, and T^* is some effective temperature at which the radicals recombine near a track, not a transient one, $T^* \approx \Delta T + T_0$, where T_0 is the bulk temperature. For high dose rate, the third term could be greater than the second term, so as

$$n_{sat} = C_1^{-1} \cdot K^{-1}(T^*)\cdot \tag{6a}.$$

The dependence n_{sat} upon irradiation temperature T_0 has a steep character. However, at very low temperatures below 20 K, the relations (6a) would give too high concentration exceeding density of radicals inside tracks of ionizing particles. It seems unreasonable. Therefore, Eq. (6) fails to predict the real density for low temperatures, and it would be justified to consider the saturated density being temperature independent at low irradiation temperatures.

Finally, qualititave temperature dependence of the saturated density of radicals together with critical density is given in Fig.2.

ICANS-XIV The Fourteenth Meeting of the International Collaboration on Advanced Neutron Sources

April 30, 1999

Dear ICANS XIV Conference Attendee,

Enclosed please find three figures from Dr. Eugene Shabalin's paper titled "On Radiation Effects In Water Ice At Low Temperatures" that were omitted from the ICANS XIV Conference Proceedings by mistake. These pages have been numbered 506-a, 506-b and 506-c and are to be inserted in Volume II after page 506.

Sincerely,

J. M. Carpenter
ICANS XIV Conference Chair
Argonne National Laboratory

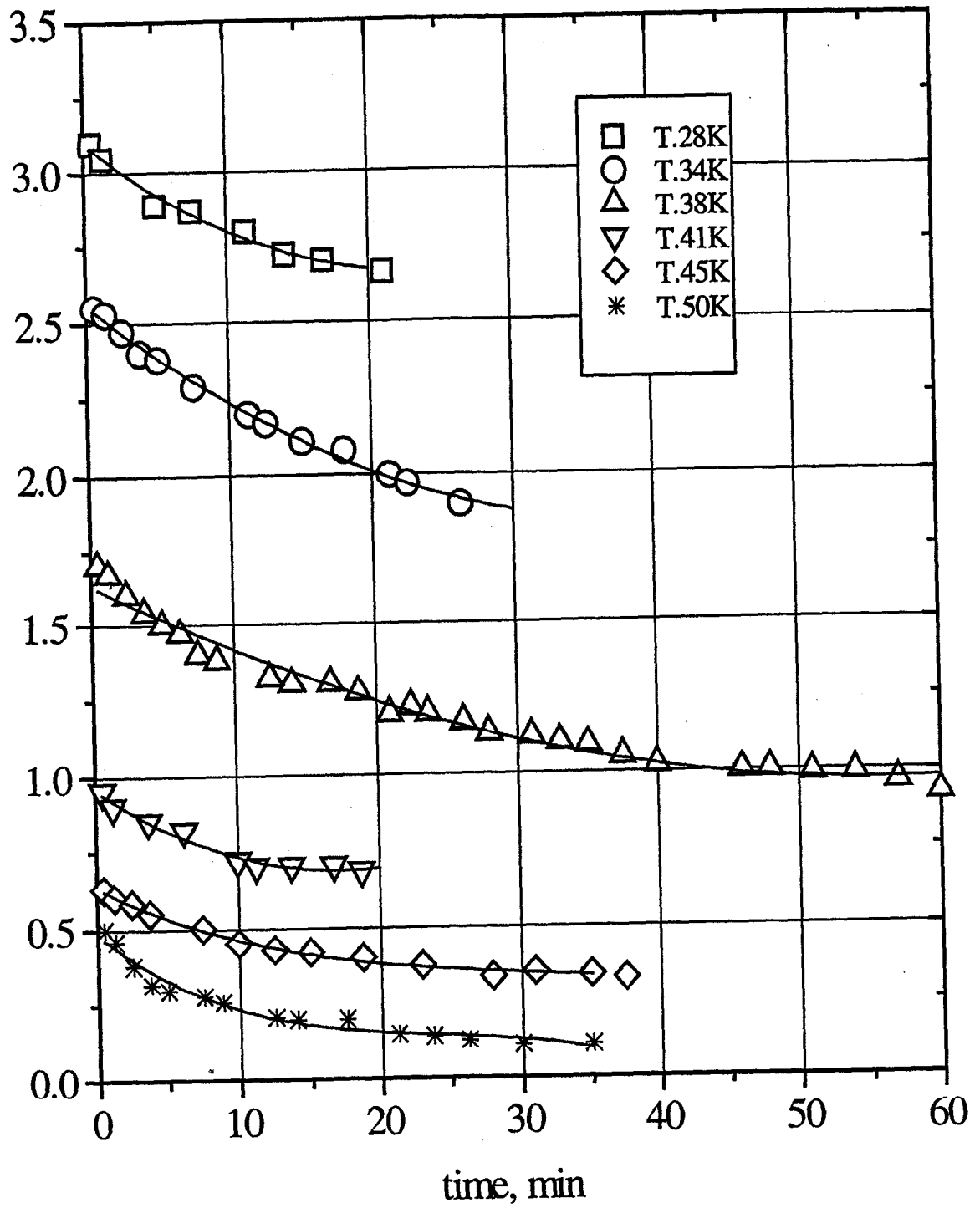

Figure 1. Disappearance of trapped H-atoms (relative concentration) in gamma-irradiated ice under isothermal conditions (see the legend for temperature); the time axis has arbitrarily been shifted to zero at the start of each isothermal measurement.

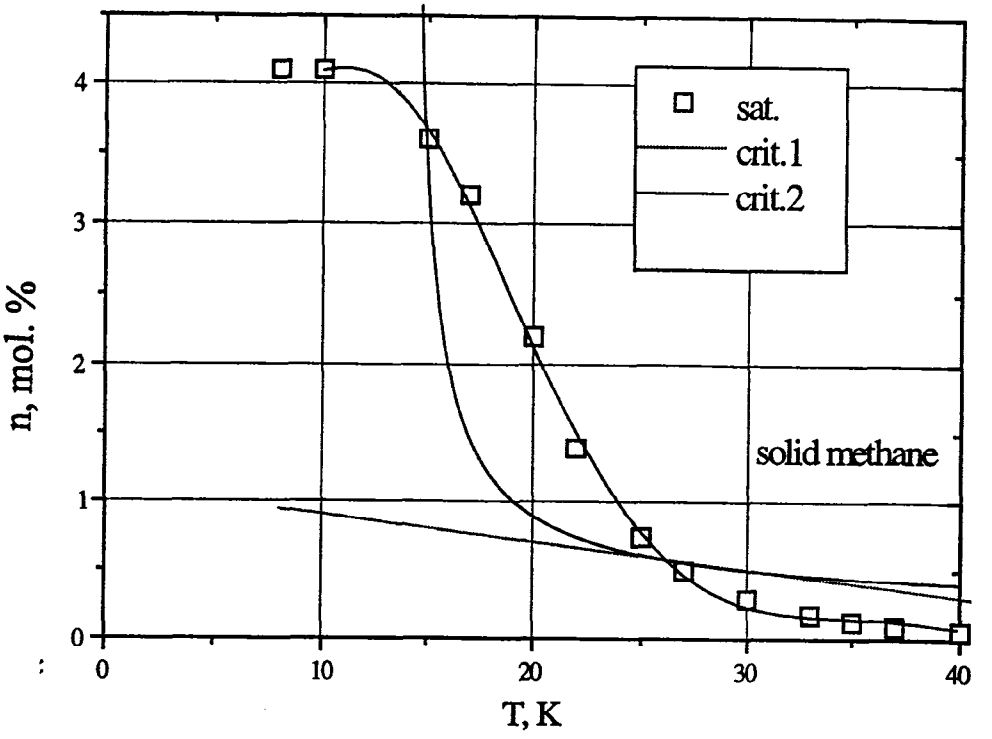

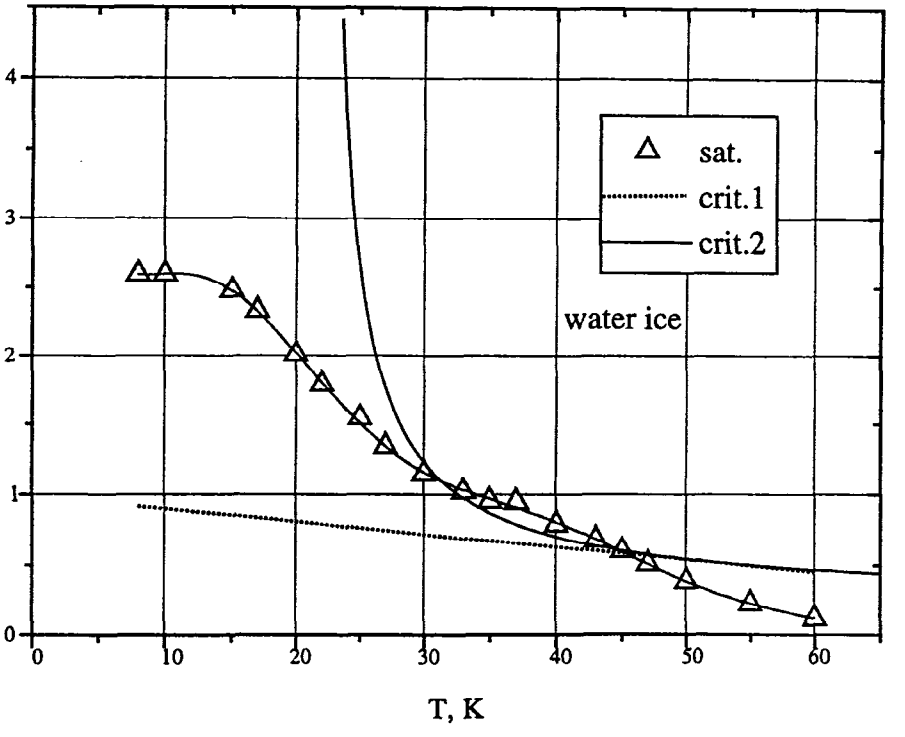

Figure 2. Irradiation temperature dependence of the concentration of radicals; "*sat*" is the saturated concentration, "*crit.*1" is the critical one to burping by Eq. (5), "*crit.* 2" is the critical one to burping by Eq. (5a). All numbers are calculated basing upon a few experimental points.

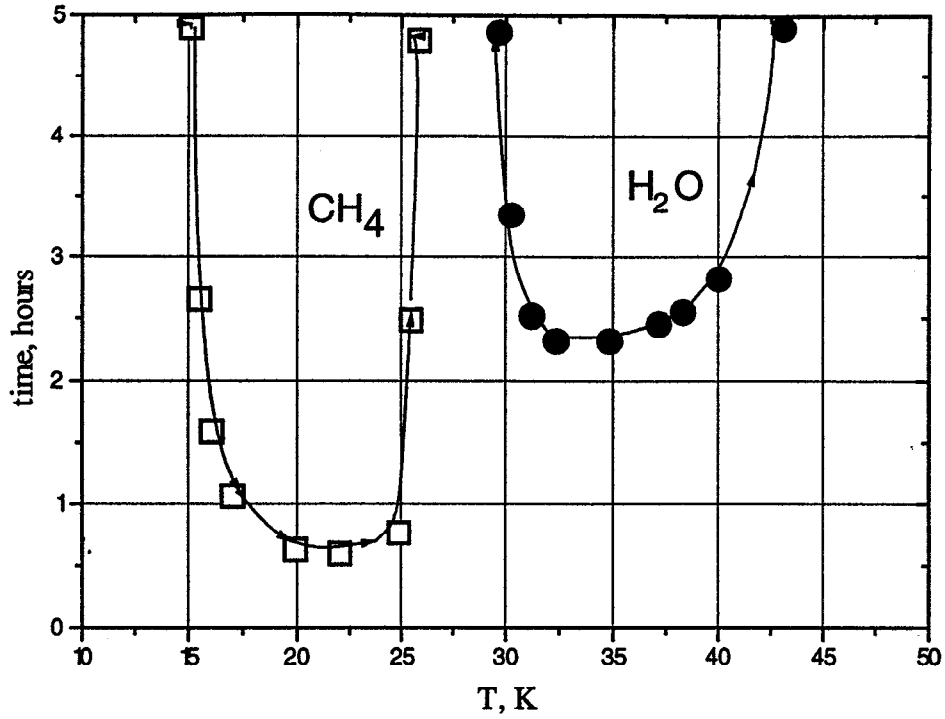

Figure 3. Estimated maximum allowable residence time of pellets in the ESS moderator versus irradiation temperature for solid methane (squares) and water ice (circles).

ICANS-XIV
14th Meeting of the International Collaboration on
Advance Neutron Sources
June 14–19, 1998
Utica, IL USA

CRYOGENIC MODERATOR SIMULATIONS: CONFRONTING REALITY

E. B. Iverson, J. M. Carpenter
Intense Pulsed Neutron Source
Argonne National Laboratory
9700 South Cass Avenue
Argonne, IL USA 60439

The Intense Pulsed Neutron Source (IPNS) at Argonne National Laboratory is a spallation neutron source dedicated to materials research. Its three cryogenic methane moderators provide twelve neutron beams to fourteen instruments and test facilities. This report concerns ongoing activities for benchmarking our Monte Carlo model of the IPNS neutron generation system.[1] This paper concentrates on the techniques (both experimental and calculational) used in such benchmarking activities.

1 IPNS Description

IPNS is a spallation neutron source in which protons are accelerated to 450 MeV and directed into a light water-cooled target composed of depleted uranium disks. A rough schematic of the target, reflector, and moderator system appears in Figure 1. The IPNS accelerator system delivers some 15 μA (time-averaged) of protons in bursts less than 100 ns long at a rate of 30 Hz. The horizontal uranium target, 250 mm long and 100 mm in diameter, is surrounded by a (vertical) graphite inner reflector 250 mm in diameter, and a beryllium outer reflector 600 mm in diameter. There are three cryogenic moderators, each decoupled from the reflector by 0.5 mm of cadmium. The "F" moderator is below the front of the uranium target (the end near the proton beam), and is composed of liquid methane (CH_4) at 100 K. The "F" moderator is 100 by 100 by 45 mm in size, and is poisoned with gadolinium 16 mm below the large faces, both of which are viewed by beam ports. The "H" moderator is above the front of the uranium target, and consists of solid methane at 30 K. The "H" moderator is also 100 by 100 by 45 mm in size, and is poisoned with gadolinium at the centerline. For both the "F" and "H" moderators, the poisoning is provided by 0.5 mm thick sheets of a gadolinium-aluminum alloy containing 17.2 weight percent gadolinium. The "C" moderator is below the rear of the uranium target, and is also solid methane at 30 K. The "C" moderator is an un-poisoned, re-entrant moderator, 100 by 100 by 80 mm, with horizontal grooves 40 mm deep and 10 mm high in the viewed face.

2 Compared Quantities

The quantities examined in benchmarking our system include the neutron energy-dependent intensity of the neutron beams and the neutron energy-dependent emission time distributions of the neutron beams. While these do not provide a complete description of the moderator's performance, such as might be required for the optimized design of a scattering instrument, these two quantities do encompass the most significant characteristics of a neutron beam.

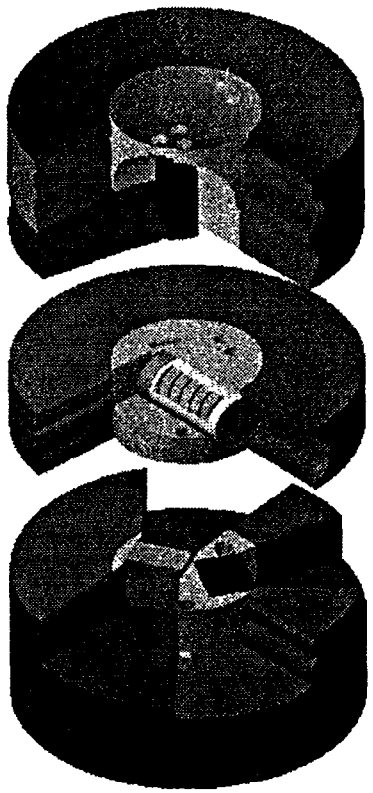

Figure 1: The IPNS target, reflector, and moderator system. Protons enter from the rear on the left in this view.

2.1 Intensity

The neutron beam intensity emitted from the moderator faces, normalized by the accelerator beam current, corresponds to what in optics terminology is a normalized "luminous intensity." This intensity is related to a measured flux;

$$i(E) = \frac{L^2}{I}\,\phi(E)|_L\,, \tag{1}$$

where $\phi(E)$ is the time-averaged flux per unit energy at a distance L far from the moderator face, and I is the time-averaged accelerator beam current. In general, the use of the luminous intensity rather than flux as a metric permits the brightness of the moderator face to be specified independently from the length of the flight path. For this metric to be useful for a re-entrant moderator such as the IPNS "C" moderator, the distance L must be either large enough that there is no significant self-shielding of the moderator face, or L must be similar to the actual distance from the real moderator to the real sample. The units of $i(E)$ are then neutrons per steradian per second per electron-Volt per micro-ampere. The commonly-quoted measure of moderator coupling effectiveness is then

$$[E \times i(E)]|_{E=1\ \mathrm{eV}}\,. \tag{2}$$

If the intensity $i(E)$ is multiplied by E, the resulting quantity is proportional to the normalized counting rate seen in a thin $1/v$ detector placed at a distance L from the moderator surface, scaled by a factor which is independent of neutron energy. Thus $E \times i(E)$ is easily compared to a time-of-flight beam intensity measurement. This quantity is calculated directly in the Monte Carlo simulations, using point detectors as

described below.

A combination of gold foil activation and time-of-flight spectrum measurements provides the absolutely normalized true intensities for the various neutron beams.[2] A low efficiency $1/v$-detector operated in a counting mode records the intensity of the neutron beam, while a cadmium-difference gold foil activation measurement (performed at the same time) provides the scale factor for the detector efficiency, and thus the absolutely normalized detector output.

The time-averaged counting rate per unit time-of-flight at time-of-flight t at the beam monitor is

$$C(t) = A\eta(E)\phi_{\mathrm{D}}(E)\frac{2E}{t} + B, \tag{3}$$

where E is the neutron energy corresponding to time-of-flight t, A is the area of the beam intercepted by the detector, η is the energy-dependent efficiency of the detector at energy E, ϕ_{D} is time-averaged flux per unit energy at the detector, and B is a steady background counting rate. For thin $1/v$-detectors (r.g., ^{3}He in ^{4}He or BF_3 in P-10), the efficiency can be expressed as

$$\eta(\lambda) = k\lambda, \tag{4}$$

where λ is the neutron wavelength corresponding to energy E, and k is a constant unique to each detector and electronic setup. Substituting Equation 4 into Equation 3, together with the de Broglie relation, gives

$$C(t) = E \times \phi_{\mathrm{D}}(E)\frac{2hkA}{mL_D} + B, \tag{5}$$

where h is Planck's constant, m is the mass of the neutron, and L_D is the length of the flight path between the moderator and the detector. We can then define an absolute efficiency (that accounts for detector geometry and position as well as intrinsic efficiency)

$$K' = \frac{2hkA}{mL_D}, \tag{6}$$

relating the flux at the detector position to the counting rate such that

$$\phi_{\mathrm{D}}(E) = \frac{C(t) - B}{EK'}. \tag{7}$$

We can modify Equation 7 to relate the flux at the foil position to the net counting rate at the detector position,

$$\phi_{\mathrm{f}}(E) = \frac{C(t) - B}{EK} = \frac{\tilde{C}(t)}{EK}, \tag{8}$$

where K is a scaled absolute efficiency

$$K = K'\frac{L_{\mathrm{f}}^2}{L_{\mathrm{D}}^2}. \tag{9}$$

Equation 8 is especially useful, as the time-averaged counting rate per unit time-of-flight $C(t)$ is easily obtained from the beam monitor, the background B is a constant at all time-of-flight values t, and the efficiency K will remain the same for any given detector, providing that the detector's configuration (e.g., discriminator setting, etc.) is not changed. In contrast, the intrinsic efficiency k is nominally provided by the manufacturer, as calculated from the cross section of the detecting medium, and its use requires knowledge of many other parameters.

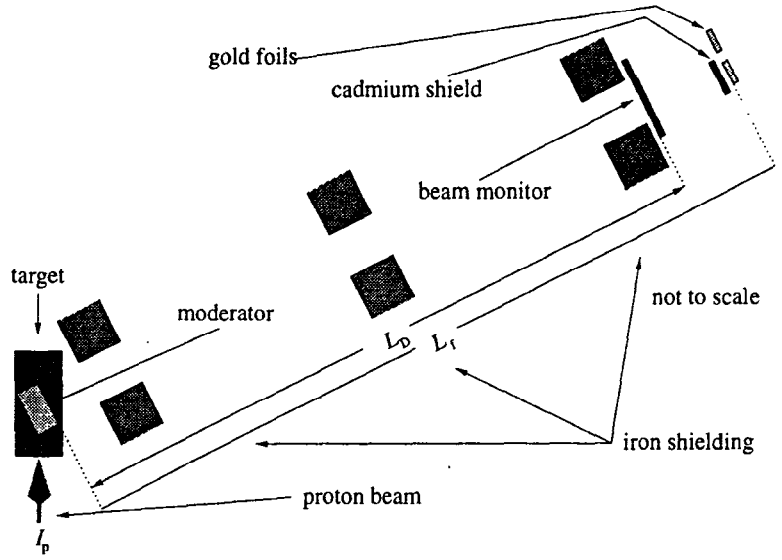

Figure 2: Experimental layout for cadmium-difference gold foil activation measurements.

To measure the efficiency K of a particular detector in a given configuration, consider a cadmium-difference gold foil activation measurement, performed downstream from this beam monitor, as in Figure 2. The neutron activation rate in the bare foil R_b is

$$R_b = N_b \int_0^\infty \sigma_{Au} \phi \, dE, \tag{10}$$

where N_b is the total number of atoms of gold in the foil and σ_{Au} is the microscopic activation cross section. For the covered foil,

$$R_c = N_c \int_0^\infty e^{-\Sigma_{Cd} s} \sigma_{Au} \phi \, dE, \tag{11}$$

where R_c and N_c apply to the covered foil, and Σ_{Cd} and s are the macroscopic total cross section and the physical thickness, respectively, for the cadmium cover. Rearranging Equations 10 and 11 and taking their difference gives

$$\frac{R_b}{N_b} - \frac{R_c}{N_c} = \int_0^\infty (1 - e^{-\Sigma_{Cd} s}) \sigma_{Au} \phi \, dE. \tag{12}$$

The quantity $(1 - e^{-\Sigma_{Cd} s})$ is very small and approximately constant at energies greater than the cadmium cutoff. If we define γ as a constant equal to the mean transmission through the cadmium cover for all energies above some energy E_1, and divide our range of integration at E_1, we have

$$\frac{R_b}{N_b} - \frac{R_c}{N_c} = \int_0^{E_1} (1 - e^{-\Sigma_{Cd} s}) \sigma_{Au} \phi \, dE + \gamma \int_{E_1}^\infty \sigma_{Au} \phi \, dE. \tag{13}$$

The second integrand in Equation 13 is from Equation 10—only the limits are different. We can therefore say

$$\begin{aligned} \frac{R_b}{N_b} - \frac{R_c}{N_c} &= \int_0^{E_1} (1 - e^{-\Sigma_{Cd} s}) \sigma_{Au} \phi \, dE - \gamma \int_0^{E_1} \sigma_{Au} \phi \, dE + \gamma \int_0^\infty \sigma_{Au} \phi \, dE \\ &= \int_0^{E_1} (1 - e^{-\Sigma_{Cd} s} - \gamma) \sigma_{Au} \phi \, dE + \gamma \frac{R_b}{N_b}. \end{aligned} \tag{14}$$

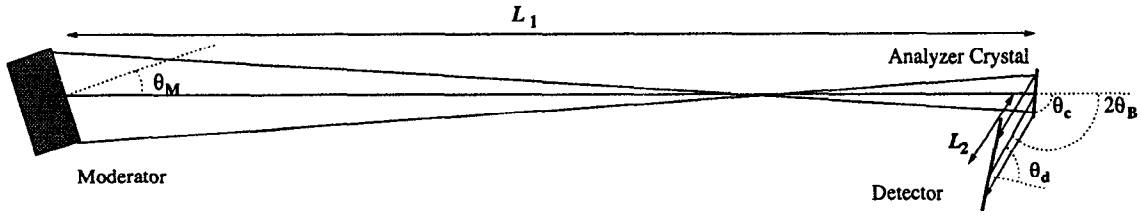

Figure 3: Experimental layout for time-focused pulse shape measurements.

Combining Equation 8 with Equation 14 and converting the integral in Equation 14 from energy to time-of-flight, then

$$\frac{R_b}{N_b}(1-\gamma) - \frac{R_c}{N_c} = \frac{2}{K}\int_{t_1}^{\infty}(1 - e^{-\Sigma_{Cd}s} - \gamma)\sigma_{Au}\frac{\tilde{C}(t)}{t}\,dt, \tag{15}$$

where the cross sections are now expressed as a function of time-of-flight, and t_1 is the time-of-flight for neutrons of energy E_1.

At very long times t, the counting rate $C(t)$ approaches B, thus allowing the upper limit of the integral in Equation 14 to be changed from ∞ to some t_2. We can now solve Equation 15 for K,

$$K = \frac{2N_cN_b}{N_cR_b(1-\gamma) - N_bR_c}\int_{t_1}^{t_2}(1 - e^{-\Sigma_{Cd}s} - \gamma)\sigma_{Au}\frac{\tilde{C}(t)}{t}\,dt. \tag{16}$$

The flux as a function of energy at the sample position can then be calculated as

$$\phi(E) = \frac{\tilde{C}(t)\left(N_cR_b(1-\gamma) - N_bR_c\right)/2N_cN_bE}{\int_{t_1}^{t_2}\sigma_{Au}(t')\frac{\tilde{C}(t')}{t'}(1-\gamma-e^{-\Sigma_{Cd}(t')s})\,dt'}, \tag{17}$$

from the counting rates $\tilde{C}(t)$ taken during the activation experiment, or from Equation 8, if using a value of K generated in a previous experiment. The cadmium-difference technique thus permits the spectrum normalization to take place even without monitor data at higher neutron energies, corresponding to time-of-flight less than t_1, where recovery from the initial prompt radiation pulse distorts the response of the detector, and where resonance effects complicate the interpretation of activation data.

The rates at which the foils are activated, R_b and R_c, are obviously equal to the saturation activity of those same foils. The saturation activity a_∞ can be determined from

$$a_\infty = \frac{a_x}{1 - e^{-\lambda_{Au}t_x}}, \tag{18}$$

where t_x is the time of exposure, λ_{Au} is the decay rate of the activation product, and a_x is the foil activity at the end of a short exposure.

2.2 Pulse Shapes

The time-dependence of the neutron emission from the moderator surface is a strong determinant of the resolution which can be achieved in any experiment involving the neutron beam. These pulse shapes have been measured, as a function of neutron energy, using a time-focused crystal analyzer system.[3,4] Figure 3 shows such a time-focused crystal analyzer.

The quantity measured in such an experiment is simply a counting rate as a function of time. A crystal reflects a series of mono-energetic pulses to a detector. The operation of the time-focused crystal analyzer is such that the dominant instrumental contribution to the resolution of the measurement is the flight time of the neutrons across a 1 mm thick crystal and their lifetime in a 1 mm thick detector. Thus, the peak shape of the counts registered in the detector matches the time distribution of the neutrons leaving the moderator surface, delayed by the known flight time of each order of reflection.

In the Monte Carlo calculations, this quantity is determined by tallying the neutrons leaving the viewed surface of the moderator as a function of time from the initial source pulse. The difference between the simulation and measurement is then limited to the minimal instrumental resolution and the flight time of the neutrons from the moderator to the detector. Unfortunately, this tally does not benefit from the use of the point detector method described below, although it does benefit from the weight windows.

Experimentally, this time distribution can be measured on a pulsed source by using a crystal analyzer to select a discrete set of neutron energies that are reflected to a detector. As in any crystal spectrometer, the mosaicity of the analyzer combines with the width and angular divergence of the beam to define the portion of phase space containing neutrons that will reach the detector. This can be represented as

$$R \sim \Delta\theta_{\mathrm{B}} \cot \theta_{\mathrm{B}}. \tag{19}$$

The challenge in making such a measurement comes about because the resolution required to accurately measure short neutron pulses (such as we see with at IPNS) implies small, tightly collimated beams, and thus low counting rates. Equation 19 indicates that the resolution can be improved (i.e., reduced) by using the spectrometer in a backscattering config-uration—as the Bragg angle θ_{B} approaches 90°, the resolution R becomes small. Unfortunately, such backscattering geometries can be somewhat difficult to use, especially when working around other dedicated instruments and associated equipment.

The backscattering analyzer can be generalized to function at other scattering angles if the correlations between scattering angle, scattering vector, and flight path lengths are accounted for and properly adjusted. Such a generalization becomes the time-focused crystal analyzer as shown in Figure 3. For a beam of transverse extent W and angular divergence α, and a crystal of mosaicity β, the variance of the resolution of such an instrument is (to first order)

$$\sigma^2 = A\alpha^2 + B\beta^2 + CW^2 + \sigma_{\mathrm{c}}^2 + \sigma_{\mathrm{d}}^2, \tag{20}$$

where A, B, and C are coefficients determined by the system geometry:

$$A = \frac{1}{v^2}\left(\frac{L_1 + L_2}{\tan\theta_{\mathrm{B}}} - L_1 \tan\theta_{\mathrm{M}} - L_2 \tan\theta_{\mathrm{d}}\right)^2, \tag{21}$$

$$B = \frac{1}{v^2 \tan^2\theta_{\mathrm{B}}}\left(L_1 + L_2 - 2L_2 \tan\theta_{\mathrm{B}} \tan\theta_{\mathrm{d}}\right)^2, \tag{22}$$

$$C = \frac{1}{3v^2}\left(\tan\theta_{\mathrm{M}} - \tan\theta_{\mathrm{c}} + \frac{\sin(2\theta_{\mathrm{B}} + \theta_{\mathrm{c}} + \theta_{\mathrm{d}})}{\cos\theta_{\mathrm{c}} \cos\theta_{\mathrm{d}}}\right)^2. \tag{23}$$

If these coefficients are set to zero, then α, β, and W can be fairly large (increasing the counting rate) without significantly impacting the instrumental resolution. Setting these terms to zero results in the following focused conditions:

$$\tan\theta_{\mathrm{M}} = \frac{1}{2}\left(1 + L_2/L_1\right)\cot\theta_{\mathrm{B}}, \tag{24}$$

$$\tan\theta_{\mathrm{d}} = \frac{1}{2}\left(1 + L_1/L_2\right)\cot\theta_{\mathrm{B}}, \tag{25}$$

$$\cot\theta_{\mathrm{c}} = \frac{\cos\theta_{\mathrm{d}} \tan\theta_{\mathrm{M}} + \sin(2\theta_{\mathrm{B}} + \theta_{\mathrm{d}})}{2\sin\theta_{\mathrm{B}} \sin(\theta_{\mathrm{B}} + \theta_{\mathrm{d}})}. \tag{26}$$

3 Simulation Methods

The simulations reported here were performed using the MCNP (version 4B)[5] and LAHET (version 2.70)[6] computer programs. These codes are extremely popular, and in general quite well validated.[7] Thus, our task is not so much benchmarking the codes as it is benchmarking our application thereof. This includes cross section data specific to cold moderator materials, the geometric model of our system, and the appropriateness and interpretation of our calculated results. These calculations were performed on an eight processor cluster of Pentium-II machines (running Linux), using MCNP's inherent support of the PVM software from Oak Ridge National Laboratory.[8]

MCNP, like any modern Monte Carlo code, has a rich selection of variance reduction features from which to chose. We employed the so-called *Weight Window* and *Point Detector* methods, described below, to speed the convergence of our calculations. Using variance reduction is absolutely essential for obtaining worthwhile estimators of cold neutron production in reasonable amounts of computer time. As an example, consider the calculation of the intensity of neutrons in a typical range of interest, say 4–14 Å. The use of these variance reduction methods speeds the calculation to a specified precision by a factor of 10^4. The MCNP4B manual describes these variance reduction methods in detail.[5] A short description of these methods appears below.

3.1 Weight Windows

Weight window variance reduction is a method of simultaneous space- and energy-dependent splitting and roulette techniques. The basic concept is that, as particles move from one region of phase space to another, more "interesting" region, they are split—i.e., replaced by multiple identical particles with the same total weight as the initial particle. These particles are then followed individually. Conversely, in the roulette instance, particles moving from one region of phase space to a *less* interesting region have some finite probability of being terminated. If the the particle survives the roulette process (the fractional probability of which is p) then its weight is multiplied by $1/p$. This process vastly increases the fraction of CPU time spent on particles in neutronically important portions of phase space, yet does not introduce a bias into the resulting calculations. The use of weight windows requires then some assessment of the importance of each region of phase space sampled within the problem. This importance function can be estimated by a skilled user, or from an adjoint multi-group calculation. MCNP also includes a very effective method for the iterative generation of the importance function.

The phase space importance function used for these calculations was constructed using this automatic generation method (called the Weight Window Generator). The importances thus calculated are subject to statistical errors, as are all quantities calculated by Monte Carlo techniques. In order to speed the convergence of the weight window generator, intermediate results were averaged for "similar" regions of geometrical space. In other words, the weight window generator might, for example, estimate the neutronic importance of several different cells, each of which was physically part of the cadmium decoupler surrounding a given moderator. When these importances are averaged, the statistical variation is smoothed somewhat, and the iterative process converges more quickly.

Finally, the resulting importance function was smoothed, in order to guarantee no severe gradients in the importance function. During the iterative process, the repeated appearance of such severe gradients in a given location indicates that adjacent regions of phase space are "too large." Breaking these regions into smaller ones, either in physical space or in energy space, results in a better importance function and a more efficient calculation.

Using a well-defined importance function can result in interesting regions of phase space (such as a viewed moderator surface between 1 meV and 1 eV) being sampled hundreds of times more frequently than they would be in a strictly analog simulation, with corresponding increases in overall computing speed.

3.2 Point Detectors

The point detector method of variance reduction is not actually a biasing of the random walks in the Monte Carlo calculation, but is instead a next event estimator. One of the great disadvantages of Monte Carlo methods is that they are intrinsically unsuited to calculating a particle flux at a given point, as opposed to averaging over a large volume. Since the production of neutron beams is essentially a low probability streaming problem, a strictly analog Monte Carlo calculation would almost never track particles in the small portion of phase space that is of interest.

If one is interested in the flux at a given location, one can instead deterministically calculate the probability that a particle at any other given point in space will contribute to the flux at that location. In MCNP, this is implemented as the point detector. At every scattering event, the transmission probability from the scattering event location to the detector location is calculated, and the point detector tally is augmented by the product of that probability and the particle's weight. Thus every single collision which takes place anywhere in the system contributes to the calculation, as opposed to only the miniscule fraction of the particles that happens to leak through the system in the correct direction.

Consider a perfectly moderating material—i.e., all scattering is inelastic, and there is no absorption. A source neutron entering this moderator has perhaps 5 MeV of energy, and will eventually leak out of the moderator. If one considers only the viewed face of the moderator, the chance that the neutron leaks out of the appropriate face is approximately 25%. Thus a tally recording all leakage through the viewed moderator face records some 0.25 contributions per source particle.

In an hydrogenous material, a 5 MeV neutron requires about twenty inelastic collisions to reach energies of 1 meV. Using a point detector, every one of those collisions contributes to the detector. Even when one considers only those scattering events below, say, 10 eV, there are a minimum of eight to ten collisions that result in desirable contributions to the tally. Once elastic collisions are included, each source particle can contribute to the tally up to twenty times or more. Thus the efficiency of the calculation per source particle increases by nearly two orders of magnitude. This increase comes at a relatively trivial cost of some ten percent or less in CPU time per source particle. This hundred-fold increase in calculation speed, when multiplied by the similar increase described above from the weight window methods, can turn a calculation that might take the better part of a year into one which will be completed in an hour with the same statistical precision.

3.3 Scattering Kernel Data

The accuracy of any Monte Carlo simulation is limited by the accuracy of the scattering kernel data used in the simulation. This is especially true in the case of under-moderated, time-dependent systems such as those we are studying. The scattering kernels of greatest importance are those for the cryogenic moderator materials. The kernels that are widely available for use with MCNP appear in Table 1, and are a part of the standard MCNP distribution. These kernels are described in greater detail elsewhere.[9] The kernels we have

Material	(K)	Material	(K)
Solid Methane	22	Liquid Methane	100
Para Hydrogen	20	Para Deuterium	20
Ortho Hydrogen	20	Ortho Deuterium	20

Table 1: Cryogenic moderator material scattering kernels available for use with MCNP.

used in these calculations are test versions of these same kernels, evaluated to somewhat higher accuracy, and at additional temperatures. These kernels are also further described elsewhere,[10] and will hopefully be

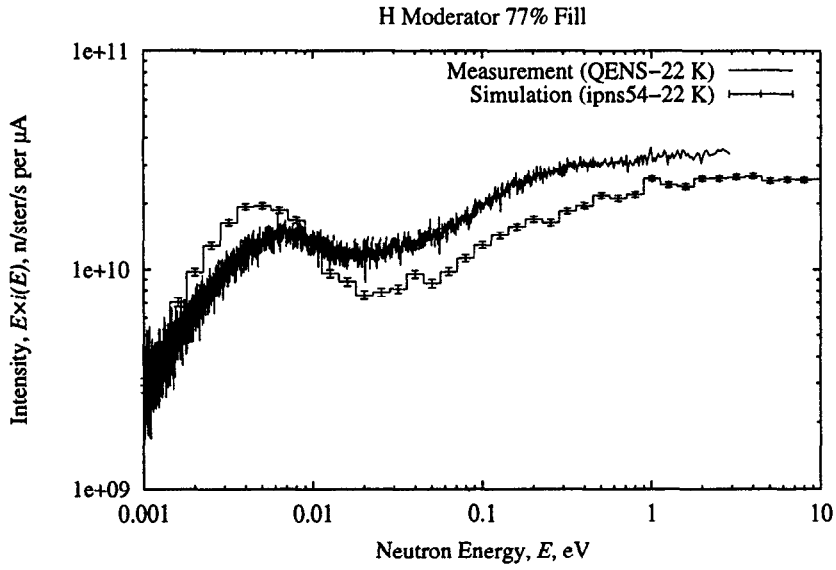

Figure 4: Absolute spectral intensity as measured on QENS from the 22 K solid methane "H" moderator.

available for general use at the time of this publication.

4 Results

We have compared the output of our Monte Carlo simulations to corresponding measurements made on the IPNS system. We have examined results from all three of the existing moderators, and we have examined both spectral intensities and wavelength/energy dependent pulse shapes. We have examined moderators composed of both liquid and solid methane, moderators with and without heterogeneous poisoning, and moderators of reentrant and non-reentrant geometries.

4.1 Spectral Intensities

We have measured the absolute spectral intensities of the neutron beams on several IPNS beam-lines. Here we will only discuss the measurements on two of these beam-lines—the QENS beam-line, viewing the solid methane "H" moderator, and the SEPD beam-line, viewing one side of the liquid methane "F" moderator. A more complete description of these measurements appears elsewhere.[11]

In the case of the solid methane moderator, the scattering kernel information used in the simulations corresponds to a temperature of 22 K, rather than the 30 K at which our solid methane moderators normally operate. With this in mind, we operated the solid methane "H" moderator at 22 K for a short time during a dedicated machine research period. The absolute spectral intensity for the QENS beam line (normal to the moderator surface), as measured at 22 K using the efficiency determined with a gold foil activation run at 30 K, is shown in Figure 4, together with the corresponding simulation results. This simulation tracked approximately 10^8 neutrons, of which some forty percent were original (spallation) source neutrons, as produced by the LAHET code following 5×10^4 450 MeV proton cascades. The point detector tally used recorded contributions not only from collisions within the moderator volume, but also from the portions of the graphite reflector which are nominally viewed through the beam line collimation, albeit perhaps after transmission through moderator and decoupler regions.

The intensity was measured over a period of approximately one hour, at an average proton current of

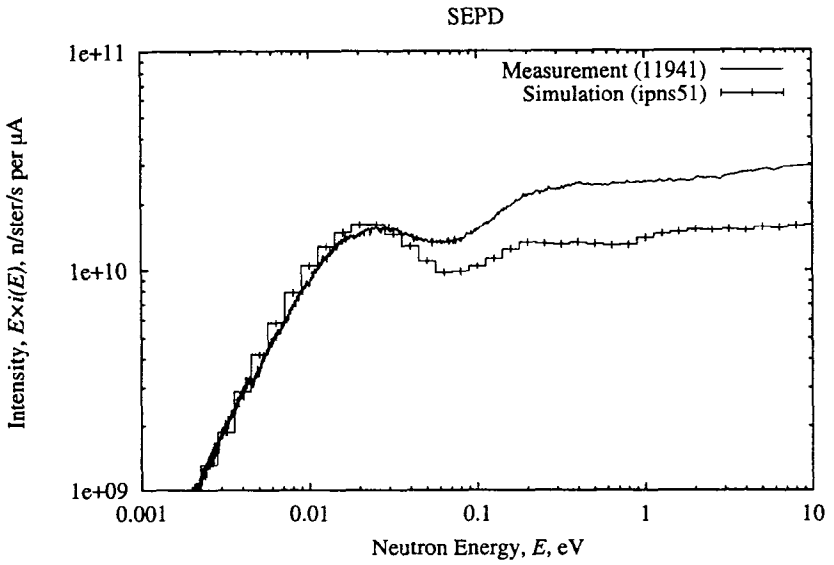

Figure 5: Absolute spectral intensity as measured on SEPD from the 100 K liquid methane "F" moderator.

12.36 μA. The measured moderator coupling is 3.3×10^{10} neutrons per steradian per second per micro-Ampere of proton current. This quantity represents the integral over the entire 100 mm by 100 mm viewed surface of the moderator. The simulation predicts a moderator coupling some 30% less than actually observed. Furthermore, the shapes of measured and simulated spectra do not match very well at all, as discussed further below. The nominal (measured) time-averaged moderator brightness at 1 eV, assuming constant proton operation at 14 μA, is 4.6×10^{13} neutrons per steradian per second per square meter.

The liquid methane "F" moderator is typically operated at 100 K, matching the temperature in the scattering kernel library. We measured the spectral intensity for the liquid methane moderator on the SEPD beam-line, normal to one side of the "F" moderator. Figure 5 shows the absolute spectral intensity as measured, again with the corresponding simulation results. These Monte Carlo results came from the same simulation as described above, tracking approximately 10^8 neutrons, as produced by the LAHET code following 5×10^4 450 MeV proton cascades and subsequent multiplication by both variance reduction methods and physical processes. This point detector tally also recorded contributions from viewed portions of the reflector as well as from the moderator volume, although the "F" moderator is distinct in that there is no reflector region immediately "behind" the moderator, as the moderator is viewed from both sides.

The intensity was measured over a period of some ninety minutes, at an average proton current of 13.95 μA. The measured moderator coupling is 2.4×10^{10} neutrons per steradian per second per micro-Ampere of proton current. As before, this quantity represents the integral over the entire 100 mm by 100 mm viewed surface of the moderator. The simulated moderator coupling and subsequent average brightness is lower than that measured by approximately 30% (1.7×10^{10} and 2.3×10^{13}, respectively). The nominal moderator brightness at 1 eV, assuming constant proton operation at 14 μA, is 3.3×10^{13} neutrons per steradian per second per square meter.

4.2 Pulse Shapes

The pulse shapes of the flat liquid methane "F" moderator, the grooved solid methane "C" moderator, and the flat solid methane "H" moderator have been measured. These measurements were performed, as de-

n	λ (Å)	E (meV)	v (km/s)
1	5.686	2.531	0.6958
3	1.895	22.78	2.087
4	1.421	40.49	2.783
5	1.137	63.27	3.479
7	0.8123	124.0	4.871
8	0.7107	162.0	5.567
9	0.6318	205.0	6.262
11	0.5169	306.2	7.654
12	0.4738	364.4	8.350
13	0.4374	427.7	9.046
15	0.3791	569.4	10.44
16	0.3554	647.8	11.13
17	0.3345	731.3	11.83
19	0.2993	913.6	13.22
20	0.2843	1012	13.92
21	0.2708	1116	14.61

Table 2: The allowed (nnn) reflections from germanium at 25 K and $2\theta = 120°$.

scribed above, using a time-focused crystal analyzer based on the (nnn) series of reflections from a cooled germanium crystal. The pulse shapes were only measured for neutron energies corresponding to these reflections at the specific scattering angle, in this case $2\theta = 120°$. Table 2 lists these reflections.

The fourth order reflection (40.49 meV neutron energy) as measured on the liquid methane "F" moderator appears in Figure 6, together with the corresponding simulation results. Space limitations prohibit the inclusion of all of the pulse shapes measured. However, one significant metric describing the neutron pulses is the pulse width. The measured pulse width as a function of neutron wavelength appears in Figure 7, and is compared to the simulated value. Note that Figure 7 does not show the often quoted full-width at half-maximum of the pulse, but rather the time width of the central eighty percent of the integrated pulse area. This metric is somewhat more robust than the FWHM for noisy pulses—the counting statistics on the measured pulses are rather poor at both extremes of the measured range, and the Monte Carlo precision is rather poor at the long-wavelength end of the range. This metric is also more sensitive to the tails of the pulses, which are poorly sampled in the simulation.

The 40.49 meV pulse shape for the solid methane "C" moderator appears in Figure 8, from both measurement and simulation. The measured pulse width for the "C" moderator as a function of neutron wavelength appears in Figure 9, and is compared to the simulated value. Finally, the pulse width from the flat, poisoned solid methane "H" moderator appears in Figure 10.

5 Discussion

The results of our simulations do, to a large extent, show strong similarity to the corresponding measurements. There are, as discussed below, some difficulties with the neutron moderation predicted in solid methane, but these difficulties are not so pervasive that we cannot use the simulation model for the optimization and analysis studies which we wish to perform. That is, we think that the calculated changes will be reliable enough to support many optimization decisions.

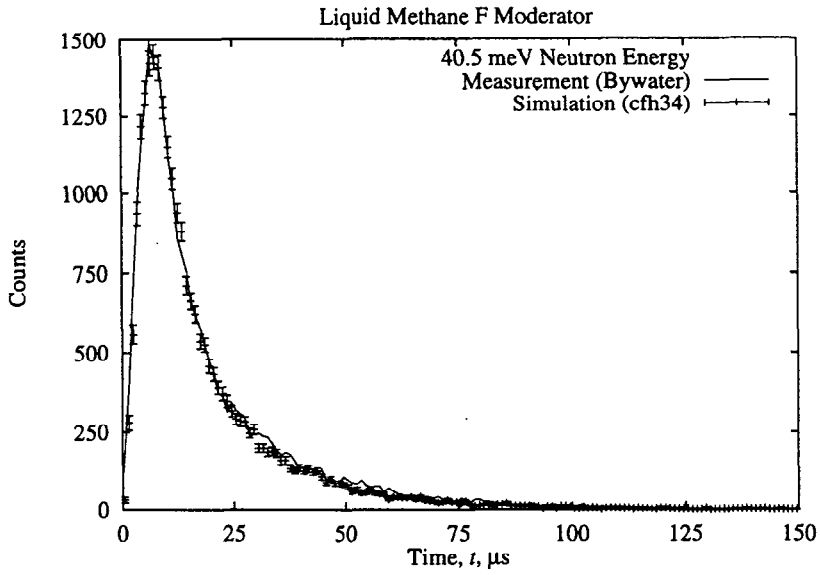

Figure 6: Time-dependent pulse shape for Ge (444) neutrons from the 100 K liquid methane "F" moderator. The line represents the measured data, while the points are the simulation results.

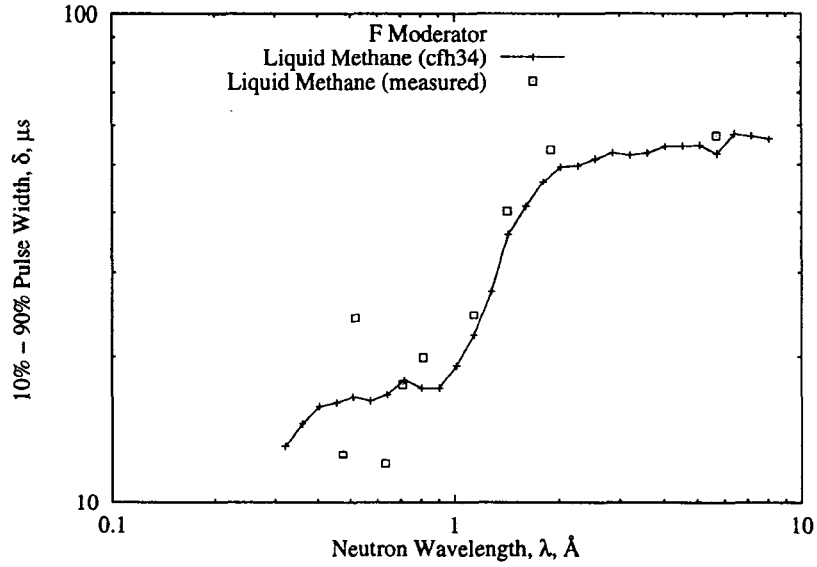

Figure 7: Pulse width as a function of neutron wavelength for the liquid methane "F" moderator.

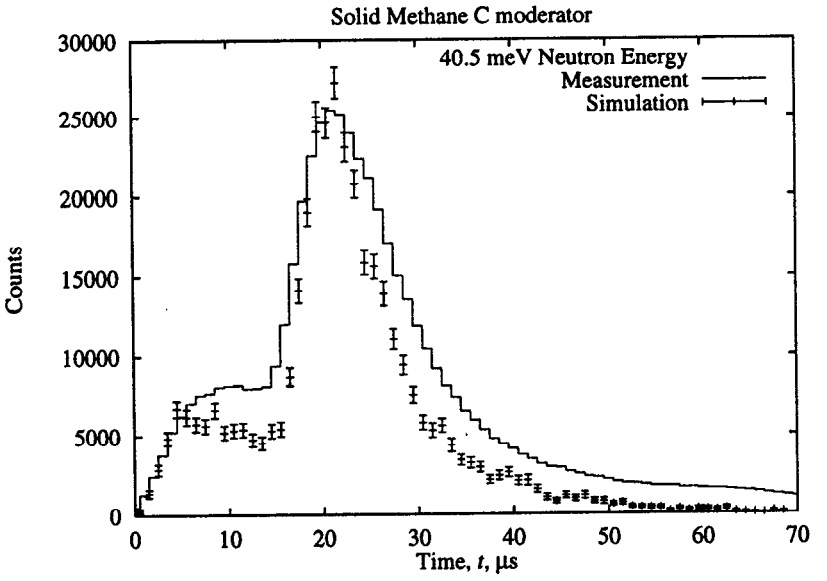

Figure 8: Time-dependent pulse shape for Ge (444) neutrons from the 30 K grooved solid methane "C" moderator.

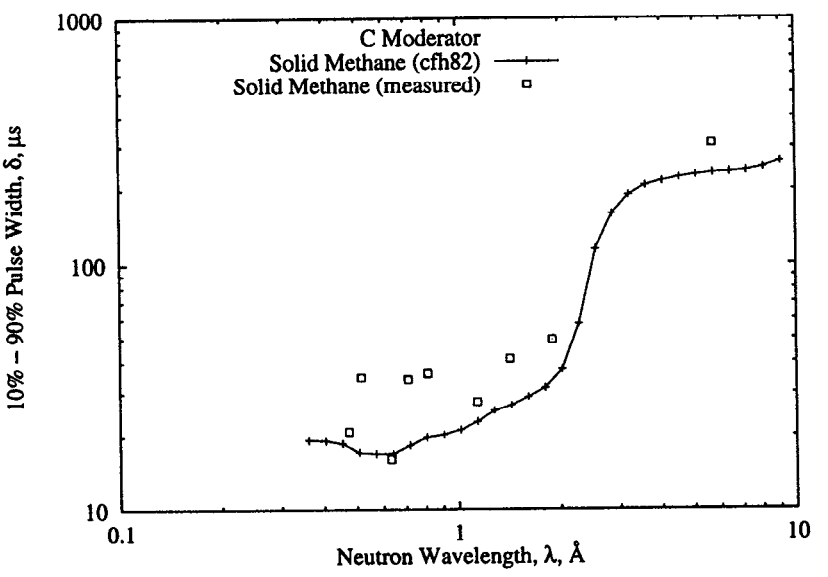

Figure 9: Pulse width as a function of neutron wavelength for the grooved solid methane "C" moderator.

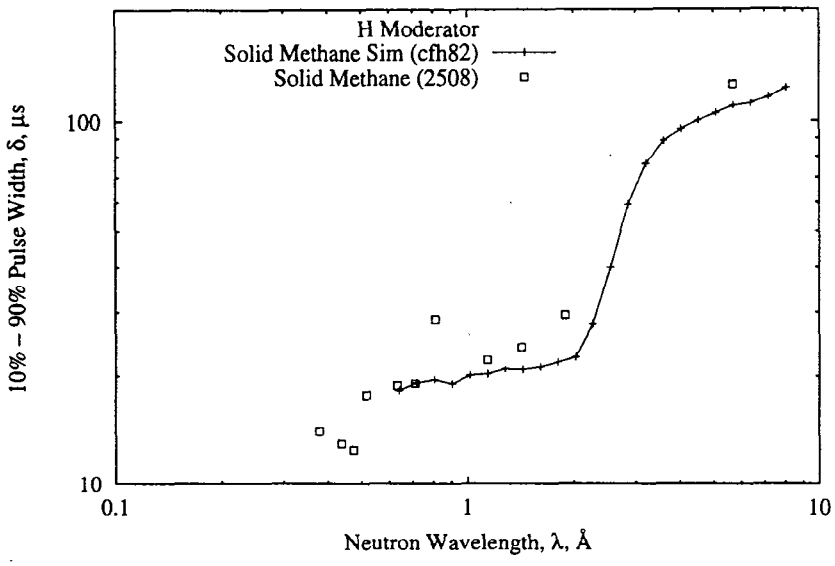

Figure 10: Pulse width as a function of neutron wavelength for the flat, poisoned solid methane "H" moderator.

5.1 Spectral Intensities

Figure 4 compares the results of simulation and measurement for the spectral intensity of the solid methane "H" moderator. While the spectrum displays many qualitative similarities, there are obvious, considerable discrepancies. The moderator coupling (the intensity at 1 eV) is under-predicted by some 30%. This is in contrast to earlier results,[1] which indicated good agreement for this parameter. The only significant aspect of the simulation which has changed in that time is a more accurate treatment of the high energy source term. Therefore, we believe that the inaccuracy in the coupling is due to flaws in the model-based calculation of neutron source term from the proton spallation on the uranium target. Similar errors have been reported elsewhere for spallation neutron production from uranium at a proton energy around 500 MeV.[12]

Furthermore, in the thermalized portion of the spectrum, there are great differences in the spectral shape. These discrepancies are so pervasive that the spectral temperature of the moderator is incorrectly estimated, as well as the actual thermal flux, as might be characterized by the thermal-to-epithermal ratio. The measured spectral temperature is approximately 4.2 meV (49 K), while the simulated spectral temperature is about 2.5 meV (29 K). Note that the maximum value of a Maxwellian in $i(E)$ when expressed as $E \times i(E)$ is located at $2k_BT$. Furthermore, the cutoff energy, defined as that energy where the flux changes from a $1/E$ behavior to a Maxwellian behavior, occurs at a significantly different energy in the simulation from that actually observed. As a result, the simulation significantly under-predicts moderator performance from 10 meV to 1 eV, the range most relevant to, say, powder diffraction and chopper spectrometer measurements, and significantly overpredicts moderator performance for cold neutrons, as relevant to quasi-elastic scattering and small-angle diffraction.

Finally, the simulated spectrum has some non-physical features, including discontinuities, below 1 eV. It is worth noting that the simulation treats the molecular scattering kernels in detail at neutron energies of 950 meV and below. The increased onset of inaccuracies and non-physical features just below 1 eV seems indicative of some problems with the scattering kernel data, coming from either inaccuracy in the molecular

description, or from discretization error in that description. The kernel is stored, in the code, as a set of equally likely final energies for each initial energy, and a set of equally likely scattering angles for each pair of energies. For this solid methane kernel, there are sixteen final energies for each incident energy, and sixty-four scattering angles for each pair of energies. The non-physical features observed are much less than those previously observed in kernels with eight energies and sixteen angles.[1]

The accuracy of the simulation of the liquid methane spectrum, as in Figure 5, is somewhat better. While the coupling and the thermal-to-epithermal ratio have discrepancies on the order of 30–50%, they offset such that the thermal flux predicted by the simulation is nearly identical to that measured. The spectral temperature is predicted very accurately. Another difficulty with the liquid methane simulation is, again, the non-physical features caused by discretization errors in the scattering kernel representation.

We previously reported[1] that the two spectra, when taken together, might indicate a possible problem in the geometric model of the system, given that the moderator coupling was accurately predicted in the case of the solid methane moderator, but not in the case of the liquid methane moderator. This no longer appears to be the case; the coupling is under-predicted by some 30–50% in each case. We feel that this is further evidence that the likely origin of the problem is the physics model for spallation in uranium at 500 MeV proton energy.

5.2 Pulse Shapes

The simulated pulse shapes from the liquid methane "F" moderator match the measured pulse shapes very well, as seen in Figure 6. Similarly, the pulse widths as shown in Figure 7 seem to behave very similarly.

The solid methane simulations were not so successful. There are significant differences in the relative heights of the the bimodal peak from the grooved moderator, as seen in Figure 8. The under-prediction of the height of the earlier peak (from the tips of the moderator fins) also results in an under-prediction of total pulse width. Examination of Figure 9 clearly shows that the solid methane simulation consistently under-predicts observed pulse widths by 30% to 40% over all wavelengths. On a more positive note, the rise time of the pulse appears to be accurately predicted. This is quite important for many instruments, as the resolving power of the instrument is largely determined by the sharpness of that rise time, as opposed to the total width of the pulse. The under-prediction of pulse widths is also seen for the flat solid methane "H" moderator in Figure 10, although not as severely as for the grooved moderator.

It is further obvious that the selection of neutron wavelengths at which the pulse shape was measured is not well matched to the physics of the solid methane system. The sharp increase in pulse width, corresponding to the increasing importance of the storage term in the pulse shape as the neutrons come into thermal equilibrium with the moderator material, is very inconveniently located in the exact range that is not measured at all in the germanium (nnn) series of reflections through $2\theta = 120°$. These measurements should be repeated for a set of wavelengths that will better match the characteristics of the solid methane moderators.

6 Conclusions

The Monte Carlo simulation of the methane moderators at IPNS shows clear difficulties with the solid methane scattering kernel as implemented with the MCNP computer code. These problems take the form of significant errors in the spectral temperature, intensity, and pulse shapes of the moderated neutron flux. These errors are not as severe in the liquid methane simulations. Furthermore, the simulations show a consistent under-prediction of the neutron production rate from the target, matching previous observations from the literature.

While these discrepancies are significant enough to warrant serious attention, we do believe that the comparison between the measurements and the simulations is good enough that we can consider our simulation model useful for some aspects of the target, moderator, and reflector system—e.g., target design, reflector material, moderator position. For studies involving detailed study of neutron moderation in solid methane,

however, our model requires further development and testing. The model will be more valuable for observing trends and making optimizations, certainly, than it will for making absolute predictions.

One avenue for further testing involves comparison of the scattering kernel used in the simulations to a scattering kernel actually measured on an inelastic neutron spectrometer. We propose that such measurements be undertaken over a wide range of Q- and ω-space for solid methane at the temperature used in the development of the simulation data. Such a program of measurements could further be extended to cover novel moderator materials, as well as conventional moderator materials at a wider range of temperature and pressure conditions than has been considered previously.

Finally, some of the measurements used for these comparisons should be extended. While the intensity measurements appear to be satisfactory, the pulse shape measurements, using this particular crystal analyzer arrangement, do not have sufficiently dense wavelength coverage. The germanium (nnn) series used reflects an adequate selection of wavelengths for the liquid methane moderators, but not for the solid methane moderators, as no reflections exist in the critical region between two and five angstroms where the pulse width changes most rapidly.

References

[1] E. B. Iverson and J. M. Carpenter. Benchmarking simulation methods for methane moderators. In John M. Carpenter and Erik B. Iverson, editors, *Proceedings of the International Workshop on Cold Moderators for Pulsed Neutron Sources*. OECD, 1998.

[2] E. B. Iverson, J. M. Carpenter, and E. J. Hill. Cold neutron beams at the Intense Pulsed Neutron Source. *Physica B*, 241–243:33–35, 1998.

[3] K. F Graham and J. M. Carpenter. Pulsed moderator studies using a time focussed crystal spectrometer. *Nuclear Instruments and Methods*, 85:163–171, 1970.

[4] Russel Lee Bywater, Jr. Neutron emission-time distributions of methane moderators at the Argonne National Laboratory Intense Pulsed Neutron Source. Master's thesis, Iowa State University, August 1989.

[5] Editor Judith F. Briesmeister. *MCNP—A General Monte Carlo N-Particle Transport Code*. Los Alamos National Laboratory, March 1997. Version 4B.

[6] Richard E. Prael and Henry Lichtenstein. *User Guide to LCS: the LAHET Code System*. Los Alamos National Laboratory, September 1989.

[7] John S. Hendricks and John D. Court. MCNP4B^{TM} verification and validation. Technical Report LA-13181, Los Alamos National Laboratory, August 1996.

[8] Al Geist, Adam Beguelin, Jack Dongarra, Weicheng Jiang, Robert Mancheck, and Vaidy Sunderam. PVM 3 User's Guide and Reference Manual. Technical Report ORNL/TM-12187, Oak Ridge National Laboratory, September 1994.

[9] R. E. MacFarlane. New thermal neutron scattring files for ENDF/B-VI release 2. Technical Report LA-12639-MS, Los Alamos National Laboratory, August 1994.

[10] G. J. Russell and R. E. MacFarlane. Report of the Working Group on scattering kernels and cross sections. In John M. Carpenter and Erik B. Iverson, editors, *Proceedings of the International Workshop on Cold Moderators for Pulsed Neutron Sources*. OECD, 1998.

[11] E. B. Iverson, J. M. Carpenter, and E. J. Hill. Absolute beam intensity measurements at the Intense Pulsed Neutron Source. In John M. Carpenter and Erik B. Iverson, editors, *Proceedings of the International Workshop on Cold Moderators for Pulsed Neutron Sources*. OECD, 1998.

[12] Bruce W. Patton, Gary J. Russell, James S. Gilmore, Phillip D. Ferguson, John D. Court, and Eric J. Pitcher. Benchmarking of the fertile to fissile conversion FERFICON water bath experiments: Integral n/p measurements. In *Topical Meeting on Nuclear Applications of Accelerator Technology*, pages 229–234. American Nuclear Society, November 1997.

ICANS XIV
14th Meeting of the International Collaboration
on Advanced Neutron Sources
June 14–19, 1998
Starved Rock Lodge, Utica, IL, USA

USE OF A COLD BERYLLIUM REFLECTOR-FILTER TO ENHANCE COLD SOURCE BRIGHTNESS AT LONG WAVELENGTHS

Eric J. Pitcher, Gary J. Russell, and Phillip D. Ferguson

Manuel Lujan, Jr. Neutron Scattering Center, Los Alamos National Laboratory, USA

ABSTRACT

Use of a cold beryllium reflector-filter to enhance cold source brightness at long wavelengths is a decades-old concept, yet it has never been implemented at any spallation source facility. Experimental investigations of its efficacy have met with limited success. Our calculations indicate that it provides a 47% boost in long-wavelength (>4 Å) brightness on a short-pulse source, while a gain factor of 1.57 is realized on a long-pulse source. Finally, calculations indicate that there is negligible benefit to its implementation on a steady-state source.

1 Introduction

The potential efficacy of a cold Be reflector-filter to enhance cold source brightness at long wavelengths has been recognized for decades. The concept takes advantage of the Bragg edge in the Be scattering cross section at 5 meV (see Figure 1). Above 5 meV, the cross section is 6.4 b. Just below 5 meV, the cross section depends on the Be temperature. At room temperature, it is 0.5 b. By cooling the Be to 77 K, the cross section drops by nearly two orders of magnitude to 8 mb, such that it is highly transparent to low-energy neutrons. At this temperature, the mean-free path of a 4-meV neutron is approximately 10 m, whereas a 7-meV neutron has a 9-mm mean-free path. Thus placement of a thick slab of 77-K Be at the emission surface of a cold moderator will reflect neutrons with energies greater than 5 meV back into the moderator while transmitting neutrons below this energy. The reflected neutrons then have another opportunity to downscatter to lower energy prior to escaping the moderator again. In this way the long-wavelength source brightness may be significantly enhanced.

Several experiments have been carried out to evaluate the effectiveness of a Be reflector-filter.[1,2] Carpenter, et al.,[1] measured the energy spectrum of a coupled, liquid hydrogen

moderator with and without a warm (300 K), 3.8-cm-thick, Be reflector-filter in place. Unfortunately, their measurements of flux were not absolute and so no conclusion about long-wavelength gain as a result of using the reflector-filter can be drawn. However, the reflector-filter did add considerable structure to the spectrum, and shows the reflector-filter configuration to have a 2-meV-to-1-eV flux ratio that is perhaps 30% greater than that of the unfiltered configuration.

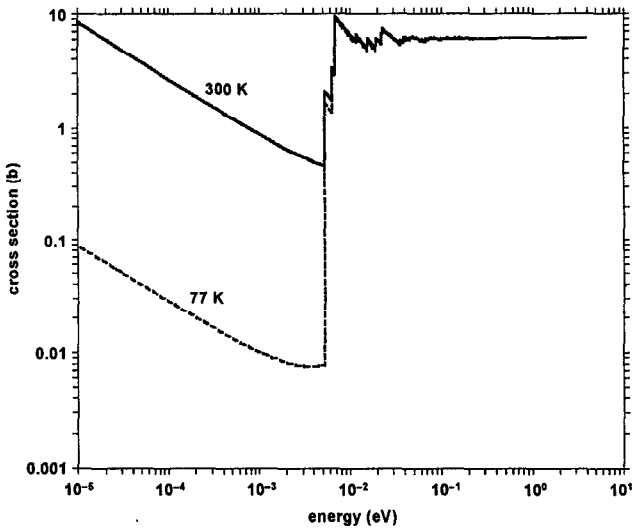

Figure 1. Total cross section of beryllium at 77 and 300 K.

Kiyanagi, et al.,[2] have measured experimentally the effect of a cold Be reflector-filter on a coupled liquid hydrogen moderator. Their experimental configuration utilized a 12×12×5-cm^3 moderator, a 2-cm-thick polyethylene premoderator, and a graphite reflector. The 1.5-cm-thick Be reflector-filter was attached directly to the hydrogen moderator so that its temperature was presumably 20 K. They measured no significant gain in the long-wavelength region due to the presence of the reflector-filter.

2 Analysis

A scattering kernel for 77-K beryllium was recently produced, allowing us to numerically analyze the performance of a cold Be reflector-filter on a variety of cold sources. Using the LAHET Code System,[3] we have investigated its efficacy on three types of sources: a short-pulse source, a long-pulse source, and a steady-state source.

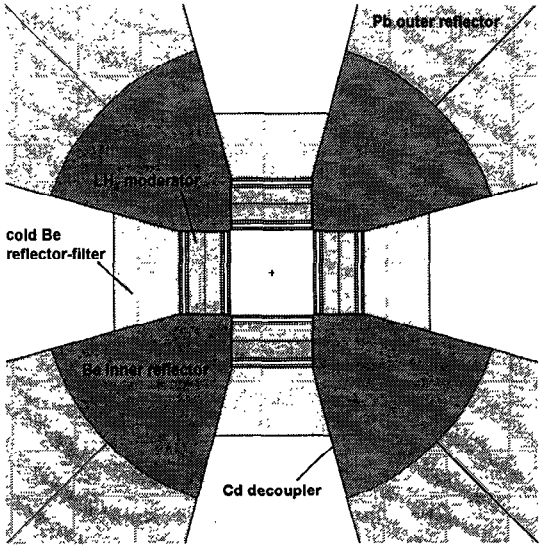

Figure 2. Short-pulse source configuration.

2.1 Short-Pulse Source Performance

We evaluated the performance of a cold Be reflector-filter installed on decoupled liquid hydrogen moderators arranged in flux-trap geometry. The decoupled moderator system chosen for this study is shown in Figure 2. The unpoisoned moderators are 12×12×5 cm^3 in size and decoupled by 0.081 cm of Cd. The flight paths have angular openings of 15° and are lined with 0.081-cm-thick Cd. The hydrogen composition is assumed to be 90% para-, 10% ortho-hydrogen. The inner reflector is room-temperature beryllium with a 70-cm diameter and height. The outer reflector is lead.

The reflector-filter thickness was varied and the source brightness, integrated below 5-meV energy, was calculated. Results are plotted in Figure 3. They show the long-wavelength brightness is 47% greater with a 10-cm reflector-filter than without one. Spectra for the unfiltered and 6-cm-thick reflector-filter configurations are plotted in Figure 4. Considerable structure is evident in the filtered case, due to reflection of neutrons with energies below 4 Å. Significant enhancement in the long-wavelength flux is also apparent. Plotted in Figure 5 is the wavelength-dependent ratio of the source brightness for these two cases. The magnitude of the dip in the ratio around 3 Å depends strongly on the reflector-filter thickness; some enhancement in the 2- to 3.5-Å range with a small penalty in long-wavelength gain may be realized by simply making the reflector-filter thinner. Because of the close proximity of the reflector-filter

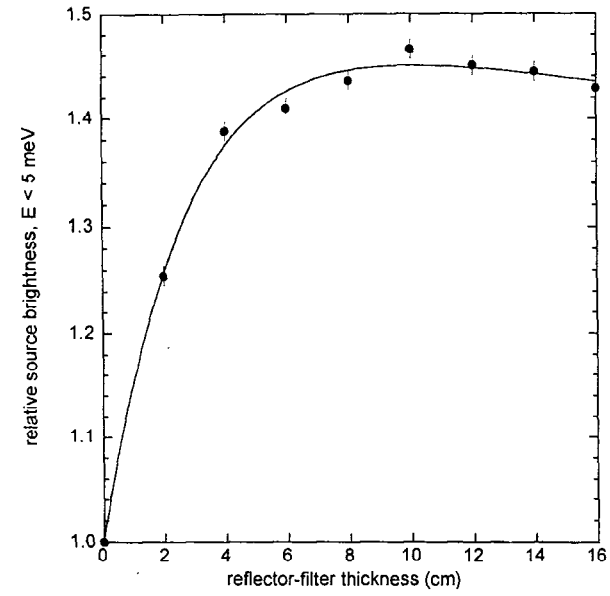

Figure 3. Relative source brightness (E < 5 meV) on a short-pulse source as a function of reflector-filter thickness.

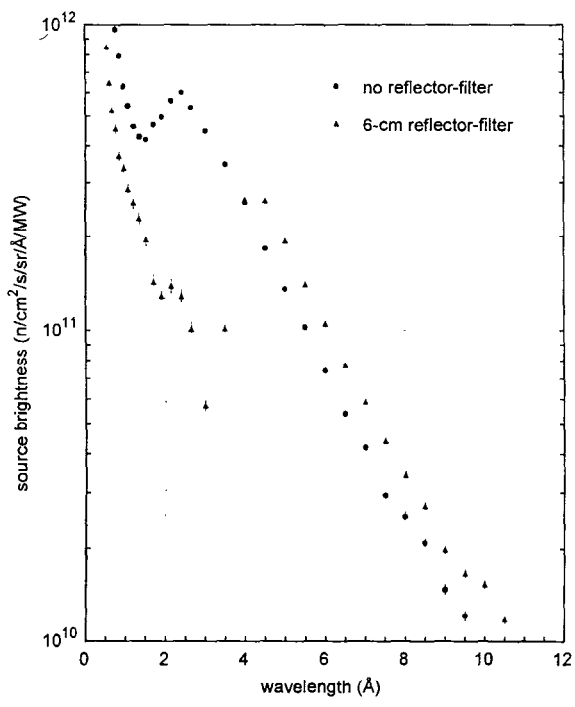

Figure 4. Wavelength-dependent source brightness of an unfiltered and filtered LH_2 moderator on a short-pulse source.

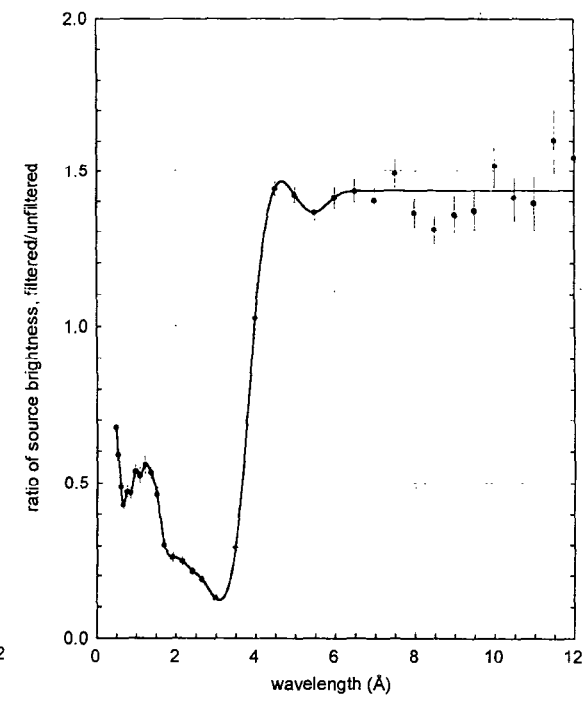

Figure 5. Ratio of source brightness for a decoupled LH_2 moderator with a 6-cm reflector-filter relative to an unfiltered one.

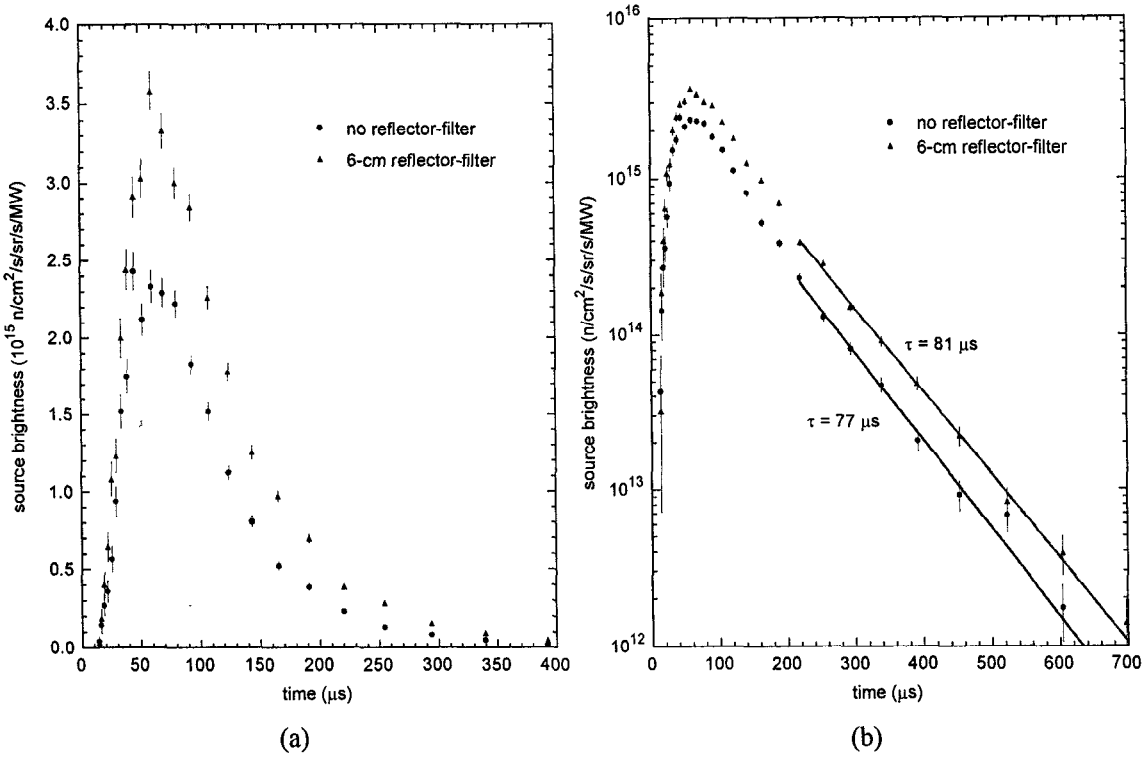

Figure 6. Time-dependent source brightness for filtered and unfiltered, decoupled LH_2 moderators, plotted on (a) linear, and (b) logarithmic time scales.

to the moderator, the enhancement in long-wavelength brightness occurs at early times in the neutron pulse, as shown in Figure 6. As seen in this figure, the decay time constants for the two cases are nearly the same.

2.2 Long-Pulse Source Performance

For evaluating the performance of a reflector-filter on a long-pulse source, we used the traditional wing moderator geometry, shown in Figure 7. The average source brightness was calculated from the four leakage surfaces of two wing moderators, one upper and one lower. The moderators are 12×12×8 cm^3 in size and composed of 90% para-, 10% ortho-hydrogen. They are coupled to a warm beryllium inner reflector with a 70-cm diameter and height, surrounded by a lead outer reflector. The inner and outer reflectors are decoupled by 0.081 cm of cadmium.

The same analysis was performed for this coupled moderator system as was performed for the decoupled moderator system. Relative integral source brightness (E < 5 meV) is plotted as a function of reflector-filter thickness in Figure 8. The long-wavelength brightness peaks at a reflector-filter thickness of 18 cm, where it is 57% brighter than the unfiltered case. Spectra for these two configurations are plotted in Figure 9, and the ratio of the spectra is shown in Figure 10. The epithermal flux in the filtered case is about half that of the unfiltered case. The high-energy portion of the Maxwellian peak of neutrons moderated in the 77-K Be can be seen between 1 and 2 Å. This feature is not observed in the flux trap geometry of the decoupled system, where the reflector filter is not strongly

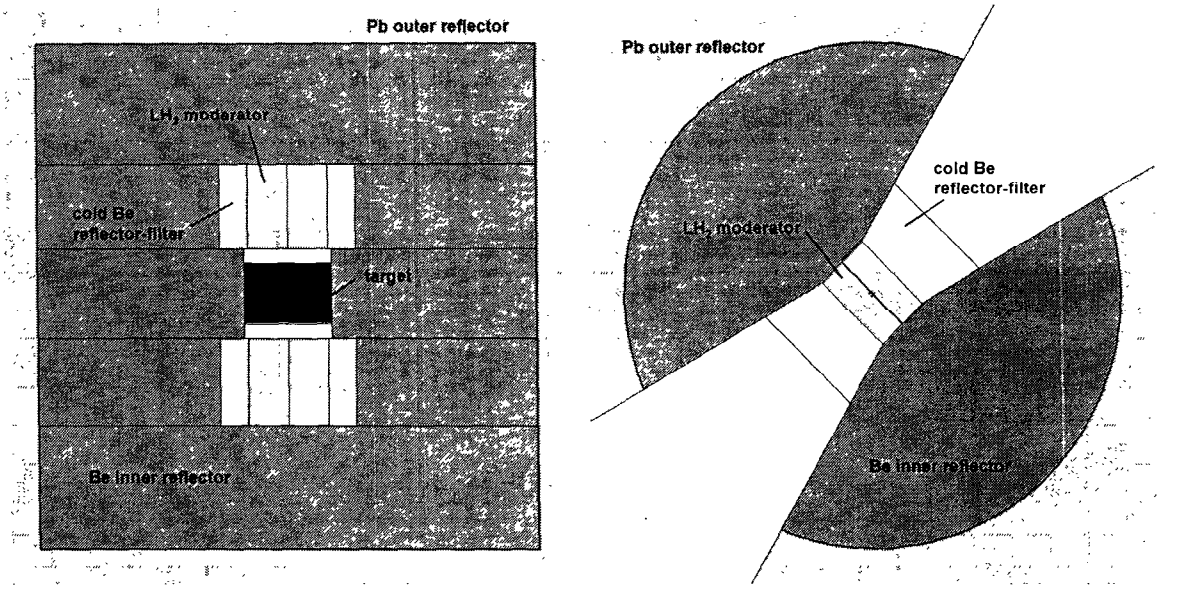

(a) (b)

Figure 7. Long-pulse source geometry: (a) vertical slice through center of moderators; (b) horizontal slice through upper wing moderator.

coupled to the target. For the wing moderator geometry, however, the reflector-filter is fed directly by the target and this is the source of the peak at ~1.5 Å. Reflection of neutrons with energies just below 4 Å is clearly evident in the lower flux of the filtered case. Significant enhancement in the long-wavelength flux is also apparent. As in the decoupled moderator system, the gain in long-wavelength brightness occurs within the peak of the neutron pulse, and not in the tail, as can be seen in Figure 11, where the time-dependent source brightness is plotted for both cases.

2.3 Steady-State Source Performance

The geometry chosen to represent a steady-state source was a lead target immersed in a 2-m-diameter by 2-m-high tank of heavy water (see Figure 12). A liquid deuterium (90% para, 10% ortho) moderator, 30 cm in diameter and 35 cm long, has its center located 42.5 cm from the proton beam centerline. Off the cylindrical surface of the moderator and perpendicular to the proton beamline is an 8-cm-wide by 12-cm-high flight path. A cold Be reflector-filter is placed directly on the moderator's cylindrical surface.

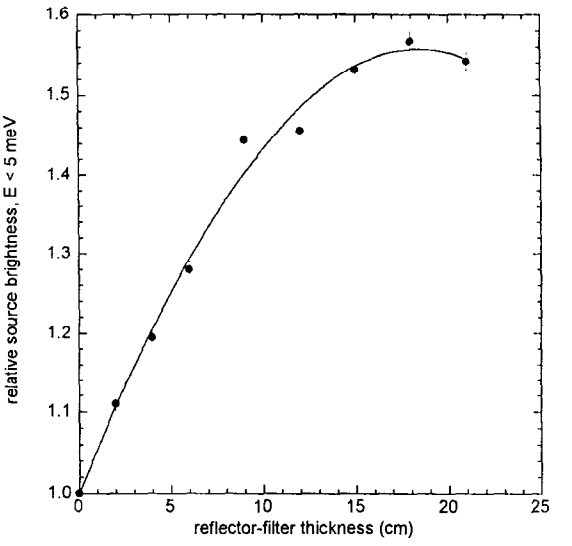

Figure 8. Relative source brightness (E < 5 meV) as a function of reflector-filter thickness for a coupled LH_2 moderator in wing geometry.

The dependence of the long-wavelength (>4 Å) source brightness on reflector-filter

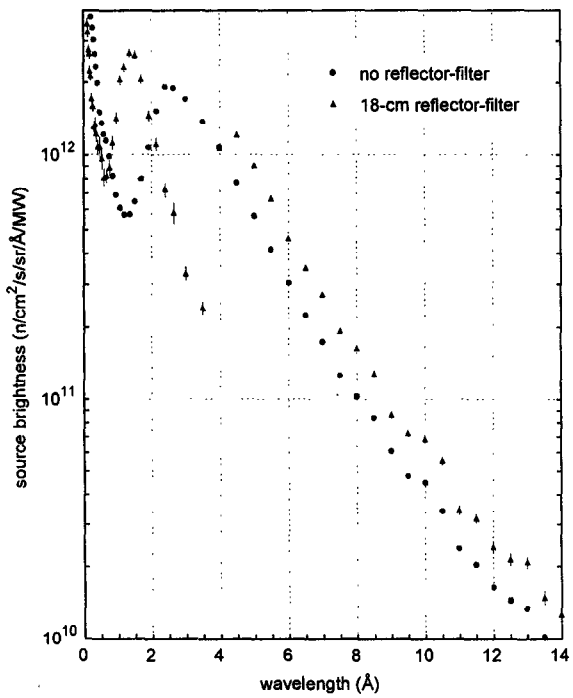

Figure 9. Source brightness as a function of wavelength for a coupled LH_2 moderator in wing geometry with and without an 18-cm reflector-filter.

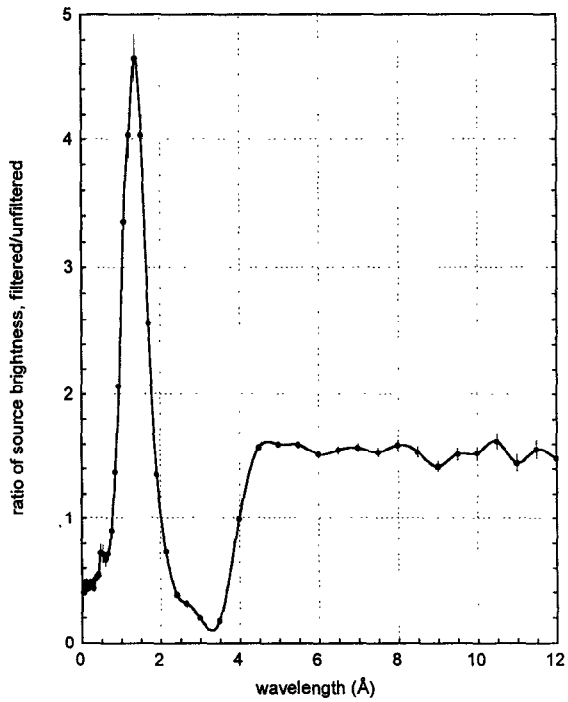

Figure 10. Source brightness as a function of wavelength for a coupled LH_2 moderator in wing geometry with an 18-cm reflector-filter relative to an unfiltered moderator.

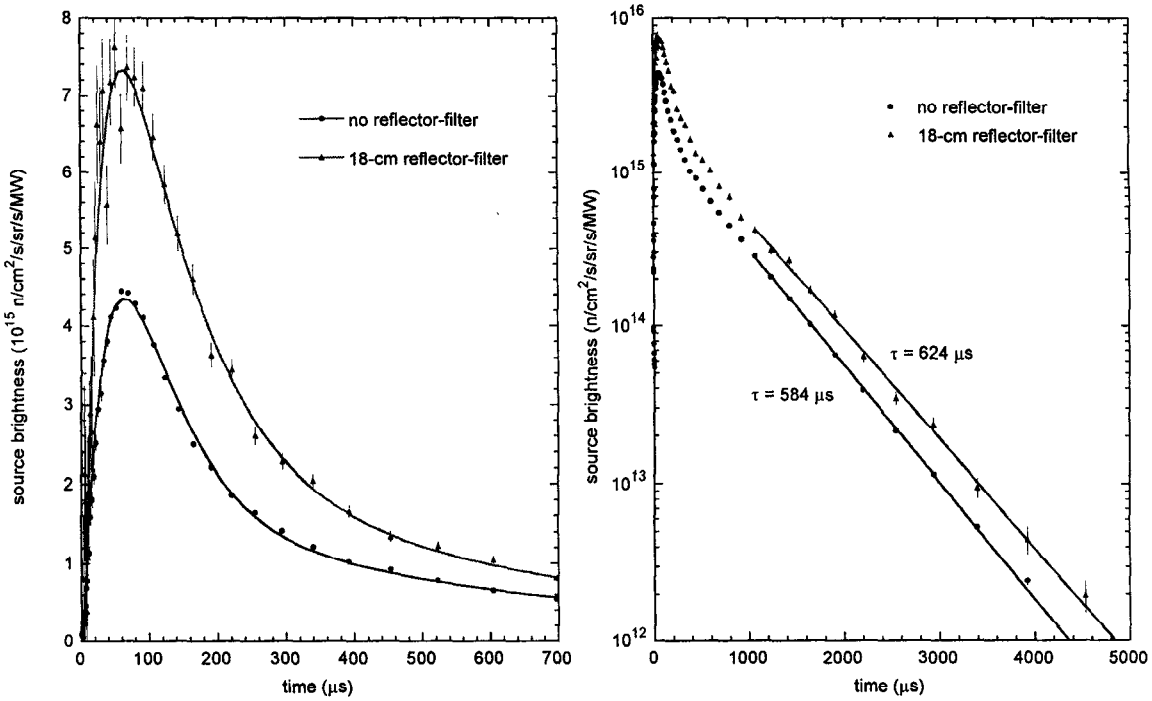

Figure 11. Time-dependent source brightness for a coupled LH_2 moderator in wing geometry with and without an 18-cm reflector-filter, plotted on (a) linear, and (b) logarithmic time scales.

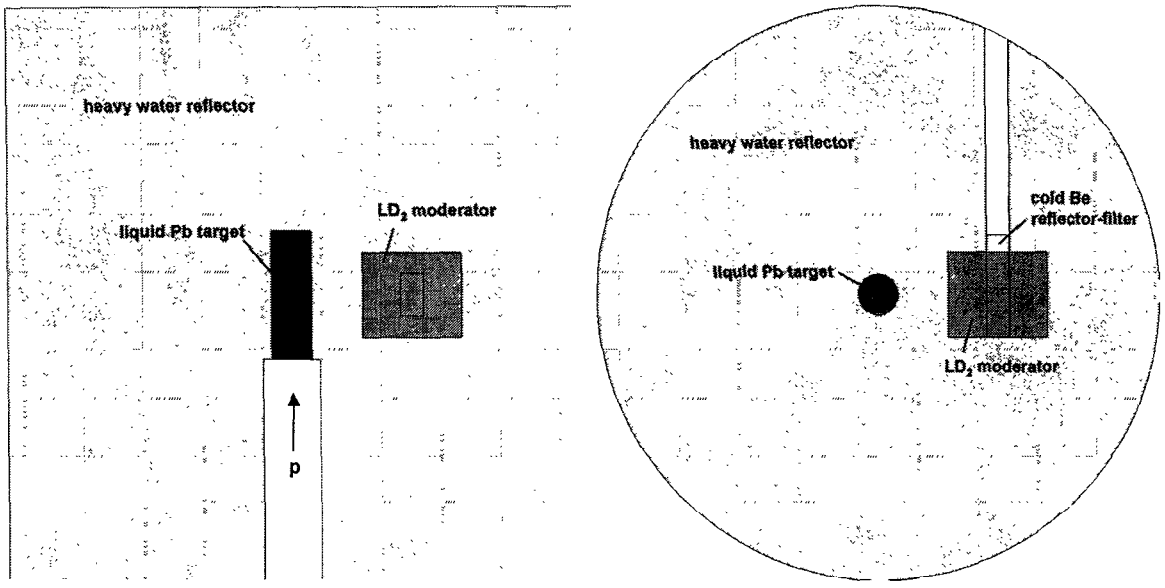

(a) (b)

Figure 12. Steady-state source geometry: (a) vertical slice through proton beam centerline; (b) horizontal slice through the central axis of the moderator.

thickness is plotted in Figure 13. It shows that there is almost no gain to be derived by using a reflector-filter in this geometry. Figure 14 shows the wavelength-dependent source brightness with and without a 6-cm reflector-filter. Again, the lack of any enhancement in the long-wavelength region is evident. From these results, it is clear that the presence of the flight path does not significantly perturb the neutron flux at the moderator leakage surface; hence, there is no benefit in using a reflector-filter in this configuration.

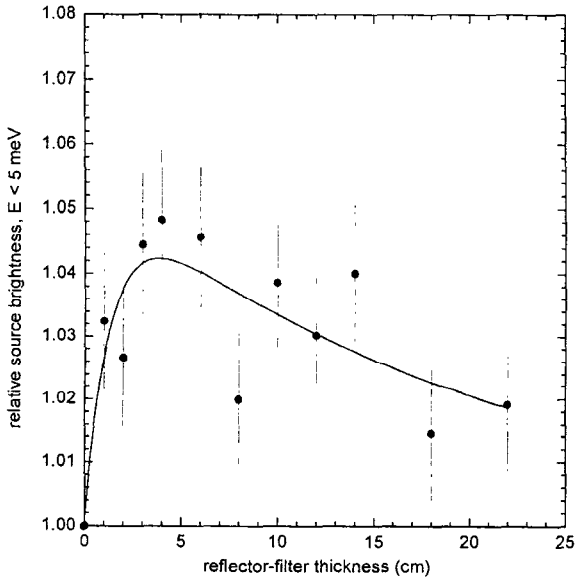

Figure 13. Low-energy (< 5 meV) relative source brightness as a function of reflector-filter thickness for a steady-state source.

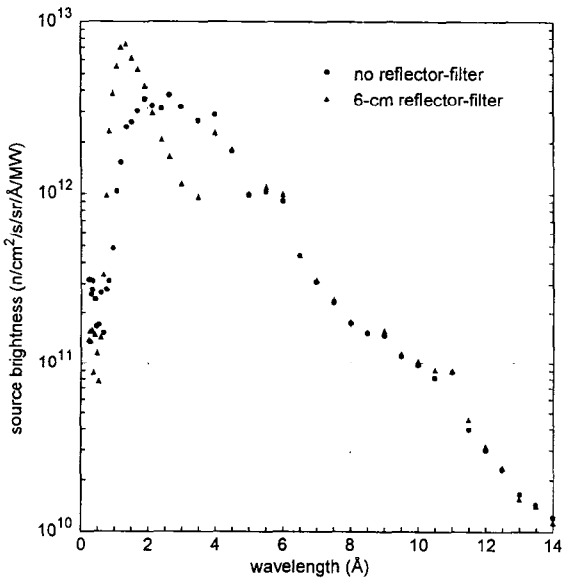

Figure 14. Spectra for a steady-state source with and without a 6-cm reflector-filter.

3 Conclusion

Simulations of various pulsed sources indicate that a cold Be reflector-filter can be effective in boosting the long-wavelength brightness of cold sources on both short- and long-pulsed sources by as much as 57%. Though not reported here, cursory calculations indicate that the magnitude of this gain may depend on the relative concentrations of ortho- and para-hydrogen, with higher ortho-hydrogen concentrations deriving a greater benefit from the use of a cold Be reflector-filter (all results reported here used a 10% ortho-hydrogen fraction). Calculations indicate that only marginal gains (~4%) in long-wavelength (>4 Å) source brightness may be realized by using a cold Be reflector-filter on a steady-state source.

4 References

[1] J. M. Carpenter, R. Kleb, T. A. Postol, R. H. Stefiuk, and D. F. R. Mildner, Nuc. Instr. Meth. **189** (1981) 405-501. Also see references 12 and 13 therein.

[1] Y. Kiyanagi, Y. Ogawa, N. Kosugi, H. Iwasa, M. Furusaka, and N. Watanabe, "Further Optimization of Coupled Liquid-Hydrogen Moderator for Intense Pulse Neutron Source," Proceedings of the 13th Meeting of the International Collaboration on Advanced Neutron Sources, September 11-14, 1995, Villigen, Switzerland.

[1] R. E. Prael and H. Lichtenstein, "User Guide to LCS: The LAHET Code System," LA-UR–89-3014, September, 1989.

ICANS XIV
14th Meeting of the International Collaboration on
Advanced Neutron Sources
June 14-19, 1998
Starved Rock Lodge, Utica, IL

THERMAL NEUTRON SCATTERING KERNELS FOR MODERATOR MATERIALS: COMPARISON OF *NJOY* RESULTS FROM A SYNTHETIC MODEL AND ITS STANDARD LIBRARY

M.M. Sbaffoni[2], V.H. Gillette[1], M.E. Pepe[2] and J.R. Granada[1*]

Comisión Nacional de Energía Atómica
[1]Centro Atómico Bariloche and Instituto Balseiro
[2]Centro Atómico Constituyentes
ARGENTINA

ABSTRACT

The Synthetic Scattering Function (SSF) allows a simple description of the incoherent interaction of slow neutrons with hydrogeneous materials. The main advantages of this model reside in the analytical expressions that it produces for double-differential cross sections, energy-transfer kernels, and total cross sections, which in turn permit the fast evaluation of neutron scattering and transport properties.

We have included the SSF routines into the NJOY code, in such a way that the cross sections can be generated with the same format either from its standard library or from our synthetic model.

In this work we briefly discuss the basic features of the SSF, some details of its implementation into NJOY, and a few examples of results obtained using those two options.

* Also at CONICET, Argentina.

1. INTRODUCTION

The scattering function $S(Q,\omega)$ is the central quantity to describe the interaction of thermal neutrons with condensed matter, as it contains all the dynamical and structural information about a scattering system [1]. First-principles theories were developed in the past to evaluate the scattering function, most of them based on the essentially exact Zemach-Glauber formalism [2], but the resulting expressions are usually not quite amenable for calculation.

In practice, and as far as neutron moderators are concerned, the compromise solution adopted in standard Nuclear Data Libraries involves the inclusion of scattering laws for a few common moderators at some selected temperatures, and data for any different material or physical condition must be 'constructed' from pieces of information actually corresponding to those few cases found in the existing files.

Those aspects were part of the main motivations for the development of a 'Synthetic Scattering Function' $T(Q,\omega;E_0)$ [3], which incorporates the main dynamical characteristics of the molecular unit, still retaining a high degree of simplicity in its formulation. The characteristic features of the synthetic model have been recently reviewed [4], and we will just briefly discuss here some of its basic hypotheses and approximations.

2. THE MODEL

The synthetic scattering function has been developed to the extent of producing analytic forms for a variety of magnitudes [3,5], and their accuracy have been verified in a number of cases [6].

The incoherent double-differential scattering cross section of a molecular unit is written, in terms of the synthetic model, as [3]

$$\frac{\partial^2\sigma}{\partial\Omega\,\partial E}=\sum_i^N n_i\frac{\sigma_b^i}{4\pi}T^i(\vec{Q},\omega,E_0)\ , \tag{1}$$

where N is the number of dynamically nonequivalent atomic species, and n_i represents the number of atoms of each equivalent atomic species with a bound scattering cross section σ_b. Finally, $T(\vec{Q},\omega,E_0)$ stands for the basic expression of the Synthetic Scattering Function (SSF):

$$T(\vec{Q},\omega,E_0)=\frac{k}{k_0}\left[S_{0,\tau_0,\Gamma}(\vec{Q},\omega)-\sum_{\lambda,\pm}^{m}C_{\lambda,\pm}\frac{\partial}{\partial\Gamma}S_{\mu_0,\tau_0,\Gamma}(\vec{Q}_{\lambda,\pm},\omega_{\lambda,\pm})\right]\ , \tag{2}$$

where k_0 and k denote the modulus of incident and scattered neutron wave vectors, respectively, $\vec{Q}=\vec{k}_0-\vec{k}$ and $\hbar\omega=E_0-E$ are the momentum and energy exchanged in the collision process. $S_{\mu_0,\tau_0,\Gamma}(\vec{Q},\omega)$ is the scattering law for the neutron interaction with a quasi-rigid molecule, and the second term on the right-hand side of Eq.(2) is a corrective one which accounts for processes where the neutron exchanges energy with the m internal modes of the atomic species, by creating or annihilating one phonon. The summation over inelastic processes is performed under the assumption that the internal modes are represented by Einstein oscillators, each with eigenfrequency ω_λ, and effective mass M_λ.

The quantities μ_0 , τ_0 and Γ represent the effective mass, temperature and vibrational factor, respectively, that the scattering nucleus would present in the interaction, and they depend explicitly on the incident neutron energy E_0. In this manner, a kind of envelope represents the combined effect of the quantum excitations of the system's internal modes. Under those conditions, $S_{\mu_0,\tau_0,\Gamma}(\vec{Q},\omega)$ may be written as

$$S_{\mu_0,\tau_0,\Gamma}(\vec{Q},\omega) = \left[\frac{\mu_0}{2\pi\ \hbar^2 Q^2 k_B \tau_0}\right]^{0.5} \exp\left[-\left(\hbar\omega - \frac{\hbar^2 Q^2}{2\,\mu_0}\right)^2 \left(\frac{\mu_0}{2\hbar^2 Q^2 k_B \tau_0}\right) - \Gamma\,\frac{\hbar^2 Q^2}{2}\right] . \quad (3)$$

The reduced number of input parameters required for the SSF and the analytic character of the derived expressions, make this formalism a powerful and practical tool for describing the slow neutron - molecule interaction. In particular, it provides in a straightforward manner analytic expressions for the scattering kernels,

$$\sigma(E_0,E) = \int_{4\pi} \frac{\partial^2 \sigma}{\partial\Omega\,\partial E} d\Omega \quad (4)$$

the total scattering cross section

$$\sigma(E_0) = \int_0^\infty \int_{4\pi} \frac{\partial^2 \sigma}{\partial\Omega\,\partial E} d\Omega\, dE \quad . \quad (5)$$

and the energy-transfer kernels [7-9]

$$\sigma_n(E_0,E) = \int_{4\pi} \frac{\partial^2 \sigma}{\partial\Omega\,\partial E} \cos^n(\theta)\, d\Omega \quad . \quad (6)$$

3. MODIFICATIONS TO THE *NJOY* CODE

In this section we briefly describe the modifications to NJOY in order to include the SSF formalism as an optional way to calculate cross sections for moderator materials.

The NJOY (94.105 version) code [10] received from RSIC was installed, as a test, on different platforms (PC, Sun Ultra with -r8 option, and Silicon Graphics). All the work presented here was done in a Sun-Ultra Spark 170 machine, with Solaris 2.5 operative system, and Fortran 77.

NJOY calculates the cross sections for moderators through two ways:

- Free-gas theory
- Calculation of the scattering matrix from the scattering law S(α,β) (calculated previously with LEAPR module) supplied in the ENDF/B-VI library.

The free-gas theory is not applicable to all the situations, while the scattering functions are available only for selected materials and temperatures, thus restricting the possibilities of nuclear data preparation to those cases.

The SSF formalism was written as a set of computer routines, which were tested through a range of application examples that involved the evaluation of neutron cross sections and thermalization properties of several moderator materials. Following the recommendations made at a recent meeting [11], we decided to tackle the problem of implementing the SSF into NJOY (94.105) as a third option to calculate cross sections for moderator materials.

Up to now, SSF input data sets are available for light and heavy water, liquid hydrogen (ortho and para), methane, glycerol, polyethylene, plexiglass, dodecane, TBP, benzene, dowtherm, metallic hydrides, but the data base will be extended in the future to other materials.

The main modifications were introduced in the THERMR module (subroutines CALCEM and SIGL, and function SIG), where new subroutines were added, adapting the formalism of the synthetic model to the NJOY system.

When NJOY calculates scattering kernels from the scattering function (iinc = 4) the initial energy grid is internally fixed (58 groups), and the final energy grid is calculated in an adaptively way, from the data provided in the $S(\alpha,\beta)$ tape. If the SSF is used (iinc = 5), the same grid of initial energies is adopted, and the same adaptive process is used for final energies determination, but from a fixed and extended grid of energy transfer (β). It consists of approximately 400 points, defined according to the values presented in ENDF/B-VI for the available moderators. The results obtained using that fixed extended grid for all the moderator materials, and using a specific one for each element were found to be in very good agreement.

Input modifications for the THERMR module:

→ In card 2, a new option for IINC was implemented. If IINC is equal to 5, the program will use the "Synthetic Scattering Module" (MODEL Subroutine) to compute the total cross section and the energy-transfer kernels.

→ In this case, new data are needed, which are given in card 5.

The first parameter (**I0**) indicates which material will be treated:

The meaning of the second and third parameters (**I1 and I2**), depends on the material , because different routines might be used for different cases. For example, in the liquid hydrogen case, I1 can take the values 1, 2, or 3 if it is ortho-hydrogen, para-hydrogen or a mix of both materials, and I2 is read only in the case of I1.eq.3 giving the percentage of ortho-hydrogen in the mix. In any other case I1 indicates the type of cross section to be calculated, and I2 specify if the data will be for a molecule or for a single atom or atom family.

4. A FEW TYPICAL RESULTS

Applications of the SSF to a variety of hydrogeneous systems were presented in the past [12], where different magnitudes were predicted and compared with available experimental data or previous theoretical results.

In this work we present NJOY results for thermal neutron scattering kernels and total cross sections of water and methane, obtained from both its original ENDF/B-VI.2 library and the Synthetic Model formalism integrated in our modified version of the code.

4.1 Water at 300 K

We wanted to begin our comparison by looking at a classic –yet complex- system: room temperature water. As far as the SSF is concerned, its predictions for thermal cross sections and diffusion parameters have been comprehensively discussed and compared with existing information [4,6].

The Table 1 contains the input data for the Synthetic Model corresponding to hydrogen in water at 300 K. This set was adopted after a thorough analysis of measured frequency spectra with particular consideration of the internal modes' weights, especially for the low frequency part where the Sachs-Teller mass concept was used for normalization purposes [13]. Besides the two vibrational modes at 0.205 eV and 0.481 eV (that are almost the same as in the LEAPR input), the model uses a single Einstein oscillator at 0.07 eV to represent the actual broad rotational band, with a weight of 0.41667 (=7.5/18) rather than 0.44444 (=8/18).

Figure 1 shows the isotropic scattering kernels produced by NJOY using (a) its ENDF/B-VI.2 library and (b) the integrated SSF option. The great similarity between both sets is evident, besides some sharper features in the model-based result related to the crude approximation involved in representing the rotational band by a single oscillator. This fact is clearly displayed in Fig.2, where the ratio (b)/(a) is shown over the same group structure; the two thin 'walls' symmetric with respect to the diagonal correspond to creation and annihilation of that single rotational 'phonon'. Over the rest of the grid the ratio is essentially equal to one, except for some small departures (groups # 30-40) in regions where the value of the scattering kernel is not significant.

The scattering cross section of hydrogen in room temperature water is shown in Fig.3, where again a very good agreement is observed between the NJOY results based on ENDF/B-VI.2 and SSF over the full thermal energy range. There is however a small systematic discrepancy between both sets below 0.1 eV, that we cannot attribute to the Synthetic Model in view of its excellent agreement with experimental data on the total cross section of water [14]. Finally, we display in Fig.4 the behaviour of the two curves in the high-energy range, showing that the ENDF/B-VI.2 evaluation is a little low, as pointed out by MacFarlane [15]; on the other hand, the SSF curve naturally approaches the free-gas (at the proper 'effective temperature') result at eV energies.

4.2 Water at 1000 K

This system was considered to test the evolution of the two evaluations with the temperature, bearing in mind that water is one of the hydrogeneous moderator with the largest temperature variation available in ENDF/B-VI.2. Concerning the SSF, it has been used in the past to predict diffusion parameters over a wide temperature range, showing good agreement with the existing integral measurements.

Another interesting point of discussion is related to the preparation of the input data for SSF. The set employed for water at 1000K is presented in Table 1, where only the two molecular vibrations enter as conforming the 'frequency spectrum', whereas the 'molecular mass' is the Sachs-Teller mass of hydrogen in the water molecule. The reason for that choice is that, in the spirit of the Synthetic Model, the single quantum oscillator representing the actual rotational band is highly excited at this temperature and therefore a quasi-classical treatment is applicable in this situation. In other words, whatever the energy of the incident neutron is, the latter will 'see' a scattering center which is part of a (thermally activated) freely-rotating molecule.

The NJOY calculated scattering kernels are shown in Fig.5, corresponding to (a) its ENDF/B-VI.2 evaluation and (b) the new SSF option. The two results are rather similar over the complete grid, except at the lower groups where the evaluation from the standard library is sharper, revealing an effective mass bigger than the Sachs-Teller mass used by the model. This fact is further emphasized in Fig.6, showing the ratio (b)/(a) which is very near to 1 everywhere but in the low energy region.

The cross section of hydrogen in this system is given in Fig.7, as produced by our NJOY version with its two options. Once again both curves are rather similar, although the SSF results are lower over most of the energy range. A more noticeable discrepancy is observed around 0.01 eV, presumably due to the lack of rotational quantum excitations in our model at this temperature (0.086 eV) which, after all, is not too high compared with the adopted characteristic energy (0.07 eV) for this motion (see Table 1) to ensure the attainment of the fully-rotating regime

As before, the approach to the free-gas limit is different for the two evaluations, as shown in Fig.8, where it seems again that ENDF/B-VI.2 produces a result too low at those high energies.

4.3 Methane at 100K

A great deal of work has been done on methane, prompted not only for being a theoretically accessible system [16], but also because of its interest as a cryogenic moderator for cold neutron sources [17]. Now, the SSF is particularly appropriate to describe a gas of spherical molecules, as CH_4 at room temperature. In this case, due to the very low energies associated to the molecular rotational motion, these modes are thermally excited and a quasi-classical treatment of them is applicable in the frame of the SSF formalism. Therefore, at all incident energies below the lower vibrational energy, the neutron will 'see' the hydrogen atoms as having a mass equal to their Sachs-Teller mass (3.4 amu); the effective temperature and vibrational factor over this region correspond to the system's temperature and the zero-point motion of the vibrational modes. Those three parameters (μ_0 , τ_0 , Γ) of the model (see Section 2) change as the neutron energy goes over the vibrations' energies (lumped into two Einstein oscillators at 0.17 eV and 0.38 eV) according to the model prescription [3].

The hypotheses discussed in the precedent paragraph are still valid for methane at 100K (~ 0.0086 eV), and in this sense the situation is equivalent to that of water at 1000K. The set of input data for the SSF is given in the Table 1.

In Fig.9 we present the results obtained for the scattering kernel of liquid methane (100 K) from the two options implemented in NJOY: (a) ENDF/B-VI.2 and (b) SSF. Some differences between both sets are apparent at the lower groups, reflecting the appropriate treatment of rotational and diffusive modes on which ENDF/B-VI.2 is based. However, as shown in Fig.10 for the ratio (b)/(a), those discrepancies are quite localized and with relatively small amplitudes.

The total scattering cross section of hydrogen in methane at 100 K is given in Fig.10 for the two evaluations. The agreement between them is not very good in this case, although the trend is similar. One may expect that at very low energies, the ENDF based calculation should give more reliable results, on account of its better description of the molecule's translation and rotations. In any case, it would be extremely useful to have experimental data over that range to elucidate this question.

In the intermediate region – at least from the point of view of the energy range covered by those NJOY calculations – the comparison between ENDF and SSF is shown in Fig.11, together with the experimental data of Rogalska [18]. The agreement between the measured points and the

Synthetic Model curve is excellent. Although this result can be confirmed at present only over a limited energy region, it is still important because that is about the expected peak position for the neutron flux emerging from a (large) liquid methane moderator, that will weigh most magnitudes of interest for neutronic calculations. Finally, the situation at high energies is shown in Fig.12, where the discrepancy observed in the previous cases is seen again here.

5. CONCLUSIONS

In this work we presented calculations performed using a modified version of the NJOY (94.105) code, in which a package of subroutines corresponding to the Synthetic Scattering Function formalism has been integrated as a new option. Results for a few moderators were used to illustrate the similarities and differences between the ENDF/B-VI.2 and SSF.

Although we have to benchmark the results based on this new option, besides the extensive applications already performed using the Synthetic Model, we expect that the powerful capabilities of this model to describe complex systems will become a useful tool after its integration into NJOY.

TABLE 1

Input data for the SSF. Energies are given in eV, and masses in amu.

	Mode 1	Mode 2	Mode 3	'Molec. Mass'
	Water 300K			
Energy	0.07	0.205	0.481	18.011
Effect. mass	2.3999	4.8078	3.2066	
	Water 1000K			
Energy	----	0.205	0.481	2.1177
Effect. mass	----	4.8078	3.2066	
	Methane 100K			
Energy	----	0.170	0.380	3.4
Effect. mass	----	2.585	3.1344	

REFERENCES

[1] S.W.Lovesey, *Theory of Neutron Scattering from Condensed Matter*, [Clarendon Press, Oxford, 1984].

[2] A.C. Zemach and R.J. Glauber, Neutron Diffraction by Gases, *Phys.Rev.* **101,** 129 (1956).

[3] J.R. Granada, Slow-neutron scattering by molecular gases: A Synthetic Scattering Function, *Phys.Rev.* **B31,** 4167 (1985).

[4] J.R. Granada and V.H. Gillette, A Review of a Synthetic Scattering Function Approach to the Thermal and Cold Neutron Scattering Kernels of Moderator Materials *J.Neutron Research* , in press (1998).

[5] J.R. Granada, V.H. Gillette and R.E. Mayer, Neutron cross sections and thermalization parameters for molecular gases using a synthetic scattering function, *Phys.Rev.* **A36,** 5585 (1987).

[6] J.R. Granada, V.H. Gillette and R.E. Mayer, Neutron cross sections and thermalization parameters using a synthetic scattering function. II: Applications to H2O, D2O and C6H6, *Phys.Rev.* **A36,** 5594 (1987).

[7] V.H. Gillette, PhD Thesis, Instituto Balseiro (Unpublished, 1989).

[8] V.H. Gillette and J.R. Granada, Analytical scattering kernels of any order for molecular gases, *Proceedings of the* VI CGEN, (Rio de Janeiro, 1996).

[9] M.K. Dede, A. Demény and J.K. Darai, Evaluation of neutron pulse measurements with Granada - Sibona plexiglass kernel, *Nucl.Instr.Meth.Phys.Res. A* **372,** 233 (1996).

[10] R.E. MacFarlane and D.W. Muir, The NJOY Nuclear Data Processing System, Version 91, Los Alamos National Laboratory Report LA-12740-M (1994)

[11] International Workshop on Cold Moderators for Pulsed Neutron Sources, Argonne National Laboratory (USA, 1997).

[12] J.R. Granada and V.H. Gillette, Evaluation of thermal neutron cross section of moderator materials using a synthetic scattering function, *Physica* **B 213&214,** 821 (1995).

[13] D. Ravignani, Thermal Neutron Scattering from HDO, MSc Thesis (in Spanish), Instituto Balseiro, Univ.Nac.Cuyo (Unpublished, 1994).

[14] J.R. Granada, R.E. Mayer and V.H. Gillette, Application of the Synthetic Scattering Function to the Design of Cold Moderators for Pulsed Neutron Sources: A Fast Response Methane Based Array, in Ref. [11].

[15] R. MacFarlane, New Thermal Neutron Scattering Files for ENDF/B-VI Release 2, LANL Report LA-12639-MS.

[16] A. K. Agrawal and S. Yip, Slow neutron scattering by molecular liquids, *Nucl.Sci.Eng.* **37,** 368 (1969).

[17] Y. Kiyanagi *et al.*, Comparison of coupled liquid hydrogen and solid methane moderators for pulsed neutron sources, *Physica* **B 213&214,** 857 (1995).

[18] Z. Rogalska, Rotational dynamics of solid methane molecules by slow neutron cross section measurements, *Acta Phys.Polonica* **XXVII,** 581 (1965).

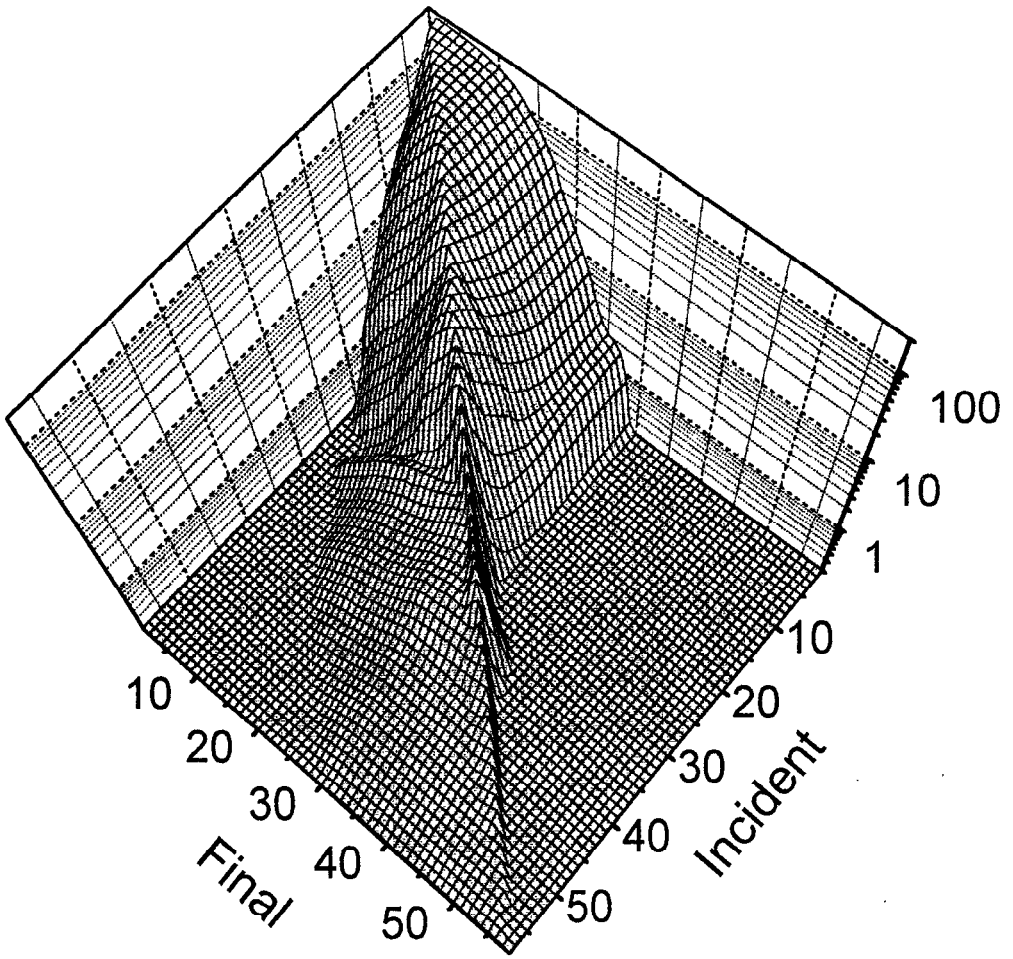

Fig.1(a): Scattering Kernel for H in H_2O at 300K, calculated by NJOY with option (a) ENDF/B-VI.2

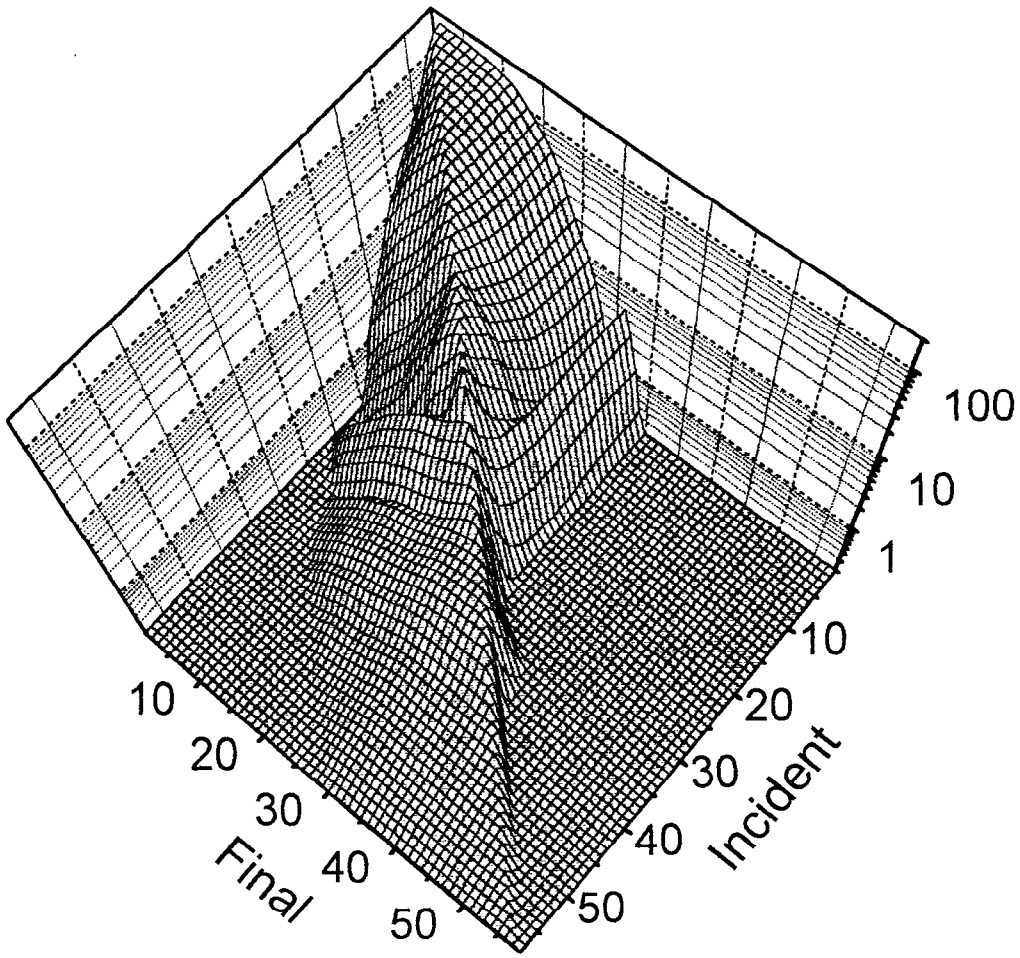

Fig.1(b): Scattering Kernel for H in H_2O at 300K, calculated by NJOY with option (b) SSF

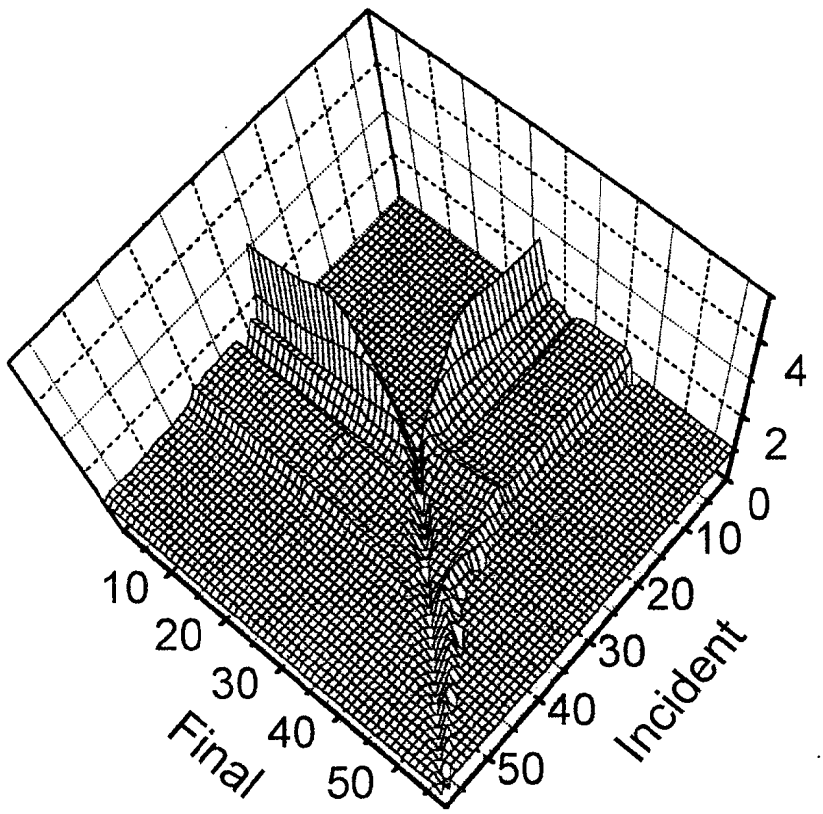

Fig.2: Ratio (b)/(a) of the Scattering Kernels for H in H_2O at 300K.

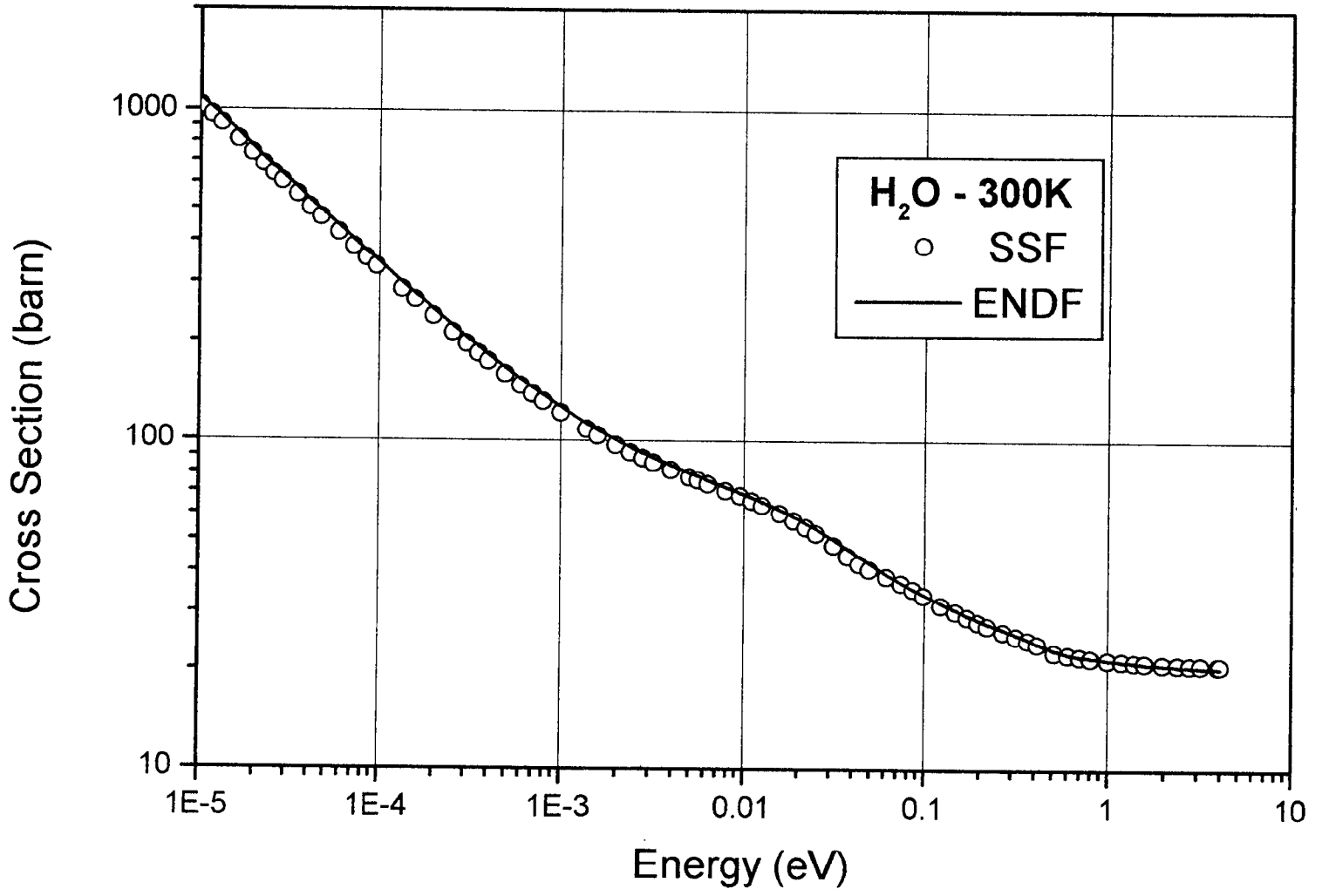

Fig.3: Cross section of H in H_2O at 300K calculated by our NJOY with its two options, over the full thermal energy range.

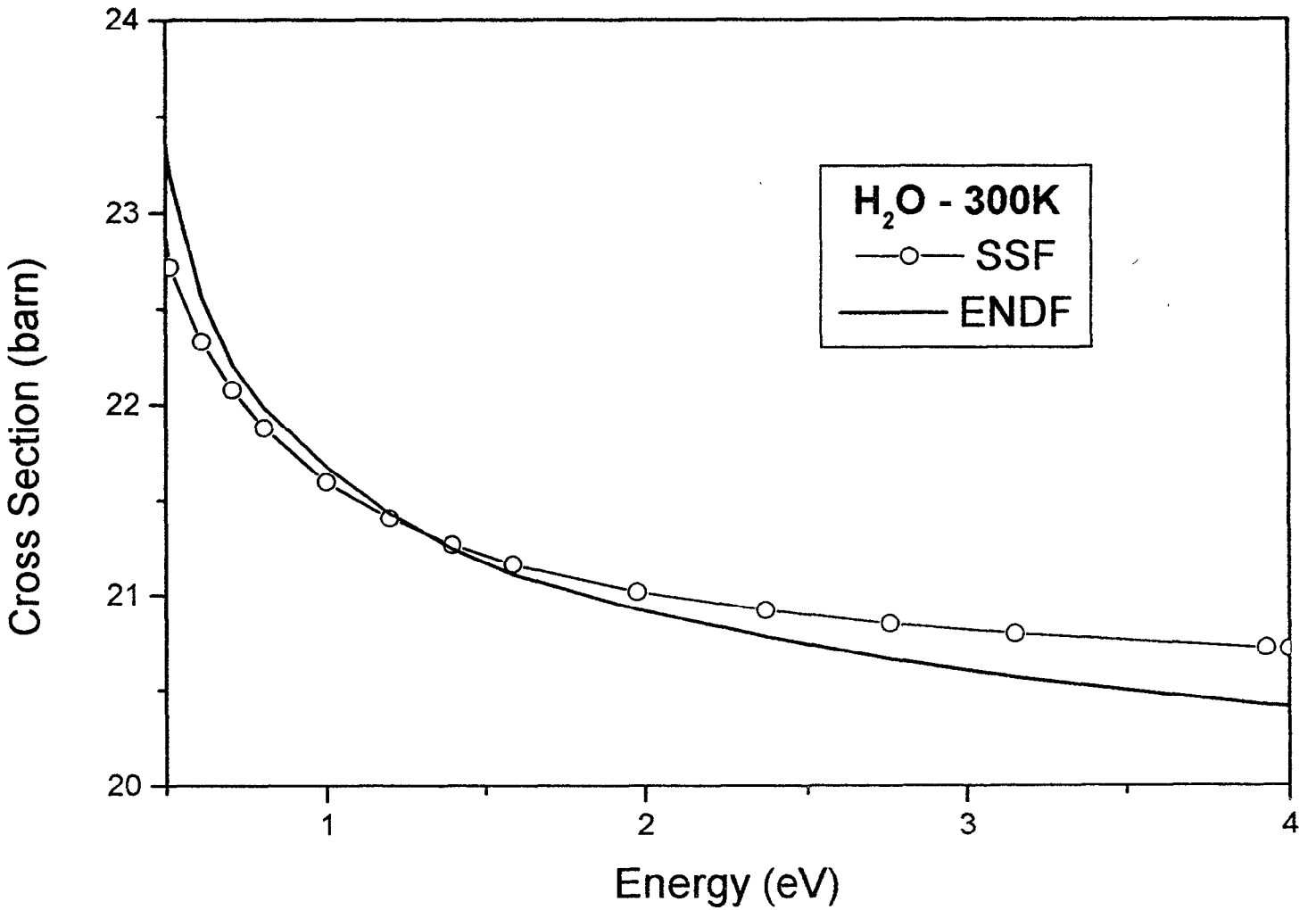

Fig.4: Cross section of H in H_2O at 300K calculated by our NJOY with its two options, over the high energy region.

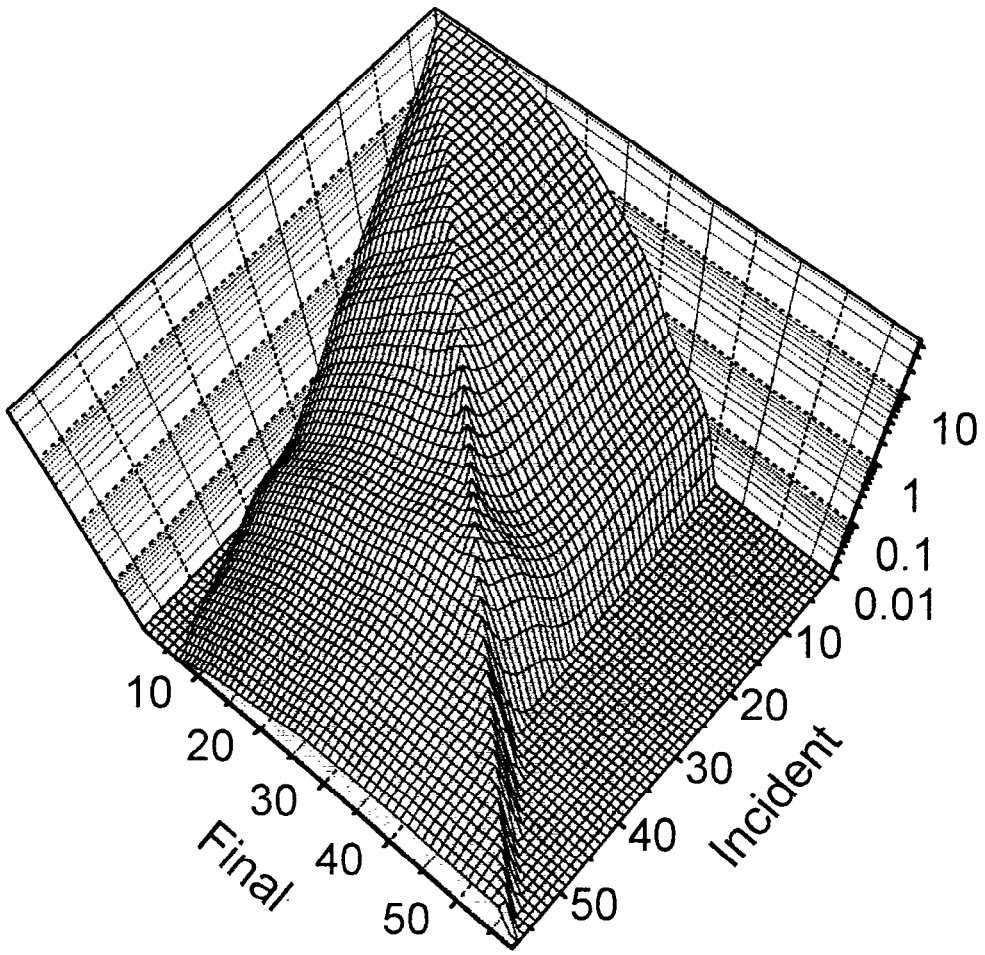

Fig.5(a): Scattering Kernel for H in H_2O at 1000K, calculated by NJOY with option (a) ENDF/B-VI.2

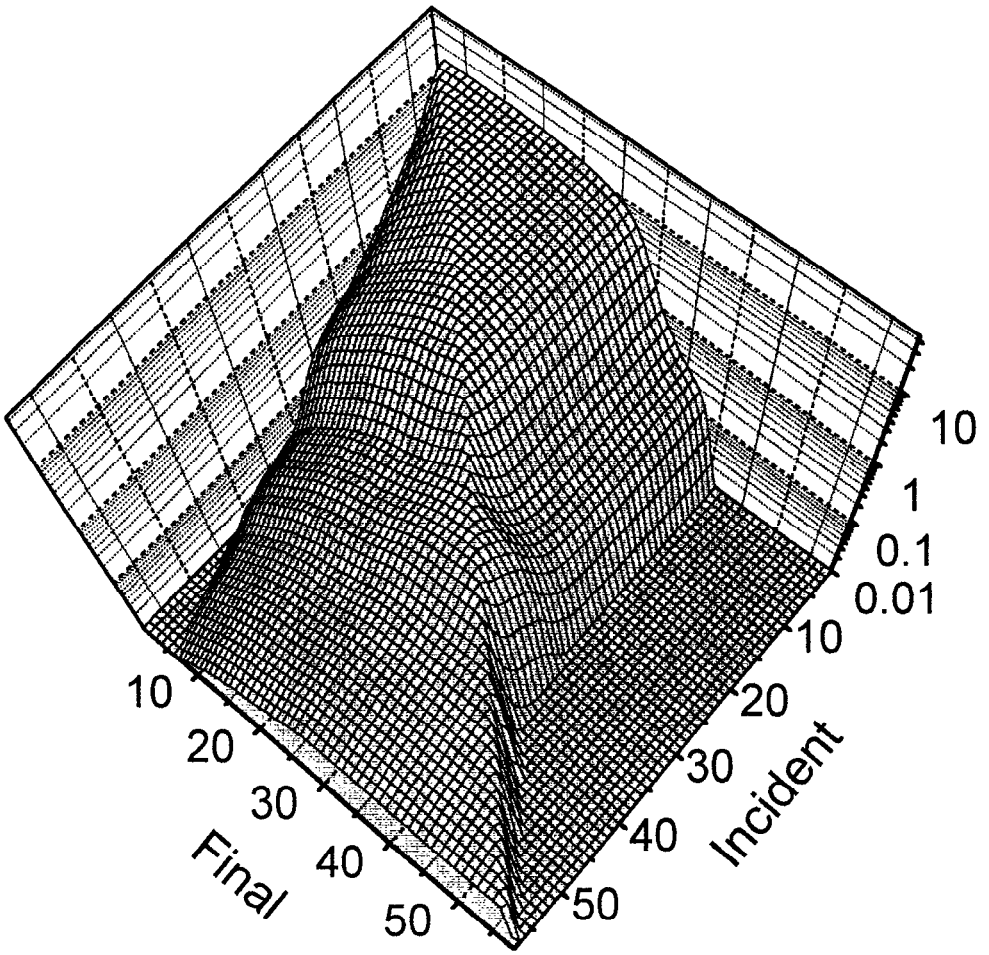

Fig.5(b): Scattering Kernel for H in H_2O at 1000K, calculated by NJOY with option (b) SSF

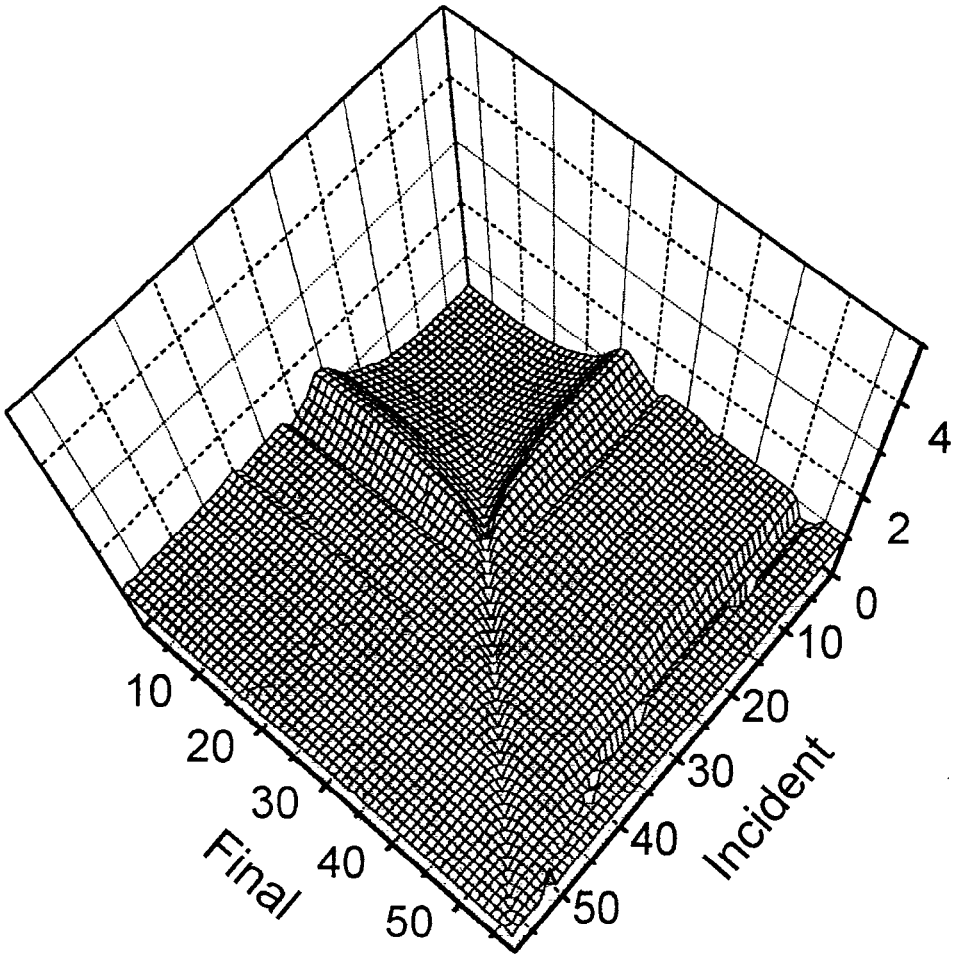

Fig.6: Ratio (b)/(a) of the Scattering Kernels for H in H_2O at 1000K.

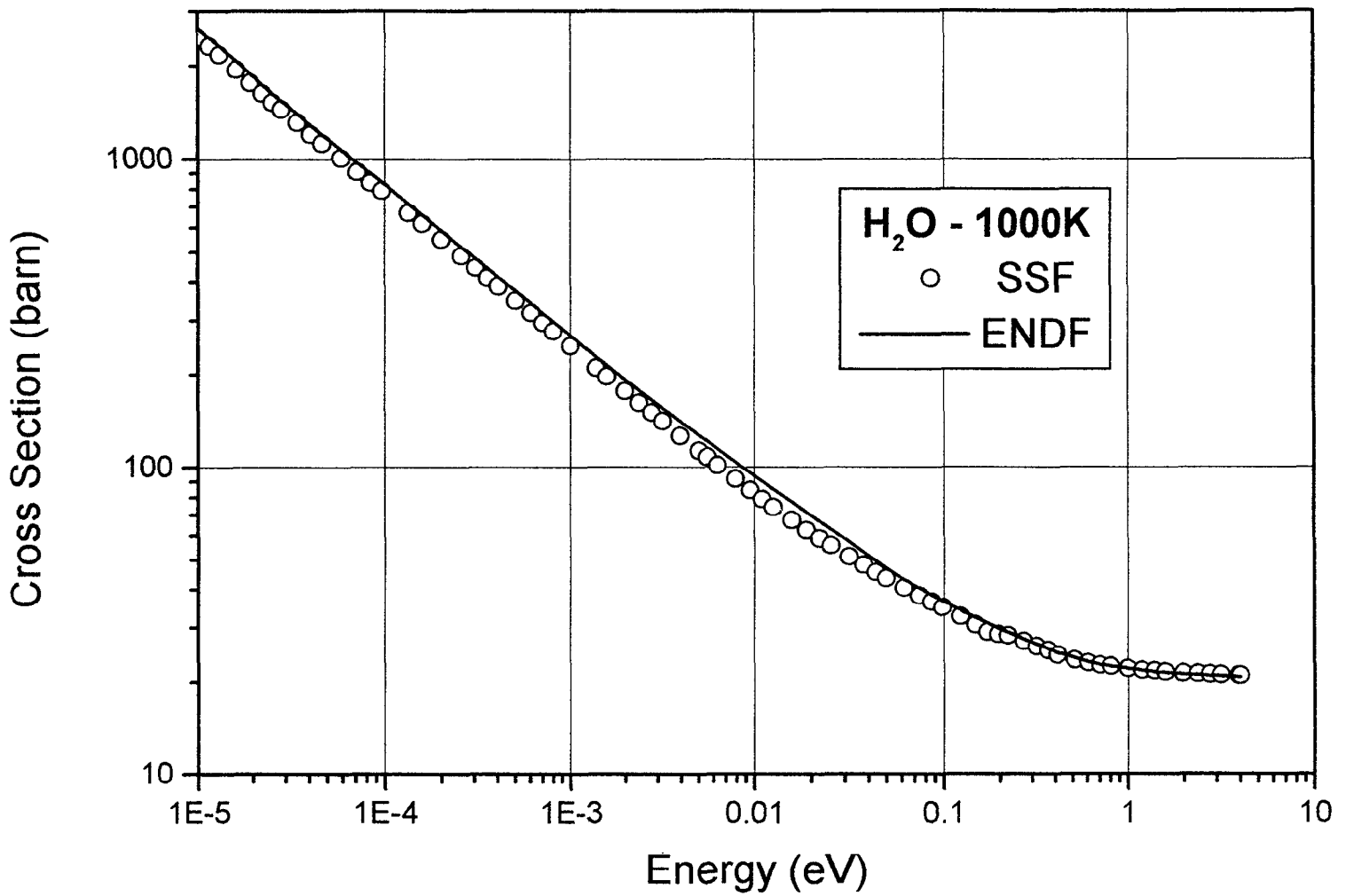

Fig.7: Cross section of H in H_2O at 1000K calculated by our NJOY with its two options, over the full thermal energy range.

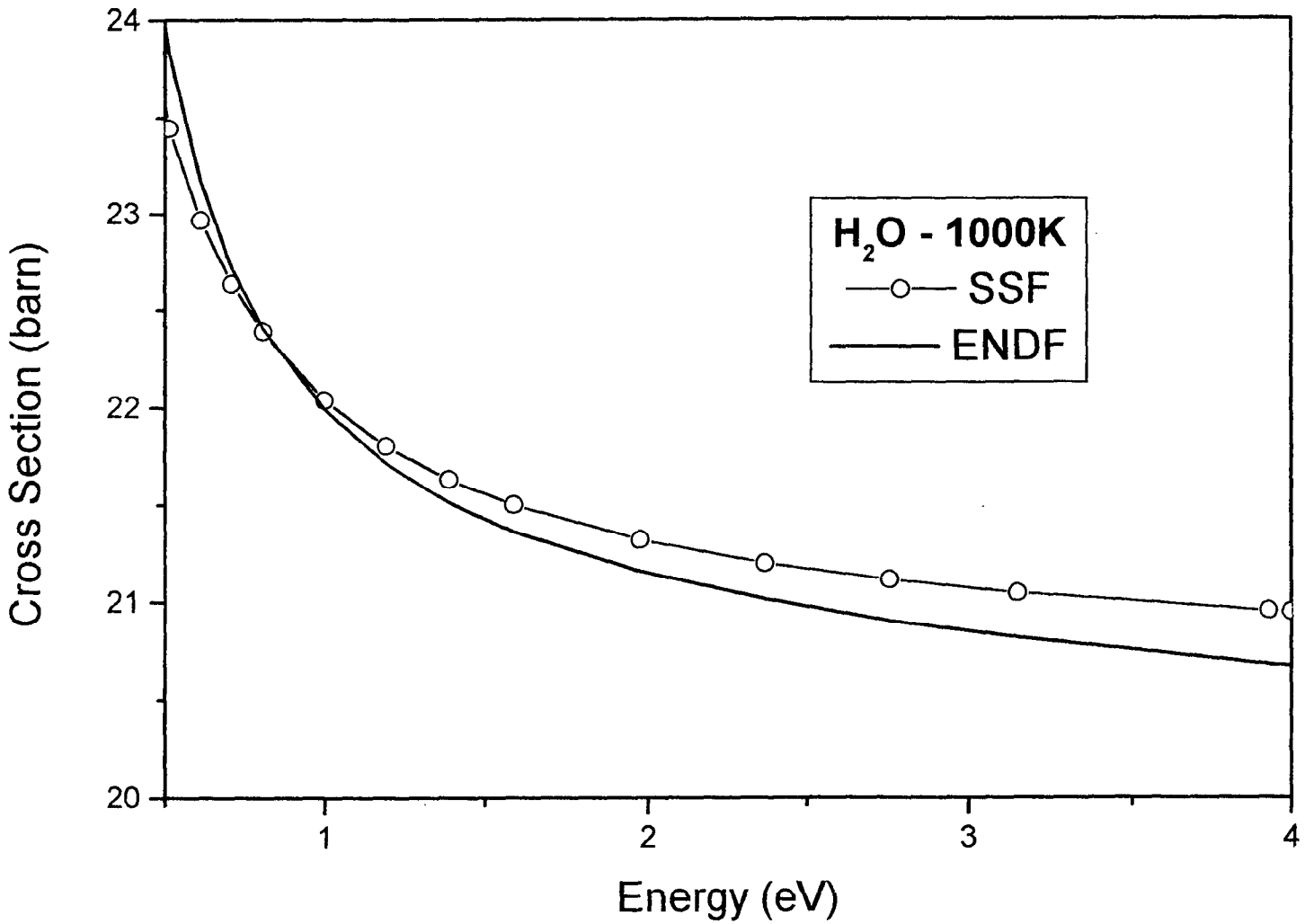

Fig.8: Cross section of H in H_2O at 1000K calculated by our NJOY with its two options, over the high energy region.

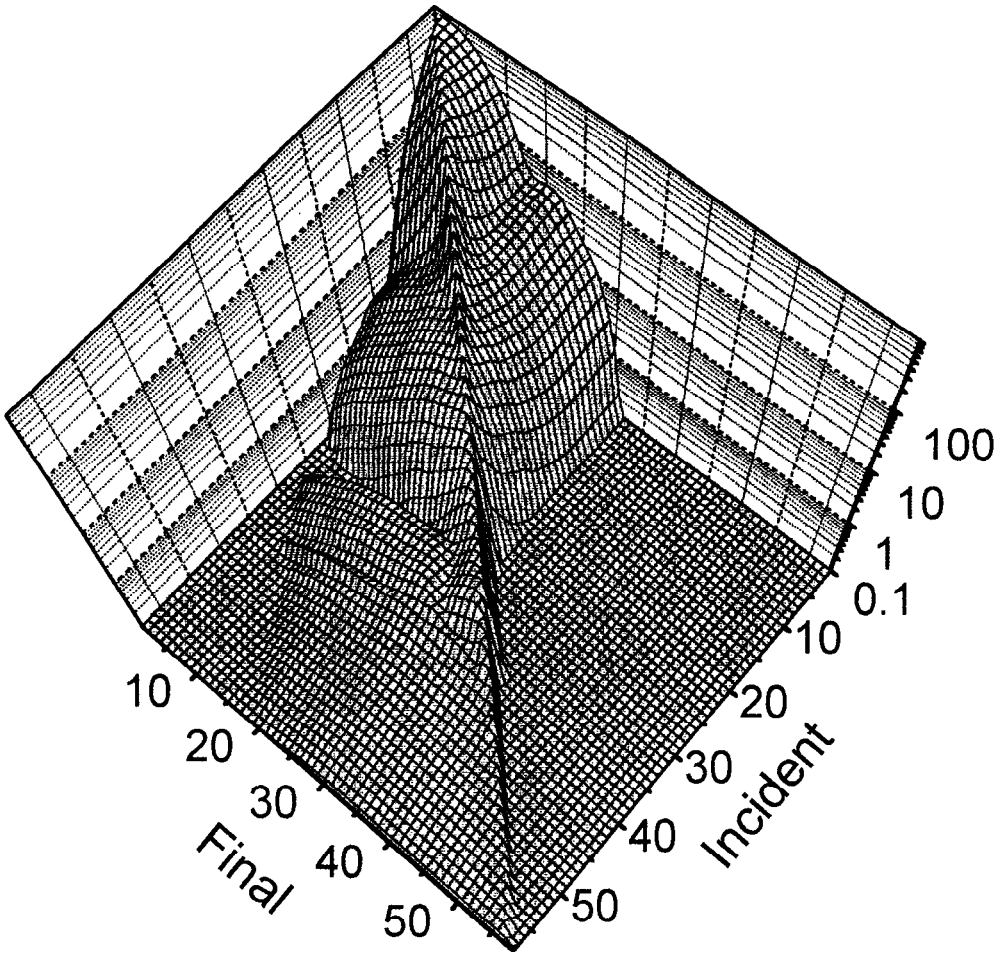

Fig.9(a): Scattering Kernel for H in CH_4 at 100K, calculated by NJOY with option (a) ENDF/B-VI.2

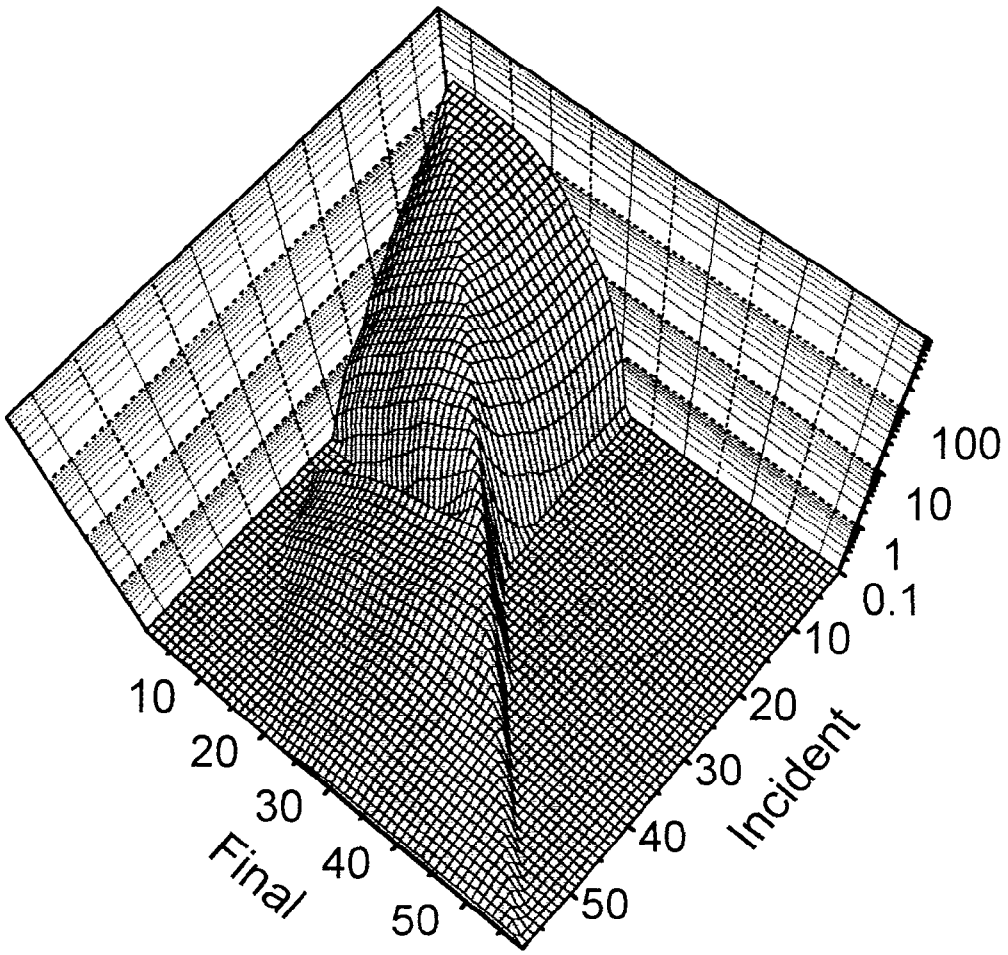

Fig.9(b): Scattering Kernel for H in CH_4 at 100K, calculated by NJOY with option (b) SSF

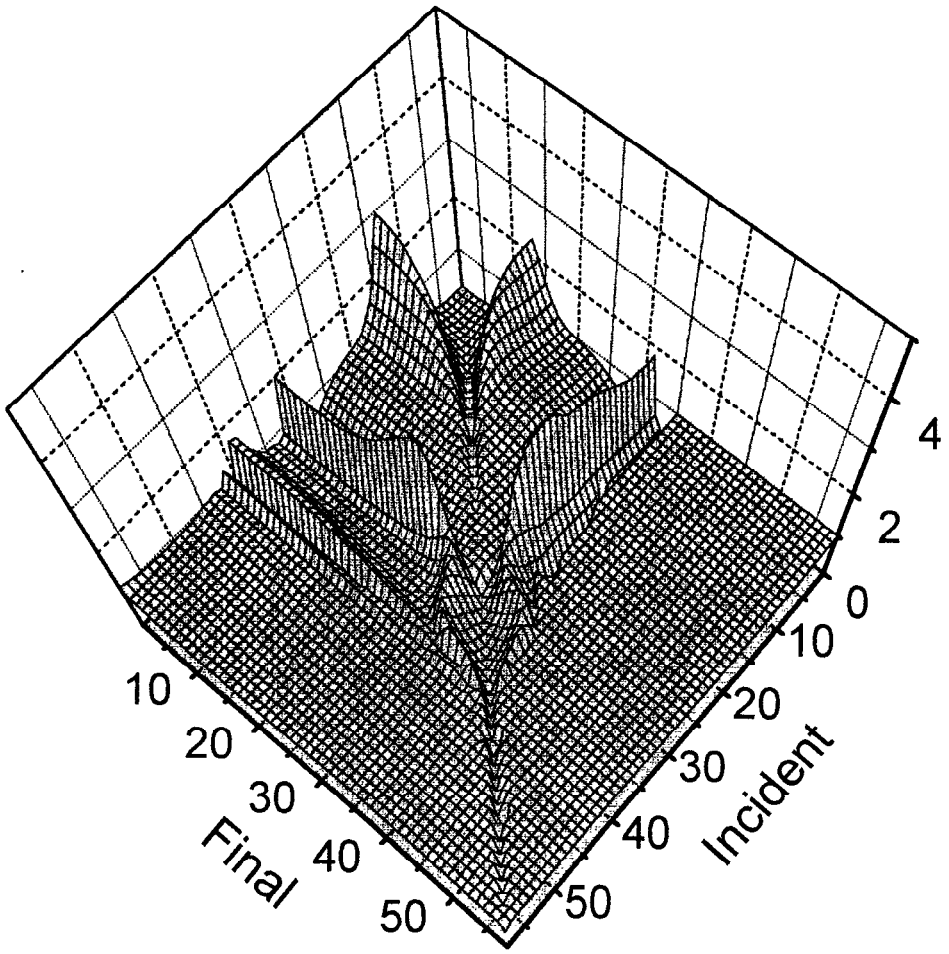

Fig.10: Ratio (b)/(a) of the Scattering Kernels for H in CH_4 at 100K.

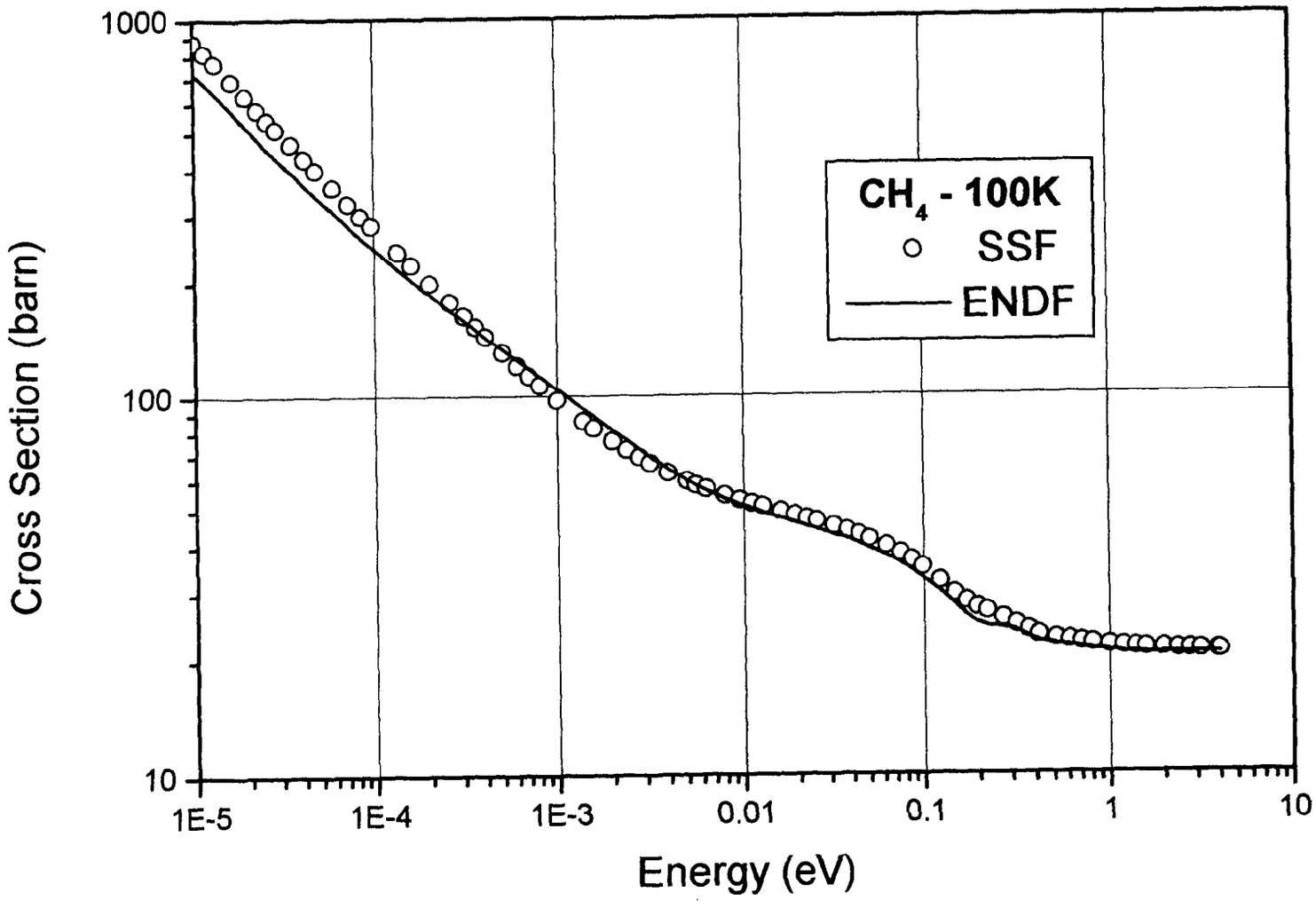

Fig.11: Cross section of H in CH_4 at 100K calculated by our NJOY with its two options, over the full thermal energy range.

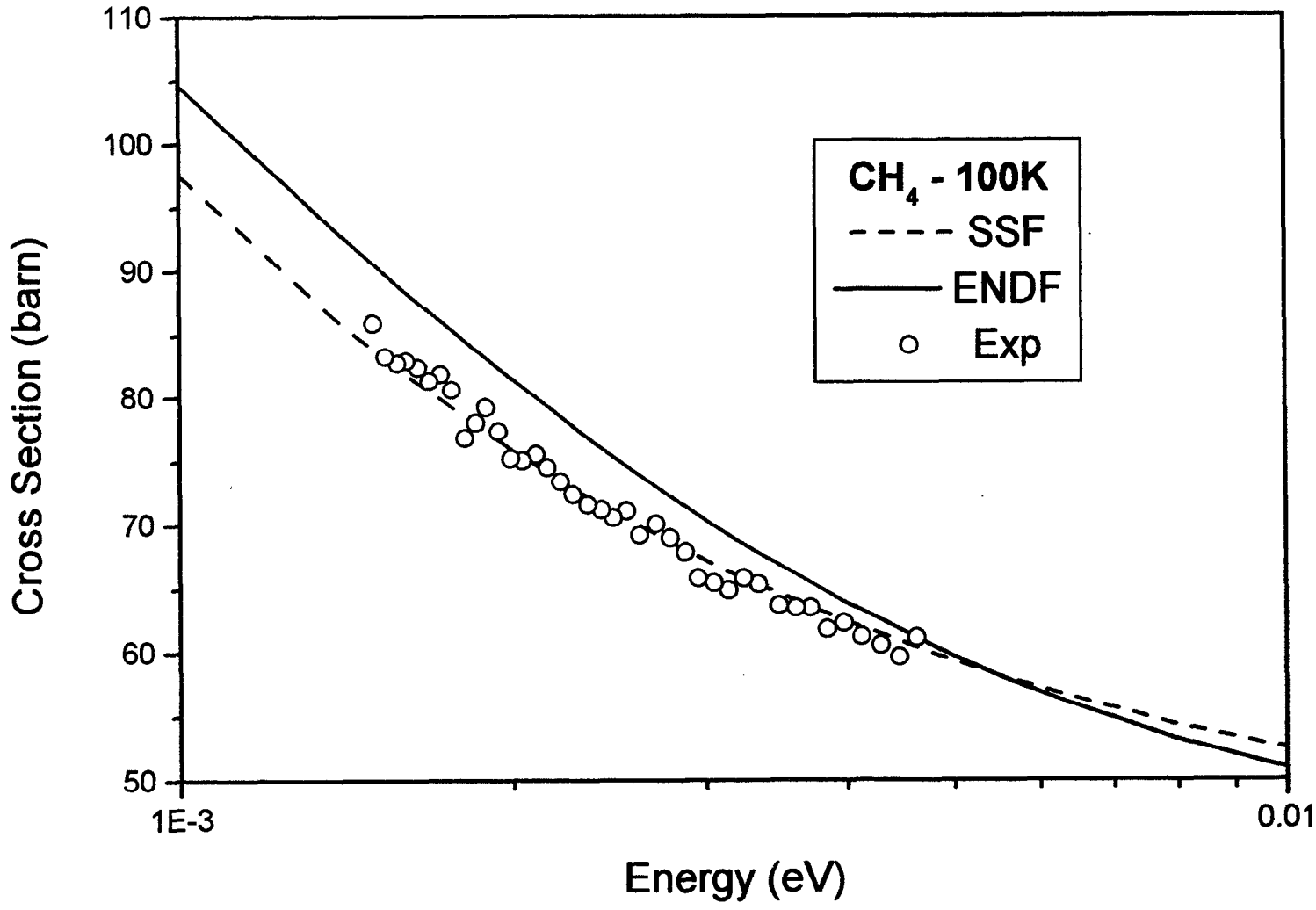

Fig.12: Cross section of H in CH_4 at 100K calculated by our NJOY with its two options, over the intermediate energy range.

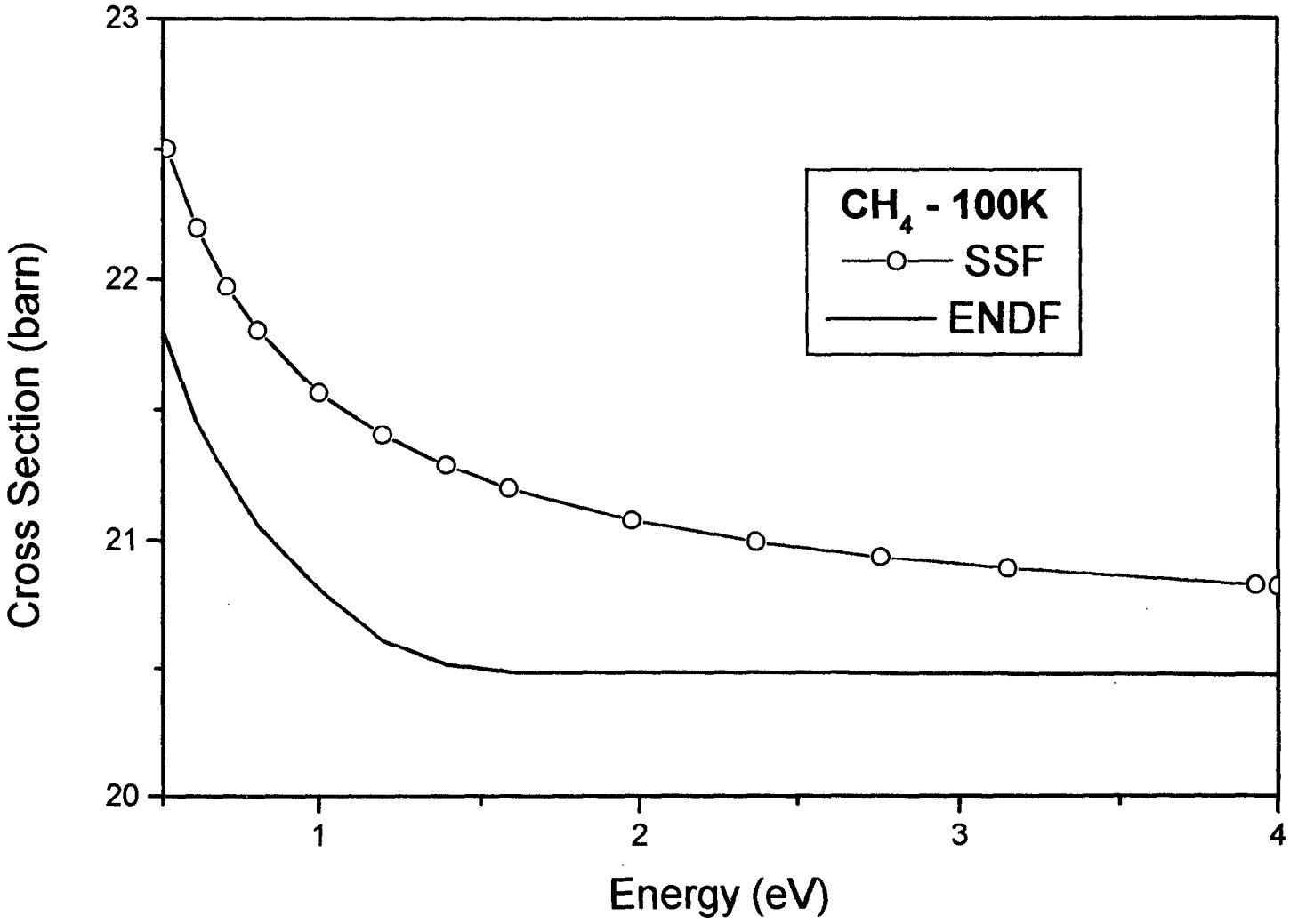

Fig.13: Cross section of H in CH_4 at 100K calculated by our NJOY with its two options, over the high energy region.

ICANS XIV
14th Meeting of the International Collaboration on
Advanced Neutron Sources
June 14-19, 1998
Starved Rock Lodge, Utica, IL

Development of a Cold Methane Pellet Moderator for ESS

H. Barnert-Wiemer, K. Döring, H. Stechemesser
Forschungszentrum Jülich GmbH
Jülich / Germany

Introduction

As part of the work for the target station of the planned European Spallation Source (ESS) the Central Department of Technology at the Forschungszentrum Jülich is also concerned with the moderators, particular attention being given to the development of cold moderators. Whereas in the USA the interest of users is focused on moderators operated at a temperature of 100 K, users in Europe are mainly interested in 20 K moderators.

Research reactors are operated with cold hydrogen or deuterium moderators whose advantage is a time-independent high flux of cold neutrons involving low radiation damage. For short-pulsed spallation sources like the ESS, H_2 and D_2 are less suited since they lead to pulse broadening due to inadequate slowing down properties.

The long-term goal of the concept and test phase only just beginning is the design of an advanced cold 20 K moderator for ESS, which is better by at least a factor of 2 than conventional H_2 moderators with respect to neutron intensity and which shows better slowing down properties in the thermal and epithermal range. The most favourable moderator material for neutrons is considered to be methane, in the liquid form for 100 K moderators and in solid form for 20 K moderators.

Methane as a Moderator

The clearly favourable neutronic properties of methane as a moderator, however, are faced with disadvantages in technical application:

- Methane is radiolysed under irradiation. During this process, energy is stored in the radicals formed and must be specifically removed at regular intervals. This can be achieved by temperature increase /1/, but every time this process has to be carried out measuring time for the user is interrupted.

- Radioactive isotopes are formed from the carbon atoms of methane (or other organic substances) due to spallation. This must be taken into account in treating the spent methane. Emission may not be possible. Known isotopes wirth half-lifes over 1 min are C-11 with a half-life of 20.3 min, Be-7 with 53.4 d, H-3 with 12.3 a and Be-10 with 1.6×10^6 a /2/.

- Neutron radiation leads to polymerization reactions in methane forming wax-like alkanes which deteriorate the moderator properties and also deposit in the moderator system. In the ISIS moderator system operated with liquid methane, wax-like alkanes occur which clog the system and cannot be completely removed by the use of solvents. Experiments are under way to slow down the formation rate of wax-like alkanes by adding further substances (e.g. propane) /3/.

- The heat conductivity of solid methane is low (< 1 mW / cm K). Due to the high heat generation in ESS moderators (~ 7.5 kW), solid methane can not be used as a compact block because the heat can not be removed fast enough, which would lead to evaporation /4/.

The problems described above have led to the following considerations:

- In order to prevent the distribution of wax-like polymers in the moderator and piping system, CH_4 is used as a solid, which is removed without melting so that

system contamination is prevented. Designs /5, 6/ that use sheets of solid methane evaporate the methane to empty the moderator container. This may lead to residue in the moderator system.

- In order to transport solid methane in the moderator system, it has been proposed to use this in the form of small pellets /4/.

- In order to ensure adequate cooling of the solid methane the small pellets should be spherical so that a defined fixed bed is formed in the moderator container through which coolant flows in a reproducible way. Designs that feature cooled metal rods in sheets of solid methane have also be published /5, 6/.

- Operating conditions must be established to allow regular warming and recooling of the solid methane to remove the energy stored.

- The problem limiting the undisturbed measuring time when using solid methane is the energy build-up, whose removal leads to frequent down-times, rather than polymer formation, which gradually deteriorates the moderator efficiency. Additions to the methane, as they are proposed for ISIS, can reduce the problem if they diminish radical formation or lead to a faster radical recombination at operating temperature thus lengthening the time between two necessary energy removal phases.

Conceptual Design for a Methane Moderator for ESS

On the basis of the above considerations, a concept for the ESS cold moderator is being examined at the Forschungszentrum Jülich, which is characterized by the following features:

- The moderator is a fixed bed of small spheres. This makes moderator vessel filling homogeneous and reproducible. Since spheres in contrast to pellets of other

shapes form a defined packed bed, good and reliable cooling of the moderator bed by H_2 is given.

- The transport of solid moderator spheres from the radiation zone largely prevents system contamination by "wax". A certain degree of abrasion must be expected however, but nothing is known so far about the abrasion resistance of solid methane spheres at 20 K.

- Good transportability of the moderator spheres due to fluidization of the bed in the moderator vessel with subsequent pneumatic transport through the pipes is given.

- The process of filling the moderator container and removing the pellets is batchwise to simplify the loading step and ensure complete removal of the spent pellets, so that no spent methane pellets accumulate in the system.

- The pellets are warmed up regularly to release the stored energy.

- The spent methane pellets are separated from the transport fluid and the methane is either purified and reused or released over the stack.Depending on the kind and amount of the radioactive isotopes present retentive measures may have to be considered.

The development of the concept for the cold source was based on the given target-moderator-reflector assembly of the ESS project. Therefore, considerations on a horizontal discharge of the pellets by a screw conveyor /7/ or swinging the moderator tank out of the beam path /5/ could not be included in the concept.

Fig. 1 shows the target-moderator-reflector assembly with top shielding /8/. The two cold moderators are arranged above and below the target. The cranked coolant pipes routed over several meters through the shielding and reflector have an inside diameter of 25 mm.

The currently valid planning documents provide for hydrogen moderators of approx. 1 l volume. When methane is used as moderator instead of hydrogen, the same amount of hydrogen has to be transported as coolant and the methane pellets must additionally be transported through the coolant pipes to the moderator container. In the chosen target-moderator-reflector assembly, additional space requirements for operating the moderator (like the screw conveyor for pellet discharge or revolving the moderator container out of ist operating position) would lead to a loss of reflector material and reduce the number of beam tubes, so that concepts requiring additional space /5, 7/ are not pursued at the Forschungszentrum Jülich.

Fig. 2 schematically shows the concept for the use of solid methane pellets. CH_4 is solidified at about 20 K and then extruded. In this way, cylindrical pellets are produced which are shaped into spheres in a spheronizer. They fall into a storage vessel from where they are proportioned into the moderator vessel via a star feeder and a stream of hydrogen.

After a given time, which is determined by the extent of the polymerization processes, they are discharged by reversing the hydrogen coolant flow and subsequently separated from the hydrogen. The methane can be purified and fed back to the solidification stage.

Alternatively, the spent methane could be emitted. In this case, the emission limits for radioactive isotopes produced are to be observed.

Not included in Fig. 2 is the configuration for the H_2 circuit during a pellet warming cycle for energy removal. It is being contemplated to temporarily send a warmer hydrogen flow, whose temperature must, of course, be below the melting point of methane, through the fixed bed of pellets so that the pellets are warmed to approx. 50 K. The process has to be optimized for rapidity, because during the warming/cooling cycle no measurments are possible.

Specific Tasks for the Development of the ESS Methane Moderator

The concept for the cold moderators contains many unsolved problems which need to be tackled step by step.The activities planned for the next three years will set in at several points:

1. Production of CH_4 pellets
   - from pure methane
   - from methane hydrate
   - from adsorber materials such as zeolites or porous substances by loading with methane

For the production of solid methane pellets it is helpful to look at fusion research were solid deuterium pellets are injected into the plasma. Extrusion cryostats are used to produce these pellets. Under changed temperature conditions these devices can also be used to produce methane pellets instead of deuterium pellets. Fig. 3 shows the cryostat adopted from fusion research. Methane is condensed in the given volume in the vertically arranged cryostat. The solid condensate is then slightly warmed and ejected downwards through a nozzle by a piston. A cutting device serves to cut pellets of the desired length.
The facility is under construction. It will serve to test and, if necessary, optimize the fabrication principle as well as to produce pellets for the COSY tests (see below). For use in ESS these cylindrical pellets would have to be rounded in a further step.

Methane hydrate is regarded as an alternative to solid methane. Gas hydrates are ice-like crystalline structures of a water lattice with cavities which contain guest gases.They are bonded by van der Vaals forces under low temperature and moderate pressures. The guest molecule is necessary to support the cavity. In the natural environment methane is the most common guest molecule /9/. It is being contemplated to have this compound produced at a university institute and test it in the COSY experiments (see below).

Furthermore, it is being considered to use methane adsorbed on porous bodies such as zeolites or porous polymer spheres. This should substantially simplify the production process and handling of the moderator pellets.

Irrespective of the neutronic properties of the different moderator pellets mentioned above, their mechanical properties are to be evaluated since the pellets are exposed to considerable mechanical loads during transport in the moderator system. Another

task is to evaluate the behaviour in the radiation field with respect to energy build-up, polymerization processes and the formation of radioactive isotopes.

2. Testing the transport phenomena of spheres in the moderator vessel and pipe systems at room temperature under similarity conditions.

A particular problem is the transport of moderator pellets in the moderator system. They must not be broken when charged into the moderator vessel, because only a-bed of spheres can guarantee an even cooling without hotspots, and they should not be destroyed during discharge, so that they can be easily separated from the coolant and to prevent fine particles from depositing in the system. The pellets must be quantitatively discharged so that no spent material accumulates in the moderator container, and the process should be carried out in a very short time so that the beam time is not significantly shortened. If the residence times of liquid methane in the ISIS moderator /10/ are used for comparison, it must be assumed that the methane in the ESS moderators may have to be replaced once a day.
The first transport tests will be carried out under similarity conditions at room temperature. A Plexiglas apparatus that allows visual inspection was set up.

3. Design and construction of the moderator test facility at JESSICA on the COSY cooler synchrotron of the Forschungszentrum Jülich.

COSY is a 2.4 GeV proton synchrotron at the Forschungszentrum Jülich. Initial experiments have shown that it is possible to completely extract the beam in one circulation /11/. This enables the setup of a moderator test facility where the performance of various moderators (solid methane pellets, methane hydrates, zeolites loaded with methane) can be measured under realistic ESS target geometries in the JESSICA facility (JESSICA = Jülich Experimental Spallation-Target Setup in COSY Area). Fig. 4 schematically shows the procedure: moderator pellets are externally produced in the laboratory (here as an example the production of solid methane pellets in the extrusion cryostat), transferred into the experimental hall of COSY and filled into the moderator vessel in a glovebox under inert gas. The pellets are kept in liquid hydrogen in the moderator vessel. A circulation cooling is not

necessary because only single pulses are measured so that the heat generation is low. The moderator vessel is cooled by a cold head.

Summary

Work for moderator design concentrates on the development of a concept for a ESS cold moderator system assuming that spherical moderator pellets will be available for the process, irrespective of the type of moderator ultimately selected. The choice of a moderator results from neutronic and technical aspects, to enable the safe and functional handling of the moderator pellets and, at the same time, satisfy the neutronic requirements.

References

/1/ Carpenter, J.M. : Nature 330 (1987) p.358-360
/2/ Broome, T.A. : Personal Communication
/3/ Broome, T.A. : The ISIS Cold Moderators, Int. Workshop on Cold Moderators for Pulsed Neutron Sources, Argonne National Laboratory,Argonne (USA), 28. 9. – 2. 10. 1997
/4/ Williamson, K.D., Lucas, A.T.: A Combined H_2/CH_4 Cold Moderator for a Short Pulsed Neutron Source, Proc. of the 10 th Meeting of the Int. Collaboration on Advanced Neutron Sources (ICANS), Los Alamos (USA), 3. –7. Oct. 1988
/5/ Jessen, N.C., Stendal, K. : Solid Methane Moderators for the ESS-project, ACoM-Meeting, PSI-Villigen(CH), 24./25. 2. 98
/6/ Beliakov,A.A. et al.: Solid Methane Cold Moderator for the IBR-2 Reactor, Workshop on Cold Moderators, Argonne National Laboratory, Argonne (USA), 28. 9. – 2.10.1997
/7/ Bauer, G.S. : Pulsed Neutron Source Moderator Engineering, Int. Workshop on Cold Moderators, Argonne National Laboratory, Argonne (USA), 28. 9. – 2.10.1997
/8/ ESS-96-53-M, Vol.3,The ESS Feasibility Study
/9/ Sloan, E.D. : Clathrate Hydrates of Natural gases, Marcel Bekker Inc. New York 1990
/10/ Broome, T.A. : Prospects for Targets and Methane Moderators at ISIS, Proc. of the 13 th Meeting of the Int. Collaboration on Advanced Neutron Sources (ICANS), Villigen(CH), 11. – 14. Oct. 1995
/11/ Neef, R.D. : ESS Target-Moderator-Reflector Mock-up Experiment at COSY, ACoM-Meeting, PSI-Villigen(CH), 24./25. 2. 98

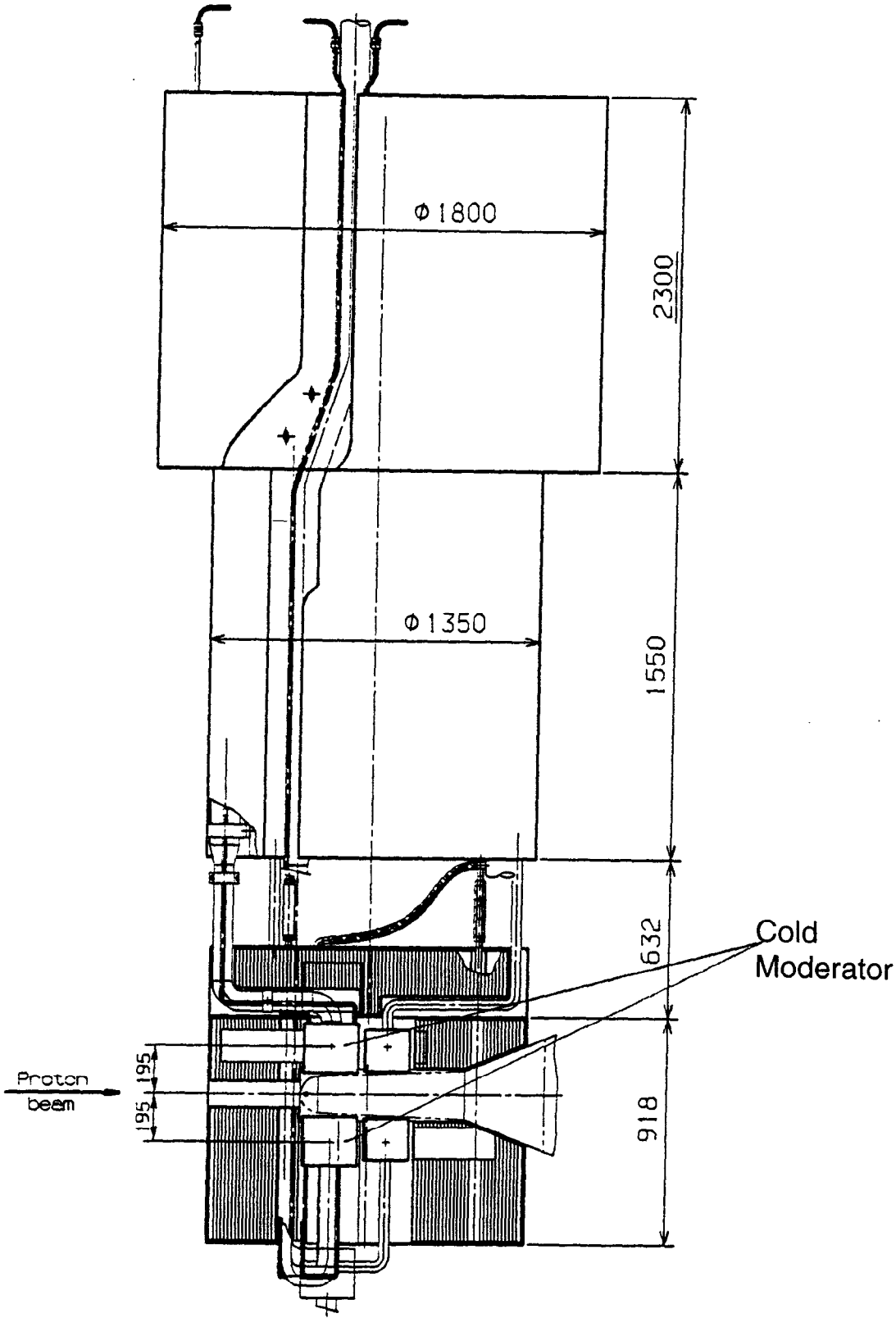

Fig. 1 : Schematic of the ESS Target-Moderator-Reflector-Assembly

Fig. 2 : Concept of the 20 K Methane Pellet Moderator System

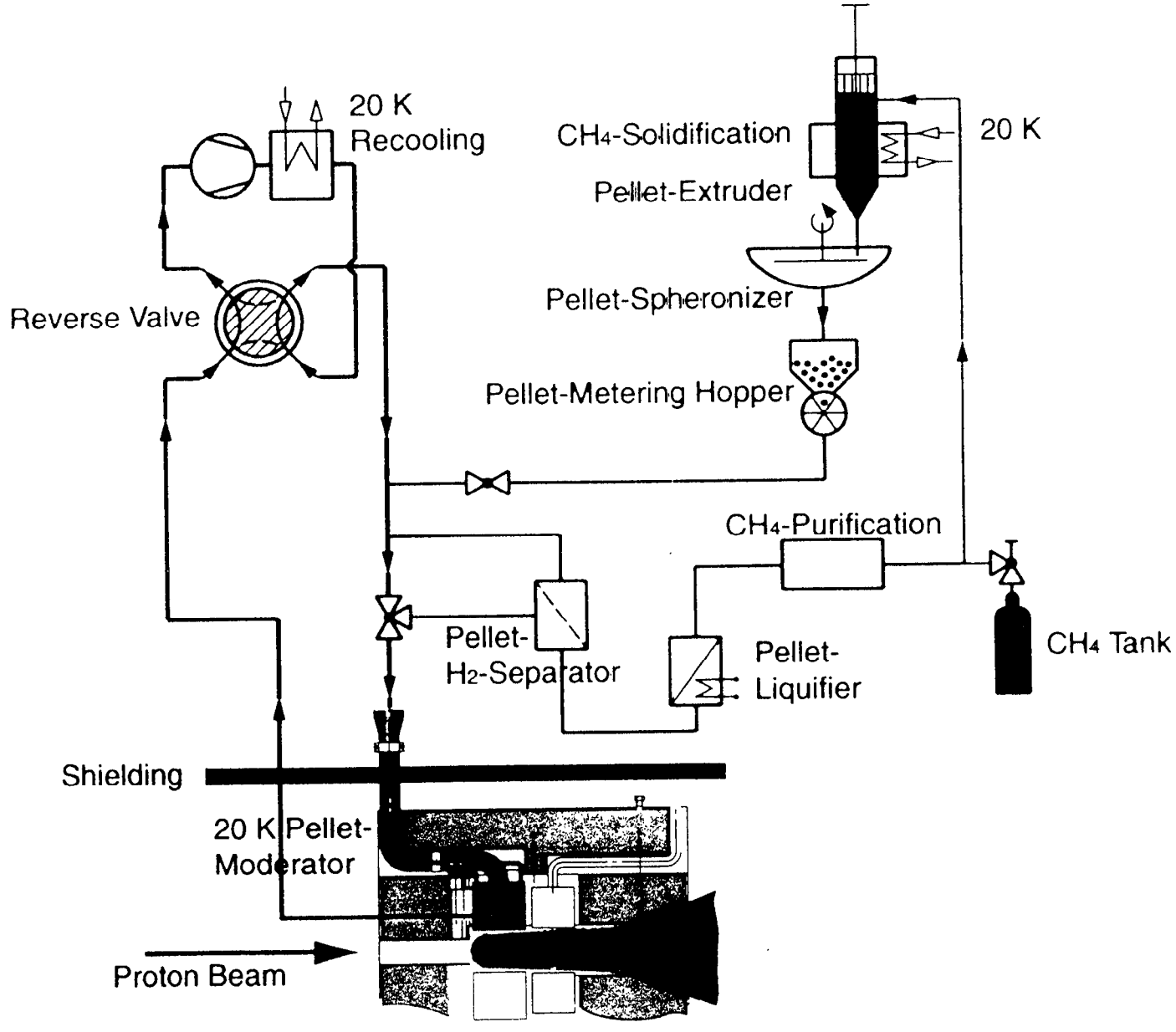

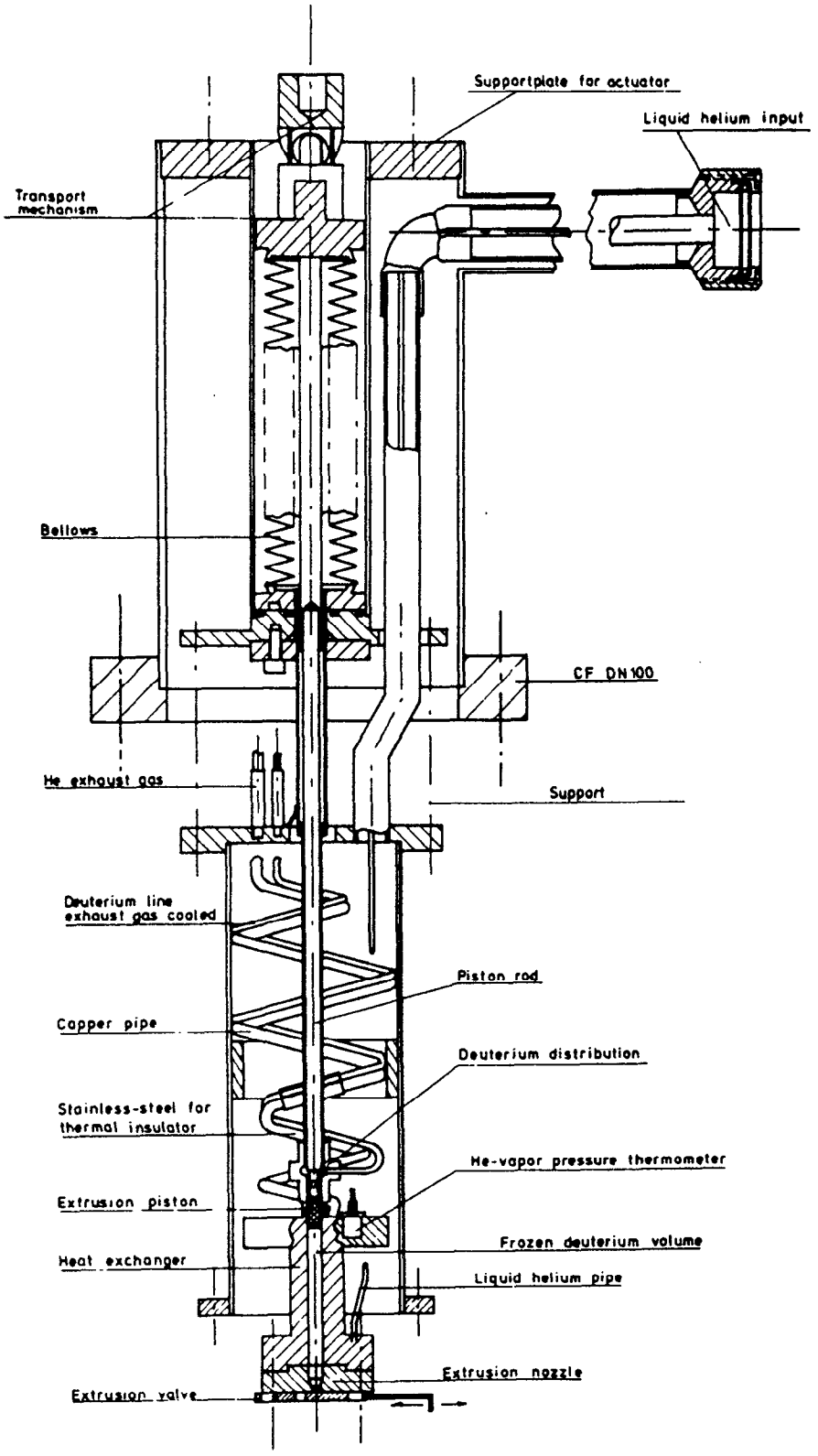

Fig. 3 : Extrusion Cryostat for the Production of Solid Methane Pellets

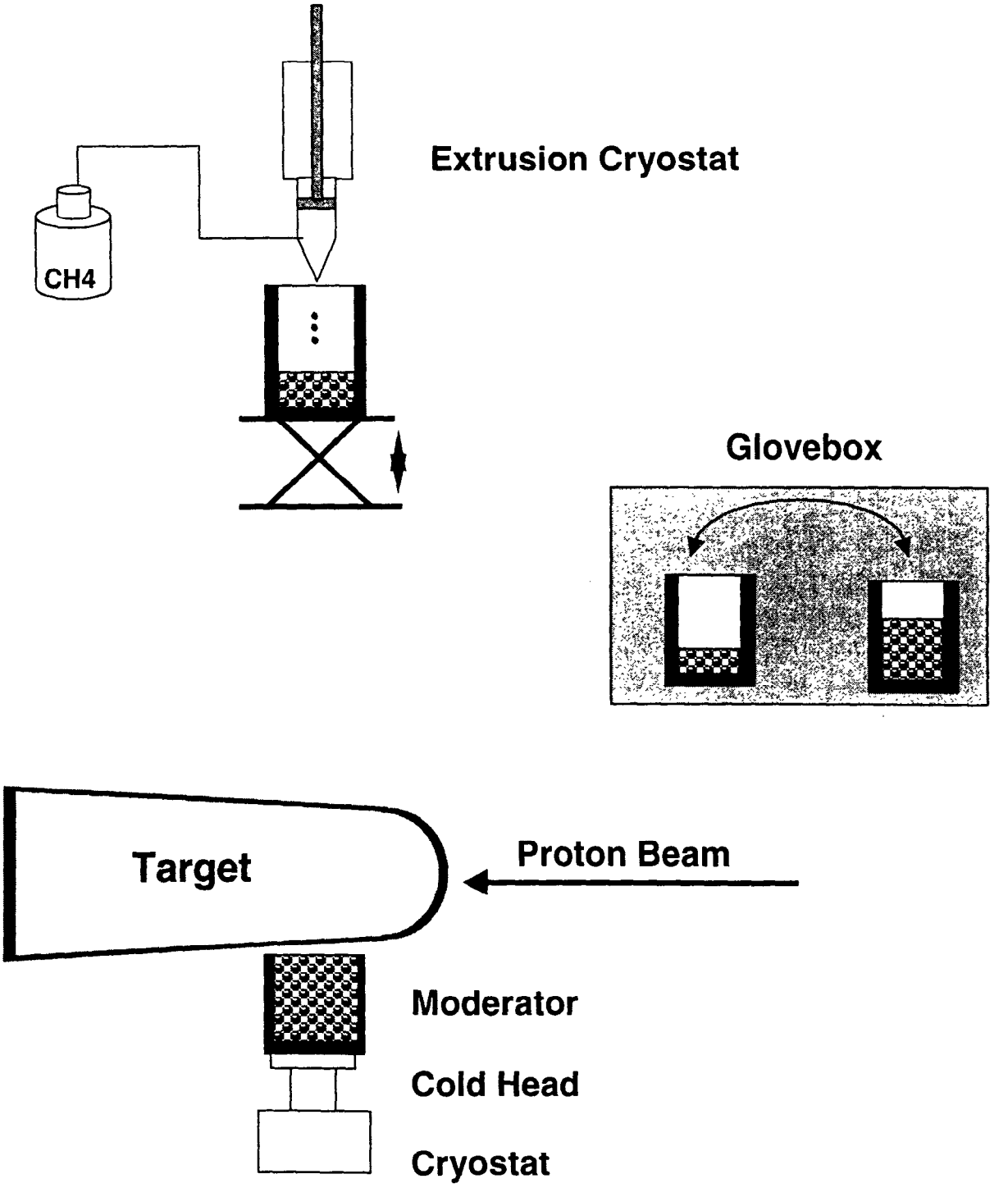

Fig. 4 : Moderator Tests at COSY

ICANS-XIV
The 14th Meeting of the International Collaboration on Advanced Neutron Sources
June 14-19, 1998
Starved Rock Lodge, Utica, Illinois

Comparison of Decoupled Cryogenic Moderators for High Resolution Experiments

Y. Ogawa, M. Konno, H. Iwasa, T. Kamiyama, Y. Kiyanagi, M. Furusaka*
and N. Watanabe**

Graduate School of Engineering, Hokkaido University, Sapporo 060-8628, Japan
*High Energy Accelerator Research Organization, Ibaraki 305-0801, Japan
** Japan Atomic Energy Research Institute, Ibaraki 319-1195, Japan

Abstract

As a cold/thermal neutron source for high-resolution experiments, we studied the neutronic performance of a mixed moderator of polyethylene particles plus liquid hydrogen, which is the first test of a mixed type moderator. The performance is better than the decoupled liquid-hydrogen moderator especially in the thermal neutron region.

As a cryogenic moderator for thermal neutron experiments, we measured neutronic performance of a poisoned liquid-methane moderator and compared the performance with that of a poisoned water moderator. The performance of the liquid-methane moderator is superior to the water moderator over the thermal region. Finally we compared the neutronic performances of a liquid-methane moderator to other various decoupled cryogenic moderators.

I. Introduction

In the future projects of MW class spallation sources, the development of efficient cryogenic moderators for high resolution scattering experiments in the cold and thermal regions is one of the important issues. In MW class spallation sources, as well known, monolithic solid methane cannot be used because of the burp and liquid methane will be very difficult to use because of the serious radiation damage although they have superior neutronic characteristics. The unique moderator material which can be used in MW class sources is liquid-hydrogen. However, a lower hydrogen number density of liquid-hydrogen causes the shortage of neutron intensity. A coupled liquid-hydrogen moderator with or without ambient temperature premoderator was proposed and gives 5 times higher intensity than a decoupled liquid-hydrogen moderator.[(1) (2)] On the other hand, the pulse width (in full width at half maximum, FWHM) of cold neutrons from a coupled moderator is much larger than that of a decoupled

Keywords: narrow pulse, mixed moderator, liquid methane moderator, neutronic performance figure of merit

one; about two times for a moderator with a premoderator and much more for without. Therefore, this type of moderator may not be used for high resolution scattering experiments without a fast chopper at a distance very close to the source and/or a very long flight path. So, it is desired to develop a cold neutron moderator providing a relatively high intensity with a narrower pulse. For this purpose, a liquid-hydrogen moderator with decoupled premoderator was proposed as a high-efficiency cold moderator, and the neutronic performance was proved to be rather good.[3]

Recently, another method was proposed; a mixed moderator of liquid-hydrogen plus hydrogenous particles.[4][5] This type of moderator could be used in a MW class spallation source if the solid particles can be circulated with the liquid to renew particles before suffering from serious radiation damage. This moderator can compensate the disadvantage of liquid-hydrogen, namely, a lower hydrogen number density. As solid particles solid methane and H_2O ice were proposed.[4][5] As the first step, we measured the intensity and pulse structure of neutrons from a mixed moderator consisting of polyethylene particles plus liquid-hydrogen, in order to understand the fundamental mechanism of neutron thermalization in a mixed moderator and also to know neutronic performance of this moderator. Polyethylene particles were chosen due to the reasons that this is a good substitution of water and easy to mix.

So far, the liquid-methane moderator is considered to be the best realistic moderator at a 100 kW source for high resolution experiments in the thermal region. However, the neutronic characteristics have not been well studied by experiments. So, we measured the neutronic performance of a liquid-methane moderator under the same target-moderator-reflector so far studied. We also measured the neutronic performance of the water moderator and compare the performance with that of the liquid-methane moderator.

We finally compare the measured neutronic performances of the liquid-methane moderator to those of various decoupled moderators; a B_4C decoupled ambient temperature light water, a Cd decoupled liquid-hydrogen, a mixed moderator and a solid methane moderator. The results are also compared in terms of a figure of merit.

II. Mixed Moderator of Polyethylene Particles and Liquid-Hydrogen

II. 1 Experiments

We performed the experiments by using a cold neutron facility at the Hokkaido linac. Figure 1 shows the target-moderator-reflector assembly used. The moderator chamber has a viewed surface of 12 cm × 12 cm and a thickness of 5 cm. We used a graphite reflector of about $1 m^3$. All moderators measured were decoupled from the reflector by 0.5 mm thick cadmium plates.

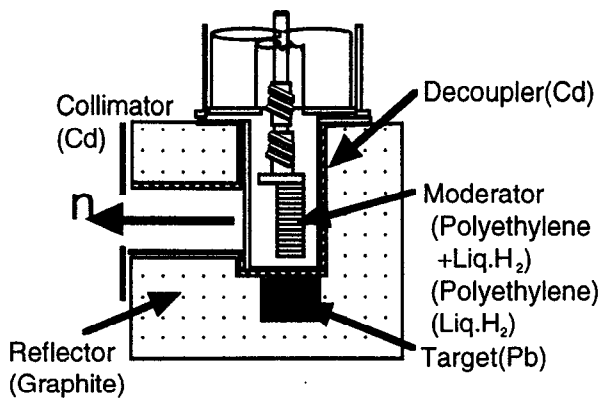

Fig. 1 Experimental setup of target-moderator-reflector assembly in study of mixed moderator.

The polyethylene particles used are low density ones with a hydrogen number density of 7.9×10^{22} H/cm^3, which is almost the same as that of solid methane. The average size is about 1 mm in diam. (ranging from 0.85 to 1.18 mm). The average diameter corresponds to the mean free path in polyethylene at the Maxwellian peak energy (~3 meV). We determined the packing factor from the weight and the volume measurements and obtained a value of 64.5 %. The overall hydrogen number density of the mixed moderator is 6.7×10^{22} H/cm^3, almost the same as that of light water (6.8×10^{22}). The average hydrogen number densities in the polyethylene particle moderator and the mixed moderator are about 1.2 times and 1.6 times higher than that of the liquid-hydrogen moderator (4.2×10^{22} H/cm^3), respectively.

We also measured the energy spectra from two pure moderators, liquid-hydrogen and polyethylene particles for comparison

II. 2 Results and Discussion

II. 2 .1 *Energy Spectra*

Figure 2 shows the measured energy spectra. The spectrum from the polyethylene particle moderator has a peak at 6-7 meV and the intensity in the slowing-down region (approximately above 20 meV) is considerably higher than that from the liquid-hydrogen one. This is due to the fact that polyethylene has a higher hydrogen number density but no effective energy exchange mode at lower energies. The neutron intensity from the mixed moderator in the slowing-down region is slightly lower than that from the polyethylene particle moderator, in spite of a higher hydrogen number density of the mixed moderator. This can be explained as follows; in the mixed moderator neutrons are transported more efficiently to a lower energy region due to a more efficient energy transfer mechanism by mixing liquid-hydrogen. This result shows, as well known, that not only the hydrogen number density but also the energy exchange mode at lower energies play an important role to determine the spectral intensity.

The neutron spectrum from the mixed moderator is characterized by the properties of the both moderator materials, polyethylene and liquid-hydrogen. Namely, in the slowing-down region, the intensity is mainly determined by the polyethylene particles, while in the equilibrium region mainly by liquid-hydrogen.

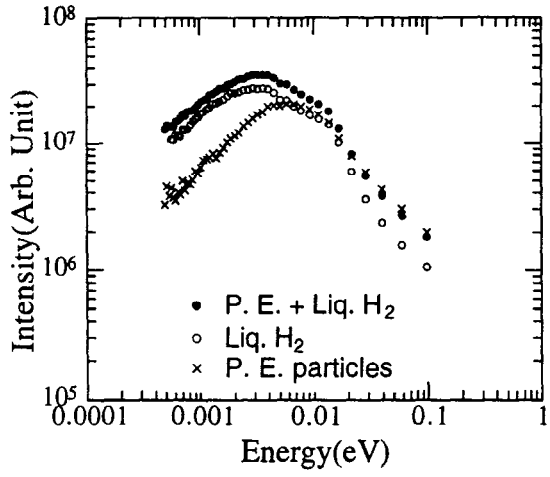

Fig. 2 Energy spectrum from the mixed moderator, compared with those from two pure moderators.

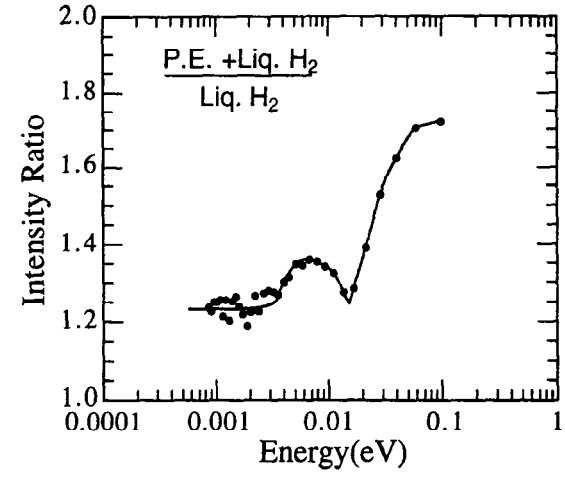

Fig. 3 Intensity ratio of mixed moderator to liquid-hydrogen moderator.

Figure 3 shows the intensity ratio of the mixed moderator to the liquid-hydrogen moderator. The neutron intensity from the mixed moderator is higher than the decoupled liquid-hydrogen moderator in all energy region. The ratio is about 1.2 at the cold neutron region but reaches to about 1.7 around 0.1 eV.

II. 2.2 *Time Distributions*

Figure 4 shows measured pulse shapes from the mixed moderator and the reference liquid-hydrogen moderator at three different energies: slowing-down, transient (between slowing-down and equilibrium) and cold equilibrium regions. Those in the left side are of the linear plots, while in the right side are of the semi-logarithmic plots. In these figures, the intensities were normalized by using the time-integrated intensities shown in Fig. 2.

In pure decoupled moderators, the pulse shapes can generally be expressed by a sum of two components; slowing-down and storage terms, as reported by Ikeda and Carpenter.[6] We found that the pulse shapes from the mixed moderator can also be expressed by the Ikeda-Carpenter formula.

In the slowing-down and transient regions the pulse widths from the mixed moderator are almost comparable to those from the pure hydrogen moderator. However, the peak intensity is significantly higher. On the other hand, in the cold equilibrium region only the width increases but the peak intensity is unchanged. From these results, it turns out that in the slowing-down region the gain in the intensity is due to the increase of the pulse height but not to the increase of the pulse width. These results indicate that the characteristics of this mixed moderator is suitable for high-resolution experiments using thermal neutrons (above 20 meV) rather than cold neutrons.

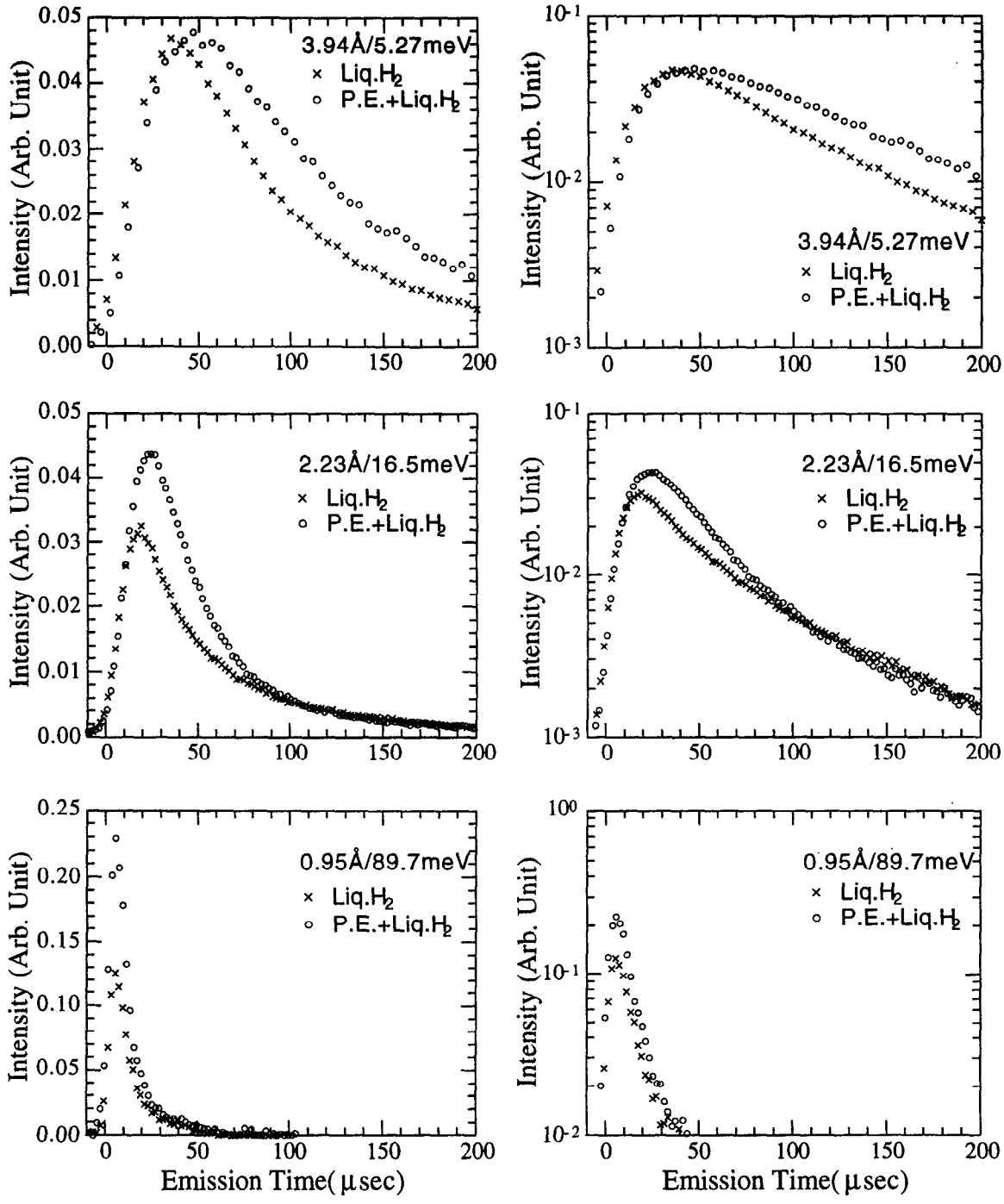

Fig. 4 Pulse shapes of mixed moderator as well as the liquid-hydrogen moderator at three energies. Left side is linear plots and right side is semi-logarithmic plots.

Figure 5 shows the pulse widths of the liquid-hydrogen and mixed moderators, in FWHM. The pulse widths of the mixed moderator is almost the same as the liquid-hydrogen one in the slowing-down and transient regions, but about 30% longer in the cold region. The pulse width broadening at lower energies is due to a higher hydrogen number density (effectively equivalent to a thicker moderator; a longer decay time) and to a poor energy exchange mechanism in polyethylene, resulting in a longer rising time as shown in Fig. 4.

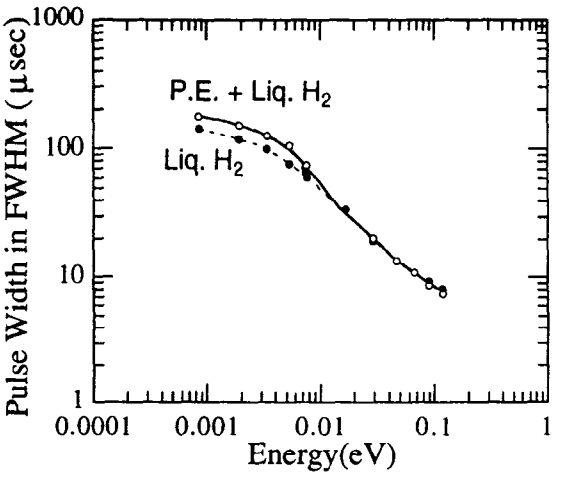

Fig. 5 Pulse width (FWHM) of neutrons from the mixed moderator as well as the liquid-hydrogen moderator as a function of neutron energy.

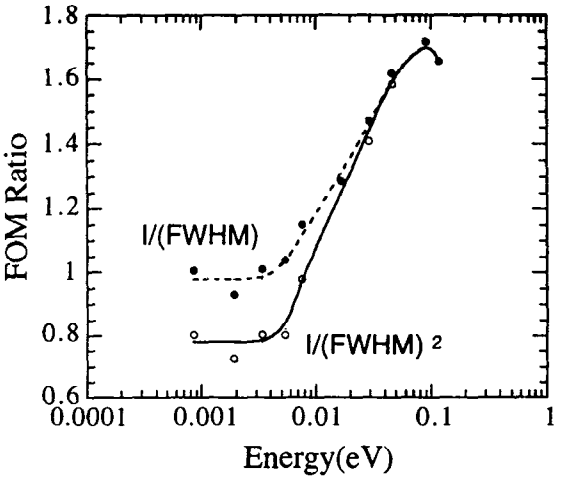

Fig. 6 Ratio of figure of merit (FOM) of the mixed moderator to the decoupled liquid-hydrogen moderator.

II. 2. 3 *Figure of Merit*

We compare the measured neutronic performance to that of a decoupled liquid-hydrogen moderator in terms of a figure of merit (FOM). The figure of merits for high-resolution experiments using thermal neutrons will be defined as $I/(FWHM)^2$ since the neutron intensity incident on a scattering sample is proportional to inverse of square of flight path length (the case without neutron guide). In the cold neutron region it is difficult to evaluate the merit of a shorter flight path since in this region a neutron guide tube can be used. If we assume the merit is proportional to the inverse of the flight path length, the FOM is defined as I/(FWHM). Figure 6 shows the ratios of the FOM's, mixed moderator to the decoupled liquid-hydrogen one, calculated by both definitions. Solid line indicates the FOM value using $FOM_1 = I/(FWHM)^2$ and broken line using $FOM_2 = I/(FWHM)$. The values will be comparable in slowing-down region, because pulse widths from the mixed moderator is almost the same as that from liquid-hydrogen moderator. The values are almost independent of the energy in the cold region, about 0.8 (FOM_1) or 1.0 (FOM_2), and reach at about 1.7 around 0.1 eV. This indicates that the mixed moderator is efficient rather in the thermal neutron region.

III. Poisoned Liquid-Methane Moderator

III. 1 Experiments

We measured the spectral intensity and pulse shapes from a poisoned liquid-methane. The target-moderator-reflector assembly used is the same as the one shown in Fig. 1 except for the moderator chamber and the decoupler. The moderator chamber has a viewed surface of 12 cm × 12 cm and a thickness of 4.5 cm. The moderator was poisoned at the center of the chamber by a 0.25 mm thick gadolinium metal plate. The moderators was decoupled from the reflector by 3 mm thick B_4C resin plates. Decoupling energy of the decoupler is about 2.5 eV. For

comparison we also measured neutronic performance of an ambient temperature H_2O moderator in the same system as the poisoned liquid methane moderator.

III. 2 Experimental Results

III. 2. 1 *Neutronic Performance of Liquid-Methane Moderator*

Figure 7 shows measured energy spectrum from the liquid-methane moderator, compared with that from H_2O moderator. In the case of H_2O moderator, the spectra consist of 1/E spectrum in slowing-down region and Maxwellian in equilibrium region. In the case of liquid-methane, there is almost flat region around 60 -100 meV.

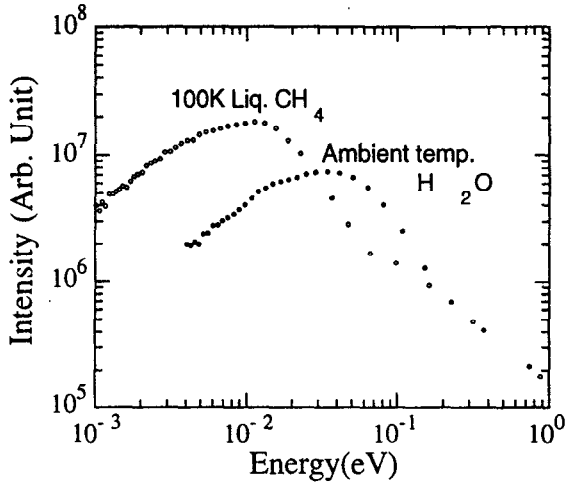

Fig. 7 Energy spectrum from liquid-methane moderator, compared with those from light water moderator.

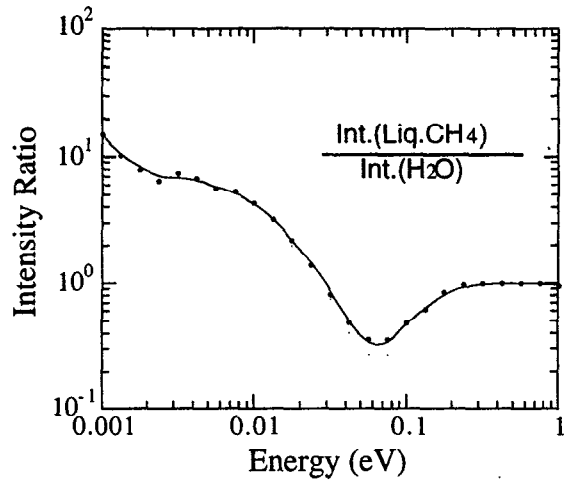

Fig. 8 Intensity ratio of liquid-methane moderator to light water moderator.

The spectral intensity of the liquid-methane is almost the same as that from the H_2O moderator in slowing-down region due to little difference in hydrogen number density. The intensity from the H_2O moderator is higher than that from the liquid-methane moderator in the range 30-200 meV. The intensity ratio of liquid-methane moderator to H_2O moderator reaches about 10 around 1 meV, as shown in Figure 8.

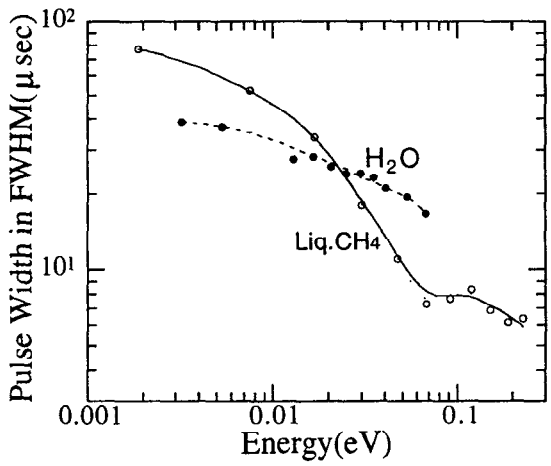

Fig. 9 Pulse width (FWHM) of neutrons from the liquid-methane moderator compared with light water moderator.

Figure 9 shows pulse width (FWHM) of neutrons from the liquid-methane moderator compared with H_2O moderator. In the range 60-100 meV where the intensity from the liquid-methane is almost constant as mentioned above, the pulse width is also unchanged and in the slowing-down region above 100 meV, the pulse width would be proportional to 1/v.

The pulse width of liquid-methane is longer in the energies below 25 meV and narrower above this energy. In the energies over 70 meV, we have no data of pulse width of H_2O, however, the pulse width of H_2O moderator would be comparable to that of liquid-methane in the slowing-down region. The pulse width in equilibrium region is about 80 μsec in the case of liquid-methane and 40 μsec in the case of H_2O.

We have calculated heat deposition in the methane-moderator in 0.6 MW case and found that the heat deposition is about 3 times higher than that in the present ISIS using Ta target.[7] If radiation damage is proportional to the heat deposition, the life will become much shorter than the present ISIS, indication that it is very difficult to use the methane moderator.

IV. Comparison of Neutronic Performances of Cryogenic Moderators

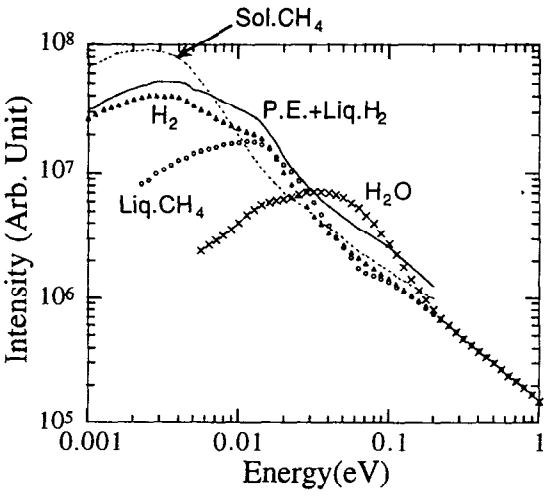

Fig. 10 Energy spectra from decoupled moderators so far measured.

A reliable comparison of the neutronic performance is indispensable for the choice of a cryogenic moderator for high-resolution thermal-neutron scattering experiments. We considered that the cryogenic moderator for high resolution experiments has to cover the energy range less than about 0.3 eV and above this energy a water moderator can provide the same neutronic performance as methane one. Our calculation indicates that we can obtain an intensity gain about 1.5 to 1.9 by reducing the decoupling energy from 2.5 to 0.5 eV. The energy spectra from five different moderators are compared in Fig. 10; a Cd decoupled liquid-hydrogen moderator with a thickness of 5 cm, a Cd decoupled mixed moderator with a thickness of 5 cm, a poisoned liquid-methane moderator with a thickness of 4.5 cm decoupled by B_4C (decoupling energy is about 2.5 eV), a Cd decoupled solid-methane moderator with a thickness of 5 cm and a B_4C decoupled poisoned water moderator with a thickness of 4.5 cm.

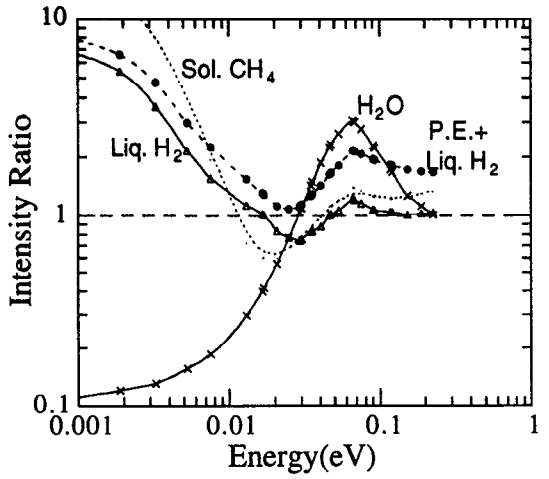

Fig. 11 Intensity ratios of various moderators to liquid-methane moderator.

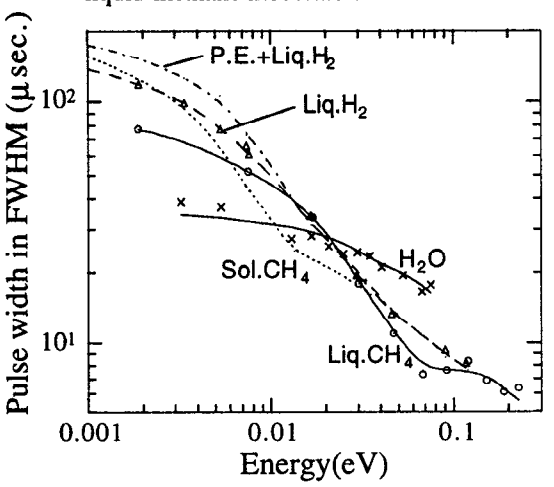

Fig. 12 Pulse Widths (FWHM) of neutrons from various decoupled moderators so far measured.

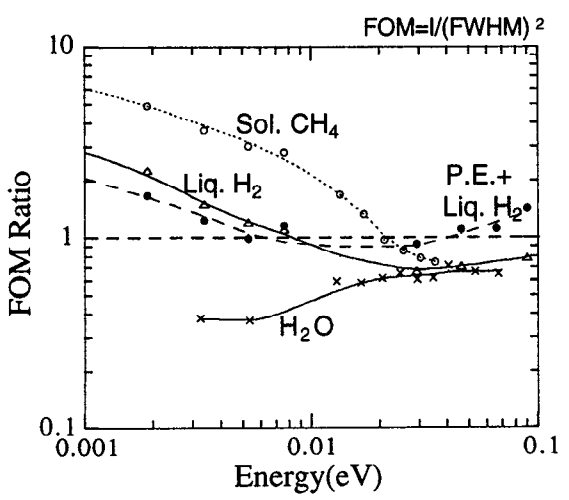

Fig. 13 Ratio of FOM's of various decoupled moderators to liquid-methane moderators.

The ratios of the intensities from moderators to that of the liquid-methane moderator are shown in Fig. 11. The pulse widths in FWHM are shown in Fig. 12. The intensity from the decoupled liquid-hydrogen is lower than that from a liquid-methane only in the region 0.015 -0.5 eV and the ratio is 0.7. Around this energy region the pulse width of the liquid-hydrogen is almost the same as or somewhat narrower than that of the liquid-methane. The intensity from the mixed moderator is higher over whole energy range. We evaluated the performance of the moderators by using the FOM defined as $I/(FWHM)^2$ and obtained ratios to that of the liquid methane. The results are shown in Fig. 13. The FOM of the water moderator is lower than others in the energy region indicated but the FOM in the higher energy region above about 0.3 eV will be almost the same as that of the methane moderators.

The FOM of the solid methane moderator is much superior to others in the lower energy region but this cannot be used in a high power source. The relative FOM value of the liquid-hydrogen is smaller than unity above 0.01 eV but the ratio is about 0.7, which is not so bad. The relative FOM value of the mixed moderator is larger than unity bellow 0.005 eV and above 0.05 eV and almost the same in the mid region.

A poisoned liquid-hydrogen moderator of somewhat a larger total volume will increase the intensity without changing the pulse width. Such experiments are important.

V. Conclusion

As a high-resolution (short pulse) moderator, a mixed moderator of liquid-hydrogen plus polyethylene particles exhibits a good neutronic performance compared with a liquid-hydrogen moderator, especially in the thermal neutron region. Therefore, this type of moderator will be suitable for high resolution experiments in the thermal region.

A liquid- methane moderator has good neutronic characteristics but the superiority is not so large compared with the liquid- hydrogen moderator. Furthermore, it is very difficult to use a liquid-methane moderator in a MW class spallation neutron source since the radiation damage in the methane moderator is too large.

A poisoned liquid-hydrogen moderator will be one of the most promising candidates as moderator for high resolution thermal neutron experiments. This type of moderator will be studied near future. For the long term study the development of an advanced type cryogenic moderators for example, a mixed moderator, is important.

References

(1) Y. Kiyanagi, N. Watanabe and H. Iwasa, Nucl. Instr. Meth. **A312**, 561(1992).

(2) G. J. Russell, E. J. Pitcher and P. D. Ferguson, Proc. ICANS XIII, Villigen, PSI, Switzerland, October 11-14, 1995, p. 495 (1995).

(3) Y. Kiyanagi, N. Kosugi, Y. Ogawa, H. Iwasa, F. Hiraga, M. Furusaka and N. Watanabe, Proc. ICANS XIII, Villigen, PSI, Switzerland, October 11-14, 1995, p. 666 (1995).

(4) K. D. Williamson and A. T. Lucas, Proc. ICANS X, Los Alamos, LANL, USA, October 3-7, 1988, p. 559 (1988).

(5) A. T. Lucas, G. S. Bauer, and C. D. Sulfredge, Proc. ICANS XIII, Villigen, PSI, Switzerland, October 11-14, 1995, p. 644 (1995).

(6) S. Ikeda and J. M. Carpenter, Nucl. Instr. Meth. **A239**, 536(1985).

(7) B. R. Diplock, Proc ICANS VI, Argonne, ANL, USA, June 27 - July 2, 1982, p328(1983)

Neutron Scattering Instruments

NEW INSTRUMENTS AND EQUIPMENT

ICANS XIV
14th Meeting of the International Collaboration on Advanced Neutron Sources
June 14-19, 1998
Starved Rock Lodge, Utica, IL

HET-II A Proposed Upgrade for HET, the High Energy Chopper Spectrometer at ISIS

R S Eccleston, S Foster and R I Bewley
ISIS Facility, CLRC Rutherford Appleton Laboratory,
Chilton, Didcot, Oxfordshire, OX11 0QX, UK.

Abstract

We propose an upgrade to the high energy chopper spectrometer, HET, at ISIS. A supermirror guide will enhance the flux of thermal energy neutrons on to the sample, and a position sensitive detector array at 2.5m from the sample covering the angular range 3° to 150° and extending out to 30° above and below the equatorial plane will provide a five fold increase in solid angle over HET. An oscillating collimator will reduce the background scattering from massive sample environment equipment such as pressure cells.

HET, the high energy transfer chopper spectrometer[1] is a member of the original suite of instruments at ISIS, and became operational as the source came on line in 1985. The unrivalled access to a wide energy range at low momentum transfer offered unique opportunities for the study of magnetic excitations. Examples of work carried out on HET include experiments on rare earths[2], heavy fermion[3] and kondo systems[4] and high temperature superconductors[5]. In addition, studies of molecular dynamics have proved very effective. Measurements on single crystals have also produced many high profile publications[5,6,7] and the work on HET and MARI provided the impetus for the construction of MAPS, a spectrometer optimised for the study of excitations in single crystals, utilising a large array of position sensitive detectors (PSDs). The commissioning of MAPS will start in early 1999. With the advent of MAPS and in the light of recent developments in the use of neutron guides and PSDs there is now an opportunity to upgrade HET so it is complementary to both MAPS and MARI, and at the same time offers a dramatic increase in performance over the present instrument. In this paper we discuss the ideal specification for HET-II setting aside the limitations associated with building on a specific beamline.

The proposed layout of HET-II is shown in figure 1. The principle features of the upgrade are a supermirror guide for the incident beam and continuous coverage from 3° to 150°, with banks of PSDs extending out to 30° above and below the equatorial plane. In addition, a removable, oscillating collimator will reduce background scattering from difficult sample environment such as pressure cells. In the design, we are also keeping in mind the possibility that the performance of ^{3}He polarising filters may, at some time in the future, be such that it would be reasonable to provide the option for polarisation of the incident beam and polarisation analysis on the spectrometer.

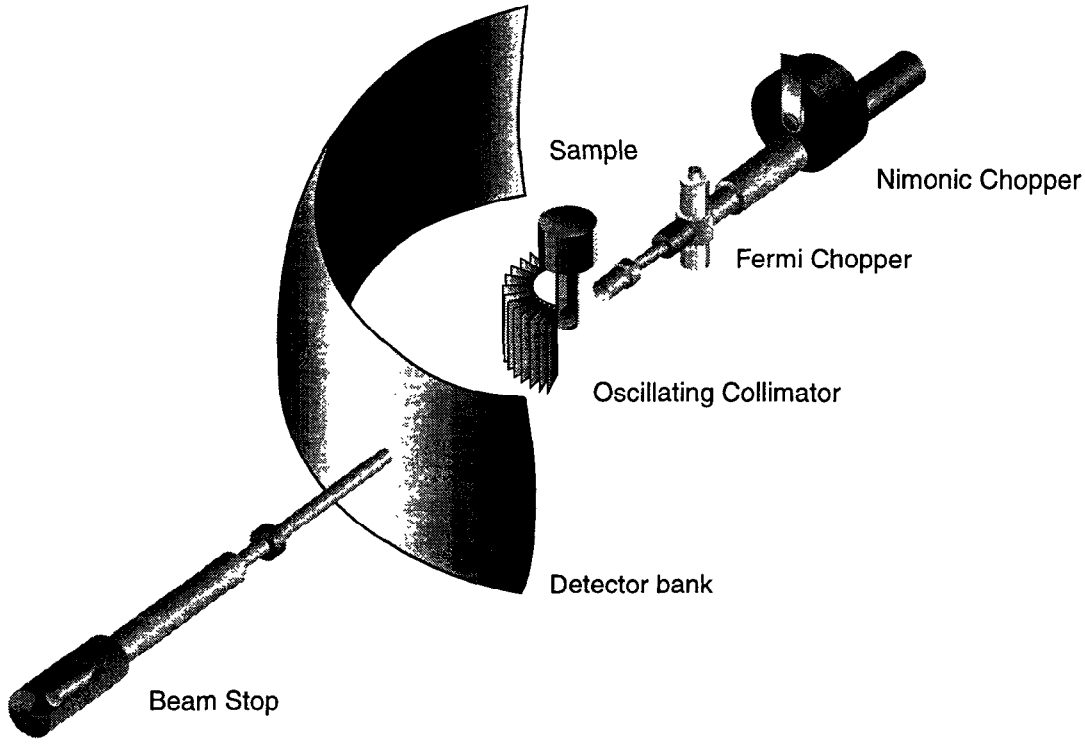

Figure 1. A schematic diagram of HET-II.

The present HET views the ambient pressure water moderator, which is poisoned at 1.5cm. The preferred choice of moderator for HET-II is a methane moderator, which offers a gain in flux of a factor of up to 10 at 20meV (figure 2).

The lengths of the primary flight path for HET-II are the same as those for HET. The nimonic or T_0 chopper will be located at 8.4m from the moderator with the Fermi chopper at 10m from the moderator and the moderator to sample distance of 11.2m. However, supermirror guides will be installed in three sections; between the moderator and the nimonic chopper, between the nimonic chopper and the Fermi chopper and between the Fermi chopper and the end of the incident beam pipe. Monte Carlo calculations for a guide with m=3 (figures 2) indicate that at low energy transfers a gain over HET of a factor of up to 100 can be achieved if HET-II was to view the methane moderator. The flux enhancement if HET-II was to view the water moderator rises to approximately 15 at 5meV. The same calculations suggest that the impact of the guides on energy transfer resolution is negligible, however, the increase in beam divergence caused by the guides will result in an increase in ΔQ for incident energies of below 100meV rising to 44% at 5meV as shown in figure 3. This loss in Q resolution could be recovered by installing a soller collimator at the end of the incident beam tube at the cost of flux. The ability to insert such a collimator when be required may be a feature of the design. The energy transfer resolution of HET-II will be the same as that of the 2.5m bank of HET, that is a HWHM of approximately 1.5 to 2.5% of the incident energy at the elastic line.

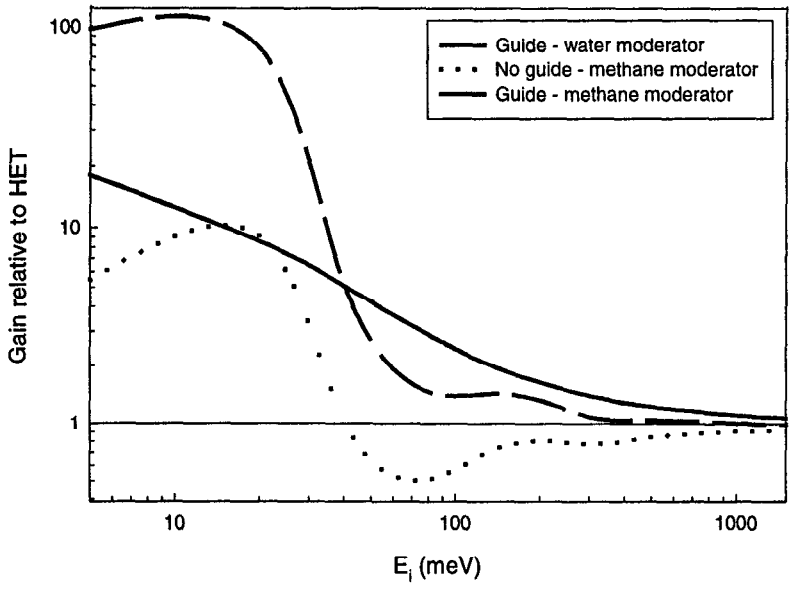

Figure 2. Anticipated gain in flux to the sample over HET, due to the installation of a guide and/or changing the moderator to methane.

HET is now equipped with beam defining jaws at the end of the incident beam tube. A further set will be installed in the Fermi chopper pit to reduce the penumbra.

The sample tank will, ideally, be cylindrical in geometry with a standard ISIS flange to accommodate all the standard ISIS sample environment equipment including the cryomagnet. However, the flange will be mounted on a goniometer assembly with vacuum bellows to provide limited movement on two arcs to facilitate easy alignment for single crystal samples. The tank will be lined with B_4C loaded epoxy to reduce background scattering and a cryo-pump will be fitted, as is the case on HET, to eliminate the build up of ice on cold samples over a period of time.

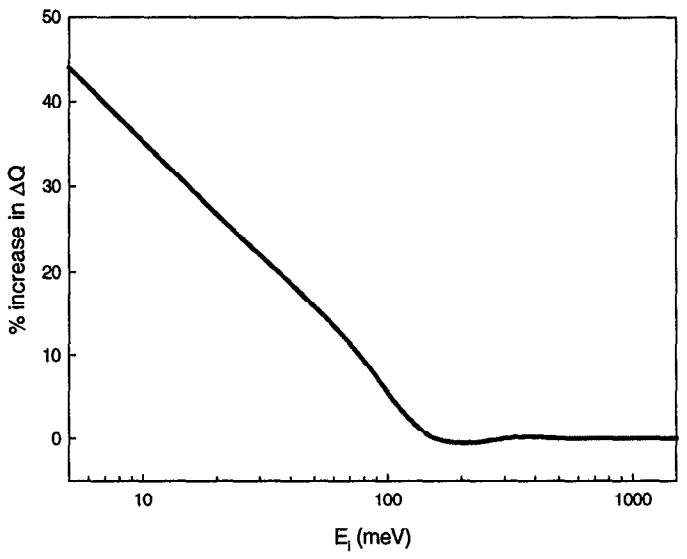

Figure 3. The calculated degradation in momentum transfer resolution as a function of incident energy arising from the use of a guide.

HET-II will use standard sample environment equipment such as CCRs and cryostats, however, the anticipated high sample throughput would justify the design and construction of a bespoke top-loading, rotating 4K CCR that would speed up sample changes for single crystal and polycrystalline samples.

The high flux and solid angle available on HET-II will facilitate the study of small sample volumes and presents the potential to use difficult sample environment such as pressure cells. In order to reduce background from sample environment an oscillating collimator will be available, surrounding the sample volume. We anticipate that the oscillating collimator will be easy to install and remove depending upon the requirements of the experiment.

Previous experience on MARI has shown the importance of vanes to prevent spurious scattering arising from reflections from the aluminium windows. In the case of HET-II we plan to stagger the position of the vanes across the face of the detector banks to reduce the number of gaps in Q,ω coverage for powder samples and care will be taken to keep the number and size of the vanes used to a minimum.

Three parallel banks of ^{3}He PSDs will be used to tile the angular range from -30 to 150° with a minimum angle of 3° on a secondary flight path of 2.5m, with detector coverage extending out to ± 30° in the azimuthal plane. The upper and lower banks will be filled with 1m PSDs, with the middle bank filled with 50cm tubes. This detector array represents a solid angle of 0.25πSr in the scattering angle range below 30°, a factor of approximately 2 increase over HET. The total solid angle of HET-II will be πSr, five times more than HET. This in itself represents a considerable gain, particularly when coupled to the gains achieved by installing the supermirror guides and viewing a methane moderator as discussed above. However, the advantages of such wide coverage with position sensitivity will have a more dramatic impact on the performance of the instrument. In total, HET-II will have over 50000 detector pixels producing a huge volume of information. Position sensitive detectors were installed on HET in May 1997. They cover the angular rang from 3° to 7° degrees on a flight path of 4m, and have already been used to great effect by several experimental teams[8]. The ability to tune Q resolution in the analysis software, and to extract arbitrary slices though the data provides a dramatic increase in flexibility, particularly for single crystal measurements.

The scientific opportunities offered by the upgrades we propose are many-fold. Increased flux will allow the use of lower sample volumes thus facilitating the study of new materials that are difficult to fabricate. High flux combined with the oscillating collimator provides the opportunity to make studies using difficult sample environment such as pressure cells or magnets, thereby open a wide range of parameter space. Short counting times also enhance the opportunities for parametric studies. The continuous detector coverage will make HET-II suitable for the molecular dynamics work which is currently carried out on MARI, but does not require the higher energy transfer resolution offered by MARI, and would benefit from higher data rates. However, the most dramatic improvement will be in the volume of information available, because such a wide area is tiled by position sensitive detectors. The ability to take arbitrary slices through four dimensional Q,ω space will provide unparalleled flexibility, particularly for single crystal experiments. Simultaneous measurements of phonons and magnetic excitation in single crystals will be possible in relatively short times with vast volumes of information attainable from only a small number of crystal orientations.

In conclusion, we have proposed an upgrade for HET that not only offers a dramatic increase in count rate, but also a huge increase in information volumes by virtue of a large bank of position sensitive detectors. The proposed instrument will complement MAPS which is optimised for higher resolution at higher energies, and MARI which also offers continuous detector coverage, but with better resolution and lower flux.

Further development in the HET-II project will be posted on the web at http://isis.rl.ac.uk/excitation/het/hetii.htm.

References

[1] B C Boland Z A Bowden T G Perring A D Taylor, Proc. ICANS-VIII, July 8-12 (1985) p535.
[2] A D Taylor R Osborn K A McEwen W G Stirling Z A Bowden W G Williams E Balcar S W Lovesey, Phys Rev Lett 61 1309 (1988).
[3] E A Goremychkin R Osborn, Phys Rev B 47 14280 (1993).
[4] A P Murani Z A Bowden A D Taylor R Osborn W G Marshall, Phys Rev B 48 13981 (1993).
[5] S M Hayden G Aeppli R Osborn A D Taylor T G Perring S-W Cheong Z Fisk, Phys Rev Lett 67 3622-3625 (1991).
[6] T G Perring A T Boothroyd D McK Paul A D Taylor R Osborn R J Newport J A Blackman H A Mook, J Appl Phys 69 6219-6221 (1991)
[7] T G Perring G Aeppli S M Hayden S A Carter J P Remeika S W Cheong, Phys Rev Lett 77 711 (1996)
[8] The commissioning and performance of the HET PSDs will be reviewed at this meeting by C D Frost.

ICANS-XIV
14th Meeting of the International Collaboration on
Advanced Neutron Sources
June 14-19, 1998
Starved Rock Lodge, Utica, Illinois, USA

THE BACKSCATTERING SPECTROMETER HERMES: DESIGN ISSUES

J.Z. Larese
Chemistry Department
Brookhaven National Laboratory
Upton, NY 11973

L.L. Daemen, P.A. Seeger, J. Eckert, T.O. Brun
Manuel Lujan, Jr. Neutron Scattering Center
Los Alamos National Laboratory
Los Alamos, NM 87545

1. Introduction

A computer model of the backscattering spectrometer HERMES was used to help answer a number of issues that arose during the conceptual design of the spectrometer. In particular, the performance of the spectrometer was evaluated on several types of moderators:

- A decoupled liquid hydrogen moderator;
- A partially coupled liquid hydrogen moderator;
- A decoupled, poisoned liquid hydrogen moderator.

Variying the degree of coupling of the moderator to the reflector , as well as poisoning the moderator can affect greatly the time and energy distribution of the neutron pulse emitted by the moderator. The proposed reflector for the LANSCE upgrade is a composite reflector made of beryllium in the immediate vicinity of the moderators. A second layer of lead completes the reflector and surrounds the inner reflector/moderators assembly.

The main purpose of the reflector is to reflect toward the moderators neutrons that would otherwise have missed the moderators and give these neutrons a second chance at moderation. While beryllium is a good reflecting material, it is also a good moderator. Therefore, in addition to returning fast (epithermal and faster) neutrons to the moderator, it also returns a large moderated neutron flux long after the target was pulsed. This increases the (time-integrated) intensity of the emitted neutron pulse, but it does so at the expense of adding a long tail to the pulse.

One can mitigate this effect by establishing a barrier between the moderator and the reflector. This barrier, a decoupler, is a material that strongly absorbs neutrons in the thermal range but is more or less transparent to faster neutrons. In this way, the reflector can only return fast neutrons to the moderator. The moderated (thermal) component of the flux returned at later times by the reflector to the moderator is eliminated. Typical decoupling materials are cadmium, gadolinium, and boral -an alloy of aluminum and boron-10. Notice that it is possible to vary the degree of coupling (or decoupling) by adjusting the thickness of the decoupler, as well as by completely or partially isolating the moderator and the reflector. The proposed partially coupled liquid hydrogen moderator for the LANSCE upgrade is not directly decoupled with any material. Its back is surrounded by the other three moderators which are decoupled. This arrangement prevents the three water moderators from returning thermal neutrons to the liquid hydrogen moderator. The flight path penetration facing the moderator does not have its walls covered with decoupling materials so that the moderator face "views" the reflector directly.

It is possible to further sharpen the pulse by poisoning the moderator. This operation consists in introducing a sheet of material such as gadolinium inside the moderator to absorb neutrons that spend too much time thermalizing in the moderator. This, effectively, produces a significantly sharper pulse at the expense of some loss of intensity.

2. Moderator Characteristics

Figure 1 shows the wavelength-emission time distribution for the three moderators mentioned above. It is clear from Figure 1 that coupling the moderator to the reflector, even partially, has a dramatic effect on the neutron pulse. Notice that in Figure 1 intensity is given in absolute units and the scale is the same for all three figures.

The pulses shown in Figure 1 were used as source terms in the Monte Carlo simulations. They are a fit to an analytical form of data obtained from a radiation transport code, MCNP, for which a detailed model of the LANSCE neutron production target station is available. The general analytical form, proposed by Ikeda and Carpenter, to represent the neutron emission time-velocity distribution of the neutron pulse is [1]:

$$\psi(\lambda,t)=\int dt'\phi(\lambda,t')\left[(1-R)\left[(1-q)\delta(t-t')+q\exp\left(-\frac{(t/\lambda)}{(t/\lambda)_0}\right)\right]+\frac{R}{\tau}\theta(t-t')\exp\left(-\frac{t-t'}{\tau}\right)\right], \tag{1}$$

where δ is the Dirac delta function, θ is the step function, $(t/\lambda)_0$ and $0<q<1$ are fitting parameter, τ is the pulse decay time constant, $R=\exp(-\lambda_0^P/\lambda^P)$ is a joining function (P and λ_0 are fitting parameters). The function ϕ is given by:

$$\phi(\lambda,t)=\frac{1}{2\alpha\lambda}\left(\frac{t}{\alpha\lambda}\right)^2\exp\left(-\frac{t}{\alpha\lambda}\right), \tag{2}$$

where α is yet another fitting parameter. In the above equation, $t>0$. Strictly speaking, the Ikeda-Carpenter equation corresponds to $q=0$. The additional parameter, q, allows a better fit to the data in certain regions of the (λ,t)-space. The convolution integral is easily calculated numerically or analytically. The first term in the equation for ψ represents basically the early part of the neutron pulse while the second term represents the exponential decay of the pulse at longer times. The quantity ψ is normalized so that integration over all λ and all $t>0$ yields unity.

The (time-averaged) spectrum was taken directly from the MCNP simulation and added to the source file as a table. No attempt was made to fit the spectrum to an analytical expression such as that used in Ref.[1]. Figure 2 shows the neutron energy spectrum between 0.1 meV and 10 meV for the three moderator considered in the present study. Table 1 below summarizes the main characteristics of the moderators used in the Monte Carlo studies.

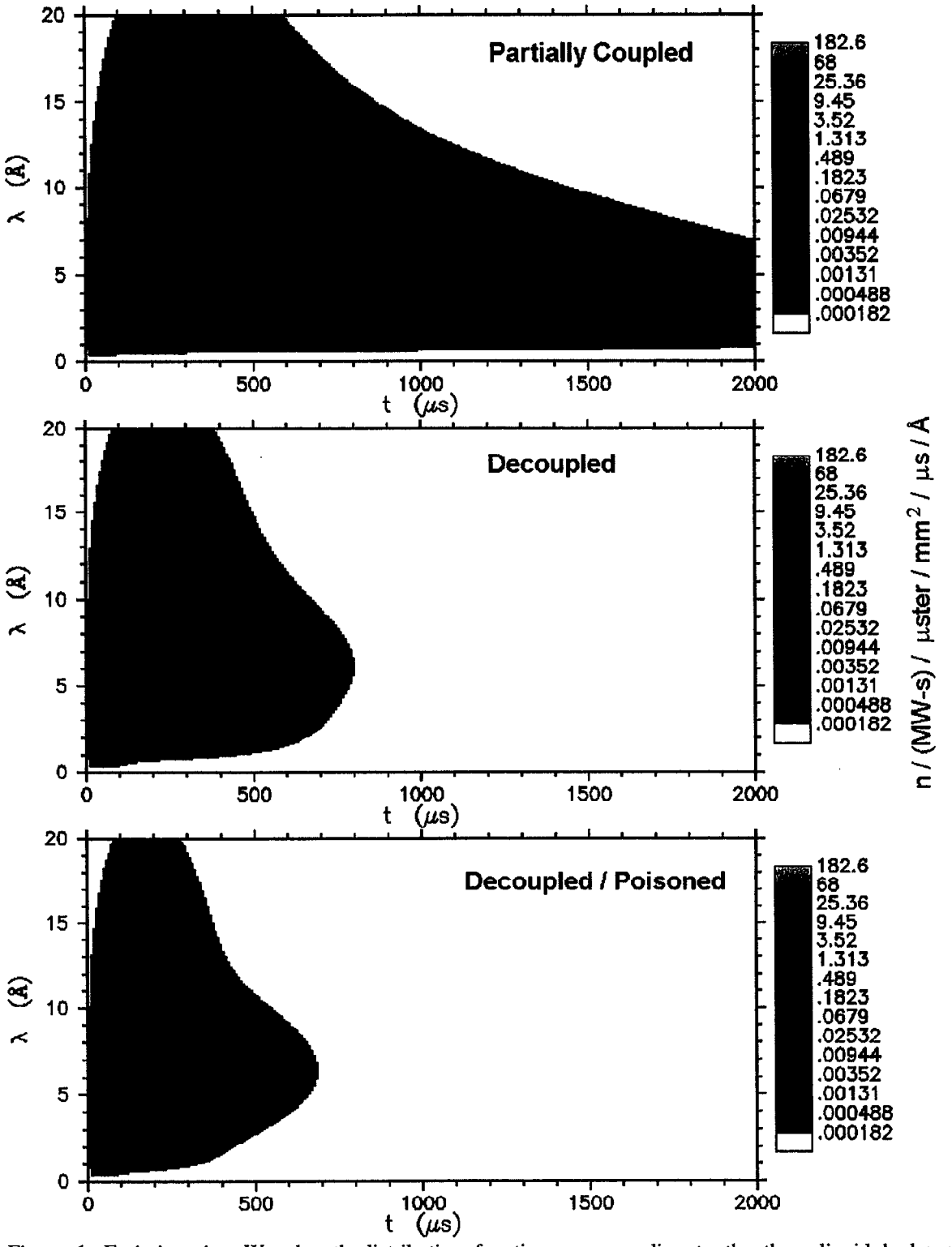

Figure 1. Emission time-Wavelength distribution function corresponding to the three liquid hydrogen moderators considered in this study. (A note on units: the flux is normalized per mm^2 of moderator surface area, per μs of emission time, per Angstrom, per μster, and per MW.s. The latter refers to the (time-averaged) energy deposited by 800 MeV protons in the neutron production target in 1 second. In order to obtain a flux per pulse, divide by the source frequency. To normalize to a 200 μA, 800 MeV proton beam, multiply by the beam power, 0.160 MW.)

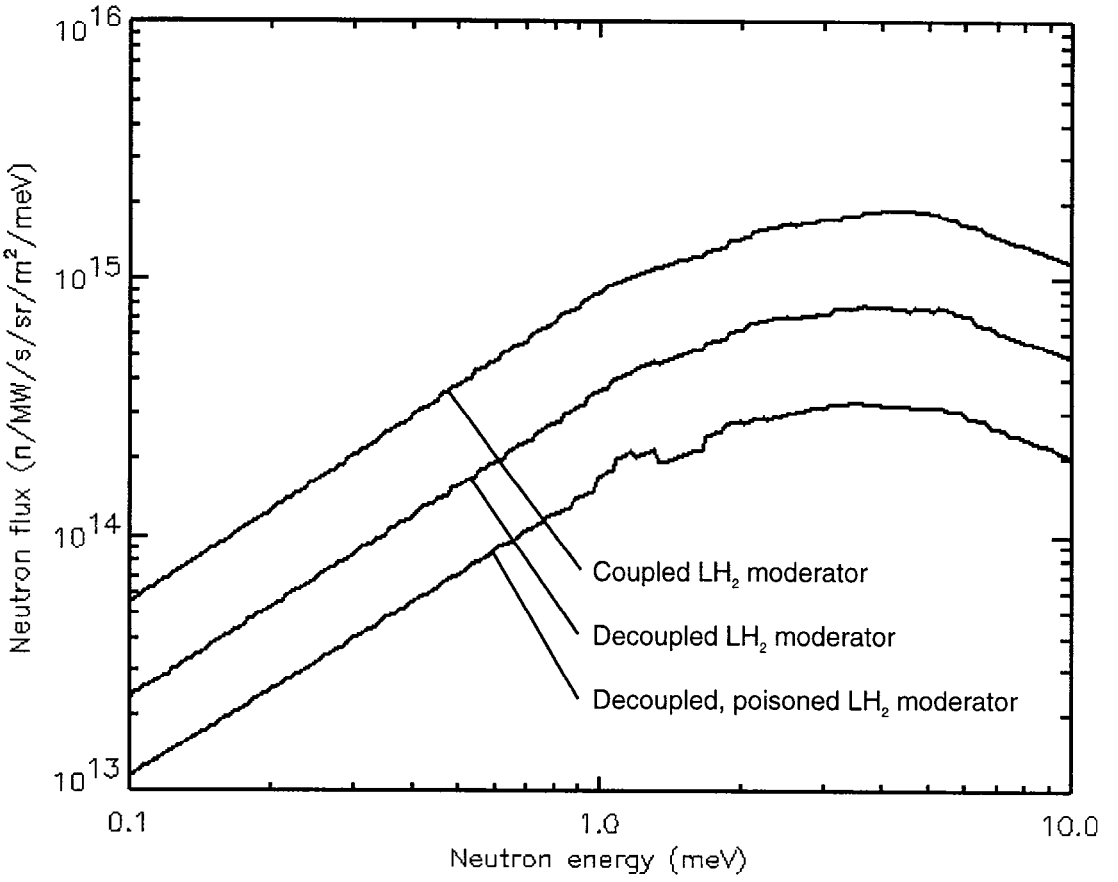

Figure 2. The (time-averaged) neutron energy spectrum for the three moderators considered in our study.

Table 1. Essential characteristics of the moderators used in our study.

MODERATING MEDIUM	LIQUID H_2 @ 20K	LIQUID H_2 @ 20K	LIQUID H_2 @ 20K
Thickness	5 cm	5 cm	5 cm
Size	12 x 12 cm^2	12 x 12 cm^2	12 x 12 cm^2
Decoupler, liner	Cd	Cd	None
Poison	Gd (17 mils), 2.5 cm depth	None	None
Surface current (0.1-5 meV range)	1.24×10^{15} n/sr/m^2/MW/s	2.89×10^{15} n/sr/m^2/MW/s	6.87×10^{15} n/sr/m^2/MW/s
Peak intensity @1.8 meV	3.30×10^{18} n/sr/m^2/μs/meV/MW/s	4.34×10^{18} n/sr/m^2/μs/meV/MW/s	5.47×10^{18} n/sr/m^2/μs/meV/MW/s
FWHM of pulse shape	80.0 μs	100.5 μs	152.0 μs
Exponential decay time constant(s)	54.5 μs	84.5 μs	100.0 μs, 400.0 μs
Rise time (10-90 %) @ 1.8 meV	24 μs	30 μs	35 μs

Table 2. Moderator parameters at 1.8 meV. The coupled moderator has one more parameter, q'=60%.

Moderator	α (μs/A)	$(t/\lambda)_0$ (μs/A)	λ_0(A)	P	Q(%)	τ_1 (τ_2) (μs)
Decoupled, poisoned	2.83	20.5	6	0.9	31.9	54.2
Decoupled	3.11	20.6	4.6	1.1	30.9	84.0
Coupled	2.0	15.0	1.5	1.79	25.0	100.0 (400.0)

From Figure 2, we see that the neutron flux for the partially coupled moderator is a factor of 5.5 larger than that that for the decoupled poisoned moderator, and a factor of 2.4 larger than the flux from the decoupled moderator. There is a factor of 2.3 in intensity between the decoupled moderator and the decoupled, poisoned moderator. The moderator pulse shape parameters at 1.8 meV are given in Table 2.

3. Monte Carlo Simulations

The Monte Carlo simulations were performed with the LANSCE Neutron Instrument Simulation Package (NISP). Most of the parameters for the simulation are easily set with the exception of parameters for the crystal analyzers. The NISP model for monochromating crystals requires one to give the lattice spacing, d, for the crystal, as well as the statistical distribution of d. While the former is well-known for pyrolytic graphite, the latter is more problematic. NISP allows the user to use a Gaussian or a Lorentzian for the statistical distribution of d, and there remains to choose a value of the standard deviation or the full width at half-maximum for the Gaussian or Lorentzian, respectively. We chose a Lorentzian distribution and set the value of the full width at half-maximum of the distribution by attempting to reproduce the elastic line shape produced by a vanadium sample (incoherent, elastic, isotropic scatterer) at the IRIS backscattering spectrometer. The reason behind this somewhat complicated way of determining the full width at half-maximum, Δd, is that its value is not known with great accuracy for graphite. A typical value, quoted by manufacturers, of $\Delta d/d$ is anywhere from 1.5×10^{-3} to 2×10^{-3} [2]. Similarly, the mosaic spread of graphite crystals is not known very well. The instrument resolution, however, is much less sensitive to this parameter which was fixed to the nominal value specified by the manufacturer. All other parameters were fixed to the appropriate values for IRIS. The primary flight path length is 36.41 m; the analyzer radius is 0.85 m; the height of the analyzer is 0.06 m; the angle of incidence on the analyzer crystals is 88.5°; and we used the decoupled moderator described above as our source term. This moderator, while calculated with the LANSCE target station model, has essentially the same characteristics as the ISIS liquid hydrogen moderator: a full width at half-maximum of the neutron pulse at λ=6.70 Angstrom of 120 μs and a decay time constant of about 84 μs.

The result is shown in Figure 3. The Monte Carlo simulation reproduces the IRIS vanadium data very well. It should be noted however that we had to use a value of $\Delta d/d$ of about 1×10^{-3} to obtain good agreement. This value is smaller than that quoted by the manufacturer. This may not be all that surprising since the graphite crystals used for the IRIS analyzer were tested individually and the better quality crystals (lower value of ?d/d) were selected systematically. The entire set of crystals should thus have an average value of $\Delta d/d$ that is smaller than the value of 2×10^{-3} quoted by the manufacturer [2].

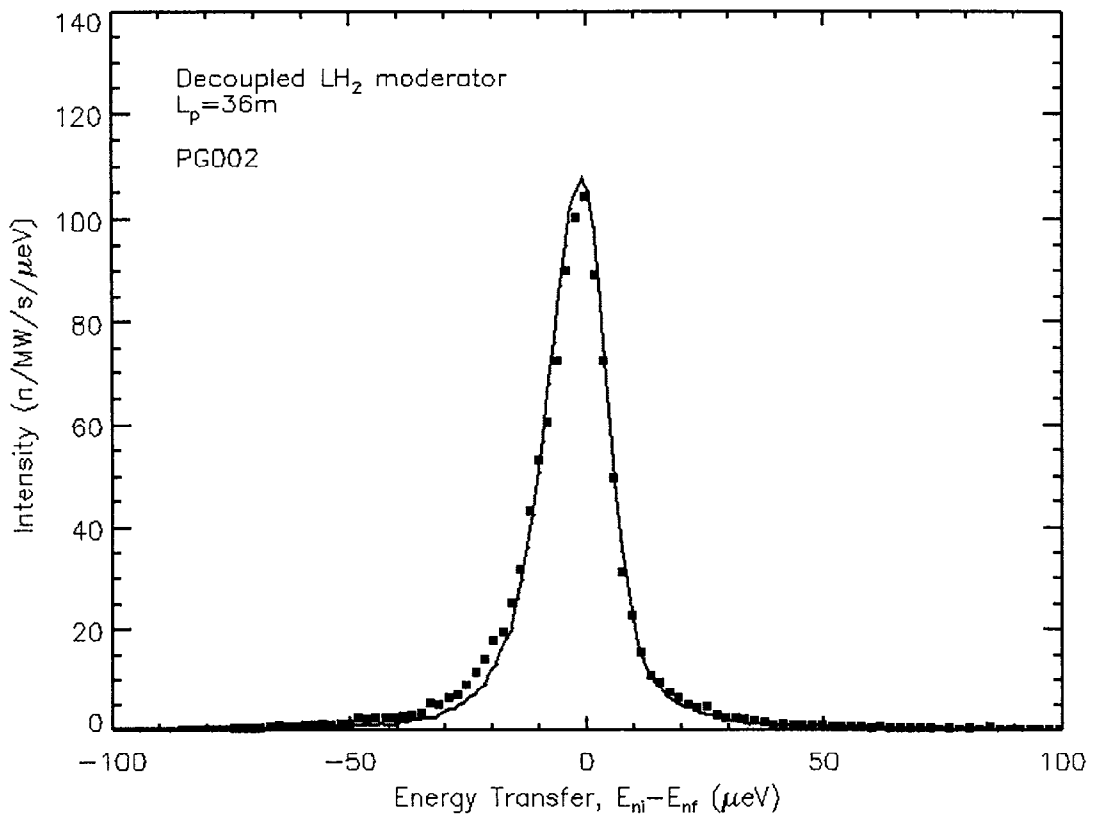

Figure 3. A comparison between the elastic line shape measured at IRIS with a vanadium sample and the results of a corresponding Monte Carlo simulation with NISP. The full width at half-maximum of the elastic line is about 14 μeV. The moderator used in this study is the decoupled moderator. This moderator has characteristics very similar to those of the ISIS liquid hydrogen moderator. These characteristics are summarized in Table 1.

In Figure 3, the calculated line shape agrees quite well with the experimental measurement, particularly for positive (neutron) energy transfers. The agreement is not quite as good for negative (neutron) energy transfers. This may be due to the fact that the neutron pulse used in the simulation corresponds to a decoupled liquid hydrogen moderator at the LANSCE target station. (A source file for the ISIS liquid hydrogen moderator is not available.) Nonetheless, the moderator used has the same full width at half-maximum (120 μs at 1.82 meV) as the IRIS liquid hydrogen moderator. The decay time constant is not known very accurately, but it would appear that the value of 84 μs corresponding to the LANSCE moderator used is fairly close to the actual value. A somewhat better agreement could be obtained by adjusting this value to a slightly smaller number, but we did not pursue this. The (energy-integrated) count rate at IRIS is approximately 335 n/s in the detector bank facing the graphite analyzer.

4. Decoupled Liquid Hydrogen Moderator

The moderating medium is liquid hydrogen at 20 K. The moderator is decoupled with cadmium on all sides except the moderator face and the corresponding flight path is also

lined with cadmium. In our simulations, we focussed mainly on the use of the graphite 002 line at the analyzer, i.e., we are interested in neutron wavelengths around 6.7 Angstrom (1.82 meV). Table 1 above summarizes the main features of the liquid hydrogen moderator. This moderator was used as a source in a Monte Carlo simulation of HERMES. The basic characteristics of the simulated instrument are:

- Primary flight path: 36 m
- Analyzer: Pyrolytic graphite mounted on equatorial strip of spherical surface
- Analyzer radius: 0.85 m
- Analyzer height: 0.3 m
  - Sample: isotropic, elastic delta scatterer
  - Analyzer: mica and graphite

The use of an idealized isotropic, elastic delta scatterer allowed us to determine the elastic resolution of the instrument. This is shown in Figure 4 where the elastic line shape calculated with the Monte Carlo package NISP appears together with the experimentally measured IRIS line shape (scaled to match the peak value of the Monte Carlo calculations). The agreement between the calculated elastic peak and the measured one is very good. Both have a full width at half-maximum of about 14 μeV.

Notice that in Figure 4, intensity is given in absolute units (n/MW/s/μeV). At a proton beam power of 160 kW, the (energy-integrated) count rate in the detector on the graphite side of the analyzer is approximately 1376 n/s. This count rate is 4.1 times that of IRIS. This is consistent with the fact that the analyzer height is five times larger (30 cm) in the present HERMES design than it is in the IRIS instrument (6 cm).

5. Partially Coupled Liquid Hydrogen Moderator

As described above, the proposed partially coupled liquid hydrogen moderator for the LANSCE upgrade has a piece of decoupler on its back, the sides have no decoupler, and the flight path is not line with decoupling material. This moderator is thus quite strongly coupled to the reflector. In order to obtain a reasonable fit to an Ikeda-Carpenter-like formula, one has to split the exponential decay term at longer times into a linear combination of two exponential terms with decay constant τ_1 and τ_2:

$$\exp\left(-\frac{t-t'}{\tau}\right) \rightarrow q'\exp\left(-\frac{t-t'}{\tau_1}\right) + (1-q')\exp\left(-\frac{t-t'}{\tau_2}\right) \qquad (3)$$

where $0<q'<1$.

At 160 kW proton beam power, the estimated (energy-integrated) count rate at the detector bank facing the graphite analyzer is approximately 3109 n/s. It is larger (by a factor of 2.25) than the 1376 n/s count rate calculated for the decoupled moderator. If we compare the peak count rates (70.4 n/s/μeV for the decoupled moderator; 118.8 n/s/μeV for the coupled moderator -a factor of 1.65 difference), however, it is evident that the increased count rate (integrated over energy) is due largely to the broadening of the elastic line and the addition of a tail at negative neutron energy transfers.

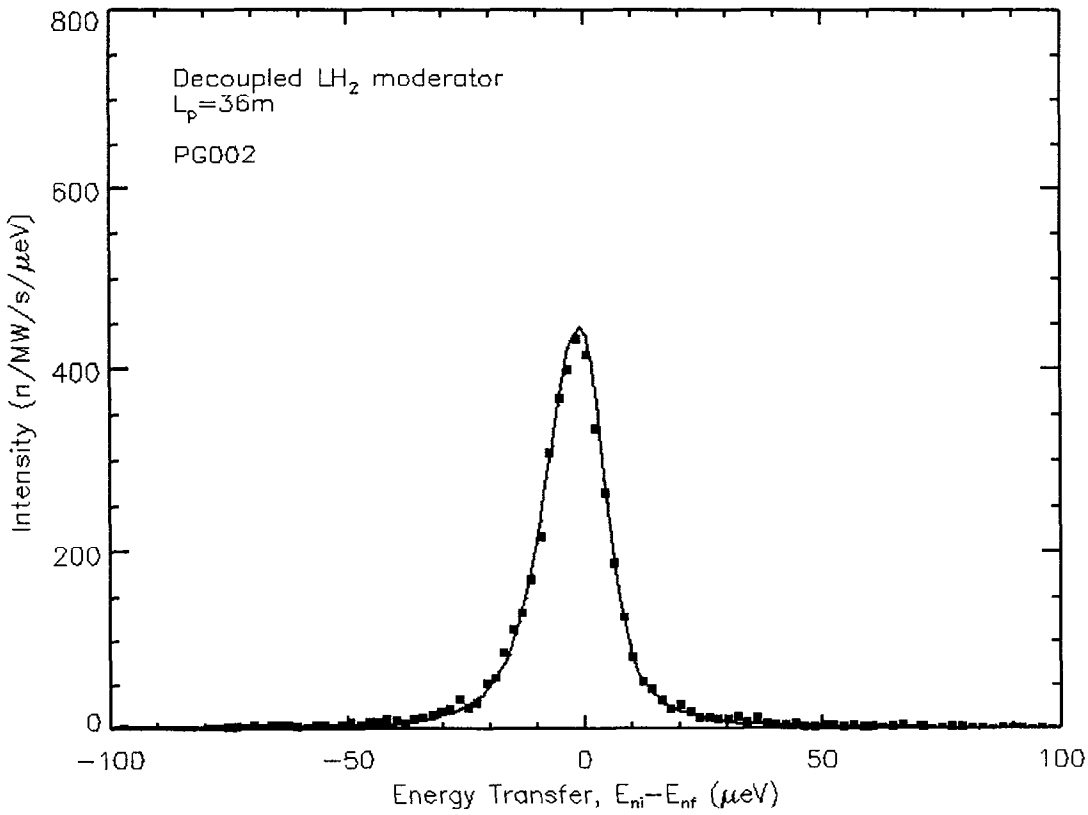

Figure 4. The elastic line shape calculated for a 36 m long instrument with a 0.3 m high analyzer (squares). The solid line is the experimentally-measured IRIS line shape scaled in magnitude to match the peak value of the Monte Carlo result. The full width at half-maximum of the elastic line is 14 μeV. The higher intensity (compared to Figure 3) is due to the larger analyzer height (0.3 m v. 0.06 m at IRIS).

It would appear at first sight that the long tail is the one feature of the neutron pulse that most affects the elastic line and that the decoupled moderator with a shorter decay time constant would be more desirable. Indeed, one may ask whether the presence of the long tail in the elastic resolution function is detrimental to the determination of small inelastic peak near the elastic line, or even to the analysis of a quasielastic spectrum. To resolve this issue, it will be necessary to perform a complete data analysis on the output of the Monte Carlo simulations.

6. Decoupled, Poisoned Liquid Hydrogen Moderator

One can further reduce the neutron pulse width by poisoning the moderator. In this calculation, we placed a 0.508 mm (17 mils) thick foil of gadolinium in the middle of the decoupled moderator. The main characteristics of the pulse are listed in Table 1. As mentioned previously, the effect of the poison is to reduce the FWHM of the neutron pulse at thermal and sub-thermal energies. This happens at the cost of sacrificing peak and integrated intensity.

Figure 6 shows the Monte Carlo-calculated elastic line shape for the decoupled poisoned moderator. Despite the relatively narrow neutron pulse (FWHM = 80 μs -compare with the decoupled, non-poisoned moderator for which FWHM = 100 μs), the FWHM of the elastic

line is virtually the same, namely 12 μeV (14 μeV for the decoupled, non-poisoned moderator). This seems to indicate that at a length of 36 m, the resolution gain to be made by using a narrower neutron pulse is quite modest indeed. The resolution is dominated by the non-zero backscattering angle and/or by the distribution of lattice spacings in the analyzer graphite crystals.

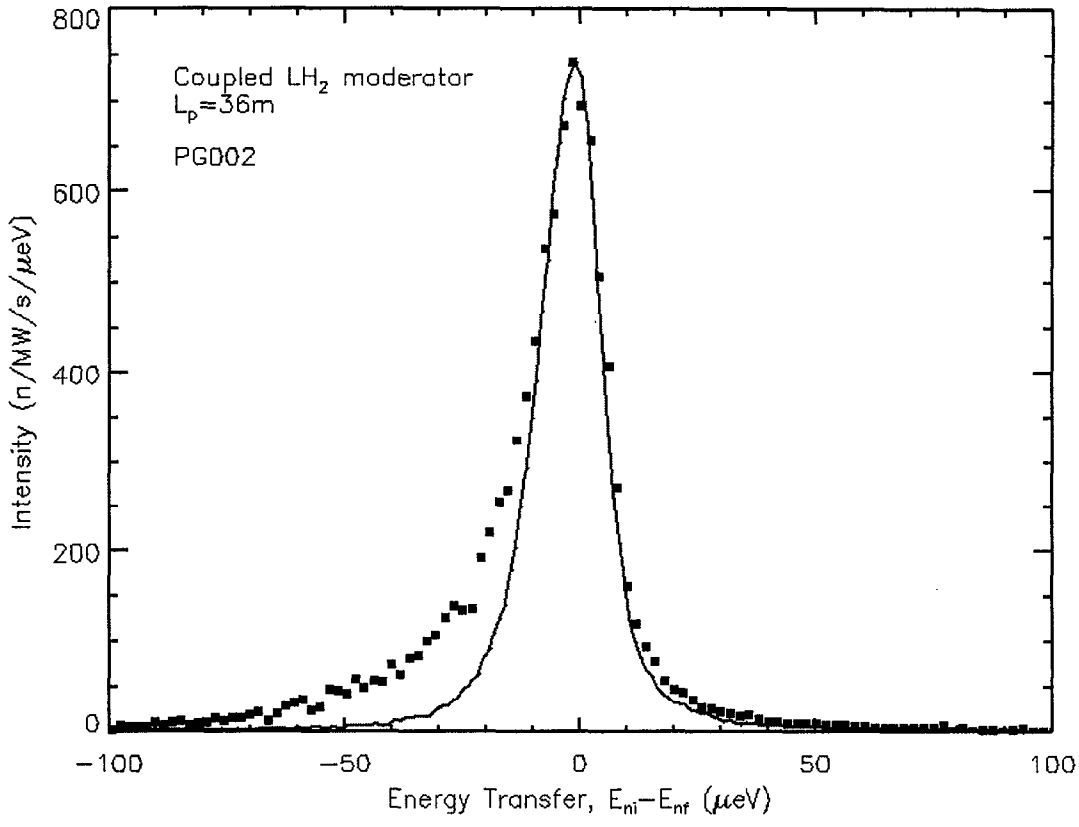

Figure 5. The calculated elastic line shape (squares) for the partially coupled liquid hydrogen moderator. The full width at half-maximum of the calculated elastic line shape is17.5 μeV. Also shown for comparison is the elastic line shape at IRIS (solid line, FWHM = 14 μeV). The large asymmetry introduced by the presence of a long tail in the neutron pulse is clearly visible.

The elastic line shape, however, is nicely symmetric with a FWHM comparable (slightly smaller) to that measured on the IRIS instrument at the Rutherford-Appleton Laboratory (U.K.).

The (energy-integrated) count rate at the detector (on the graphite side of the analyzer) is now about 587 n/s, significantly lower than the count rate of 1376 n/s calculated for the decoupled (non-poisoned) moderator, and somewhat larger than the IRIS count rate despite the analyzer surface area being 5 times that of IRIS.

7. Conclusion: Performance Comparison

Table 3 summarizes some of the results discussed above. Refer to it in the following discussion.

If we compare all three moderators, it would appear that the decoupled, non-poisoned moderator is ideal for HERMES.

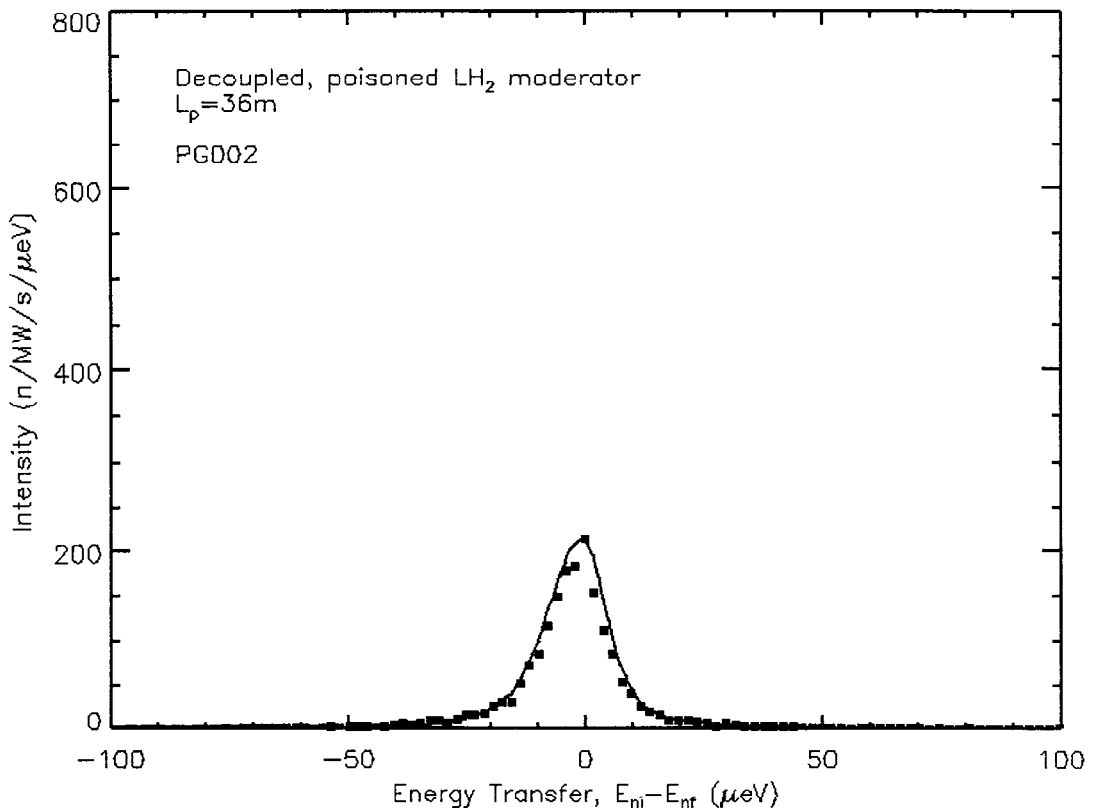

Figure 6. The elastic line shape for the decoupled, poisoned liquid hydrogen moderator. The FWHM of the peak from the Monte Carlo simulation (squares) is 12 μeV. The FWHM of the measured peak (solid line) is 14 μeV.

Indeed, the coupled moderator leads to a larger count rate (2.4 times the count rate for the decoupled moderator), but a significant fraction of the increase is due to an increase in line width and the addition of a tail to the elastic peak rather than an increase in peak intensity (which is a factor of 1.65 only).

The decoupled poisoned moderator leads to a very modest increase in line width at the cost of a decrease in count rate at the detector of a factor of about 2.3 compared to the decoupled, non-poisoned moderator case. This means that the pulse from the decoupled, non-poisoned moderator comes close to matching the backscattering angle and the $\Delta d/d$ uncertainty for graphite on HERMES. No further gain in resolution can be achieved by means of using a narrower pulse. Instead, better resolution should be attained by using other crystals, e.g., mica, with a smaller value of $\Delta d/d$. For such crystals, it might be worth

considering a decoupled poisoned moderator in order to further improve the elastic resolution of the instrument.

Comparison of Figure 3 and Figure 4 shows the intensity of the elastic line is about five times larger at the proposed HERMES instrument on a decoupled moderator than it is at IRIS. Yet, the FWHM of the peak is the same in both cases. The difference between the two simulations (besides a modest 41 cm difference in primary flight path) is the height of the analyzer: 30 cm on HERMES compared to 6 cm for IRIS. (The same moderator was used in both simulations.) Notice that the elastic line in Figure 4 remains highly symmetric.

Table 3. Performance comparison. Notice that the analyzer at HERMES has five times the height of the IRIS analyzer.

Instrument	Moderator	FWHM (μs)	Count Rate (n/s)	Peak Count Rate (n/s/μeV)
IRIS	Decoupled	14	335	16.7
HERMES	Decoupled, poisoned	12.5	587	34.2
HERMES	Decoupled	14	1376	70.4
HERMES	Coupled	17.5	3109	118.8

References

[1] S. Ikeda and J.M. Carpenter, *Nucl.Instr.Meth.*, **A239**, 536 (1985).
[2] C.J. Carlile and M.A. Adams, *Physica B*, **182**, 431 (1992).

ICANS XIV
14th Meeting of the International Collaboration on
Advanced Neutron Sources
June 14-19, 1998
Starved Rock Lodge, Utica, IL

HELIOS: A High Intensity Chopper Spectrometer at LANSCE

T.E. Mason[1,2], C. Broholm[3], B. Fult[4], R. Osborn[5], R.A. Robinson[6], G. Aeppli[7], H.A. Mook[1], S.E. Nagler[1], B. Keimer[8] and S. Kern[9]

[1]Oak Ridge National Laboratory, Oak Ridge TN 37831
[2]Department of Physics, University of Toronto, Toronto, ON M5S 1A7, Canada
[3]Department of Physics and Astronomy, The Johns Hopkins University, Baltimore MD 21218
[4]Department of Materials Science, California Institute of Technology, Pasadena CA 91125
[5]Argonne National Laboratory, Argonne IL 60439
[6]Los Alamos National Laboratory, Los Alamos NM 87545
[7]NEC Research Institute, 4 Independence Way, Princeton NJ 08540
[8]Department of Physics, Princeton University, Princeton NJ 08544
[9]Department of Physics, Colorado State University, Fort Collins CO 80523

Abstract

A proposal to construct a high intensity chopper spectrometer at LANSCE as part of the SPSS upgrade project is discussed. HELIOS will be optimized for science requiring high sensitivity neutron spectroscopy. This includes studies of phonon density of states in small polycrystalline samples, magnetic excitations in quantum magnets and highly correlated electron systems, as well as parametric studies (as a function of pressure, temperature, or magnetic field) of $S(\mathbf{Q},\omega)$. By employing a compact design together with the use of supermirror guide in the incident flight path the neutron flux at HELIOS will be significantly higher than any other comparable instrument now operating.

Introduction

We propose the construction of a high intensity, direct-geometry, time-of-flight spectrometer, HELIOS, on flight path 8 at the Lujan Center. HELIOS will be optimized to provide the highest possible neutron flux at the sample, high detection efficiency, and sufficient energy resolution to study dynamical processes in a wide variety of materials. The spectrometer will be capable of using the full energy spectrum of neutrons provided by a water moderator at a spallation neutron source, making it useful for studies of excitations from a few meV to several hundred meV. The performance at the lower end of this range will be boosted by supermirrors in the incident flight path. HELIOS will be compact, with a source-sample distance of 7.1 m and a secondary flight path of 2.5 m. The short secondary flight path will allow for a dense array of position-sensitive detectors that will be able to detect the direction and velocity of almost 10% of the neutrons scattered by the sample. Design calculations show that HELIOS would be the most efficient chopper spectrometer at any spallation neutron source.

The scientific mission for HELIOS is to enhance our fundamental understanding of materials by providing detailed information about their dynamic processes. Research topics include: (i) studies of vibrational excitations and their relationship to phase diagrams and equations of state of materials, including materials with correlated electrons, and (ii) studies of spin correlations in magnets, superconductors, and materials close to metal-insulator transitions. The projects described in the proposal are at the forefront of current civilian research in condensed matter physics and materials science, but some are relevant to the SBSS program. For example studies of the phase diagram of cerium and electronic correlations in f-electron metals are closely linked to understanding the complicated phase diagram of plutonium. In addition HELIOS would be the instrument of choice for studies of phonons and the magnetic susceptibility of plutonium metal under pressure or over a range of temperatures.

Optimized for efficiency, the HELIOS spectrometer would enable civilian and weapons programs to acquire data over a range of physical parameters, such as mapping dynamic processes in solids as a function of temperature, pressure and composition. Such parametric studies on HELIOS will provide physical trends in microscopic dynamical properties over energies from 1-500 meV. Mapping such physical trends is largely impractical with today's instrumentation at LANSCE or elsewhere.

The design of a new chopper spectrometer and its integration into the Lujan Center facilities will require an extensive effort on instrument design. Much of this work will be done under the auspices of the instrumentation R&D program of the Spallation Neutron Source, a collaboration between Oak Ridge and Argonne. Funding for the design effort will be obtained largely from the SNS allowing an immediate start, independent of Los Alamos funding commitments. It is expected that the design will be ready once construction funds are available in late 1999.

The HELIOS spectrometer is a natural complement to the higher resolution PHAROS instrument at LANSCE. Having both instruments at the same laboratory will allow the design of experiments where initial surveys and parametric studies are conducted on HELIOS, while details of energy spectra under selected conditions are measured by PHAROS. The addition of the HELIOS spectrometer will provide the Lujan Center a unique opportunity to become an international center for experimental research at the forefront of condensed matter physics and materials science.

1 Scientific Justification

Neutron spectroscopy provides unique information about dynamic properties of condensed matter. Time and again this experimental technique has yielded critical information towards the understanding of the fundamental properties of condensed matter. Neutron spectroscopy provided comprehensive evidence for phonons and the first evidence for spin waves by directly probing the corresponding dispersion relations. Brockhouse was awarded the 1994 Nobel Prize in physics for such work.

A neutron spectrometer provides optimal sensitivity and resolution only in a limited range of energy and wave vector transfer. So, while there are a number of highly productive neutron scattering spectrometers currently operating in the United States, no instrument offers state-of-the-art sensitivity towards wave vector resolved magnetic and vibrational dynamics in the energy range from 50 to 500 meV. None have the efficiency of the proposed HELIOS instrument, which will enable rapid data acquisition over a wide range of experimental parameter space. In this section we discuss the scientific areas which are currently suffering from this lack of suitable instrumentation and which would greatly benefit from an instrument such as HELIOS.

1.1 Lattice Dynamics

The past two decades have seen a steady growth in our understanding of alloy phase diagrams. There has been excellent progress in the ab-initio microscopic approach, which provides a free energy function by combining total electronic energy calculations with an entropy from statistical mechanics[1]. Almost every experimental discovery of an important new alloy such as a high temperature superconductor or a high strength transition metal aluminide is now followed quickly by a phase diagram calculation. While these phase diagrams are not necessarily precise in detail, they are helpful for further materials development. B. Fultz and his group would use the HELIOS spectrometer for investigations in the field of alloy phase stability, specifically on the vibrational entropy of alloy phases. The free energy, F, of an alloy phase is:

$$F = E - T(S_{config} + S_{vibr}) \quad . \quad (1)$$

The configurational entropy, S_{config}, is well known, and methods for calculating S_{config} are well developed. Until recently, however, S_{vibr}, has been essentially unknown and assumed to be small. Precision calorimetry measurements[2,3,4,5] have shown that for chemically ordered and disordered Ni_3Al, Fe_3Al, Cu_3Au, and Co_3V, the difference in vibrational entropy between alloys phases is typically 0.2 k_B/atom. This is about half the size of the difference in configurational entropy during a phase transition, and vibrational entropy will therefore make a major contribution to the alloy free energy. The difference in vibrational entropy originates with the phonon density of states (DOS, g(E)) of the alloy. In the high temperature limit the difference in

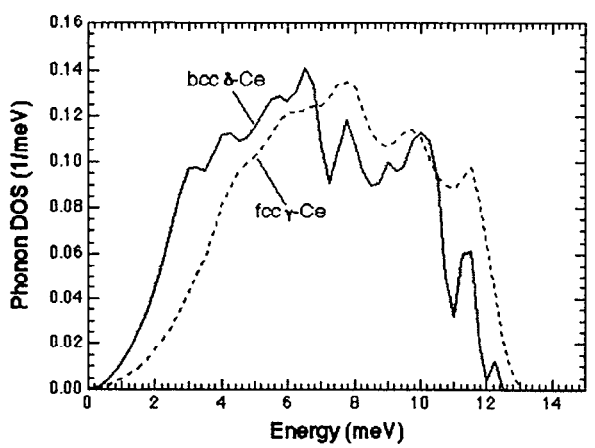

Figure 1: Phonon DOS curves of fcc cerium at 984 K and bcc cerium at 1028 K. Spectra were acquired at 5 values of **Q**, chosen by prior calculation of the polycrystalline average of the coherent scattering from the fcc phase. Spectra were corrected individually for multi-phonon scattering and background, and summed.

vibrational entropy between two phases, α and β, is:

$$\Delta S_{vibr}^{\alpha-\beta} = 3k_B \int_0^\infty [g^\beta(E) - g^\alpha(E)] \ln(E) dE \qquad (2)$$

where the difference of normalized DOS functions avoids problems with the dimensionality of the logarithm. B. Fultz's group is now actively measuring differences in the phonon DOS curves of different alloys phases. The disordered states of most materials of interest cannot be obtained in single crystals, so polycrystalline materials must be used for the neutron scattering measurements. Measurements on Fe_3Al, Ni_3Al, Ni_3V, and Co_3V, gave DOS curves in good agreement with calorimetry results[2,3,5,6,7] (using the finite temperature equivalent of Eq. (2). We are also investigating how microstructural features affect the vibrational entropies of materials[8,9]. In collaboration with R. A. Robinson (LANL), G. H. Kwei (LANL), R. J. McQueeney (LANL), and J. L. Robertson (ORNL), B. Fultz's group recently made inelastic neutron scattering measurements at HFIR, ORNL on the fcc - bcc phase transition in cerium metal. Tentative DOS curves are presented in Figure 1.

Notice that the phonon DOS of the bcc phase is shifted significantly to lower energies with respect to the fcc curve, suggesting a softening of one or more of the transverse branches. Most significantly, the observed change in phonon DOS predicts a change in vibrational entropy of 0.6 k_B/atom, using Eq. (2). This is actually larger than expected from the latent heat of the fcc - bcc transition, and suggests that there may be a change in the electronic entropy of cerium during the fcc - bcc transition. Our experiments to measure phonon DOS curves of different alloy phases almost invariably require the use of polycrystalline samples, for which a direct-geometry time-of-flight spectrometer offers advantages such as the absence of contamination wavelengths and simultaneous data collection over a wide range in **Q**. The energy resolution need not be particularly high, since we are interested primarily in comparative studies between different states of a material. For the purpose of obtaining thermodynamic information, high energy resolution is not required anyhow, since Eq. (2) is an average over the phonon DOS. In general we do not need to identify specific features of phonon DOS curves. In cases where this need arises, however, the PHAROS II spectrometer will be a well-matched companion. The HELIOS spectrometer would be ideal for much of our present work, and will provide new research opportunities. For example, it is now impractical for us to obtain more than two or three phonon DOS curves in an experimental session. With HELIOS, however, we expect to be able to follow the evolution of the phonon DOS at intermediate states of a phase transition. The evolution of vibrational entropy may play a central role in the kinetics of some phase transitions, but this is as yet an unexplored topic in materials science.

1.2 Magnetic Dynamics

Direct-geometry time-of-flight spectrometers offer a powerful probe for studying the magnetic dynamics in materials, offering a wide range of frequencies together with the ability to map out a large region of reciprocal space. Many of the most celebrated successes in applying the direct-geometry time-of-flight method to studies of magnetic dynamics have been in the study of low-dimensional materials. In such systems it is possible to arrange the scattering geometry so the simultaneous variation of momentum and energy transfer along a time of flight trajectory is projected out - giving full coverage of the 1D or 2D reciprocal space. This is not essential however, a recent example is the measurements obtained on HET showing a cut through the very three dimensional dispersion surface of a manganese oxide, one of the so called Colossal Magneto-Resistive (CMR) compounds[10], shown in Figure 2.

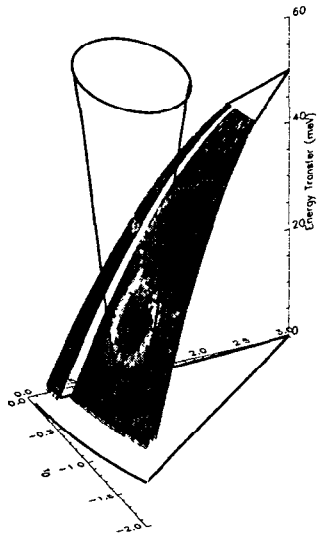

Figure 2: Time of flight spectra obtained on HET from the CMR compound $La_{0.7}Pb_{0.3}MnO_3$ in the ferromagnetic phase at T=10 K. The intersection of the dispersion surface extracted from fits to the data with the neutron trajectories in (**Q**,ω) space is shown schematically.

Note that the range of energy transfers accessed in this measurement (0-50 meV) is much lower than that generally thought to be optimal for this class of instrument. The provision of incident flight path supermirror guides on HELIOS will further improve its efficiency below about 25 meV.

An example of the use of a direct-geometry time-of-flight spectrometer for the studies of the magnetic dynamics in a low-dimensional material is a measurement of the spin wave in $FeGe_2$ (a quasi-one-dimensional itinerant antiferromagnet) performed on HET, mapping out the c-axis dispersion up to 400 meV. Figure 3 shows data obtained in ~6 hours using an incident energy of 120 meV at 11 K. In low-dimensional compounds it is possible to characterize a large fraction of the dispersion surface in a single geometry since the variation of **Q** along a weakly coupled direction in the (**Q**,ω) trajectories does not affect the excitation energy. In the case of $FeGe_2$ the Q_a variation is negligible so the (Q_c,ω) dispersion is mapped out from 40 - 100 meV[11].

G. Aeppli, C. Broholm, B. Keimer, T. E. Mason, H. A. Mook, R. Osborn, and R. A. Robinson share an interest in the structure and spin dynamics in correlated electronic materials. The quest for a theoretical description of materials with strong electron-electron interactions is currently at the forefront of condensed matter physics, and the correlation functions measurable by inelastic magnetic neutron scattering provide unique and incisive constraints for theories of the electronic many-body states realized in these materials. Unfortunately there is, however, no instrument in the US that can efficiently probe electronic correlations at energies beyond 50 meV. This has limited the application of neutron spectroscopy to a relatively small class of materials with low temperature anomalies of little technological significance. By increasing the range of energies and reducing the required sample size, HELIOS would expand the range of materials that can be studied by neutron spectroscopy. With HELIOS we could study spin dynamics in correlated metals with energy scales from 10-500 meV. There is no reason to expect the microscopic information about electronic correlations in these materials to be less interesting than what we learned from neutron spectroscopy in heavy fermion systems where the energy scales are an order of magnitude smaller. High T_c superconductors are important examples of interesting correlated metals but we may also make progress in understanding seemingly less exotic 3d metals such as chromium, yttrium, vanadium, or even copper, where the energy scale for magnetic excitations is set by the Fermi energy. Experiments in magnetic multilayers have shown that these materials have considerable **Q**-dependence in their magnetic susceptibility. New microscopic information about electronic correlations in these systems could have an important impact on our understanding of electronic correlations in the metallic state.

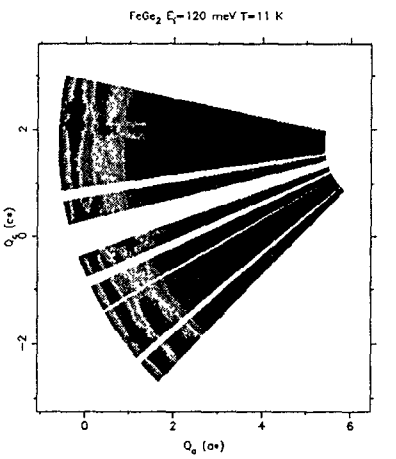

Figure 3: Spin wave and phonon scattering from $FeGe_2$ at 11 K for energy transfers from -10 to 120 meV (left to right) projected onto the (Q_a,Q_c) plane.

1.2.1 High Temperature Superconductivity

The supreme challenge in the field of strongly correlated electron systems is an explanation of high temperature superconductivity in the quasi-two dimensional cuprates. A central question in the theory of high temperature superconductors is the relationship between the microscopic spin dynamics and the transport and superconducting properties of the cuprates. To this end, knowledge of the spin correlations over a wide energy range is essential. Until recently, such experiments were confined to excitation energies below ~ 40 meV, larger than the superconducting energy gap but smaller than the intralayer superexchange J ~ 120 meV which sets the energy scale for spin excitations in the

undoped antiferromagnetic precursor compounds. In recent pioneering studies, many of the members of this SDT have extended these measurements to higher energies and established the presence of significant spectral weight at energies comparable to J in the $La_{2-x}Sr_xCuO_4$ and $YBa_2Cu_3O_{6+x}$ families of superconducting cuprates[12,13,14]. The capability of carrying out such high-energy studies with sufficient intensity is currently lacking in the United States, and all of these important experiments were carried out at ISIS or European reactor sources with hot moderators. The HELIOS spectrometer would thus fill a critical need in this regard. Regular access to a high-intensity spectrometer would enable us to obtain detailed, quantitative measurements of the temperature and doping dependence of the high energy spin dynamics in the cuprate high-T_c materials which are essential for microscopic theories of high temperature superconductivity.

Crystal field spectroscopy is another promising tool to study the electronic state of the cuprate superconductors. S. Kern's research has been primarily focused on studying the excitations in polycrystalline samples, both electronic and lattice. A high-intensity spectrometer is useful for detecting the often weak response from magnetic systems. The ability to investigate electronic transitions and quasielastic scattering both at large and small incident energies makes a machine such as HELIOS very useful. For example, Kern has used an incident energy of 4 meV on HRMECS to determine the presence of ~ 1 meV crystal-field level in an Erbium high T_c material[15]. The line width of crystal field excitations has been shown to contain important information about the electronic susceptibility and the pairing state in the cuprates[16]. R. Osborn and collaborators have reported transitions in f-electron systems reaching to the 1 eV range[17]. In S. Kern's recent investigations of the interactions between the electrons and phonons in the rare-earth phosphates, both small scattering angle coverage (low **Q**) for the electronic transitions and wide angle coverage for the phonons (high **Q**) were needed. Low noise in the forward scattering direction is required for accurate determination of magnetic response.

A quantitative understanding of high temperature superconductivity in the cuprates will ultimately require broad, systematic studies of transition metal oxides as a function of parameters such as the carrier concentration, dimensionality, the width of the valence band, correlation and charge transfer energies, and disorder. Many of the members of this SDT collaborate actively with solid state chemists and materials scientists at their institutions and elsewhere who are capable of growing high quality single crystals of a wide variety of these materials.

1.2.2 One Dimensional Quantum Magnets

Undoped spin chain compounds are arguably the simplest realizations of quantum many body systems and have for years served as a unique "laboratory" for many-body physics. Some idealized spin chain Hamiltonians can actually be solved exactly; their excitation spectra consist of sharp, dispersive modes and excitation continua. While the spin-wave-like dispersive modes have been studied by neutron scattering since the 1970's, the quantitative exploration of excitation continua has been greatly advanced by direct-geometry time-of-flight spectrometers at pulsed neutron sources. A high flux chopper spectrometer like HELIOS would be the ideal instrument for investigating such broad, diffuse inelastic scattering, and would have a large impact on research in this area. For

example, S. E. Nagler's work employed MARI to study the free spinon continuum spectrum in the S=1/2 Heisenberg antiferromagnetic chain system $KCuF_3$[18]. Direct measurements of the dynamic spin correlation function, $S^{\alpha\alpha}(\mathbf{Q},\omega)$, were made possible by orienting the sample with the chain axis parallel to the incident neutron direction, resulting in magnetic scattering with azimuthal symmetry. This allowed integration of the signal over many detectors without loss of information. A complementary approach (see for example, work on $CuGeO_3$ by M. Arai and co-workers) attempts to survey large regions of reciprocal space simultaneously. This method was used to measure a similar continuum in the spin-Peierls compound $CuGeO_3$[19]. These experiments have tested many aspects of one-dimensional quantum magnetism for the first time, and have also revealed unanticipated features such as a "double gap" structure in alternating spin chains[20,21]. Other members of this collaboration have focused on the effect of high magnetic fields on organic and inorganic spin chain compounds and discovered novel field-induced fluctuations[22] and phase transitions[23]. The theoretical description of these phenomena is still in its infancy. HELIOS will open up many new experimental opportunities along these lines, such as the study of new spin chain compounds with different alternation parameters, higher-lying excitations continua etc.

The gap from one to two dimensions can be bridged by spin-ladders, realized in compounds with two or more directly adjacent, strongly interacting spin chains[24]. Several cuprate spin ladders have been identified, including one that can be doped and becomes superconducting under pressure[25]. Since many of these materials are characterized by exchange constants comparable to or larger than the high-T_c compounds[26], HELIOS would again be well suited to study their spin dynamics. Efforts to synthesize large crystals of cuprate and cobaltate spin ladders are underway in the laboratory of R. Cava at Princeton University, a collaborator of B. Keimer, using a new floating zone furnace. S. E. Nagler's group is studying chain/ladder systems in the vanadium phosphate family[20].

1.2.3 Metal Insulator Transition in Oxides

Oxides of 3d metals other than copper also show intriguing behavior dominated by electronic correlations. R. Osborn has started a program to study the magnetic correlations close to the metal-insulator transition in $La_{1-x}Sr_xTiO_3$, a three-dimensional electron analogue to the well known hole-doped cuprate $La_{2-x}Sr_xCuO_4$. These compounds undergo a Mott-Hubbard transition at $x \sim 0.05$, which is accompanied by a divergence of the d-electron effective mass according to specific heat and magnetic susceptibility[27]. This is predicted to produce a narrowing of the energy scale of d-electron magnetic fluctuations into the range accessible by HELIOS. Early studies indicate that the response is enhanced close to the transition, but is difficult to determine unambiguously because of the limited sensitivity of current instrumentation. Optimized for sensitivity in the relevant energy range, HELIOS will enable single crystal investigations of the transition to the Mott-insulating antiferromagnetic phase. G. Aeppli and collaborators are studying manganites of composition $La_{1-x}Pb_xMnO_3$ which are fully spin polarized metals by virtue of the double-exchange mechanism. The same microscopic physics also underlies the recently discovered "colossal magnetoresistance" effect that has potential for technological applications. While these materials have been known for more than 40 years, an experimental characterization of the excitations of the

double-exchange Hamiltonian has only recently been achieved through studies at ISIS[10]. The manganites show rich phase diagrams with competing charge-localized and metallic states whose spin dynamics is only beginning to be probed. The flexibility and dynamic range of HELIOS will undoubtedly prove useful in this area as well.

Whereas various 3d metal oxides are currently under intense investigation in laboratories around the world, compounds based on 4d/5d transition metals are potentially very interesting materials that are only now beginning to attract serious attention of condensed matter physicists. The large size of the outer electron cloud in the 4d/5d series results in greatly increased hybridization and potentially new physics. For this reason we call such materials "extended electron" compounds. Examples of recent interest include $SrRuO_3$, which is a "badly metallic" ferromagnet (i.e. with electronic properties similar to those of the normal state of high Tc superconductors, fullerenes, and organic metals), and the derivative compound Sr_2RuO_4, now suspected to be a p-wave superconductor[28]. There is much to be learned by studying the magnetic fluctuation spectrum of such materials, and in some cases perhaps even optical phonons. There are several technically challenging aspects of such measurements that may be well suited to HELIOS. The rapidly diminishing form factors force measurements with high energy transfers at small wavevectors. Typically only small single crystals or powders are available. The itinerant nature of the magnetism in many of these materials also can result in excitation continua. The effective dimensionality of the ruthenates, as well as that of the cuprates, can be systematically changed in the Ruddlesden-Popper scheme which interpolates quasi-continuously between two and three dimensional electronic structure by changing the number of directly adjacent transition metal oxide layers, resulting in compounds such as Sr_2RuO_4, $Sr_3Ru_2O_7$, etc. Ruthenates of this series will be studied by S. E. Nagler, while B. Keimer plans experiments on analogous cuprate compounds to be synthesized in R. Cava's laboratory.

1.2.4 Heavy Fermion Magnetism

There are also exciting developments in the area of heavy fermion systems to which experiments at HELIOS could make important contributions. R. Osborn will use HELIOS in studies of the dynamic susceptibility of disordered heavy fermions, usually containing uranium ions that exhibit unusual power-law correlations at low temperature. Pulsed neutron spectroscopy at IPNS and ISIS have already revealed a novel scaling of the magnetic response which is universal in ω/T over a very wide dynamic range of frequencies and temperatures[29]. This is believed to result from quantum critical scattering associated with the proximity to a T=0 phase transition. A key question to be resolved is the dimensionality of the correlations. At high temperatures (>30K), the scattering is single-ion in nature but there is evidence of a crossover at low temperatures to a quantum-disordered regime showing weak antiferromagnetic correlations. The scaling properties are reminiscent of marginal Fermi liquids, proposed to explain the unusual normal-state properties of high-temperature superconductors, which also undergo quantum phase transitions as a function of doping. We intend to pursue the systematics of this scaling as a function of composition and other thermodynamic variables. Pulsed neutron time-of-flight spectrometers have been especially valuable in determining this

scaling behavior because of the wide range of accessible energies and angles. The angular range is also necessary in subtracting the phonon scattering reliably[30].

1.2.5 Characterization of Novel Magnetic Materials

The vast majority of novel magnetic materials are developed by solid state chemists through guided trial and error using susceptibility and perhaps specific heat measurements as the diagnostic tools. Because current neutron scattering instrumentation requires large amounts of material this powerful sample characterization tool is typically only applied by specialists as a means of explaining previously discovered anomalies. Optimized for high sensitivity HELIOS will enable rapid surveys of spin fluctuations in new materials that are available only in small quantities. We expect that this will make neutron spectroscopy an important tool for the initial characterization of novel magnetic materials thus bringing more detailed information about a larger amount of different materials to a broader community of materials scientists.

1.3 Relevance of HELIOS to the Weapons Program

1.3.1 Introduction

While we are primarily interested in f-electron systems because of their fascinating correlated-electron properties, as manifest in heavy fermion, non-Fermi-liquid, superconducting and other behaviors, the same issues are important in understanding the basic properties of nuclear-weapons materials, in particular plutonium. It has long been known that, part way across the actinide row of the Periodic Table, there is a transition from itinerant electronic behavior (as typically occurs in the transition metals) to more localized f-electron behavior (as in the rare earths). Plutonium lies right at the crossover between the two regimes[31,32]. This means that first-principles one-electron band-structure calculations of plutonium are not reliable, and there is a need for experimental data (on phonons and the enhanced generalized magnetic susceptibility) on the various different phases of plutonium. Given such data, it should be possible to learn how to include correlations within the electronic-structure calculations. Accurate electronic structure calculations of actinides are an important part of the Science Based Stockpile Stewardship Program. We envisage a strong interplay between work on plutonium and civilian basic research on f-electron systems more generally, because the underlying physics is so closely related.

The PHAROS spectrometer at LANSCE is beginning to make important contributions to the LANL effort in Science Based Stockpile Stewardship. In the next LANSCE operating cycle, it is expected that a number of important measurements on ^{242}Pu will be performed with PHAROS. The excellent energy resolution of the PHAROS spectrometer makes it an ideal instrument for measuring the phonon densities of states and neutron Brillouin scattering from ^{242}Pu at ambient temperature and pressure. It is also expected that PHAROS will be an excellent instrument for measuring dispersion curves from δ-^{242}Pu once a single crystal is available. As described here, however, there are a number of important experiments for which the HELIOS spectrometer would be much more suitable than PHAROS, and HELIOS should enable new experimental investigations.

Most importantly, the HELIOS spectrometer will make possible experiments on Pu under pressure. The difficulty with neutron inelastic scattering experiments with samples under pressure is the scattering from the pressure cell. Scattering from the pressure cell can readily overwhelm the scattering from a small sample of a specialty isotope. The HELIOS design, with its high-intensity and oscillating radial collimators, will be ideal for measurements on small samples in a pressure cell. If HELIOS construction starts within a year, the pressure experiments on HELIOS should match well the timetable for the completion of a number of important experiments on ^{242}Pu with the PHAROS spectrometer. Although such work is classified, we present here some ideas for experiments on HELIOS, and we suggest these experiments are relevant to the SBSS mission.

1.3.2 Work on Ce Metal and its Relationship to Pu

Over the past year there has developed a collaboration between B. Fultz at Caltech and R. A. Robinson and G. H. Kwei at Los Alamos. Together with a bright LANL postdoctoral fellow, R. J. McQueeney, this group has already undertaken several productive collaborations on studies of phonons in metals using inelastic neutron scattering. We hope this ongoing interaction between university and LANL personnel will move forward into experiments of high relevance to the SBSS effort.

Quite independently, G. H. Kwei and B. Fultz recognized that the difficulty of performing experiments on plutonium would require practice with an analog material. Both concluded that cerium metal is the obvious choice. Cerium assumes four crystal structures at atmospheric pressure, and some transformations between these phases are related to electronic instabilities of its valence electrons. In this respect, cerium has similarities to plutonium metal, but is much easier to study. Experimental techniques for making measurements at different temperatures and pressures are now being refined through work on cerium metal, and these methods should later be applicable to studies on plutonium metal.

The first experiment resulted in a manuscript submitted to Phys. Rev. Lett.[33]. It reports inelastic neutron scattering measurements on Ce metal at temperatures near the fcc (γ) to bcc (δ) transition, and presents approximate phonon DOS curves. A large difference in the phonon DOS of the γ-Ce and δ-Ce was found, providing a change in vibrational entropy at the γ-δ transition temperature of $(0.51\pm0.05)\ k_B\ \text{atom}^{-1}$. To be consistent with the latent heat of the γ-δ transition, this large change in vibrational entropy must be accompanied by a thermodynamically significant change in electronic entropy of the opposite sign. This is the first evidence for a large electronic entropy contribution to the γ-δ phase transition. It is an exciting result, since it is the first case of a high-temperature structural phase transition in a material where electronic entropy is important. We expect that electronic entropy will play a similar role in the stability of the different solid phases of Pu metal.

Two more experiments on Ce were performed with the LRMECS spectrometer at IPNS at the Argonne National Lab. Data analysis for these measurements on Ce at low and high temperatures is still underway. It is expected that the anharmonicity of the phonons in fcc

γ-Ce will be determined. The heat capacity of γ-Ce has been measured at elevated temperatures, and it is considerably higher than the classical limit for a harmonic solid. Some of this excess heat capacity can be associated with the softening of the phonon DOS, but we also expect a contribution from the temperature-dependence of the electronic entropy in γ-Ce. Without electronic entropy, it can be shown that:

$$9\,Bv\,\alpha^2\,T = C_p(T) - C_V(T) = -\frac{T\Delta S_{vib}}{\Delta T}, \quad (3)$$

where ΔS_{vib} is defined as the change in vibrational entropy caused by the change in phonon DOS over the temperature range ΔT. While the first equality is rigorous (we derive this equality to impress students of thermodynamics with the power of the Maxwell relations), the second equality is true only if the electronic entropy is negligible. We are testing this relationship with the temperature dependence of the phonon DOS of γ-Ce. The same sort of experiments on δ- and δ'-Pu should be even more interesting, since their negative thermal expansion indicates that their anharmonicity is even larger. A temperature-dependence of the electronic entropy is a possible reason why phases in plutonium metal undergo negative thermal expansion.

In a preliminary experiment during our last beamtime allocation at LRMECS, we measured the phonon DOS of the shape memory alloy Ni-Ti[34]. Data analysis is nearly complete, and some results are clear. There is a substantial difference between the phonon DOS of the high temperature "austenite" and low temperature "martensite" phases of NiTi. This difference is approximately consistent with the latent heat of the transformation measured by calorimetry. More specifically, it appears that most of this difference in vibrational entropy is caused by changes in low energy phonons. It is interesting that low energy phonons have also been associated with the displacive mechanism of the phase transformation in Ni-Ti[35].

1.3.3 Issues with Pu Metal

The phonon DOS of anharmonic solids will usually stiffen under pressure, leading to reduced entropy, for example. Another important consequence is an increase in the velocities of sound. At high pressures the increased speed of sound makes it possible to generate a shock wavefront that propagates through the material. Measuring the pressure dependence of phonon dispersion curves of a metal is an excellent way to understand the pressure conditions required for shock wave generation.

An unusual phenomenon should occur when driving high-pressure waves through a material with negative coefficient of thermal expansion such as δ-Pu. Negative thermal expansion indicates a negative Grüneisen constant, meaning that the phonon DOS of δ-Pu softens with increasing pressure. This would tend to suppress shock wave formation. However, it is not obvious that all phonon modes will have negative mode Grüneisen constants. For example, the phonon softening in Co_3V at elevated temperature is predicted very poorly with an average Grüneisen constant[36].

Studies on single crystals under pressure would provide the most useful data. Nevertheless, it should be possible to obtain some of this information with a mix of neutron Brillouin scattering and phonon DOS measurements. With the configuration of the PHAROS I spectrometer, B. Fultz, R. A. Robinson, and G. H. Kwei will soon attempt to measure an average dispersion of longitudinal waves from polycrystalline Ce metal. These neutron Brillouin scattering experiments can provide crystallographically averaged cuts through the dispersion surface of long wavelength phonons. Changes with temperature of the average intensities in the constant-energy cuts from these data, for example, should reveal the temperature-dependence of the average speed of longitudinal sound waves. The shapes of these measured intensity dispersions should provide the distribution of sound velocities along different crystallographic directions.

Beam collimation to suppress scattering from a pressure cell is difficult in forward geometry, however, so experiments with the sample under pressure cannot be performed so readily. Although these measurements will be attempted on PHAROS, it is likely that Brillouin scattering experiments will not be possible with the sample under pressure. It is most practical to characterize thoroughly the phonon DOS of Ce and ^{242}Pu with the PHAROS spectrometer with the sample at various temperatures. Pressure-dependent experiments are less appropriate for PHAROS.

The HELIOS spectrometer would be the ideal instrument for experiments on metals under pressure, owing to its higher intensity and its oscillating radial collimators. It is expected that by the time the HELIOS spectrometer is completed, the features of the phonon DOS of Ce and ^{242}Pu will be adequately understood so that it will be known which features of the phonon DOS correspond to which phonon polarizations.

Plutonium metal should exhibit a rich set of phase transitions at relatively modest pressures. We do not have access to classified literature on this subject, so the following comments must be considered speculative. Thermodynamically, however, the large specific volume of fcc δ-Pu must make it quite unstable against pressure-driven transformations (to α-Pu, perhaps), and these should occur at pressures of several kbar. If the latent heat of these transformations have been measured under pressure, we should be able to determine independently the pressure dependencies of the electronic and phonon entropies. Furthermore, phonon softening may be a precursor to some of the low-temperature transformations in plutonium metal, which likely occur by diffusionless processes. Interpretations of the thermodynamics and kinetics of these transformations would proceed along the lines we are following for the work on NiTi[34].

1.3.4 Complementarity of HELIOS and PHAROS

The PHAROS weapons research effort will benefit from the development of HELIOS. An important part of the work on Pu will be the measurement of phonon dispersion curves from single crystals. This work will require a significant effort to develop experimental techniques and software for the analysis of phonon dispersion curves with a time-of-flight instrument. Software for this work will be developed in the software effort proposed for the HELIOS spectrometer. A larger user program and a higher level of

scientific activity associated with the presence of HELIOS will help the development of experimental methods needed for single crystal work with PHAROS.

Some experimental problems will benefit from the use of both PHAROS and HELIOS. Measurements of phonon dispersion curves from small single crystals of ^{242}Pu are expected to be limited by neutron flux. The most appropriate way to perform these experiments is to start by making several precise measurements on PHAROS. The excellent energy resolution of the PHAROS spectrometer will facilitate the identification of the phonon dispersion curves. For measurements at many different crystal orientations or at different pressures and temperatures, however, it would be most appropriate to use an instrument such as HELIOS, which offers much stronger signals. The flexibility of having the HELIOS instrument to complement PHAROS will facilitate all inelastic scattering research at LANSCE, including the weapons efforts.

1.4 User Program

Because the energy resolution of HELIOS will be similar to that currently attainable on thermal beam triple axis spectrometers, to some extent, the user base will mirror that of that class of instruments. However, HELIOS will offer dramatically improved efficiency for measurements of dynamics over wide ranges of frequency and momentum space. Firstly, HELIOS will offer dramatically improved sensitivity to inelastic scattering with energy transfer between 50 meV and 500 meV. Secondly, the large solid angle detector bank will enable experiments on systems where the scattering is distributed over a wide range of energies and momenta, as is the case for many novel magnetic systems that do not possess well-defined dispersion surfaces. Even for more traditional mapping of dispersion surfaces the phase space gains can be substantial since large regions of $(\mathbf{Q},\omega)$ must be surveyed in order to locate all propagating modes.

2 Instrument Description

HELIOS will be installed on Flight Path 8 in ER-1 viewing the high intensity water moderator. The layout of the instrument is shown in Figure 5. The philosophy guiding the design of the instrument is the desire to maximize the flux at the sample position and the solid angle detector coverage. This must be achieved with an energy resolution appropriate for the scientific program described in Section 1 (typically 2-5% of E_i, similar to that commonly employed on triple axis spectrometers). The instrument is designed for single crystal measurements from the outset. This implies a goniometer for crystal rotation and a detector array consisting of linear position sensitive detectors where gaps in coverage are minimized. The short 2.5 m secondary flight path allows us to span scattering angles between –20 and 140° in the horizontal plane and ±10° in the vertical plane with a relatively inexpensive 5.5 m^2 detector bank. We will use the LRMECS spectrometer at Argonne for component testing as needed. A detailed description of the essential features of the design follows in Sections 3.1-3.4.

Wherever possible we have tried to adopt hardware that is similar to that employed on PHAROS. This simplifies things from both the user and facility perspective. There are a number of interface issues that must be coordinated with LANSCE:

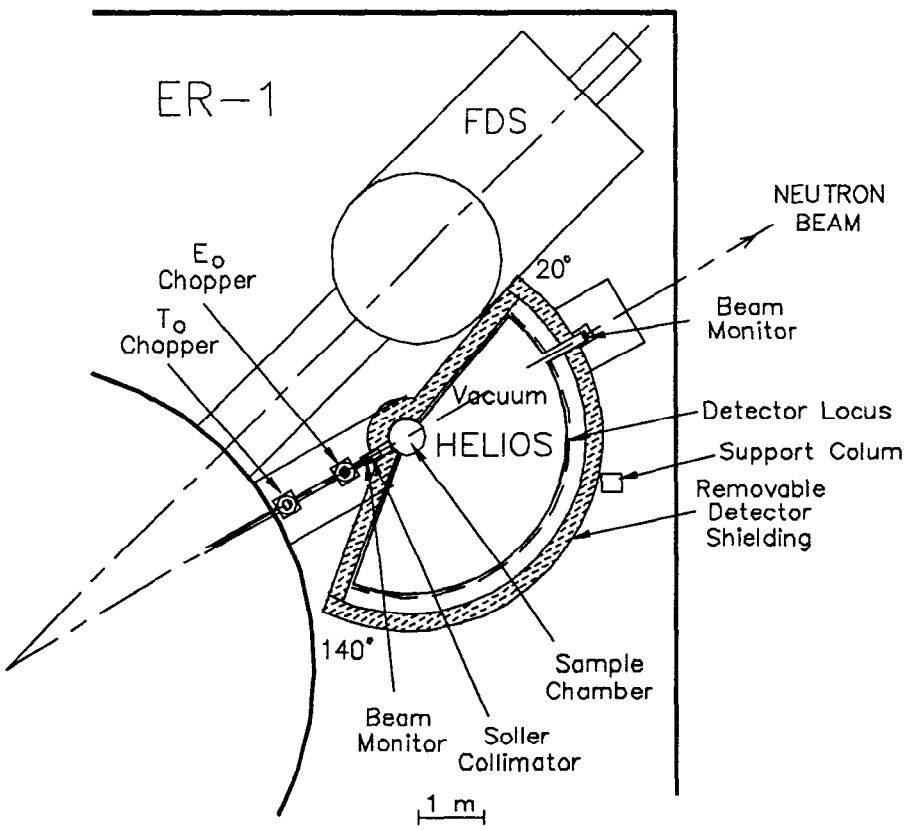

Figure 5: Layout of HELIOS on Flight Path 8 in ER-1.

- The spectrometer is being installed in a very restricted space in ER-1. This does not pose a major problem due to the desire for a compact instrument to maximize neutron intensity. However, there is a load bearing post very close to FP-8 (shown in Figure 5) which will make accessing the detectors for installation and servicing difficult if the design is not carefully thought out.
- The phasing of the chopper to the source will require a TTL pulse, likely HELIOS will operate slaved to PHAROS which has much more stringent timing specifications due to its higher resolution.
- The catwalk providing access to the back of ER-1 runs over top of FP-8. Support currently in place may have to be reconfigured. There is not a large load associated with this so it can likely be incorporated into the bulk shielding and vacuum vessel.
- The sample environment inserts will be subject to the same safety concerns as other cryogenic and furnace systems in use at the Lujan Center.
- The vacuum vessel, while not as large as that being installed on PHAROS, still requires careful engineering to insure it can be operated safely.

2.1 Incident Flight Path

HELIOS will be located on flight path 8 in ER-1 viewing the "high–intensity" H_2O moderator. For much of the energy range, this provides a twofold increase in intensity over the "high–resolution" H_2O moderator viewed by PHAROS, and the pulse widths,

which vary from 4μs at 1eV to 25μs at 10 meV, are better matched to the reduced primary and secondary flight paths. We estimate that the incident flux will be at least factor three greater than available on HET for the equivalent elastic resolution of 5% of the incident energy (FWHM) (see Section 3.4).

The main components of the beam–line outside the biological shielding are:

1) The background–suppressing T–zero chopper
2) The monochromating Fermi chopper
3) Adjustable slits
4) Supermirror guide

One of the important advantages of direct–geometry chopper spectrometers on pulsed neutron sources is the flexibility that they provide the experimenter in optimizing the incident energy and resolution of the measurements. The incident energy can be varied from 10 meV to 1 eV by changing the Fermi chopper phase, speed, and, occasionally, the slit package. HELIOS will take full advantage of this flexibility with three Fermi chopper slit packages to allow the measurement of energy transfers from 1meV to 500 meV.

2.1.1 Biological Shielding

The visible area of the "high–intensity" H_2O moderator viewed by HELIOS is 12.5 x 12.5 cm^2. The primary collimation within the biological shielding consists of B_4C apertures of tapering size. One of the options that we wish to consider in more detail is the ability to switch between this standard collimation and a supermirror guide, also installed in the biological shielding. This would have substantial intensity benefits at the lower end of the HELIOS energy spectrum, below 40 meV, particularly if coupled to focusing guides before the sample position. Such guides have been successfully installed close to the cold sources of reactors without suffering significant radiation damage. However, it may not be compatible with the current mercury shutter mechanism used most commonly at MLNSC. We will perform more detailed Monte Carlo estimates of the flux gains before proceeding with this option.

2.1.2 T_0 Chopper

The purpose of the T–zero (T_0) chopper, which will be located just outside the biological shielding at about 5.1 m from the moderator, is to suppress both the prompt pulse of fast neutrons produced when the proton–beam strikes the target and the time–independent background arising from delayed neutrons from the moderator. The HET spectrometer at ISIS has a nimonic alloy chopper with two fins that block the beam only during the prompt pulse. Since this has no effect on the delayed neutrons, the backgrounds were considerably higher when the uranium target was in operation. Moreover, the downstream Fermi chopper modulated the delayed neutron background making it extremely difficult to subtract reliably.

We therefore propose to use a coarse Fermi chopper which can be phased to the incident energy of the monochromating Fermi chopper while running at a lower multiple of the source pulse frequency. Beryllium-bodied choppers running on mechanical bearings have proved to be very effective on the HRMECS and LRMECS spectrometers at IPNS. They

are identical in design to the Fermi choppers but have no collimating slit packages so the transmission for in–phase neutrons is 100%. The kinematics of the neutron scattering processes ensure that the chopper is closed up to very high fractional energy transfers so that backgrounds are reduced over the useful portion of the time frame. Care has to be taken that detector backgrounds are not increased during subsequent open periods of the chopper.

2.1.3 Fermi Chopper

The Fermi chopper will be located at 6.1 m from the moderator. Its purpose is to produce a monochromatic burst of neutrons whose energy is determined by the chopper phase. The intensity and resolution of the neutron pulse incident on the sample is governed by both the chopper rotation frequency, which can be any integer multiple of the source frequency up to a maximum of 600 Hz, and the dimensions of the curved collimation slits within the chopper. The relevant dimensions are the slit width, the slat width, radius of curvature and external radius of the chopper body. Although precise optimization of the intensity and resolution requires the ability to vary all these parameters, a set of three chopper slit packages provide adequate performance over the entire range of accessible energy transfers, from 1 to 500 meV.

We present in Figure 7 (Section 3.4) estimates of the intensity and resolution of three different chopper slit packages. They are labeled by the energy of their maximum transmission at a rotation frequency of 600 Hz. The following parameters were used:

	Slit Width	Slit Width	Curvature	Body size
250 meV	1.29 mm	0.55 mm	920 mm	49 mm
100 meV	2.58 mm	0.55 mm	580 mm	49 mm
12 meV	5.77 mm	0.55 mm	200 mm	49 mm

In order to achieve rotation speeds up to 600 Hz, the Fermi chopper will employ magnetic bearings. These have the added advantage of better phase stability than mechanical–bearing choppers.

A critical development priority for the HELIOS project is to determine how the Fermi chopper system will be timed to the source pulse. At present, the MLNSC has only one chopper spectrometer, PHAROS. The phase of its Fermi chopper tracks frequency variations in the external power supply and triggers the proton beam injection accordingly. There are proposals to change the timing electronics of the PHAROS chopper system, so HELIOS will be designed in conjunction with those changes. There is also considerable investment in chopper electronic and computer control developments by SNS and IPNS. The chopper phasing mechanisms will be tested during the development phase on the LRMECS spectrometer before final construction at Los Alamos.

2.1.4 Adjustable Slits

We will install two sets of adjustable slits in order to reduce backgrounds when samples smaller than the overall beam size are being measured. They will be installed both in the Fermi chopper housing and just before the sample chamber with both horizontal and vertical adjustment. Since both locations will be inaccessible when safety interlocks are in place, the slits will be fitted with stepper-motor drives for remote operation.

2.1.5 Supermirror guide

The angle subtended by a detector pixel is 0.6° (see Section 3.3) corresponding to a FWHM angular divergence of 0.3° for a point sample. The distance collimation associated with a point sample viewing a 12.5 x 12.5 cm^2 moderator at 7.1 m is 0.5° giving a reasonably well matched initial and final divergence, particularly once the effect of finite sample size (which impacts final divergence to a greater extent due to shorter distance) are taken into account. Nevertheless, there are many cases where the increased intensity that can be achieved at the expense of beam divergence by using supermirror guide in the incident flight path. In principle the guide should extend as far back to the source as possible, into the biological shield described in 3.1.1. However this may be ruled out by compatibility with the mercury shutter. In the event this is the case we would still include a shorter guide section in the section between the two choppers. This would be installed on a cylindrical drum that is aligned parallel to the beam thus permitting a variety of beam conditioning optical elements to be remotely inserted as dictated by the needs of the experiment. The detailed choices for insertion would be based on the results of the Monte Carlo optimization but the flexibility offered by straight and tapered guide sections, along with smaller aperture channels for smaller samples with reduced background would greatly increase the flexibility of HELIOS. The cost estimate in Section 4 is based on the assumption a full guide section can be installed. If we are restricted to a shorter section then the savings in guide costs can be devoted to the rotating insertion device.

2.2 Vacuum Vessel

The vacuum vessel of HELIOS serves three purposes. It provides an evacuated secondary flight path, a low background environment for the detector bank, and vacuum insulation for certain sample environments. The inner volume of the vessel will be a 160 degree wedge of a cylinder with a radius of approximately 2.6 m and height 1.1 m. With these dimensions the inner volume of the vessel will be 10 m^3 while the surface area is 33 m^2. The vacuum vessel will be built from approximately 0.75" thick steal plates with a total mass of 4×10^3 kg. The mass of support structures is estimated to be 2×10^3 kg so that the total mass of the vacuum vessel will be about 6 metric tons. This exceeds the capacity of the crane in ER-1 so we plan to use rollers in combination with a fork truck to bring the vessel to its location there. At present we anticipate that the detectors will be mounted in vacuum within the vessel since we estimate that it is easier to create a vacuum feed-through for the detector cables than establish thin windows which sustain an atmosphere. No extra expenditure will be made for non-magnetic steel since a magnetically polarizable vacuum vessel should not preclude future production or detection of polarized

neutrons. In addition much of the science to be pursued does not require polarization analysis.

Because of the high ability of the internal neutron shielding (crispy mix) to adsorb water it is probably not practical to pump the whole vacuum vessel down to the cryogenic vacuum required for sample environments. The vessel will therefore have a sample vacuum separated from the main vacuum by a very thin aluminum or sapphire membrane at beam height (<0.1 mm). This differential shield will only have to support a pressure difference of approximately 0.1 mbar corresponding to a force of 10^{-2} N/m^2 and it will be stationary with respect to the incident beam. The main cost for this item, estimated at $10,000, will go to developing the evacuation and safety interlock system to prevent there from being a pressure difference larger than 0.1 mbar between the sample and detector volumes.

2.2.1 Shielding requirements

For maximum dynamic range in inelastic scattering experiments it will be crucial to provide a low background environment for the HELIOS detector bank. For this reason the vacuum vessel will be surrounded by a 20-30 cm thick shell of shielding. Thin walled steel containers will be filled with a mixture of wax and borax ($Na_2B_4O_7$), for moderation and absorption of neutrons which would otherwise enter the detector bank from the outside. To determine the thickness and composition of the shielding required experiments will be conducted at Flight Path 8 with a single PSD detector in a small shielded volume of varying composition and wall thickness. In anticipation of future proton current upgrades and taking into account previous unpleasant experiences in which shielding requirements were underestimated we will tend to be generous with shielding material. With a mass ratio of 25% borax powder and 75% wax the density of the shielding material will be approximately 1 g/cm^3. There will be shielding on all sides of the vacuum vessel and the corresponding shielding volume will be 6-9 m^3 with a mass of 6-9 metric tons. Naturally this shielding will be segmented so that it can be brought into place using the crane in ER-1. At an estimated price of 1000$/$m^2$ the total cost of shielding the vacuum vessel will be $33,000 including design costs. Special attention must of course be paid to shielding around the incident beam path and to completely coating the inside of the vessel with boron loaded epoxy (crispy mix). The price for crispy mix is $2000/$m^2$ so we will use $66,000 for this purpose.

2.2.2 Vacuum pumping system

The pumping system will be designed with the following constraints.

1. It must be completely automated and equipped with interlocks for safety and to protect the investment
2. It must be able to bring the entire vacuum vessel from ambient pressure to base pressure in 1 hour.

3. It must achieve a base pressure of 10^{-3} mbar in the main vessel and 10^{-6} mbar in the sample vacuum chamber.
4. It must avoid cryopumping of water and other material onto a sample held at 3.6 K.
5. It should not require service or regeneration under normal operating conditions over the period of a typical LANSCE beam cycle

For rapid pump down of the entire vessel to 10^{-3} mbar we shall use a root pump backed by a conventional rotary pump. The required pumping speed is of order 1000 cubic feet per minute. A suitable system costs approximately $ 60,000. To reach a pressure of 10^{-6} mbar in the sample vacuum we shall use a turbo molecular pump at a price of $15,000. To avoid cryopumping onto the sample the sample volume will also be pumped by a cryo-pump (poly-cold) estimated to cost $30,000. Finally to maintain a dry atmosphere in the vessel at all times we shall purchase a dry air venting system estimated at $15,000. From the experience building PHAROS we estimate that design and construction of the pumping automation and interlock system will cost $15,000.

2.3 Detectors

The detector array on HELIOS will consist of 262 linear position sensitive detectors (LPSDs) of the same type used on PHAROS. These are 2.5 cm x 90 cm tubes which will be electronically resolved as 36 2.5 cm x 2.5 cm pixels, for a total of 9432 individual detector elements. Each pixel will subtend 0.6°, corresponding to a FWHM angular resolution of 0.3°, comparable to the mosaic spread of typical single crystals. For powder samples the detector array will be decomposed into Debye-Scherrer rings. Angles from –20° to +140° in the horizontal plane and ±10 degrees vertically will be accessed with even spacing of the detectors to the extent possible while maintaining the structural integrity of the vacuum vessel. The detector array and associated electronics are the single most expensive component of HELIOS. However, the wide angle coverage translates directly into improved detection efficiency and the combination of low angles for magnetic studies and high angles for phonon measurements is essential to the two components of the scientific program.

2.4 Computer systems

The data acquisition and analysis systems will be built using commodity components following the standard under development at LANSCE and IPNS. Software for HELIOS will benefit from (and provide benefits to) similar systems employed on PHAROS and ISIS. The software required to visualize and carry out lineshape analysis of data obtained on HELIOS will be developed at Oak Ridge in a generic form making it suitable for single crystal time of flight data obtained at any facility. By adhering to the emerging, HDF based, NeXus data format portability of HELIOS data to this (or any other analysis package) will be ensured.

2.4.1 Data acquisition

The data acquisition hardware will be a modular VME based system which will provide the necessary event timing and positioning. An ethernet connection to the host UNIX or Windows NT computer will be sufficient for the data rates anticipated on HELIOS (the

full detector images are large but for typical inelastic experiments counting times are long so a delay of a few seconds is tolerable). The user interface to the data acquisition will be via a web browser, decoupling the location and operating system of the spectrometer from those of the user. The sample environment will also be controlled via a web browser interface though the use of Labview and IEEE-488 or RS-232 interfaces. Password based security, which is specific to a given experiment, will ensure safe and secure remote operation. Only systems that can be modified without compromising safe operation will be remotely controllable although all relevant machine parameters will be viewable.

2.4.2 Experiment simulator

An online experiment simulator will be built up from the Monte Carlo code used to optimize HELIOS. In order to be useful for real time experiment optimization it will be restricted to resolution modeling (i.e. the full instrument performance including background will not be simulated). This will be accessed from the same software interface as the analysis package or as a callable routine from user supplied software.

2.4.3 Data analysis and presentation

One of the computational challenges facing large solid angle chopper instruments is dealing with the visualization of thousands (9432 for HELIOS) of time of flight scans each constituting a trajectory through the four dimensional ($\mathbf{Q}$,ω) space of a single crystal sample. Each time of flight trajectory itself consists of thousands of microsecond time bins. The software must correctly transform the data from (ϕ,t) [angle and time] into ($\mathbf{Q}$,ω) keeping track of resolution volume, statistical uncertainty, detector efficiency, and crystal coordinate transforms. Having done this the data must then be projected onto a two dimensional space appropriate for the scientist to view and make decisions about the next step in the experiment. The data from a single setting of the spectrometer will be projected, sliced, viewed, and modeled in attempt to reconstruct the important features of the dynamical response of the sample being measured.

Fortunately, powerful tools exist for manipulating and visualizing large arrays of data. Commercial programs such as IDL and Matlab greatly reduce the development time for specialized software to handle this problem. However, HELIOS and PHAROS II will have more than an order of magnitude more detector elements than any existing time of flight spectrometer (due to the use of spacially resolving LPSDs) so they will tax the hardware and software capabilities of whatever system is adopted.

2.5 Sample environment

Sample environments will be provided by units that mount on a rotating stage atop the HELIOS vacuum vessel. The stage will have a rotating vacuum seal large enough to enclose the LANSCE standard bolt circle. The different systems for sample environment to be mounted with this bolt circle are:

1. Thimble, a thin-walled aluminum containment to separate the spectrometer vacuum from a cylindrical specimen region at ambient pressure. Specialized sample environments provided by users will fit within this thimble.
2. Low temperature heliplex system for experimentation from 3.6 K to 350 K. This unit is a closed-cycle refrigerator with enhanced low temperature capability provided by a Joule-Thompson heat exchanger.
3. Displex/heater unit for a temperature range of <30 - 650 K.
4. High temperature furnace unit capable of temperatures from 600 - 2073 K.

These units are described in detail below. An over-riding consideration in choosing these units was their ease-of-use. Especially in the early years of HELIOS, all users will be inexperienced with its characteristics. Further risk to the users' experiments caused by complexities of cryostat control, for example, are important to avoid. Displex units also provide for more convenient computer interfacing, and promise a greater degree of automatic control of data acquisition.

2.5.1 Sample rotation stage

Much of the science to be done on HELIOS involves single crystal samples. For these experiments it is necessary to orient the reciprocal space of the sample with respect to the wave vector transfer probed by the spectrometer. For a given choice of E_i a conventional triple axis spectrometer can probe the neutron scattering cross section for wave-vector transfer on part of a circle of radius k_f which is displaced from the origin by $\mathbf{k}_i$. For a given value of $Q=|\mathbf{k}_i-\mathbf{k}_f|$ there are at most two orientations of the sample which will bring a given reciprocal lattice direction into coincidence with $\mathbf{k}_i-\mathbf{k}_f$. To probe an arbitrary value of wave *vector* transfer to the sample it is therefore necessary on such an instrument to select the tilt of the sample about an arbitrary horizontal axis as well as to rotate the sample about a vertical axis. On HELIOS the tall Position Sensitive Detectors (PSD) subtend a vertical angular range of 20 degrees such that for a given choice of E_i the detector bank probes an equatorial band on the surface of a sphere of radius k_f which is displaced by $\mathbf{k}_i$ from the origin of reciprocal space. The detector bank thus probes an area in reciprocal space and there are lines along this spherical band which correspond to specific values of $Q=|\mathbf{k}_i-\mathbf{k}_f|$. This implies that for a given choice of E_i and E_f a volume of reciprocal space can be accessed on the HELIOS detector bank with just a vertical axis of rotation for the sample. If only values of wave vector transfer within a specific reciprocal lattice plane are of interest, it will be necessary to orient this plane of the crystal lattice to within 5 degrees of the horizontal plane. This level of accuracy is easily obtained using well-established alignment techniques. It is therefore sufficient on HELIOS to implement a rotation stage capable of rotating the sample about a vertical axis.

The rotation stage will include the flange for mounting the sample environment units atop the vacuum vessel. This requires the design of a rotating vacuum feed through. The diameter of the LANSCE standard bolt circle (as on PHAROS) will set the size of the sample environment units. In cases where further degrees of freedom for sample orientation with respect to the spectrometer are required this will have to be accomplished through specialized goniometers within the sample environment. The sample rotation

stage will be based on a commercial rotation table. A stepping motor and associated controller connected to the data acquisition software through an IEEE interface will control the angular setting of the rotation stage to within an accuracy of 0.01 degrees.

2.5.2 Thimble for specialized sample environments

While most sample environments will use the vacuum of the HELIOS vacuum vessel to provide an evacuated scattering volume and thermal insulation is necessary there are cases in which special conditions require a separate sample vacuum. Examples of such cases are

1. When the HELIOS vacuum vessel does not provide adequate thermal insulation as for example in the case of a dilution refrigerator.
2. When there is a risk that the sample may disintegrate and contaminate the main vacuum vessel as in the case of the high temperature furnace.
3. When it is necessary to have access to a sample vacuum prior to availability of the HELIOS vacuum vessel.
4. When a specialized sample environment, which cannot be mounted directly on the rotating vacuum flange, is to be used.

For these and other cases there will be an ambient pressure thimble that can be mounted on the rotating vacuum flange to provide ambient pressure and temperature access to the HELIOS scattering volume. The thimble will be made of aluminum tube stock and have a thin aluminum window at beam height to minimize scattering from this part of the sample environment. The thickness of this window will be in the range 1-2 mm as dictated by strength and safety considerations. All parts of the thimble outside of beam height will be coated with neutron absorbing material such as boron loaded epoxy on the side facing the vacuum vessel.

2.5.3 Oscillating radial collimator

Important parts of the scientific projects to be pursued on HELIOS involve sample environments that necessarily place significant amounts of material in the incident beam path. Examples are the high temperature furnace and various high pressure cells to be used on the instrument. Owing to their different flight paths, neutrons which scatter elastically from material that is not at the sample position will in general arrive at the detector bank at different times than neutrons which scatter elastically from the sample. The result can be intense spurions that are difficult to distinguish from inelastic scattering from the sample itself.

To suppress these spurions and background, HELIOS will be equipped with an oscillating radial collimator. The collimator will be located in the detector vacuum vessel in such a way that it can be used in combination with any sample environment including the ambient pressure thimble. The collimator will cover the full angular range of the detector bank and the blade spacing will be chosen so as to define a cylindrical scattering volume with a diameter of order 1 cm. With an inner diameter of approximately 0.5 m this

requires a collimation of approximately 140 minutes of arc per channel. Assuming a blade length of 30 cm, the entire collimator would have of order 60 blades separated by approximately 1.2 cm. There are several companies that have delivered such collimators in the past. We are basing our price estimate on the cost for the radial collimator purchased by John Copley of NIST from Euro Collimator in 1997. One innovation would be the necessity of using a neutron absorbing material such as boron, which remains efficient up to neutron energies of order 500 meV. Given the large blade spacing we believe this problem can be solved without reducing the transmission of the device below 90 %.

The radial collimator will be mounted on a rotation stage to provide the oscillating motion that prevents permanent shading of specific directions. Not only the collimator blades but also the frame from which the blades are suspended and the rotation stage will be coated with neutron absorbing material to avoid spurious scattering processes. Provisions will be made to automatically lower or raise the collimator out of the beam path when it is unnecessary.

2.5.4 Low temperature closed-cycle refrigerator (3.6 - 350 K)

A closed-cycle refrigerator unit is already in place at LANSCE for use on PHAROS, and we expect this unit to be adaptable to HELIOS. Since low temperatures are required for much of the scientific program, it is important to acquire another displex unit. We may choose to duplicate the PHAROS unit, but our preference is to obtain a unit with extended low temperature capability. One approach is taken by APD Cryogenics in their commercial Heliplex design. It uses a closed-cycle refrigerator in combination with a Joule-Thompson heat exchanger to achieve base temperatures below 3.6 K. A temperature controller dedicated to this device will be purchased.

2.5.5 High temperature closed-cycle refrigerator (<30 - 650 K)

Ross W. Erwin of NIST has modified a closed-cycle refrigerator to enable it to reach temperatures of 650 K. The trick is to use a sapphire spacer between the cooling head and heating stage. The thermal conductivity of sapphire is temperature-dependent so that it provides better heat conduction at low temperatures than at higher temperatures. The NIST group is agreeable to providing us with drawings and technical advice. We plan to build our own unit, however, which is based on a closed-cycle refrigerator unit from APD or Leybold, a heating stage from Air Products, and a sapphire link between them. Although the closed-cycle refrigerator has a base temperature of 6.5 K, we expect that with the sapphire spacer the base temperature should be between 25 and 30 K. A temperature controller dedicated to this refrigerator will be purchased.

2.5.6 Furnace (600 - 2073 K)

We have evaluated the performance and reliability of several high temperature furnaces that have been used previously for neutron scattering work. The clear choice is the "ILL" furnace manufactured by AS Scientific Products, Abingdon, England, and shown below

in Figure 6. This unit uses a cylindrical Nb heating element around the sample, which can be as large as 4.5 cm diameter and 10 cm high. Cylindrical Nb radiation shields surround the heating element, and the water-cooled housing has thin Al windows for 360° neutron access around the sample. Neutron access is ±20° out of the plane of the spectrometer. This unit has relatively low background, but the background will be essentially negligible with incident beam collimation and the use of radial collimators in the HELIOS vacuum vessel. The unit is reasonably priced, about 65 k$ with vacuum system, power supply, interlocks, and miscellaneous spare parts.

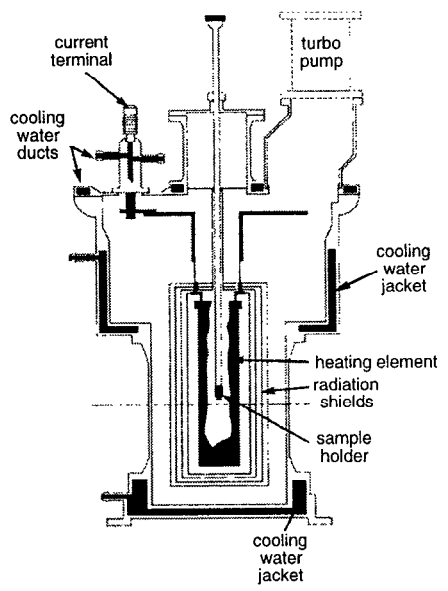

Figure 6: The ILL high temperature furnace. The thin Nb heating element and Nb radiation shields are in the neutron beam, but we have had little trouble with spurious scattering in reactor experiments with collimated beams at ORNL.

An important advantage of this ILL furnace is that it is a mature product, with an integrated vacuum system, temperature controller, power supply, and safety interlocks. It will likely be useful for other experimental facilities at LANSCE — certainly it will be useful on PHAROS. There is a possibility that an ILL high temperature furnaces will be procured for the PHAROS spectrometer. Depending on timetable and funding for HELIOS, it may be possible to find partial external support for this furnace as it is being purchased for work on PHAROS.

2.5.7 Issues with pressure cells

Pressure experiments with a samples having masses of tens of grams and greater are often performed by mounting the sample in a canister that can be compressed in a hydraulic press, and then locked in a compressed position. Upon removal from the hydraulic press, the pressure is maintained in this "pressure cell", which is a compact unit that can be moved into the specimen region of the HELIOS spectrometer, for example. An obvious feature of the pressure cell is that it is made of high strength materials such as sapphire or steel, and typically more such material when higher pressures are required. For pressures of 10 kbar or higher, spurious scattering from the pressure cell can overwhelm the scattering from the sample itself. This problem can be alleviated considerably by collimation. The incident beam is collimated to have a width comparable to the sample, and the scattered beam is collimated with the oscillating radial collimators. The small size of the vacuum vessel of HELIOS facilitates such scattered beam collimation with oscillating radial collimators. For this reason we expect it to be easier to perform high pressure experiments with HELIOS than with the PHAROS spectrometer.

2.6 Projected system performance

To complement PHAROS II, which was optimized for high resolution, HELIOS will be optimized for high flux and sensitivity with a correspondingly coarser energy resolution. As a rough measure of the overall sensitivity of the two instruments we take:

$$\eta=\Omega_i \ \Delta E_i/E_i \ \Omega_f \text{, (4)}$$

where Ω_i is the solid angle by which the moderator is viewed from the sample position, Ω_f is the total solid angle of the detection system, and $\Delta E_i/E_i$ is the relative energy resolution of the Fermi chopper system. The estimated values for these quantities are:

Instrument	Ω_i (steradians)	$\Delta E_i/E_I$	Ω_f (steradians)
PHAROS II	$3.9\text{x}10^{-5}$	0.5%	0.65
HELIOS	$3.1\text{x}10^{-4}$	5%	1.1

For HELIOS we have not taken into account the enhancement in solid angle Ω_i by as much as a factor of 2 for E_i<30 meV which will be achieved through the use of a super mirror guide in the incident beam path. Nor have we considered the higher flux at the coupled HELIOS moderator as compared to the decoupled water moderator at PHAROS. From these numbers we obtain a lower bound on the ratio of sensitivity between the two instruments:

$$\eta_{HELIOS}/\eta_{PHAROS}>2\text{x}10^2 \text{ (5)}$$

This estimate is perhaps the best argument for building HELIOS. For scientific projects such as those described in Section 2 which do not require very good energy resolution, it will be possible to complete experiments on HELIOS in days, which could not be completed on PHAROS in an entire cycle. On the other hand HELIOS does *not* supersede PHAROS because it will not be useful for experiments which do require $\Delta E_i/E_i$<3 %. Nor will it provide access to the very low angle regime which is important for probing sound waves in amorphous solids and liquids. The two spectrometers are therefore manifestly complementary. With both, LANSCE will have a productive suite of spectrometers around which to develop a world class scientific program in the important fields of condensed matter physics and materials science outlined in this proposal. With only PHAROS, LANSCE will *not* be competitive for probing dynamics of solids in the important thermal and epithermal energy ranges.

For an absolute comparison of HELIOS to similar instrumentation at other spallation sources, T. G. Perring calculated flux and resolution as a function of incident neutron energy using software that he has developed and verified for accuracy at ISIS. Again we seek a conservative estimate so the calculation does not taken into account the supermirror guide or the coupled moderator which will enhance the flux without

compromising resolution. The parameters which went into the calculation are listed in Table 1. The result of the calculations are shown in Figure 7.

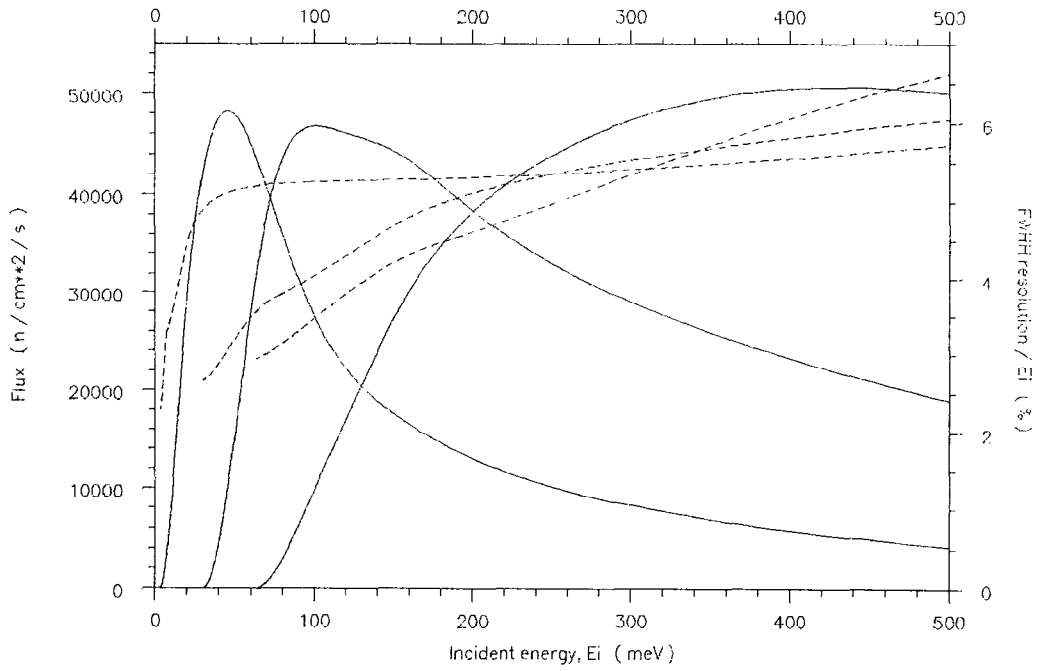

Figure 7: Estimated neutron flux at the sample position (solid) and energy resolution (dashed) vs E_i for three different chopper slit packages described in the text. The high, medium, and low energy slit packages result in the intensity curves arrayed from right to left. The resolution curves from bottom to top on the left hand side correspond to high to low energy respectively.

There are three pairs of curves showing flux and resolution for three different Fermi chopper slit packs optimized for E_i=20 meV, E_i= 100 meV, and E_i= 400meV and $\Delta E_i/E_i$=5%. One important observation is that the peak flux and relative energy resolution for these chopper systems is almost energy independent from 20-500 meV. It is also clear from these calculations that this impressive energy range can only be accessed with several different Fermi chopper slit packs. The HELIOS chopper system will be designed to minimize turn around time for changing the incident energy and the Fermi chopper. The energy resolution plotted is the elastic linewidth, the energy resolution decreases as the energy transfer is increased so most excitations will be measured with tighter resolution than that implied by Figure 7.

Moderator to Chopper Distance	6.1 m
Chopper to sample distance	1 m
Sample to detector distance	2.5 m
Moderator area	12.5 cm x 12.5 cm
Moderator type	Water T=316 K poisoned at 1.5 cm

Target	ISIS Tantalum target
Proton beam power	160 kW

Table 1. Specifications underlying the flux and resolution calculations of Figure 7.

The other important message from Figure 7 is the absolute flux numbers. At Ei=100 meV the flux on HELIOS will exceed the maximum monochromatic flux which can currently be obtained on MARI by roughly a factor 3. Of course this is simply due to the larger incident bandwidth and beam divergence on HELIOS. This does mean, however, that HELIOS would bring a world record in pulsed monochromatic flux to LANSCE, and that it would attract experimenters with projects which require high sensitivity at a relative energy resolution similar to that of a triple axis spectrometer.

3 Conclusions

HELIOS combines the relatively coarse resolution, and therefore high single to noise, of a thermal triple axis spectrometer with the dynamic range and efficiency of a high solid angle direct geometry time of flight spectrometer. It will permit the application of neutron spectroscopy to a wide range of problems that currently cannot be addressed due to limitations associated with small sample size, weak scattering, or demanding sample environments.

Acknowledgements

We would like to thank T.G. Perring for assistance with comparisons of flux and resolution with ISIS instruments. Work at Oak Ridge was carried out under U.S. Department of Energy Contract No. DE-AC05-960R22464. T.E.M. acknowledges the support of NSERC, CIAR, and the A.P. Sloan Foundation for work carried out at the University of Toronto.

References

[1] See, for example: F. Ducastelle, Order and Phase Stability in Alloys, (North Holland, Amsterdam, 1991).
[2] L. Anthony, J. K. Okamoto, and B. Fultz, "Vibrational Entropy of Ordered and Disordered Ni_3Al, Phys. Rev. Lett. 70 (1993) 1128-1130.
[3] L. Anthony, L. J. Nagel, J. K. Okamoto, and B. Fultz "The magnitude and origin of the difference in vibrational entropy between ordered and disordered Fe_3Al", Phys. Rev. Lett. 73 (1994) 3034-3037.
[4] L. J. Nagel, L. Anthony and B. Fultz, "Differences in vibrational entropy of disordered and ordered Cu_3Au", Philos. Mag. Lett. 72 (1995) 421-427.

[5] L. J. Nagel, B. Fultz, and J. L. Robertson, "Vibrational Entropies of Phases of Co_3V Measured by Inelastic Neutron Scattering and Cryogenic Calorimetry", Philos. Mag. B, in press.
[6] B. Fultz, L. Anthony, L. J. Nagel, R. M. Nicklow and S. Spooner, "Phonon densities of states and vibrational entropies of ordered and disordered Ni_3Al", Phys. Rev. B 52 (1995) 3315-3321.
[7] L. J. Nagel, B. Fultz, J. L. Robertson, and S. Spooner, "Vibrational entropy and microstructural effects on the thermodynamics of partially-disordered and ordered Ni_3V", Phys. Rev. B, 55 (1997) 2903-2911.
[8] B. Fultz, J. L. Robertson, T. A. Stephens, L. J. Nagel and S. Spooner, "Phonon density of states of nanocrystalline Fe prepared by high energy ball milling", J. Appl. Phys. 79 (1996) 8318-8322.
[9] H. N. Frase, L. J. Nagel, J. L. Robertson, and B. Fultz, "Vibrational Density of States in Nanocrystalline Ni_3Fe", Philos. Mag. B 75 (1997) 335.
[10] T.G. Perring, G. Aeppli, S.M. Hayden, S.A. Carter, J.P. Remeika, and S.-W. Cheong, "Spin waves throughout the Brillouin zone of a double-exchange ferromagnet", Phys. Rev. Lett. 77 (1996) 711-714.
[11] T.E. Mason, C.P. Adams, S.A.M. Mentink, E. Fawcett, A.Z. Menshikov, C.D. Frost, J.B. Forsyth, T.G. Perring, and T.M. Holden, Physica B 237-238 (1997) 449-452.
[12] K. Yamada *et al.*, "An overall energy spectrum of magnetic fluctuations in the superconducting $La_{1.85}Sr_{0.15}CuO_4$", J. Phys. Soc. Jpn. 64 (1995) 2742.
[13] S.M. Hayden, G. Aeppli, H.A. Mook, T.G. Perring, T.E. Mason, S.-W. Cheong, and Z. Fisk, "Comparison of the high-frequency magnetic fluctuations in insulating and superconducting $La_{2-x}Sr_xCuO_4$", Phys. Rev. Lett. 76 (1996) 1344.
[14] P. Bourges, H.F. Fong, L.P. Regnault, J. Bossy, C. Vettier, D.L. Milius, I.A. Aksay, and B. Keimer, "High Energy Spin Excitations in $YBa_2Cu_3O_{6.5}$", Phys. Rev. B 56 (1997) R11439.
[15] L. Soderholm, C.-K. Loong, and S. Kern, Phys. Rev. B 45 (1992) 10062.
[16] R. Osborn, S. W. Lovesey, A. D. Taylor, and E. Balcar, "Intermultiplet transitions using neutron spectroscopy" in Handbook on the Physics and Chemistry of Rare Earths, edited by K. A. Gschneidner, Jr. and L. Eyring (North-Holland, Amsterdam, 1991), Vol. 14, p. 1.
[17] A.T. Boothroyd, A. Mukherjee, A.P. Murani, "Evidence for extreme gap anisotropy in $Ho_{0.1}Y_{0.9}Ba_2Cu_3O_7$ from neutron spectroscopy of Ho^{3+}", Phys. Rev. Lett. 77 (1996) 1600.
[18] D.A. Tennant, R.A. Cowley, S.E. Nagler, *et al.*, "Measurement of the Spin-Excitation Continuum in One-Dimensional $KCuF_3$ using Neutron Scattering", Phys. Rev. B 52 (1995) 13368.
[19] M. Arai, M. Fujita, M. Motokawa, *et al.*, "Quantum spin excitations in the spin-peierls system $CuGeO_3$", Phys. Rev. Lett. 77 (1996) 3649.
[20] A.W. Garrett, S.E. Nagler, *et al.*, "Magnetic excitations in the S=1/2 alternating chain compound $(VO)_2P_2O_7$", Phys. Rev. Lett. 79 (1997) 745.
[21] M. Ain, J.E. Lorenzo, L.P. Regnault, *et al.*, "Double gap and solitonic excitations in the spin-Peierls chain $CuGeO_3$", Phys. Rev. Lett. 78 (1997) 1560.

[22] D.C. Dender , P.R. Hammar, D.H. Reich, C. Broholm *et al.* "Direct observation of field-induced incommensurate fluctuations in a one-dimensional S=1/2 antiferromagnet", Phys. Rev. Lett. 79 (1997) 1750.
[23] V. Kiryukhin, B. Keimer, J.P. Hill and A. Vigliante, ``Soliton Lattice in Pure and Diluted $CuGeO_3$", Phys. Rev. Lett. 76 (1996) 4608.
[24] For a review, see E. Dagotto, T.M. Rice, "Surprises on the way from one- to two-dimensional quantum magnets: The ladder materials", Science 271 (1995) 618.
[25] M. Uehara , T. Nagata , J. Akimitsu, *et al.*, "Superconductivity in the ladder material $Sr_{0.4}Ca_{13.6}Cu_{24}O_{41.84}$", J. Phys. Soc. Jpn. 65 (1996) 2764.
[26] N. Motoyama, H. Eisaki , S. Uchida , "Magnetic susceptibility of ideal spin 1/2 Heisenberg antiferromagnetic chain systems, Sr_2CuO_3 and $SrCuO_2$", Phys. Rev. Lett. 76 (1996) 3212.
[27] See, for example, T. Katsufuji et al., "Spectral Weight Transfer of the Optical Conductivity in Doped Mott Insulators", Phys. Rev. Lett. 75 (1995) 3497, and references therein.
[28] Y. Maeno *et al.*, "Superconductivity in a layered perovskite without copper", Nature 372 (1994) 532.
[29] M. C. Aronson, R. Osborn, R. A. Robinson, J. W. Lynn, R. Chau, C. L. Seaman, and M. B. Maple, "Non-Fermi liquid scaling of the magnetic response in $UCu_{5-x}Pd_x$ (x=1,1.5)" Phys. Rev. Lett. 75 (1995) 725.
[30] E. A. Goremychkin and R. Osborn, "Crystal field excitations in $CeCu_2Si_2$", Phys. Rev. B 47 (1993) 14280.
[31] P. Soderlind, O. Eriksson, B. Johansson, J. M. Wills and A. M. Boring, Nature 374, 524 (1995), and references therein.
[32] P. Soderlind, J. M. Wills, B. Johansson and O. Eriksson, Phys. Rev. B 55, 1997 (1997).
[33] J. L. Robertson, H. N. Frase, B. Fultz and R. J. McQueeney "Phonon densities of states of γ-Ce and δ-Ce measured by inelastic neutron scattering", submitted to Phys Rev. Lett.
[34] P. D. Bogdanoff, B. Fultz, J. L. Robertson, R. J. McQueeney, S. Rosenkranz, "Phonon Density of States and Heat Capacity of the Austenite-Martensite Transformation in the Shape Memory Alloy NiTi", manuscript in preparation.
[35] S. K. Satija, S. M. Shapiro, M. B. Salamon, and C. M. Wayman, "Phonon Softening in $Ni_{46.8}Ti_{50}Fe_{3.2}$", Phys. Rev. B 29 (1984) 6031. H. Chou and S. M. Shapiro, "Observation of predicted phonon anomalies in β-phase $Ni_{50}Al_{50}$", Phys. Rev. B 48 (1993) 16088.
[36] L. J. Nagel, B. Fultz, and J. L. Robertson, "Vibrational Entropies of Phases of Co_3V Measured by Inelastic Neutron Scattering and Cryogenic Calorimetry", Philos. Mag. B 75 (1997) 681-699.

ICANS XIV
14th Meeting of the International Collaboration on
Advanced Neutron Sources
June 14-19, 1998
Starved Rock Lodge, Utica, IL

A DESIGN FOR A HIGH RESOLUTION VERY-LOW-Q TIME-OF-FLIGHT DIFFRACTOMETER

Rex P. Hjelm & Phillip A Seeger
Manuel Lujan Jr. Neutron Scattering Center , Los Alamos National Laboratory, Los Alamos, NM 87545
P. Thiyagarajan & Lahsen Assoufid
Intense Pulsed Neutron Source and Advanced Photon Source, Argonne National Laboratory, Argonne, IL 60139
Louis R. Bertolini
Accelerator Technology Engineering, Engineering Directorate, Lawrence Livermore National Laboratory, Livermore, CA
Brent J. Heuser
Department of Nuclear Engineering, University of Illinois at Urbana-Champaign, Urbana, IL 61801

Abstract

The design of a high resolution very low-Q time of flight diffractometer was motivated by the anticipated need to perform small-angle neutron scattering measurements at far lower momentum transfer and higher precision than currently available at either pulsed or steady state sources. In addition, it was recognized that flexibility in the configuration of the instrument and ease in which data is acquired are important. The design offers two configurations, a high intensity/very low Q geometry employing a focusing mirror and a medium to high Q-precision/low Q configuration using standard pinhole collimation geometry. The quality of the mirror optics is very important to the performance of the high intensity/very low Q configuration. We believe that the necessary technology exists to fabricate the high quality mirror optics required for the instrument.

Objective:

Our objective was to design a Time-of-flight (TOF), Very Low-Q Diffractometer (VLQD) with capabilities not currently available in existing small-angle neutron scattering (SANS) instruments. These capabilities include having configurations for high Q-precision measurements and for minimum Q, Q_{min}, substantially less than 0.001 Å. The instrument will operate in either of two configurations:

- A high intensity, mirror-focused configuration with a Q_{min} in the 0.0002 to 0.0005 $Å^{-1}$ range with 10%, $\sigma(Q)/Q$ root mean squared (rms) resolution at $Q = 0.005$ $Å^{-1}$.
- A high resolution, pin hole collimated configuration, with $Q_{min} = 0.0014$ $Å^{-1}$ with variable resolution (5-15% rms) coupled with a variable Q-measurement domain.

Background:

One conclusion of the Berkeley Long Pulsed Spallation Source (LPSS) Workshop [1] was that SANS instrumentation at a neutron scattering facility should have the following characteristics:

- Q_{min} less than 0.001 $Å^{-1}$, Q_{max} up to 0.5 $Å^{-1}$.
- Choice of rms Q-resolution between 2 and 10% $\sigma(Q)/Q$.
- Flux on the sample as high as achievable.
- With backgrounds as low as possible.

The report of the SANS working group in the Oak Ridge Spallation Neutron Source (SNS) report) [2] supported this conclusion, and went further in emphasizing the need to have an instrument with extended Q_{min} capability down to as small as 1 10^{-4} $Å^{-1}$.

Practical considerations dictate that no single SANS instrument can meet all of the requirements needed to achieve these characteristics. Further, limitations imposed by the available beam brilliance at TOF spallation sources limits the feasibility of some of the characteristics, particularly at lower value of Q_{min} and more precise Q-resolution. Consequently operational SANS instruments at TOF spallation sources have relatively modest $\sigma(Q)/Q$ and Q_{min}. LQD, the SANS instrument at the Lujan Center for example was designed with $\sigma(Q)/Q = 10\%$ at $Q = 0.1 Å^{-1}$ and concentrates on the middle Q-range from 0.002 to 0.3 $Å^{-1}$. On higher powered sources radiation shielding issues force the sample areas to be no less than 10 m from the source. In addition, it may be difficult to place complex collimation inside the bulk shield. These concerns drive toward longer instruments.

Planned upgrades and antcipated new spallation source will improve the brilliance from cold moderators. These developments provide opportunity to expand neutron measurement capabilities with new designs beyond the capabilities available at any existing facility by removing some of the intensity limitations. Taking the Lujan Center upgrade as an example, the increased flux, ϕ, will result in part from the increased brilliance due to increases in the proton beam current (1.8 times increase), and by setting the source frequency to 30 Hz (1.5 increase), a value that optimizes the performance of a TOF-SANS instrument. The use of a partially decoupled or fully coupled cold moderator with time structure matched to SANS resolution will provide factors, respectively, of 2.5 and 5 to 6 times the neutron output of standard decoupled, liquid hydrogen moderators. The total gain in ϕ available from the Lujan Center upgrade is therefore a factor of 6 to 16.

We designed a flexible TOF-SANS instrument that will take advantage of the promise of higher neutron fluxes and provide capabilities not available in current SANS instruments. In a high-intensity, mirror focused configuration, the instrument will go to Q_{min} of better than 0.0005 $Å^{-1}$. In a high-resolution configuration pinhole configuration, it will provide variable $\sigma(Q)/Q$ between 2 and 10% over $Q > 0.0146$ $Å^{-1}$. The pinhole configuration will be optimized to somewhat low Q-values than current TOF-SANS instruments. We propose the two interchangeable configuration, which are essentially two instruments on one beam line, as a means of best utilizing available beam lines. The new capabilities provided by the proposed design are complementary, and will not replace those available on present SANS instruments. Current TOF-SANS instruments are designed to work well over the middle Q-range.

The new design pioneers principles for TOF-SANS. These include:

- The use of mirror optics to increase intensity and provide for very low-Q measurements.
- The use of phased choppers to vary bandwidth.
- The use of variable instrument length to tune the Q-domain to the needs of the measurement.
- The use of variable collimation to change the Q-precision of the measurement.
- The use of a coupled cold moderator to increase neutron detector currents

There are a few implementation and several suggested ways of providing extension of the Q_{min} for SANS. Two pinhole cameras have been built at reactors that are capable of $Q \leq 0.001 Å^{-1}$, D-11 at the Institut Laue-Langevin ($Q_{min} \approx 7\ 10^{-4}$ $Å^{-1}$) and the KWA instruments at the Forschungszentrum, Jülich ($Q_{min} \approx 1\ 10^{-3}$ $Å^{-1}$). These instruments require either the use of long neutron wavelengths ($\lambda \approx 20$ Å for KWA) or long source to detector distance (up to 80 m for D-11). Thus, either a very bright source or long counting times are required. The large L and λ values imply a loss in Q-precision due to gravitational droop of the beam. There has been a proposal for a long, 36 m pinhole instrument for an advanced spallation source [3] that uses TOF to correct for gravitational effects. Multiple pinhole collimators are usedto provide a useable current on the detector. Even so the anticipated measurement times are likely to be too long until very sources much more powerful than the 160 kW anticipated for the Lujan upgrade become available.

Lower Q_{min} than measured by pinhole geometry cameras have been accessed at reactors using the double crystal (Bonse-Hart) geometry. Such an instrument could be built on a cold spallation source in the 1 MW range, roughly a factor of 6 more powerful than the upgraded Lujan source. The data from such instruments suffer from smearing effects from the anisotropy of the collimation. The extremely small beam divergence from the collimation and analyzer crystals leads to a tiny fraction of the total beam current reaching on the detector. These factors, plus the difficulty in setting up the double crystal geometry for each measurement has limited their use to only special problems with high scattering cross-sections. Thus, we do not consider such a design to be viable for a general purpose machine.

Mirrors that focus the beam to a small spot on the detector have been proposed as an alternative method for making measurements down to around $Q = 0.0001$ $Å^{-1}$ [4]. Indeed, such a mirror has been shown to work for the small-

angle scattering geometry on the ILL neutron spin echo instrument, IN-14 [5], and a similar design is under construction at Jülich. Scattering can be measured down to a Q smaller than 0.001 $Å^{-1}$ with a factor of 15 greater count rate than that measured for the same Q using a pinhole geometry. The higher count rate is at the expense of relatively high divergence of the beam. Recent improvements in mirror fabrication for synchrotron sources and orbiting x-ray telescopes lead us to conclude that a mirror can be build that will have sufficiently good optical properties to be useable for SANS. This mirror is the basis for the high-intensity, very low Q configuration for our design. We consider the use of a mirror to be the only practical method to reach very low-Q at the neutron currents anticipated from the enhanced Lujan Center cold moderators.

Description of the Instrument:

Overview

The instrument is shown schematically in Fig. 1 and a description of the major components are given in Table I. The instrument will use a coupled liquid H_2 moderator. A fully coupled moderator is preferred due to a larger integrated flux. The factor of 5 to 6 in Φ over decoupled moderators and 2 over a partially decoupled moderator are important to the total performance of the instrument and affects the $\sigma(Q)$ and Q_{min} that can be reached.

A mechanical shutter assembly will be used, similar to that currently operating on the Lujan Center low-Q diffractometer, LQD. This type of shutter has the advantage of 10 second opening and closing times, and allows for the insertion of additional optics elements in the flight path as needed.

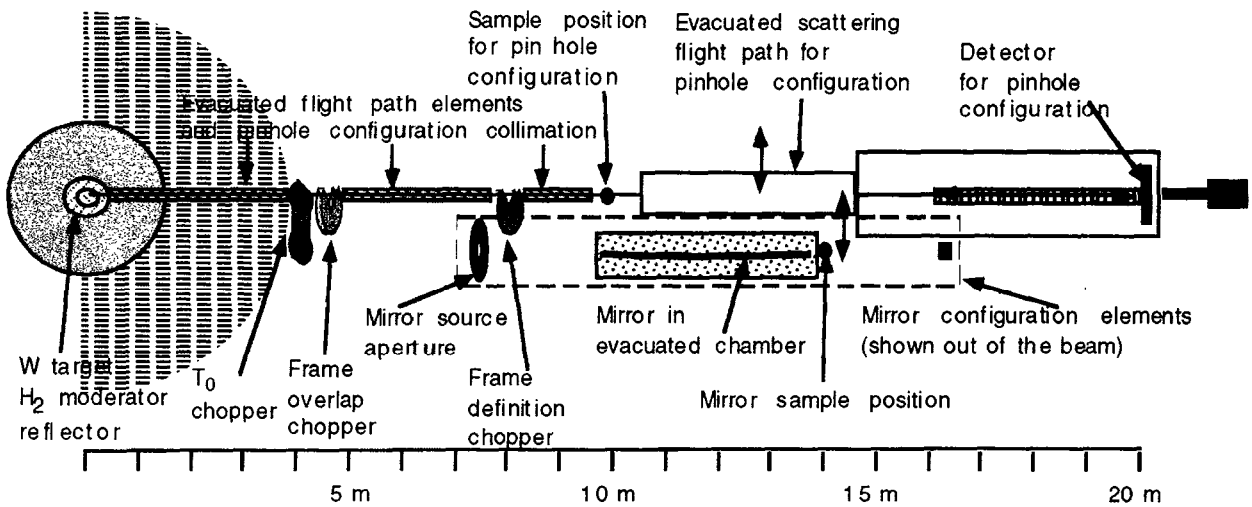

Fig. 1: Schematic layout of the VLQD. Pinhole configuration is shown in place. Mirror collimation elements are enclosed in the box bordered by dashed lines. Double arrows indicate relative motion of elements in changing instrument configurations.

The primary flight path includes three choppers and interchangeable collimation elements. The three-chopper configuration is needed to reduce background and define the neutron TOF frame at the detector. The T_0 chopper is used to remove the high-energy neutron and γ pulse. The frame-overlap (tail) chopper prevents cross talk between frames. The frame-definition chopper serves to limit the bandwidth so that TOF frames do not overlap at the detector, and sets the midrange of the bandwidth. The T_o chopper is positioned at 4.2 m from the source; the frame overlap chopper at 4.8 m; and the frame definition chopper at 8.1 m. The evacuated sections of the primary flight path includes the collimation elements for the high-resolution pinhole configurations and the mirror source aperture. The interchangeable pinhole apertures are located on a wheel positioning mechanism located just inside the bulk shielding. A second, matching aperture is located on the gravity focuser just before the pinhole configuration sample position,. There are several matching pinhole apertures for different sample to detector distances and resolution selections. A satisfactory implementation of multiple aperture collimation to increase intensity while maintaining resolution is highly beneficial and is essential for the high-resolution configurations.

The major pinhole configuration elements after the frame definition chopper, the sample area and moveable scattering tanks, interchange with the corresponding mirror configuration elements. Because of the substantial differences between the pinhole and mirror geometries, the sample areas for each are in different parts of the instrument. In the pinhole configuration the sample area is located 10 m from the source. The sample area is followed by a removable

section of secondary (scattering) flight path tube. This tube is followed by a stationary scattering tube, which contains the main detector. The detector is moved inside the tube to allow for source to detector lengths between 16 m and 20 m. The 20 m configuration will give a Q_{min} of 0.0014 $Å^{-1}$.

The mirror elements (Fig. 2) include a 4 m long elliptical mirror located inside an evacuated tank, followed by a sample area. The detector for the mirror configuration is inside the stationary evacuated scattering tube, and will be mounted so that it can be either pulled out of the way or used as a auxiliary, high-angle detector for a pinhole measurement. These elements are described in Table I. This mirror geometry will give a Q_{min} = 0.000015 $Å^{-1}$, if the mirror optics are perfect.

Table I
Major subsystems

Subsystem	Description	Notes
Moderator	Coupled or partially decoupled liquid Hydrogen	ϕ from coupled & partially decoupled moderator are, respectively 2.5- and 5-6-times, that from decoupled moderator.
Choppers	T_0	Background suppression
	Frame overlap Frame definition	Adjustment of bandwidth to region of interest and sample to detector distance.
Pinhole collimation	Interchangeable converging collimation. Gravity focus.	Different aperture and multi-aperture elements to match resolution requirements and retain cone rule for different sample to detector distances.
Sample area	1 m long, 1 m side to side clearance optical bench.	Designed for easy access and quick interchange and alignment.
Mirror	Ellipsoidal, 9.142 m major axis, and 0.223 m minor axis. Dimensions: 4.000 m x 92 mm	ULE, ^{58}Ni. Surface roughness: 3 Å rms. Maximum slope error: 100 μrad. Background < 10^{-4}.
Secondary Flight Path	One stationary section, one removable section. 9 m total length.	Trace for moving pinhole detector for source to detector distances from 16 to 20 m.
Mirror Detector	^{3}He multi-wire position-sensitive, proportional counters. ≤1.5 mm wire pitch. 256 wires in x and y.	Time stamping required (under development). 10^5 Hz per wire, 10^6 Hz overall.
Pinhole Detector	^{3}He multi-wire position-sensitive, proportional counters. 5 mm wire pitch. Active area 68x68 – 100x100 cm	Time stamping required (under development). 10^5 Hz per wire, 10^6 Hz overall.

Design Considerations

General

The instrument characteristics that determine the Q measurement domain, defined as $Q_{min} \leq Q \leq Q_{max}$ and the rms resolution in Q, $\sigma(Q)$ for a TOF-Low-Q diffractometer derive directly from the definition of the magnitude of the scattering vector,

$$Q = \frac{4\pi}{\lambda}\sin(\theta) \quad , \qquad 1.$$

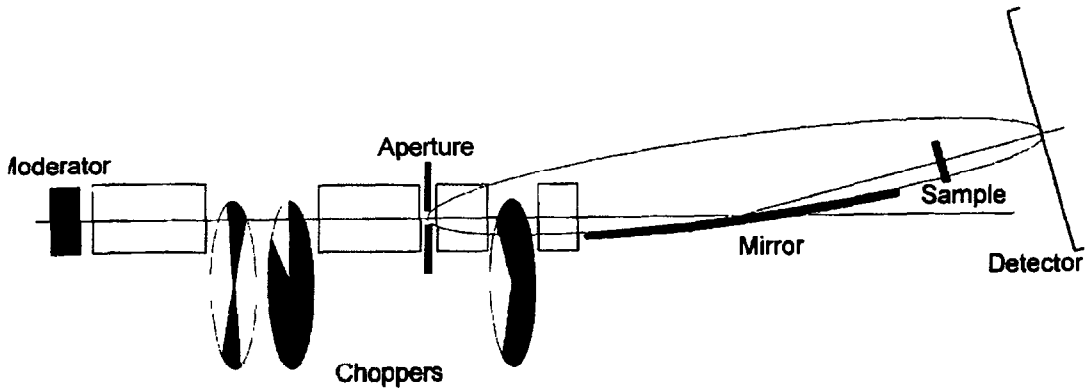

Fig. 2: Elements of the VLQD mirror configuration. The vertical dimensions are exaggerated for clarity.

where 2θ is the scattering angle and λ is the incident neutron wavelength. From Eq. 1 it is easy to see that the geometry of the instrument must be such that the lowest 2θ possible be measured with the longest wavelength possible to obtain the lowest Q_{min}.

The rms resolution in Q is obtained from Eq 1 by the usual methods to give

$$\frac{\sigma(Q)}{Q} = \left[\frac{\sigma(\lambda)^2}{\lambda^2} + \cot^2(\theta)\sigma(\theta)^2\right]^{\frac{1}{2}} \quad . \qquad 2.$$

The variance in the scattering angle is given by,

$$\sigma^2(\theta) = \frac{R_1^2(l + L_2)^2 + R_2^2(L_c + l + L_2)^2}{4L_c^2L_2^2} + \frac{\Delta x_d^2 + \Delta y_d^2}{24L_2^2} + \sigma^2(c) \quad , \qquad 3.$$

where the first term is the contribution from the collimation, in this case pinhole collimation, and the last two terms are due to the detector pixel size and encoding errors, respectively. The dimensions in Eq. 4 are: l, L_c and L_2 are the moderator to collimator distance, the collimator length and sample to detector distance, respectively; R_1 and R_2 are the radii of the collimator entrance and exit apertures. In all equations $\sigma(x)$ refers to the rms error in the measurement of x.

The neutron current in the nth time channel on the detector elements for a pin hole geometry instrument as

$$I_n = K\Lambda(\lambda)\Delta\lambda_n\left[\frac{\pi R_1 R_2}{L_1}\right]^2\frac{\Delta x \Delta y}{L_2^2} \quad . \qquad 4.$$

Eq. 4 is in terms of the source brilliance, $\Lambda(\lambda)$ ($n\ cm^{-2}sterad^{-1}s^{-1}Å^{-1}$), the entrance and exit aperture radii, R_1 and R_2, the distance between the collimation apertures, L_1, and the sample to detector distance, L_2. Here, K is a constant, $\Delta\lambda_n$ is the bandwidth of the nth time channel, and $\Delta x\ \Delta y$ is the area of the detector elements.

The basic design issues that need to be considered are the instrument geometry, the source characteristics and the number, positions and phasing of choppers. The basic rules for optimal instrument geometry have been understood for some time [6]. The issues here are the optimal instrument length, L, which is interrelated with choppers, source characteristics, Q_{min} and $\sigma(Q)$, and the practical limitations to the instrument resolution. We consider the optimal length that optimizes resolution and intensity given by Eqs. 1-4. We also look at the function of choppers, and analyze the rules governing performance on a SANS. The balance between the pulse length and the total integrated flux must be considered as well.

Source Characteristics:

The source characteristics determine the Q-domain accessible to the instrument by giving the range of λ that is available (Eq. 1). Since one objective of the VLQD design is to measure as small a Q as possible, Eq. 1 dictates a cold source. The SANS instrument is affected mostly by two characteristics: the peak brilliance and the peak shape. The source brilliance in Eq. 4 is the output of the moderator integrated over time, t, at which a neutron of a given wavelength, λ, is emitted from the moderator during a single pulse,

$$\Lambda(\lambda) = \int \Lambda(t,\lambda)dt \quad . \qquad 5.$$

Consequently, the pulse height, shape and width affect the source $\Lambda(\lambda)$ as seen by the instrument. Such an integrated effect naturally affects the time-of-flight resolution of the experiment, $\sigma(\lambda)$, as well (Eq. 2). Thus, there is a balance that must be considered in determining the optimal source characteristics.. The peak shape is modeled by a main peak function convoluted with one or two exponential functions describing the tails of the pulse in time [6], the latter of which is characterized by the time constant(s), τ. For pulses emitted from a partially decoupled or full coupled cold moderator we expect $\sigma(t,\lambda) \approx \tau$, where we take the value to be that of the longest exponential tail for a pulse at long wavelengths. The condition for τ being consistent with the Q-resolution found directly from the relationship between measured TOF, T and λ,

$$\lambda = \frac{h\,T}{m\,L} \qquad 6.$$

and Eqs 1 and 2 is,

$$\tau \le \frac{1}{\sqrt{2}\,h/m} L\lambda \frac{\sigma(Q)}{Q} = \frac{1}{h/m} L\lambda \frac{\sigma(\theta)}{\theta'}, \text{ or } \frac{\lambda}{\theta'} \ge \frac{h}{m}\frac{\tau}{L\sigma(\theta)} \qquad 7.$$

Thus, τ limits the usable ratio $\frac{\lambda}{\theta'}$ at a given source to detector distance, L and angular resolution, $\sigma(\theta)$. The latter two quantities are fixed for any given instrument configuration, and θ' is the minimum angle on the detector that data can be used consistent with $\sigma(Q)/Q$. Thus, the source characteristics of total neutron pulse length, given by τ, along with, $\sigma(\theta)$ and L, determine the minimum wavelength and the fraction of the detector that can be used. This condition along with the frame overlap condition gives the total bandwidth as,

$$\max\begin{bmatrix} \frac{h}{m}\frac{\tau\theta'}{L\sigma(\theta)}, \text{resolution condition} \\ \frac{h}{m}\frac{n\Delta T}{L}, \text{frame overlap condition} \end{bmatrix} \le \lambda \le \frac{h}{m}\frac{(n+p)\Delta T}{L}. \qquad 8.$$

Here, n is the frame number after the pulse in which the neutron is counted and p is the number of source frequency intervals of duration, ΔT, between pulses used in the counting frame. Thus, the choice of τ impacts the minimum wavelength that we can use for a given maximum value of $\sigma(\theta)/\theta$, but only if we chose to count in the first frame. These considerations which determine the amount of the moderator output that can be used must be taken into account in order to properly match the instrument with the moderator characteristics.

The $\Lambda(t,\lambda)$ of the decoupled liquid hydrogen Lujan Center moderator is shown in Fig. 3A along with its replacement being implemented as part of the SPSS enhancement project in Fig. 3B. The replacement moderator is partially decoupled from the reflector. Fig. 3C shows the brilliance for the a fully coupled cold moderator also being built as part of the Lujan Center upgrade. It is obvious that the $\Lambda(t,\lambda)$ differ largely by the length of the tails. For the partially decoupled moderator the tails have $\tau \approx 400$ µs at long wavelengths and for the fully coupled moderator $\tau \approx 460$ µs. For reference $\sigma(t,\lambda) \approx 100$ µs for long wavelengths from the decoupled cold moderator. The integrated cold neutron pulse (Eq. 5) for the partially decoupled and coupled moderators, respectively, are predicted to be about 2.5 and 5 to 6 times that of the decoupled cold moderator. Thus, the new moderators will provide enhanced ϕ over their predecessor.

The effect of the pulse tail from a coupled cold moderator with $\tau = 500$ µs is shown if Fig. 4, which is a plot of the bandwidth conditions given in Eqs. 7 and 8 as a function of $\sigma(Q)/Q$ for the L = 16 and 20 m detector positions, assuming a $\lambda_{max} = 10$ Å for the frame. At the 16 m position all $\sigma(Q)/Q < 0.1$ limits the bandwidth, where as $\sigma(Q)/Q < 0.04$ limits the bandwidth for the 20 m position. Thus, for this particular value of λ_{max} one anticipates a loss in detector current for $\sigma(Q)/Q < 0.04$ due to bandwidth losses in addition to losses due to smaller aperture size.

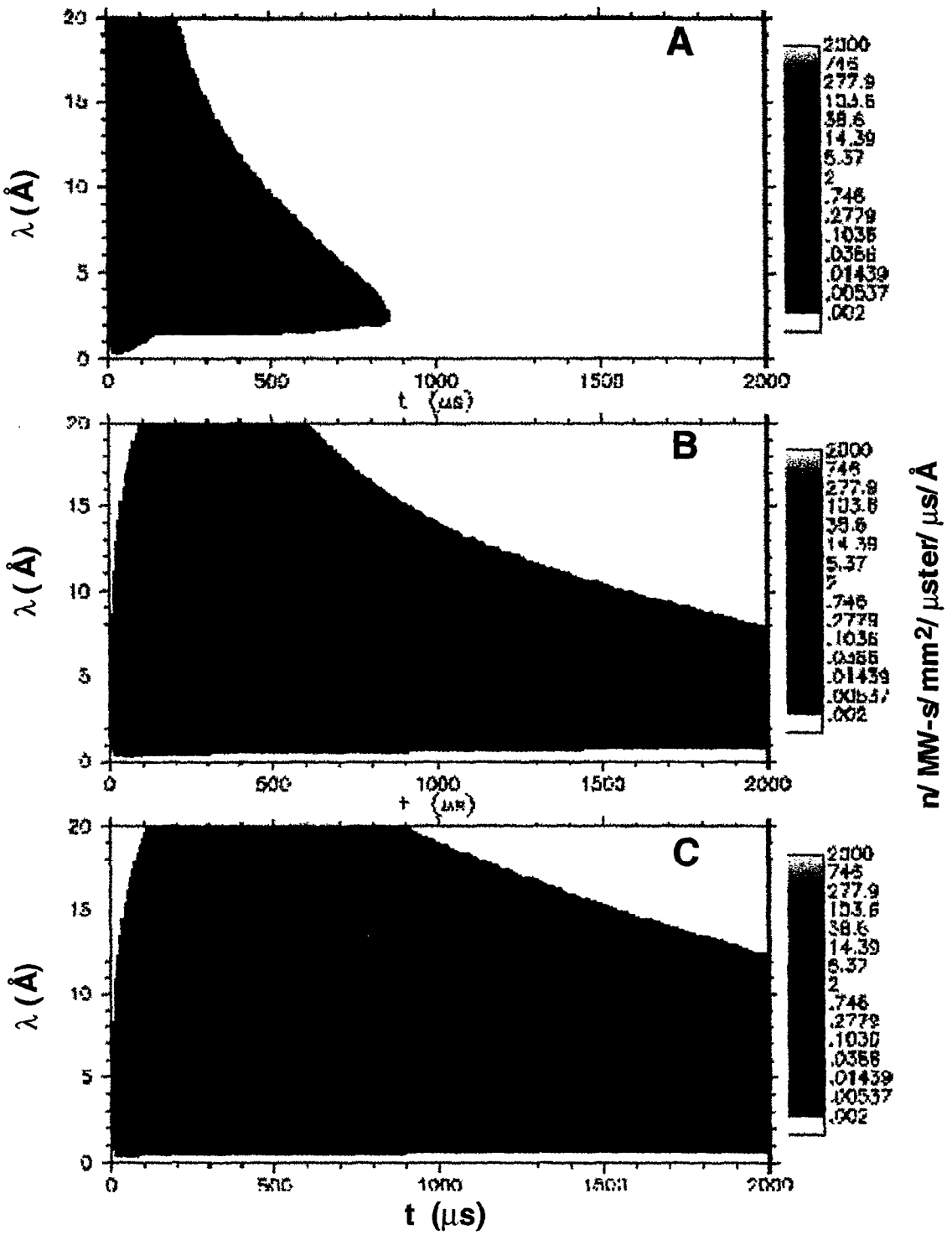

Figure 3. $\Lambda(t,\lambda)$. A: the decoupled liquid hydrogen moderator; B: The predicted performance of the partially coupled liquid hydrogen moderator being installed as part of the Lujan Center upgrade; C: The predicted performance of the coupled liquid hydrogen moderator being installed as part of the Lujan Center upgrade.

Choppers

The choppers sample $\Lambda(t,\lambda)$. The neutron wavelengths that reach the detector are the intersection of the areas defined between each pair of lines given by $\lambda = h/m(t_c-t)/L_c$,and $t - (mL_c/h)\lambda = t_c + \Delta t_c$, where L_c is the distance from

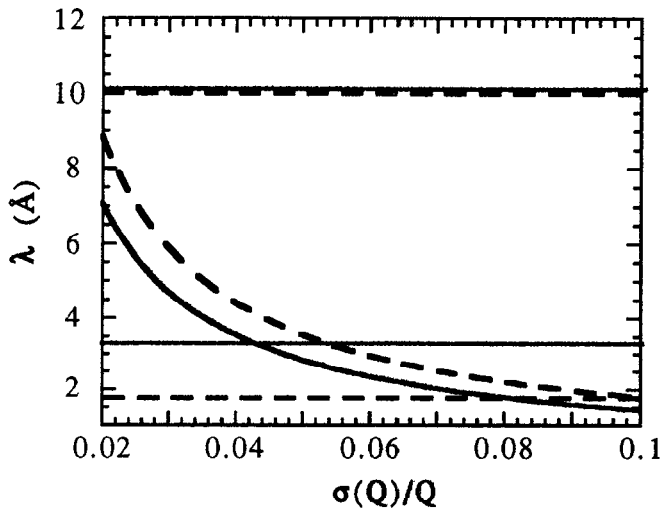

Figure 4. The bandwidth available as a function of resolution. Upper and lower straight lines are the band limitations given by the frame overlap condition of Eq. 8 with λ_{max} = 10 Å. ———, L = 20 m; — — —, L = 16 Å.

the source to the chopper, t is the time that a neutron of wavelength, λ, is emitted from the moderator, and t_c, Δt_c are the time at which the chopper opens and the open duration, respectively.

The T_0 chopper limits the available bandwidth at the detector. From a simple geometric argument, the wavelength bandwidth of neutrons emitted at the same time from the moderator passed by the chopper, Δλ, is related to the time interval over which the chopper is open by $\Delta\lambda = h/m(\Delta t_c / L_c)$. Thus, the best possible position for the T_0 chopper on a broad band instrument such as SANS is close to the source up to the limit that the maximum usable wavelength, $\lambda_{max} = {}^{h}\!/_{m}(n+p)\Delta T / L$, is passed. These considerations give the optimal position as $L_c = (1 - \Delta t_s / \Delta T)L/(n+p)$, where Δt is the source pulse length. Because the T_0 chopper is fixed in position, the upper and lower wavelengths that are likely to be used should be considered carefully and the T_0 chopper position determined accordingly, consistent with minimizing the maintenance and engineering difficulties of running a chopper in a high radiation environment. For a general-purpose instrument, Δλ is set by the lowest Q required and the dynamic range, and we take the former to be more important. We set Q_{min} to 0.0014 $Å^{-1}$ for 20 m pinhole collimation, and this requirement relates λ_{max} and L, through Eq. 1 in the subsequent optimization. The T_0 chopper position should be less than 5 m for a 30 Hz source, given the optimal instrument length determined below. Accessibility and cost issues constrain the position to just outside the bulk shield.

The frame definition and frame overlap chopper positions also affect Δ(λ). The range of wavelengths that is passed by the chopper is constant for the entire pulse width starting at $\lambda_{min} = {}^{h}\!/_{m}\left({}^{t_c}\!/_{L_c}\right)$, and has a bandwidth

$$\Delta\lambda = \frac{h}{m}\frac{(\Delta t_c - \Delta t_s)}{L_c}, \qquad 9.$$

provided that $\Delta t_s < \Delta t_c$, which is a requirement for the existence of this region. This bandwidth defines the "umbra". There are two "penumbra" regions where the wavelengths sampled change linearly with TOF. The bandwidth of each penumbra region is $\Delta\lambda' = {}^{h}\!/_{m}\left({}^{\Delta t_s}\!/_{L_c}\right)$. This expression combined with the requirement that the full Δλ fit within ΔT gives the relation,

$$\Delta T = \frac{L}{L_c}(\Delta t_c + \Delta t_s) - \Delta t_s. \qquad 10.$$

Eq. 9 shows that the bandwidth of the "umbra" scales with Δt_c, and Eqs. 9 and 10 taken together show that by moving the chopper away from the source as far as possible, Δt_c can be made as large as practical, thus increasing the fraction of the "umbra" in the TOF frame, as

$$\frac{\Delta t_u}{\Delta T} = \frac{L(\Delta t_c - \Delta t_s) + L_c \Delta t_s}{L(\Delta t_c + \Delta t_s) - L_c \Delta t_s}, \qquad 11.$$

where Δt_u is the duration of TOF for the "umbra". The chopper positions, however, cannot be too close to the sample in order that the chopper be adequately shielded.

We used NISP [8] to calculate the integral for the part of Λ(t,λ) passed by the chopper system, taking into account the complete characteristics of Λ(t,λ) computed for a coupled cold moderator and anticipated error in chopper phasing and jitter. From this calculation we find [7] that the "penumbra effect" has a significant effect on both λ_{min} and

on the detector count rate when the choppers are too close to the source. We also use these calculations to determine the optimal disk chopper positions to be between 4.2 and 5.6 m from the source for the overlap chopper and greater than 7 m for the frame definition chopper for a 30 Hz pulse. The positions of the T_0 chopper and the pinhole collimation elements set these distances at 5.3 and 8.1 m for the frame over lap and frame definition choppers, respectively.

Optimization of the Pinhole Configuration

To calculate the optimal instrument configuration we maximize a figure of merit (FOM),

$$FOM = \frac{I(Q)}{\sigma^2(Q)} \ln\left(\frac{Q_{min}}{Q_{max}}\right) \quad . \qquad 12.$$

The natural logarithm of the ratio of the maximum and minimum Q-values is proportional to the number of resolution elements in the reduced data, as $\sigma(Q)/Q$ is constant. Thus, this particular FOM corresponds with that derived from Shannon information theory [10].

Optimization was done by NISP simulation of a δ-scatterer, which scatters only at one Q value, and finding the instrument configuration with the maximum I(Q) at a given $\sigma(Q)$ and Q_{min}. Here, $\sigma(Q)/Q$ was set equal to 0.1, and Q_{min} was set at 0.0014 $Å^{-1}$ for the 20 m configuration. The optimal sample position is at one half the source to detector distance, in agreement with the cone rule. The collimator entrance aperture radius, R_1, should be twice the radius of the exit aperture, R_2. Deviations from the optimal relationship between moderator to sample length, L_1 and sample to detector length, L_2, that $L_1 = L_2$, requires that the relation between the aperture radii be given by,

$$R_2 = R_1 \frac{L_1}{L_1 + L_2} \quad . \qquad 13.$$

We found that the optimal instrument length is different in the two cases studied, Q = 0.01 and Q = 0.07 $Å^{-1}$. The instrument length was 16 m for optimization at Q = 0.07 $Å^{-1}$ and 18 m for optimization at Q = 0.01 $Å^{-1}$.

We can see why this is so from the R-T map (detector radius versus TOF) in Fig.5. This simulation was for a Long Pulsed Spallation Source, LPSS, but serves to illustrate our point. The scattering at large Q runs off the detector if the instrument is too long for the region of interest. If the sample to detector distance is too short, then the required $\sigma(Q)$ cannot be achieved using the entire detector. This is because TOF channels differ in data quality at a given Q largely because the signal is taken from a different part of the detector [11]. Therefore, optimization of a SANS instrument using TOF is a balance of detector geometry needed to access a particular range of Q values and the $\sigma(Q)$ needed for a particular measurement.

Because there are different optimal instrument lengths depending on the region of interest in Q, we conclude that TOF instrument built on a 30 Hz source should have a variable L, rather than a fixed length prevalent in first generation TOF instruments. This implies that the frame definition and frame overlap choppers be phased relative to the source to adjust the bandwidth of the instrument to match the length. According to Eq. 13, this also implies that different collimation aperture sizes be used, to preserve the cone rule for focusing the beam onto the detector.

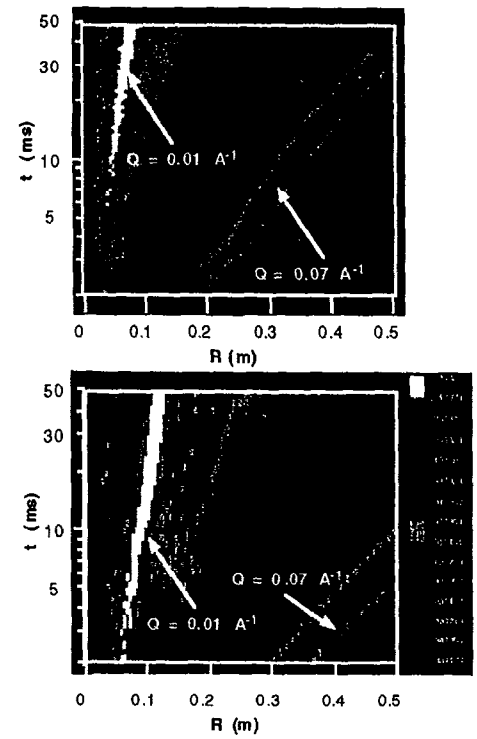

Fig. 5: R-T plots of δ-scatterers. Vertical scale is TOF and horizontal is detector radius. Lines of intensity are at Q = 0.01 $Å^{-1}$ and 0.07 $Å^{-1}$, as labeled. Upper panel is the simulation for a 16 m SANS on a 60 Hz, 1 ms LPSS. The lower panel is for an 18 m instrument.

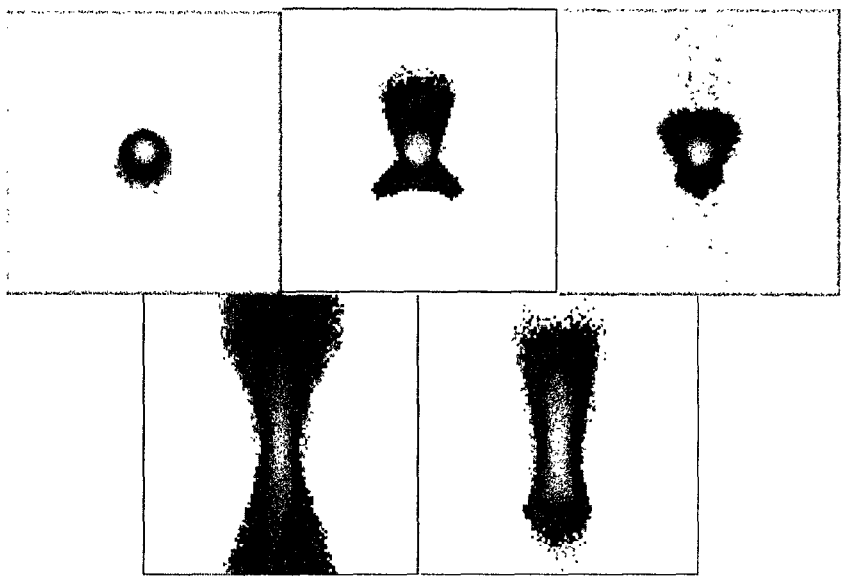

Fig. 6: Beam spot profiles. Upper: Ellipsoid, Toroid, 8 Toroids. Lower: 8 Cylinders, 20 Cylinders. Figures are approximately twice actual size. The intensity scale is logarithmic.

Mirrors

Fig. 6 illustrates that an ellipse is the best option for a mirror. An ellipsoid approximated by a series of toroids, used IN-14, is the next best approximation.

We discuss the specifics of the mirror geometry where L = 17.5 m. We assume a detector with a 1.5-mm square pixel size, and that we require the width of a Q-bin to be 0.0003 $Å^{-1}$ at λ = 15 Å. Then from Eq. 2 and $\Delta x = \Delta y$ = (1.5 mm)/L_2, the required sample-to-detector distance L_2 is 2.1 m or greater. We choose L_2 = 2.25 m, and next assume a 40x40 mm^2 sample, so the desired beam convergence angle at the detector is ±(20 mm)/(2.25 m) = ±0.009 in both the x- and y-planes. To view the entire 130x130 mm^2 moderator with this convergence, the resolution-defining aperture must be placed 7.3 m from the moderator surface. This aperture will be at one focus of the ellipsoidal mirror, with the detector placed at the other focus. The distance from the aperture or detector (i.e., a focal point) to the mirror center is the semi-major axis of the ellipsoid, which is thus 5.10 m to obtain a total instrument length of 17.5 m. The width of the mirror at its center must be 92 mm for full illumination.

Next consider the mirror bend angle. Suppose the mirror surface is ^{58}Ni, with a scattering-length density of 13.15×10^{10} cm^{-2}. The critical angle for 5-Å neutrons is 0.6°, so the angle of the mirror should be small. On the other hand, it is important that the angle be large enough that no direct rays from the aperture may strike the sample. This requires a total bend angle greater than 1.8°. Yet another consideration is that the total length of the mirror which must be illuminated becomes longer as the angle is shallower. If we take 4 m as a practical limit of the mirror length, then the mirror inclination is 0.8°. We thus use a bend angle of 1.8°. The critical wavelength is about 8 Å. The ellipsoid semi-minor axis is sin(0.9°)(5.1 m) = 0.0801 m. Smaller sample sizes are possible by using a sample-defining aperture at the sample position, or by moving the sample closer to the detector. By using the former method the sample can in principle be made arbitrarily small, but the current at the detector will decrease as the area of the sample. The latter method allows the sample size to scale with the distance to the detector with little loss in neutron current on the detector, but with a resultant degradation in $\sigma(\theta)$ and Q_{min}. The mirror parameters and specifications are given in Table I.

Because of the low surface microroughness, all of the manufacturers favor ULE due to its low porosity, although 3 Å microroughness has been accomplished for the 4 m long zerodur toroidal mirror coated with Cu in IN15. The mirror has to be made in several sections that will be connected together and aligned to form a full mirror. The alignment of the mirror is easily possible based on the experience on the IN15 instrument at ILL where 8 small mirrors were aligned to make a 4 m long toroidal mirror.

One manufacturer proposed to make the mirror in three ULE sections (Corning): one 1400-mm-long central section and two 1350-mm-long identical end sections. The middle section is a toroid and the two end sections are portions

of a true ellipsoid. Simulations using NISP showed that the rms of the beam spot formed by 1400 mm long mirror increases from 0.7 mm to 0.9 mm when the ellipsoid is replaced by a toroid. (Fig. 7). This degradation of the source image was comparable to the effect of the distortions simulated below, and thus should be satisfactory. Another manufacturer proposed a mirror four ULE 1 m ellipsoid segments with 20 arcsec slope error from the desired shape. The costs for this option were considerably higher than for a central toroid segment.

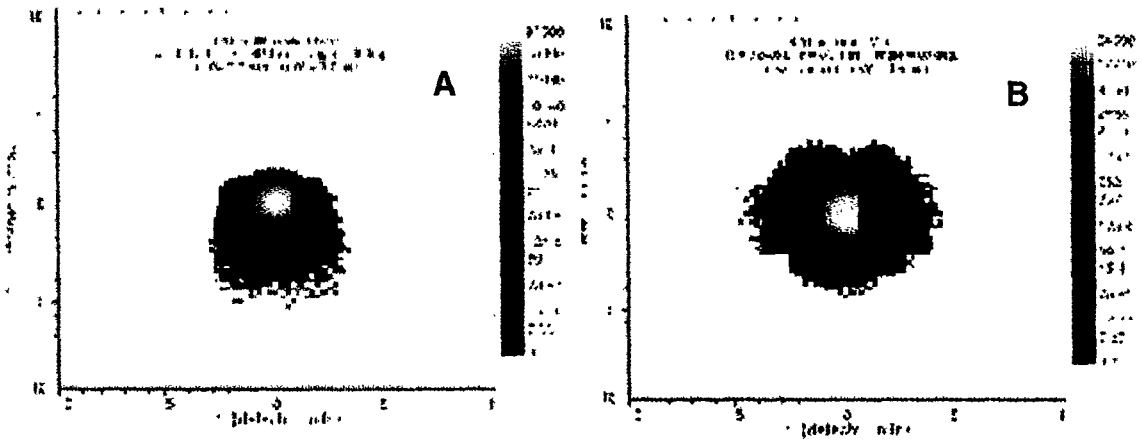

Fig. 7: Effect of approximating the central part of the ellipsoid with a toroid: A: perfect ellipsoid; B: Central segment approximated by a toroid.

Instrument Performance

Pinhole Configuration

We compare the pinhole geometry configuration with a continuous wave (CW) instrument. Each instrument is optimized for its particular type of source, using the methods described above, with s(Q)/Q equal to 10% at Q = 0.01 $Å^{-1}$. The CW source is the liquid hydrogen cold source CS-1 at the ILL. For the pulsed source we rescale the simulations from the LANSCE II study [12] and our recent work [7] on a 1 MW LPSS to the brilliance anticipated for the new cold moderators at the Lujan Center. The CW source in calculated for a nominal 60 MW reactor, which is the power of the ILL HFR. The CW instrument uses a "monochromatic" incident neutron beam, which has a triangular probability distribution for λ with a 12% FWHM (4.9% $\sigma(\lambda)/\lambda$) spread. Single pinhole collimation is assumed for each instrument.

First, we look at the intensity and resolution of the instrument for a δ-scatterer at Q = 0.01 $Å^{-1}$ (Table II). Here we have used the result of simulations for VLQD in an 18-m configuration.

Table II
Scattering at Q = 0.01 $Å^{-1}$ for Optimized Configurations of VLQD and CW

Source [1]	I(Q) (s^{-1}) [2]	σ(Q) ($Å^{-1}$) [3]	Q range ($Å^{-1}$) [4]
VLQD (λ_{max} = 10.7 Å; 18 m)	0.26 x 10^5	0.001	0.002 - 0.10
VLQD (λ_{max} = 10.7 Å; 20 m)	0.13 x 10^4	0.0005	0.0018-0.09
VLQD (λ_{max} = 10.7 Å; 20 m)	0.4 x 10^3	0.00025	0.0018-0.09
D11 @ ILL (10 Å, 21 m) CONSTANZE Velocity Selector	1.1 x 10^5	0.001	0.002 - 0.03

[1] Numbers in parentheses for VLQD refer to the source to sample distance. The numbers for D11 refer to the mean wavelength and source to detector distance.
[2] The intensity values are for 160 kW for the VLQD and 60 MW for D11.
[3] The rms of Q at Q = 0.01 $Å^{-1}$.
[4] The Q range accessed in a single instrument configuration, as noted.

In Table II we also show the count rates expected for the VLQD at the longest camera setting of 20 m with 5 and 2.5% resolution determined by rescaling the Monte Carlo result using Eqs. 4 and 8. The rate at 5% resolution is only 1/20-times that of the 10% case at a shorter camera distance. This will only be practical using a multi-aperture collimator. 2.5% resolution appears impractical on this instrument.

We can extend the calculation to δ-scatterers for other Q values for the optimized instruments and for other instrument configurations, taking into account the variable detector position in our design, to calculate the response of each instrument as a function of Q. The 18-m configuration has resolution comparable to D11 with a 21m configuration (Fig. 8). The count rates for the proposed instrument and D11 are shown in Fig. 9. The VLQD 18-m configuration on the upgraded Lujan Center source has an anticipated count rate about quarter that for D11.

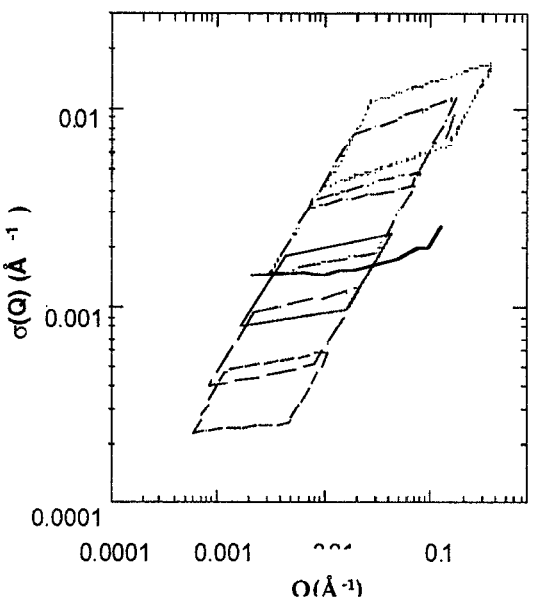

Fig. 8: Resolution of VLQD and a CW instrument. Closed light boxes are for D11 at different instrument configurations with the shortest (3.6 m), to the longest (76 m), total length from top to bottom. The solid line is for VLQD at 18 m.

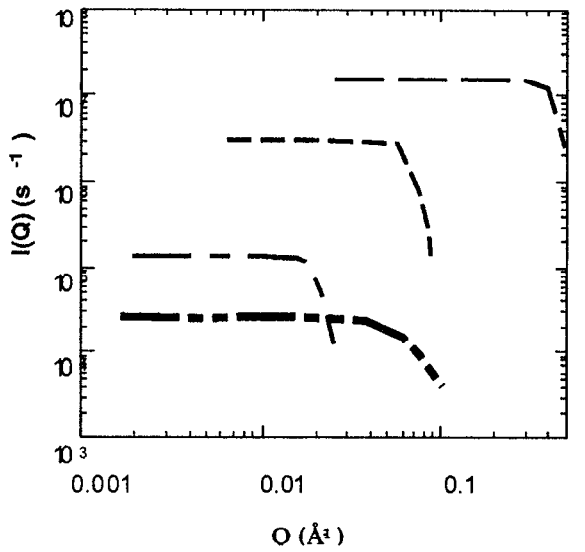

Fig. 9: Count rates of VLQD and a CW instrument. D11: __ __ __, 3.6 m λ= 4.5 Å; _ _ _ _,11 m λ=5.5 Å; __ _ _ _ _, 21 m λ= 10 Å. VLQD 18 m: __ _ _ _ _.

The response functions shown in Figs. 8 and 9 and in Table II do not give the entire picture. Comparisons between instruments on different sources depend on the measurement. To illustrate this we looked at scattering from a spherical particle to simulate an actual measurement, asking the question: How much time is required to do a measurement over a given Q domain for a 'hard sphere' scatterer with R = 150 Å? The results are shown in Table III. The scattering measurements on the proposed instrument with pinhole collimation require one configuration. The CW case, two or more camera settings would be required to cover the full Q range. It is difficult to match the σ(Q) of the pulsed source (see Fig. 9) with the corresponding CW camera settings. The lowest camera number of camera settings for the CW case is tabulated in Table III and VLQD at the upgraded Lujan source requires ~ 3 time longer measurement time relative to D11. Multiple apertures would make the comparison more favorable by increasing the

Table III

Hard Sphere Scattering (R = 150 Å) for VLQD and CW

Source	Q-Range (Å^{-1})	Time (s)	R (Å)	Rg (Å)
VLQD (λ_{max} = 10.7 Å; 18 m)	0.002 - 0.11	19	149.9 ± 0.9	115.8 ± 0.8
D11@ILL (10 Å, 21m) CONSTANZE velocity selector	0.002 - 0.029	6.8	141.3 ± 2.5	116.0 ± 0.6

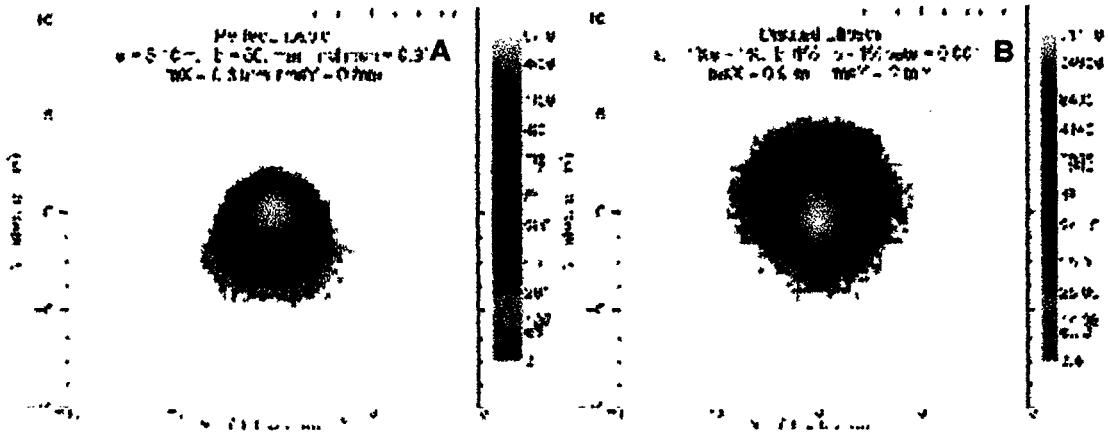

Fig. 10: Some pictures of beam spots for various distortions. The central circle is 2-mm diameter, equal to the entrance aperture. If the detector pixel is 2-mm square, it will convolute an additional 0.6 mm with $\sigma(x)$ and with $\sigma(y)$. These amounts of distortion do not seriously affect the overall resolution of the instrument. A: Perfect ellipse; B: ellipsoid distorted by 1% and with waviness.

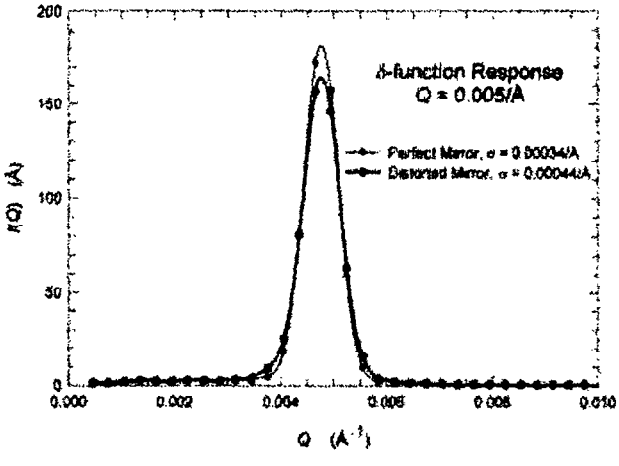

Fig. 11: Radial averaged spot profile from a perfect and disported ellipsoid

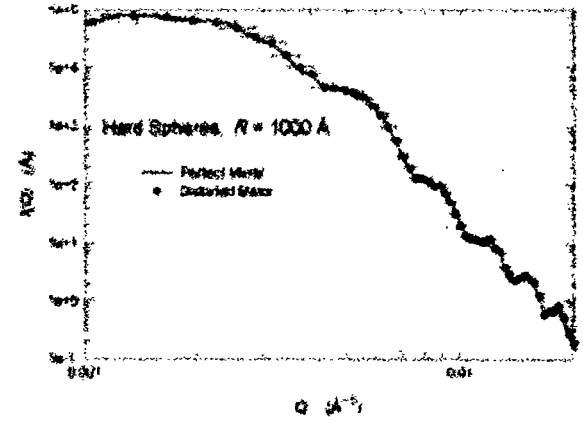

Fig. 12: Hard sphere scattering using a perfect and distorted ellipsoidal mirror

total current on the detector by roughly the number of aperture holes.

Mirror geometry:

Limits on the figure error (major and minor axes) have been studied using NISP. Such errors, if uniform, result in a change of the mirror focal length and inclination angle and can be corrected shifting the alignment. Three "scatterers" were simulated: no sample, to observe the beam spot shape and statistics (Fig. 10); a d-scatterer at Q = 0.005 $Å^{-1}$ to calculate resolution (Fig. 11); and hard spheres of radius 1000 Å, to illustrate data quality (Fig. 12). For the latter two systems, the detector was recorded in 1.5-mm square pixels with no encoding error. Each case was run with a "Perfect" ellipsoidal mirror and also with a "Distorted" mirror. The distortion was accomplished by dividing the mirror into quarters, with the major axis increased by 1% in the first section and decreased by 1% in the second, the minor axis increased by 1% in the third and decreased by 1% in the fourth. A surface waviness with a maximum angular deviation of 100 μrad (rms 58 μrad) was applied to the entire mirror. While this distortion leads to a considerably worse beam-spot profile (Fig. 10), and has an effect of 30% on the low-Q resolution (Fig. 11), there is little degradation of data taken over a wide Q-range (Fig. 12). From these results we conclude that given likely imperfections in the mirror optics that Q_{min} would be at least 0.0005 $Å^{-1}$. Thus, the main issue for the implementation of this optics is obtaining peak to background of better than 10^{-4}. Meeting this goal will have to be the objective of further research and development. We note that the intensity for the hard sphere scatter is about 10 to 15 times that of the pinhole configuration at the same Q. Such current on the detector would bring the intensity performance into the range offered by D-22 at comparable resolutions (a factor of 4 to 5 greater than the D-11 simula-

tions shown in Fig. 9). This would make the VLQD mirror an interesting development, even if accessing the lowest values of Q proved impractical.

References:

1. Proceedings of the Workshop on Neutron Instrumentation for a Long-Pulse Spallation Source, E. O. Lawrence Berkeley National Laboratory Report No. LBL-37880, Berkeley, California, April 18 - 21, 1995, pp II-23 - II-28.

2. Magid, L., Bates, F., Crawford, R.K., Glinka, C., Olah, G., Penfold, J., Thiyagarajan, P., Timmins, P., and Wignall, G., "Report of the Small-angle Scattering Working Group", *Instrumentation fo a High-Power Pulsed Spallation Neutron Source, Proceedings of the Workshop on Instrumentation Needs and Performance Metrics for the National Spallation Neutron Source*, pp 35-44, Oak Ridge National Laboratory, Oak Ridge, TN (1997).

3. Seeger, P.A. and Hjelm, R.P., "Design and Implementation of Low-Q Diffractometers at Spallation Sources", *Transactions of the American Crystallographic Association*, (1993).
Seeger, P.A. and Hjelm, R.P., "A Very-Low-Q Diffractometer for an Advanced Spallation Source", *Proceedings of the 12th Meeting of the International Collaboration on Advanced Neutron Sources*, May 22-26, 1993, Rutherford, Oxford, UK, I-172-184 (1993).

4. Maier-Leibnitz, H. and Springer, T., "The use of neutron optical devices on beam-hole experiments," *Reactor Science and Technology* (*J. Nucl. Energy A/B* **17**) 217-225 (1963).

5. Copley, J. R. D., "Simulations of neutron focusing with curved mirrors," *Rev. Sci. Instrum.* **67**, 188-194 (1996).
Hayes, C., Alefeld, B., Copley, J.R.D., Lartigue, C., and Mezei, F., "On the use if a Toroidal Mirror to Focus at the ILL Neutron Spin Echo Spectrometer, IN15", *Proceeding of a Workshop on Methods for Neutron Scattering Instrumentation Design*, R.P. Hjelm, ed., E.O. Lawrence Berkeley National Laboratory, Berkeley, California (CONF-9609353), pp 102-111 (1997).

6. I. Ikeda and J. Carpenter, Wide-Energy-Range, High-Resolution Measurements of Neutron Pulse Shapes of Polyethlene Moderators, Nucl. Instr. Meth. **A239**, 536-544, 1985.

7. Olah, G.A. and Hjelm, R.P. "Analysis and Simulations of a Small-angle Neutron Scattering Instrument on a 1 MW Long Pulsed Spallation Source", *J. Neutron Res.*, **6**, 79-93 (1997)

8. Seeger, P. A., "The MCLIB Library: Monte Carlo simulation of neutron scattering instruments," 13th Meeting of the International Collaboration on Advanced Neutron Sources, October 11–14, 1995, Paul Scherrer Institut, Villigen, Switzerland, *PSI Proceedings* **95-02**, pp. 194–212.
Seeger, P.A., "The MCLIB Library: New Features", ", *Proceeding of a Workshop on Methods for Neutron Scattering Instrumentation Design*, R.P. Hjelm, ed., E.O. Lawrence Berkeley Naitonal Laboratory, Berkeley, California (CONF-9609353), pp 62-77 (1997).

9. W. Schmatz, T. Springer, J. Schelten, and K. Ibel, Neutron Small-Angle Scattering: Experimental Techniques and Applications , J. Appl. Cryst. 7, 96-116, 1974.

10. M. W. Johnson, The Information Bandwidth of Neutron Scattering Instruments, The Council for the Central Laboratory of the Research Councils, Rutherford Appleton Laboratory, Chilton, UK, Technical Report No. RAL-TR-95-011, 1995.

11. R.P. Hjelm, "Resolution of Time-of-Flight Low-Q diffractometers: Instrumental, Data Acquisition and Reduction Factors", *J. Appl. Crystal.*, **21**, 618-628 (1988).
P. A. Seeger and R. P. Hjelm, "Small-Angle Neutron Scattering at Pulsed Spallation Sources", *J. Appl. Crystal.*, **24**, 467-478 (1991).

12. Hjelm, R.P. Fitzsimmons, M., Schoenborn, B., Roberts, J., Seeger. P.A., Von Dreele, R., Larson, A., Smith, G.,Sommer, W., Borden., M., Lysaught, P., Nelson, R., Eckert, J., Robinson, R., "Neutron Scattering Instrumentation for a High Powered Spallation Source", *Los Alamos National Laboratory Report, LA-UR 97*-1272 pp 1-178 (1997). (http://www.lansce.lanl.gov/Laur_97-1272.pdf)

ICANS-XIV
14th Meeting of the International Collaboration on
Advanced Neutron Sources
June 14-19, 1998
Starved Rock Lodge, Utica, Illinois, USA

Optimisation of PRISMA at ISIS for cold neutron single crystal spectroscopy

Martyn Bull[1,2], Mark Harris[2], Mark Hagen[3], Uschi Steigenberger[2], Caterina Petrillo[4], Francesco Sacchetti[4] and Keith McEwen[1]

[1]Department of Physics & Astronomy, University College London, Gower Street, London WC1E 6BT, UK
[2]ISIS Facility, CLRC Rutherford Appleton Laboratory, Chilton, Didcot OX11 0QX, UK
[3]Department of Physics, Keele University, Keele ST5 5BG, UK
[4]Dipartimento di Fisica, Universitá di Perugia, Via A. Pascogli, I-06100, Perugia, Italy

ABSTRACT

The PRISMA spectrometer at ISIS is being developed into an instrument optimised for cold neutron single crystal spectroscopy. The conversion of the beamline to accept interchangeable detector modules is complete and the current layout of the instrument and detector systems is described. The second phase of the development will be the installation of a supermirror neutron guide that will increase the cold neutron flux by factors of up to 20, with a corresponding impact on the scope of the scientific programme. The implications for the final guide design of several example beamline configurations evaluated by Monte Carlo calculations are discussed.

1. Introduction

The PRISMA indirect geometry crystal analyser spectrometer at ISIS has been operational for 10 years, and has proved to be particularly successful for overview experiments in single crystals in the thermal neutron energy range 20 - 80 meV and also for diffuse and critical scattering studies. Over the past 4 years, PRISMA has been converted into a modular instrument with a suite of three interchangeable detector modules allowing significantly greater experimental flexibility: (i) the original single-analyser system, (ii) a new high resolution double-analyser system, and (iii) a high resolution diffraction detector. The double-analyser system has been highly successful at obtaining high energy and wavevector resolution for analysing energies between 2 meV and 14 meV and is the first stage in the optimisation of PRISMA for cold neutron experiments. The beamline is to be further developed through the installation of a supermirror neutron guide leading to incident flux increases of factors between 10 and 15 for neutrons between 1 meV and 10 meV that will consequently allow new scientific areas to be opened up and will make PRISMA competitive with the best cold source triple axis spectrometers at reactor sources (which are already heavily oversubscribed). This work is being carried out within an R&D network for Cold Neutron Optimisation supported by the EU TMR-RTD programme. The development ties in strongly with the recommendations for R&D projects identified by the ESS technical feasibility study, particularly in the improvement of neutron optics and focussing devices, and the exploitation of cold neutrons at spallation sources for single crystal spectroscopy [1].

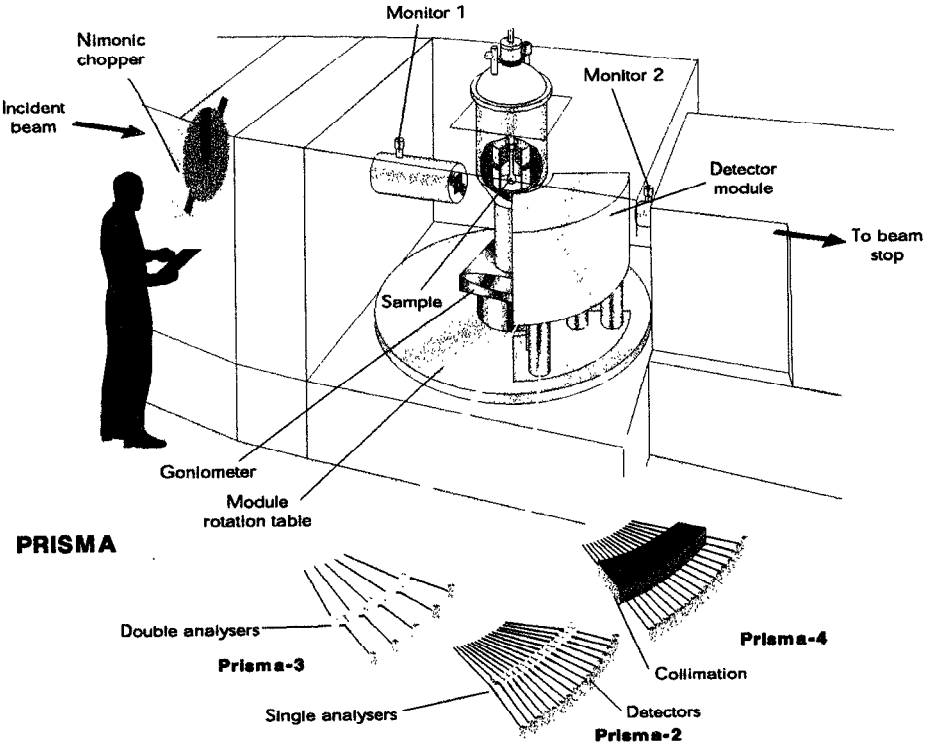

Figure 1 Schematic drawing of the PRISMA sample area

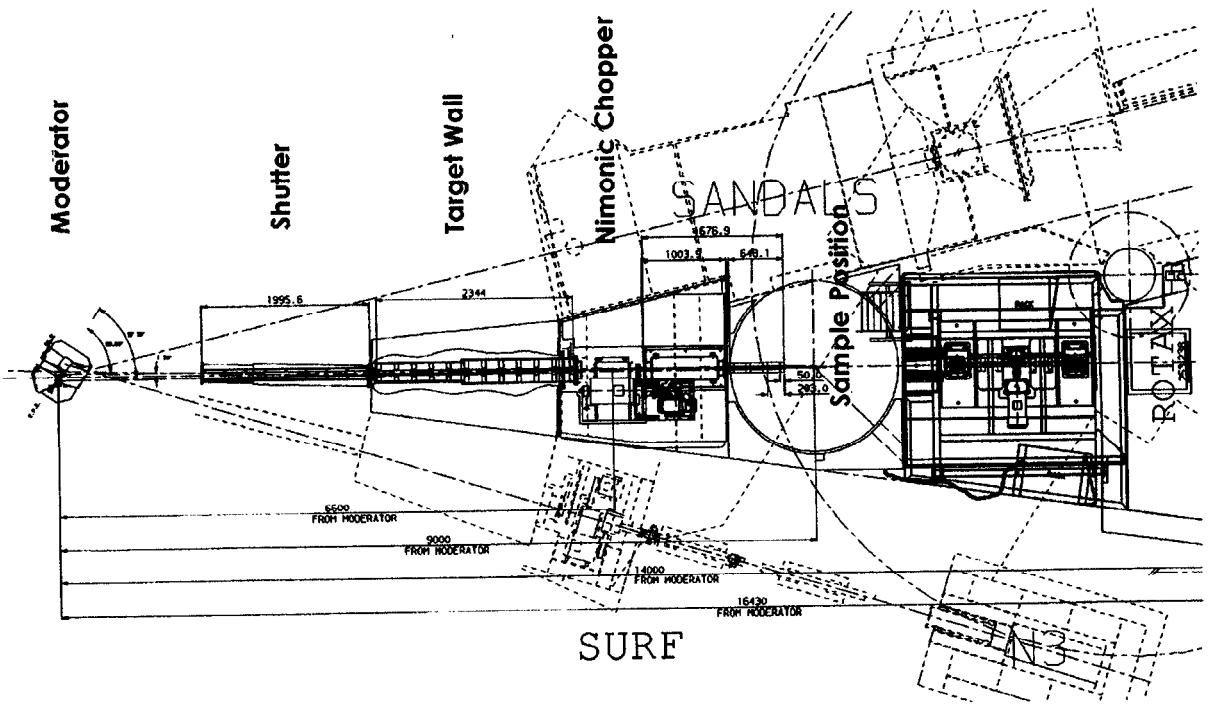

Figure 2 Engineering layout of the PRISMA beamline

2. Conversion to a modular instrument

PRISMA was originally designed to operate with final energies in the thermal energy range 20-50 meV [2] with an array of 16 analyser-detector arms separated by 2° in ϕ providing a close spacing of the TOF detector trajectories in reciprocal space. Whilst many successful experiments were performed with this arrangement, the continued and increasing interest in low energy excitations

required considerably lower final energies in the cold neutron range 1-12 meV to obtain good resolution. However, to obtain $E_f < 12$ meV with the (002) reflections of a pyrolytic graphite (PG) analyser, the detector must be positioned at a scattering angle $2\theta_A > 50°$, an unattainable situation with the single-analyser detector system since adjacent detector arms collide. To overcome this mechanical constraint, a new high resolution low-E_f detector system has been constructed, requiring the parallel conversion of the original spectrometer into a modular instrument by rebuilding the beamline shielding around the sample area.

A schematic drawing of the PRISMA sample area is shown in Figure 1. A goniometer allows sample environment equipment to be oriented in the beam, and detector systems enclosed in individual shielding modules are mounted on a rotating table centred on the sample position. Removable roof shielding allows detector modules to be interchanged on a time scale of around 8 hours. The arrangement of the remaining beamline components are shown in the engineering layout of Figure 2. PRISMA views a 100 K methane moderator at 90° with the sample position located at a distance of 9.035 m. A 2 m thick steel shutter is located immediately outside the ISIS target vessel (1.714 m from the moderator) followed by 2 m of target wall shielding and a 50 Hz nimonic background chopper to block the epithermal flux from the moderator with a cadmium tail cutter to reduce the background

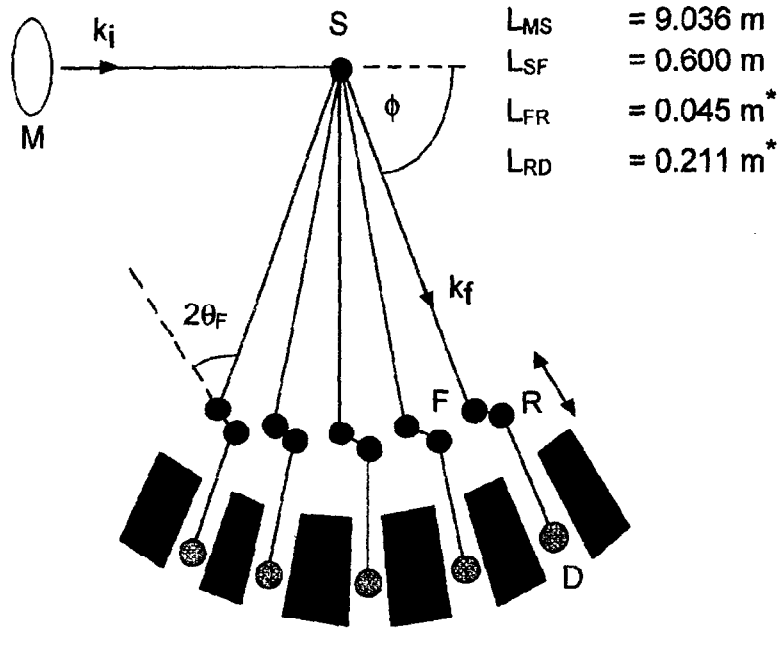

Figure 3 Schematic view of the double-analyser detector system. Starred lengths are defined when L_{FR} is at 90° to L_{SF}.

from neutrons arriving after 12 ms in each 20 ms ISIS frame. The incident beam collimation is castellated with sintered B_4C edges surrounded by iron shot, B_4C and resin giving a horizontal divergence of 30' and a vertical divergence of 60' with a beam exit cross-section of 3 x 5 cm (width x height) at the sample position. Note that immediately behind PRISMA is the shutter of the ROTAX powder diffractometer and that the SURF reflectometer and SANDALS diffractometer are located on either side.

The high resolution, low-E_f detector module, Figure 3, contains five double-analyser detector arms each consisting of Soller collimation, two PG analyser crystals and a Reuter-Stokes 10 atm 1/2" ^{3}He

gas detector [3,4]. The analyser arms are separated by 10° in ϕ, but a sequence of interleaving data sets can be collected for finer reciprocal space coverage. E_f is set by aligning both analysers to the appropriate Bragg angle with respect to the scattered beam direction, whilst the rear analyser is additionally mounted on a translation unit permitting movement towards or away from the fixed detector to maximise the signal. This arrangement gives an energy resolution $\Delta E_f / E_f \approx 4\%$ with final collimation 60'-open for $E_f < 12$ meV. With such low final energies, the overlap of the signal from λ and $\lambda/2$ reflections becomes significant and sets of PG or beryllium filters are available if required. Since there is no direct path from the sample to the detectors, an additional alignment detector consisting of five squashed ^{3}He tubes has also been constructed in a fixed 90° position. This reduces the time required for sample alignment and allows measurements of lattice parameters and d-spacings to be easily made during experiments.

In addition to the two inelastic detector modules, a third high resolution diffraction module is also available, optimised for diffuse scattering and critical scattering studies with 10' collimation [5]. Because of the small size of this module, it can be installed simultaneously with the double-analyser system, allowing inelastic and elastic data to be collected in the same experiment.

3. Improving the flux

The second stage in the optimisation of PRISMA will be the installation of a supermirror neutron guide between the target void vessel and the sample area. The close proximity of the instruments surrounding PRISMA imposes tight constraints upon the design options, the most significant being that the guide must be straight or tapered since there is insufficient space to install a curved guide.

```
1000000 1 0 8.0
[moderator]                    % 100 K methane moderator
9.035 0.0 0.0 0.1 0.1 0.0
95. 37.15 9.0 39.1
[guide]                        % shutter section
300 1
7.320 0.0 0.0 0.062 0.086
5.321 0.0 0.0 0.050 0.070
[guide]                        % target wall section
300 1
5.320 0.0 0.0 0.050 0.070
2.821 0.0 0.0 0.036 0.051
[chopper]                      % nimonic chopper
2.421 0.0 0.0 0.040 0.060
300.0 10300.0 20000.0
[soller]                       % chopper to sample pit
1 1
2.820 0.0 0.0 0.036 0.051
0.421 0.0 0.0 0.036 0.051
[area]                         % PRISMA sample position
50 50
0.000 0.0 0.0 0.125 0.125
[monitor]
[stop]
```

Figure 4 A typical PRMON input file. The first line specifies the number of neutrons and whether the neutron will be emitted towards the first element with a fixed or random energy defined by the flux shape in the moderator component. Each component is defined by its distance from the sample position, displacement from the central axis of the beam, and its width and height, with other parameters as required. Area detector components allow the flux distribution to be viewed, and monitor components record the time of flight profile of transmitted neutrons.

One advantage of this design is that experience will be gained with a considerably different guide system to those already existing at ISIS on the IRIS, OSIRIS and HRPD instruments.

To assess the parameters for the guide design, we are using a generalised Fortran Monte Carlo code PRMON developed by Mark Hagen. Components such as neutron guides, Soller collimation, nimonic choppers, area detectors or monitors can be assembled in any order to model a particular beamline configuration. A typical input file is shown in Figure 4. Simulation of the secondary part of the spectrometer including scattering from a sample is under development. Extensive testing of the code comparing simple beamline arrangements with analytical calculations has been carried out with excellent agreement found between the two methods. Here, six examples that illustrate the influence of various parameters upon the neutron intensity at the sample position are considered. The results of

	Normalised Intensity (n/cm^2)		**Intensity gain over tapered collimation**		**α (°)**	**Energy integrated Intensity PRISMA**		**Energy integrated intensity ROTAX**	
	11 meV	**2 meV**	**11 meV**	**2 meV**		**(n/cm^2)**	**Gain**	**(n/cm^2)**	**Gain**
Tapered collimation (3 cm x 5 cm exit)	*0.8*	*0.2*	*1.0*	*1.0*	*0.4*	*645*	*1.0*	*10.5*	*1.0*
Tapered guide (3 cm x 5 cm exit)	6.8	3.7	8.5	18.5	2.3	5595	8.7	19.7	1.9
Tapered guide - shutter only (3 cm x 5 cm exit)	1.4	0.4	1.8	2.0	0.5	870	1.3	10.5	1.0
Tapered guide - no chopper gap (3 cm x 5 cm exit)	8.0	5.0	10.0	25.0	4.2	9285	14.4	23.7	2.3
Straight guide (2 cm x 4 cm exit)	4.4	2.3	5.5	11.3	1.5	3257	5.1	6.8	0.6
Tapered guide (2 cm x 4 cm exit)	4.5	2.5	5.6	12.5	2.0	3792	5.9	9.1	0.9

Table 1 Intensity and horizontal divergence, α, of several example beamline arrangements calculated using PRMON for the PRISMA and ROTAX sample positions. 'Tapered collimation' represents the current beamline configuration. Normalised intensity values have been calculated by dividing PRMON intensity values by the exit area of the beam.

the calculations are summarised in Table 1 with the intensity at the ROTAX sample position also listed (ROTAX has 3 cm x 5 cm straight collimation through its shutter). Fixed beamline parameters included in the calculations are the 9.035 m moderator to sample distance, the 10 x 10 cm^2 moderator size and orientation of the beamline with respect to this, and the inclusion of a 0.75 m gap to accommodate the nimonic chopper. For these calculations, guide sections all have m = 3 supermirrors and intensities have been normalised to the exit beam area of the particular guide configuration.

All comparisons of intensity gains and divergence angles will be made with respect to the values for the existing tapered collimation. It can be seen from Table 1 that replacing the collimation with a guide system with an identical taper will produce a huge increase in the cold neutron intensity with factors of up to 20 above the present situation, and a correspondingly large increase at the ROTAX sample position. In fact, a factor 2 gain in intensity can be obtained just by installing a guide in the shutter section of the beamline. This increase in itself is significant, since the upgrades to the beamline will take place in separate stages during ISIS shutdown periods, leaving the instrument

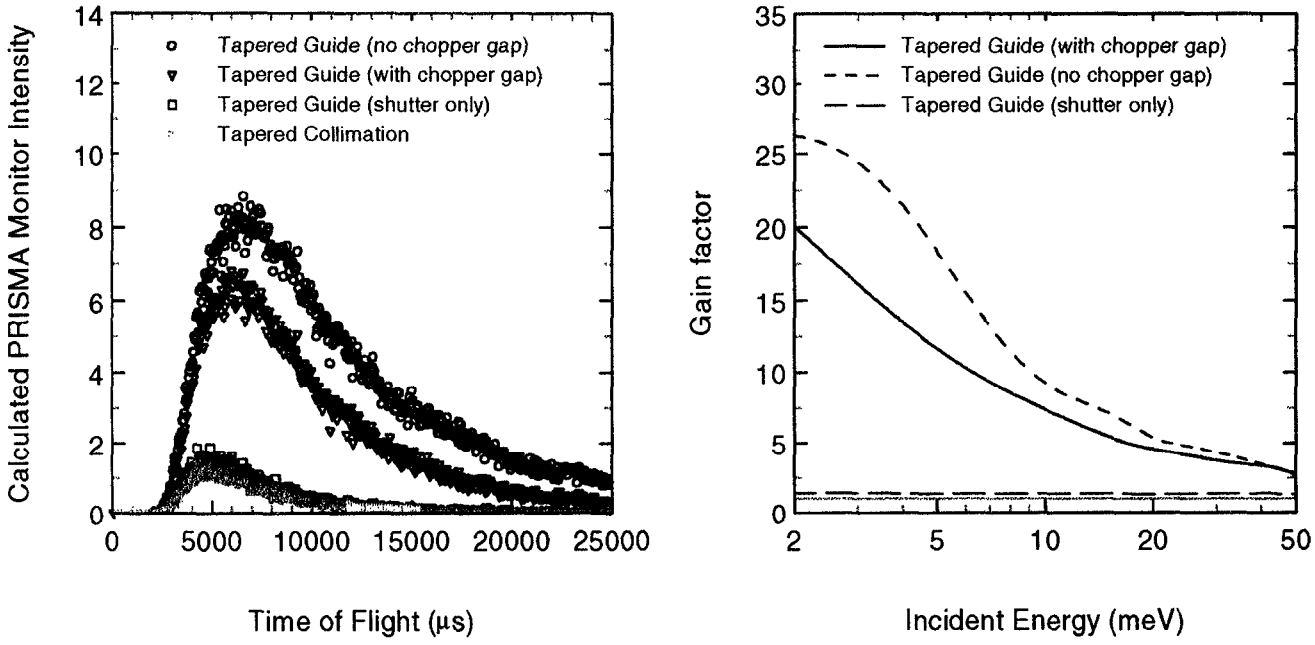

Figure 5 Calculated monitor intensities at the PRISMA sample position for the existing tapered collimation and incremental replacements of the collimation with m = 3 supermirror guide. The gain factors vs. incident energy over the present situation are also shown.

operational during experimental cycles. Consequently, users will experience the benefits of the instrument development long before the final completion date.

One of the most significant parameters affecting the transmitted intensity is the gap provided for the nimonic chopper. By replacing the gap with a section of neutron guide the intensity is enhanced by gain factors of 25 and above, but with an associated exit divergence of over 4°, principally due to neutrons with energy < 1 meV. Given that the lowest incident energy of the instrument will be 2 meV (see below), one useful feature of the chopper gap will be the removal of these unwanted neutrons. In Figure 5, the calculated monitor spectra for these three tapered guide arrangements are shown and compared to that of the tapered collimation. The gain factors for each configuration are also shown.

Since most samples rarely exceed 1-2 cm^3 and the beamline is to be optimised for a high signal:noise ratio in the presence of complex sample environment, a small final beam size, e.g. 2 cm width and 4 cm height, will be required to match the incident beam to the sample size. In Table 1, the calculated intensities for a straight guide with this cross-section, and a guide with the same taper as the existing collimation are also listed, and the calculated divergences are shown in Figure 6. As expected, the tapered collimation has a triangular divergence, which is preserved for the straight guide but with a larger divergence due to the critical angle of the supermirror. The tapered guide produces a rather interesting fringe pattern, with a sequence of minima occurring at integer multiples of the guide taper angle. Whilst the reduction in cross-section still leads to large gain factors for PRISMA, there is a detrimental effect for the ROTAX sample position due to the non-optimum matching of the beam size across the PRISMA sample area. Thus, despite the restraints upon the guide geometry, it can be appreciated from the examples given here that there are still many parameters that can be adjusted to optimise the guide system, and that furthermore, the impact upon the *entire* beamline of each parameter must be considered in the design.

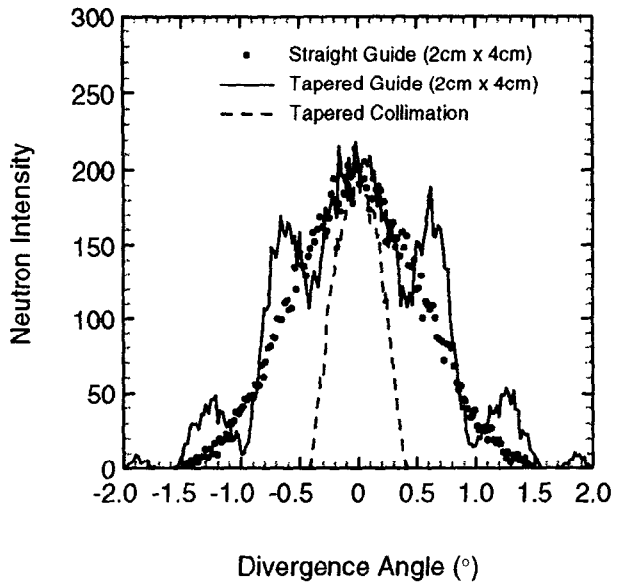

Figure 6 Calculated horizontal divergence profiles for neutron guides with 2 cm x 4 cm cross section compared with the divergence of the existing beamline collimation.

4. Optimising the beamline

The scientific case for the upgrade of the PRISMA beamline has identified three areas where the enhanced low energy flux could make a significant impact: (i) quantum critical phenomena of small moment heavy-fermion systems under pressure; (ii) lattice dynamics at high pressure, and (iii) phase transitions and dynamics of unconventional magnetic materials. All three areas will require an instrument with a high signal:noise ratio, and it is planned to install a range of devices to reduce the background of the beamline. In addition to the nimonic chopper to reduce the epithermal neutron flux, a variable aperture double disk chopper will allow the required energy window for a particular experiment to be stringently defined. Incident neutrons with $E_i > 80$ meV will also be filtered out by a removable 100 mm perfect single crystal of sapphire, and the exit beam size will be further reducable by a set of variable neutron absorbing slits. Other options will be available to allow the beam characteristics to be tailored to a particular experimental situation, including a focussing supermirror nose and Soller collimation to reduce the divergence of the exit beam.

At a spallation neutron source, tight fitting shielding around the supermirrors is critical in minimising the background from neutron and gamma radiation passing down the beam tube around the outside of the guide. Conventional guide systems are constructed from supermirror components deposited on glass substrates attached to the inside of evacuated beam tubes, but it has recently been demonstrated [6] at the ILL that m = 3 Ni/Ti supermirrors can be deposited on polished metal substrates, including steel, with equivalent reflectivity profiles to conventional supermirrors. This is a highly significant development and it is planned to construct the PRISMA neutron guide from supermirrors coated on the steel components that will be used for the insert assemblies. It is anticipated that that this will also lead to a considerable reduction in the background levels in the sample area.

The substantial increase in incident flux at low incident energies provided by the neutron guide will lead to a significant frame overlap problem. Hence, neutrons with $E_i < 2$ meV will be removed from the incident beam by a frame overlap supermirror on a glass or etched silicon substrate. The shallow critical angle will result in a length of around 1.7 m to cover the entire beam area and it will be

located inside the target wall guide section where any possibility of an increased background at the sample position from the scattered beam will be minimised.

5. Summary

The development of the PRISMA instrument at ISIS into a high intensity cold neutron spectrometer optimised for single crystal experiments and extreme sample environment conditions has been described. The design phase of the supermirror neutron guide is in progress using Monte Carlo modelling techniques with completion expected within the next 6 months. Installation of the guide system will take place in stages over the next 2 years with final commissioning of the instrument during the year 2000.

[1] "ESS: A next generation source for Europe" (1997), ESS Council, Vols. I, II, III.
[2] C. Adreani, C.J. Carlile, F. Cilloco, C. Petrillo, F. Sacchetti, G.C. Stirling and C.G. Windsor, Nucl. Inst. Methods A254 (1987) 333; U. Steigenberger, M. Hagen, R. Caciuffo, C. Petrillo, F. Cillocco and F. Sacchetti, Nucl. Inst. Methods B53 (1991) 87
[3] C. Petrillo, F. Sacchetti, U. Steigenberger and M. Hagen, J. Neutron Research, 3 (1996) 93
[4] M.J. Bull, M.J. Harris, U. Steigenberger, M. Hagen, C. Petrillo and F. Sacchetti, Physica B 234-236 (1997) 1061
[5] M. Hagen and S.J. Payne (1995), Rutherford Appleton Laboratory Technical Report, RAL-TR-95-034
[6] Ian Anderson, ILL. Private communication.

ICANS XIV
14th Meeting of the International Collaboration on
Advanced Neutron Sources
June 14-19, 1998
Starved Rock Lodge, Utica, IL

RECENT DEVELOPMENTS OF NEUTRON DIFFRACTION INSTRUMENTS AT THE IBR-2 PULSED REACTOR

Anatoli M. Balagurov

Frank Laboratory of Neutron Physics, Joint Institute for Nuclear Research, 141980 Dubna, Russia, e-mail: bala@nf.jinr.ru

ABSTRACT

Improvements in the performance of the high resolution Fourier diffractometer, HRFD, diffractometer for high pressure studies, DN-12, and single crystal diffractometer, DN-2, at the IBR-2 pulsed reactor in Dubna are discussed. On HRFD, a second back-scattering detector bank started operation and a geometrical contribution to the resolution function was reduced. On DN-12, a new supermirror neutron guide tube was installed, which substantially increases the neutron flux. On DN-2, a new two-dimensional detector is used. That allows registering three-dimensional intensity distributions. Examples of experimental results are also presented.

1. Introduction

The IBR-2 pulsed reactor in Dubna is one of the most effective neutron sources for condensed matter studies. A high neutron flux (about 10^{16} n/cm^2/s in pulse) and a low repetition rate (5 Hz) provide good conditions for various types of neutron scattering investigations. Together with inelastic and small angle scattering, reflectometry and polarized neutron optics, neutron diffraction is an essential scientific area at IBR-2 [1]. All together five diffractometers are in operation: HRFD, for high resolution powder and single crystal studies; DN-2, medium resolution, multipurpose diffractometer; SNIM, diffractometer with a high pulsed magnetic field; DN-12, for experiments with micro samples, and NSVR, diffractometer for texture studies. During the last two years the upgrading of some of them is accomplished and in this paper the new characteristics of HRFD, DN-2, and DN-12 together with examples of recent results are discussed.

2. HRFD, high resolution RTOF Fourier diffractometer

HRFD is the TOF correlation spectrometer using a fast Fourier chopper for modulating the intensity of the incident neutron beam and the reverse TOF-method (RTOF) for data acquisition. The detailed description of the method, HRFD design, and the reasons why it is very suitable for high resolution powder diffraction at long pulse neutron sources were earlier presented in papers [2,3] and at ICANS conferences [4,5]. The HRFD *d*-spacing resolution depends on the highest frequency of intensity modulation (highest chopper rotating speed, V_m) and on geometrical contribution and could be as small as 0.05%. In reality this level can

be reached only with a special collimator at the incident beam and a sample of very high quality.

In the last two years on HRFD a second back-scattering detector bank at $2\theta = -152°$ was put into operation, which reduced the time of experiments, and final adjustment of the detector elements was done, which decreased the geometrical component of the resolution function. In Fig.1, one of the diffraction peaks from La_2CuO_4 single crystal measured at V_m=8000 rpm is shown. The relative full width of the peak (d=1.335 Å), that can be regarded as the HRFD resolution at this point, is about $9 \cdot 10^{-4}$. For powder samples of even very high quality like the Al_2O_3 sintered reference sample, the lowest limit in the same conditions is $11.5 \cdot 10^{-4}$ (at d=1.5 Å). Nevertheless, at this resolution level the famous Al_2O_3 doublet (433) / (432) (R3c setting) is quite well separated (Fig.2). The diffraction line width dependence on d-spacing is linear in a wide d-range, which makes it possible to use only one model for the line shape [2].

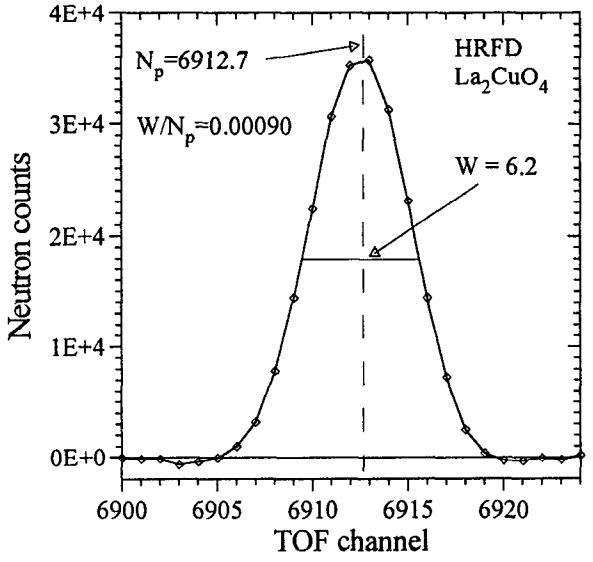

Fig.1. *A typical Bragg peak for a La_2CuO_4 single crystal measured at V_m=8000 rpm with the TOF channel width of 2 μs. The position and the full width of the peak are equal to 6912.7 and 6.2 TOF channels, respectively, i.e. the relative resolution is about 0.0009. Small negative deeps on both sides of the peak are due to the correlation nature of counts.*

At present HRFD is used for structure refinements of powders, for experiments with single crystals if it's a very high d-spacing resolution is needed, and for residual stress investigations in bulk samples. Recently the results of high-resolution powder studies of $HgBa_2CuO_{4+\delta}$ [6] and $HgBa_2CuO_4F_\delta$ [7] structures, investigation of phase separation phenomenon in $La_2CuO_{4+\delta}$ [8], and semiconductor – metal phase transition in CMR compounds [9] were published.

Figure 3 shows an example of the Rietveld refinement of the $La_{0.8}Ba_{0.2}MnO_3$ diffraction pattern. For $La_{0.35}Pr_{0.35}Ca_{0.30}MnO_3$, the analysis of the characteristic bond length (Fig.4) reveals that coherent deviation of oxygen octahedra is not significant at room temperature and in the FM phase ($T_c \approx 160$ K). The axial distance Mn-O1 is slightly shortening with decreasing of temperature from room temperature to 40 K while equatorial Mn-O21 and Mn-O22 distances significantly and simultaneously change at $T \approx 200$ K. This fact proves the ordering of static Jahn-Teller distortions in the equatorial plane of MnO_6 octahedra at this temperature [9].

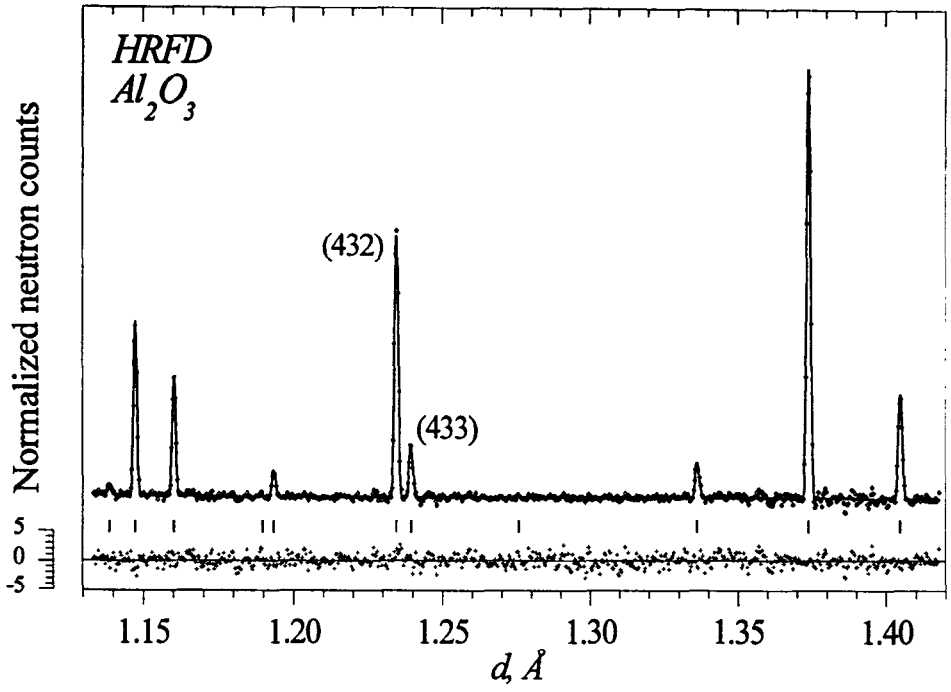

Fig.2. *A part of the diffraction pattern of the reference Al_2O_3 sample measured with HRFD at V_m=8000 rpm and processed by the Rietveld method. The difference curve is normalized on the mean-square deviation.*

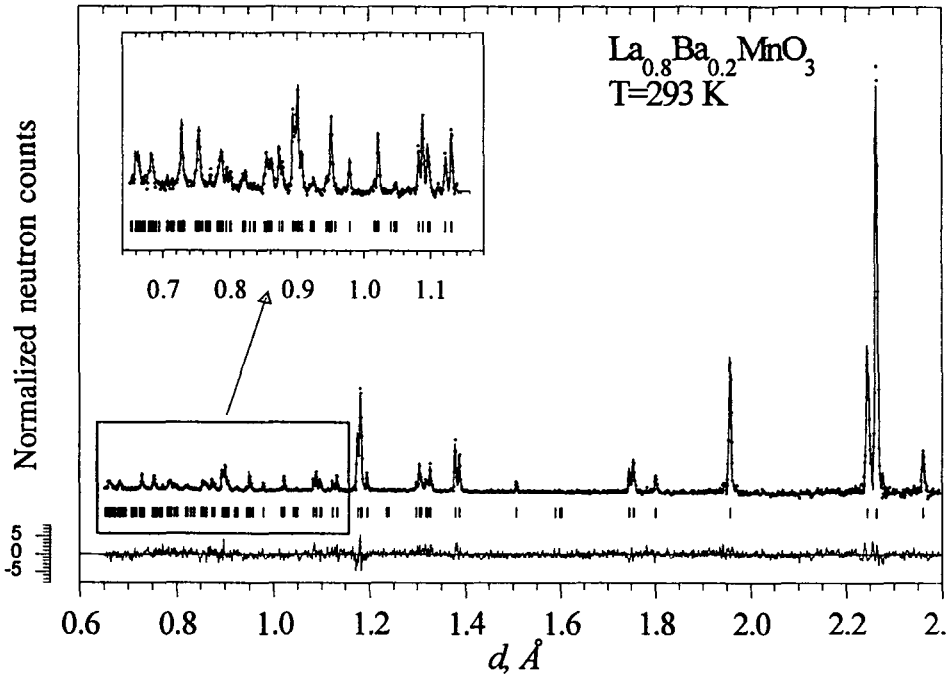

Fig.3. T*he diffraction pattern of the La(Ba)MnO_3 sample measured at V_m=8000 rpm and processed by the Rietveld method. The difference curve is normalized on the mean-square deviation.*

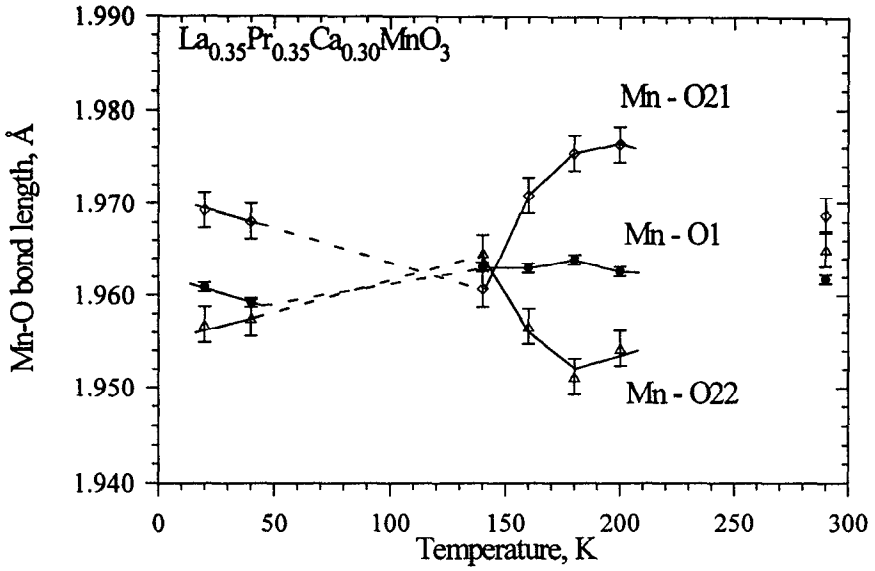

Fig.4. *Mn–O bond lengths of $La_{0.35}Pr_{0.35}Ca_{0.3}MnO_3$ vs temperature. T≈175 K is the onset temperature of the semiconductor – metal phase transition. At T≈140 K the FM state is fully accomplished.*

3. DN-12, TOF spectrometer for micro samples studies under high pressure

The first stage of the DN-12 spectrometer for high-pressure studies was put into operation three years ago [10,11]. After the first successful experiments [12] DN-12 developments continued. To increase the neutron flux, improve background conditions, and extend the wavelength range, a curved supermirror neutron guide tube is installed (Fig.5). As a result, the total flux on the sample increases twice and the flux of long wavelength neutrons increases several times (up to 9 for λ=3.8 Å) (Fig.6). At present, the DN-12 detector consists of two 800 mm in diameter rings, positioned in the vertical plane. Both rings are assembled of 16 ^{3}He counters and can be moved along the beam axis providing a scattering angle interval from 45° to 135°. For inelastic neutron scattering investigations a Be filter can be placed in front of one of the rings. The results of the NH_4Cl vibrational spectrum study can be found in Ref. [13].

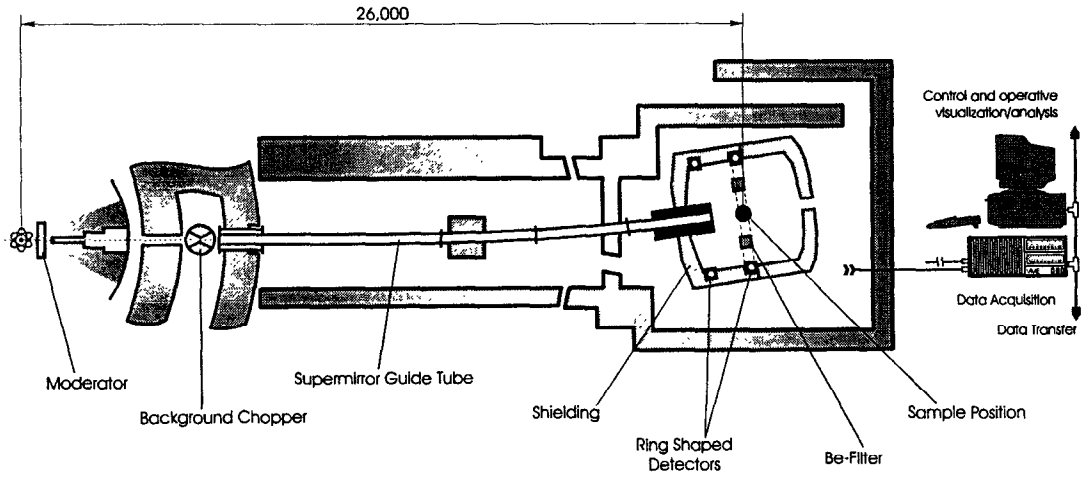

Fig.5. *The lay-out of the new design of the DN-12 spectrometer at the IBR-2 reactor.*

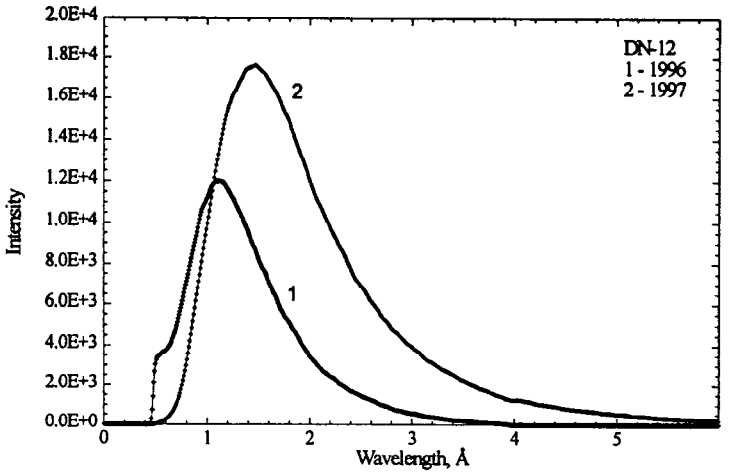

Fig.6. *The neutron intensity at the sample position measured before (1) and after (2) installation of a supermirror neutron guide.*

Figure 7 shows an example of the C_{60} diffraction pattern of a 0.5 cm^3 sample, measured at ambient conditions in 1 h. The hematite Fe_2O_3 is studied at pressures up to 3.7 GPa. At P=2.5 GPa in this compound the magnetic phase transition occurs (Fig.8).

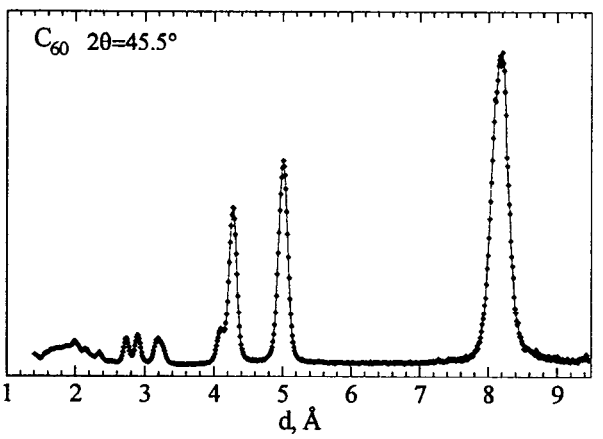

Fig.7. *The diffraction pattern of C_{60} measured from a 0.5 cm^3 sample at ambient pressure in 1 hour.*

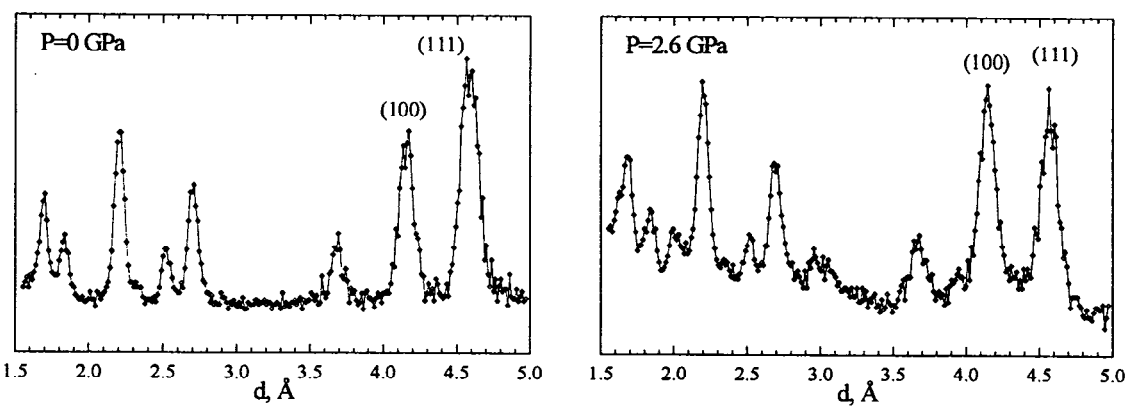

Fig.8. *The diffraction patterns of Fe_2O_3 measured before (left) and after (right) the magnetic phase transition at P=2.5 GPa. The sample volume is about 0.5 mm^3, time of experiment is 24 h.*

4. DN-2, TOF diffractometer

DN-2 is a high intensity diffractometer mainly for single crystal but also for real-time studies. Recently, the characteristics of DN-2 were noticeably improved after a two-dimensional detector (320x280 mm^2) with the position resolution about 2.5 mm in two directions started operation. In addition to time-of-flight analysis, this detector allows registering the three-dimensional intensity distribution in the reciprocal space of the crystal without rotating the sample or the detector. Figure 9 illustrates a two-dimensional intensity distribution in the (220) and (440) reciprocal lattice sites in a $La_2CuO_{4+\delta}$ single crystal following the tetragonal to orthorhombic phase transition and twin structure formation.

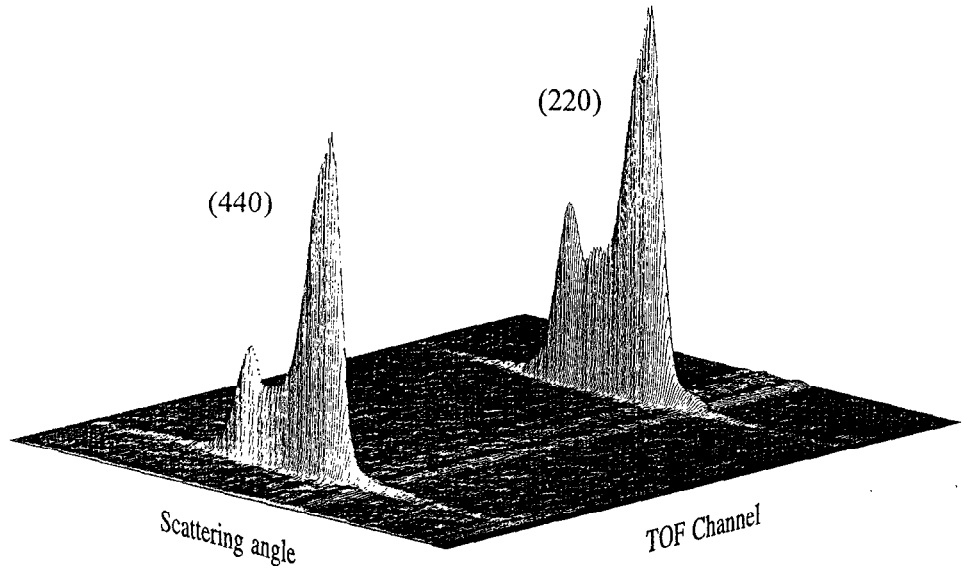

Fig.9. *The diffraction pattern along the (hh0) direction of a La_2CuO_4 single crystal (in the ferroelastic phase) measured with a two-dimensional PSD and summed over the vertical coordinate of the detector.*

The problem of the coexistence of superconductivity and an ordered magnetic state in two different kinds of these $La_2CuO_{4+\delta}$ single crystals – macroscopically homogeneous and phase separated – have been studied intensively with both HRFD and DN-2 diffractometers [8,14]. To check whether the observed by μSR technique magnetic transitions in $La_2CuO_{4.02}$ and $La_2CuO_{4.04}$ samples lead to the true long-range AFM order, the neutron diffraction spectra along the [100] direction were measured on DN-2. According to the μSR data, one could expect to find the (100) magnetic peak below T_N. Indeed, in the $La_2CuO_{4.04}$ sample, this peak is well pronounced (Fig.10), whereas in the $La_2CuO_{4.02}$ sample, neutron diffraction reveals no traces of such reflection (insert in Fig.10).

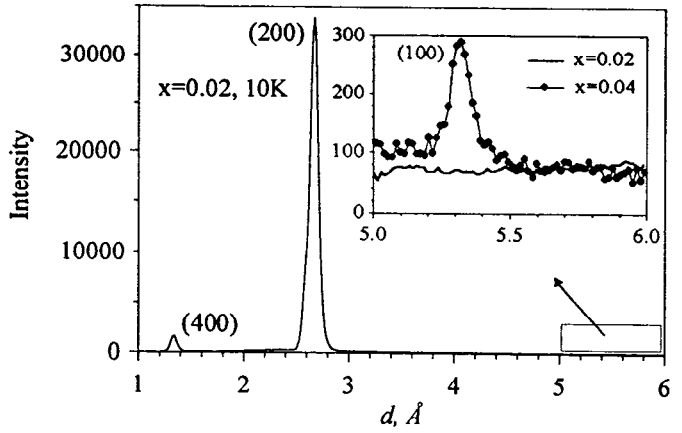

Fig.10. *The diffraction pattern from the (h00) plane for $La_2CuO_{4.02}$ measured at T=10 K. The insert shows fragments of (h00) diffraction patterns for $La_2CuO_{4.02}$ and $La_2CuO_{4.04}$ near the (100) AFM peak.*

In conclusion, it can be confidently forecasted that the joint operation of improved HRFD, DN-12, and DN-2 diffractometers at the IBR-2 pulsed reactor will make a visible scientific impact in powder precision structural, powder high pressure, and single crystal neutron diffraction studies.

Acknowledgements

All of the work discussed in this paper is the result of effort by many people of FLNP (Dubna), RSC KI (Moscow), and PNPI (Gatchina). It was financed by the JINR (Dubna) in the frame of the JINR and BMBF (Germany) agreement on co-operation and supported by the Russian Science Foundation (grant 96-02-17823).

References

1. A.M.Balagurov, Neutron News, 7(3), 10 (1996).
2. V.L.Aksenov, A.M.Balagurov, V.G.Simkin et al., J.of Neutron Research, **5**, 181 (1997).
3. V.L.Aksenov, A.M.Balagurov, V.A.Trounov, J.of Neutron Research, **6**, 135 (1997).
4. V.L.Aksenov, A.M.Balagurov, V.G.Simkin et al., ICANS-XII, RAL Report 94-025, **1**, 124, Abingdon (1993).
5. V.L.Aksenov, A.M.Balagurov, V.A.Trounov, P.Hiismaki, ICANS-XIII, PSI Proceedings 95-02, **1**, 235, Villigen (1995).
6. V.L.Aksenov, E.V.Antipov, A.M.Balagurov et al., Phys. Rev. B, **55**, 3966 (1997).
7. A.M.Abakumov, V.L.Aksenov, V.A.Alyoshin et al., Phys. Rev. Letters, **80**, 385 (1998).
8. A.M.Balagurov, V.Yu.Pomjakushin, V.G.Simkin, A.A.Zakharov, Physica B, **234-236**, 797 (1997).
9. A.M.Balagurov, V.Yu.Pomjakushin, V.L.Aksenov et al., JETP Letters (1998), to be published.
10. V.L.Aksenov, A.M.Balagurov, S.L.Platonov et al., High Press. Research, **14**, 181 (1995).
11. V.L.Aksenov, A.M.Balagurov, S.L.Platonov et al., *ICANS-XIII*, PSI Proceedings 95-02, **1**, 93, Villigen (1995).
12. V.L.Aksenov, A.M.Balagurov, B.N.Savenko et al., Physica C, **275**, 87 (1997).
13. A.M.Balagurov, B.N.Savenko, V.A.Somenkov et al., High Press. Research, **14**, 55 (1995).
14. V.Yu.Pomjakushin, A.A.Zakharov, A.M.Balagurov et al., Phys. Rev. B, (1998), submitted.

ICANS XIV
14th Meeting of the International Collaboration on
Advanced Neutron Sources
June 14-19, 1998
Starved Rock Lodge, Utica, IL

DESIGN AND PLACEMENT CONSIDERATIONS FOR PROPELLER-TYPE T-ZERO CHOPPERS

R. A. Robinson, Los Alamos National Laboratory, Los Alamos, NM 87545

We discuss factors to do with placement and running speeds of "propeller-type" t-zero choppers, as implemented at ISIS (on chopper spectrometers) and at LANSCE (on a reflectometer, chopper spectrometer and small-angle scattering instrument).

Propeller-syle t-zero choppers have been used at spallation sources since the HET chopper spectrometer was originally constructed[1], and similar t-zero choppers have been installed on other chopper instruments[2] at ISIS, as well as on the SPEAR reflectometer, the PHAROS chopper spectrometer[3] and, more recently, the LQD small-angle machine at LANSCE. In all cases, the purpose is to block the burst of high-energy neutrons that emanates from the source when the proton beam strikes the target, and still be fully open when the thermal neutrons of interest pass through the space occupied by the t-zero chopper. In general, roughly 30 cm of high-strength high-Ni alloy (like nimonic or inconel) is placed in the beam, and for background purposes, it is desirable to place the chopper as far upstream as possible. Examples of rotor geometries are shown in Fig. 1, while Fig. 2 is a photograph of the 341 kg inconel rotor used in the PHAROS t-zero chopper.

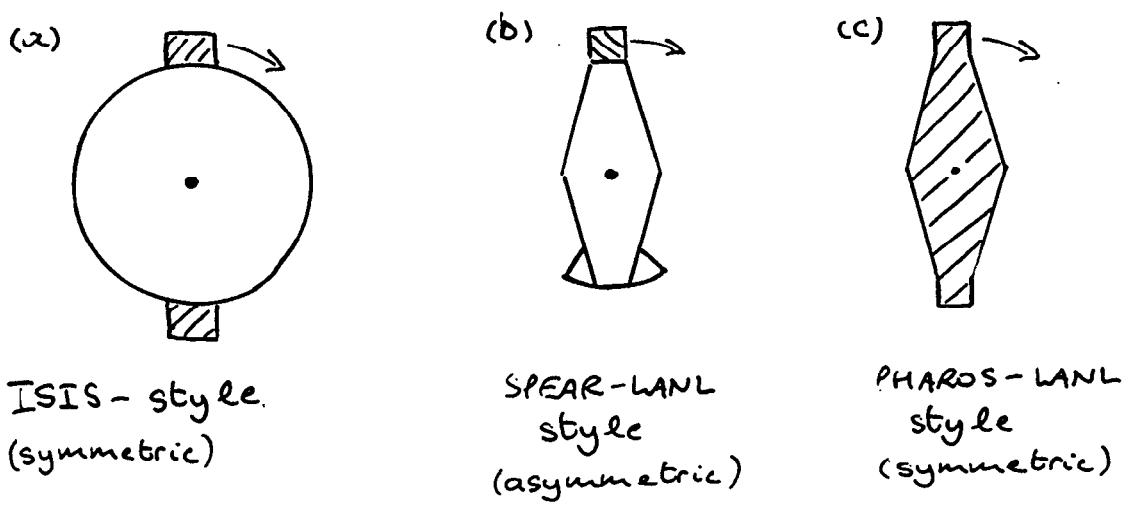

Figure 1 Schematic diagram showing t-zero choppers as implemented (a) at ISIS, (b) on SPEAR and LQD at LANSCE, and (c) on PHAROS at LANSCE. The neutron-attenuating material is shown by the shading and an alumunium alloy is typically used for the other structural components. (a) and (c) are *symmetrically* balanced, with the rotor entering the beam twice per revolution, while (b) is *asymmetrically* balanced and enters only once per revolution.

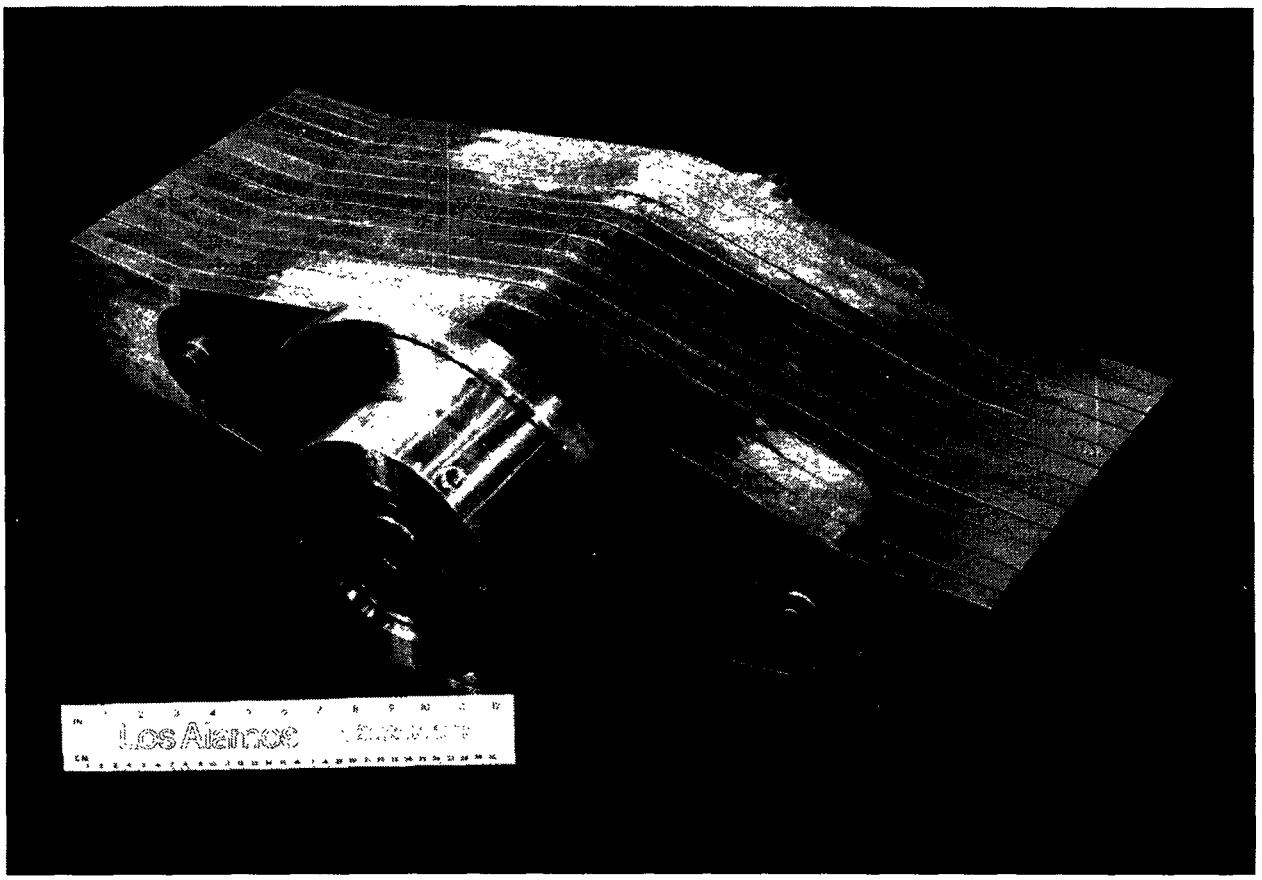

Figure 2 Photograph of the rotor for the t-zero chopper on the high-resolution chopper spectrometer PHAROS (see Ref. 3) at LANSCE. The rotor is symmetrically balanced, and the neutron beam passes throught the square sections at the ends of the blades. It is constructed from a set of twelve 25-mm thick plates of Inconel X-750, and weighs 341 kg.

Table I lists those parameters that are available to perform an optimisation, along with constraints, typical outer bounds and the values actually used on the high-resolution chopper spectrometer PHAROS[3] at LANSCE. As regards materials, we use Inconel X-750 [4], a high-tensile-strength high-nickel alloy (density ρ = 8.3 g cm^{-3}; yield strength σ_{yield} = 690 MPa; fast-neutron mean free path = 3.4 cm) as the neutronic element in our t-zero choppers. Following practice at ISIS, we have used 30 cm of inconel (as measured along the neutron beam path), which corresponds to ~ 8.8 fast-neutron mean free paths. The next constraint to consider is the maximum rotational frequency ν_{max} at which such a chopper can be run, without disintegrating. For a rotating straight homogeneous bar, with width « length, ν_{max} is given by

$$\nu_{max} = \frac{1}{2\pi}\sqrt{\frac{2\sigma_{yield}}{\rho R^2}} \qquad (1),$$

where σ_{yield} is the yield stress for the bar material, ρ is its density, R is the overall radius of the rotor and the maximum stress is at the centre of rotation. Assuming an additional engineering safety factor S (which should typically be ~3), the equation becomes

$$\nu_{max} = \frac{1}{2\pi}\sqrt{\frac{2\sigma_{yield}}{S\rho R^2}} \qquad (2).$$

and this limit is shown as a function of R in Fig. 3.

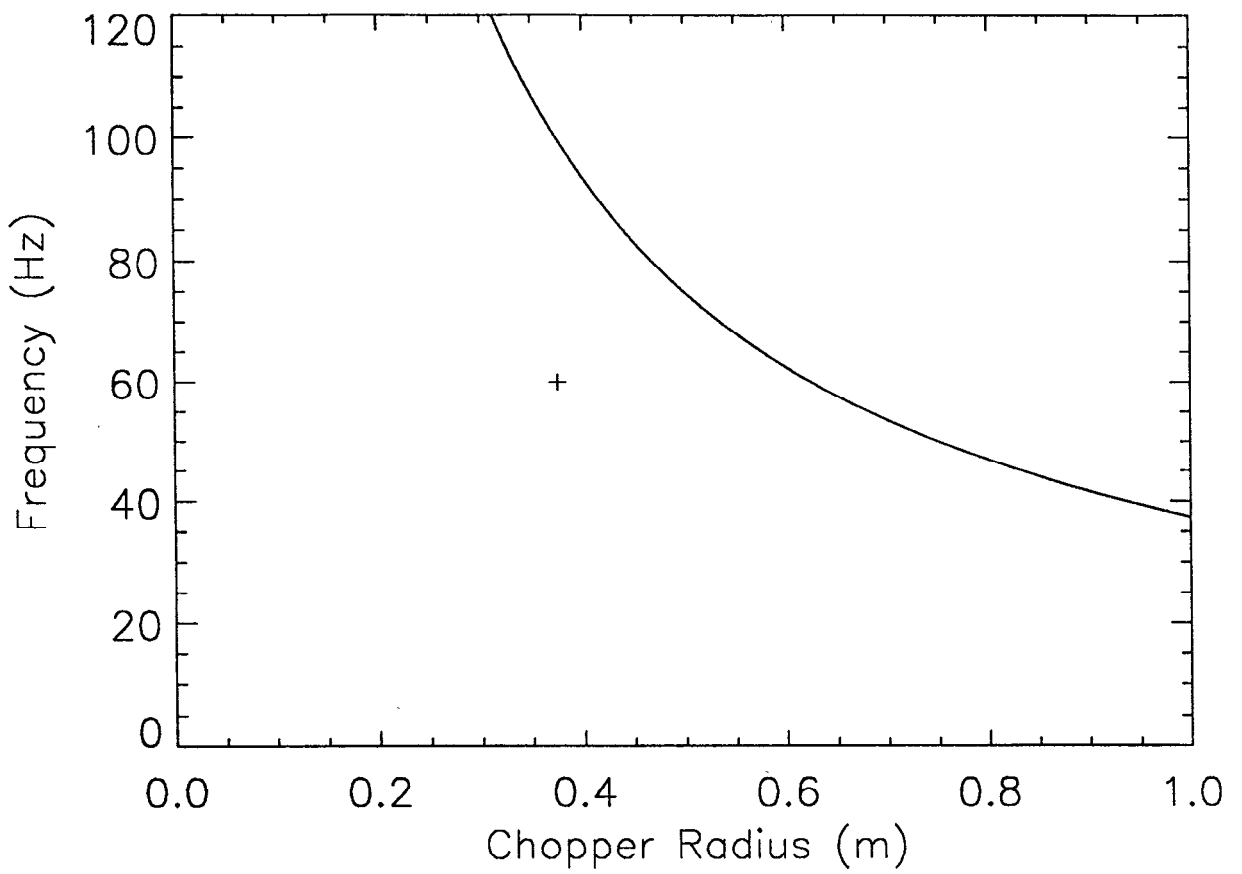

Figure 3 Chopper frequency - radius bounds determined from the yield stress and density of Inconel X-750, using Equation (2) with an engineering safety factor S = 3. In designing the chopper, one must remain on the lower left-hand side of the line. The (+) symbol represents the rotor used on PHAROS.

The next consideration is the spatial extent of the neutron beam, at the chopper location. Normal thermal beams are defined by a series of thermal-neutron apertures, typically sintered B_4C or a low-epoxy/B_4C composite (crispy-mix). Between these apertures, but with larger width, there is likely some fast-neutron shielding, typically consisting of some combination of steel and a hydrogenous material (e.g. polyethylene or epoxy resin, possibly doped with borax), as shown in Fig. 4(a). It is advantageous to think of a *thermal-neutron* beam and a larger *fast-neutron* beam coexisting at the chopper position. Similar ideas apply to beams with guides, as shown in Fig. 4(b), but it is not so clear in this case what the shape and extent of the fast-neutron beam is. In both cases, it is clearly desirable to sweep the chopper blade across the shortest dimension of the beam, and this may have consequences regarding whether the rotation axis of the rotor is below (or above) the neutron beam or is translated to one side. **The main function of the t-zero chopper is to block the fast neutron beam as fully as possible, when protons strike the**

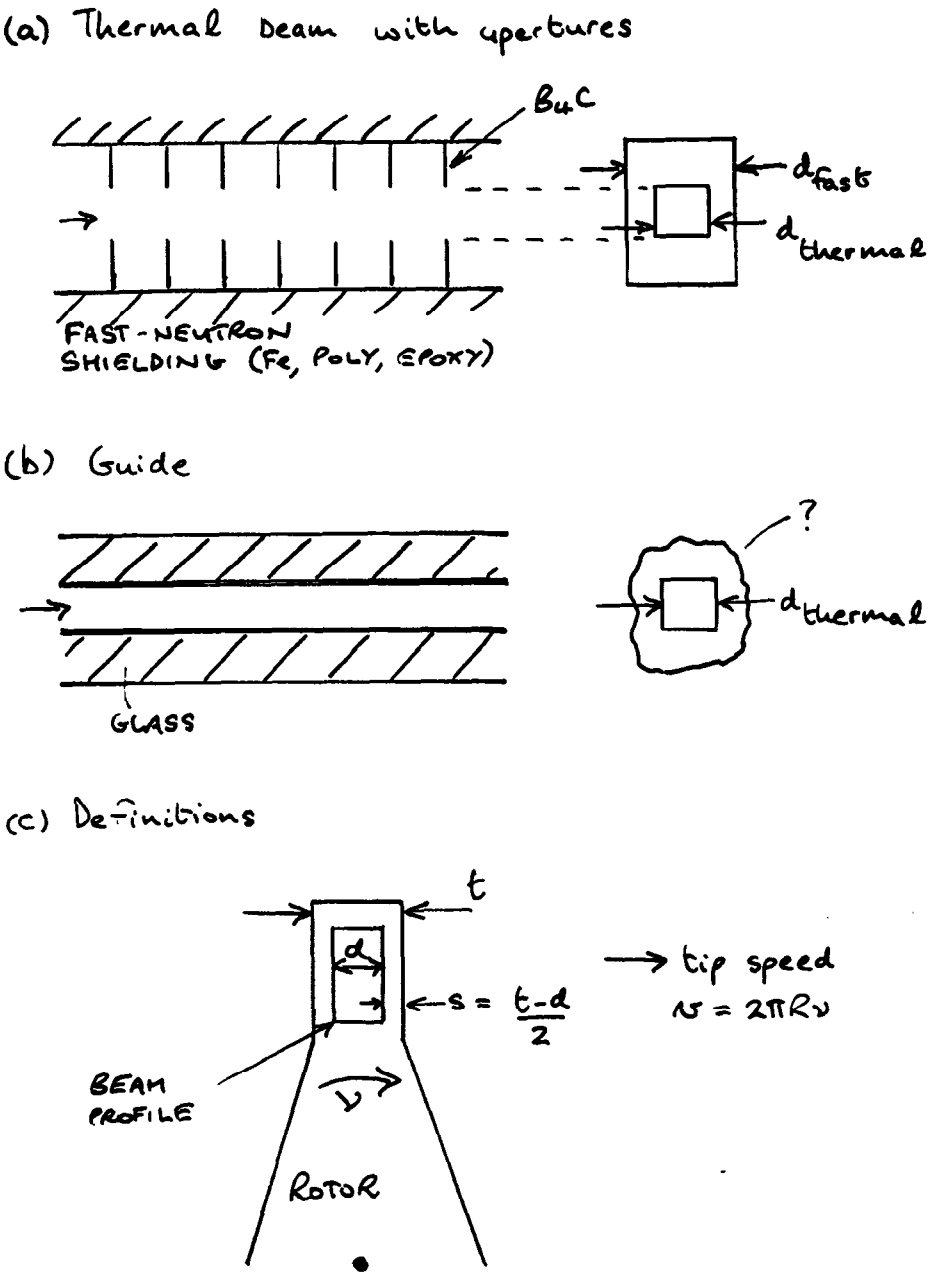

Figure 4 Schematic diagram showing the thermal and fast-neutron beams for (a) a normal thermal beam using apertures (B_4C) and larger aperture fast-neutron shielding (steel, polyethylene, epoxy resin), and (b) for a guide, in which the fast-neutron aperture is less well-defined. In (a) and (c), some of the symbols used in the text for chopper and beam dimensions are shown.

spallation target, and yet have the thermal beam fully open in time for the highest energy neutrons of interest to pass through completely unimpeded. The latter condition is not so straightforward, and the ISIS t-zero choppers on HET and MARI are not fully open at 1eV, for instance. If one simply considers a fixed point on the chopper sweeping across the thermal beam of width $d_{thermal}$, the maximum neutron energy E_{max} that can pass through is

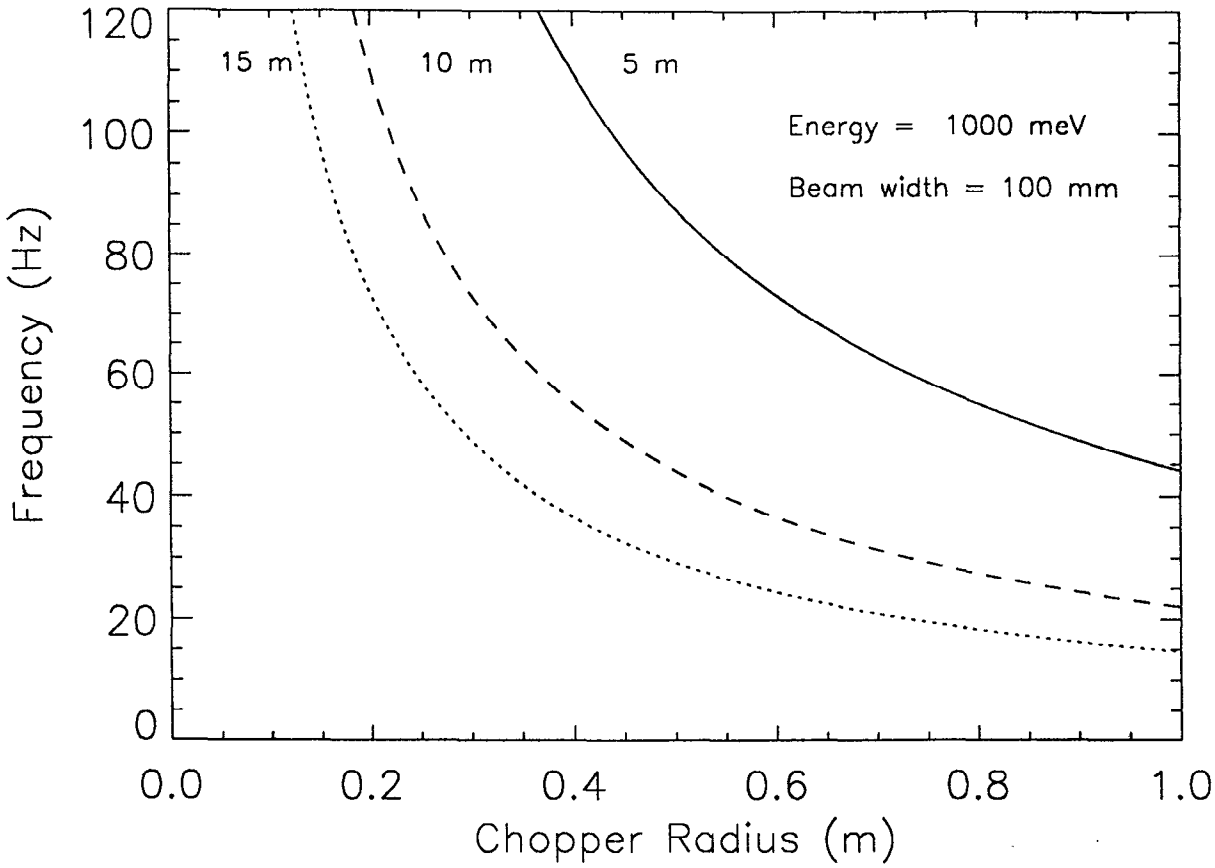

Figure 5 Chopper frequency - radius bounds determined from the desired maximum useful neutron energy E_{max}, beam width $d_{thermal}$ and for source-chopper distance = 5, 10 and 15 m, using Equation (3). For the example shown here, we assume E_{max} = 1 eV and $d_{thermal}$ = 10 cm. The chopper must operate in the region to the upper right-hand side of the curve.

$$E_{max}(\text{meV}) = 5.22697 \times 10^{-6} \left(\frac{2\pi \nu R L}{d_{thermal}} \right)^2 \qquad (3).$$

The parameters that are available to the instrument designer, for a given desired E_{max} and beam width $d_{thermal}$, are the chopper rotational frequency ν, the chopper radius R and the distance L at which chopper is placed, measured from the source. As an example, Fig. 5 shows a set of frequency-radius curves for different chopper placements, assuming a 10-cm wide beam and the use of neutrons up to 1eV. One needs to be to the upper-right side of these lines, and it is very difficult to achieve this, by placing the chopper at the edge of the biological shield (say at 5m) - it involves either a very large or a very fast rotor. Equations (2) and (3) can now be combined into a very useful rule of thumb for chopper design, because they both have the same $\nu = 1/R$ functional dependence:

$$\frac{d_{thermal}}{2\pi L} \sqrt{\frac{E_{max}(\text{meV})}{5.22697 \times 10^{-6}}} < R\nu < \frac{1}{2\pi} \sqrt{\frac{2\sigma_{yield}}{S\rho}} \qquad (4),$$

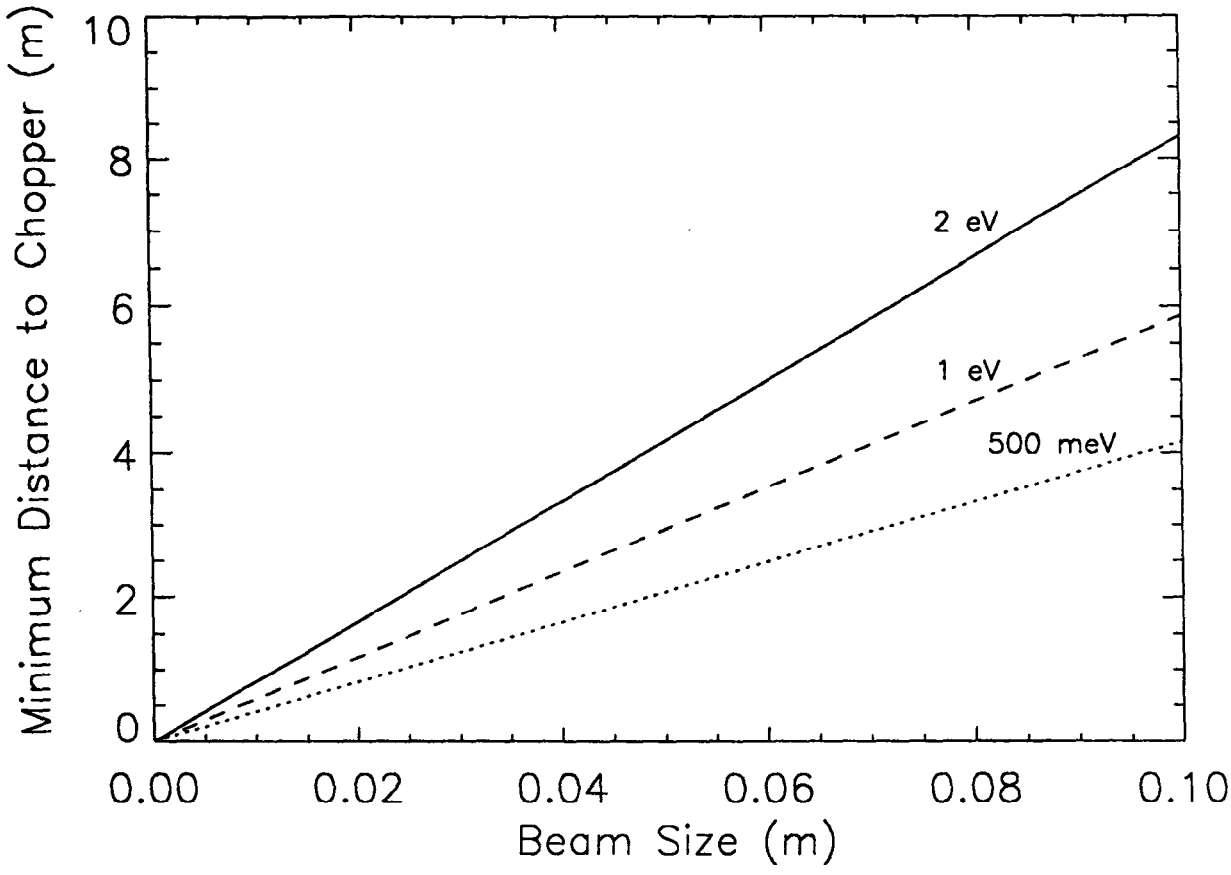

Figure 6 Plot of closest possible chopper position versus beam size for several neutron energies, following Equation (5). The numbers presented here, which assume the use of Inconel X-750 and a safety factor S = 3, take no account of the overlap of the chopper, beyond the beam size. This effect can be included simply by using s + d in place of d for the beam size in Equation (5).

or stated another way that is independent of R and ν,

$$L > d_{thermal}\sqrt{\frac{E_{max}(meV)}{5.22697\times10^{-6}}\frac{S\rho}{2\sigma_{yield}}} \qquad (5).$$

This linear L-versus-d variation is plotted in Fig. 6 for several neutron energies. Note that this expression is independent of both chopper radius R and chopper frequency ν, with the consequence that there are minimum acceptable source-chopper distances, irrespective of how one changes R and ν.

Now, Equation (3) and Fig. 5 correspond to the situation of having a chopper blade with width exactly equal to the beam size, with no overlap. In other words, it may not stop the whole fast-neutron beam which can proceed into the instrument and cause background problems, nor does it allow any margin for error in synchronising the chopper with the source. It is clearly desirable to make the chopper blade somewhat wider (say, with width t) as shown in Fig. 4(c), and one can

then define neutron energies at which the thermal beam starts to open (E_{start}) and at which it is fully open (E_{full}):

$$E_{start} = 5.22697\times10^{-6}\left(\frac{2\pi\nu RL}{s_{thermal}}\right)^2 \qquad (6)$$

$$= 5.22697\times10^{-6}\left(\frac{4\pi\nu RL}{t-d_{thermal}}\right)^2$$

and

$$E_{full} = 5.22697\times10^{-6}\left(\frac{2\pi\nu RL}{s_{thermal}+d_{thermal}}\right)^2 \qquad (7),$$

$$= 5.22697\times10^{-6}\left(\frac{4\pi\nu RL}{t+d_{thermal}}\right)^2$$

where s is the degree of overlap on the trailing edge of the chopper blade, and the second line of each equation assumes that the chopper blade is centred on the neutron beam when protons hit the target. **Equation 7 is particularly useful for determining how much overlap one can tolerate, given a desired value of E_{full}.** Of course, for the fast-neutron beam, there are corresponding equations in which $s_{thermal}$ and $d_{thermal}$ are replaced by s_{fast} and d_{fast}.

The overlap s_{fast} (see Fig. 4(c)) also determines how well the chopper and accelerator must be phased to each other, or how much jitter is acceptable in the chopper-accelerator timing-control system:

$$t_{jitter}(\mu s) = \frac{10^6 s_{fast}}{2\pi\nu R} = \frac{10^6(t-d_{fast})}{4\pi\nu R} \qquad (8)$$

and one can replace s_{fast} and d_{fast} by $s_{thermal}$ and $d_{thermal}$ to give the equivalent fast-neutron jitter.

One also has to choose whether to construct the chopper such that it is *symmetrically* balanced, with the rotor entering the beam every 180°, or *asymmetrically* balanced in such a way that the rotor only re-enters the beam after a full revolution, as shown in Fig. 1(b). This effect is shown schematically in Fig. 7(a), for the PHAROS t-zero chopper parameters, in the time domain. Symmetric choppers are generally undesirable for broad-band cold-neutron applications, because the rotor re-enters the beam at a time corresponding to useful neutron bandwidth, and the uninterrupted wavelength bandwidth can be doubled using an asymmetric rotor - such choppers are used on SPEAR and LQD at LANSCE. However, asymmetric rotors can be more complicated to fabricate and balance. The energies at which the rotor re-enters the beam are

$$E_{180}(\text{meV}) = 5.22697\times10^{-6}\left(\frac{2L}{\nu}\right)^2 \qquad (9)$$

and

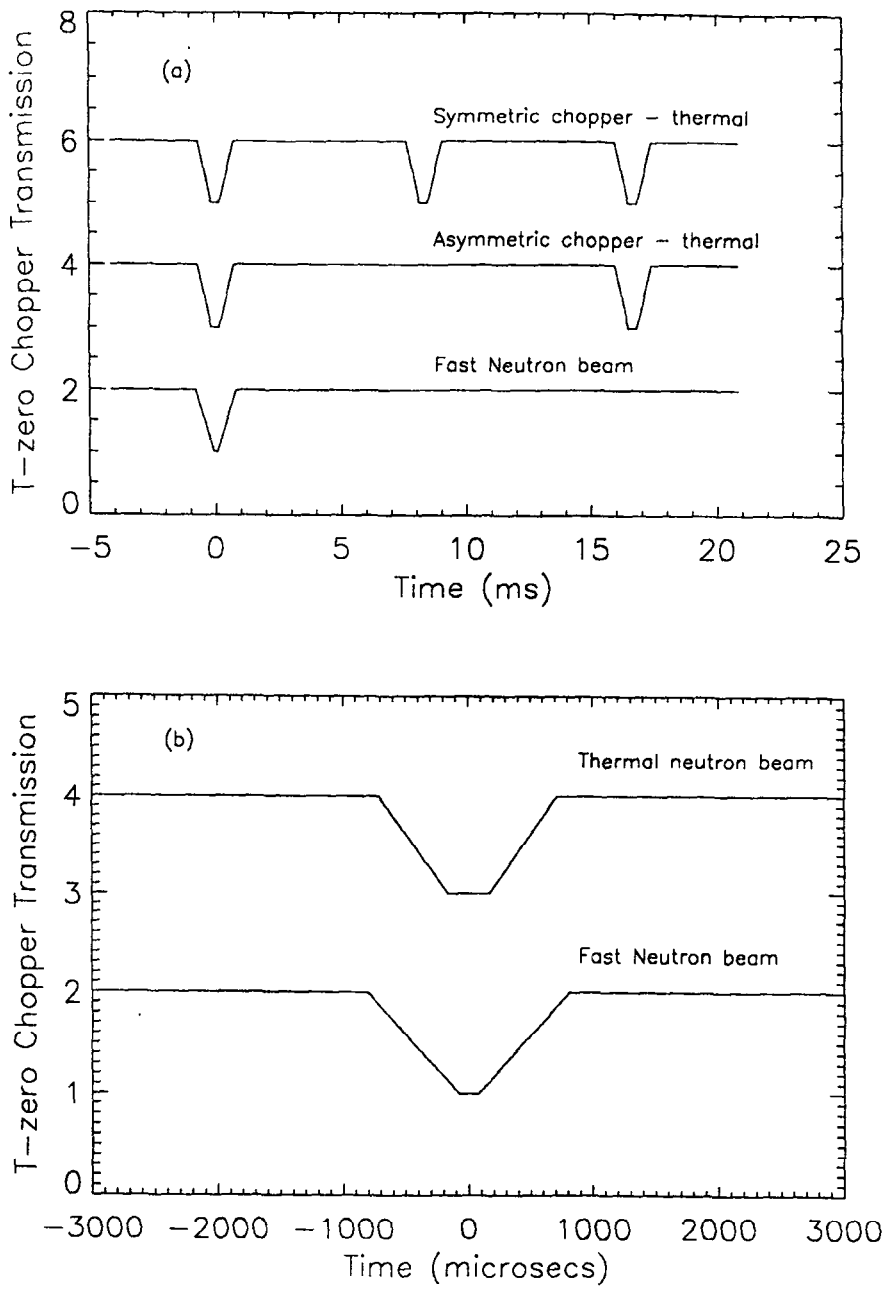

Figure 7 Calculated neutron-beam transmissions for the PHAROS t-zero chopper (see Tables I and II, and/or Ref. 3, for parameters), assuming that the chopper is completely black and that the both the thermal and fast-neutron apertures are perfect absorbers. The real geometry has been approximated by one in which the edges of the chopper blade are radial from the shaft axis. In (a), the thermal-beam performance of the real symmetric chopper is shown, followed by an equivalent asymmetric chopper and the fast-neutron performance. In (b) the thermal and fast-neutron performance in the region close to t = 0 is shown. Note that the larger fast-neutron beam is fully closed for a shorter time than the thermal beam, in agreement with the values given in Table II.

$$E_{360}\,(\mathrm{meV}) = 5.22697\times 10^{-6}\left(\frac{L}{v}\right)^2 \qquad (10)$$

where E_{180} and E_{360} correspond to the symmetric and asymmetric cases respectively.

Of course, the chopper must work for every neutron pulse that the accelerator delivers, and it must therefore spin at a frequency which is an integer multiple of the accelerator frequency, for asymmetric rotors, or an integer multiple of half the accelerator frequency for symmetric rotors, as listed in Table I. Table II gives all of the relevant parameters for the PHAROS t-zero chopper, in addition to results from Equations (3) and (6-10)

For the future, there are number of assumptions that have been made in this very simple treatment. The first is that 30 cm of inconel is the "right" stopping length for this application. As far as I know, this question has not been studied in detail, beyond estimating the number of mean free paths in the MeV range. Using conservative approximations for the high-energy neutron cross sections of the constituent elements in inconel[4], 30 cm corresponds to 8.8 mean free paths, or an attenuation to 0.015% of the incident fast-neutron flux. This might be a fruitful area for future study using Monte-Carlo simulations.

The second assumption is that there is a well-defined "fast-neutron" beam that is larger than the thermal beam, as shown in Fig. 4. It would be worthwhile to investigate what the fast-neutron beam profile looks like for both simple beams with apertures and for guides, using Monte-Carlo simulation. The question of possible streaming around the chopper, and matching it to the neighbouring apertures (which have penumbra effects), could also be investigated.

It would also be worthwhile to investigate whether it is beneficial to include any other materials, like hydrogenous materials or thermal-neutron absorbers such as boron, cadmium or gadolinium, into the rotor or its surfaces.

Finally, it seems that the actual performance of such choppers has never been measured, and it would be desirable to do so in an experiment with detectors placed before and after the rotor.

ACKNOWLEDGEMENTS

I am grateful for discussion with Mark Taylor and Ben Etuk regarding the mechanical engineering aspects discussed here, and to Phil Seeger and Luc Daemen for useful discussion. This work was supported in part by the division of Basic Energy Sciences of the U.S. Department of Energy under contract number W-7405-ENG-36.

REFERENCES

1. "Neutron Scattering Instruments at the SNS - A Guide for Potential Users", Rutherford Appleton Laboratory, February 1985

2. see for instance the MARI spectrometer in "Experimental Facilities at ISIS", RAL-88-030, February 1988

3. R. A. Robinson, M. Nutter, R. L. Ricketts, E. Larson, J. P. Sandoval, P. Lysaght and B. J. Olivier, in proceedings of ICANS-XII, Abingdon, U.K., 24-28 May 1993, Rutherford Appleton Laboratory Report 94-025, Vol. I, p.44-51.

4. Inconel X-750 has nominal composition 73.0 wt.% Ni, 15.5 wt.% Cr, 7.0 wt.% Fe, 2.5 wt.% Ti, 1.0 wt. % Nb, 0.7 wt.% Al, 0.04 wt.% C. from ASM Metals Reference Book, 3rd Ed. (ASM International, Materials Park 1993) p. 383.

Table I: Parameters that affect t-zero chopper performance

	Constraints	Typical sensible values	Value for PHAROS
Material	mechanically strong strong fast-neutron scatterer high-Z material	Inconel, Nimonic, Be	Inconel X-750
Neutron path length through the material	> some number of fast-neutron mean free paths	not known	30 cm ~ 8.8 mean free paths
Rotation frequency, ν	$n * \nu_{source}$ (for asymmetric rotor) $0.5 * n * \nu_{source}$ (for symmetric rotor)	$10 < \nu < 120$ Hz	$\nu = 60$ Hz (symmetric)
Width of blade, t	t > fast-neutron beam size (d_{fast})	$10 < t < 500$ mm	t = 116 mm
Radius of rotor, R	$2 * t < R < 0.5 *$ distance to adjacent beam	$100 < R < 1000$ mm	R = 0.35 m
Source-Rotor distance, L	beyond biological shield, but before sample	$5 < L < 20$ m	L = 14 m

Table II: Parameters and Characterisics for the t-zero chopper on PHAROS[3] at LANSCE.

Parameter	Symbol	Standard/Thermal	Fast-Neutron
source-chopper distance	L	14 m	
chopper radius	R	350 mm	
chopper rotation frequency	ν	60 Hz	
chopper tip speed	v	132 ms^{-1}	
beam width	d	72.5 mm	96.9 mm
chopper blade width	t	116.0 mm	
Idealised maximum energy	E_{max}	3.39 eV	1.90 eV
Energy at which beam begins opening	E_{start}	37.7 eV	195 eV
Energy at which beam is fully open	E_{full}	1.86 eV	1.47 eV
Energy when other blade re-enters beam	E_{180}	14.75 meV (12.5 - 17.6 meV)	
Energy when original blade re-enters beam	E_{360}	3.69 meV (3.4 - 4.0 meV)	
allowable jitter	t_{jitter} (μs)	165 μs	72.4 μs

Targets and Moderators

TARGET AND MODERATOR NEUTRONICS

ICANS-XIV
14th Meeting of the International Collaboration on
Advanced Neutron Sources
June 14-19, 1998
Starved Rock Lodge, Utica, Illinois, U.S.A.

COMPARISONS OF MCNP THERMAL SCATTERING KERNELS IN A CALCULATION OF THE SPECTRUM FROM THE RAL LIQUID HYDROGEN MODERATOR.

D.J. Picton, T.D. Beynon and T.A. Broome

School of Physics and Space Research, The University of Birmingham,
Birmingham B15 2TT, England

ABSTRACT

A comparison was made between MCNP calculations, for varying ortho/para concentrations, with experimental measurements of the neutron spectrum from the ISIS liquid hydrogen moderator.

The original calculations were performed using the standard $S(\alpha, \beta)$ thermal scattering kernels, HPARA and HORTHO. Unfortunately the agreement between the calculated and measured spectra was poor. In particular, the calculated flux showed strong fluctuations with energy, which are not seen in the measured spectra.

This problem was reported by other authors, including G. Russel et al., during the Cold Moderator workshop at Argonne, Sept. 28 - Oct 2 1997. It was reported that the cause had been identified; the angular bin structure used in the preparation of the kernels was too coarse. A new set of kernels (PARAH and ORTHOH) had been calculated using finer bins, and had been shown to produce reasonable results. It was agreed that these kernels would be made available to workshop participants on a pre-release basis.

We subsequently repeated our calculations with the new kernels, and our results also show greatly improved agreement between measured and calculated spectra. A best fit was obtained for 100% para hydrogen, and the new results showed close agreement between calculated and measured spectra up to about 5.5 Å. For longer wavelengths the results diverge, with the calculated fluxes apparently overestimating the measured spectrum.

Keywords: Kernels, ISIS, hydrogen, moderator

1. Introduction

An original set of calculations on the ISIS liquid hydrogen moderator was presented at the Cold Moderator Workshop, for varying ortho/para compositions 1. For these calculations we applied a patch to MCNP to permit the mixing of $S(\alpha, \beta)$ scattering laws for ortho- and para-hydrogen. Unfortunately a bug was found in the modified code; it apparently failed [2] to calculate a correct value for the total cross section of an ortho-para mixture.

We therefore repeated all our calculations using a well-tested scheme [3] involving modified copies of cross section sets. For para-hydrogen we used the standard neutron scattering and thermal $S(\alpha, \beta)$ cross sections, but for ortho-hydrogen we prepared copies with a fictitious atomic mass number (but with the actual atomic mass left unchanged.) Para-hydrogen and ortho-hydrogen then had separate nuclide identifiers and could be mixed without any modifications to MCNP itself.

Section 2 summarizes the results of our comparison between measured and calculated spectra from the liquid hydrogen moderator at RAL. The results from the original kernels show poor agreement between measurements and calculations. The calculated spectra show spurious structure which is not seen in the measurements. This problem had been seen by others at the Workshop, and its cause had been diagnosed as a deficiency in the preparation of the standard MCNP kernels [5]. We have now repeated our calculations using corrected kernels [4] which were made available to Workshop participants. The results show a dramatic improvement in the agreement between calculated and measured data, although the fit is still not perfect.

Our conclusions, and suggestions for future studies, are given in Section 3.

2. Comparisons between calculated and measured spectra from the RAL liquid hydrogen moderator.

The calculations were carried out using the LCS codes (LAHET and HMCNP4A). A series of HMCNP4A cases was run to determine the variation in the neutron spectrum with ortho-hydrogen concentration.

All the results presented in this section have been repeated using the reliable method described in Section 1, in which ortho/para mixing is achieved using modified cross section files. Two other improvements were made: a finer energy bin structure was specified, and the spectrum was corrected for transmission through aluminium.

Fig. 1 shows the geometry of the aluminium transmission calculation. A uniformly distributed and outwardly directed source was specified at the moderator surface. The angular dependence of the source was chosen so that the flux close to the moderator surface obeyed a cosine distribution ($\phi(\theta) \propto \cos\theta$ where θ is the angle relative to the normal.) The spectrum used for the source was the calculated spectrum for pure para-hydrogen. A temperature of 20K was specified for the liquid hydrogen and the innermost can. Other materials were at ambient temperature (300K).

A special 'scoring region' was defined at a distance of 15cm from the moderator surface, and the flux in the scoring region was calculated. The aluminium cans of the hydrogen moderator were then

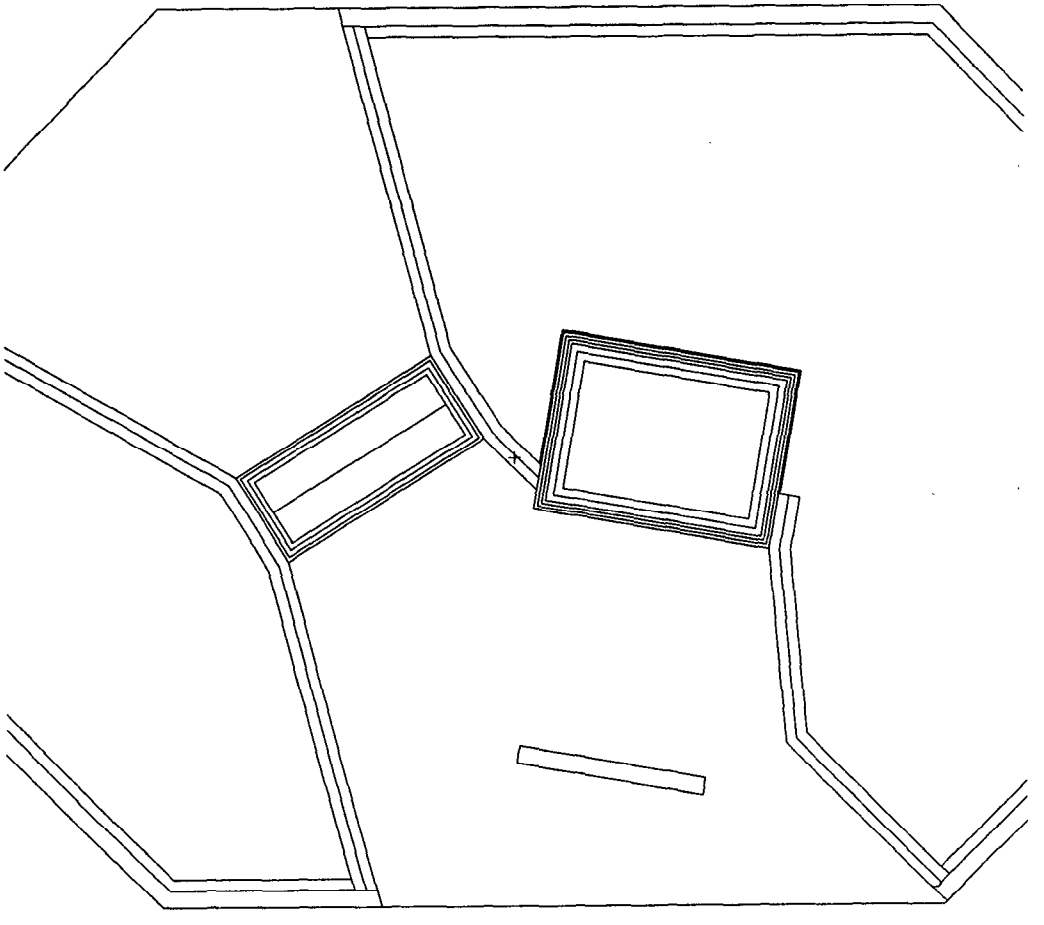

Fig. 1. Geometry used for the aluminium transmission correction, showing the liquid hydrogen moderator (right) and its three aluminium cans, and the 'scoring region' (below).

replaced by void cells, and the calculation repeated. The ratio between the two sets of results was used as a correction factor.

The accuracy of our correction factor is limited by the lack of a suitable scattering kernel for aluminium; the free gas model had to be used and therefore the results do not take into account the long-wavelength effects, e.g. Bragg scattering, which are clearly evident in the measured spectrum. The calculated factor did not vary greatly with wavelength in the range of interest (up to about 7Å) and therefore had little effect on the shape of the calculated spectrum.

Results which used the standard HPARA and HORTHO scattering kernels were unsatisfactory because the calculated spectra exhibited spurious structure which is not present in the measured spectrum (see Figs. 2 and 3). The presentation of G.Russel et al. [5] confirmed this finding. They had diagnosed the cause as the use of insufficiently fine angular bins in the preparation of the data. The kernels had been recalculated and it was shown that the resulting spectra agreed much more closely with experimental measurements. Although the new kernels [4] (PARAH and ORTHOH) will not be released to the general user community until later in 1988, it was announced that they would be made available to Workshop participants. We subsequently obtained the new kernels and used them in a new set of calculations.

Figs. 2 and 3 compare the calculated spectra for low ortho-H_2 concentrations with the measured spectrum. Fig. 2 shows the results calculated using the standard ORTHOH/PARAH kernels, and Fig. 3 shows the results with the improved HORTHO/HPARA kernels. In each case the measured spectrum is shown, normalized to give the best fit to the 100% para-H_2 case. For completeness the corresponding results for higher ortho-H_2 concentrations are also shown, in Figs. 4 and 5.

3. Conclusions

The results, particularly when calculated with the new kernels, uphold our earlier conclusion that the best fit to the measured spectrum occurs for pure para-hydrogen.

It is clear that the new kernels provide the expected improvement in the calculated results, which are now much closer to the experimental measurements. Up to about 5.5Å the agreement between the calculated curve for 100% para-hydrogen with the measured curve (Fig. 3) is within about 10%. However, the curves appear to diverge at longer wavelengths. In order to clarify this issue, it would be desirable for the experimental measurements to be extended to longer wavelengths and for a more accurate estimate of the aluminium transmission factor to be used.

Another issue for future study is the approximate geometry used in the current ISIS model, in which a rectangular form is used for all moderators (see Fig. 1). It would be desirable to determine whether a more realistic moderator geometry, using curved surfaces with appropriate radii, would further improve the agreement between the calculated and measured spectra.

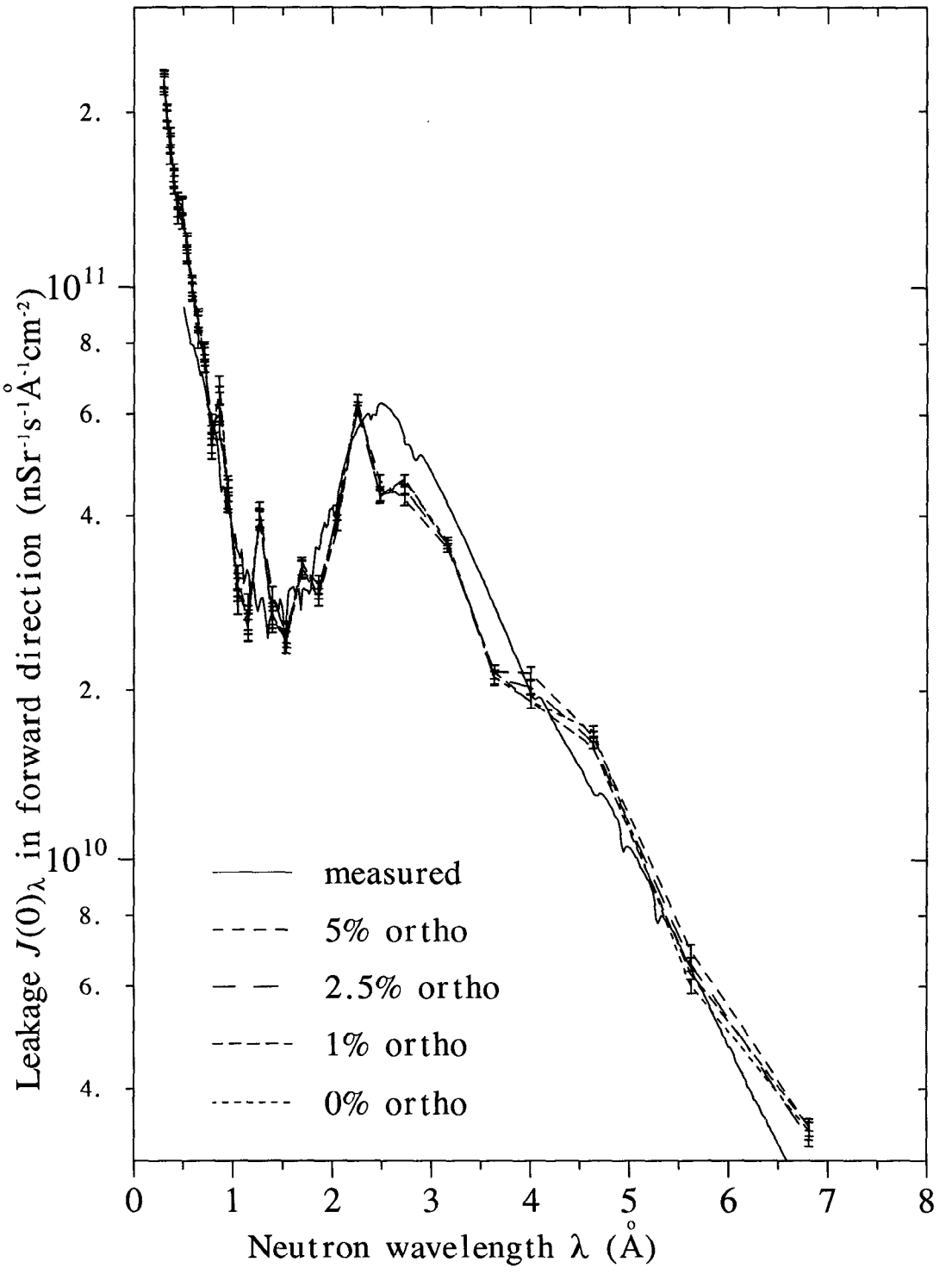

Fig. 2. Comparison of experimentally measured with calculated spectra for low ortho-H_2 concentrations using the standard (PARAH/ORTHOH) kernels.

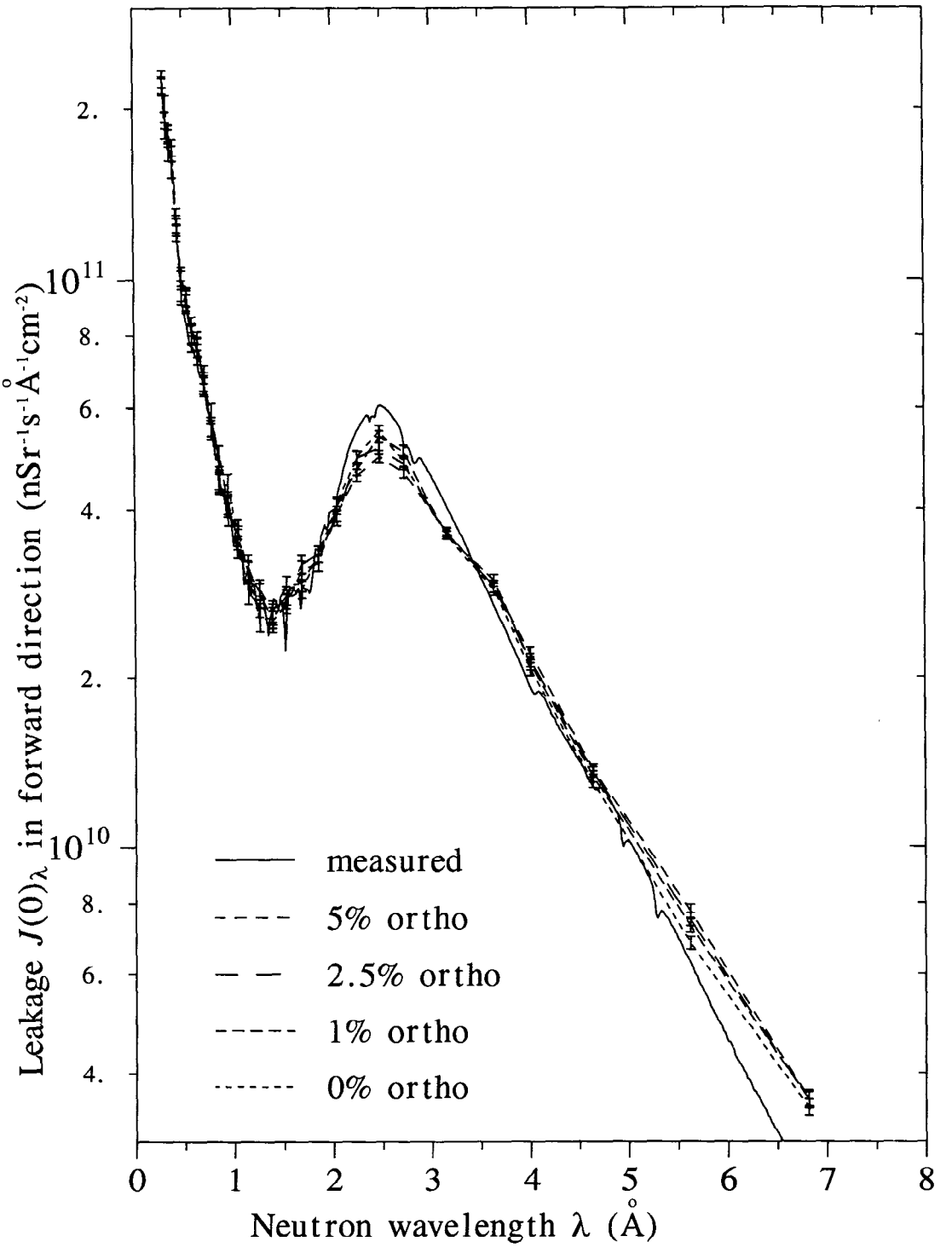

Fig. 3. Comparison of experimentally measured with calculated spectra for low ortho-H_2 concentrations using the new (HORTHO/HPARA) kernels.

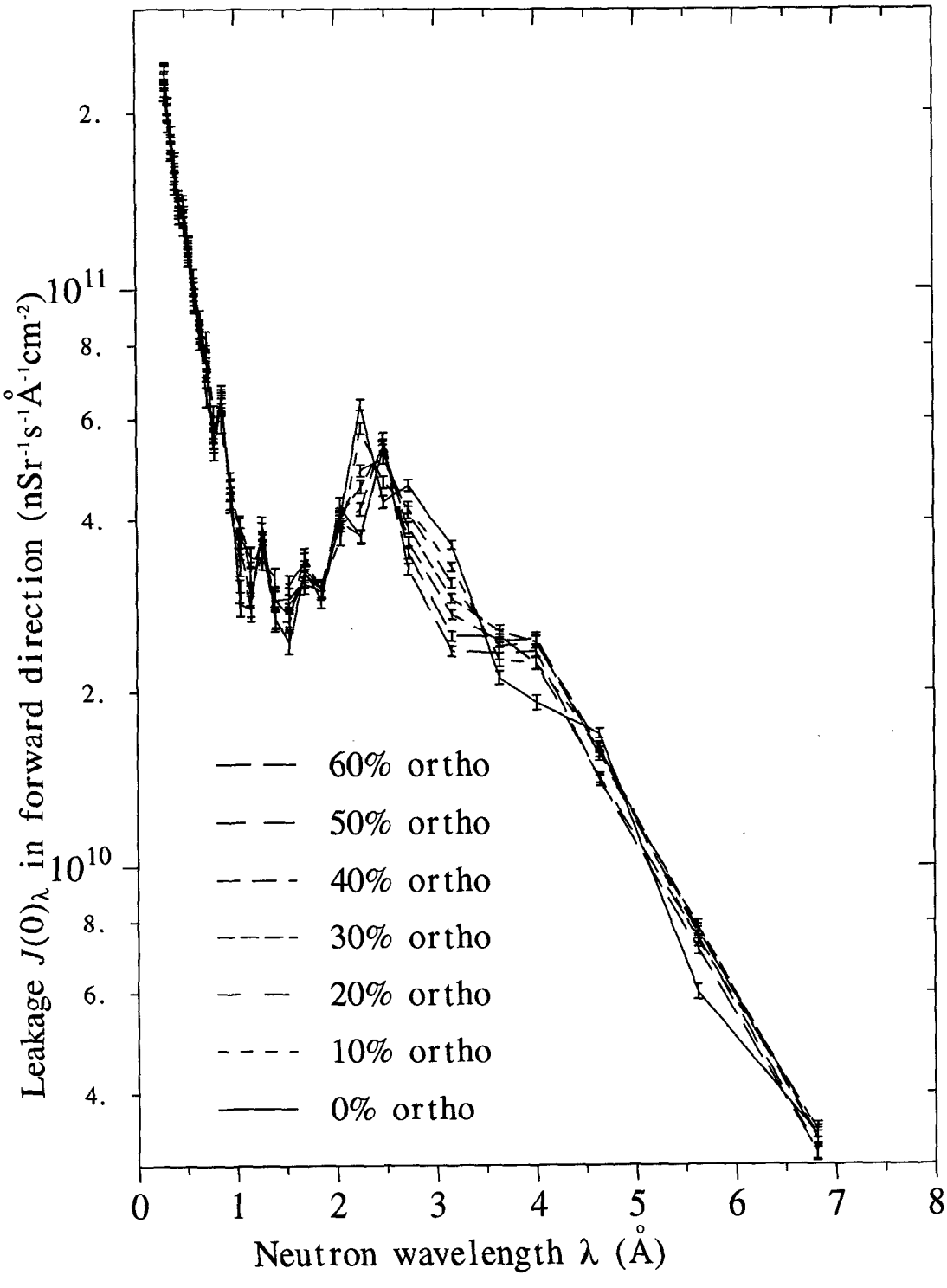

Fig. 4. Calculated spectra for high ortho-H_2 concentrations with standard PARAH/ORTHOH kernels.

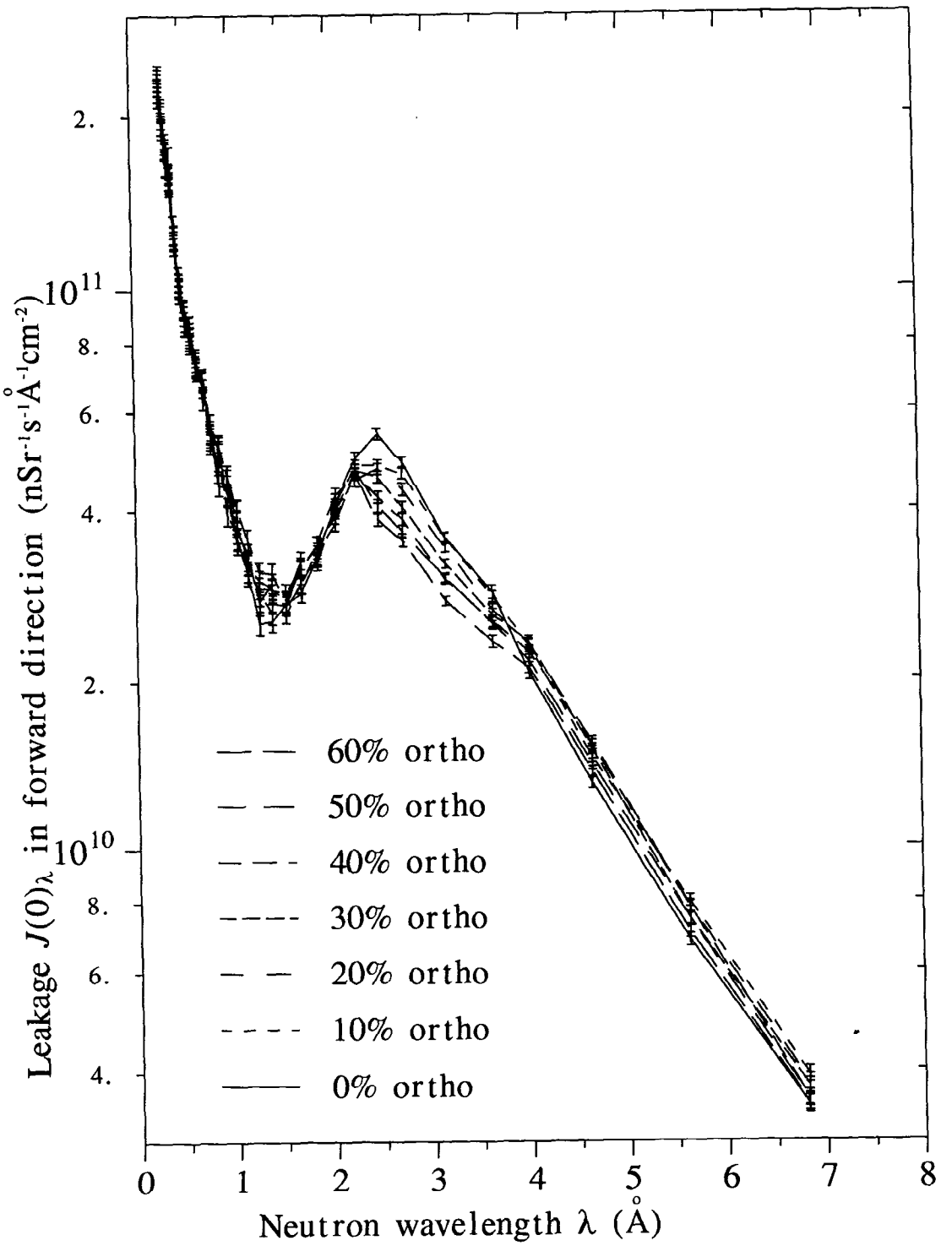

Fig. 5. Calculated spectra for high ortho-H_2 concentrations with the new (HORTHO/HPARA) kernels. correction.

4. References.

1. D.J. Picton, T.D. Beynon and T.A. Broome,"Hydrogen Moderator Performance Calculations." Paper presented at the International Workshop on Cold Moderators, September 28 - October 2 1997, Argonne, Illinois, U.S.A.

2. Hiroyuki Kadotani, private communication.

3. R.E. Prael, "Ortho/Para Mixing". Los Alamos memorandum no. X-6:REP-90-179, 9 March 1990.

4. P. Ferguson, private communication.

5. G. Russel, P. Ferguson, E. Pitcher and B. Patton, "Lujan Center Cold Moderator Comparisons." Paper presented at the International Workshop on Cold Moderators for Pulsed Neutron Sources, September 28 - October 2, 1997, Argonne, Illinois, U.S.A.

PROGRESS REPORT: SNS NEUTRONICS STUDIES

L. A. Charlton, J. M. Barnes, J. O. Johnson and T. A. Gabriel

Oak Ridge National Laboratory,* P.O. Box 2008, Oak Ridge, TN 37831-6363

1. Introduction

The proposed Spallation Neutron Source (SNS) facility (see Fig. 1) will consist of two parts: (1) a high-energy (1-GeV) and high-powered (1-MW) proton accelerator (linac) and accumulator ring, and (2) a target station that produces low-energy (<2-eV) neutrons and delivers them to the neutron scattering instruments. It will be a 60-Hz facility, delivering 6×10^{15} protons each second in 60 1-μs pulses with a linac length of 490 m and an accumulator ring circumference of 220 m.

This paper deals with the second part of the facility: the design and development of the SNS target station proposed for Oak Ridge National Laboratory (ORNL). Some of the more recent work will be presented, including a premoderator study, validation comparisons with experiment, sensitivity studies of cryogenic H_2 moderator output to assumed ortho/para admixtures, and the construction of a more detailed model geometry.

2. Methodology

The neutronic behavior of the target system can be obtained by using Monte Carlo techniques to track the progress of various subatomic particles as they proceed through the target geometry. For low-energy transport, the MCNP [1] code was used; for high-energy transport, the codes HETC [2] and LAHET [3] were used. The various target station geometries are discussed in more detail in Ref. 4.

3. Premoderator Study

A premoderator, used together with a cryogenic moderator, can be very effective in reducing the heat deposited in the moderator material. This combination reduces demands on the cryogenic system and allows it to be made more simply and cheaper.

For this study a H_2O premoderator was placed between the target and the liquid H_2 moderator (see Fig. 2). The size of the premoderator in the plane parallel to the target surface was the same as the moderator. The thickness (distance from the side of the premoderator next to the

* Managed by Lockheed Martin Energy Research Corporation for the U.S. Department of Energy under Contract No. DE-AC05-96OR22464.

Keywords: Spallation Neutron Source, neutronics, cryogenic H_2 moderators, SNS target station

surface of the target to the side of the premoderator next to the moderator itself) was varied to assess the premoderator performance.

Both the thermal neutron current and the energy deposition in the moderator are shown vs premoderator thickness in Fig. 3. As the thickness is increased, there is first an increase and then a decrease in the current with a continuous decrease in the energy deposition. Both are normalized to unity when no premoderator is present. The decrease in the current (expressed as a fraction of the zero thickness current) is a good deal less than the decrease in the energy deposition (also expressed as a fraction of the zero thickness energy deposition). The energy deposition (and thus the cost of the cryogenic system needed to remove the energy) can be decreased by a large amount with a much smaller decrease in the neutron current. A 3-cm premoderator can reduce the energy deposition by 50%, with only a 15% loss of neutron current.

In Fig. 4 the neutron spectrum with no premoderator is shown, along with the ratio of the current when a 5-cm premoderator is used to that when no premoderator is used. The current loss at an energy corresponding to the peak in the spectrum is very small (5%), even with the large premoderator. As may be seen the thermal current loss shown in the previous figure comes mainly from higher-energy neutron loss. As the energy is increased, the current loss reaches 10% at ~30 meV, which is the approximate location of the peak in the spectrum from a H_2O moderator. Thus appreciable loss occurs only for neutrons that would be better obtained from a H_2O moderator. The penalty, in terms of current loss, is very small for neutrons in the energy range that would typically be obtained from a cryogenic H_2 moderator. A 3-cm premoderator is being incorporated into the SNS cryogenic H_2-moderator design.

4. Comparison with Activation Data [5]

In June of 1997 a series of experiments were performed at the alternative gradient synchrotron (AGS) facility at Brookhaven National Laboratory (BNL) to study the effects of proton bombardment of a container of Hg. One of the experiments consisted of placing foils at the edge of the Hg container and finding the resultant foil isotopic content by measuring the gamma-ray intensity and energy. The shape of the Hg container was that of a cylinder with a half-spherical nose on the end where the 1.5-GeV protons entered. The number of nuclei in each foil was calculated in the same manner and with the same codes being used in the SNS study. Thus the success or failure of the comparison with the activation data provides a strong test of the Hg cross sections used and of the general reliability of the SNS neutronic studies.

Typical results from this study are shown in Fig. 5, where the number of nuclei measured in the foil sample (N_0) is compared with the number calculated. This comparison is done as a function of z (the distance from the tip of the Hg longitudinally to the foil sample). In order to find the calculational prediction, one must know the total number of incident protons(N_p). Measured values for N_p varied.[6] The calculated values for N_0 using the largest and smallest values for N_p are shown in the figure. The points labeled "1-on" are for a series of foils with the same azimuthal angle. The points labeled "azimuthal average" are an average of points with the same z

but with differing azimuthal angles. As may be seen, the measured values are close to or between the largest and smallest calculated values. These values are regarded as indicating a better-than-adequate agreement given the uncertainties. For more details, see Ref. 7.

5. Sensitivity Studies of Cryogenic H_2 Moderator Output to Output from Assumed Ortho/Para Admixtures

A continuing issue when using cryogenic H_2, particularly in the presence of radiation, is the ortho/para admixture. At room temperature, H_2 has a ~70%/30% ortho/para content. As the temperature is lowered to cryogenic values, the para content should increase because after a sufficiently long period of time the H_2 should have a 100% para content in the absence of radiation. However, the admixture in a cryogenic H_2 moderator in use is usually unknown. Comparisons with experiments where the calculated neutron spectrum is matched to the measured spectrum by varying the ortho/para content give a large para content. (Picton et al. [6] found a 100% para content, for instance). The SNS studies have routinely assumed a 100% para content. The neutron output from a H_2 moderator in typical SNS geometry is shown in Fig. 6 for varying ortho/para content. The smallest neutron flux from the moderator face occurs when a 100% para content is assumed. As expected, it rapidly increases when an admixture of ortho is included. It would, obviously, be very desirable to have a known admixture when doing design studies. However, the difference between the extremes is <50%, and the use of pure para underestimates the output. Thus the SNS studies are probably conservative in their projections of neutron output from H_2 moderators. Indications are, however, that the calculations are well within a factor of 2. It is unlikely that an exact admixture will be known for the SNS studies. It is planned that sensitivity studies will be done routinely for calculations where the admixture is likely to be important.

6. The Construction of a More Detailed Model Geometry

The SNS design is an iterative process where a specific engineering design is used to produce information that then changes the engineering design, causing different information to be produced, and so on. A new rather detailed neutronic model has been constructed recently to start a new cycle. The early Hg container and H_2O shroud models used boxlike structures. The new neutronic model geometry for the current Hg container is shown in Fig. 7. The planned Hg cooling flow is represented in great detail. In the figure the main section is seen at the top with the central nose portion removed and rotated by 90°. The quarter spheres located on the sides of the nose are also shown. The main body of the Hg container,along with the surrounding H_2O shroud, is seen again in Fig. 8. Analogous detail is contained in the rest of the geometry. This model will allow detailed calculations of the material damage needed for the proper selection of materials. It will also allow an accurate calculation of the energy deposition so that the heat removal system can be planned in more detail. Many other parts of the design process will also be done more accurately and with more confidence.

7. Summary

Several calculational studies were conducted for the proposed SNS. These studies were described briefly, and the results were presented. Certain conclusions may be drawn from the results of these studies: First, the use of a premoderator allows the energy deposition in a cryogenic H_2 moderator to be greatly decreased with little penalty in neutron current loss at energies where a H_2 moderator would typically be used. Second, a comparison has been made between the results of the neutronics codes used in the SNS design and experimental activation data. This comparison tends to validate both the Hg cross sections used in the calculations and the general integrity of the neutronics calculations. Third, a sensitivity study has been made of the effect of the ortho/para admixture of H_2 in a cryogenic H_2 moderator on the neutron output of the moderator. This study indicates that the previous calculations of the H_2 moderator performance were conservative but were correct to better than a factor of 2.

A new geometry incorporating the latest engineering design features has been constructed and will be used to perform detailed studies, including calculations of neutron output, materials damage, energy deposition, shielding, and activation. The neutronics design and optimization analyses are now well beyond the infancy phase. It is anticipated that the general features of the SNS engineering design will be fixed in the next year and the neutronics modeling and calculations will be consistent with this design.

References

[1] J. F. Briesmeister, Ed. "MCNP-A General Purpose Monte Carlo Code for Neutron and Photon Transport," LASL Report LA-7396-M, Rev.2 (Sept. 1986)

[2] T. A. Gabriel et al., "CALOR87: HETC87, MICAP, EGS4, and SPECT, A Code System for Analyzing Detectors for Use in High Energy Physics Experiments," Proc.Workshop on Detector Simulation for the SSC, ANL, Aug. 24–28, (1987).

[3] R. E. Prael and H. Lichtenstein, "User Guide to LSC: The LAHET Code System," Los Alamos National Laboratory.

[4] L. A. Charlton, J. M. Barnes, J. O. Johnson and T. A. Gabriel, "Neutronic Design Studies for the National Spallation Neutron Source (NSNS)." Proc. Topical Meeting on Nuclear Applications of Accelerator Technology, Albuquerque, NM, Nov 16–20, 1997, 281.

[5] The work in this section was done as part of the ASTE (AGS Spallation Target Experiment)collaboration.

[6] H. Takada, "Measurement of Total Number of Incident protons with Activation Method," Presented at the 2nd General Meeting of the AGS Spallation Target Experiment (ASTE), Paris, France, Sept. 25 and 26, 1997.

[7] L. A. Charlton, E. Jerde, D. C. Glasgow and T. A. Gabriel, "Foil Analysis of 1.5 GeV Proton Bombardment of a Hg Target," Submitted to *Nuc. Inst. and Meths.*

[8] D. J. Picton, T. D. Beynon and T. A. Broome, "Hydrogen Moderator Performance Calculations," International Workshop on Cold Moderators for Pulsed Neutron Sources, Sept. 28–Oct 2, 1997, Argonne National Laboratory, (1997).

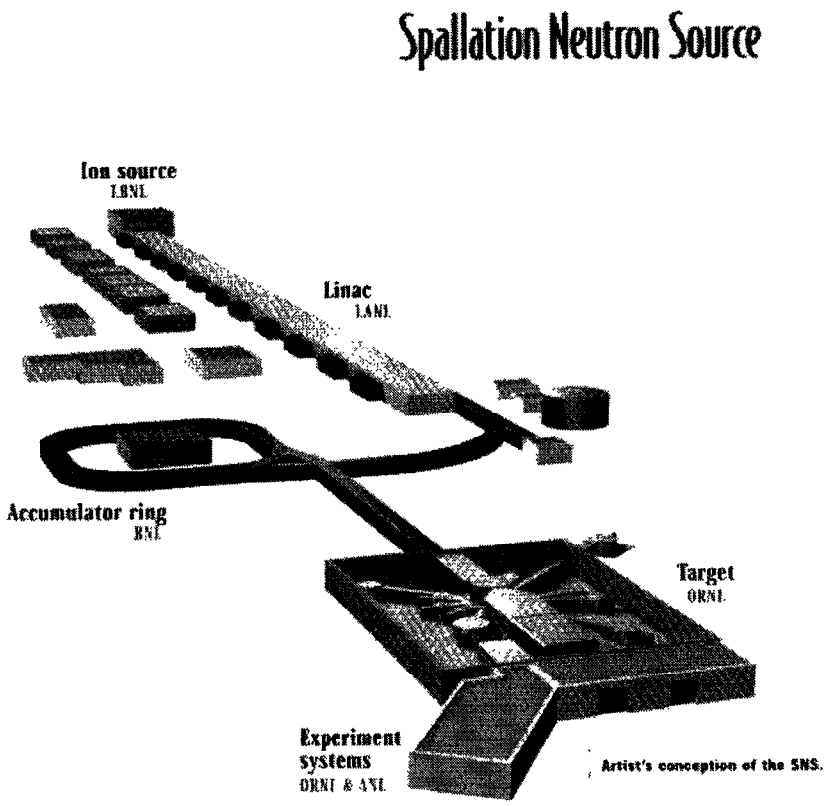

Fig. 1. Artist's conception of the Spallation Neutron Source (SNS).

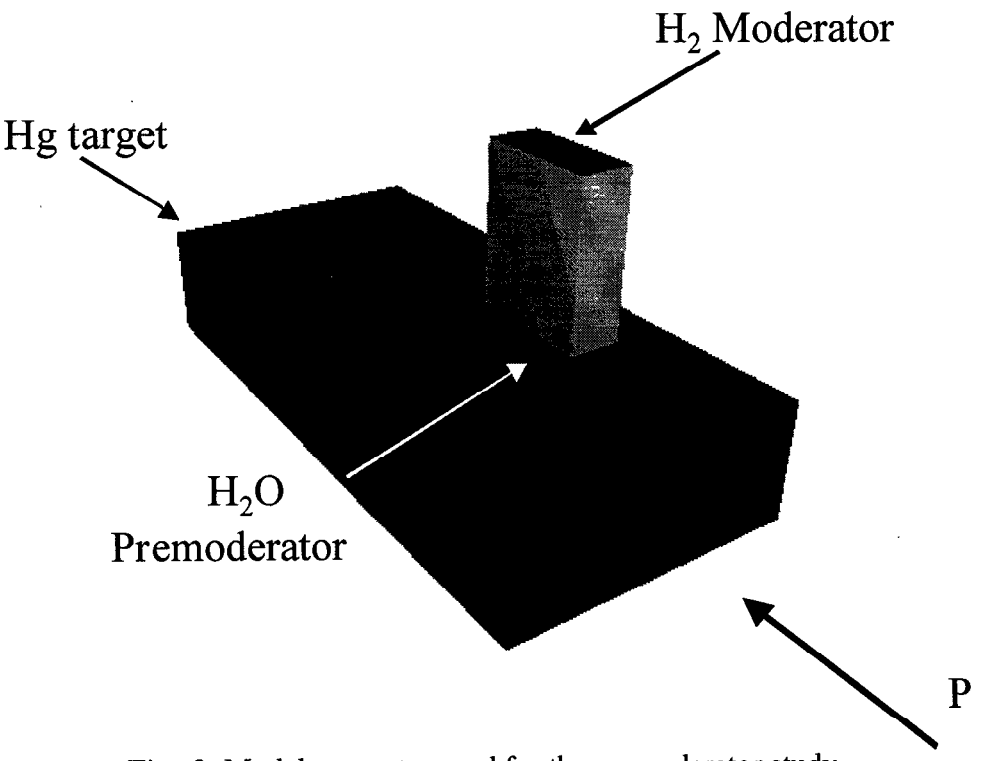

Fig. 2. Model geometry used for the premoderator study.

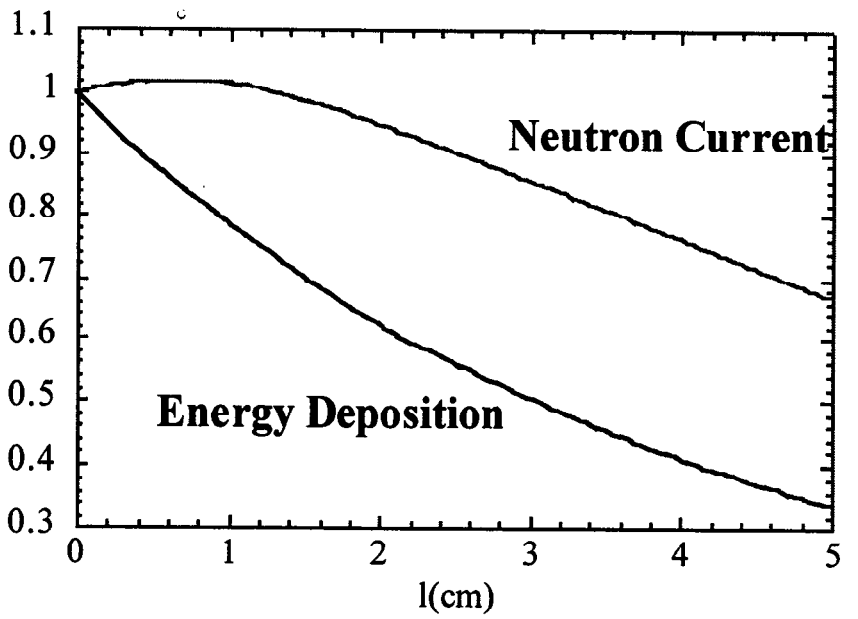

Fig. 3. Thermal neutron current and energy deposition vs the premoderator thickness (l).

Fig.4. Spectrum with no premoderator and the ratio of the spectrum with no premoderator to that

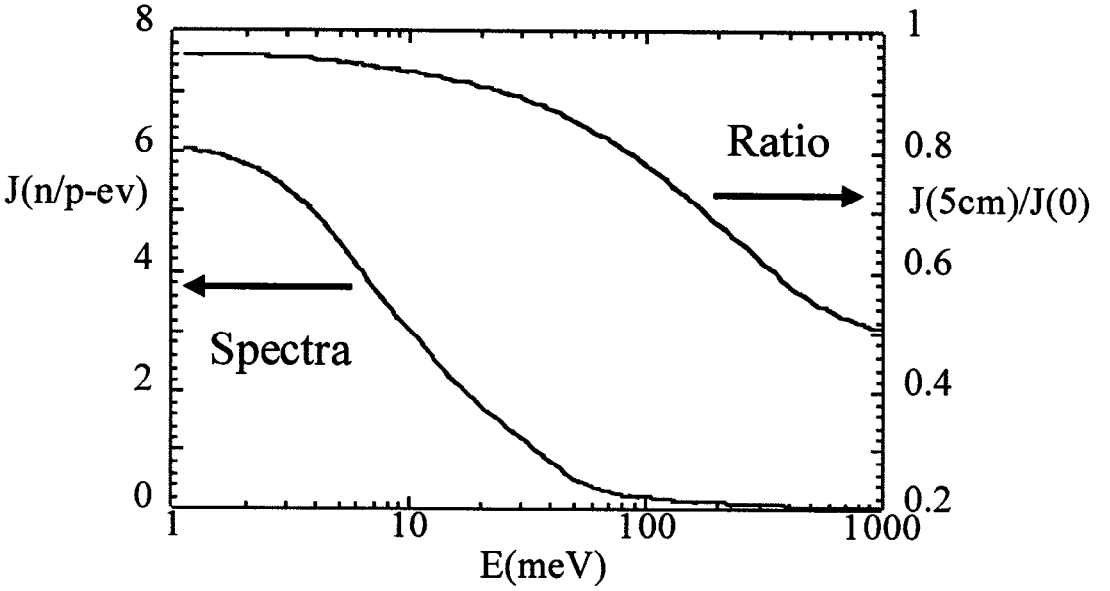

with a 5-cm premoderator included.

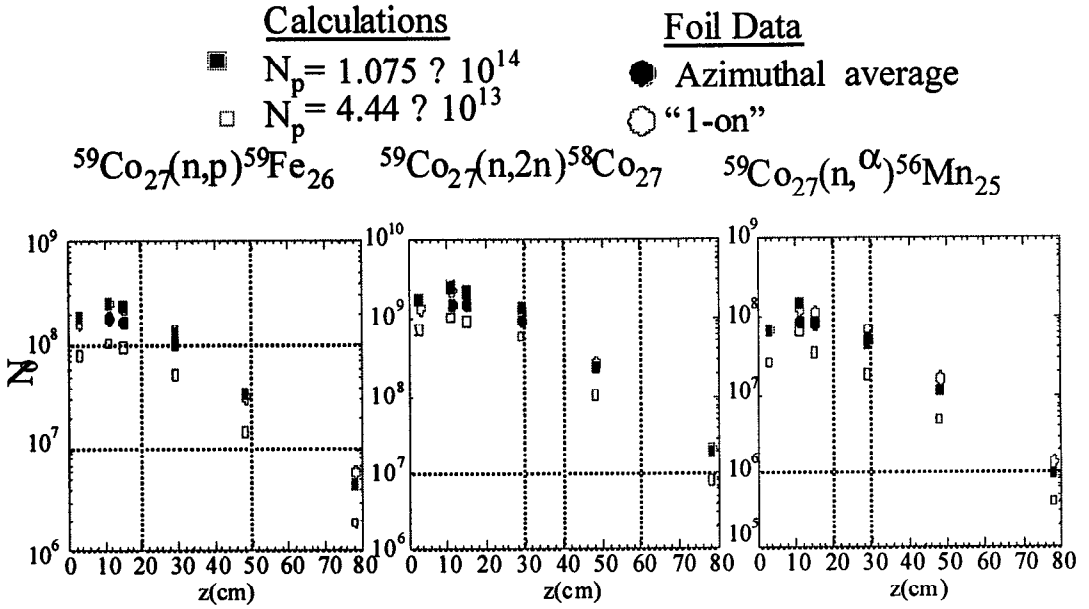

Fig. 5. Comparison between calculational and experimental results show good spatial agreement.

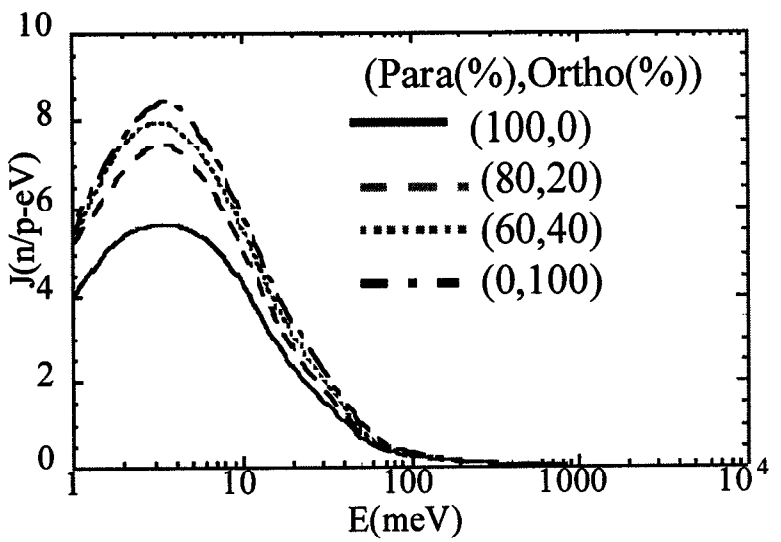

Fig. 6. Neutron spectra from cryogenic H_2 moderator for varying ortho/para admixtures.

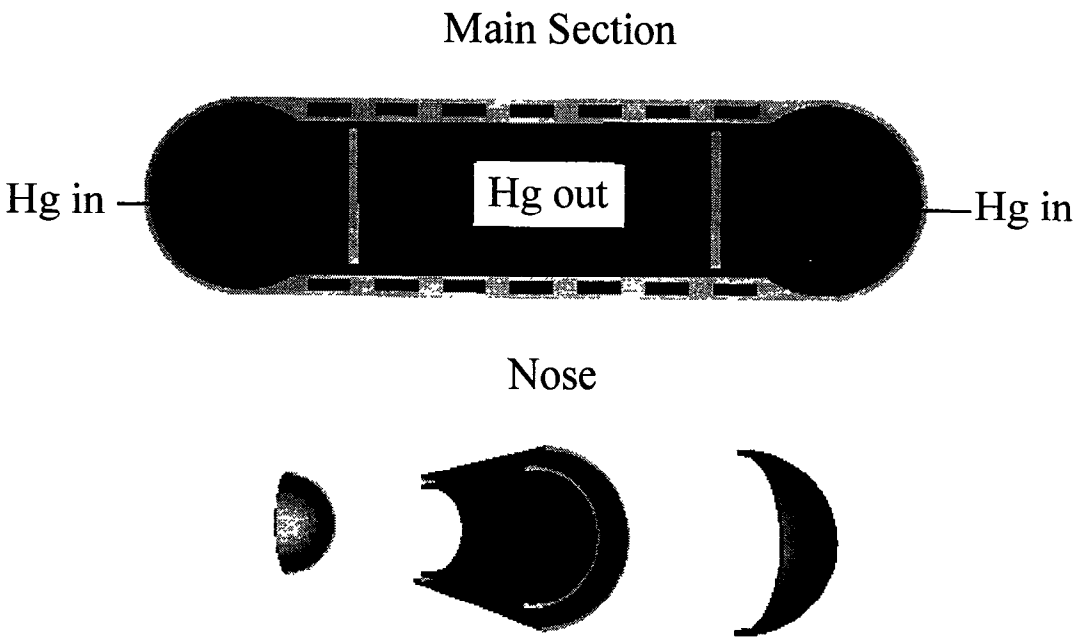

Fig. 7. New neutronic model: Hg container.

Fig. 8. New neutronic model: Main sections of the Hg container and H_2O shroud.

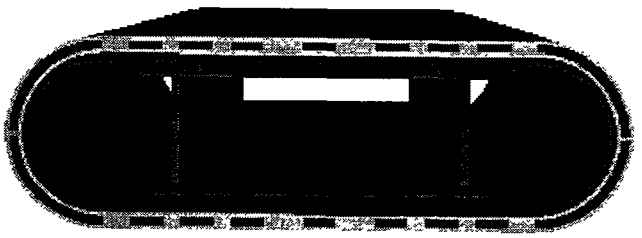

Outer section – H_2O Shroud
Inner section - Hg Container

ICANS XIV
14th Meeting of the International Collaboration on Advanced Neutron Sources
June 14–19, 1998
Starved Rock Lodge, Utica, Illinois, USA

A Modular Approach to the Design of Cold Moderators

A.T.Lucas

Oak Ridge National Laboratory, TN, USA

Abstract

Cold moderators are usually designed to the specific requirements of the parent neutron source. However since all cryogenic moderators within a broad design envelope require certain common parameters, it should be possible to create a central core design served by smaller packages designed, or selected to satisfy a wide range of individual requirements. This paper describes a modular design philosophy that has been applied to two very different cold sources with only minor changes to two of the modules in the system. Both of the systems and the basic differences between them are described in detail.

Applications

Two major projects are under way at the Oak Ridge National Laboratory. One is an upgrade program for the High Flux Isotope Reactor (HFIR) and the other, with the collaboration of four other 'U.S Department of Energy' national laboratories, is the design, and planned, construction of a Spallation Neutron Source (SNS). Both will require cryogenic moderators to provide high fluxes of cold and very cold neutrons. In each case hydrogen at supercritical pressure was chosen for the moderator material to avoid two phase flow problems normally associated with a lower pressure. A typical flow diagram (HFIR system) is shown in figure 1.

The HFIR moderator is situated in a very high radiation area, close to the reactor core which produces a heat load in the cryogenic hydrogen and the aluminum alloy moderator vessel. The total heat load is about 2.2 kW and has to be removed by the supercritical cryogenic hydrogen, (@15 bars,17K) which is circulated at a flow rate of 1 L/s. A 3-dimensional thermal-hydraulic 'CFD' analysis of the moderator vessel was carried out to determine the flow requirements and the vessel configuration to provide the necessary energy removal. A thorough stress analysis was

also carried out to optimize the vessel design for minimum material mass. In addition, a potential manufacturer of the vessel was consulted for input on machining and fabrication considerations in order to achieve an overall optimal design.

The 'SNS' spallation source has two cryogenic moderators each of which represents a heat load of 1 kW. These moderators are coupled together in a series configuration requiring one moderator to have a mean temperature about 1.5 K lower than the other. However, the series configuration gives better flow control than a parallel arrangement, allowing full flow to both moderators without a complicated balancing valve system.
Since the HFIR & SNS systems represent a very similar overall heat load, the basic hydrogen loops and automatic control systems are of similar design. Although each system has very different basic design characteristics and installation requirements it was found possible to use an identical basic cryogenic design with identical major component modules. It is not implied that a common design philosophy can be applied to all cold moderator requirements, but careful design can result in a modular system encompassing a broad operating spectrum which is scaleable to function in other similar systems. The majority of successful cold moderator systems use the passive thermo-siphon principle thereby eliminating an active pumping system. This is classically simple in operation and is, to some extent self regulating. However such a system requires careful planning of transfer line routes which usually tend to be larger than those needed for mechanically circulated systems. On the other hand active systems normally operate best with a single phase fluid (vapor or liquid). This requires the hydrogen to be pressurized, to allow it to be circulated as sub-cooled liquid, or in a supercritical phase. Operation under this scenario requires that all hydrogen in the loop has to be of high density and safety considerations dictate a careful consideration of the overall hydrogen inventory. However, there is an over-riding requirement for the cooling of the moderator vessel walls. Unless this is independently provided by a separate cryogenic loop, cooling will depend totally on the neutron moderating hydrogen flow. Future cold moderator systems are likely to be required to operate in higher radiation fluxes (therefore energy) that will require fluid flows not easily achievable with a thermo-siphon system. Also shielding demands are likely to become more challenging, making remote handling of active components more difficult. This will tend to make the more compact active circulated system a more natural choice for most applications. The availability of more reliable circulators, installed redundancy and the ability to replace a failed circulator on line will help eliminate safety and operational concerns.

What is modular

In the present context, modular is defined as a complete cryogenic system designed around a system of core units (modules) that contains those basic components that are common to a wide range of cold moderator applications. An example is the pump module. Supporting sub-systems which could differ with the application, are grouped into smaller modules: the gas handling module, purge module, vacuum stations, and standby module. Each module and its function are described later and table 'A' lists individual components. The extent of modular breakdown is a question of judgment and could vary with development, but in addition to the obvious advantage of flexibility it improves maintenance operations. It should be relatively easy to localize system problems to a specific module and to effect servicing without the need to spoil the entire vacuum

system.
Other items, such as transfer lines and even the refrigerator, could also be referred to as modules since they operate as functional packages whose purpose can be identified and redesigned. The refrigerator in this case can be switched into a standby mode to function passively at a level sufficient to keep the temperature of the moderator vessel within safe limits. Transfer lines could suit other applications with a change in length only.
The moderator vessel assembly is very specific to the particular application, but can also be described as a module.

Specific Applications

The HFIR upgrade and the SNS projects are different applications, but both have been satisfied by using a basically identical cold moderator system and modifying only two of the modules. For safety reasons a secondary inert blanket surrounds all hydrogen bearing regions over the entire system providing double containment of ambient temperature areas and triple containment of cold vacuum insulated areas.

The HFIR Reactor Cold source

The HFIR cold moderator will produce a continuous flux of cold neutrons are least equal equal in brightness to any currently available sources. The moderator is situated very close to the reactor core and a heat load of 2.2 kW is generated in it, 75% of this being deposited in the aluminum alloy material. Ref. figure 2. A design flow of 1 L/s is needed to provide vessel cooling. This flow-rate is provided by a high density cryogenic circulator. To ensure continuous operability, this system module contains an identical backup (or redundant) spare circulator. This spare is under automatic control to be activated if circulation failure is detected. Both circulators are independently electrically driven centrifugal cryogenic pumps. They have no rotating seals as the motor operates in ambient temperature hydrogen gas that is directly connected to the cold loop. Either one can be isolated from the loop, blown down to atmospheric pressure, evacuated and filled with dry helium gas through a purging system. It is then possible to replace a faulty circulator without breaking the double containment philosophy.

The moderator vessel is cylindrical with a hemispherical end and a flow smoothing inlet and outlet flared section. A roughly elliptical shape between the flow and return ways is the cold neutron viewing area that illuminates three divergent beam guides providing cold neutrons to the scattering instruments. The vessel shape is designed to optimize the conflicting requirements of good coolant flow characteristics, low mass and acceptable stress levels, while providing good neutron moderation and minimal beam interference.

The critical pressure of hydrogen is approximately 13 bar abs and the system includes gas handling equipment designed to maintain a higher pressure than that at all times. For safety reasons the system can be operated in a standby state to allow the reactor to continue at full power (but without cold neutron production) in the event of a cold source failure. This is

achieved by cooling a lower density hydrogen gas with liquid nitrogen and increasing the circulation rate to 2.25 L/s. A separate lower power circulator provides enough hydrogen flow to hold the aluminum moderator vessel in a safe condition.

The main hydrogen loop and all enclosed systems (including vacuum and inert blankets) are protected against positive pressure excursions by rupture discs and relief valves that are vented to a nitrogen purged manifold before being released to the atmosphere through an elevated stack .

The SNS Spallation source cold moderators

The spallation source will require two cold moderators placed above the mercury target. These are coupled together in a series configuration to allow a single refrigerator and hydrogen loop. This means that the first moderator in line has an average temperature about 1.5 K cooler than the other; however, full flow through each ensures adequate cooling. The total heat load is 2kW which is very close to that of the HFIR system but the installation geometry is very different. However, the main cryogenic systems are similar in most aspects as described below. Ref. figure 3.

Individual modules

i) Pump Module

(High Flux Isotope Reactor - HIFR)

This module is the heart of the system and incorporates the heat exchanger that interfaces the hydrogen loop with the refrigerant, all three circulators, double valving for the circulators, three pressure and temperature sensor systems and the loop pressure interface vessel. The stainless steel containment housing is about 8 feet in diameter and 4 feet tall and is double walled to incorporate part of the inert gas blanket. A flow diagram is shown in figure 4.

(Spallation Source - SNS)

This is virtually identical to that for the HFIR but the appendage that contains the low density (standby state) circulator has been removed and blanked off. Instead it is planned to develop a variable geometry circulator (in which the effective thickness of the impeller can be changed by a stepper motor that axially moves the entire rotor and shaft assembly). Together with speed adjustment this allows a single circulator to cover both normal and standby operational requirements. It also allows infinite adjustment of the flow during cool-down by causing the power drawn by the main electric motor to remain constant as fluid density increases. This should result in greatly improved stability and smoother transitions between normal and standby states.

ii) Refrigerator (HFIR & SNS)

The refrigerator selected is an 'off-the-shelf' design (which uses helium as the refrigerant with liquid nitrogen pre-cooling), up to five screw compressors and four reciprocating expander engines provide a maximum power of 3.5 kW at 20K. It will operate at the maximum power required for normal operation (approximately 2.5 kW) plus a small contingency which will be finely controlled by an electrically powered control heater. A special feature allows the helium refrigerant to bypass the expanders and cool the hydrogen directly using the liquid nitrogen pre-cooler, this is termed the standby state. No compressors are required in that condition as helium flow will be provided by an auxiliary gas circulator. No temperature control is required since temperatures would be limited by the liquid nitrogen. This makes the standby state available over a wide range of system failures. Since the refrigerator is considered an independent module, alternative refrigerator choices would be workable.

iii) Transfer lines (HFIR & SNS)

The transfer line design will be similar for both applications, differing only in length. The transfer lines are made from spirally convoluted stainless steel tubes. A concentric pipe configuration is used, which minimizes heat loss and transfer line footprint. This transfer line design is easily transported in long lengths and expansion/contraction of the cold inner tubes, due to temperature differences, are self compensating. The main line is a five-concentric-tube design for flow-vacuum-return-vacuum (with multi-layer insulation) -inert gas blanket (the two vacuums are interconnected). A second transfer line connects the refrigerator to the pump module. This is similar in design, but since the transport fluid is helium gas it does not require the outer helium tube. The concentric pipe arrangement is shown in figure 5.

iv) Gas handling system (HFIR & SNS)

The gas handling system is in three parts and is shown schematically in figure 6:

- A large double walled hydrogen storage vessel which allows the system to reside at a uniform pressure of 4 bar abs under total shutdown conditions.

- A hydrogen gas transfer pump that raises the main loop pressure to 14 bar abs at the start of a cool-down and maintains this pressure by adding gas from the storage tank.

- A vacuum vessel that contains the hydrogen feed vessel and all valves associated with the ambient temperature gas handling system.

At the start of a cool-down, gas is drawn from the storage vessel to raise the loop pressures to 14 bar abs. As the gas cools and its density increases, the loop supercritical pressure is maintained. Under operating conditions the storage vessel is reduced in pressure to a partial vacuum. The loop pressure is controlled thereafter by opening the inlet valve from the feed vessel, or the return valve to the storage vessel in response to the hydrogen loop automatic control system. The inert

blanket for the gas handling system is low vacuum rather than helium gas. This is a safety measure since the main storage vessel operates at partial vacuum under normal conditions. It also provides insulation when cold gas is admitted to the storage vessel during system shut-down. This mode of operation reduces the overall hydrogen inventory since the majority of it is utilized in the loop. If an application did not require such a mode of operation it could be replaced by a more appropriate system.

v) Purge module (HFIR and SNS)
The purge module comprises a helium gas vessel containing the purge pump and valves. This module allows either of the high density circulators to be isolated, blown down, evacuated and filled with dry helium for replacement. The module also includes relief systems to protect sections of piping that could be isolated by the closure of two valves at the same time. The module will also allow initial purging of whole hydrogen system. The circuitry of this module could be changed considerably to suit specific requirements. The outer housing comprises an integral part of the inert blanket system.

vi) Vacuum modules (HFIR & SNS)
The HFIR system has three (3) separate vacuum systems and the Spallation Source two (2). These provide insulation for the following sections of the loop:

- The moderator assembly – this is separated from the rest of the loop to limit contamination in the event of a failure.

- The pump module, heat exchanger and transfer line

The HFIR has the following additional vacuum system:

- The transfer line between the point of entry through the wall of the reactor building and the moderator vessel assembly.

Each vacuum system is maintained by a vacuum station which comprises a helium housing that containing isolation valves, a turbo pump and a backing pumps. The housing comprises a part of the inert blanket system but is designed to allow quick replacement in the event of failure, without breaking the double containment philosophy. Each vacuum system is equipped with a gas analyzer to monitor for leaks of hydrogen or helium and a pressure relief system to protect the vessel from overpressure. Ref. figure 7.

vii) Vent system (HFIR & SNS)
Although the hydrogen operates in a closed loop, it is pressure protected by relief valves and rupture discs in the event of a pressure excursion. The vacuum and inert blanket systems are also protected from pressure excursions above 3 bar abs. More vulnerable components are housed in a safe room that is constantly ventilated. A hydrogen sensor in the ventilation system initiates a rise in flow rate to the equivalent of one air change/min. All rupture discs, relief valves and vacuum pump exhausts are fed to a common vent manifold that is maintained at 1.5 bar abs with a nitrogen gas purge. In the event of the operation of a relief system the manifold exhausts into a

dedicated elevated vent stack. Ref. figure 8.

viii) Control system (HFIR & SNS)
The control system is PC based using readily available software and hardware. It controls the gas handling system and cold moderator operating conditions. It also monitors the circulators and initiates changeover if an operating circulator malfunctions. In extreme cases it is capable of deriving a signals to initiate reactor scrams. The control system will have built-in redundancy and an automatic transition will be initiated in the event of a control system problem. The refrigerator is set up to operate at its maximum anticipated power requirement and a control heater in the helium line substitutes for the power of the reactor. When the reactor is started, power in the control heater is reduced until the system is in equilibrium. The temperature control is not required during standby operation since the minimum temperature is limited to 77K. The high flow (but lower density) circulator is used during cool-down and a control sensor in the heat exchanger limits the temperature of the heat exchanger to avoid freezing of the low density hydrogen. When the temperature reaches about 50K, the control system switches temperature control to a sensor in the main feed line. It is ultimately planned to allow the control system to transition the system into standby automatically in the event of a cold loop problem.

ix) Moderator Vessel Assembly
This will always be specific to the application, but in many cases its design will have an impact on the configuration of one or more of the other modules.

(HFIR)
This comprises the moderator vessel which is mounted inside a vacuum chamber. The complete assembly is shrink fitted into the beam tube and the cryogenic lines are passed through the rear beam collimator section.
The complete assembly is about 13'-0" long and replacement would be a major task. Ref.figure 9.

(SNS)
The two moderator units are mounted into a vertical circular plug, which is replaced as a complete unit. However the moderator assembly can be replaced in a hot cell though it is unlikely that it could be serviced and is regarded as dispensable. Ref. figure 10.

x) Standby service module (HFIR & SNS)
This is a single walled vacuum chamber that is outside of the inert blanket. It contains a helium circulator used for the standby state, isolation valves and bypass valve. It also contains the main loop temperature control heater.

Conclusion

By the substitution of one or more modules, the entire system can be reconfigured to operate over a wide range of requirements. Within the modules themselves specific components, such as circulators, could also be readily substituted without major design or structural changes. Overall, the modular philosophy could not only minimize design effort, but offers the advantage of using a proven system that has already undergone development and operating stages.

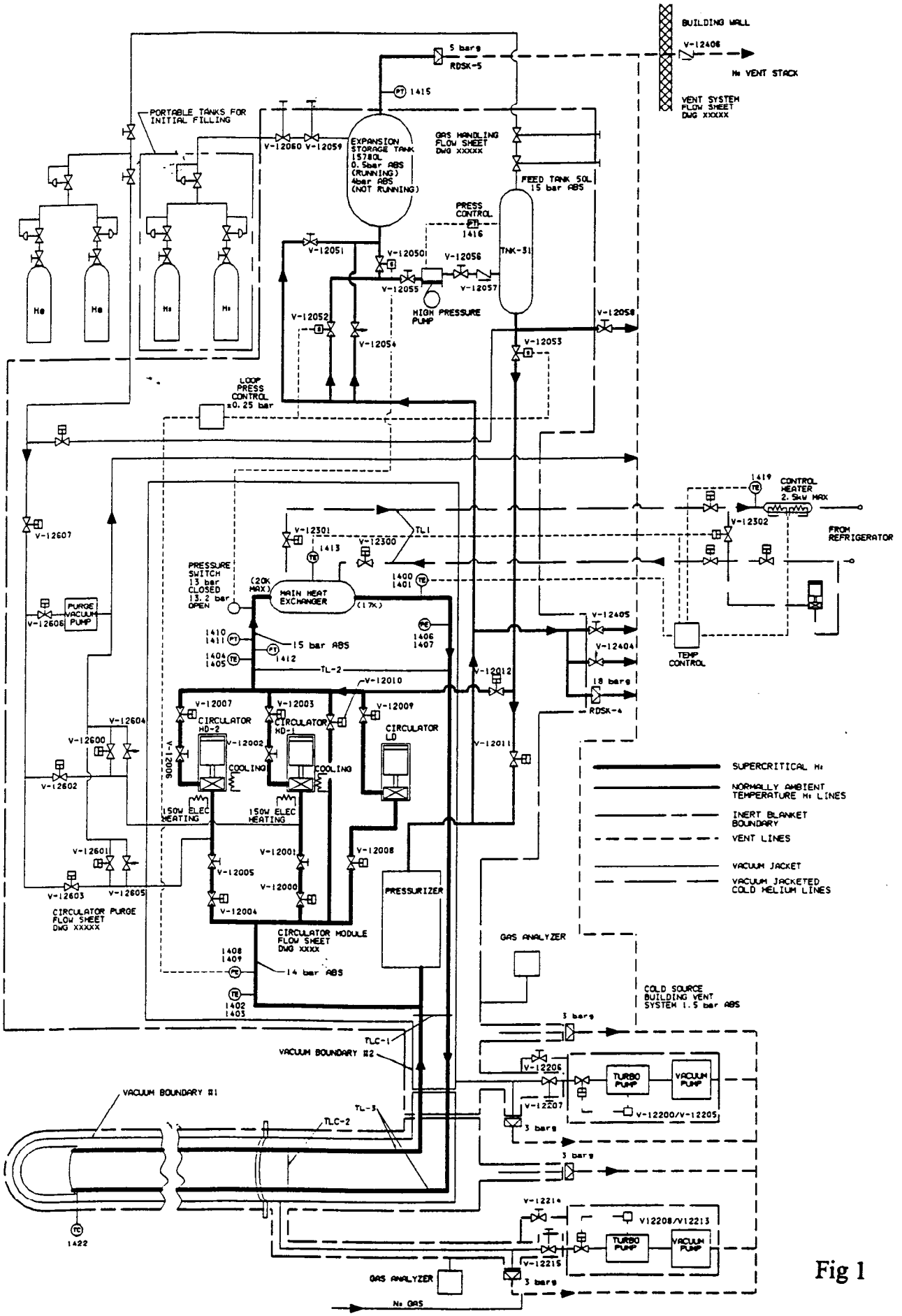

Fig 1

Flow Diagram of HFIR Cold Source system

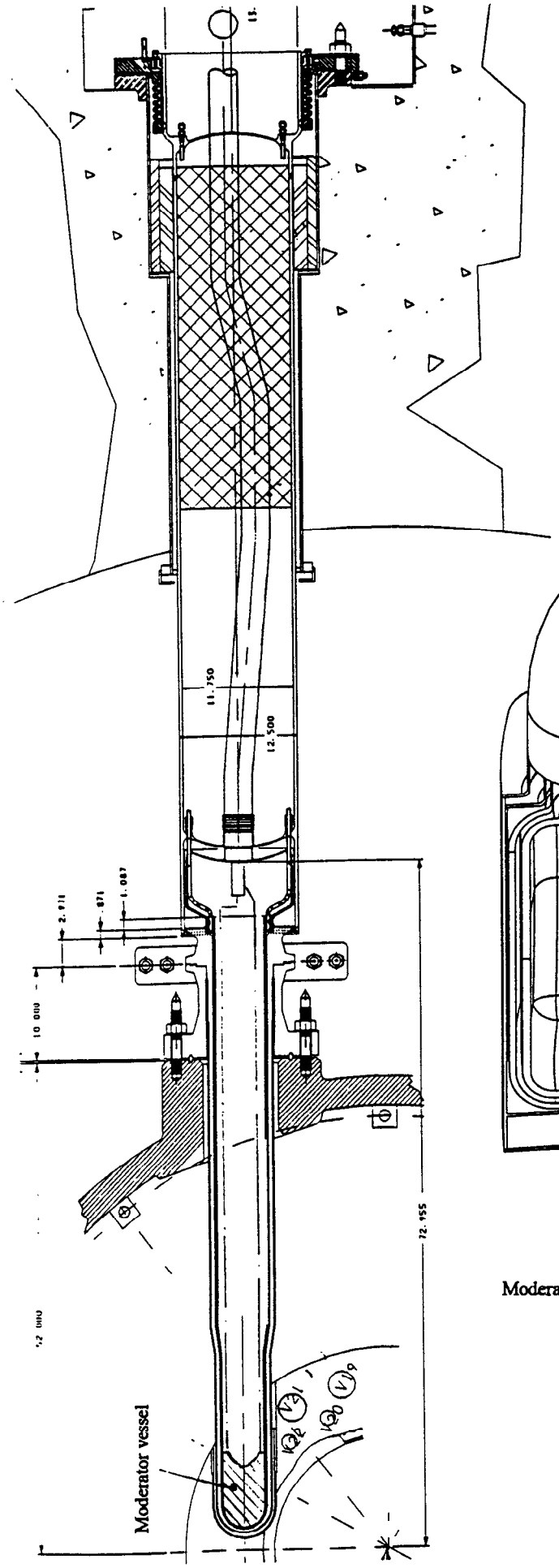

Fig 2

HFIR cold source installation

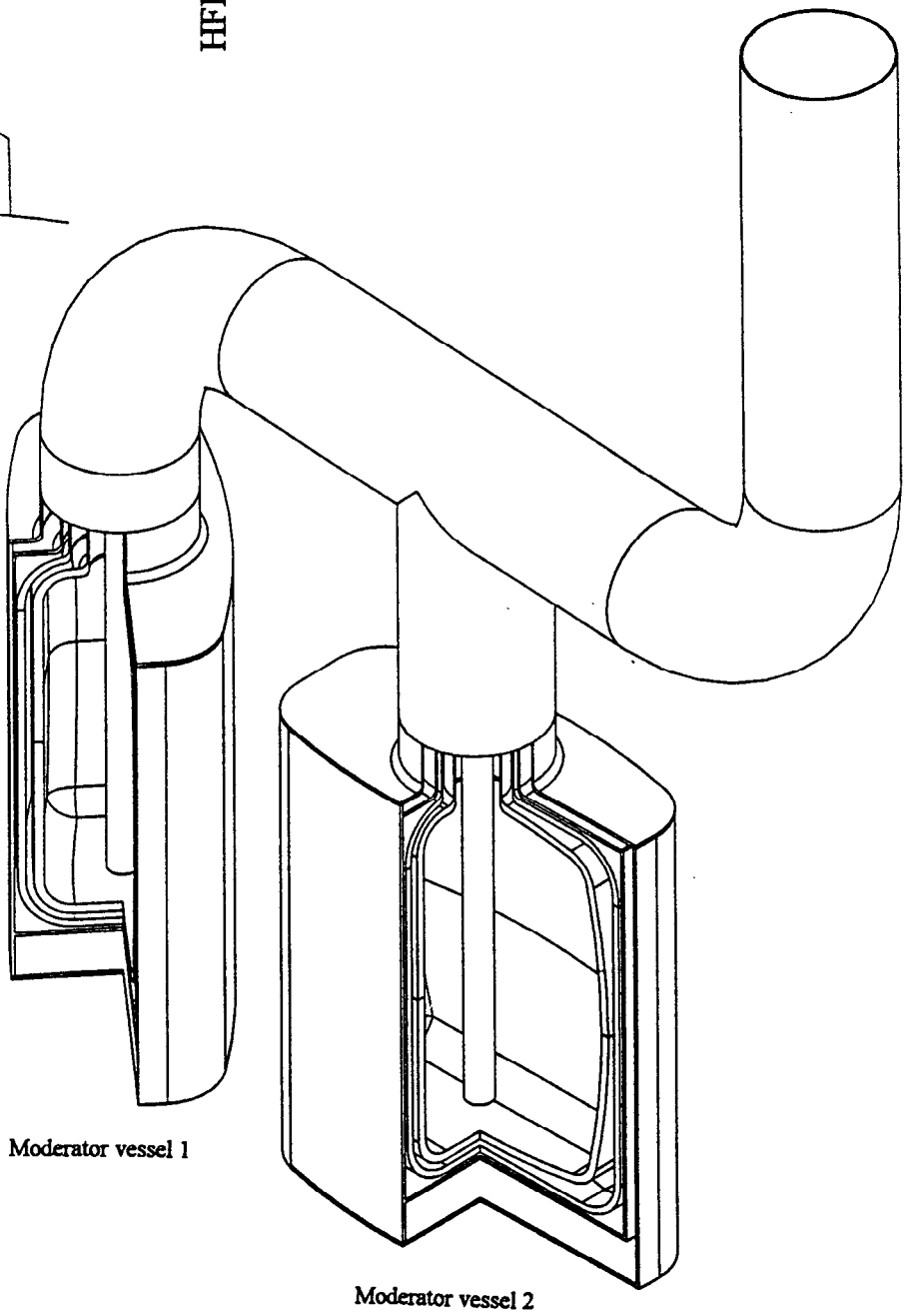

Fig 3

SNS moderator arrangement

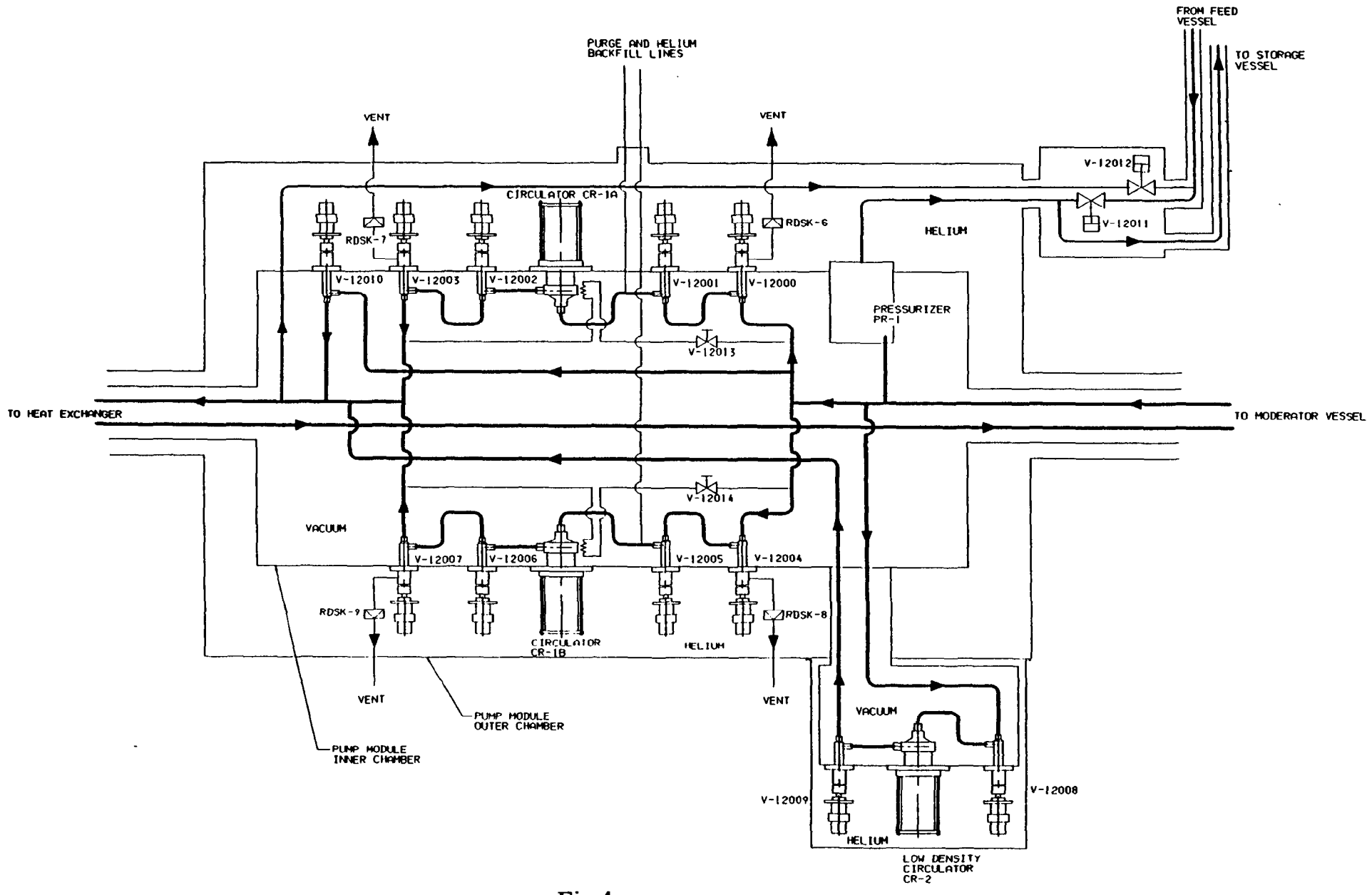

Fig 4

Schematic diagram of Gas Handling system

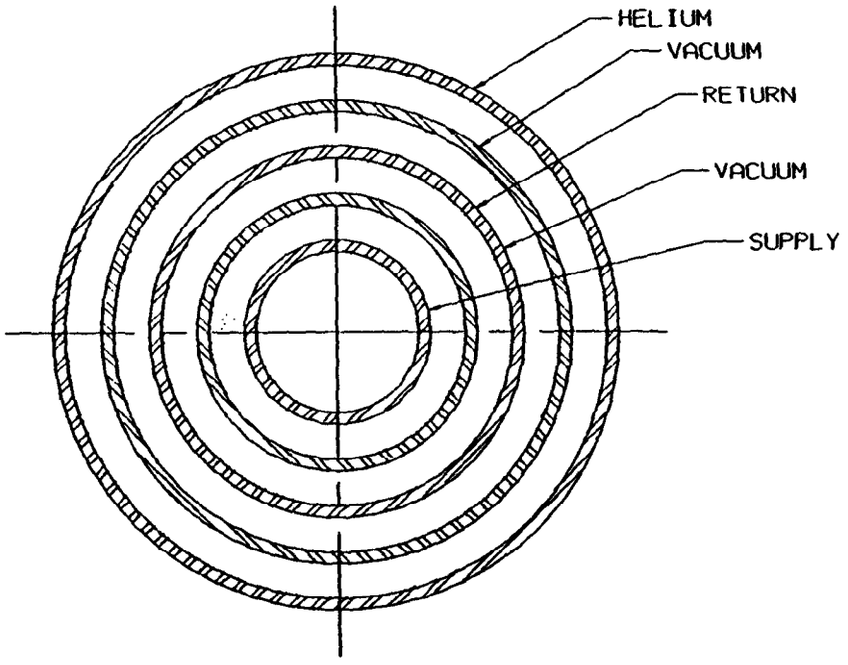

Fig 5
Transfer line pipe configuration

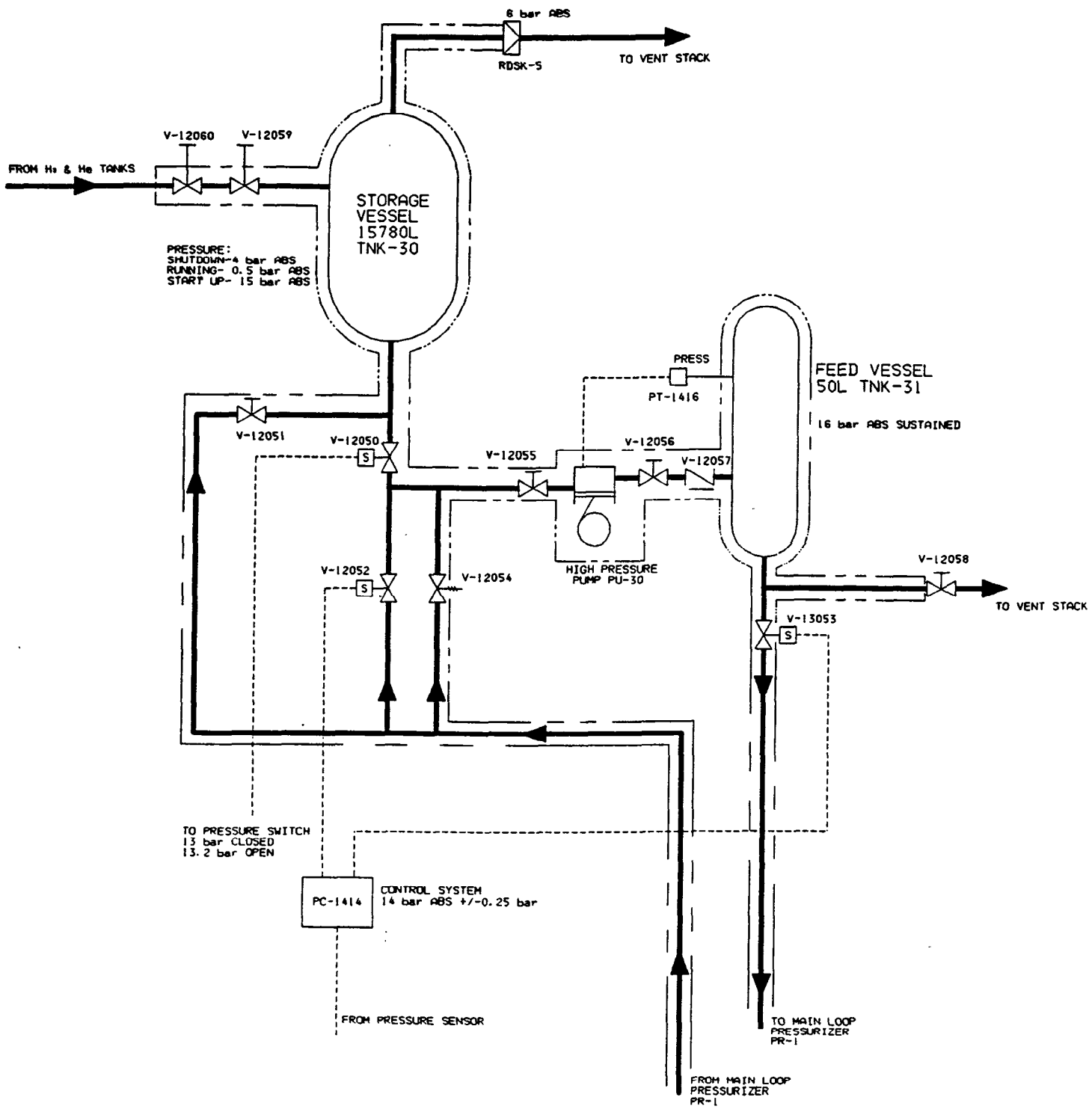

Fig 6
Gas handling arangement

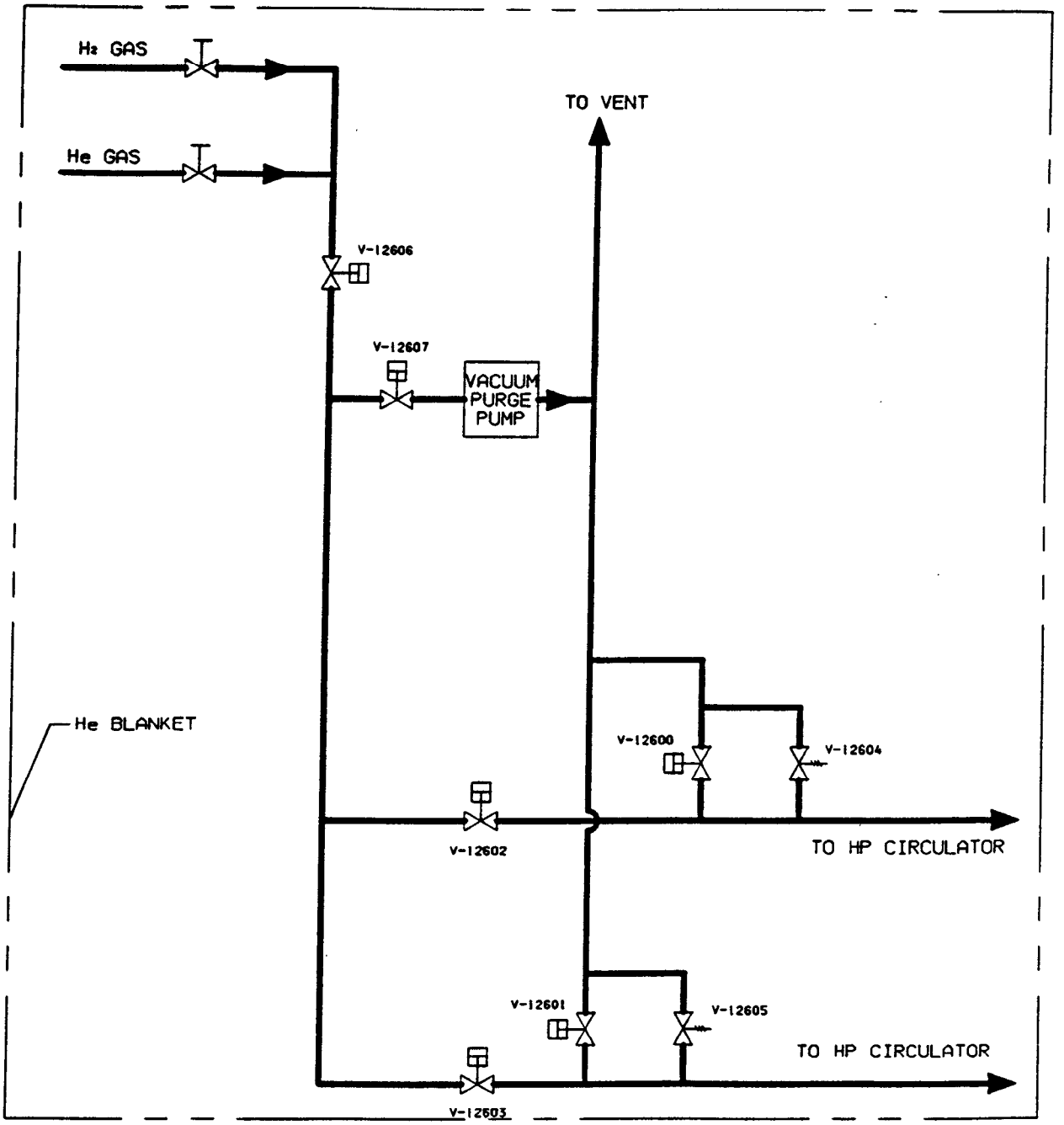

Fig 7
Purge module

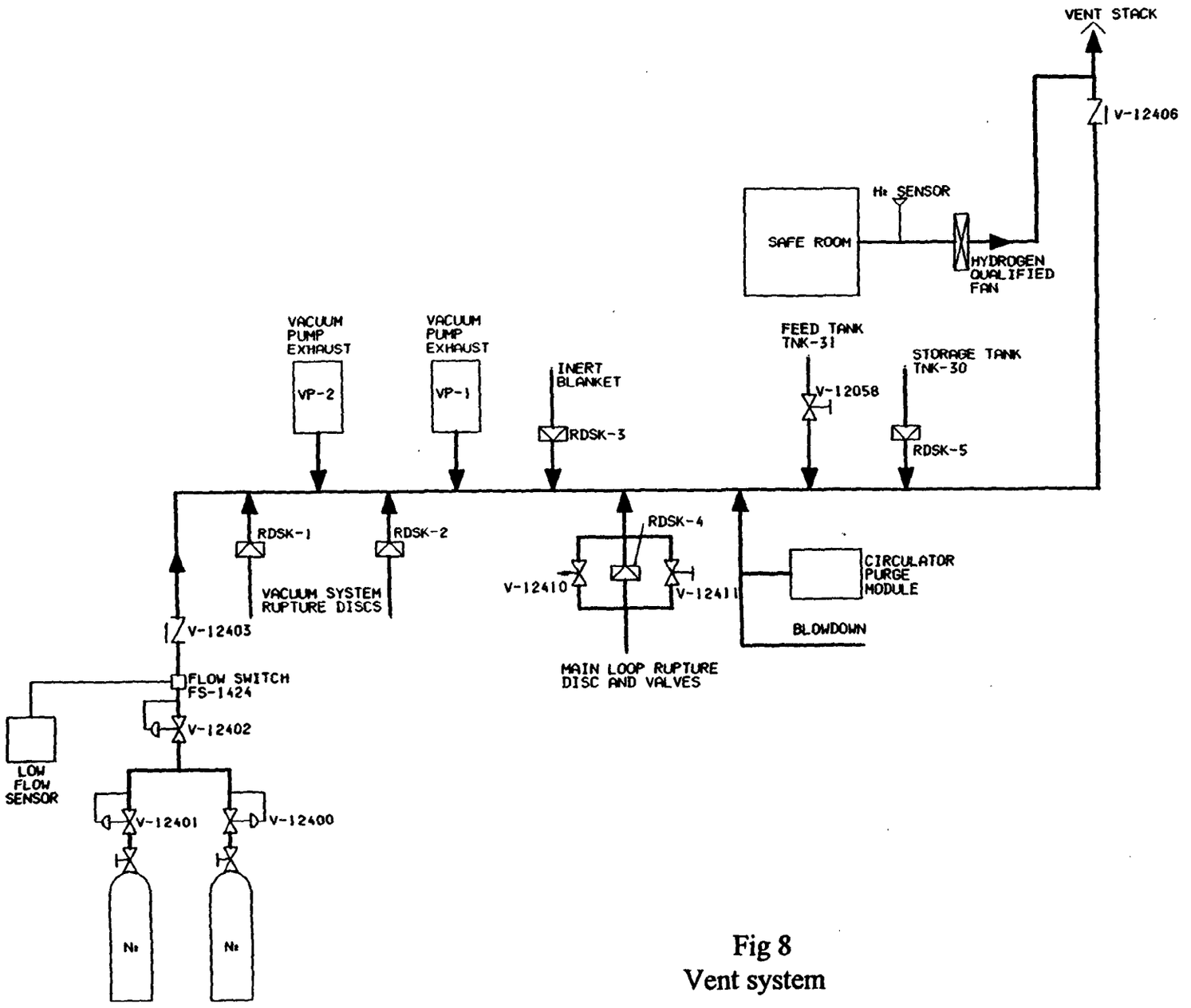

Fig 8
Vent system

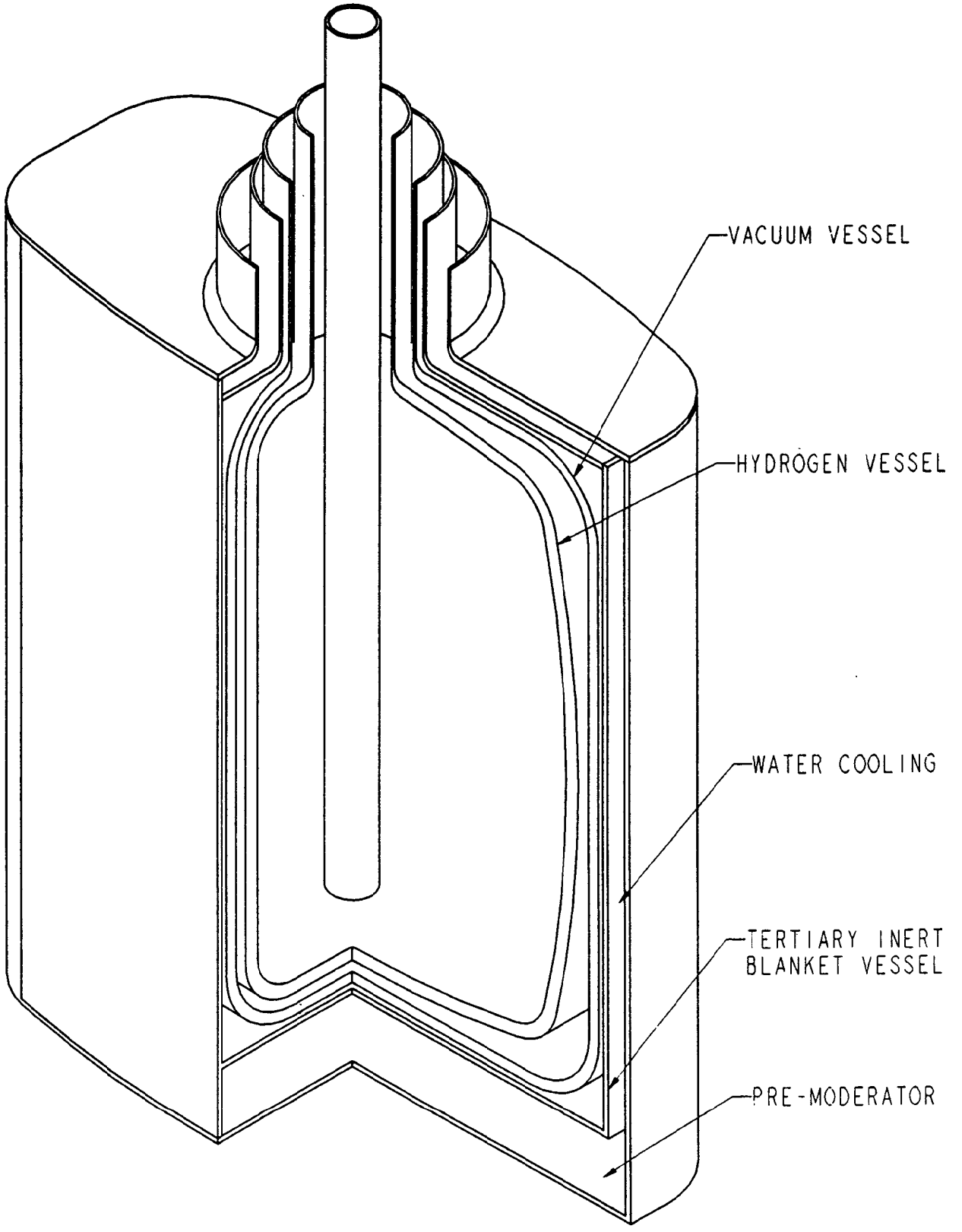

Fig 10
SNS Moderator vessel Assembly

ICANS-XIV
14th Meeting of the International Collaboration on Advanced Neutron Sources
Starved Rock Lodge, Utica Ill., USA
June 14-19, 1998

Target Options for SINQ - A Neutronic Assessment

G.S. Bauer, A. Dementyev *, E. Lehmann
* Guest from Institute for Nuclear Research Moscow, Russia

Paul Scherrer Institut, CH-5232 Villigen-PSI, Switzerland

Abstract

In order to raise the neutron output of SINQ, now operating with a Zircaloy rod bundle target, several options of varying complexity are conceivable. This includes liquid metal targets as well as lead-based rod targets with different cladding materials, but also composite targets where the highest loaded zone is made from a different material than the bulk of the target, to keep thermal neutron absorption as low as possible.

Using the LAHET code system the neutronic performance of the various target concepts was examined in a first round in order to provide some guidance on the effect of different possible choices on the overall source performance.

This report will summaries some of the investigations for different target concepts and a parameter study related to a composite target with a tungsten core embedded in a lead body.

1. Introduction

Being a continuous neutron source with a large D_2O tank surrounding the target for neutron moderation and reflection, SINQ is particularly sensitive to neutron absorbing materials in or in the vicinity of its target. Different variants of targets for SINQ using solid and liquid target materials were initially studies by Atchison [1], [2], [3]. A thorough neutronic assessment was carried out for the system finally chosen for the commissioning and initial operating phases of the neutron source [4], namely a target made up from Zircaloy rods. These calculations were made with the HETC code for the high energy transport calculations and a locally extensively modified version of the O5R code with ENDF/B-IV cross section data for sub 15 MeV neutron transport. In the mean time the LCS code system [5] is being widely used for such calculations and it was of interest to apply this package to the SINQ case in order to be consistent with other groups and to compare results. First calculations with this system for the SINQ Zircaloy target

Keywords: Rod Target, SINQ, Neutron Flux, Composite target, Liquid metal target

were reported in a different paper [6]. Although results from earlier calculations could generally be confirmed, it was observed that flux values obtained with the LCS package tend to be lower than the earlier results. In cases where measurements on the actual system allowed direct comparison, good agreement with the LCS-result was found [7]. Therefore, in order to study options for the future development of the SINQ target, calculations were started and continue to be performed, using the LAHET-based code. Some special cases were modelled considering different target materials and the influences of structural materials.

As a first step, the rod bundle of the zircaloy target was described in detail to study its properties [6]. Next the consequences of modifications in the second target were studied [8], which will contain a number of test rods to examine radiation effects under the specific operating conditions of SINQ [9]. The present report describes preliminary results for alternative target concepts aiming at improving the neutronic performance and life time predictability of the SINQ target.

It is generally accepted that for a continuous neutron source as SINQ, lead will be the best target material from a neutronic point of view, because it gives good neutron yield and has low neutron absorption. However, the need to remove the heat from the target during operation will require either to introduce a cooling medium into the target material or to allow melting to move the lead in a circuit. The last option favours use of a low melting eutectic alloy (e.g. Pb-Bi) to operate at temperatures as low as possible. In terms of computer modelling, this target concept is relatively simple.

More complex models are needed if heterogeneous target designs are to be analysed that contain coolant and target material in relatively complicated arrangements. Besides neutronic performance the most important questions relate to power deposition in the target material and transmutation and gas production which can be the reason for life time limitations.

The most straight forward step in the development of the SINQ target is replacing the Zircaloy rods by lead filled tubes. In this case the choice of cladding (tube) material is of importance for neutronic reasons as well as for the safety of the target operation, especially in off-normal situations, where (partial) melting of the lead may occur.

Alternatively, it is conceivable to go for a composite target with an inner region of a highly temperature resistant (refractory) heavy metal and an outer ring and downstream part using lead. Both zones have to be cooled with heavy water. For practical reasons, all zones of this target will have a rod bundle structure, with corresponding materials filling of the cladding tubes.

2. Geometric model

In order to describe the SINQ facility regarding its use as efficient neutron source the outer zones like the moderator tank and shielding have to be accounted for in addition to the central target zone. This configuration is illustrated in Fig. 1 where the target region is represented only symbolically without any details.

The structure in the target region is shown in Fig. 2 for three different target versions as outlined above, version c consisting of different components with variable dimensions. This parameters

will be investigated concerning their effect on performance The radius R and the height L of the refractory metal (tantalum) cylinder will be considered as parameters for the optimisation of the target performance. The lead zone around the tantalum will change in size accordingly, maintaining the outer dimensions to fit in the existing SINQ geometry.

For the current scoping study the targets were modelled to different degrees of detail: While the rod targets (Zircaloy and clad lead) were described as built up from individual rods and tubes as in the real design [6], no internal structure was assumed to exist in the liquid target models and the composite target was generated by varying the composition of individual zones in the target model as shown in Fig. 2c.

The beam profile used for all cases is as given in Ref. [6], a cylindrical beam with normalised Gaussian intensity distribution of standard deviation $\sigma = 3.7$ cm in both directions and truncated at a radius c*a, with c taken as 2. For the present purpose this approximates sufficiently well the distribution with $\sigma_x = 3.3$ cm and $\sigma_y = 3.83$ cm obtained from beam dynamics calculations. The beam energy is 570 MeV and all calculations are for 1 mA on target.

Since this study only aims at scoping calculations, no details of the materials distribution in the moderator tank were taken into account.

3. Thermal neutron field in the D_2O tank for the different target variants

3.1 Overview of results

In all calculations the zero level of the z-coordinate was taken as the centre of the moderator tank which coincides with the centre of the hemispherical bottom cap of the target container.

For the liquid metal target versions a completely filled 2 mm thick steel container with a radius of 9.6 cm was assumed and the safety hull was omitted. Clearly, this configuration can only give a first approximation to the target performance and more detail will have to be included as a design matures.

The isoflux contours obtained for the different target variants are shown in Fig 3.

Apart from the different maximum flux values obtained, the position of the flux maximum in the moderator tank (i.e. relative to the target) varies greatly. This is a consequence of the different average density on the one hand and of thermal neutron absorption in the target on the other. In the axial direction this effect could be compensated for by adjusting the target length if any of these variants were used. The difference being as much as 30 cm between Zircaloy and Mercury, this is an important piece of information. With the flux maximum being at the position of the beam tubes now, a Mercury target would have to be about 30 cm shorter in order to obtain the same situation again.

Although not immediately obvious from the contour plots, it is also observed that the radial position of the flux maximum varies markedly for the different target variants. This is due to the

absence of moderation in the liquid metal targets on the one hand and to the flux depression near the target surface caused by absorbing materials on the other. In Fig. 4 the radial flux distributions found at the heights of the respective maxima are shown.

As expected, targets that contain only weakly absorbing materials produce a thermal neutron flux maximum near the target surface, while neutron absorption in the target results in a more or less pronounced flux depression near the target surface and in a flux peak at some distance from the target. Since the average position of the beam tube noses at SINQ is at a radius of about 25 cm with a width of 8 cm, it is the flux in this region which is important for the intercomparison. For the cold moderator the flux at the mean position of 40 cm and averaged over 20 cm is important These regions are marked in Fig 4. Some details and the results of parameter variations will be discussed in the following for the different target concepts.

3.2. Liquid metal targets

The most important technical problem with liquid metal targets is the operating temperature, because it immediately bears on the choice of the structural material, the concept of heat removal and on the precautions necessary for keeping the target molten at all times to avoid structural damage that might result from volume changes in the solid state and to ensure operational readiness after beam trips of any duration. Clearly a low operating temperature is most desirable. This is why the PbBi-eutectic mixture with a melting point of 125°C is most favoured. The only heavy metal with an even lower melting point (-39°C) is Mercury, which has a very high thermal neutron absorption cross section of 380 barns. In view of this high absorption it is surprising to see that even a Mercury target would give a significant flux improvement (70%) at the beam tube positions over the present Zircaloy target in SINQ. This is without any optimisation in terms of geometry, which might still be possible.

Clearly, with the high thermal neutron absorption in Mercury the thickness of the container wall should not play a role and has, therefore, not been investigated. This is different in the case of Lead-Bismuth. Fig 5 shows the results obtained for a variation of the thickness of the assumed steel container in the case of PbBi.

Due to the low intrinsic absorption in the PbBi, the absorption in the container wall has a marked influence on the source performance and great care will have to be taken in the optimisation procedure. It should be noted that, due to the power deposition in the container window, a thick wall will result in higher stress than a thin one, especially if cooling is to be accomplished via the liquid metal only. So far, no structural materials other than steel have been considered for PbBi, because too little is known about the behaviour of possible alternatives under the anticipated operating conditions. Also, in a more detailed study the internal structure of a liquid metal target will have to be accounted for in order to judge the real benefits in terms of neutronic performance. (Another benefit would, of course, be the absence of cooling water in the target volume, which is the source of most of the radioactivity in the cooling water plant room due to the production of ^{7}Be by spallation in the oxygen.)

3.3. Lead rod targets with different cladding materials

While the development of a liquid metal target still requires significant amounts of R&D work, the most straight forward way to improve SINQ's neutronic performance seems to be the use of lead rods instead of Zircaloy, as noted above. Since Lead, due to its corrosive and mechanical properties, cannot be used in water directly, some kind of cladding is required. In order to ensure sufficient mechanical stability of the rods, the temperature of the lead must either be kept below a value where creep becomes an issue, or the tubes must be rigid enough to be independent of the mechanical properties of Lead. This bears immediately on the choice of the cladding material and method. For reasons of simplicity of manufacturing it is assumed that Lead rods will be produced either by filling molten Lead into tubes or by inserting solid rods with a tight fit. One problem arising in this context is the high thermal expansion of lead, which might result in significant hoop stress in the tube walls upon heating. For this reason methods were investigated to establish good thermal contact between the lead filling and the tubes with the goal of being able to use Aluminium as tube material [10], [11]. Preliminary studies have shown, however, that the lead is likely to creep sufficiently rapidly even at moderate temperatures to expand into gaps that are left at the ends of the lead filling, so that no dangerous stress levels are reached in tubes of reasonable strength [12]. Of course, next to safety, the choice of the tube material is influenced by the neutron flux that can be expected in the moderator. Therefore different candidate materials were examined in a first run. Without accounting in detail for the fact that, from a mechanical point of view, the required wall thickness might depend on the material chosen, the wall thickness was assumed to be 0.75 mm in the cases of Aluminium and Zircaloy and 0.5 mm in the case of steel. The corresponding materials fractions were distributed homogeneously over the volumes of the rods but the heterogeneous distribution of rod material and coolant (D_2O) was simulated correctly. In all cases a target support structure (hexagonal casing) of Zircaloy was retained. The results of this study are shown in Fig. 6

According to these results, Zircaloy would be the best cladding material despite its higher neutron absorption cross section relative to Aluminium. This is attributed to the neutron production in the Zircaloy itself. The question whether Zircaloy can actually be used depends strongly on the effect of the hydrogen produced in the Lead and in the Zircaloy itself and mandates further investigation. Aluminium would be suitable if sufficient mechanical strength could be secured under all circumstances. However, since abnormal operating conditions (bypassing of Target E upstream of SINQ by part of the beam, see below) cannot be excluded, softening or even partial melting of the Lead inside the tubes should be an allowable situation. In this case, Aluminium is not considered a suitable structural material at least in the region of highest beam heating. The question, whether different tube materials can be used in different regions of the target needs yet to be investigated. For the time being, steel cladding is considered the safest choice, at least until sufficient data on the other options is available. This choice will yield a 60% increase of the neutron flux at the beam tubes over solid Zircaloy rods, although it will only yield 85% of the flux obtainable with Lead and Zircaloy cladding.

3.4. Composite Target

The phase space distribution of the proton beam on the SINQ target depends crucially on the interaction of the beam with the pion and muon production target "E" which the beam passes before being deflected onto SINQ. This is a rotating graphite target of 6 cm length and 6 mm width. The width is matched to the diameter of the proton beam at that position in order to optimise the output of surface muons. As a consequence of the interaction in this target the beam energy is lowered from 590 to 570 MeV and the phase space occupied by the beam is increased considerably, especially in transverse direction. Behind the target "E" the beam is scraped from its halo and reshaped for further low loss transport to SINQ [13]. If all beam hits the target "E", this results in the beam profile used for the present calculations. However, if part of the beam goes past target "E" unscattered, this results in an increase of the maximum current density on the SINQ target. The radial current density distribution on the SINQ window as a function of the fraction ε of the beam missing target "E" can be approximated by a sum of two Gaussian distributions:

$$i(r) = I_0 * [\varepsilon/(\pi\sigma_1^2)*\exp(-r/\sigma_1)^2 + \alpha(1-\varepsilon)/(\pi\sigma_2^2)*\exp(-r/\sigma_2)^2], \qquad (1)$$

with I_0 being the current delivered by the accelerator and α the fraction of the collided beam that can be recollected and transported to SINQ ($\alpha \approx 0.57$) and σ_1 and σ_2 representing the standard deviations of the uncollided and the collided beam respectively. In our calculations we used 37mm for σ_2; σ_1 has been quoted as 13.4 mm [14], [15].

From equ. (1) it is obvious that the peak current density (at r = 0) more than doubles if 10% of the beam miss target E and goes up by more than a factor of 13 if all beam would go through uncollided. As can be seen from Fig. 7, however, all current density increase is inside a circle with a radius of 2.3 cm. Outside this area the current density decreases.

While it is likely that an Aluminium window will be able to cope with such an increase [15], the Lead in the target rods would certainly melt. This may not be a problem if the cladding material stays in tact, but if it is unacceptable, a target concept could be considered, where this central region is made up of a much more temperature resistant material, such as Tantalum or Tungsten, which show good neutron yield but are unsuitable for the full SINQ target because of their strong neutron absorption. As a first approach to such a concept the configuration shown in Fig. 2c with a Tantalum core was examined with respect to its neutronic and thermal characteristics under standard operating conditions, i.e. with the full beam passing through target "E". The thermal flux distributions for the reference core dimensions of 3 cm radius and 8 cm height have already been included in Figs. 3 and 4. It can be seen that, relative to a Zircaloy rod target the expected gain for this configuration is about a factor of 1.6, similar to a steel clad lead rod target.

In order to examine the effect of the size of the Tantalum core on the neutron flux in the moderator, its height and diameter were varied. The results obtained for the position at z = 15 cm and r = 20 cm are displayed in Fig. 8.

While there is obviously a marked dependence on the diameter, the effect of the length is moderate. (Note that the whole range of flux variation shown in Fig 8 is only about 12%!). From a neutronics point of view the optimum dimensions of the Tantalum core seem to be 5 cm in diameter and 6 to 8 cm in length. This diameter would be sufficient to avoid power surges in the Lead as a consequence of part of the beam missing target "E". The effect of the core length on the power density in the downstream Lead sector will be discussed in the next section.

4. Power deposition

Data on the power deposition in rod targets with Zircaloy and Lead as target material have already been given elsewhere [8]. Here we give some additional results on the composite target. Although the idea behind the composite target is to make power densities more manageable even in abnormal operating conditions, these questions will be examined in detail later. For the time being the change of the power density was investigated for the different dimensions of the inner tantalum cylinder and the corresponding outer lead zones only for the standard situation and in view of the effect on the downstream part of the target.

As for the Tantalum insert itself, its mean power density clearly changes as the diameter is varied because of the beam profile. The effect is less pronounced when the length of the insert is varied, probably because of build-up effects. The total effect for all cases considered (from volumes of 75 cm^3 to 400 cm^3) is in the region of about 20 % only.

The power deposition in the downstream Lead block is reduced by about 40% as the length of the Tantalum insert is varied from 4 to 14 cm.

The power deposited in the first Pb block also depends on the radius of the tantalum block, of course, because its inner radius changes accordingly. With the length of this lead zone is unchanged, the data given in Table 1 illustrate that there is a small reduction in the total power and in the sum of tantalum and the first lead block if the radius of the tantalum block is enlarged.

	radius of the Ta block [cm]		
	2	3	4
Ta	23.51	48.41	77.28
Pb 1	145.5	118.5	87.4
sum	169.01	166.91	164.68
Pb 2	148.3	146.3	144.6
total	317.31	313.21	309.28

Table 1: Distribution of the beam power (MeV/ proton) deposited in the different target zones and its shift when the diameter of the central Ta insert is varied

5. Conclusions

The present results clearly confirm that there is a potential for increasing the neutronic performance of SINQ significantly even with a solid target. The question, how closely the performance of a liquid metal target can be approached depends on the type and amount of structural material that must be employed in both cases. Table 2 gives an overview of relevant results.

	flux at 25 cm [cm^{-2} s^{-1} mA^{-1}]	relative to Zr	relative to Pb-Bi	flux at 40 cm [cm^{-2} s^{-1} mA^{-1}]	relative to Zr	relative to Pb-Bi
Zircaloy rods	3.25E+13	1.00	0.40	2.19E+13	1.00	0.38
Lead-Bismuth-eutecticum (2mm container)	8.15E+13	2.51	1.00	5.74E+13	2.62	1.00
Mercury	5.62E+13	1.73	0.69	4.07E+13	1.86	0.71
Lead rods without cladding	6.85E+13	2.11	0.84	4.47E+13	2.04	0.78
Lead rods with Zircaloy cladding (0.7 mm)	6.11E+13	1.88	0.75	4.02E+13	1.83	0.70
Lead rods with Aluminium cladding (0.7 mm)	5.84E+13	1.79	0.72	3.85E+13	1.75	0.67
Lead rods with Iron cladding (0.5 mm)	5.18E+13	1.59	0.64	3.49E+13	1.59	0.61
Lead rod target with Ta core	5.51E+13	1.69	0.68	3.52E+13	1.61	0.61

Table 2: Comparison of the expected thermal neutron flux levels for different target options for SINQ

If designing against large fractions of the beam missing the upstream target "E" becomes an issue, a composite target with a central insert of refractory metal may be a solution, provided that thermal hydraulics allow to cope with the high heat density. Possibly the flow of coolant must be influenced accordingly, since the fraction of beam power deposited in the insert would increase sharply as the beam narrows. In any case, the calculations show that, to a certain extent, absorbing material in the innermost region of the target can be tolerated without excessive penalties on the neutron flux in the moderator. This is corroborated by the observation that even a full size Mercury target would still perform approximately as well as a Lead rod target with steel cladding in terms of thermal neutron flux at the beam tube noses. More detailed calculations are, of course, required before a final decision is made.

References:

[1] F. Atchison, "Thermal fluxes for SINQ with alternative target systems", PSI-internal report SINQ/816/AF38-001 (1990)

[2] F. Atchison, " A Quantitative Study of the Effect of Absorption on Thermal Fluxes in SINQ" PSI-internal report SINQ/810/AF38-003 (1990)

[3] F. Atchison "The Neutronic Performance of Solid-Target Alternatives for SINQ" Proc ICANS XI, KEK-report 90-25 (1991) pp 319-334

[4] F. Atchison "Calculated Neutron Intensities for SINQ" PSI-Bericht Nr 98-03 (1998)

[5] R. Prael, H. Lichtenstein, User Guide to LCS: The LAHET Code system, LA-UR-89-3014

[6] A. Dementyev, E. Lehmann, and G:S: Bauer "Computational Modelling and Assessment of SINQ with Zircaloy Target by the Code System LAHET" PSI-internal report TM-36-97-03 (1998)

[7] L. Tobler, "Neutronenflussbestimmung in der Rohrpostanlage (1RP) für die Neutronenaktivierungsanalyse" Internal report PSI: TM-32-98-01 (1998)TM

[8] A. Dementyev, G.S Bauer, Y. Dai and E. Lehmann, "Neutronic Aspects of the SINQ Mark 2 Target with Irradiation Test Samples" this conference, ,

[9] G.S. Bauer, Y. Dai and L. Ni "Experience and Research on Target and Structural Materials at PSI" submitted to Proc Int. Workshop on JHF Science (JHF98), to be published as KEK report and PSI Bericht Nr 98-04(1998)

[10] G. Heidenreich u. A. Malik "Programm und Stand der Entwicklung des Pb-Feststofftargets fuer SINQ" PSI-internal report TM13-97-01 (1997)

[11] A. Malik, G. S. Bauer and G. Heidenreich "Target Materials Development for SINQ and Out of Beam Testing", this conference

[12] L. Ni and G S. Bauer, "Heat Transfer and Thermomechanic Analyses on the Test Rods in the SINQ Target Mark 2" this conference

[13] G.S. Bauer, W.E. Fischer, U. Rohrer, U. Schryber "Commissioning of the 1 MW Spallation Neutron Source SINQ" Proc. PAC '97, 1997 Particle Accelerator Conference, Vancouver, BC, 12.-16. May 1997

[14] U. Rohrer "Protonenstrahl für die SINQ" internal report SINQ/851/RU13-001.

[15] Heidenreich " Preliminary Thermal and Stress Analysis of the SINQ Window" Proc ICANS XI, report KEK 90-25 pp 536-550 (1990)

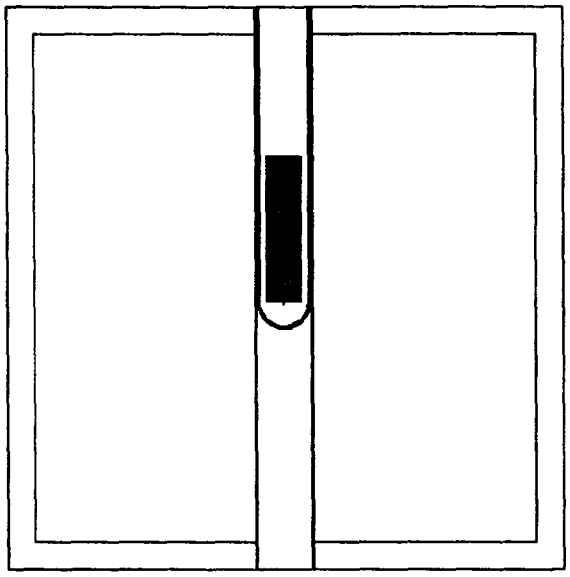

Fig. 1: Simplified model of the inner components of the spallation source SINQ without accounting for installations inside the moderator tank

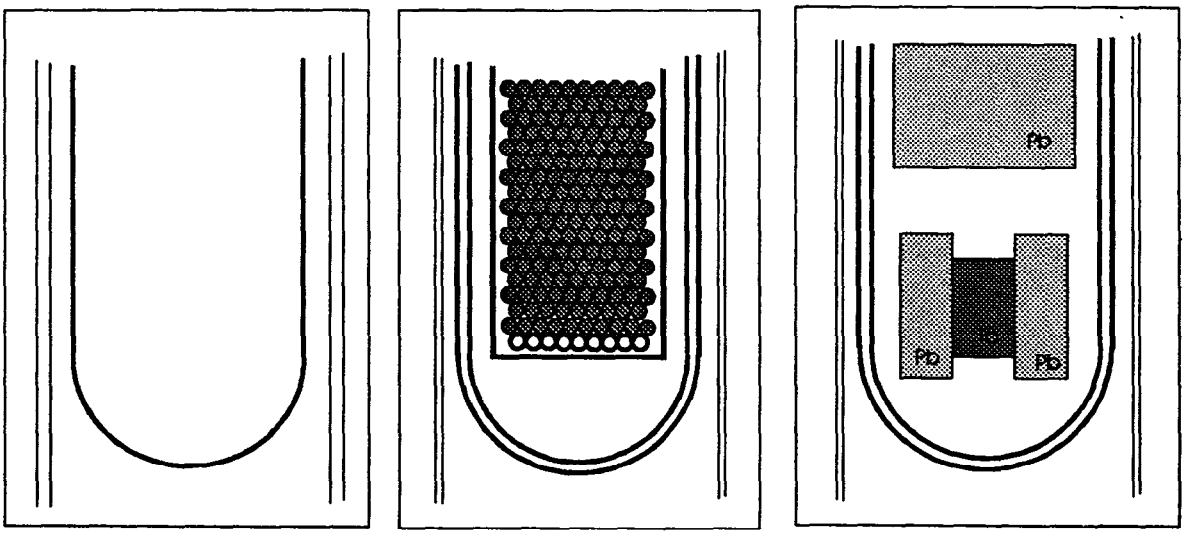

a **b** **c**

Fig. 2: Models of the SINQ target versions considered: (a) liquid metal, (b) simple rod target, (c) composite target. Version (c) consists of different zones with varying dimensions and material compositions in the rod bundle structure.

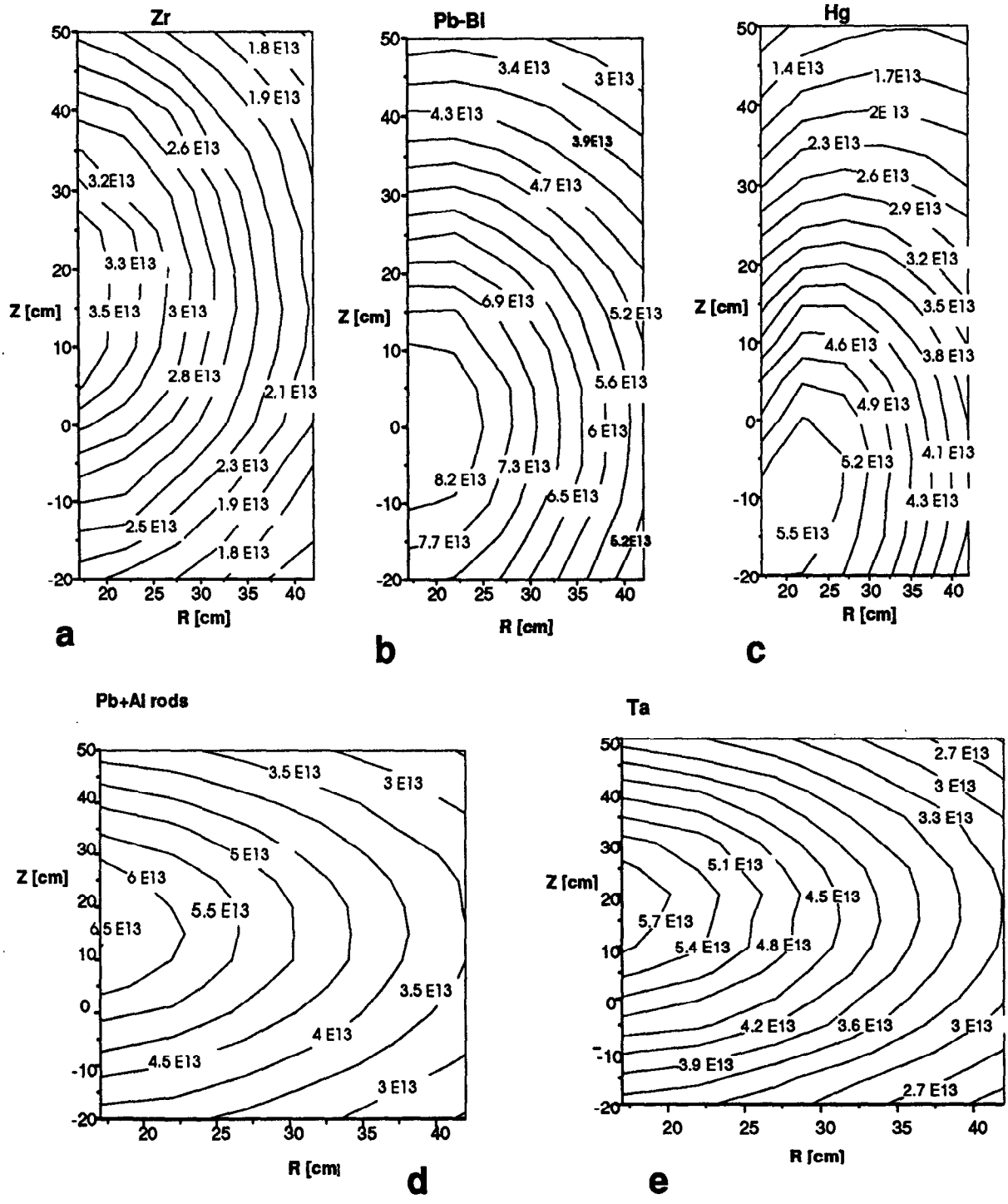

Fig. 3: Isoflux contours of thermal neutrons in the moderator for different target variants considered. (a) Zircaloy rod target; (b) PbBi-eutectic target; (c) Mercury target, (d) rod target with lead in aluminium tubes (e) composite target with 6 cm diameter and 8 cm high Tantalum block embedded in Lead and a gap width of 0 cm between the upper and lower part of the target

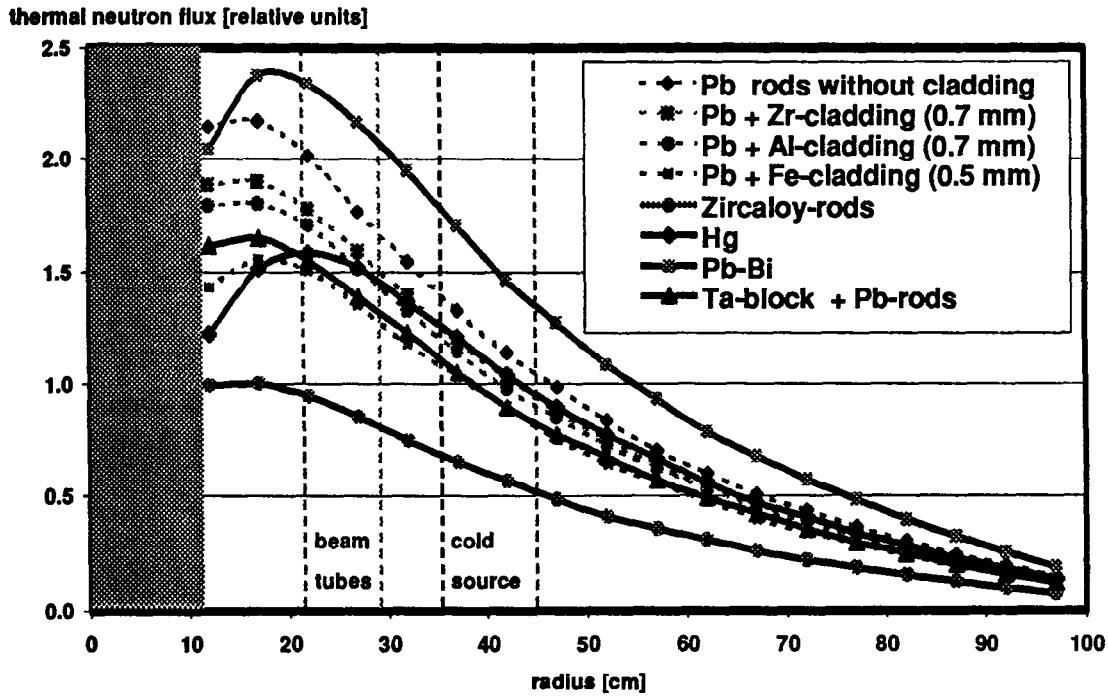

Fig. 4: Comparison of the radial distribution of the thermal neutron flux around the target region of the different target versions shown in Fig. 3 – viewed areas for thermal and cold neutrons are indicated

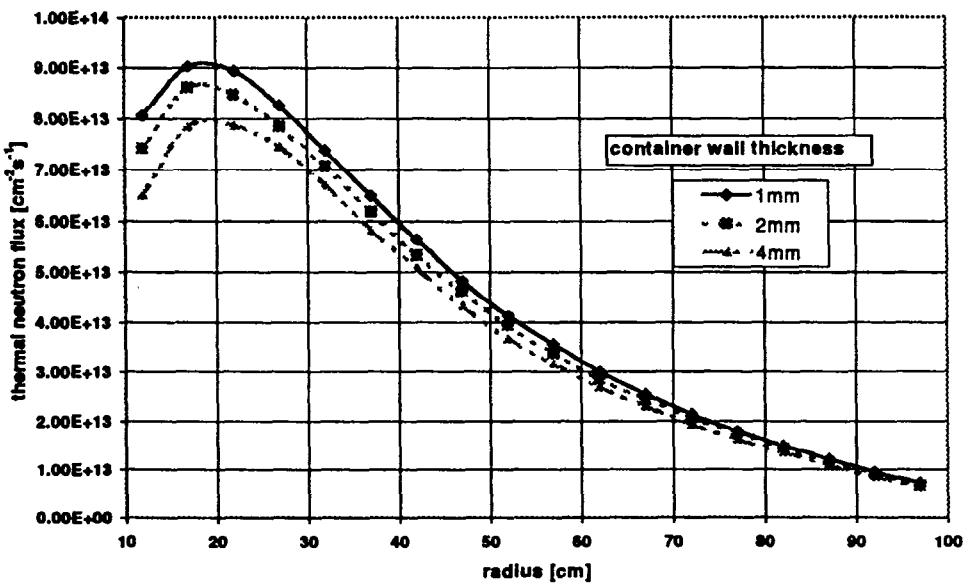

Fig. 5 Effect of the thickness of a steel container for the PbBi-target on the unperturbed thermal flux in the moderator of SINQ

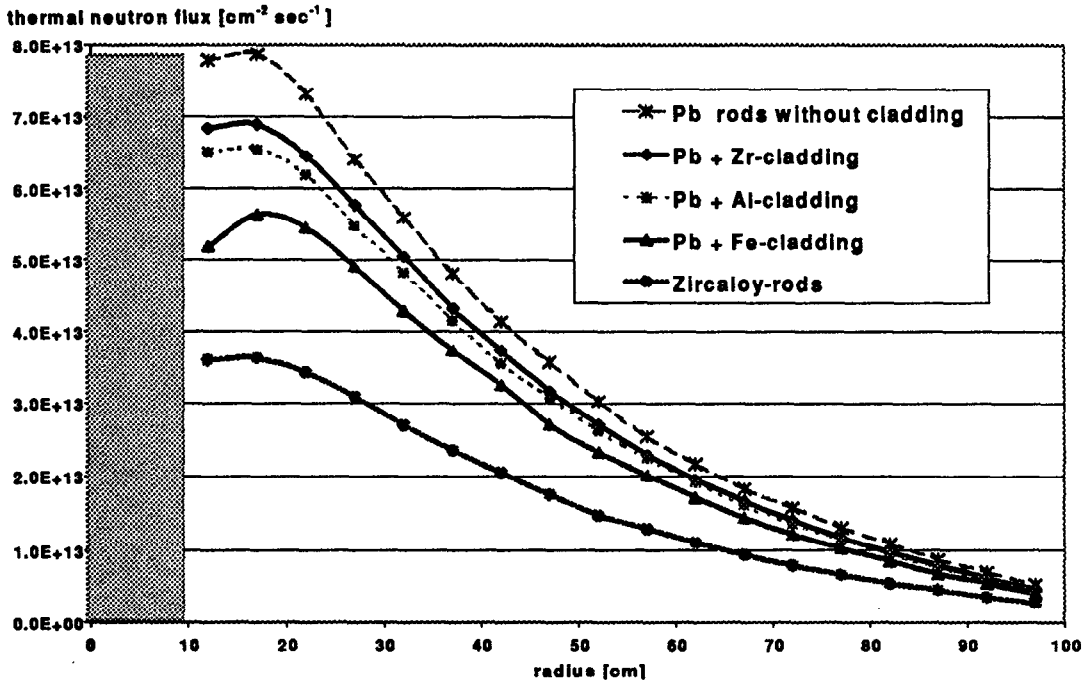

Fig. 6 Radial distributions of the calculated unperturbed thermal neutron flux in the SINQ moderator tank at the axial position of the flux maximum (z=15 cm) for Lead target rods with different tube materials. For comparison, the cases of Zircaloy rods and unclad Lead rods have also been included.

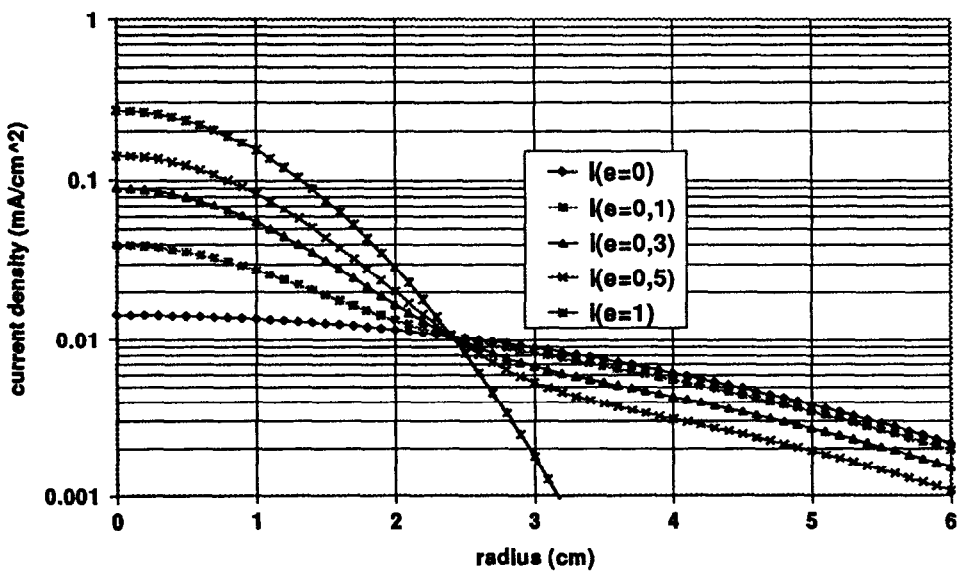

Fig. 7 Current density on the SINQ target window as a function of radius for different fractions e of the total beam current (1.5 mA) by passing target E

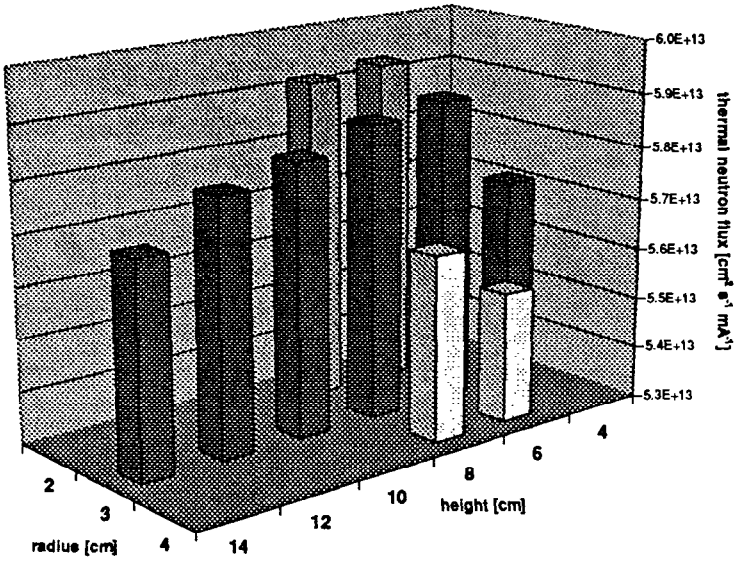

Fig. 8 Dependence of the thermal neutron flux at the position z = 15 cm, r = 20 cm on the dimensions of the Tantalum core of the composite target. The inner diameter of the Lead ring corresponded to the outer diameter of the tantalum core. The height of the lead ring was the same in all cases (14 cm).

ICANS-XIV
14th Meeting of the International Collaboration on Advanced Neutron Sources
Starved Rock Lodge, Utica Ill., USA
June 14-19, 1998

Neutronic Aspects of the SINQ Mark 2 Target with Irradiation Test Samples

A. Dementyev *), G.S. Bauer, Y. Dai and E. Lehmann
*) Guest from Institute for Nuclear Research Moscow, Russia

Paul Scherrer Institut, CH-5232 Villigen-PSI, Switzerland

Abstract

The radiation fields and power deposition levels in a heavy water cooled Zircaloy rod target for SINQ are examined, with particular attention to so called "experimental rods" which contain miniature radiation effects test samples of steel between filler pieces in Zircaloy tubes. Because the geometric model is a very detailed one, we were able to analyse individual rods in their discrete environment. As result, the radiation environment and the power distribution in the different target versions could be compared in detail. Furthermore, some results for rod bundles containing Lead in Aluminium cladding are reported.

1. Introduction

The target for the commissioning phase of the continuous spallation neutron source SINQ consists of Zircaloy-2 rods which are arranged perpendicular to the proton beam. This array is welded into the hexagonal target case and is cooled by heavy water (to avoid neutron losses by absorption which would occur if light water is used). This target concept was chosen for its simplicity and because very limited information was available on the behaviour of materials under irradiation in a spallation source radiation field. With Zircaloy, a proven reactor material, the most serious worry is embrittlement due to formation of hydride.

Since, according to calculations [1], the neutron yield of this target is by a factor of 2-2.5 lower than what could be achieved by an optimally designed target on the basis of Lead as spallation material, there is a strong incentive to change to a different target concept.

For this transition, and also for future spallation sources like ESS [2] it is very important to know the effects of irradiation on structural materials in order to be able to assess the life expectancy and operational safety of the target. There are some favourite alloys for use as cladding material

Keywords: SINQ Target, Rod Target, Neutronic Performance, Radiation Fields, Power deposition

for Lead or as containers for liquid metals, but knowledge on their behaviour under high level irradiation is very limited, because there are doubts whether the results from reactor irradiation are valid due to the much higher gas production (He and H) in a spallation environment

Therefore, it was decided to launch a materials programme at PSI [3]. As part of this programme several of the standard Zircaloy rods along the beam axis are replaced by experimental rods in the second target for SINQ which will be used from July 1998 on. These experimental rods have a Zircaloy cladding and contain a large number of miniature samples of the material to be investigated which are embedded between filling material of Aluminium or Zircaloy. The 1500 micro samples have dimensions from 3 to 24 mm [4]. Fig. 1 illustrates how the 10 rods are positioned in the rod bundle matrix. It also shows some more special target elements on off-axis positions which are either solid steel or prototypes of steel clad lead rods.

Because the experimental rods represent a deviation from the licensed standard target and in order to estimate the thermal, stress and flux conditions under which the specimens would be irradiated, a thorough assessment of the nuclear and mechanical loads in the new target was necessary. In this paper we report on the nuclear and neutronic part of the work; the mechanical aspects, for which these results served as a basis are reported elsewhere [5].

2. Calculational modelling

Using a rather detailed geometric model [6] which represents the rods and tubes in the target individually and part of which is shown in Fig. 2, the power deposition and flux distribution in the target were studied. The intensity in the incident proton has been given [7] as being of elliptic cross section with a truncated Gaussian distribution:

$$i(r) = I_0/(2\pi ab)*\exp(-1/2[(x/a)^2+(y/b)^2]) / [1-\exp(-c^2/2)], \quad (1)$$

where a and b are the standard deviations of the Gaussian distributions in x and y and the cut-off is given by the condition

$$(x/a)^2 + (y/b)^2 \leq c^2. \quad (2)$$

To a first approximation the beam can be described as having the form of a Gaussian with radial symmetry and a standard deviation $a = b = \sigma$ of 3.7 cm. Taking $c = 2$, the intensity distribution can be represented with $r^2=x^2+y^2$ as:

$$i(r) = I_0*/(2\pi\sigma^2)*\exp(-r^2/2\sigma^2)/ [1- e^{-2}], \quad (3)$$

This relation describes the one given in [7] fairly well and was used in the present calculations.

Whereas the heat deposition can be calculated by the high energy code LAHET [8] alone, the coupled MCNP code must be used to determine the thermal flux distribution around the target region, which is much more time consuming.

The modified rods where described as homogeneous mixtures of the materials contained in them. Three cases were considered:

- a mixture of aluminium and iron in the Zircaloy tube as replacement for the Zircaloy rods
- substitution of additional four rods by stainless steel as shown in Fig. 1.
- Lead rods with aluminium as cladding material.

3. Spectral and flux conditions in the target region

3.1 Proton energy and flux

As the proton beam penetrated into the target its average energy and intensity decrease, while its energy spread at each position increases. Knowledge of theses spectral details is important for the final evaluation of the radiation damage measured in the post irradiation examination of the test specimens. The change of intensity and spectral composition of the proton beam was, therefore, examined at the position of each one of the experimental rods. The results, averaged over a length of 2 cm around the middle of each rod, are shown in Fig 3 with the proton energy as independent variable and the rod number as parameter. Rod # 1 is the rod closest to the beam window. The total proton flux at each position is the integral under the respective curve.

In order to estimate the power distribution along the rods as the beam widens while it penetrates into the target, each rod was subdivided into 9 segments and the total number of protons hitting each segment was counted. The results are shown in Fig 4 in units of total proton flux per mA beam. It may be assumed that, to a first approximation, the spectral distribution remains unchanged over the length of the rod.

Clearly, as the beam penetrates into the target it widens and the intensity distribution along the rods becomes flatter. The peak values of the neutron flux for all experimental rods will be shown together with the neutron fluxes in the next section.

3.2 Neutron spectra and intensities

The neutron spectrum in the energy range between about 1meV up to 1 MeV shows little variation for the positions of the different rods. (Fig. 5). As for the thermal part of the spectrum no significant variation would be expected due to the long transport length of a heavy water moderated and reflected system with low absorption in the target region.

Also, since cascade neutrons are preferentially emitted in the forward direction, less variation is observed in the high energy neutron flux (above 20 MeV) than in the proton flux, as can be seen from Fig. 6.

For the radiation damage generated in the material the proton flux as well as the neutron flux above 0.1 to 0.5 MeV play the dominant role. In Figs 7 and 8 we compare the peak values of the proton flux at the positions of the experimental rods to the neutron flux above 0.1 and 0.5 MeV respectively. It is obvious that a large contribution comes from neutrons between the two energies.

4. Power dissipation in the target region

Since it is very time consuming to compute in detail the power dissipation in each rod as a function of position, this was done for one case only and all the following comparisons were made for the average power in individual rods only. Fig. 9 shows the power density calculated for the first Zircaloy rod in the target in comparison to the mean value obtained from an independent calculation. It can be seen that, in Zircaloy, the power dissipation is almost completely determined by the proton beam distribution. In cases where absorption of longer range secondary particles play a more dominant role, the peak-to-average ratio will be lower than that of the proton beam and therefore, using the distributions given in Fig 4 will always yield a peak power distribution that is on the safe side when used for temperature and stress calculations.

The average power densities in the experimental rods for the cases where Aluminium or Zircaloy is used as filler material is shown in Fig 10 in comparison to the case, of pure Zircaloy rods. The irregular behaviour stems from the fact that the steel content varies from one rod to the next. Fig. 10 shows that, by adding the steel samples to the rods, some 5% increase of average power density is generated, if Zircaloy is used as filler material, but can even be made lower than in pure Zircaloy by using Aluminium as filler material. The case of the massive steel rods was also examined and it was found that the power density in this case is increased by 30% over Zircaloy.

Finally the power dissipation in all target rods was examined for the case of lead filled Aluminium rods relative to Zircaloy and Lead rods only. This complements earlier work [9] and allows to compare the results obtained from using different code systems. In the case of Lead in the target its higher stopping power for protons plays an important role. Fig. 11 shows the average power density in the individual rods as a function of their layer number (position along the proton beam). It can be seen that, at the proton energy of 570 MeV available at SINQ, a Bragg peak still exists at the end of the range but is rather smeared out and not very intense.

It can be seen from Fig. 11 that, while about 46 layers of rods are required to range out the protons completely for Zircaloy, 40 will be enough for the case of lead filled aluminium tubes.

5. Neutron flux in the moderator

Clearly, introducing a small amount of steel and aluminium into 1o out of 450 target rods would not be expected to result in any significant changes in the flux or spectral distribution in the D_2O moderator surrounding the target. However, since it could be done conveniently, the neutron spectra were sampled at a point 20 cm from the target axis and 15 cm above the centre of the hemispherical bottom end of the target shell (i.e. the lower ege of the rod bundle (cf Fig 1). The results are shown for the whole energy range from 1 meV to 10 MeV in Fig 12 and for the thermal regime alone in Fig. 13. As expected, the differences are barely discernible and no adverse effects will be seen by the users due to the experimental rods in the target.

6. Conclusions

The analysis presented in this paper shows that introducing the experimental rods in the SINQ target Mark 2 will not affect the neutron flux in the reflector of SINQ but the radiation levels in the target and their spatial and spectral distributions will be suitable for the planned investigations on the test samples. Expected power densities were determined and can be used to examine the thermo-mechanical situation in the test rods in detail. Results of this work will be reported elsewhere. Using Aluminium as a filler material for the experimental rods will result in a total power per rod which is lower than for pure Zircaloy, but even for Zircaloy fillers the heat flux on the rod surfaces will be very moderate.

References:

[1] G.S. Bauer, A. Dementyev , E. Lehmann "Target Options for SINQ - A Neutronic Assessment" this conference

[2] ESS-Final Report, G.S. Bauer, T. Broome, D. Filges, H. Jones, H. Lengeler, A. Letchford, G. Rees, H. Stechemesser and G. Thomas, eds. "ESS, a Next Generation Neutron Source for Europe ", Vol III, The Ess Technical Study, ESS 96-53-M (1996),ISBN 90 237 6 659

[3] G.S. Bauer, Spallation neutron source material research at SINQ, Research proposal dated 21.10.1996

[4] G.S. Bauer, Y. Dai and L. Ni "Experience and Research on Target and structural Materials at PSI", submitted to Proc Int. Workshop on JHF Science, KEK, Tsukuba, Japan and PSI-report 98-04 (1998)

[5] L. Ni, and G.S. Bauer, "Thermal Structure Analyses on the Test Rods in the SINQ target Mark 2" this conference

[6] D. Dementyev, E. Lehmann, and G.S. Bauer "Computational Modelling and Assessment of SINQ with Zircaloy Target by the Code System LAHET" internal report PSI TM-36-97-02 (1998)

[7] U. Rohrer "Protonenstrahl für die SINQ" internal report SINQ/851/RU13-001.-

[8] R. Prael, H. Lichtenstein, User Guide to LCS: The LAHET Code system, LA-UR-89-3014

[9] F. Atchison, Operational Parameters for the Canneloni-Target, TM-816/AF30-303

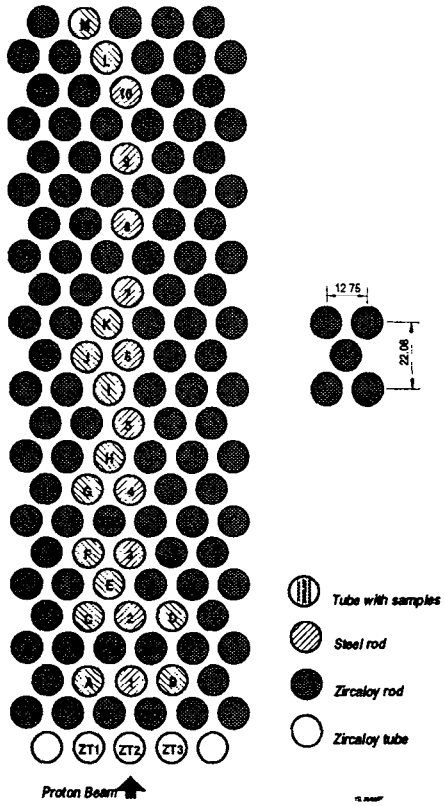

Fig. 1: Vertical section through the lower part of the modified zircaloy rod bundle equipped for investigations of the irradiation behaviour of structural material samples

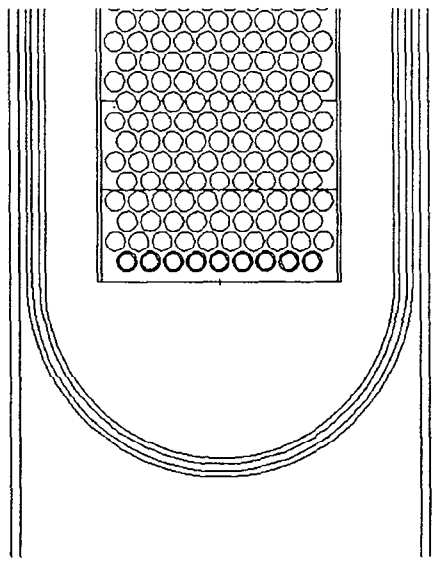

Fig. 2: Part of the model for the target of SINQ accounting each individual rod

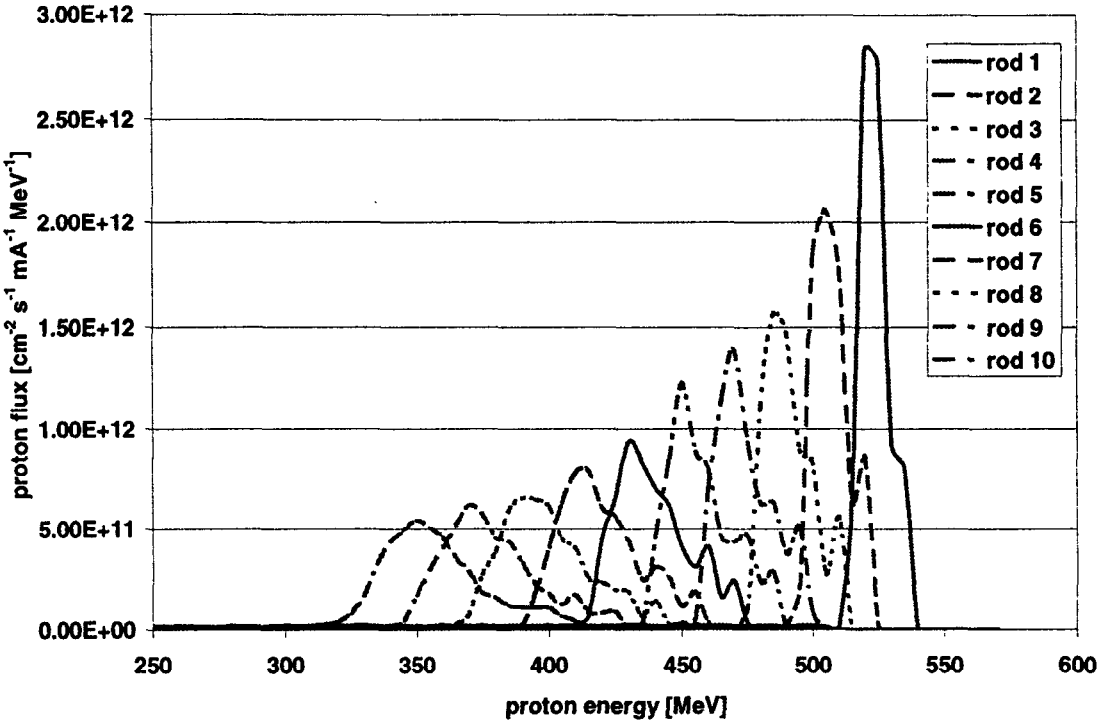

Fig 3: Proton flux spectra in the individual rods (cf Fig. 1) in the centre line of the modified Zircaloy target, averaged over the middle 2 cm of each rod

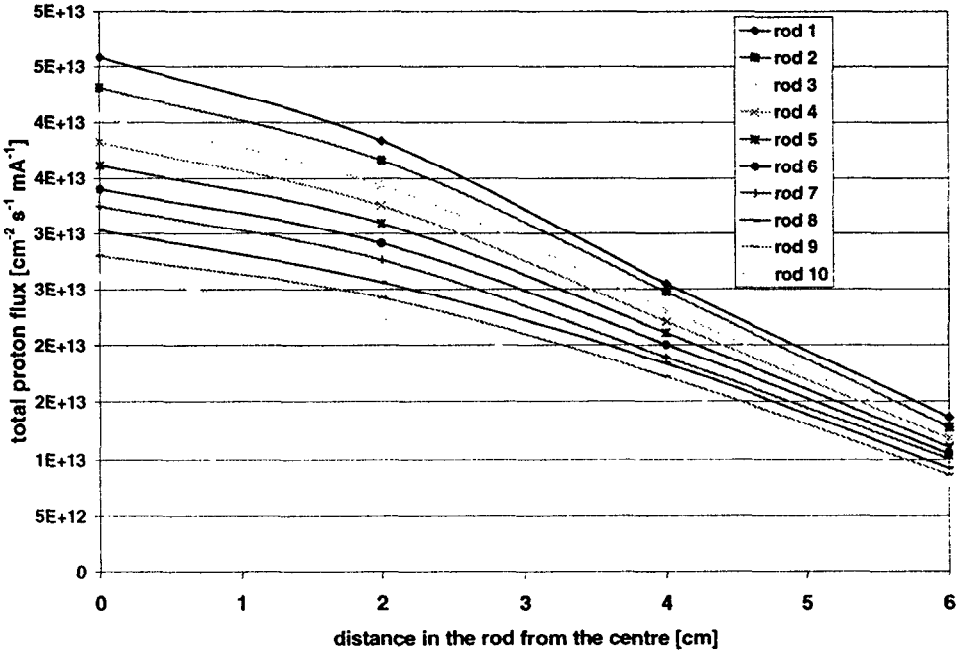

Fig. 4: Proton flux in the 10 experimental rods as a function of position along the rods.

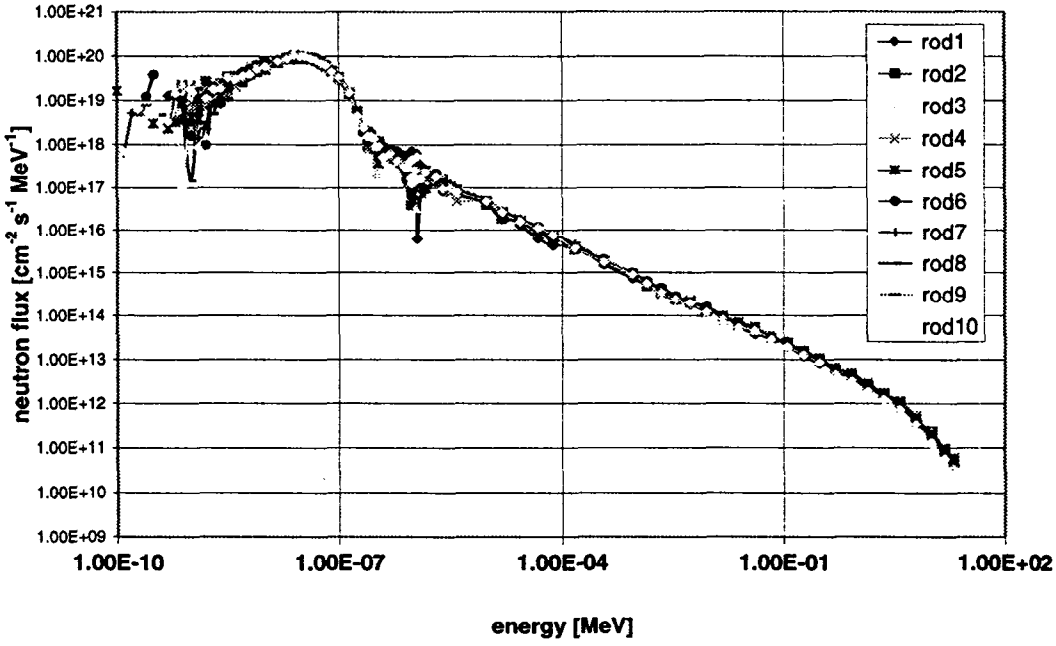

Fig. 5: Neutron spectra at the 10 modified rods of the zircaloy rod bundle target

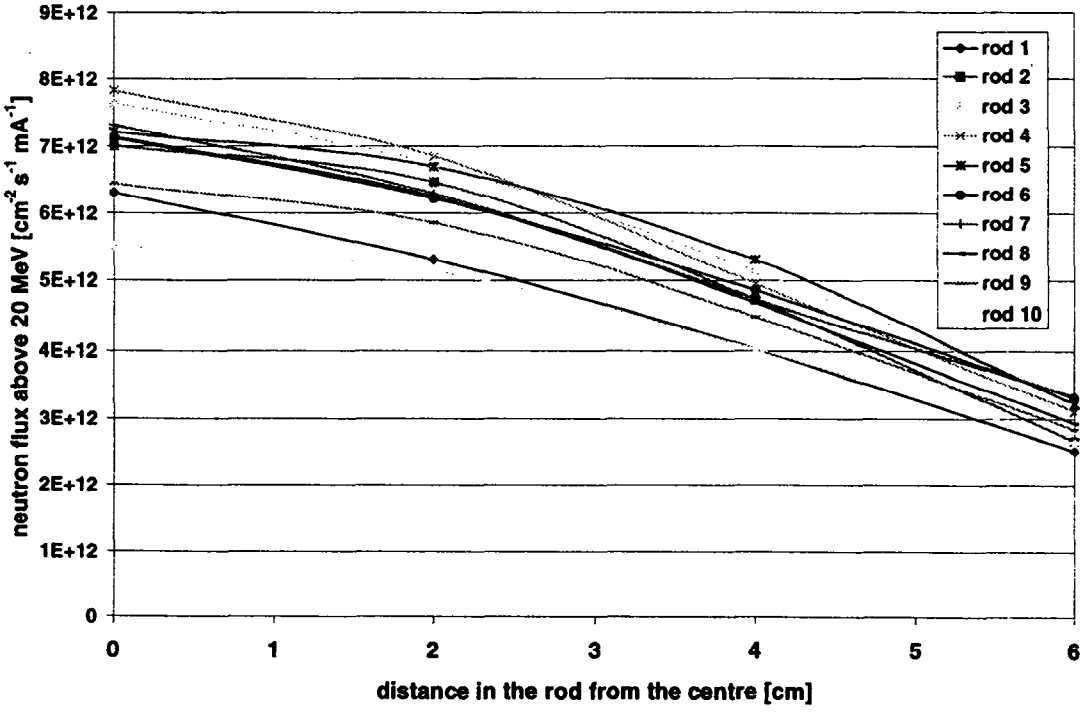

Fig. 6: Distribution of the high energy flux (above 20 MeV) along the 10 expeimental rods

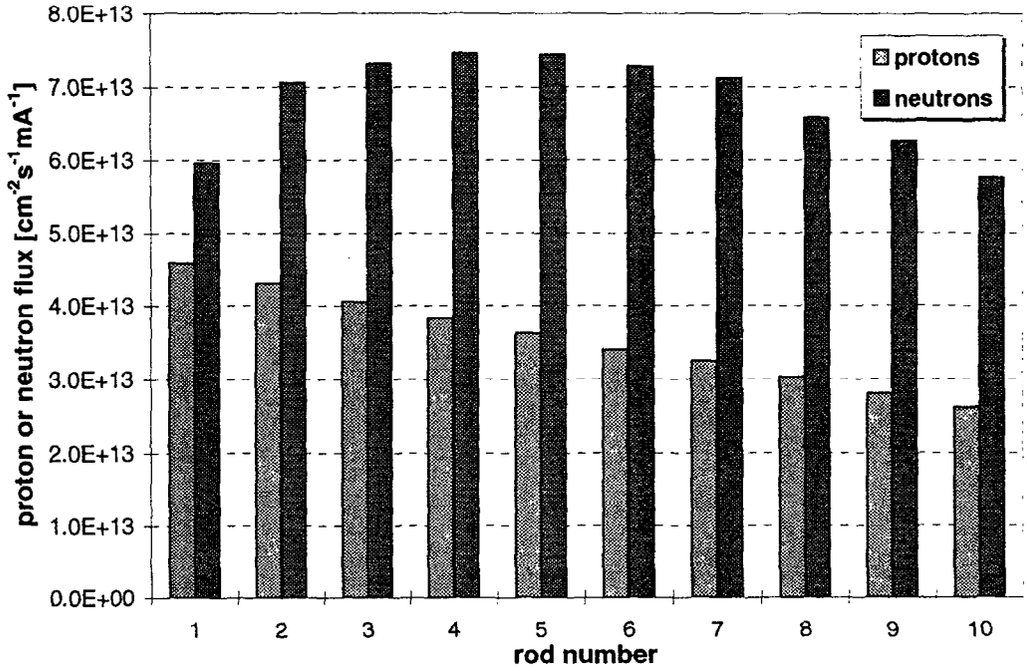

Fig. 7: Maximum proton and neutron flux (above 0.1 MeV) at the positions of the experimental rods

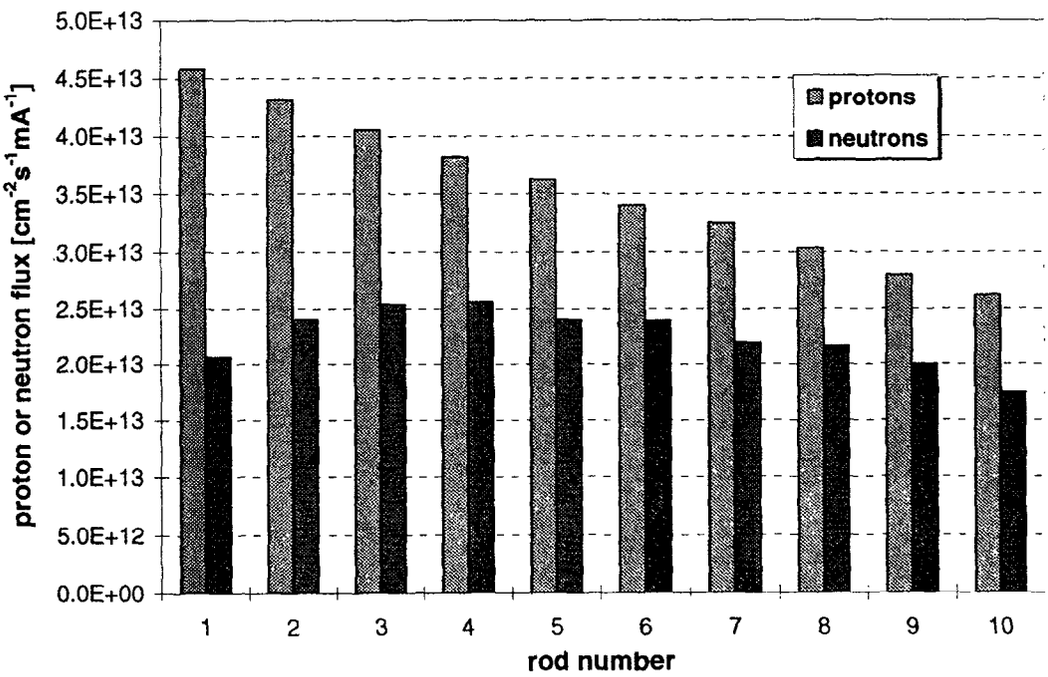

Fig. 8: Maximum proton and neutron flux (above 0.5 MeV) at the positions of the experimental rods.

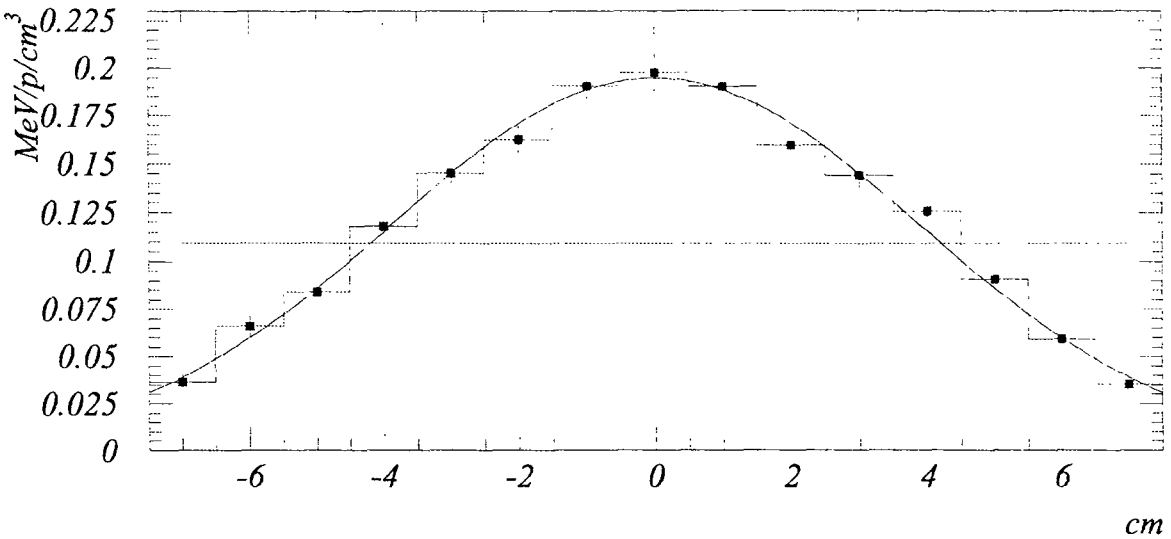

Fig. 9: Power density along the rod in the first line of the Zircaloy target compared to the average value of this rod

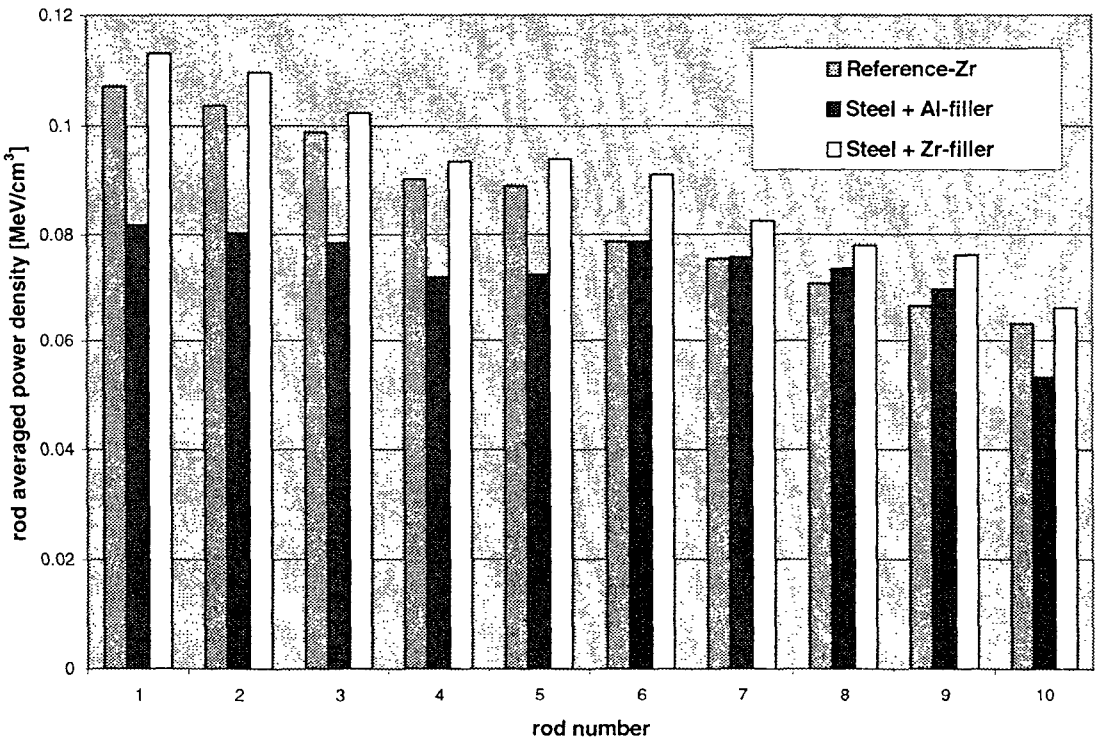

Fig. 10: Average power densities of the experimental target rods in the central plane (see Fig.1) in comparison to the Zircaloy rods

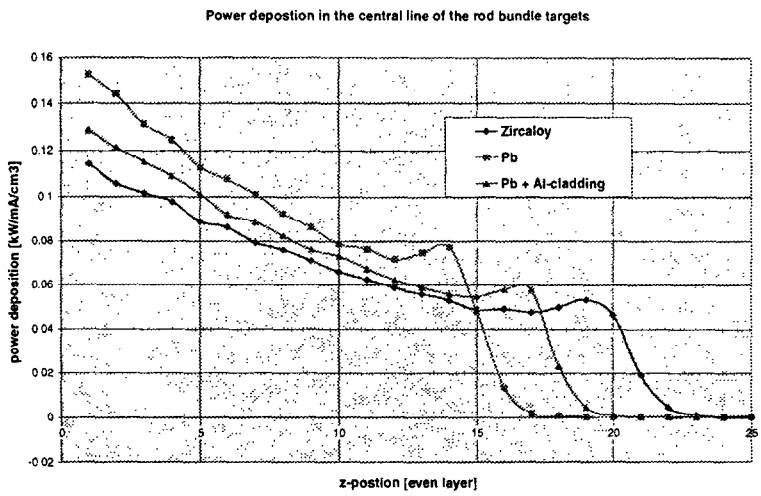

Fig. 11: Average power density in the target rods located in the central plane for different rod bundle targets for different target materials

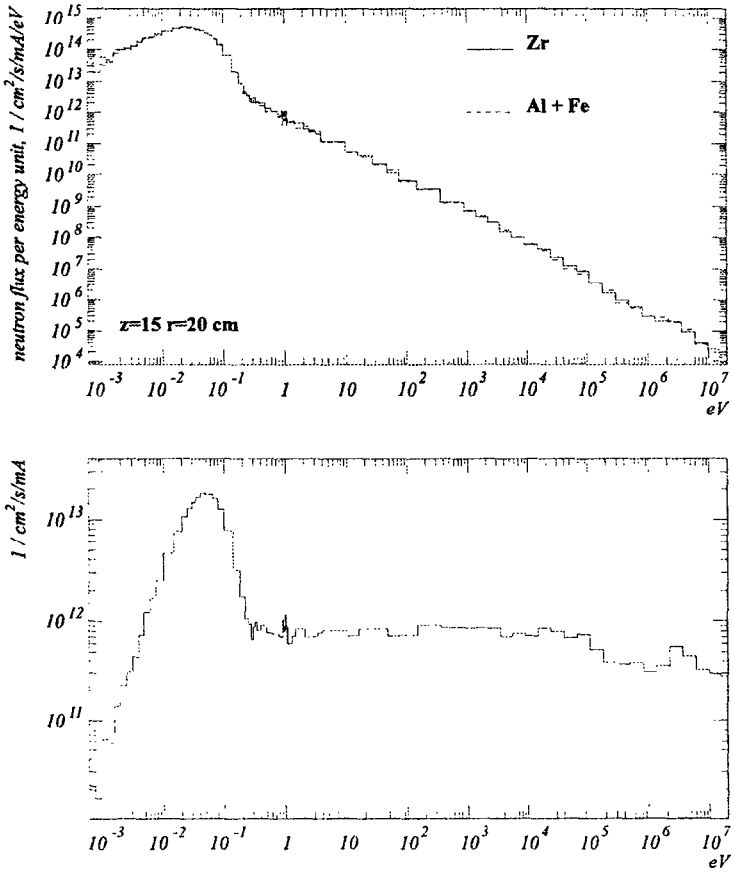

Fig. 12: Neutron spectra inside the moderator tank at the position r = 20 cm z =15 cm for the Zircaloy rod targets with and without the experimental rods. No visible difference is found. (Top: spectrum per neutron energy, below: lethargy representation).

ICANS-XIV
14th Meeting of the International Collaboration
on Advanced Neutron Sources
June 14-19, 1998
Starved Rock Lodge, Utica, Illinois, USA

A Conceptual Design Study of Target-Moderator-Reflector System for JAERI 5 MW Spallation Source

N. Watanabe, M. Teshigawara, H. Takada, H. Nakashima, Y. Oyama, T. Nagao,
T. Kai, Y. Ikeda and K. Kosako*
Japan Atomic Energy Research Institute, Tokai-mura, Naka-gun, Ibaraki, 319-1195 Japan
*Sumitomo Atomic Power Industries, 2-10-14 Ryogoku, Sumida-ku, Tokyo, 130 -0026 Japan

Abstract

The fundamental design concept of the JAERI 5 MW spallation source is proposed with some new ideas on the target-moderator-reflector system. Extensive optimization efforts have been devoted, mainly from the neutronic point of view and various important information have been obtained with various technical issues associated with the present concept. The concept was reviewed by comparing the predicted performance with those of the other projected intense sources. Although the engineering feasibility to realize some of the important parameters optimized here are still under examination or R&D, the performance at the present stage is satisfactory to justify the present concept.

1. Introduction

As a next-generation neutron source the construction of a 5 MW class intense spallation neutron source is under planning at Japan Atomic Energy Research Institute (JAERI). The neutron source program is the most important part of the Neutron Science Project in JAERI with the nuclear energy application program (R&D of accelerator-driven nuclear-transmutation-system). The project includes R&D and the construction of a high-power proton (P/H^-) accelerator of about 8 MW in total beam power. After extensive discussions a basic design concept of the neutron source facility, especially of the target station and the target-moderator-reflector system, has almost settled. Based on the basic concept and various requirements, the effects of various source parameters, such as the target material/shape/size, type of moderators with their various parameters, target-moderator coupling, reflector material/size, etc. on the neutronic performance, including pulse characteristics, are being studied.

Although the optimization studies of parameters are still continuing, the present concept has to be justified by comparing the predicted performance with the optimized parameters at the present stage, to those in other high power spallation sources.

Another important issue is the energy deposition in cryogenic moderators : How to minimize the deposition and how to realize the required H_2 flow rate. In an intense pulsed spallation source this issue is equally serious to the target problem, since the moderator volume is rather small (about 0.5-0.7 litters) and the total energy deposition is in a range of several kW with a

much higher local deposition rate near the target.

The present paper describes the proposed basic concept and overviews the present status of the design studies with various technical issues on the JAERI 5 MW spallation source, especially focused on the optimization with some new ideas.

2. Outline and basic concept of JAERI 5 MW spallation source

2.1 Accelerator

The main accelerator proposed for the Neutron Science Project is a superconducting P/H^- linac of the following specifications;

Proton energy	1.5 GeV
Peak beam current	30 mA
Total beam power	8 MW
Beam power for spallation source	5 MW at 50 Hz (finally)
	1.5 MW (early stage).

A superconducting linac was chosen for the common use (multipurpose use) of a high power accelerator with other research fields, mainly of the nuclear technology (accelerator-driven nuclear-energy-system). How to efficiently utilize the proton beam of such a modest peak current (30 mA) for an intense spallation source is the most important issue in the JAERI spallation source project. After extensive discussions we decided to put priority at a short pulse spallation source (SPSS) with a long pulse spallation source (LPSS) in the second priority. For an SPSS compressor ring(s) is indispensable which is more expensive and technically challenging. In order to accumulate the proton beam into compressor ring(s) up to a level corresponding to 5 MW at 50 Hz, the charge exchange injection over a long pulse duration of about 3.7 ms becomes indispensable due to a modest peak current, which shall be compared to 105 mA in the ESS project. In order to overcome the technical difficulties associated with the conventional charge exchange injection method utilizing stripping foils, a new method which utilize undulators and a laser beam for ionizing H^0 beam has been proposed by Y. Suzuki [1]. It is expected to promote R&D works on this idea by an international collaboration.

2.2 Target station

After extensive discussions we reached at a basic concept for the neutron source facility and the target station [2]. Important items are as follows;

(1). A horizontal beam injection;

(2). One target station and one experimental hall at the early stage, but finally two sets;

(3). The first target station acceptable the full power (5 MW at 50 Hz);

(4). Four moderators on one target (the first target station);

(5). All moderators at the highest luminosity position on the target;

(6). As many neutron beams as possible (design goal: acceptable more than 40 instruments including packed beam extractions and multiple use of one beam by several instruments (as in a guide hall at a high-flux reactor);

(7). Equal number of beams for experiments utilizing cold, thermal and epithermal neutrons (tentative decision);

(8). Each neutron beam viewing a fixed moderator (no flexibility for viewing a different moderator, which is effective to increase the total number of the beam and simplify the design of beam shutters, beam windows, etc.)

(9) Minimum angular occupation around the target station for the proton beam injection (upstream) and for the target remote handling (down stream) in order to increase the number of

available beams;
(10). The smallest target void vessel or crypt in order to minimize leakage fast and high-energy neutrons around the slow neutron beams;
(11). Beam shutters of an ISIS type (simple up-down movement);
(12). Target remote handling cell downstream; Not decided yet for the cryogenic moderator handling (upward or downstream);

3. Basic concept for target-moderator-reflector system

Based on the concept described above we reached at a concept for the target-moderator-reflector system [2], which is described below.

3.1 Target

The major considerations and decisions are as follows;
(1). The use of a mercury target due to the reasons discussed later;
(2). Adopting a flat beam and a flat target as shown in Fig. 1, from a neutronic point of view (optimal flatness is discussed later);
(3). Assuming the maximum acceptable proton-current-density on the target to be 48 $\mu A/cm^2$, judging from the integrity of the target beam window under the proton irradiation;
(4). Assuming a beam current density distribution as close as an uniform distribution from the neutronic and mechanical points of view (A Gaussian profile is not acceptable. A Moffet or, at least, a parabolic distribution is acceptable. A perfect uniform distribution, rectangular distribution, is not acceptable due to a higher stress in the beam window by the pressure wave.);
(5). Assuming the minimum beam size determined by (3) and (4);
(6). Assuming the smallest lateral target dimensions, beam size plus 1.5 cm to up and down directions (towards moderators) and 2 cm to the left and right directions, in order to maximize the target-moderator coupling (the engineering feasibility must be considered separately);

3.2 Moderator and reflector

3.2.1 Choice of moderators

Since we assumed that one third of the total available angles around the source is allocated to each field of experiments utilizing cold, thermal or epithermal neutrons (basic concept (7) in

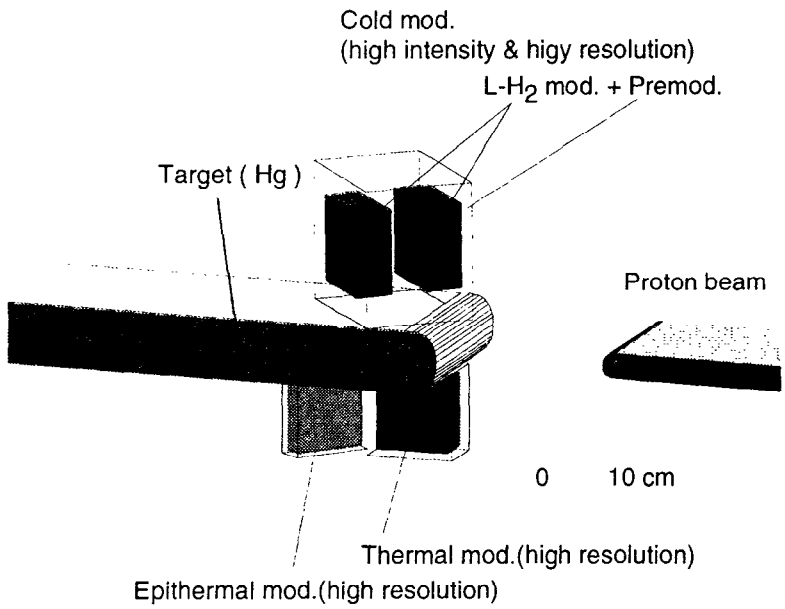

Fig. 1 Illustration of target and moderator layout

section 2.2), the required angular coverage for each kind of moderator(s) becomes about 100 degrees [2], which cannot be covered by one viewed surface, but two viewed surface becomes indispensable. For a moderator having only one viewed surface, two such moderators are required. Thus, four moderators as listed in Table 1 are considered.

Cold neutron moderator: For a cold neutron source we adopted a coupled composite moderator composed of liquid-hydrogen or supercritical hydrogen (H_2) plus hydrogenous premoderator (practically H_2O) at ambient temperature (sometimes called a coupled H_2 with premoderator), which has been developed to provide a higher time-integrated and simultaneously a higher peak cold neutron intensity than a conventional decoupled H_2 or solid methane moderator [4-6]. This moderator can satisfy high-intensity experiments such as SANS, reflectometry, etc. in which the time-integrated intensity is important [7], together with high-resolution experiments in which the peak intensity is essential [7]. We assumed two such moderators since this moderator has only one viewed surface.

Thermal neutron moderator: For high-resolution thermal neutron experiments we assumed a decoupled H_2 moderator with a interleave poison sheet, since a decoupled solid or liquid methane moderator so far been successfully used cannot be utilized at MW sources. R&D of a mixed moderator for this purpose (for example, [8]) will require a long period. Optimization studies on a decoupled poisoned H_2 moderator is under progress.

At the present stage of the design work we are not thinking to install a high-intensity thermal neutron moderator, since high-resolution thermal neutron experiments are much more promising than high-intensity ones at SPSS.

Epithermal neutron moderator: For a high-resolution epithermal-neutron-moderator we are assuming an H_2O moderator of an appropriate thickness, tentatively 3 cm thick. The optimal thickness will be determined after extensive discussions by users on the most interesting energy range in future science.

3.2.2 Moderator layout

Figure 2 shows moderator layout we proposed; two coupled composite moderators above the target and two decoupled moderators, one poisoned H_2 and one H_2O, below the target. In order to make it possible to put two coupled moderators at the highest luminosity region on the target, we proposed an idea of sharing a backside premoderator as shown in Fig. 2. Similarly we put two decoupled moderators such that both can take the best place by positioning them adjacently each other. One concern with this configuration was a possible cross talk between

Table 1 Main parameters of moderators

Purpose	High-resolution & high-intensity cold neutrons	High-resolution thermal neutrons	High-resolution epithermal neutrons
Main moderator	H_2	Poisoned H_2	H_2O
size (cm^3)	12 x 12 x 5	10 x 10 x 5	10 x 10 x 3
Moderator temp.	20 K	20 K	Room temp.
Premoderator	H_2O (2.5 cm thick)	Non	Non
Coupling	Coupled	Decoupled	Decoupled
Cut - off energy	--	1 eV	1 eV
Angular coverage	50°×1	50°×2	50°×2
No. of viewed surface / moderator	2 / 2	2 / 1	2 / 1

two adjacent viewed surfaces. However, it was confirmed by a simulation that such cross talk will not be important.
The neutronic performance of this configuration will be discussed later.

3.2.3 Reflector

We assumed a reflector as shown in Fig. 2 as a reference size (80^W x 160^H x 120^L cm^3) and compared the performance with a smaller one (60^W x 140^H x 90^L cm^3) to discuss the required size, especially for coupled moderators. Each reflector has neutron-beam extraction holes as shown in Fig. 2.

4. Optimization

4.1 Calculation

Calculational model was essentially the same as the model shown in Fig. 2. When the size of the target or a moderator, or the bottom premoderator thicknesses were changed, the positions of moderators and beam extraction holes were also changed accordingly. All the inside surface of the beam extraction holes in the reflector for the decoupled moderators were covered by liners made of B_4C. The thickness of the decouplers and the liners was fixed at 3 mm and a

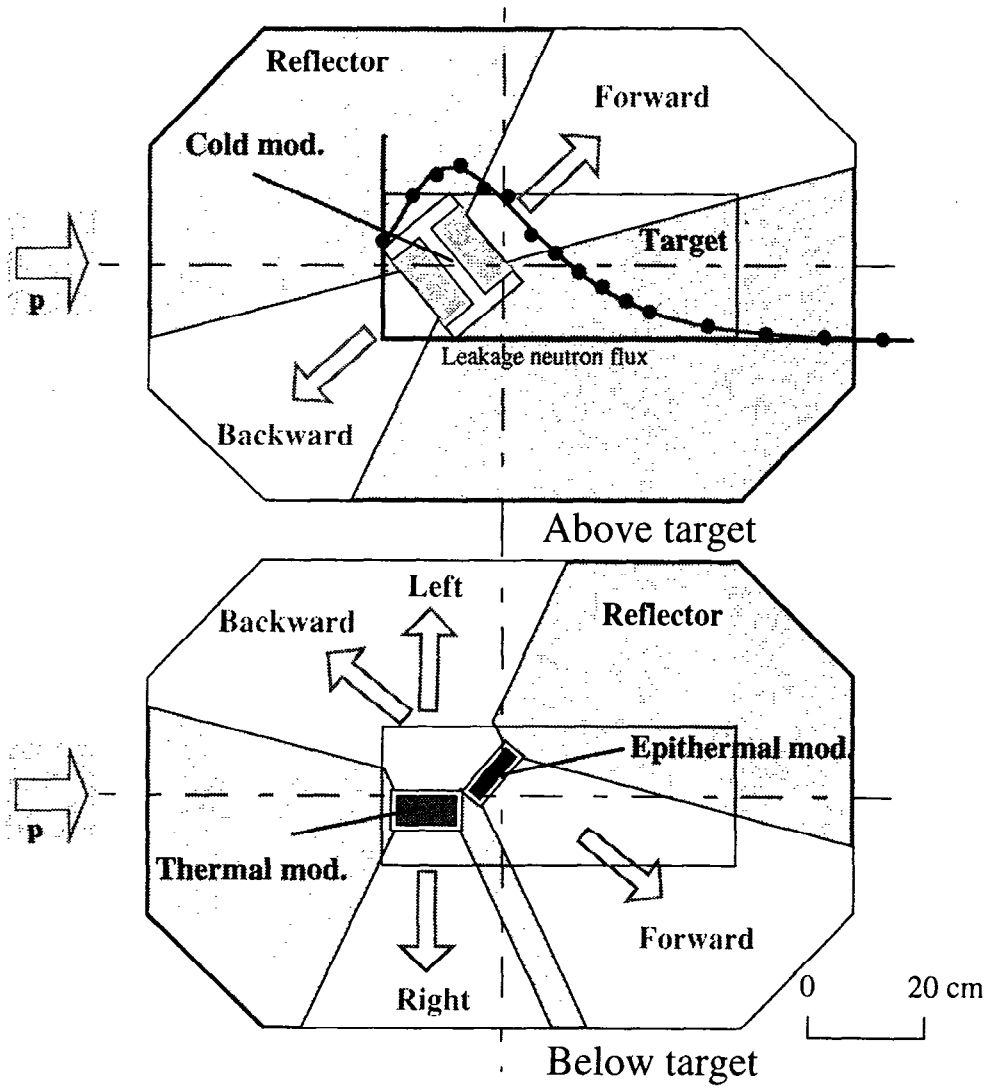

Fig. 2 Layout of target-moderator-reflactor system

required cut-off energy was controlled by adjusting the number density of B_4C. The cut-off energy was tentatively fixed at 1 eV.

In the case of a water cooled solid target, a homogeneous mixture of the metals and the coolant was assumed as usual. The target and moderator vessels were also treated as homogenous mixtures, including metals, cooling water and void of 1 cm thick in total for both vessels.

Codes, cross sections and the number of protons used for the present calculations are almost the same as those described at the separate article in this ICANS [9].

4.2 Choice of target material and shape

Assuming that the use of a liquid metal target is indispensable, we compared mercury (Hg) and lead bismuth (Pb-Bi) as a target material from the neutronic point of view. To understand the bare target neutronics the leakage neutron intensities at 2 cm from the target surface towards moderators were calculated for the two different target materials of various shapes and sizes. The lateral dimensions of the targets were automatically determined from the assumed proton beam size (beam size plus 1.5 cm up and down directions, and plus 2 cm to the left and the right directions). The results are shown in Fig. 3. An Hg target gives always a higher intensity than a Pb-Bi target of the same geometry. A flat target (of a rectangular cross section) provides a higher intensity than a cylindrical one under the same condition in the maximum proton current density (48 $\mu A/cm^2$, i.e., the same beam cross sectional-area). Since Hg has a larger slow neutron absorption cross section, the final decision shall be done after comparing slow neutron intensities.

Figure 4 shows leakage neutron distributions on the five different horizontal regions for flat targets. Although the maximum intensity is approximately comparable of different flatness, the flatter one provides a larger high luminosity region (horizontally).

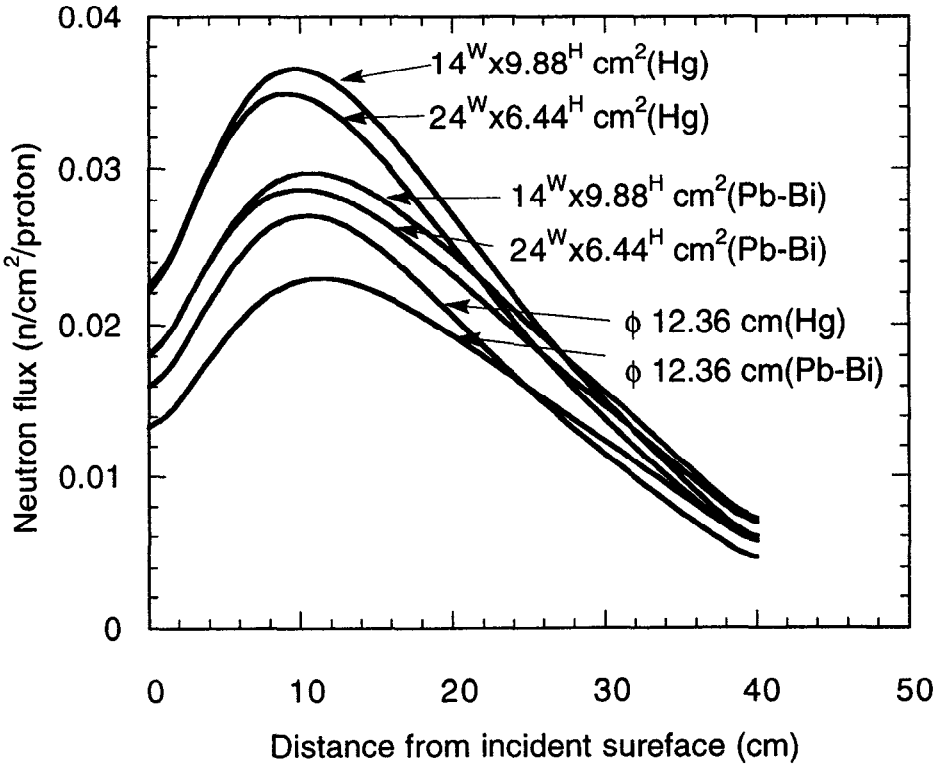

Fig. 3 Spatial (axial) distribution of leakage neutron intensities from various targets

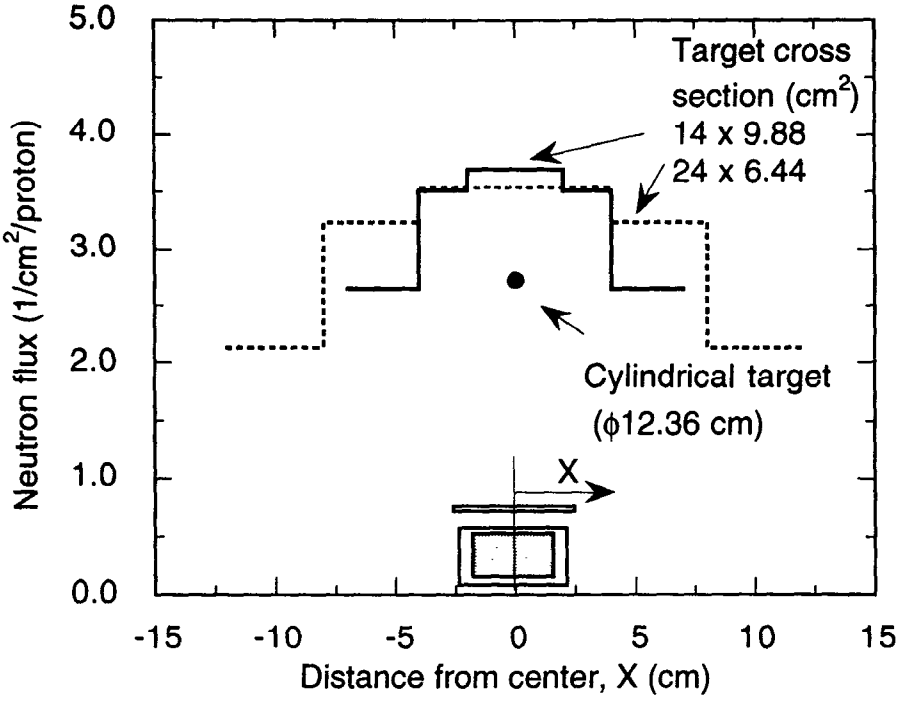

Fig. 4 Spatial (lateral) distributions of leakage neutron intensity from flat Hg targets

4.3 Target shape and size

The effects of the target shape and size on slow neutron intensities were studied. Some results for the case of the Hg targets with a Pb reflector are shown in Fig. 5, where slow neutron intensities from various moderators are compared for various beam sizes and shapes (in terms of the aspect ratio, b/a, where a and b are the horizontal and the vertical beam sizes, respectively). The target sizes and shapes are automatically defined from these values. Note that the data indicated by open circles are for a reduced beam current density (two third of the assumed maximum acceptable value), which corresponds to a larger beam size, accordingly a larger target size. Judging from this result, one important conclusion comes out: the slow neutron intensity is almost unchanged for a large variety of the beam aspect ratio, b/a, and for a different (larger) target size. **This fact will provide a larger flexibility for the target engineering.** This is a rather surprising result for Hg targets, since Hg target has been considered to act as a sort of a large decoupler due to a larger slow neutron absorption cross section. The reason will be due to the fact that a flatter (a smaller b/a) target gives a wider maximum luminosity region on the target than a less flat one as shown in Fig. 4, but absorbs more slow neutrons, canceling the former effect.

4.4 Effect of reflector

The effects of the reflector material and the size on slow neutron intensities and pulse shapes were studied. The intensities calculated with a Be reflector of the same size as the Pb reflector are also plotted in Fig. 3 (for the case of b/a=3.44/20). The Be reflector gives higher time-integrated intensities (J's) for all moderators, especially for coupled composite moderators, compared to the Pb reflector. Figure 6 compares time distributions (pulse shapes) of cold neutrons at 2.1 meV (2.0-2.2 meV) from the reference coupled composite moderator in the Be and the Pb reflectors.

The result shows that although a Be reflector can provide a higher integrated intensity with a

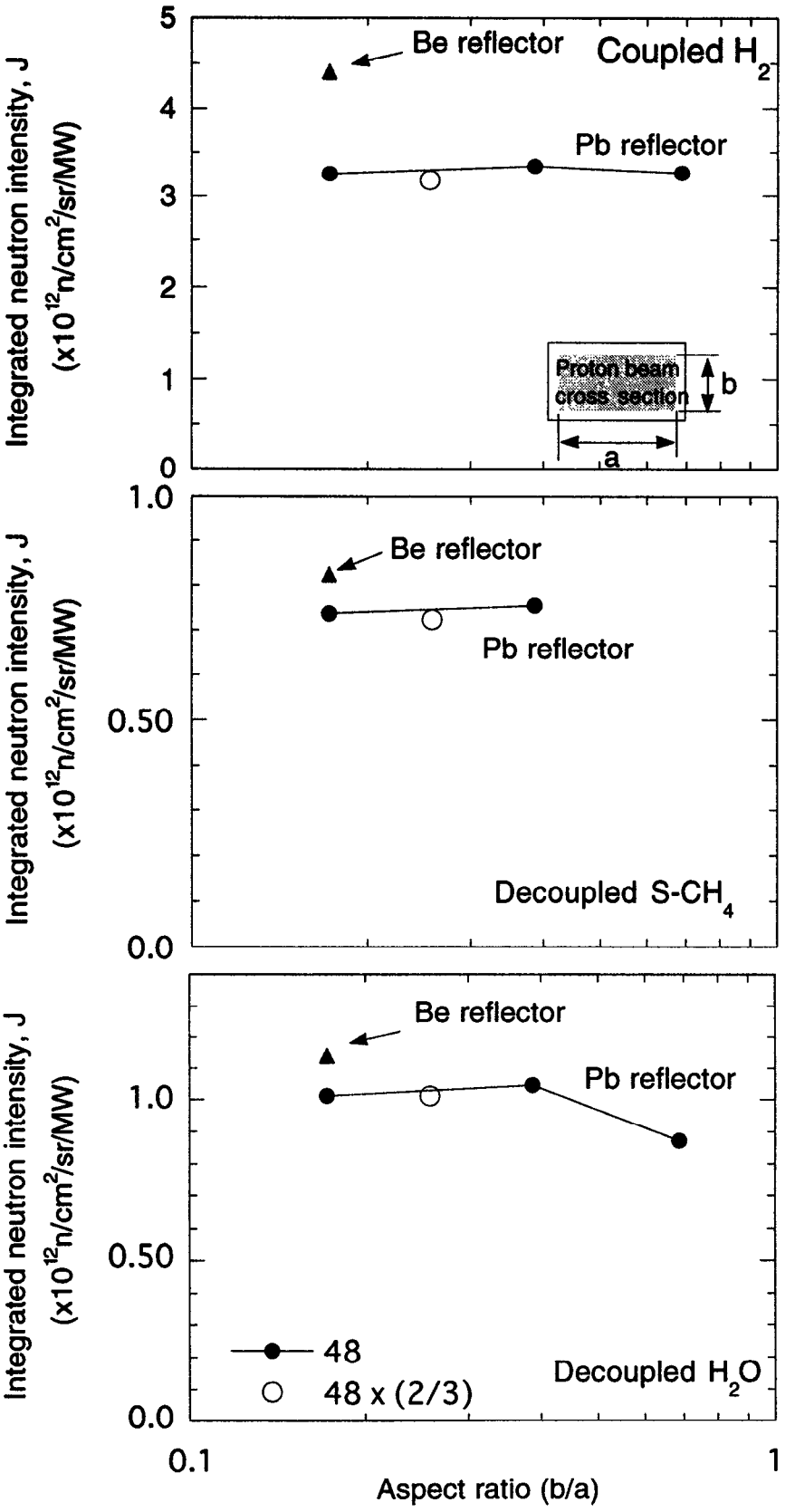

Fig. 5 Beam aspect-ratio dependence of integrated neutron intesity, J, from various moderators

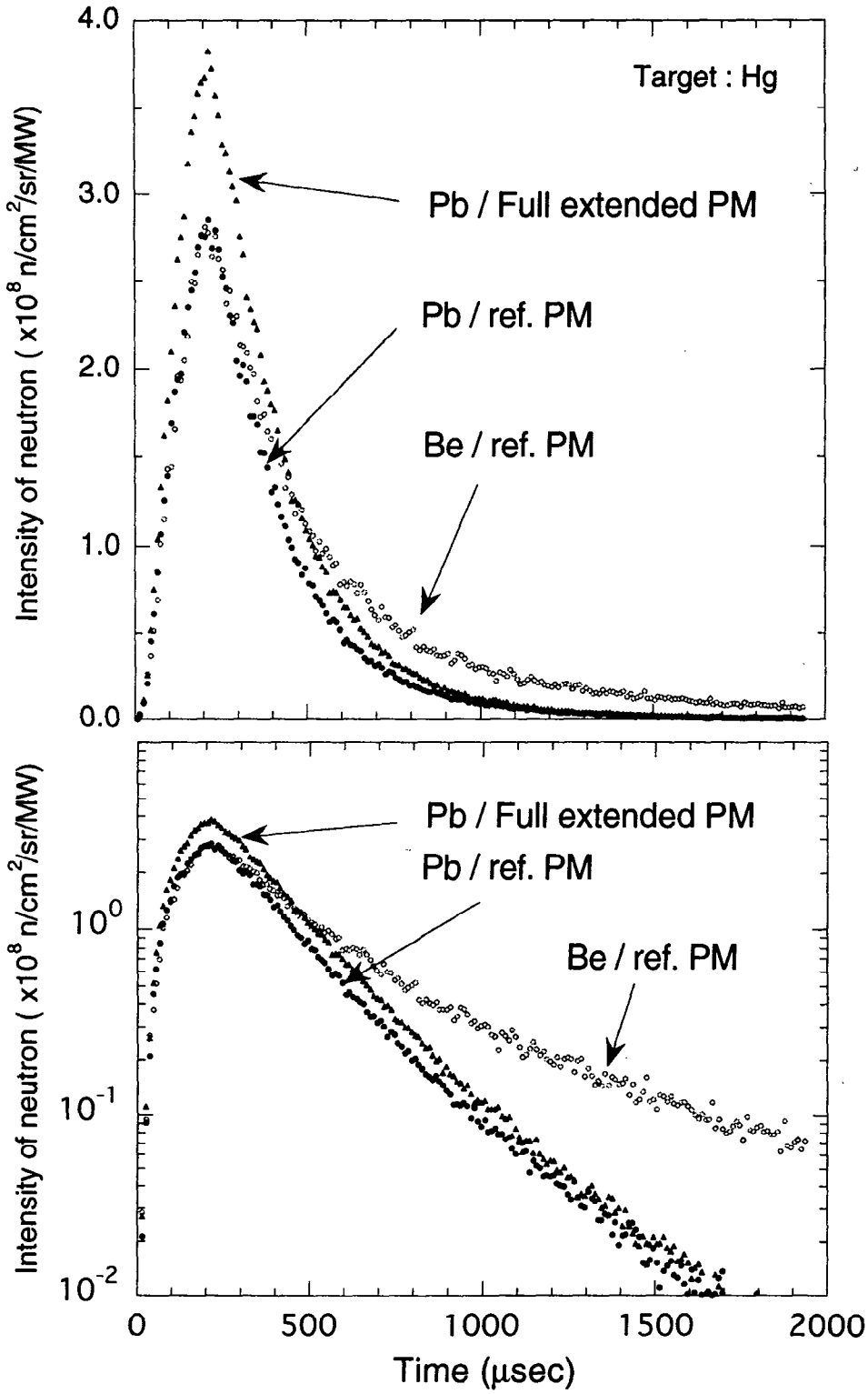

Fig. 6 Time distributions of neutron at E=2.0-2.2 meV from coupled composite moderators

lower energy deposition, as described later, than a Pb reflector, if we compare the pulse characteristics, the latter with an optimized premoderator, as described in a separete article [9], gives much higher peak intensity with a narrower pulse width than the former. This suggests the superiority of a Pb reflected system as far as the neutronic performance is concerned. The integrated cold neutron intensity from a Be reflected system will also increased to some extent by adopting a similar fully extended premoderator. However the gain factor by this will not be as large as in the case of the Pb reflected system. Such comparison is under progress.

The neutronic performance with a smaller Pb reflector was compared to that with the reference size one. The result shows that in the case of a Pb reflector the time-integrated intensities are more or less lower than those of the reference size case, especially for a coupled composite moderator.

4.5 Moderator position relative to target

The effects of the relative position of a moderator to the target on time-integrated intensities (J's) were studied changing the position of the target in the fixed moderator-reflector configuration. This is nearly equivalent to that the moderators were moved as a set relative to the target. The relative position was changed by 5 cm upstream and downstream from the reference position. The intensities from various moderators at the three positions are plotted in Fig. 7 for the case of the Pb-Bi target with the Pb reflector of the reference size. Judging from this result, it can be said that the present moderator layout at the reference position is almost at the optimal, not only in the sum of the intensities from the two moderators above and below the target, respectively, but also for each moderator, i.e., all moderators are positioned at the first class sheet as envisaged. More exactly speaking, the optimal position for the set of two coupled composite moderators is about X = -5 cm. This conclusion will be true also for other combination of target and reflector. The intensities with the reference Hg target combined with a Pb and a Be reflector are also plotted in the figure only at the reference position.

5. Nuclear heating in cryogenic moderator

The nuclear heating in cryogenic moderators is one of the most important technical issues in the design study of an intense spallation source. We calculated the energy deposition in the main cryogenic moderator (H_2) for various cases, a simple decoupled H_2 moderator, a coupled composite moderator with the reference premoderator and with fully extended premoderator. In all cases two different reflectors, Be and Pb, were compared. The results on the total energy depositions are summarized in Table 2 and the spatial distributions are compared in Fig. 8. The

Table 2 Total energy deposition in cryogenic moderators

Case	Moderator	Moderator size (cm^3)	Reflector	Premoderator	Heat deposition (kW)
(1)	Composite*	12 x 12 x 5	Pb	PM (2.5 cm)	2.79
(2)	Composite*	12 x 12 x 5	Be	PM (2.5 cm)	2.06
(3)	Composite*	12 x 12 x 5	Pb	Full (3.5 cm)**	1.94
(4)	Decoupled H_2	10 x 10 x 5	Pb	non	3.95
(5)	Decoupled L-CH_4	10 x 10 x 5	Pb	non	5.77
(6)	Decoupled L-CH_4	10 x 10 x 5	Be	non	4.68

*Coupled composite moderator composed of H_2 + premoderator

** A fully extended premoderator with 3.5 cm thick bottom premoderator (see ref. [9])

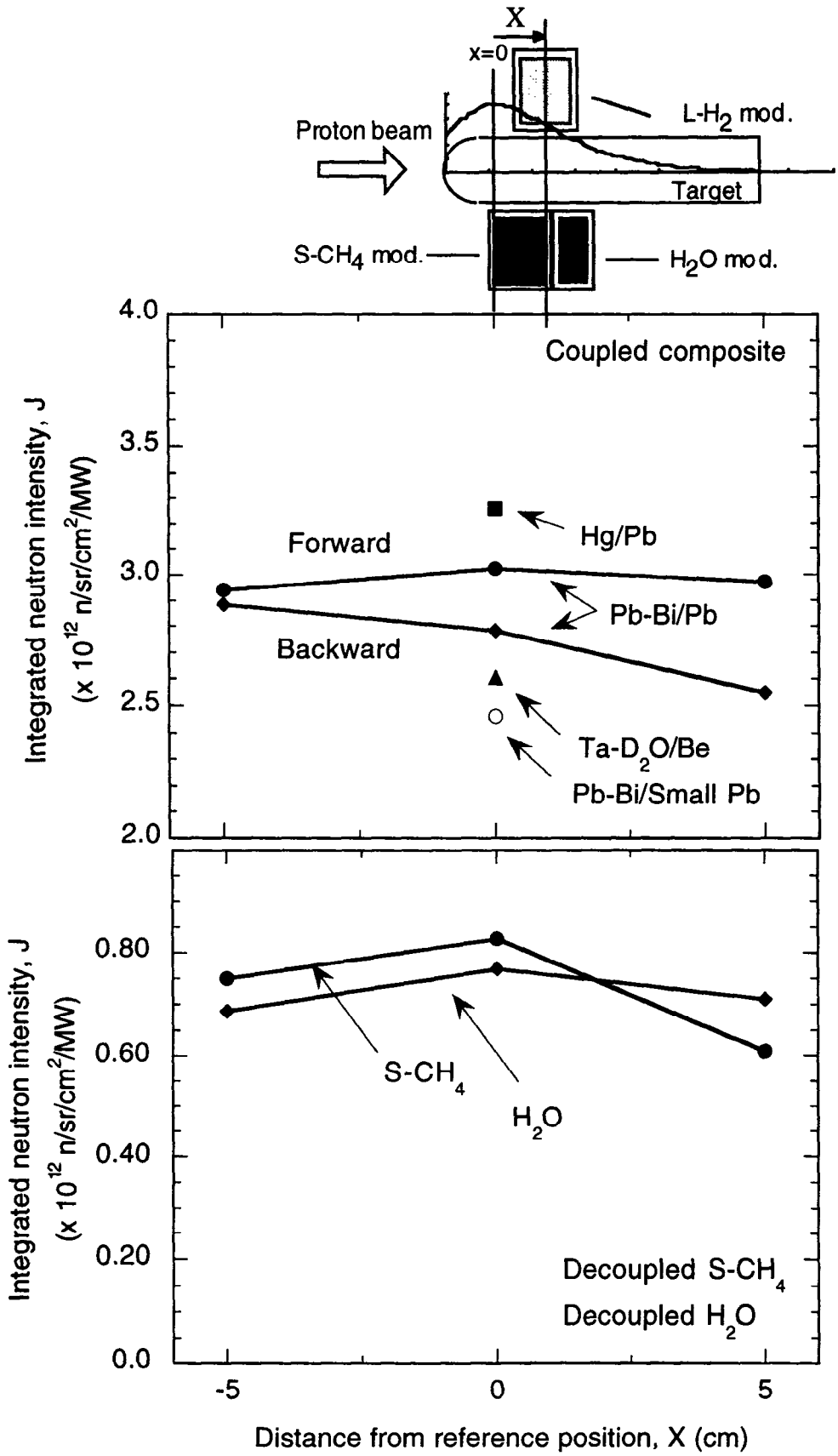

Fig. 7 Integrated neutron intensities, J's, from various moderators at three different positions

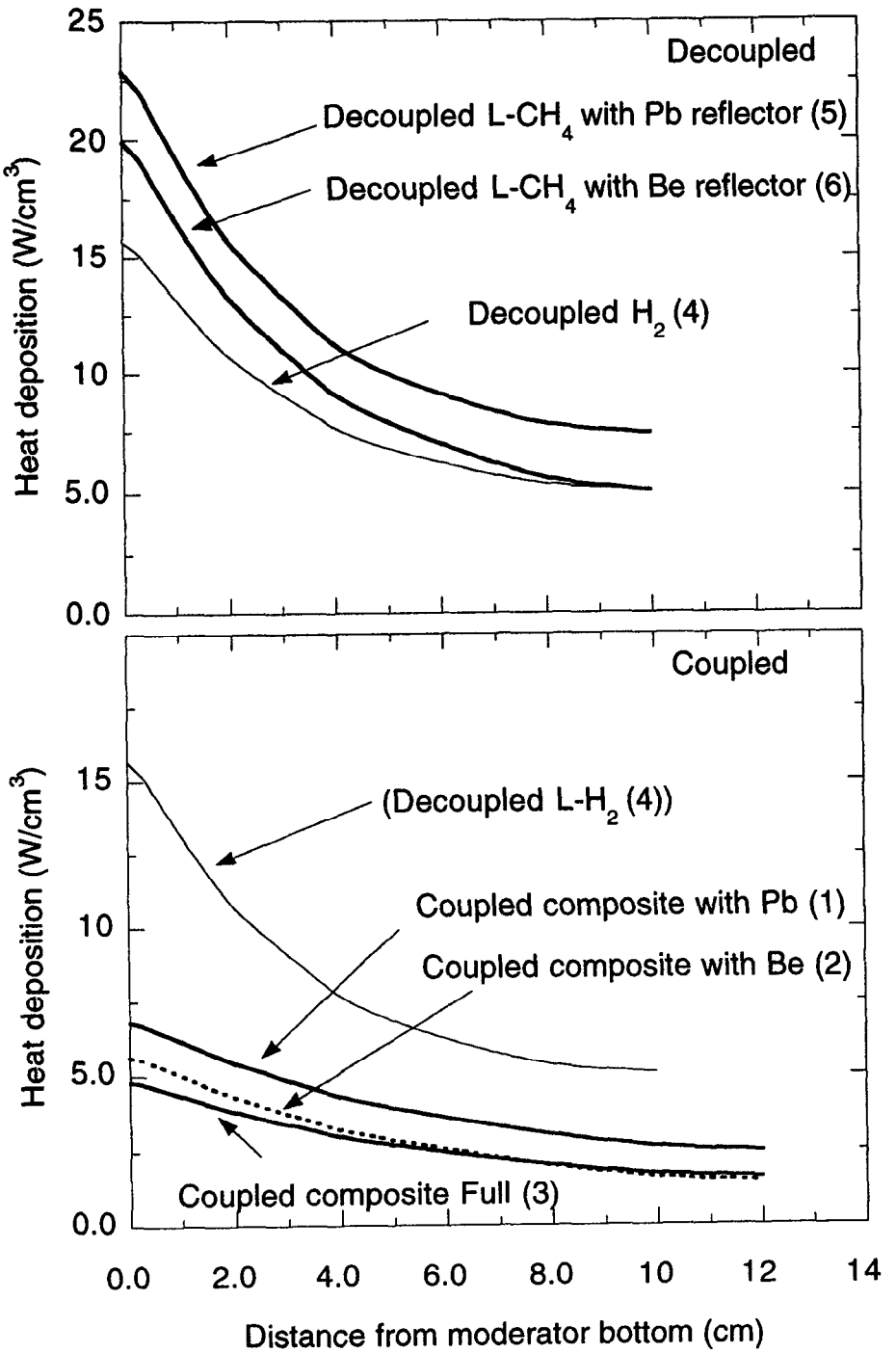

Fig. 8 Spatial distributions of heat deposition in cryogenic moderator as a function of distance from moderator bottom

energy deposition can be decreased by the use of a premoderator as already well known, but we found, with various efforts as described in the separate paper in this ICANS [9], a further reduction in the nuclear heating is feasible incorporated with a higher cold neutron intensity without sacrificing the pulse characteristics for example by the use of a fully extended premoderator. The choice of the reflector is another important issue. The energy depositions can be reduced to some extents by adopting a Be reflector, also as well known. However, the reduction rate at the hottest region close to the target is rather small as shown in Fig. 8. Note that even with a Pb reflector the energy deposition can be reduced to the same level as with a Be reflector by adopting a fully extended premoderator as described above.

The level of the nuclear heating for a coupled moderator with premoderator is in an acceptable range even at the full power (5 MW at the full repetition rate of 50 Hz): it ranges from 2 to 2.8 kW. However, for a decoupled H_2 moderator, which we are thinking to use as a high-resolution thermal neutron moderator probably with an interleave poison sheet, the level becomes very high, especially in the case with a Pb reflector, which reaches at about 8 kW/liter. If we compare the power density, our value is a much higher than other sources due to full pulse use (50 Hz). Some important parameters on cryogenic moderators in various intense sources are compared in Table 3. The use of supercritical hydrogen, is, of course, indispensable. However, one important problem is a very high temperature rise of H_2 during the passage through the moderator chamber, even assuming a higher hydrogen flow rate of 2 liters per second, which is technically very ambitious for such a small moderator volume. The average temperature rise reaches at about 5.8 K. If we assume a possible flow disturbance such as a recirculation flow, a local temperature rise beyond the critical temperature may occur, resulting in the break of the supercritical state over the whole moderator and eventually in the destroy of the cryogenic moderator. Extensive studies how to prevent such flow instabilities has just started [9].

Table 3 Comparison of important parameters of cryogenic moderators in various neutron sources

	ISIS	HFIR	ANS	SNS	JAERI*
Energy deposition (total, kW)	0.4	0.6+1.4	15+15	2	3.95
Moderator volume (liter)	1.06		30		0.5 (1)
Average power density (kW/liter)	0.4		1		7.9
Volumetric flow rate (liters/sec)	0.5	1	30	1	2
Temperature rise (K)	1.1	3	2.3	3	2.9 (5.8)

* The values for pulsed spallation source are for a decoupled H2 moderator. Our value is for the case of (4) in Table 2. The values in parenthesis are for the case of 1 liter moderator volume.

6. Discussions and conclusions

How to judge or justify the present concept of the target-moderator-reflector? A direct comparison of the predicted performance based on the present model with those of other similar project will be the most persuasive way. Since the calculation methods are almost well established, such comparisons will be fair, provided that the model is realistic in engineering feasi-

bility. Thus, neutron spectral intensities and time-integrated intensities (J's) from various moderators combined with an Hg target of a given size were calculated. An example of the results on cold neutron intensity obtained from the reference coupled composite moderator (in detail, see Fig. 1 of a separate paper presented at this ICANS [9]) coupled to the reference Be reflector is shown in Fig. 9 in a liner scale compared with reported values at a medium power SPSS (LANSCE Upgrade, about 160 kW [10]). From these results it can be said that the cold neutron intensity per MW of the present model is at least comparable to or higher than those in other project including a medium power one. The results justify the present concept of the target-moderator-reflector system as far as the neutronic performance is concerned. By adopting a fully extended premoderator an additional gain will be obtained also in the case of a Be reflected system, although the gain may not as large as in a Pb reflected system.

As described above, the superiority of a Pb reflector for coupled composite moderator has been proved in the case a fully extended premoderator : a higher peak cold neutron intensity with approximately a comparable time-integrated intensity, but with a narrower pulse width and a lower energy deposition compared to the reference Be reflected system. For decoupled moderators, the advantage of a Pb reflector is not clear. Extensive calculation on the time distribution of thermal and epithermal neutrons from decoupled moderators are under progress.

Next It was found that the slow neutron intensities are not strongly depend upon the target (Hg) geometry (size and aspect ratio), bringing about a large flexibility in the target engineering.

It also turned out that the energy deposition in a decoupled H_2 moderator is very high, especially in power density which requires a very high H_2 flow rete. To ensure the engineering feasibility to realize the optimized parameters, further R&D efforts are necessary.

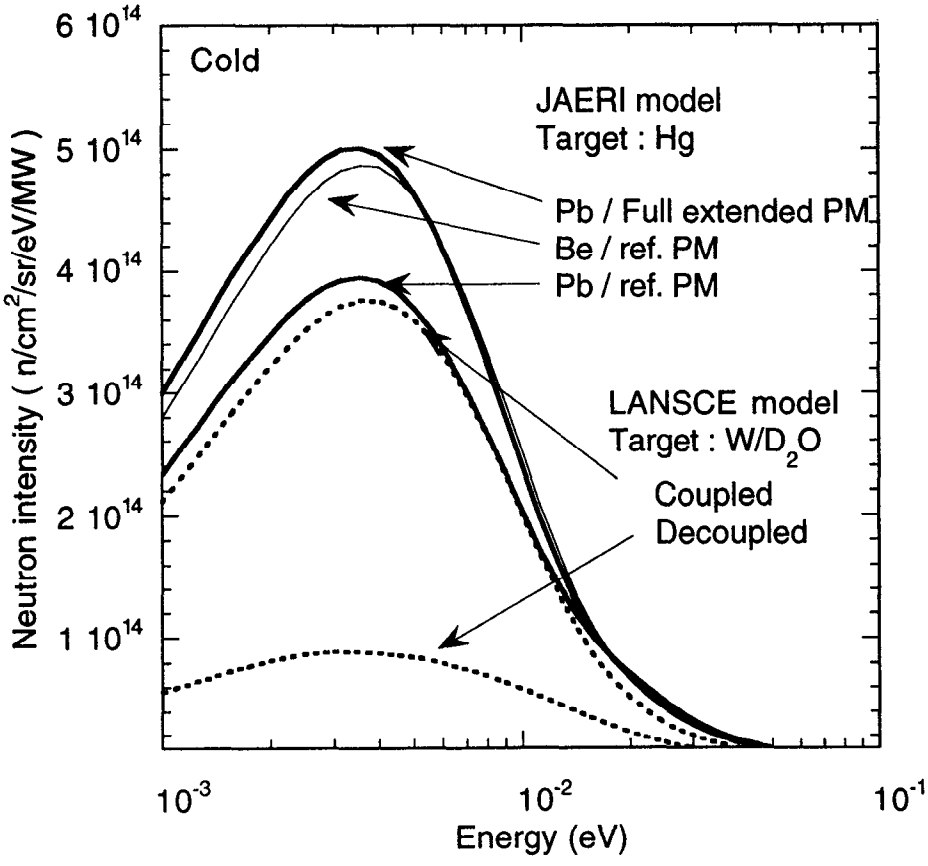

Fig. 9 Slow neutron spectral intensities for various moderator in a liner scale

References

[1]. Y. Suzuki, M. Kinsho, F. Noda, M. Mizumoto and I. Yamane: A new scheme of charge exchange injection for high intensity proton storage ring with high injection energy , poster presented at ICANS-XIV (Starved Rock, June 15-19, 1998)

[2]. N. Watanabe, M. Teshigawara, H. Takada, H. Nakashima, J. Suzuki, K. Aizawa, Y. Oyama and K. Kosako: Neutronic performance of cold moderators in JAERI 5 MW pulsed spallation source, Proc. Int. Workshop on Cold Moderators for Pulsed Neutron Source (Argonne, Oct. 28 - Sept. 2, 1997), in press.

[3]. N. Watanabe, M. Teshigawara, K. Aizawa, J. Suzuki and Y. Oyama: A target-moderator-reflector concept of the JAERI 5 MW pulsed spallation neutron source, JAERI-Tech 98-011 (March 1998)

[4,5]. Y. Kiyanagi, N. Watanabe and H. Iwasa: Nucl. Instr. Meth. A312 (1992) 561. A343 (1944) 558.

[6]. Y. Kiyanagi, S. Sato, H. Iwasa, F. Hiraga and N. Watanabe: Physics B 213 & 214 (1995) 857.

[7]. N. Watanabe and Y. Kiyanagi: Pysica B 180 &181 (1992) 893.

[8]. A. T. Lucas, G. S. Bauer and C. D. Sulfredge: a pelletized solid methane moderator for a medium-to-high power neutron source, Proc. ICANS-XIII (PSI, Villigen, Switzerland, Oct. 11-14, 1995) 644.

[9]. N. Watanabe, M. Teshigawara, H. Takada, H. Nakashima, Y. Oyama, T. Nagao, T. Kai and K. Kosako: Toward a high-efficiency pulsed cold neutron source, presented at ICANS-XIV (Starved Rock, June 15-19,1998)..

[10]. T. Aso, A. Terada, S. Ishikura, M. Teshigawara, T. Kai, H. Hino and N. Watanabe: Structural and hydraulic study on cold source moderator, poster presented at ICANS-XIV (Starved Rock, June 15-19, 1998).

[11]. P. D. Ferguson, G. J. Russell and E. J. Pitcher: Reference moderator calculated performance for the LANSCE Upgrade Project, Proc. ICANS-XIV (PSI, Villigen, Switzerland, Oct. 11-14, 1997) 510.

ICANS-XIV
14th Meeting of the International Collaboration
on Advanced Neutron Sources
June 14-19, 1998
Starved Rock Lodge, Utica, Illinois, USA

Towards a high-efficiency pulsed cold neutron source

N. Watanabe, M. Teshigawara, H. Takada, H. Nakashima, Y. Oyama, T. Kai,
T. Nagao and K. Kosako*

Japan Atomic Energy Research Institute, Tokai-mura, Ibaraki, 319-1195 Japan

*Sumitomo Atomic Power Industries, 2-10-14 Ryogoku, Sumida-ku, Tokyo 130-0026 Japan

Abstract

A high efficiency cold neutron moderator has been developed by adopting a fully extended premoderator of the optimized thickness in a coupled composite moderator system consisting of liquid-hydrogen and hydrogenous premoderator at ambient temperature. An additional gain factor of about 24% has been achieved in the time-integrated and peak cold neutron intensities compared with the reference moderator so far been studied, without sacrificing the pulse characteristics. In addition to the better neutronic performance the nuclear heating in liquid hydrogen can be decreased by about 19% with a fully extended premoderator.

1. Introduction

A coupled composite moderator system, which consists of liquid or supercritical hydrogen (H_2) plus hydrogenous premoderator (PM) at ambient temperature coupled to a reflector, was proposed [1,2] in order to improve the shortage in the time integrated cold neutron intensity in a decoupled H_2 moderator and extensive optimization studies have already been carried out [3-6]. An intensity gain factor of about 6 relative to a decoupled H_2 moderator has been confirmed with a polyethylene premoderator [3]. This gain is about 2 times larger even compared with a decoupled solid methane (CH_4) moderator at 20 K, the best pulsed cold neutron moderator so far been used. The peak intensity of pulsed cold neutrons from the composite moderator is approximately 2 times higher than that from a decoupled one and almost comparable to that from a decoupled CH_4 moderator [3]. If we replace polyethylene by light water, since polyethylene cannot be utilized at an intense spallation source and light water would be an unique material for premoderator, the gain factor decreases to a value of about 5 due to a lower hydrogen number density of water [5]. In spite of a great deal of efforts so far devoted to increase the gain factor, it has not succeeded to obtain a further gain except for the case of a coupled composite moderator utilizing a grooved H_2 moderator [7] and for a partially enhanced moderator (in the spatial distribution) [8]. Although a finite gain relative to the reference case (5 cm thick H_2 plus 2.5 cm H_2O) has been obtained in each case, the former is not practical for a supercritical hydrogen system with a very high mass-flow rate required and the application of the latter is limited to a certain class of experiments such as small angle scattering, reflectometry, etc.

We decided to use coupled composite moderators for high-intensity as well as for high-resolution experiments and performed extensive neutronic calculations to seek the optimal parameters and predict the performance of the proposed source [9,10]. We have confirmed excellent

cold neutron intensities (per MW), which are at least comparable to a corresponding value obtained for a medium power source (a coupled H_2 moderator without premoderator but with a very large reflector in LANSCE Upgrade [11]). In the process of our optimization study based on the proposed target-moderator-reflector concept, we found that the energy deposition (nuclear heating) in H_2 was rather high in spite of the existence of a premoderator [9,10]. We thought this is due to the fast neutrons which obliquely incident upon the viewed surface of the H_2 moderator from a part of primary neutron source (target) through the beam extraction hole in the reflector, where no premoderator exists. We thought that, if this is true, by extending a bottom premoderator (target side) towards neutron extracting direction to some extent, it should be possible to decrease the energy deposition and hopefully increase the cold neutron intensity, since a very small but a finite intensity gain (about 5%) has already been confirmed by a measurement using an electron-linac-base pulsed-neutron-source [3]. Based on this idea we performed an optimization study by calculation on the proposed coupled composite moderator system. This paper reports the results of the present investigation.

2. Moderator model

The model target-moderator-reflector system used for the present calculations is the same as shown in Fig.1 in a separate paper [10]. The configurations of the H_2 moderators and premoderators used for the calculations are shown in Fig.1. The main moderator (H_2, we assumed normal hydrogen) has fixed dimensions of 12^W x 12^H x 5^L cm^3 and located at a fixed position on the target. Six cases were studied; three cases for different bottom premoderator thickness of 1.5, 2.5 (reference case) and 3.5 cm, one case for an extended bottom-premoderators of 2.5 cm thick and two cases for fully extended premoderators (the inside surface of the beam extraction hole in the reflector was completely covered by the premoderator and the bottom-premoderator thickness was 2.5 cm or 3.5 cm). For all cases we assumed a lead (Pb) reflector about 80^W x 160^H x 120^L cm^3 [9,10]. Table 1 summarizes the cases studied.

For the calculations a high-energy hadron transport code NMTC/JAERI and a low-energy transport code MCNP-4A were used with a cross section set (FSXLIB-JFF, FSXLIB-JFNS and THERXS) . For mercury the cross section set recently evaluated at JAERI was used. The num-

Table 1 Calculational model

Proton beam		
Proton energy	Current density	Total beam power
1.5 GeV	48 μA/cm²	5 MW
Cryogenic moderator		
Temperature		Material
20 K		Normal H2 (Ortho para ratio = 75 :25)
Premoderaotor		
Temperature		Material
Ambient		Light water
Calculation		
Calculational model	Thickness of bottom PM (cm)	Extended/Normal
a	1.5	Normal
b (ref.)	2.5	Normal
c	3.5	Normal
d	2.5	Bottom extended
e	2.5	Full
f	3.5	Full

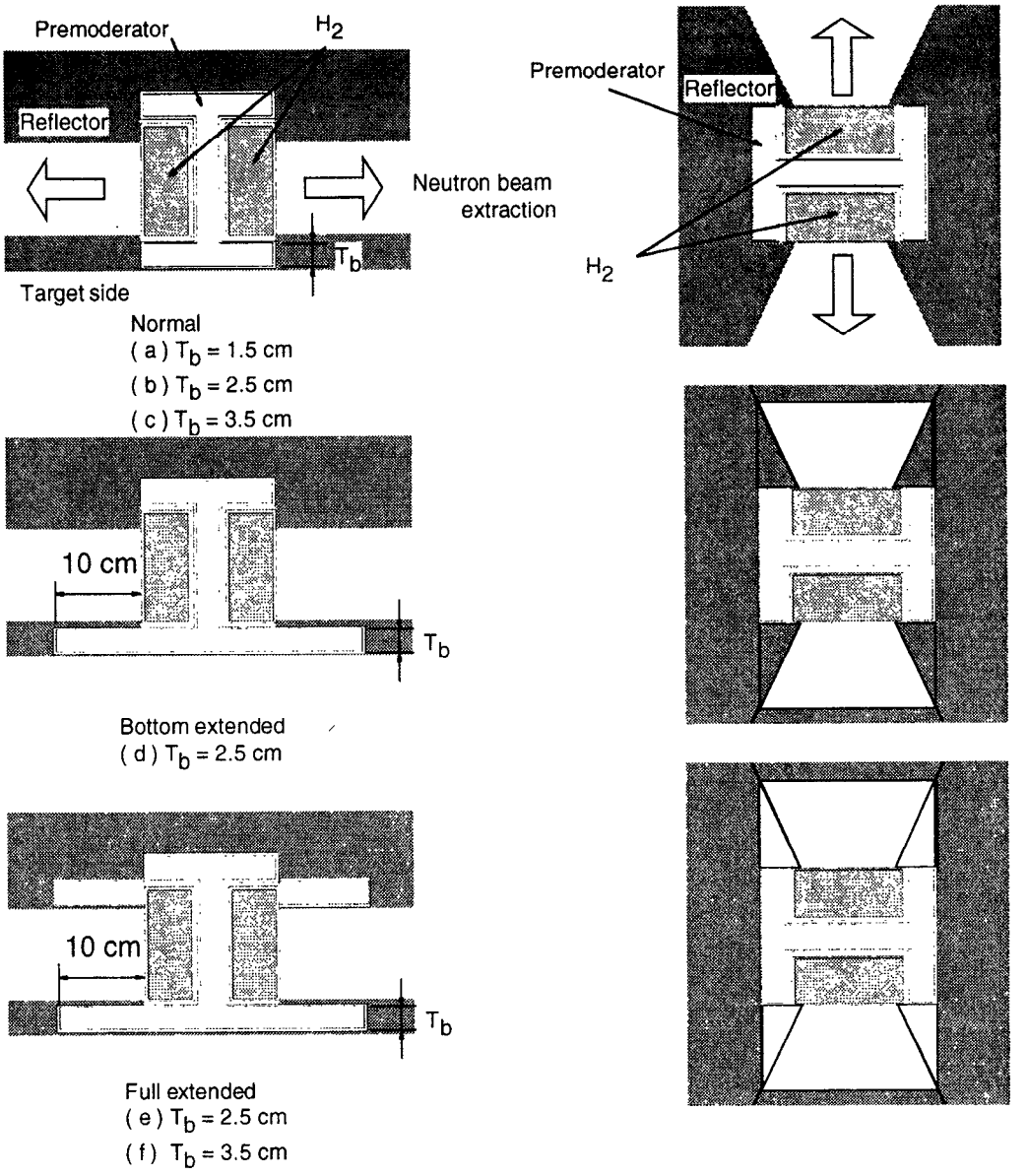

Fig. 1 Calculational model of H_2 moderator with premoderator

ber of protons used for the present calculations were in a range (0.6-1.2) x 10^6 for each calculation.

3. Results and discussions

3.1 Spectral intensity and energy deposition

Spectral intensities and energy depositions for three different bottom-premoderator thicknesses were calculated (cases (a)-(c)). The results are shown in Fig. 2. The time- and energy-integrated cold neutron intensity does not strongly depend on the thickness, but the thickness of 2.5 cm is approximately at the optimal as already known [4]. On the other hand the energy deposition exhibits a monotonic decrease with increasing bottom premoderator thickness. The fact suggests that a possible choice of a thicker premoderator, provided that the pulse width broadening is in an acceptable range. The pulse shapes will be discussed later.

Next, the effect of an extended premoderator (case (d) in Fig. 1) was studied. The result is also shown in Fig. 2. An appreciable intensity increase can be recognized with an additional decrease in the energy deposition. Encouraged by this result we examined fully extended premoderator cases ((e) and (f) in Fig. 1). Higher gain factors, more than expected, have been obtained with further decreases in the energy deposition as shown in Fig. 2.

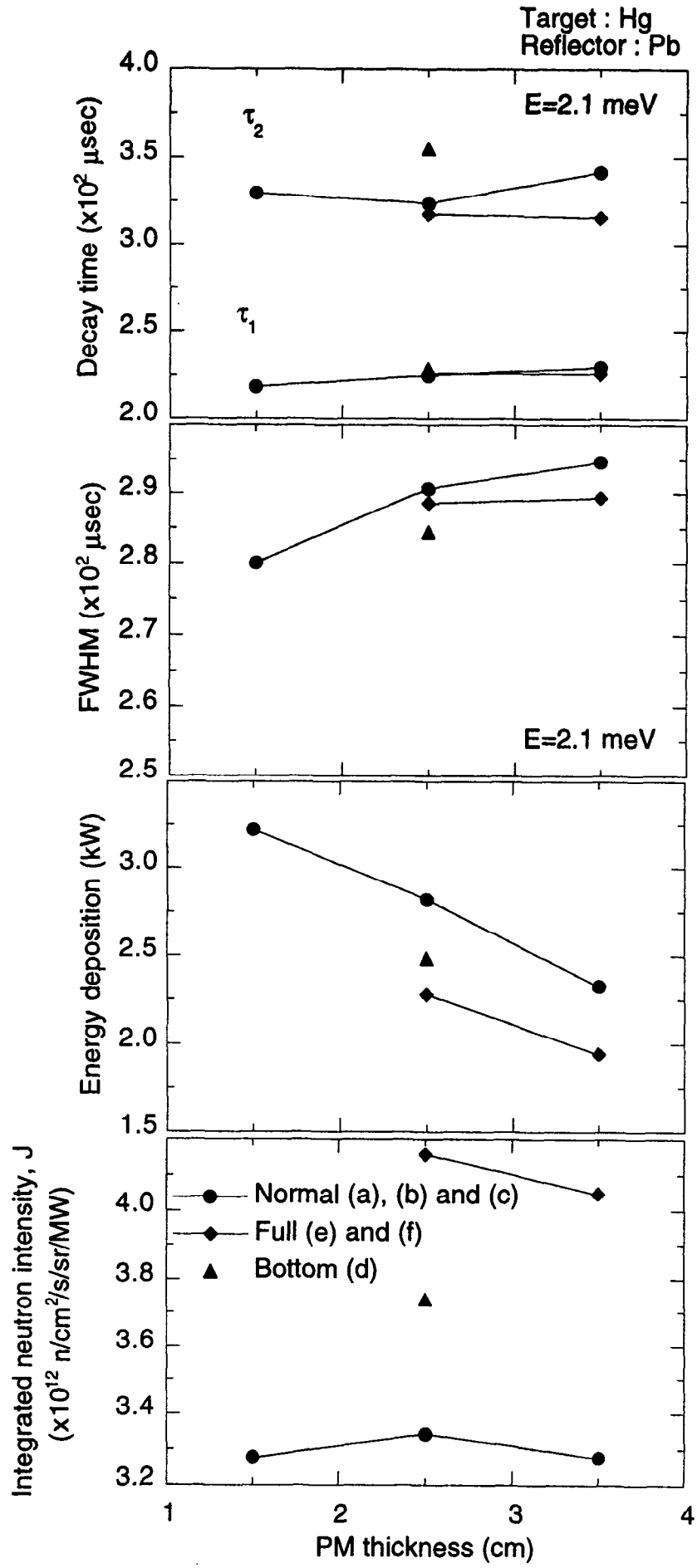

Fig. 2 Premoderator thickness dependence of integrated neutron intensity (J), energy deposition, FWHM and decay time

Table 2 Total energy deposition in H_2 for Pb reflected system

Calulational case	Total energy deposition (kW)
a	3.22
b (ref.)	2.82
c	2.33
d	2.49
e	2.28
f	1.94

The intensity gains relative to the reference case, (b), are plotted in Fig. 3 as a function of the neutron energy. For all moderators there is no energy dependence in the gain factor in the cold neutron region.

Figure 4 compares the spatial distribution of the energy deposition in H_2 for various cases. The ratios relative to the reference case are plotted in Fig. 5. Total energy depositions in H_2 for various cases are summarized in Table 2.

The above results clearly show that as far as the spectral intensity of cold neutrons and the energy deposition are concerned, a fully extended premoderator is much superior to the reference case.

3.2 Pulse characteristics

When we discuss the performance of a pulsed neutron source the time distribution is another important factor in addition to the spectral intensity (time-integrated intensity). Calculated pulse shapes of cold neutrons from the moderators in the reference case (b), with the extended bottom premoderator (d) and with the fully extended premoderator (2.5 cm thick bottom premoderator (e)) are compared in Fig. 6. The most distinguishing feature of the moderators (e) and (f) is that a higher gain factor is achieved in the time-integrated and the peak intensities without pulse

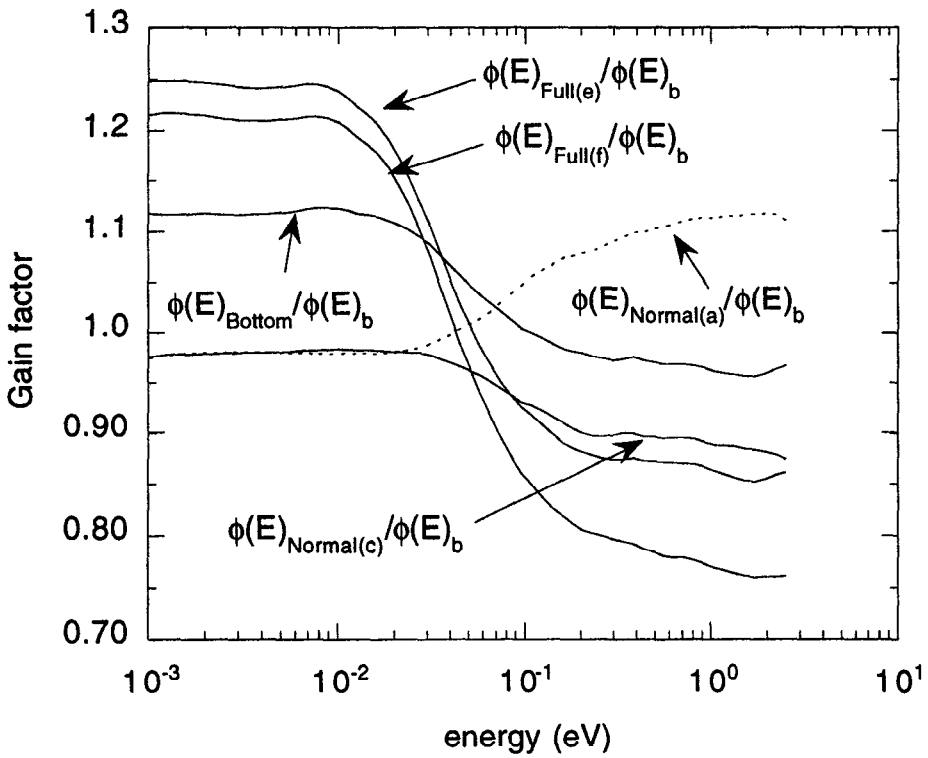

Fig. 3 Gain factor of neutron intensity relative to the reference case as a function of energy

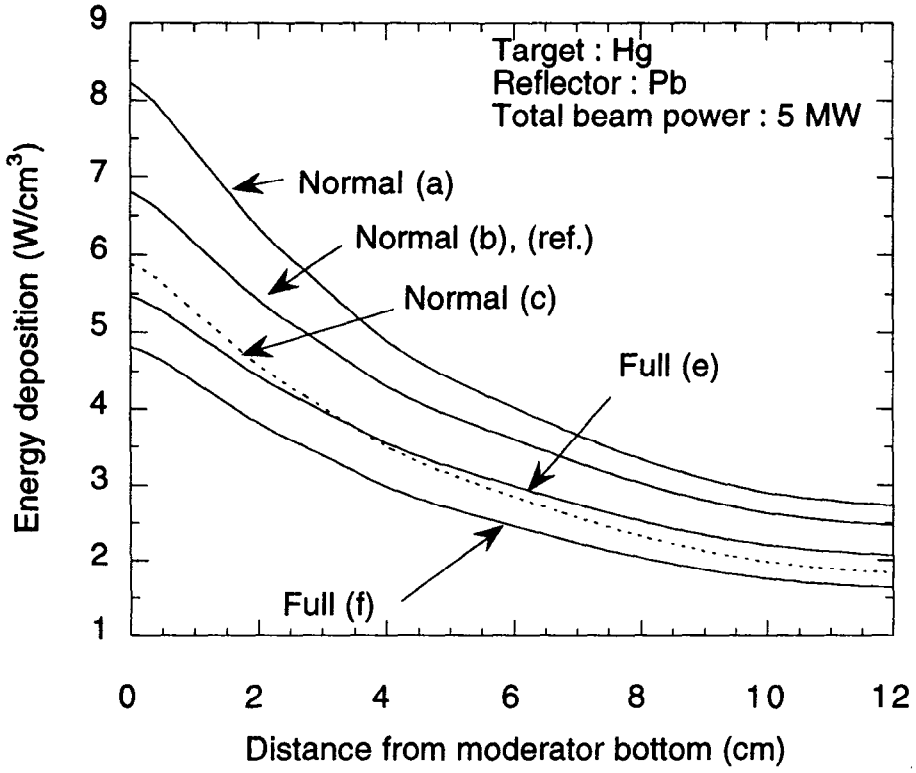

Fig. 4 Energy depsition in H_2 for different configulation of PM

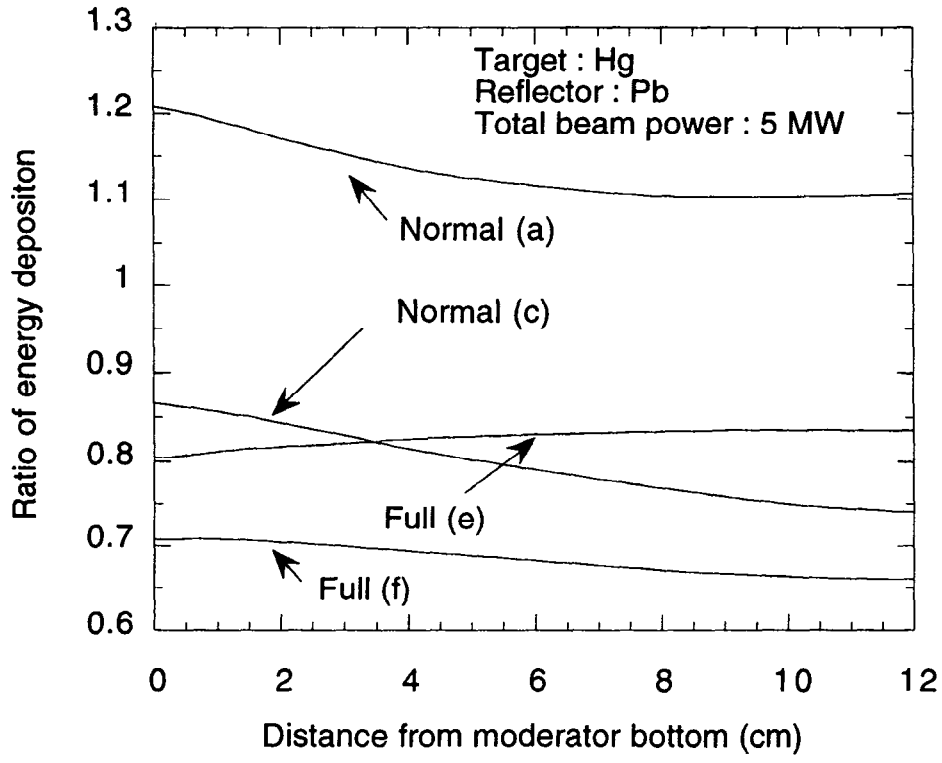

Fig. 5 Ratio of energy depositons relative to the reference case (b)

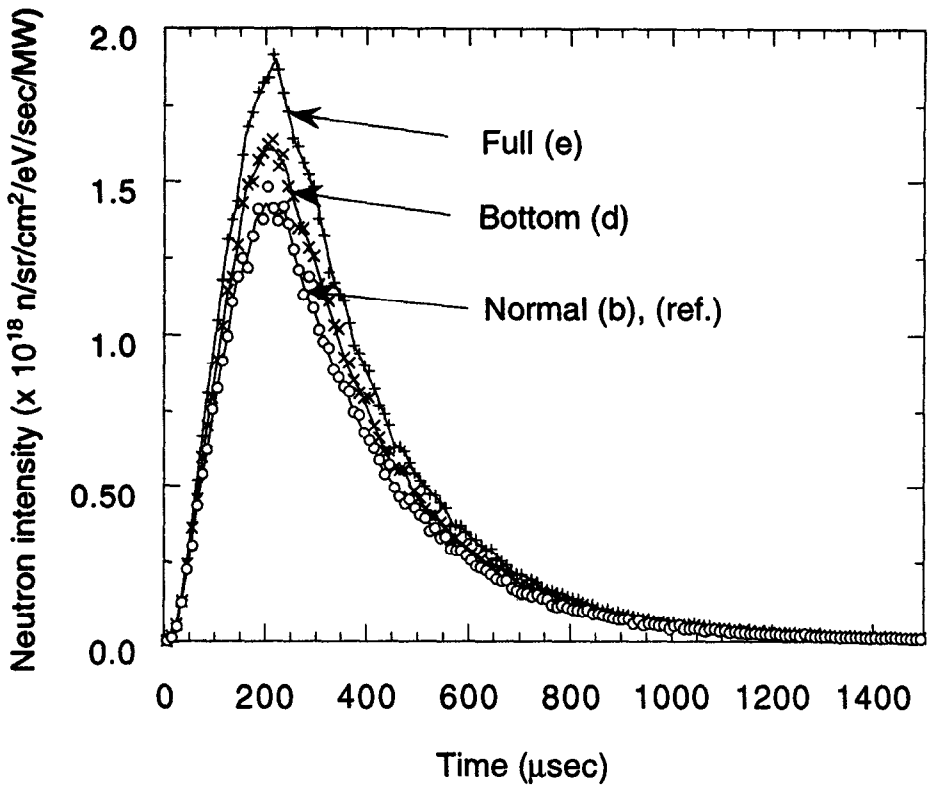

Fig. 6 Time distributions of neutrons at E=2.0-2.2 meV for cases (b), (d) and (e)

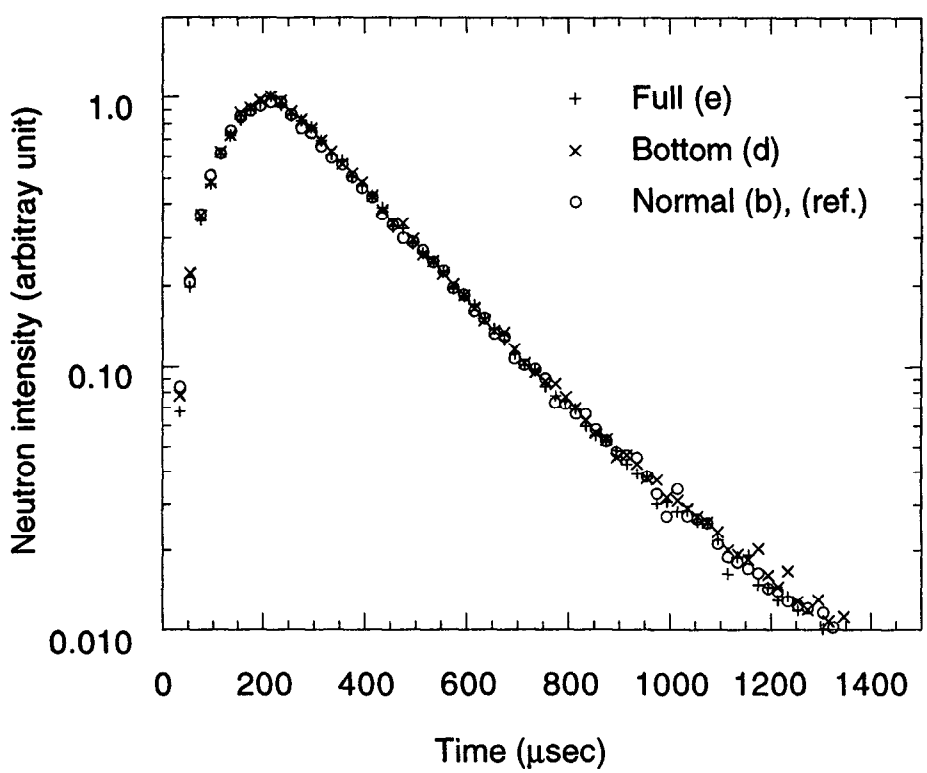

Fig. 7 Time distributions (E=2.0-2.2 meV) normalized at the peak in semi-logarithmic scale

width broadening: in the case (e) a relative gain factor to the reference case is about 24%. The pulse shapes for three different cases ((b), (d) and (e)) are plotted in Fig. 7 in a semilogarithmic scale normalized at the peak intensity. We cannot recognize any difference between the three. This is a great advantage for a pulsed cold neutron source. The pulse widths in full width at half maximum (FWHM) for all moderators are also plotted in Fig. 2.

In order to discuss the decay characteristics at a longer tail, the calculated pulse shapes were fitted by two exponentially decaying terms characterized by two decay times, τ_1 and τ_2, respectively, although there is no physical base to express the pulse shape only by two exponentially decaying terms. The decay times are also plotted in Fig. 2. Judging from the pulse width and two decay times, the pulse characteristics of the fully extended moderator is almost unchanged compared to the reference moderator.

4. Summary and conclusion

It has been shown that a coupled composite moderator of H_2 and a fully extended premoderator of the optimized thickness can provide a considerably higher time-integrated and peak cold neutron intensities compared to a conventional composite moderator so far been discussed, and that these advantage can be achieved without sacrificing the pulse characteristics and, furthermore, with a much lower energy deposition in H_2: triple merits have been realized simultaneously.

In concluding we could say that a coupled composite moderator consisting of H_2 and an optimally designed premoderator has a potential to improve the neutronic performance further with a reduced nuclear heating in the maim cryogenic moderator (H_2) by introducing various ideas. Such efforts are under progress.

References

[1]. N. Watanabe: Advanced Neutron Sources 1988, Institute of Physics, Bristle and New York, p.763.

[2]. N. Watanabe, Y. Kiyanagi, K. Inoue, M. Furusaka, S. Ikeda, M. Arai and H. Iwasa: Advanced Neutron Sources 1988, Institute of Physic, Bristle and New York, p.767.

[3,4]. Y. Kiyanagi, N. Watanabe and H. Iwasa: Nucl. Instr. Meth. A312 (1992) 561, A343 (1944) 558.

[5]. Y. Kiyanagi, S. Sato, H. Iwasa, F. Hiraga and N. Watanabe: Physica B 213 & 214 (1995) 857.

[6]. N. Watanabe, Y. Kiyanagi and M. Furusaka: Recent progress in developing high-efficiency cryogenic moderators, Proc. ICANS-XIII (PSI, Villigen, Switzerland, Oct. 11-14, 1995) 659.

[7]. Y. Ogawa, Y. Kiyanagi, M. Furusaka and N. Watanabe: J. Neutron Research (1997) T-196.

[8]. Y. Kiyanagi, Y. Ogawa, N. Kosugi, H. Iwasa, M. Furusaka and N. Watanabe: Further optimization of coupled liquid hydrogen moderator for intense pulsed neutron source, Proc. ICANS-XIII (PSI, Villigen, Switzerland, Oct. 11-14, 1996) 654.

[9]. N. Watanabe, M. Teshigawara, H. Takada, H. Nakashima, J. Suzuki, K. Aizawa, Y. Oyama and K. Kosako: Neutronic performance of cold moderators in JAERI 5 MW pulsed spallation source, Proc. Int. Workshop on Cold Moderators for Pulsed Neutron Sources (Argonne, Oct. 28 - Sept. 2, 1997), in press.

[10]. N. Watanabe, M. Teshigawara, H. Takada, H. Nakashima, Y. Oyama, T. Nagao, T. Kai, Y. Ikeda and K. Kosako: A conceptual design study of target-moderator-reflector system for JAERI 5 MW spallation source, to be published in Proc. ICANS-XIV.

[11]. P. D. Ferguson, G. J. Russell and E. J. Pitcher: Reference moderator calculated performance for the LANSCE Upgrade Project, Proc. ICANS-XIII (PSI, Villigen, Switzerland, Oct. 11-14, 1997) 510.

ICANS-XIV
14th Meeting of the International Collaboration on
Advance Neutron Sources
June 14–19, 1998
Utica, IL USA

Neutron Production Enhancements for the Intense Pulsed Neutron Source

E. B. Iverson, J. M. Carpenter, T. L. Scott, M. E. Miller, L. D. Peters, M. W. Schlueter
Intense Pulsed Neutron Source
Argonne National Laboratory
9700 South Cass Avenue
Argonne, IL USA 60439

The Intense Pulsed Neutron Source (IPNS) was the first high energy spallation neutron source in the United States dedicated to materials research. It has operated for sixteen years, and in that time has had a very prolific record concerning the development of new target and moderator systems for pulsed spallation sources. IPNS supports a very productive user program on its thirteen instruments, which are oversubscribed by more than two times, meanwhile having an excellent overall reliability of 95%. Although the proton beam power is relatively low at 7 kW, the target and moderator systems are very efficient. The typical beam power which gives an equivalent flux for long-wavelength neutrons is about 60 kW, due to the use of a uranium target and liquid and solid methane moderators, precluded at some sources due to a higher accelerator power.

The development of new target and moderator systems is by no means stagnant at IPNS. We are presently considering numerous enhancements to the target and moderators that offer prospects for increasing the useful neutron production by substantial factors. Many of these enhancements could be combined, although their combined benefit has not yet been well established. Meanwhile, IPNS is embarking on a coherent program of study concerning these improvements and their possible combination and implementation. Moreover, any improvements accomplished at IPNS would immediately increase the performance of IPNS instruments.

1 Enhancements In Progress

A number of enhancements to IPNS neutron production are already in progress. Design choices for these enhancements have largely been made, and engineering questions are all that remain to be answered, whether by experiment or calculation. These enhancements are relatively well-defined, with clearly demonstrable benefits. They include a re-designed booster target, based on experience with the booster target used from 1988–1991, re-designed solid methane moderators for use with the booster target, a moderator-reflector assembly designed for rapid moderator replacement, and experimental studies of minor moderator modifications.

1.1 New Booster Target

IPNS has operated with a depleted uranium target from 1981–1988 and since 1992. For three years, 1988–1991, we operated with a booster target composed of the same alloy of α-phase uranium enriched to 77% ^{235}U, and of the same physical design as the depleted target. This subcritical target had a multiplication factor k_{eff} of approximately 0.80, and resulted in neutron production of about two and one-half times the production rate with the depleted uranium target.

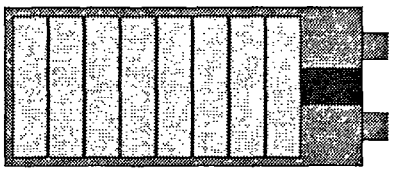

Figure 1: The IPNS target, composed of uranium disks cooled by water.

The booster target failed at approximately the expected end of its design life, as did the first depleted uranium target. Examination of the failed depleted uranium target indicated that the failure was due to anisotropic growth, caused by the rhombohedral α-phase crystal structure. A new booster target of enriched uranium with ten weight percent molybdenum in a cubic γ-phase was then designed which would be stable against anisotropic growth under irradiation. Stability and manufacturing methods for the U-10Mo alloy have been experimentally verified in the German SNQ study. The new target would have the same multiplication factor, and thus the same gain in neutron production, as the original booster target. The new booster target is predicted to have a significantly longer lifetime than the original booster target, which was nonetheless acceptable. The new target would be physically similar to the existing target.

There are a number of challenges to be met involving the use of an enriched booster target. Current Department of Energy policies require proof that highly enriched materials offer benefits which cannot be obtained by the use of materials of lower (less than 20%) enrichment. Detailed calculations demonstrating these benefits have been performed by Roger Blomquist of the Reactor Analysis division of ANL. If the booster target is to be combined with a beryllium reflector, the Safety Analysis Report will need to be modified slightly. Finally, use of the booster target will exacerbate the operational difficulties presently experienced in the solid methane moderators, discussed in greater depth below.

In spite of the benefits to be gained from the use a booster target, the penalties and challenges of its use have lead us to decide that it is simply not practical.

1.2 Solid Methane Moderators with Increased Neutron Yield

The C and H moderators are composed of solid methane, which displays a "burping" phenomenon under irradiation. This behavior is currently being controlled by an annealing procedure performed manually every two to three days during operations. Any increase in target yield, whether from a booster target or some other modification, will result in a shortening of the allowable time between annealing operations. The annealing procedure currently in use is to be automated, which will allow more flexibility in the annealing schedule, reduce manpower requirements, and reduce the operational down time for anneals. A task force has been assigned that is currently in the planning stage of this project with an estimated project completion of February 2000.

A cooperative research program with the Nuclear Engineering Department at Pennsylvania State University has been explored to study the behavior of solid methane under heavy neutron irradiation. This program is expected to provide insight into the dynamics of the spontaneous energy release and the hydrogen release and the associated pressure surge, possibly leading to techniques for controlling or mitigating the effect of radiation damage and/or resulting pressurization. This program is currently on hold. Finally, the moderator container may be amenable to redesign against fatigue effects based on calculation of the stresses resulting from the pressure surge associated with the burping phenomenon. This possibility has not yet been explored.

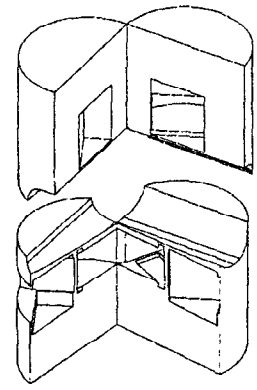

Figure 2: A "clamshell" reflector.

1.3 Rapid Moderator Replacement

The moderator and reflector assembly can be markedly improved to facilitate rapid moderator replacement. The present reflector assembly must be laboriously disassembled to provide access to the moderators, resulting in considerable time expenditure and radiation exposure. The use of "clamshell" reflector and shield plug assemblies, which would split open vertically to allow ready access to the moderators, would increase the availability of the moderator system, and reduce time and personnel irradiation during maintenance. Such a reflector design is on hold until resources become available to complete the design. A quick connection system for plumbing and wiring is also being designed to save operational down time and reduce personnel radiation exposure during moderator replacement. The design for the quick connect system is in progress with an estimated design completion of March 1999.

1.4 Grooved Moderator Reconfiguration

A program of Monte Carlo simulations directed toward optimizing the groove configurations of the C moderator was carried out at the University of Illinois, Urbana-Champaign under the direction of Professor Brent Heuser of the Nuclear Engineering Department. The results of these simulations indicate that exchanging the current solid methane moderator with horizontal grooves for a similar moderator with vertical grooves would increase the neutron intensity seen by the POSY instruments by a factor of 1.3–1.6. These simulations further predict that the neutron intensity at the SAD and SAND instruments, which also view the C moderator, would not be compromised. The vertical grooved moderator is currently being fabricated in Argonne shops, with an estimated completion date of March 1999.

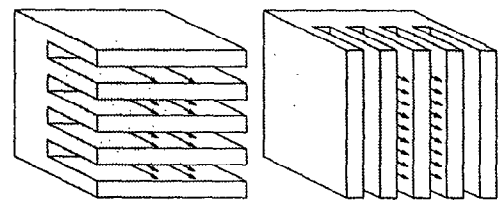

Figure 3: Grooved moderators from the POSY viewpoint.

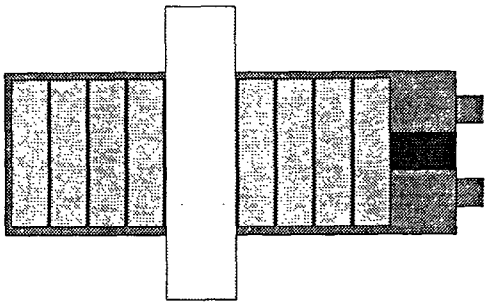

Figure 4: A split target with a tall moderator in the flux trap region.

1.5 Exotic Moderator Materials

Experimental studies of exotic moderator materials at Hokkaido University in Japan are in progress. The materials included in this study are partially deuterated liquid hydrogen (H_2+HD), partially deuterated liquid methane, and partially deuterated solid methane (CH_4+CH_3D). We anticipate improvements in the thermalization capabilities of these materials relative to the protonated versions, which would stem from the richer rotational levels of the asymmetric molecules. The benefit of such moderator materials include a roughly estimated gain of a factor of 1.2 in the intensity of long-wavelength neutrons. The materials to perform these experiments have been ordered, and should be received in October. The actual experiments will follow, according to the run schedule for the Hokkaido facility.

2 Computational Studies of Potential Enhancements

A number of possibilities for potential enhancement of the neutron production at IPNS are being investigated by computational Monte Carlo studies. The benefits of these design changes are in general less precisely known, and such calculations will provide a useful assessment of their value to IPNS, as well as to the pulsed neutron community in general.

2.1 Split Target

The present target system is composed of a set of eight zircalloy-clad uranium disks, cooled by water. Each disk is four inches in diameter and one inch thick. These disks are spaced one-sixteenth of an inch apart, and the moderators are centered along the length of the target assembly. By "splitting" the target, i.e., separating two of the intermediate disks by a larger space, it is conceivable that the intensity gains from appropriately positioned moderators could reach a factor of three over the present target arrangement. A split target could be employed with either the new booster target design, or with the present depleted uranium design. The space between the two halves of the split target might be useful as a flux-trap moderator. The flux-trap moderator could be "tall," i.e., oblong, in such a way that it provides more neutrons to those instruments which would not suffer from the reduced angular resolution in the vertical dimension. This design is similar to that which forms a central part of the current upgrade at the Manuel Lujan, Jr., Neutron Scattering Center.

2.2 Squat Target

Japanese experience at KENS indicates that a target which presents an oblong cross section to the oncoming proton beam may result in large intensity gains—greater than a factor of two in some cases. This cross section would have the major axis comparable to the diameter of the present circular target. If premoderators (discussed below) were found to provide an additional benefit, use of the oblong target at IPNS

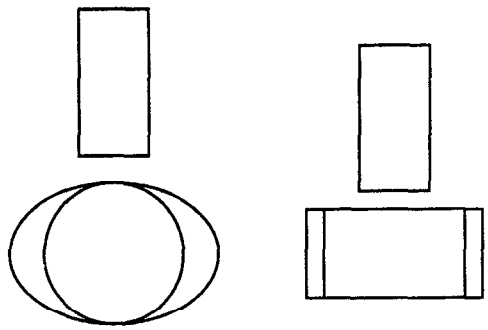

Figure 5: A squat target (right) allows moderators to be closer to the target itself.

might not require moving the moderators (and thus the neutron beam-lines). The new target might further require modifying the incident proton beam, either in position or footprint. Implementation of the squat target might require moving some or all of the neutron beam-lines and instruments up or down.

2.3 Combined C and H Moderators

The three moderators (C, F, and H) now in use serve twelve neutron beam-lines. Six of these beam-lines view the F moderator, beneath the target; three view the C moderator, also beneath the target; and three view the H moderator, above the target. Combining the functions of the C and H moderators could enhance the beam intensity available from all moderators by as much as a factor of 1.5, due to the increase reflector efficiency which would result.

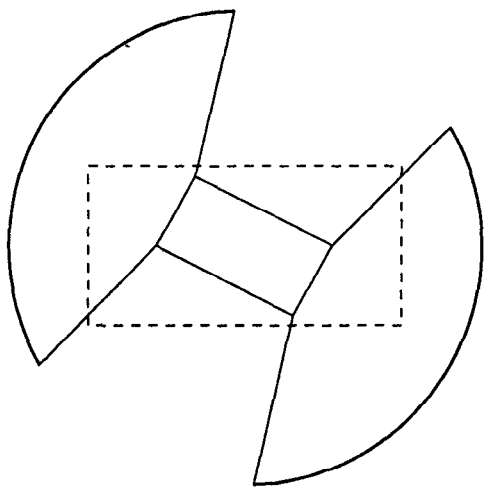

Figure 6: Combining the functions of the C and H moderators.

2.4 Solid Methane F Moderator

Of the current moderators, the C and H moderators are composed of solid methane at 30 K, while the F moderator is composed of liquid methane at 110 K. Replacing the moderator material in the F moderator with solid methane would increase the intensity of longer wavelength neutrons by a factor of six, although reducing the intensity at intermediate wavelengths by a factor of two. This reduction is partially countered

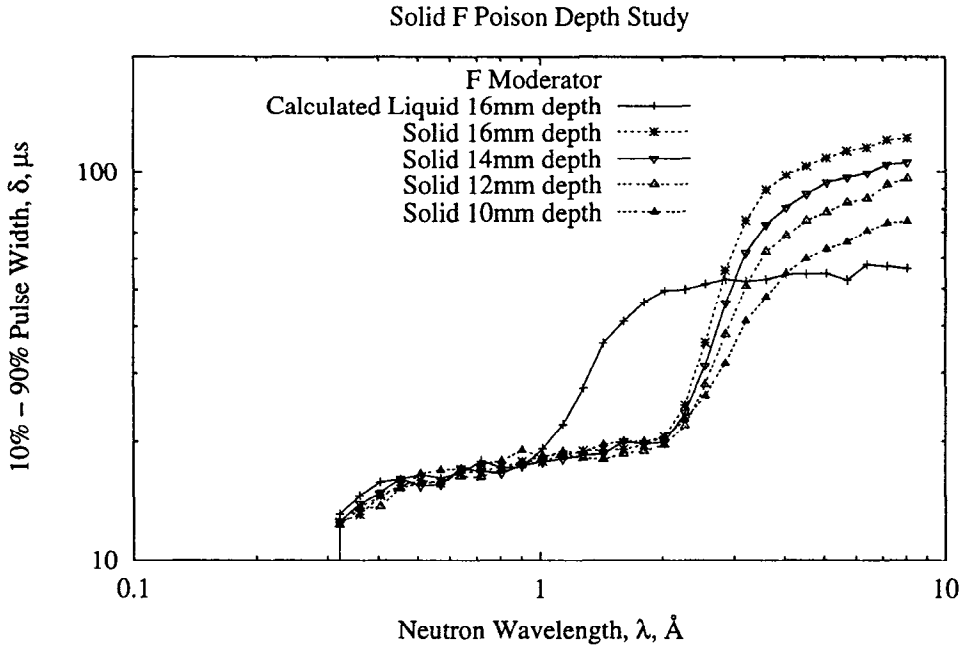

Figure 7: Pulse widths as a function of poison depth for a solid methane F moderator, as compared to the present liquid methane moderator.

by an improvement (reduction) in the pulse resolution of a factor of 0.8 at intermediate wavelengths, and 0.9 at shorter wavelengths. The interest in such a proposal stems from the ever-present desire to have more long-wavelength neutrons.

2.5 Pre-Moderators

In the present moderator-reflector configuration, there is neither moderating nor reflecting material between the target and the moderators. The use of "pre-moderators," moderating material at room temperature placed between the target and the viewed moderator, would reduce cooling requirements on the cryogenic moderators; especially important if other IPNS improvements were to increase the neutron yield of the target system, requiring more frequent annealing of the solid methane moderators. Calculations performed as part of a Japanese study have further indicated the possibility that pre-moderators would result in intensity gains in the neutron beams.

2.6 Composite (Pre)Moderators

Typical moderators at pulsed neutron sources are, like those at IPNS, poisoned with a heterogeneous layer of neutron absorbing material. This layer provides a more advantageous pulse shape to the neutron beam. Moderators which employ more complex arrangements and more diverse materials offer the ability to tailor the neutron spectrum and increase the neutron intensity. Such composite moderators may also provide the possibility of duplicating the 100 K spectrum available from a liquid methane moderator without using liquid methane, which suffers serious radiation-induced decomposition at higher heat loads.

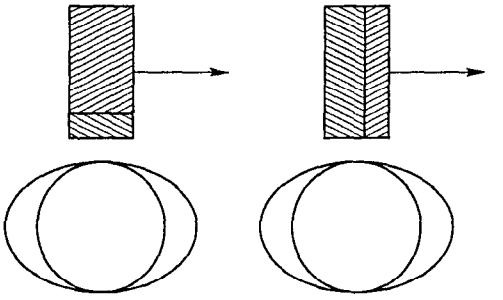

Figure 8: A pre-moderator (left) and a composite moderator.

2.7 Decoupler Materials

The present moderators are all decoupled from the rest of the moderator-reflector assembly by 0.5 mm thick layers of cadmium. Changing the decoupler material to gadolinium or some other neutron absorber exhibiting a different energy dependent cross section would result in a different balance between lengthened tails in the neutron pulse structure and neutron intensity. This balance might further be influenced by cooling the reflector assembly, which is presently at ambient temperature. Figure 9 shows an approximate time-average neutron spectrum in the reflector, $F(E)$, and the fraction of neutrons transmitted by decoupling layers of Cd and Gd. Actual attenuation of isotropically distributed neutrons is greater than shown, computed for normally incident particles. The decoupler must exclude long-lived neutrons from the Maxwellian (low-energy) part of the spectrum, yet should pass epithermal (higher energy) neutrons which fall off rapidly. The gadolinium decoupler passes more epithermal neutrons than does the cadmium, at the expense of broadening the pulse in the moderator.

2.8 Reflector Material

The target and moderators are contained within a large two-region reflector assembly, currently composed of beryllium and graphite. Changing the inner reflector material from graphite to beryllium would result in greater intensity in the neutron beams from some or all of the moderators. Rough calculations indicate that this gain in intensity would be of the order of a factor of 1.15.

2.9 Larger Moderators

The present moderators have viewed surfaces with dimensions of ten by ten centimeters. Enlarging the viewed face of the moderator from ten by ten centimeters to, for example, twelve by twelve centimeters

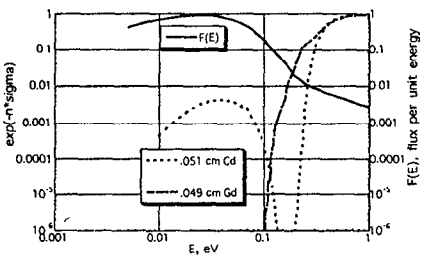

Figure 9: The neutron spectrum in reflector compared to decoupler transmission fractions.

would provide a gain in neutron intensity at the cost of angular resolution.

2.10 Exotic Moderator Materials

The experiments previously described (concerning exotic moderator materials) taking place at Hokkaido University should be accompanied by computational analysis of the potential benefit of these materials. As mentioned above, these partially deuterated moderator materials—$H_xD_{2-x}(\ell)$, $CH_xD_{4-x}(\ell)$, and $CH_xD_{4-x}(s)$—offer the possibility of gains of a factor of 1.2 in intensity for longer wavelength neutrons. The primary obstacle to calculation of the moderating capabilities of these materials is the lack of knowledge of their scattering kernels at cryogenic temperatures.

3 Long-Term Enhancements

Finally, there are some long-term possibilities for study. These concepts would require a considerable amount of study before they could be determined to be feasible, and their benefits are not well characterized. The knowledge and experienced gained would be enormously useful to the pulsed neutron source community, and they would require a great deal of additional study prior to implementation.

3.1 Intermediate Spectrum Booster

The present design for a sub-critical booster target uses primarily ^{235}U, deriving most of the neutron multiplication from fast neutron induced fissions. A booster target which relied more upon fissions induced by neutrons of lower intermediate energies accomplished by including more coolant/moderator might require lower enrichment uranium for the target material. A target composed of lower enrichment uranium would provide a solution to the political difficulties surrounding the use of highly enriched uranium.

3.2 Circulating Solid Methane Moderator

One of the difficulties described previously concerning the use of solid methane as a moderator material is that, while solid methane is neutronically superior to any other material presently used, its behavior under radiation exposure leads to gas evolution and attendant "burping"—sudden surges in temperature and pressure resulting in often permanent structural damage to the physical structure of the moderator assembly. While there are other avenues of exploration intended to counter this problem, one attractive concept is the use of *circulating* solid methane in a moderator. Several systems have been proposed, including small particles of solid methane suspended in liquid hydrogen. Development of a circulating solid methane moderator would have considerable benefit to the entire pulsed neutron community. This concept is presently under active development by various members of the ACoM collaboration (the collaboration for Advanced Cold Moderators); this collaboration and its work are discussed elsewhere in these proceedings.

4 Summary

IPNS has a history of innovative developments in spallation neutron production for neutron scattering. The new efforts described herein will continue to improve the state-of-the-art neutron scattering research that takes place at IPNS, and will benefit companion efforts underway elsewhere in the country and throughout the world.

POSTERS

ICANS-XIV
14th Meeting of the International Collaboration on
Advanced Neutron Sources
June 14-19, 1998
Starved Rock Lodge & Conference Centre, Box 570, Utica, IL 61373, USA.

The IRIS 4.2 K Cold Graphite Analyser Design.

M.A. Adams , J.J.P. Balchin , T.A. Broome , C.J. Carlile , D.A. Cragg ,J. Tomkinson , C.N. Uden
ISIS Facility , CLRC Rutherford Appleton Laboratory , Chilton , Didcot , Oxfordshire , UK , OX11 0QX
Tel: + 44(0)1235 821900
Fax: +44(0)1235 445720

Abstract:

Summary.

This presentation describes a new Cryogenic Cooling system for the IRIS Graphite Analyser on the ISIS Spallation Neutron Source. The paper includes a brief description of the scientific requirements, the concept behind the cooling system, reference to an increase in the area covered by the analyser using a mixed array of the original Le Carbonne and new Atomgraph Pyrolitic Graphite crystals, design layouts supporting the new proposed design and CAD 2-D & 3-D views showing the current design status.

The requirements of the new graphite analyser cooling system are:

1. To cool the Graphite Analyser Crystals to 5 Kelvin or below.
2. To increase the area covered by Crystals both Longitudinally & Latitudinally.

Background:

The IRIS instrument graphite analyser is located within a vacuum vessel some 36.5 m from the liquid hydrogen moderator on the ISIS pulsed neutron source. The cylindrical vessel, 2.0 m in diameter & 0.6 m in height contains two crystal analyser banks, Muscovite Mica & Pyrolitic Graphite, arranged in inverted geometry close to back scattering. Each analyser consists of a spherical surface reflecting scattered neutrons to an array of scintillation detectors below the sample position. The precise crystalline structure of each analyser material provide peak neutron reflection intensities (Bragg angle scattering) for discrete neutron energies from different atomic planes. Using a series of beam choppers to select different energies allows the instrument to measure d-spacings for a range of materials within several ranges of instrument resolution.

The present graphite analyser is cooled to 25 Kelvin using a 2-stage gaseous Helium closed cycle refrigerator circulating through a pipe brazed to the rear of the analyser mounting plate. The Helium refrigerator & cooling head, liquid Nitrogen feed pipework & storage vessel near the main vacuum vessel are linked to it via insulated lines. Operation at this temperature reduces background neutron scattering caused by the effect of Thermal Diffuse Scattering (TDS) & is caused by neutron interactions with phonons within the graphite. Measurements conducted on the IRIS instrument suggest that reducing the analyser temperature produces a proportional reduction in TDS. An improvement in instrument signal background up to a factor of four is achievable by a four fold reduction in Thermal Diffuse Scattering. Cooling the graphite to 5 Kelvin using liquid Helium is expected to improve the instrument signal background from 1250:1 to 5000:1. Further reductions in TDS may be achievable by reducing temperatures still further if pumping on the Helium reservoir takes place (this is not covered here but may be incorporated at a later date).

In order to achieve this temperature a cryostat design is required which will connect to the IRIS vacuum vessel. This will supply liquid Helium to an analyser support surrounded by a radiation heat shield cooled to liquid Nitrogen temperature, 77 Kelvin. The current cooling installation will be retained for improved cryopumping of the instrument vessel. The graphite analyser crystals, together with Cadmium shielding plates will be secured to a new cooling loop within the vessel in a manner to provide good heat transfer characteristics and the required back scattering geometry.

In parallel with the installation of the cryostat, a new analyser plate is required to increase the graphite analyser coverage. Latitude angles are increased by 5.4° for low & high angle scattering, together with an increase in the solid angle subtended by the analyser in the longitudinal axis from 4.2° to 11.2°.(Subject to modifications to the collimation / beryllium filter assembly). The design mixes the original Le Carbonne & new Atomgraph crystals to give a uniform resolution function.

THE IRIS 4.2 K COLD GRAPHITE ANALYSER

M.A. Adams J.J.P.Balchin T.A. Broome C.J. Carlile D.A. Cragg J. Tomkinson C.N. Uden

CLRC ISIS

THE IRIS INSTRUMENT

The IRIS Spectrometer incorporates two Analyser arrays. An ambient temperature array of Muscovite Mica Crystals and a Pyrolitic Graphite Crystal array cooled to 25 Kelvin using a gaseous Helium CCR cooling system. Each array is arranged to a geometry suitable for near backscattering experiments. A cooling system is proposed to further cool the Graphite Analyser array to a temperature of 4.2 Kelvin to produce an improved instrument Signal : Background ratio of 5000 : 1. This reduces the Thermal Diffuse Scattering effects of the analyser material. It is also proposed to increase the Graphite area coverage x 3 to improve the neutron flux at the detectors.

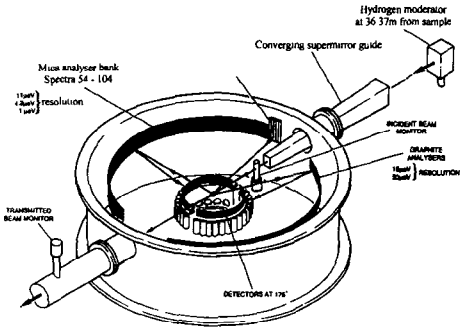

FIGURE 1 - IRIS INSTRUMENT VACUUM VESSEL
GRAPHITE (LHS) MICA (RHS)

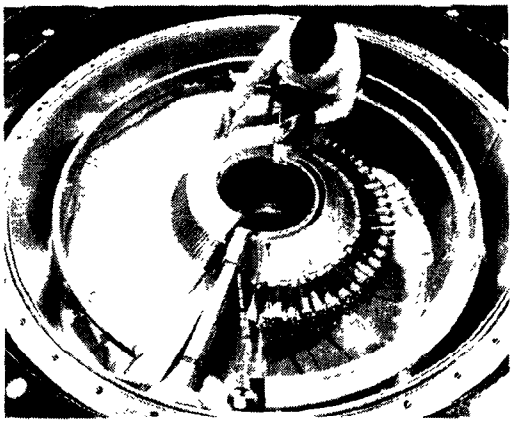

THE IRIS COLD ANALYSER CIRCUIT

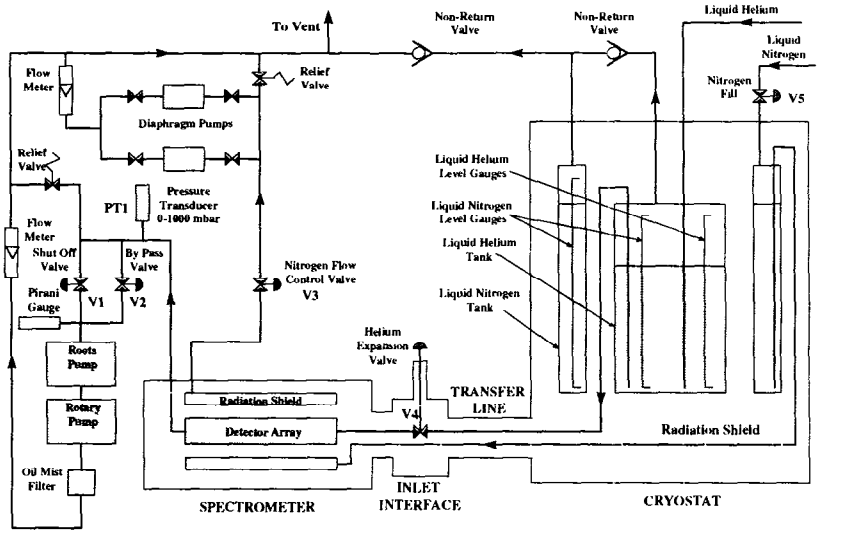

FIGURE 2. IRIS SPECTROMETER CRYOGENIC CIRCUIT

A continuous flow cooling system is proposed, supplied from a Custom designed and built Helium Storage Vessel. To reduce Helium losses the storage vessel is designed to incorporate a Liquid Nitrogen jacket which also provides a balanced feed to the Nitrogen cooled radiation shield and a supply for pre-cooling of the Analyser to 77 Kelvin prior to base temperature cool-down. Both Helium and Nitrogen cryogens are pumped through a heat-exchange coil on the rear of the analyser mounting / radiation shield respectively. To ensure optimal heat transfer a square wall tube is used for each coil, electron beam welded to the component being cooled. The analyser and transfer lines are instrumented for temperature and pressure to allow automated operation

THERMAL DIFFUSE SCATTERING (TDS)

Thermal diffuse scattering originates in a temporal variation of d-spacing of the analyser crystal at elevated temperatures. The vibration of atoms either side of the crystal lattice position results in a spread in the Bragg scattering angle akin to chromatic abberations in optical systems.

In an instrument without collimation this results in low energy neutrons being lost to adjacent detector modules. This increases the background noise of the instrument. As a result the resolution of the instrument tails off as energies decrease.

By lowering the temperature the atomic vibration is lowered and the scatter of low energy neutrons can be reliably detected above the noise floor of the instrument. Both the instrument operating bandwidth and signal-to-noise ratio are improved.

FIGURE 3. IMPROVEMENT IN TDS OF GRAPHITE AS A FUNCTION OF TEMPERATURE

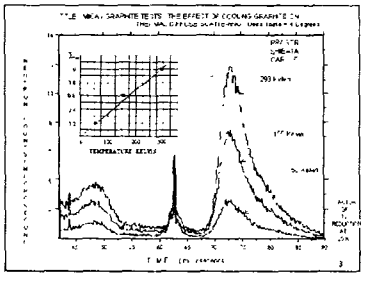

FIGURE 5. THE IRIS CRYSTAL ANALYSERS :- GRAPHITE (LHS) & MICA (RHS)

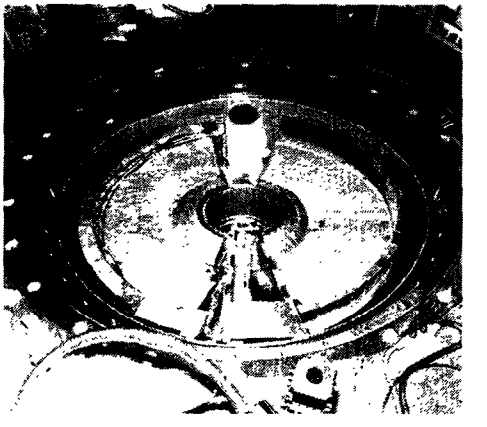

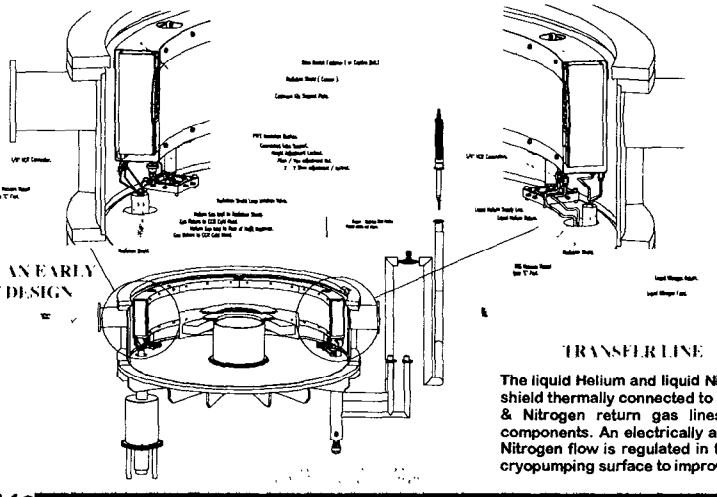

FIGURE 4. AN EARLY CONCEPT DESIGN

TRANSFER LINE

The liquid Helium and liquid Nitrogen transfer line is a vacuum insulated design incorporating a radiation shield thermally connected to the Nitrogen line. At the point of entry to the IRIS vacuum vessel the Helium & Nitrogen return gas lines provide additional thermal isolation from the ambient temperature components. An electrically actuated Kammer Helium control valve is included to regulate Helium flow. Nitrogen flow is regulated in the exhaust line. The existing CCR cold head will be retained to provide a cryopumping surface to improve the vacuum in the instrument.

THE IRIS 4.2 K COLD GRAPHITE ANALYSER

M.A. Adams J.J.P.Balchin T.A. Broome C.J. Carlile D.A. Cragg J. Tomkinson C.N. Uden

FIGURE 7: THE GRAPHITE ANALYSER

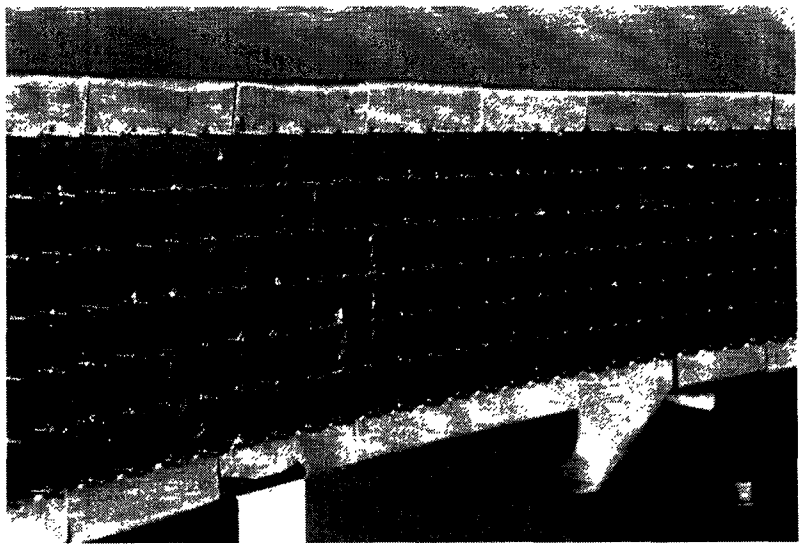

FIGURE 8: THE INTEGRATED INTENSITIES OF PHONON CREATION AND PHONON ANNIHILATION PEAKS IN GRAPHITE AS A FUNCTION OF TEMPERATURE

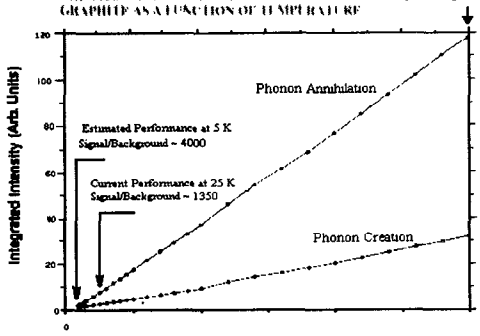

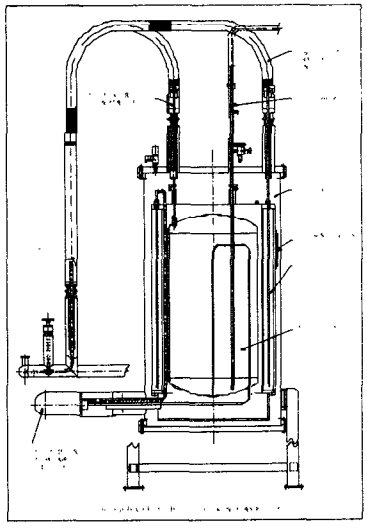

FIGURE 9: THE INTERMEDIATE STORAGE VESSEL.

This vessel is sited outside ISIS Hall 3, within the IRIS liquid nitrogen storage compound. It is supplied via a fill line, from 200 l helium dewars, and via a permanent transfer line, from the existing nitrogen storage vessel. A central 214 litre capacity helium reservoir is enclosed within a circumcircular 163 litre capacity nitrogen reservoir. Phase separation tanks prevent impurities entering the transfer lines. The outer shell of the vessel includes an evacuated radiation shield with superinsulation. Future installation of a lambda plate to pump superfluid helium within the helium reservoir is envisaged.

THE IRIS COOLING SYSTEM INSTALLATION

This shows the layout of the LN2 storage vessel, Intermediate storage vessel, transfer line, IRIS & OSIRIS Instruments, helium & nitrogen exhaust lines , heat exchangers and associated pumping & flow control equipment within the IRIS blister in Hall 3. All the equipment within Hall 3 is located at floor level beneath the IRIS platform to allow for later modification to a transfer line connected to analysers in the OSIRIS instrument.

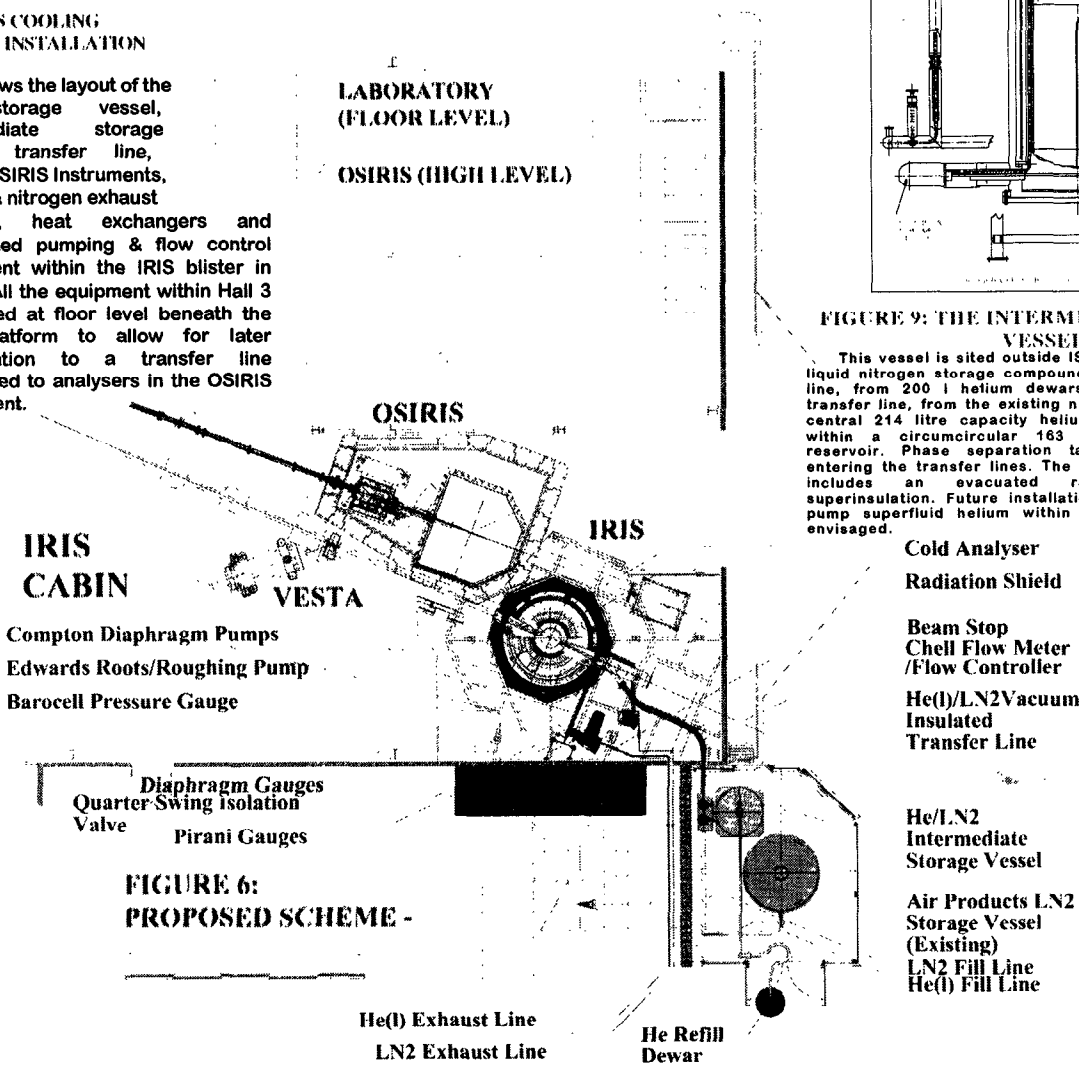

FIGURE 6:
PROPOSED SCHEME -

ICANS-XIV
14th Meeting of the International Collaboration on Advanced Neutron Sources
June 14-19, 1998
Starved Rock Lodge, Utica, Illinois, USA

Membrane Windows with Get-Lost Tubes for Use at Small Scattering Angles in Neutron Spectrometers

Henry Belch, Robert Kleb, John M. Carpenter and R. Kent Crawford
Intense Pulsed Neutron Source
Argonne National Laboratory
Argonne, Illinois

Introduction

Many types of spectrometers require an evacuated incident beam path before and after the scattering sample to reduce the background due to scattering from air or gas otherwise present. When in the same instrument, detectors are located outside of the flight path vacuum and therefore thin windows must be used to reduce transmission losses and window-scattered background. Windows of membrane design are most efficient in this application. When in addition detectors are at small scattering angles close to the scattered beam, it is necessary to provide an opening in the window. This provides an extension of the flight path vacuum to some point distant from the detectors where it is easy to shield against the scattering at the exit window. We have found that the alternative, a beam stop within the vacuum, cannot provide the needed shielding of the window and at the same time avoid the scattered neutron background that it itself produces.

Our design and installation of "get-lost" tubes integral to large area membrane windows preserves the thinness of the window, yet provides strength for a safe extension of the vacuum path to a remote exit window. We have designed a window of this type for the HRMECS spectrometer at IPNS and have installed one in the GLAD diffractometer, which we describe. The window with get-lost tube reduced the background in GLAD by better than a factor of two below that accomplishable with our best-effort internal beam stop. The window size is 24.5 inches (62.23 cm) square. Window edges are clamped with a frame bolted at 2-inch intervals and o-ring sealed.

Analysis

The key tools used in the design and evaluation were the linear and non-linear analysis features of the NASTRAN finite element analysis code. Initial non-linear calculations based on available stress strain curves provided the shape and resulting maximum and residual stress levels of the deformed window, which were designed to be formed hydrostatically from 6061-T4 aluminum alloy, 0.063 inches (1.60 mm) thick (Figure 1). A fatigue analysis then determined the initial amount of the cumulative fatigue damage. A subsequent elastic stress analysis of the welded assembly assumed a final structure tempered to T-6 hardness after fabrication (Figure 2). Several support options for the extension tube were evaluated to determine the optimal design criteria. The tube structure was designed to be thinner in the area of the weld to the window to increase compliance and reduce stresses in the weld joint. A final fatigue analysis of maximum stressed areas including stress concentration, surface, reliability and safety factors was then performed to determine the expected life of 50 years based on a conservative estimate of subsequent 500 normal loading cycles per year. An analysis of the welded joint based upon the loading conditions was then performed to confirm the resulting stresses determined by the finite element analysis.

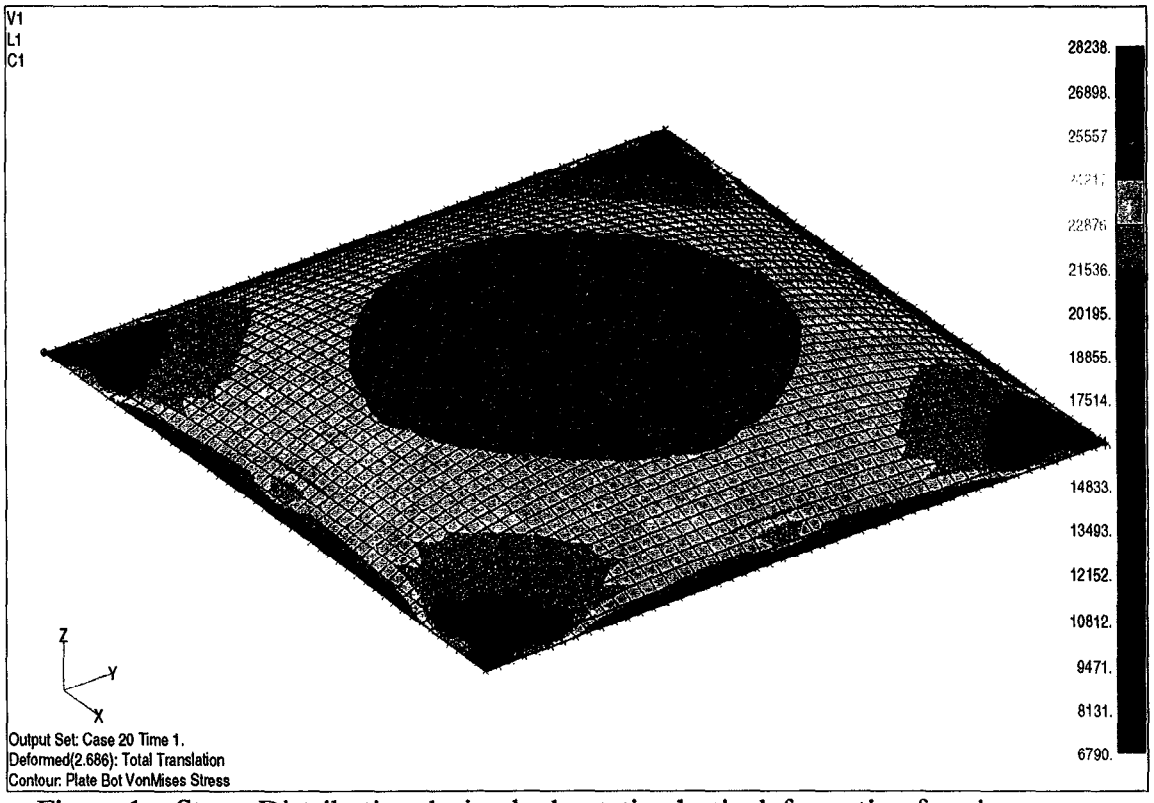

Figure 1 – Stress Distribution during hydrostatic plastic deformation forming process

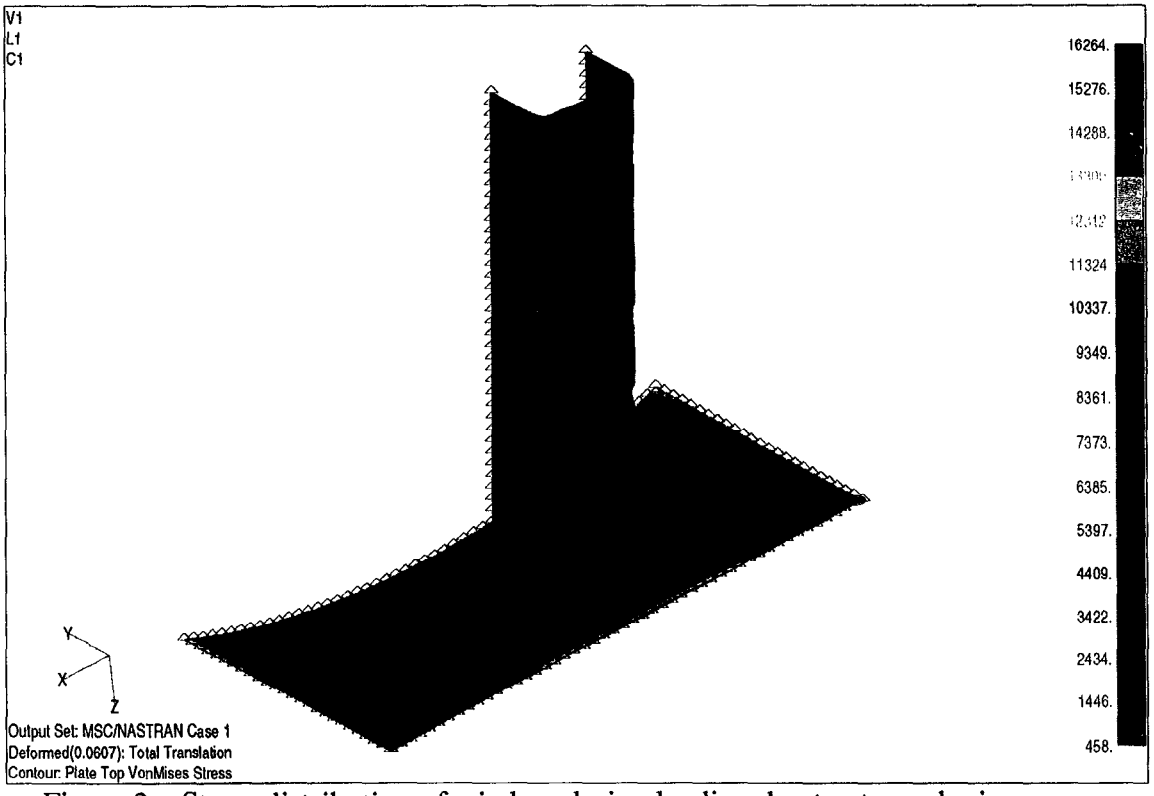

Figure 2 – Stress distribution of window during loading due to atmospheric pressure

Manufacture and Testing

The window structure consists of a rectangular welded tube section (the size of which is based upon the measured beam profile) shaped to match its intersection with the membrane, welded to the deformed membrane sheet after deformation, with supporting constraints which were found to reduce local stresses by substantial factors. Clamping forces from a heavy window frame support the membrane at the edges. Figure 3 shows the overall window/extension tube design. Modifications to the "membrane-forming fixture" were designed to test the welded assembly hydrostatically to 2 atmospheres of pressure after completion (Figure 4).

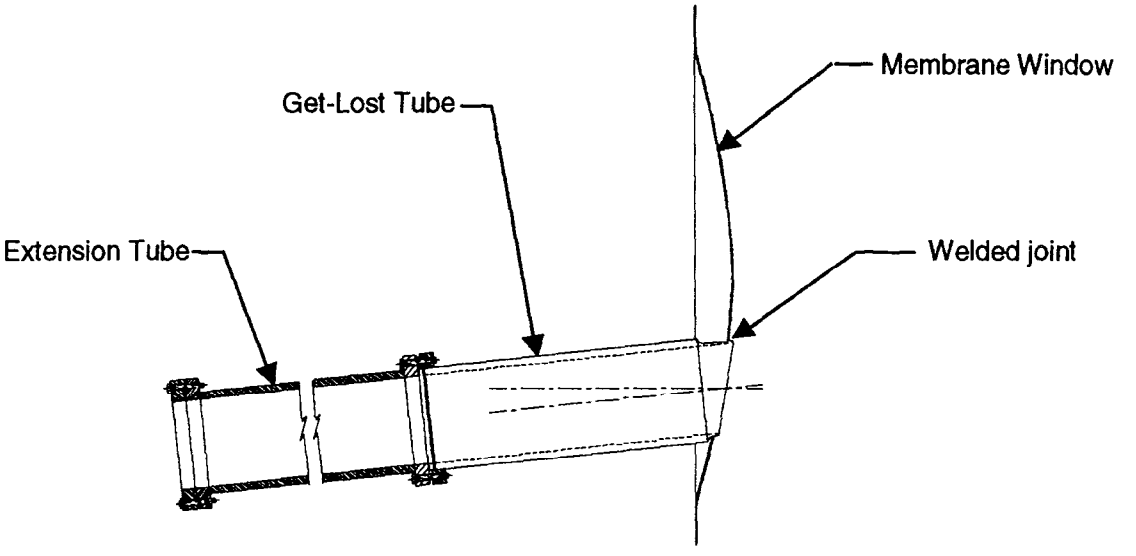

Figure 3 – Assembly of Get-Lost Tube to window (Instrument not shown for clarity)

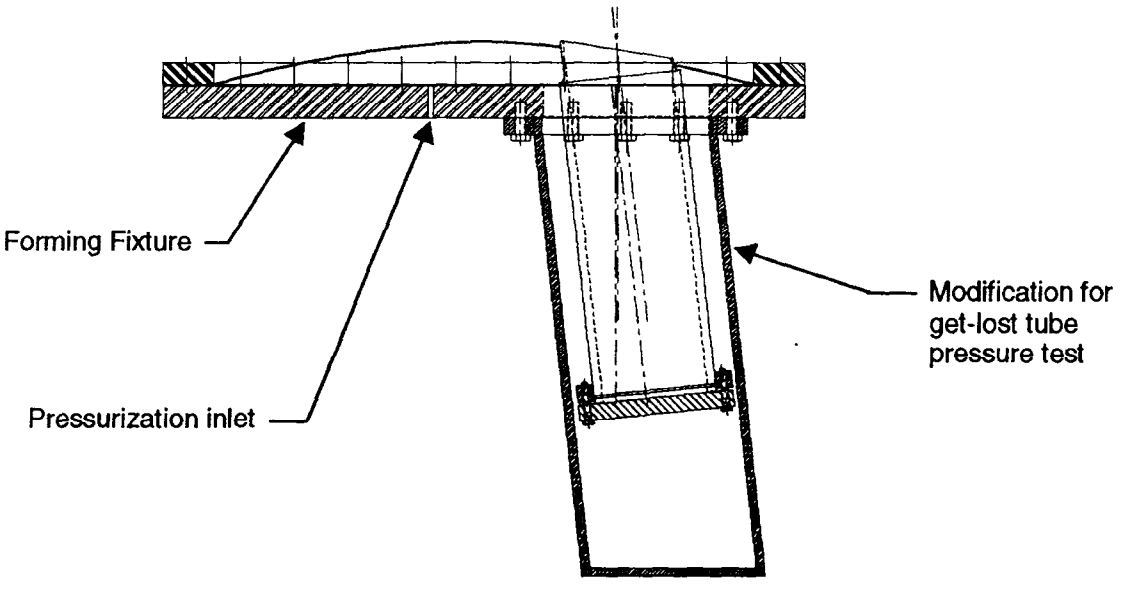

Figure 4 – Modification to membrane forming fixture for hydrostatic test

Detector Array Modifications

The supports for the vacuum flight path extension were designed into the detector array structure as shown in Figure 5. The detector array was modified to include horizontal as well as vertical linear position sensitive detectors that surround the vacuum extension tube. The calibration bars for the linear position sensitive detector array were modified using several gear driven mechanisms to provide calibration capabilities to both horizontal and vertical detectors.

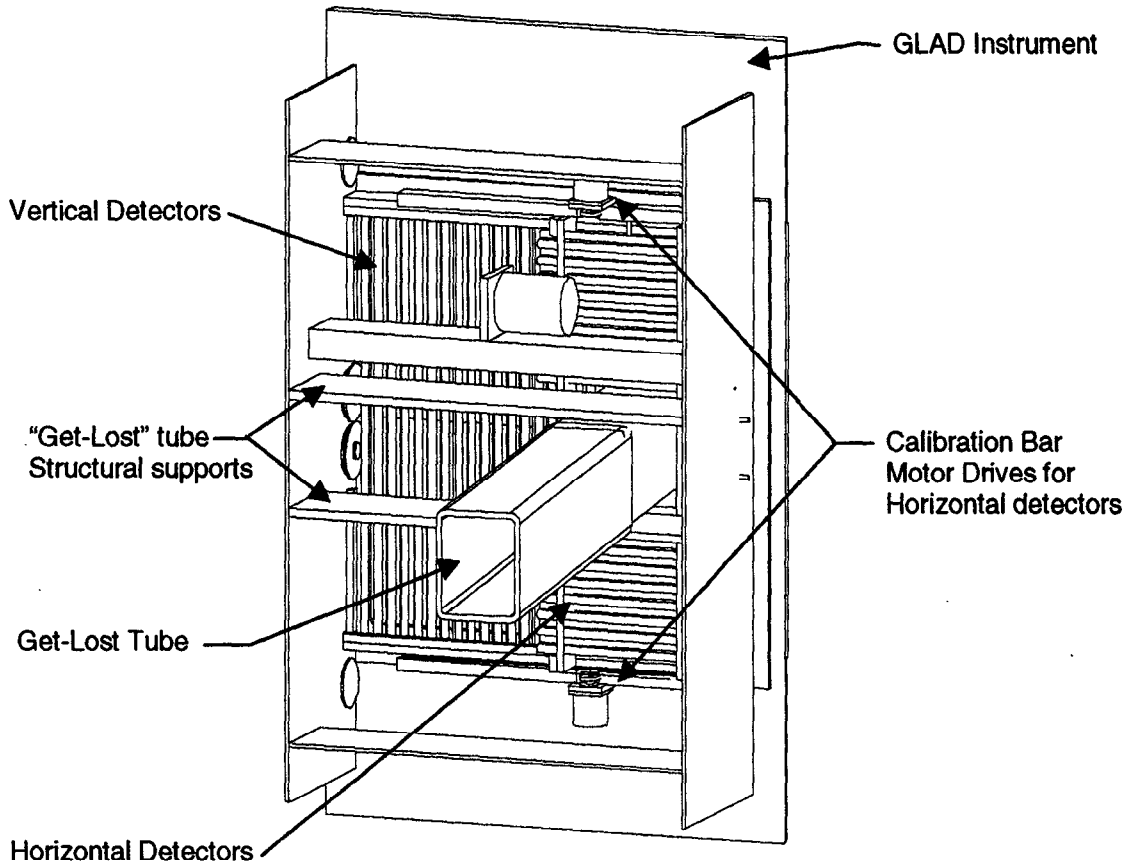

Figure 5 – Modified LPSD array (covers and electronics removed for clarity)

Conclusion

The GLAD window has been in place since August 1997 and the background is at least a factor of two lower than the level accomplished using the best internal beam stop arrangement.

Acknowledgements : We thank Richard Vitt, Ken Violin, Phil Calahan, Lynette Jirik, Dave Leach, Yaspal Badyal, Argonne Central Shops, and all who provided installation assistance.

The submitted manuscript has been created by the University of Chicago as Operator of Argonne National Laboratory under Contract No. W-31-109-ENG-38 with the U.S. Department of Energy. The U.S. Government retains for itself, and others acting on its behalf, a paid up, nonexclusive, irrevocable worldwide license in said article to reproduce, prepare derivative works, distribute copies to the public, and perform publicity and display publicly, by or on behalf of the Government.

ICANS XIV
14th Meeting of the International Collaboration on Advanced Neutron Sources

Starved Rock Lodge, Utica, IL
June 14-19, 1998

Development and Modernization of the System for the Diagnostics of the State of the Pulsed Neutron Source IBR-2

Pepyolyshev Yu.N., Belushkin A.V., Vinogradov A.V.
Frank Laboratory of Neutron Physics (FLNP), Joint Institute
for Nuclear Research (JINR),
141980 Dubna, Moscow Region, Russia

The fast neutron reactor of periodic operation IBR-2 generates neutron pulses with the frequency 5 Hz and the average power 2 MW /1/. The reactor is characterized by a high sensitivity to reactivity fluctuations and the existence of a massive mechanical structure, the reactivity modulator (RM), which rotates close to the reactor core and essentially influences neutron pulse fluctuations. An increase in the sensitivity is of fundamental character. This is caused by several reasons. First, when the reactor operates in the pulsed mode its sensitivity to reactivity fluctuations sharply increases. Second, energy fluctuations of power pulses increase significantly compared to steady-state reactors because of additional sources of reactivity fluctuations such as, for example, vibrations of the RM blades. In the pulsed mode as compared to the steady-state mode of operation (without rotation of RM), the main characteristics of the reactor change significantly. For example, the kinetic, dynamic and thermodynamic characteristics of the reactor vary. Thus, when controlling the state of the pulsed reactor, in addition to the usual requirements the control over the change in the noises of the reactor and vibrations of RM, as well as over the change in dynamic characteristics of the reactor core, which influence the instability /2/, should be exerted

Therefore, to carry out the diagnostics of the IBR-2 state in investigations during physical and energy startups and in the process of the exploitation of the reactor, the methods of noise diagnostics are used. The main stages of reactor investigations where the methods of noise diagnostics are widely used include.

1977 – 1984 The IBR-2 reactor physical and energy startups. Experimental investigations of the reactor. The main studies in that period were aimed at determining and optimization of the performance characteristics and improving the quality of the reactor as a pulsed neutron source.

1984 – 1997 Exploitation of the reactor. Investigations and monitoring of the principal reactor parameters. Experimental substantiation of a reliable and safe mode of the reactor operation.

1997 – 2000 Creation of a new information and diagnostics system for the reactor users.

The main elements of IBR-2 whose states are analyzed by the methods of noise diagnostics are:

1. Reactor core. Energy fluctuations of neutron pulses. Analysis of the fast neutron pulse shape.
2. The first contour of the sodium cooling system. Fluctuations of the inlet and outlet temperatures of the cooling agent. Fluctuations of the cooling agent expenditure in two loops of the first contour of the cooling system of the reactor core.
3. Reactivity modulator as a complex rotational machine. Axial vibrations of the blades of the main and auxiliary movable reflectors. Vibrations and displacements of supports for the shaft of the main movable reflector.

To analyze time series, the methods of spectral and correlation analysis, image identification, multidimensional data compression for visualization of the data are accepted. At present, the new updated system for the examination and diagnostics of IBR-2 is being created. The general state of the reactor will be analyzed on the basis of a total of 40 measured reactor parameters.

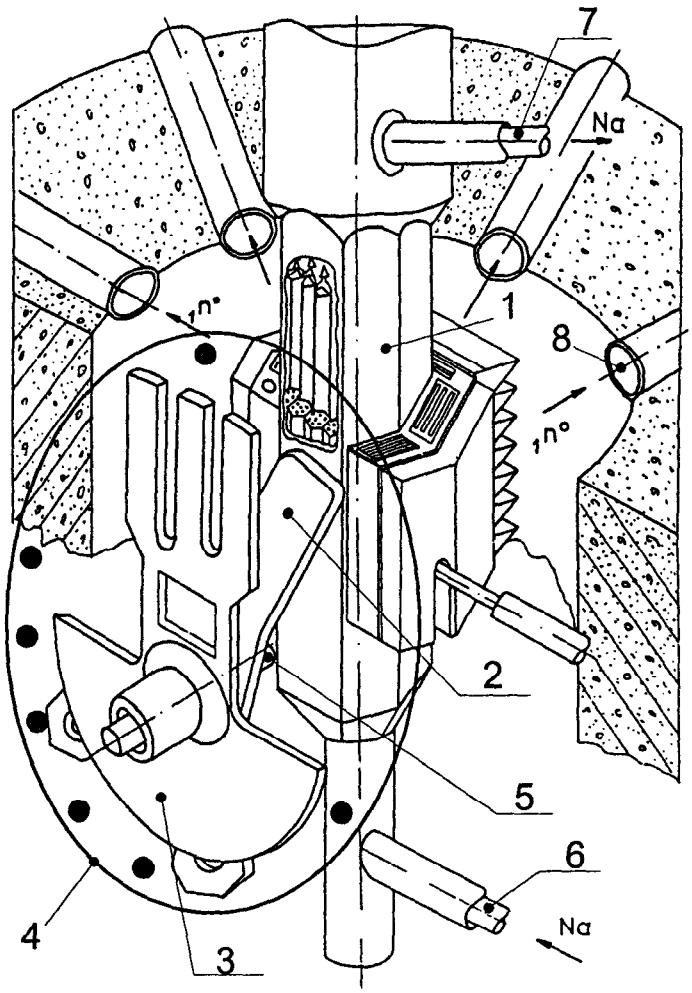

Fig. 1. The principal scheme of the IBR-2 reactor and positioning of sensors: 1 – reactor vessel, 2 – main movable reflector (MMR), 3 – auxiliary movable reflector (AMR), 4 – RM jacket with 16 sensors of MMR and AMR blade positions, 5 – vibration pickups and AMR front support displacement pickups, 6 – sodium temperature sensor in the inlet collector, 7 – sodium temperature sensor in the outlet collector, 8 - neutron flux detectors (fission ionization chambers).

Regular measurements of dynamic characteristics of the reactor using controlled single or repeated changes of the reactivity will complement noise diagnostics. Important is that the new system gives access for neutron beam users to part of the information in the close to real time mode through FLNP net servers. Work to develop a system with advanced hardware and software using modern computing means is now in progress at the IBR-2 reactor. The main functions of the system are as follows:

1. Availability of operative information for neutron users and the reactor staff;
2. Measuring of not less than 40 principal reactor parameters with a frequency equal to the pulse repetition rate 5 Hz during each two-week reactor cycle;
3. Preliminary noise diagnostics. Data processing in the real-time mode. Creation of a data base;
4. Processing over full data (over all reactor cycles) in the close to real time mode to search for anomalies and compute trends;
5. Possibility of performing additional investigations of the reactor (dynamic characteristics);
6. Evaluation of the vibration state of the reactivity modulator as a complicated rotating machine;
7. Fast neutron pulse shape measurements. Operative evaluation of kinetic parameters.

The system is oriented for powerful PC-class machines and the FLNP net server as shown in fig. 2.

Access to data is realized via user passwords automatically defining the necessary data volume for a particular user from any machine with the net support. A distributed automatic system for IBR-2 users with generation of a Web page on the FLNP net server has existed in FLNP since November 1996 and is the prototype of one of the components of the discussed system. In particular, it is possible to have current information about the reactor power and the state of a neutron guide (open-closed) together with some other information from the following address:

http://nfdnf.jinr.ru/flnph/ibr-2/cycles/ibr2_monitoring.html

Information is updated every 10 minutes of the reactor operation.

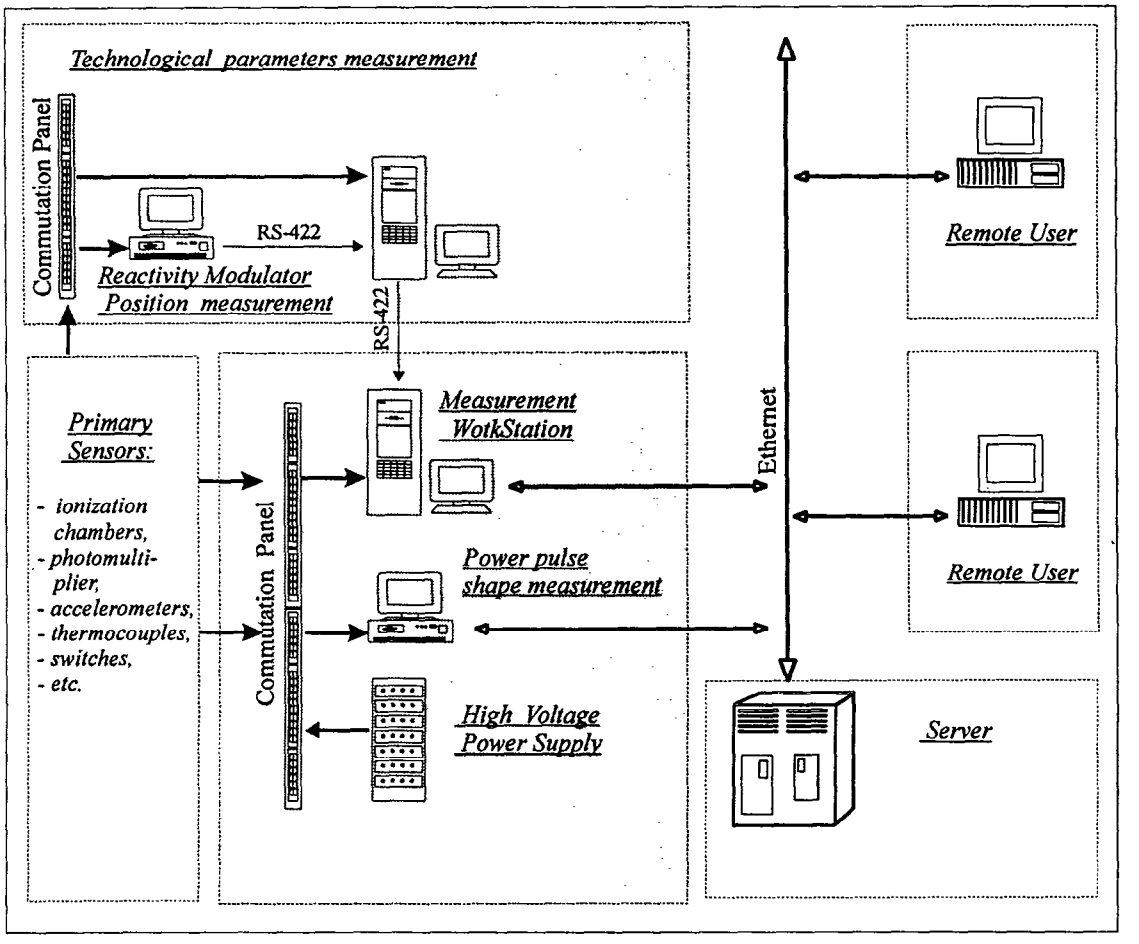

Fig.2. The scheme of the diagnostics system.

Following are some experimental results obtained in the operation of the IBR-2 reactor. Under any change of the mean power or the coolant flow rate through the reactor core the character of power fluctuations (spectrum shape and absolute deviations) changes. As an illustration, Fig.3 shows relative changes of pulse energy fluctuations as the power decreases from 1.8 to 0.82 MW.

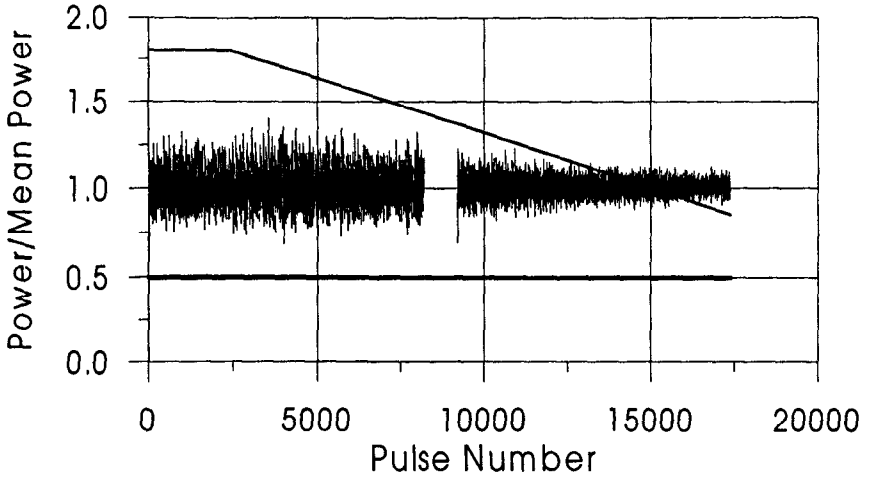

Fig.3. Changes in relative power noises as the power was decreased from 1.8 to 0.82 MW for the coolant flow rate 80 m^3/h .The upper curve shows the power (MW). At 0.5 the lower limit for the reactor shutdown is marked. On the abscissa the number of registered power pulses is plotted. The total time of the cycle is one hour and three minutes. The break in the pattern is connected with an interruption in the measurements.

Some partial components of the spectrum density of pulse energy fluctuations depend on the power and the coolant flow rate in a different manner. The absolute deviations of pulse energy fluctuations in the low frequency region are shown in fig. 4. As is seen in figs. 3,4 the dependence of pulse energy fluctuations on the mean power and the coolant flow rate has a complex character. For example, in the region from 1.5 to 1.8 MW, low frequency oscillations sharply increase and their amplitude essentially depends on the coolant flow rate.

The second important task of the control over the state of the pulsed reactor consists, as mentioned above, in determining current dynamic characteristics of the reactor. It is well known that while the reactor is in operation, neutron-physical, thermohydraulic and mechanical characteristics of the reactor core change. The changes can be due to natural processes connected with the burn of fuel elements or changes in the core due to reloading or replacement with fresh ones of fuel elements leading to changing of dynamic characteristics of the reactor. For example, the important characteristics of the reactor, such as the power reactivity coefficient or its separate components, alter. Knowledge of the current characteristics of the power feedback is necessary for estimating the behaviour of the reactor in various transitions and emergencies. It is especially important for a pulsed reactor since it has some limiting power above which it becomes unstable. The value of the limiting power depends on fast components of the power feedback. Therefore, a monitoring system for fast components of the feedback using the rectangular reactivity oscillations method is created at the IBR-2 reactor. The data obtained in the operation of the system during the period from 1989 to present is used to analyse the physical nature of changes occurring in the core and, also, to substantiate a reliable and safe mode of operation of the reactor.

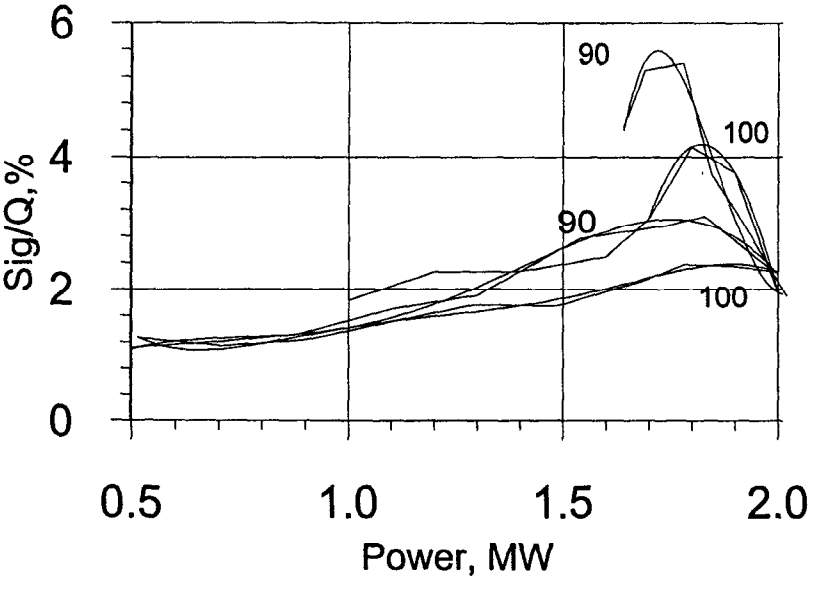

Fig.4. Changes in mean square root deviations of the energy of power pulses in the low-frequency region of the spectrum (0.01-0.4 Hz) as the power increases up to 2 MW and decreases from 2 MW at the sodium flow rate 90 and 100 m^3/h in contour I. Two upper curves were measured as the power decreased.

In the stable pulsed mode of reactor operation, a periodically varied reactivity of "meander" type is introduced into the reactor. An acute reactivity change is realised between power pulses (in less than 0.2 s). For periodic changes of external reactivity, stationary oscillations of the deterministic oscillations of pulse energy with imposed statistical power fluctuations are established. Identification of the deterministic component is only possible by smoothing measurements over many periods because of large power fluctuations ($\sigma q/Q$ =8%). As an example, the measured deterministic component of power oscillations averaged over four hours is presented in Fig.5. The 1989 to 1997 experience with the power feedback characteristics (PFC) monitoring system for the average Pu-239 burn from 1 to 4% shows that PFC of the IBR-2 reactor depends on the coolant flow rate through the core and the mean reactor power /3/.

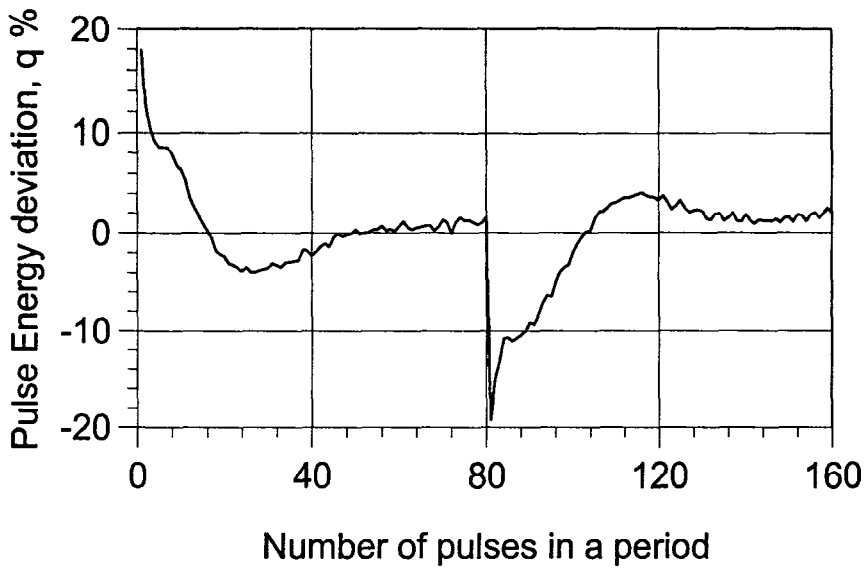

Fig.5. The defining component of power oscillations under external reactivity modulation with the repetition rate 160 reactor pulses. Averaging is performed over 600 periods. The amplitude of the modulating reactivity is $8 \cdot 10^{-6}$ $\Delta K/K$. On the ordinate axis, pulse energy deviations from the mean value are shown.

The presented report outlines only part of problems connected with the research and diagnostics of the IBR-2 reactor. It is apparent that the task of the diagnostics of the reactor is much broader than it has been discussed. We hope that in connection with the development of pulsed neutron sources in different countries there will be a good chance for joint effort in the field of diagnostics and increasing the safety of the existing and future pulsed neutron sources.

References

1. Ananiev V.P., Vinogradov A.V., The IBR-2 pulsed research reactor: status report. Proceedings of PANS-II Second International Seminar "Advanced Pulsed Neutron Sources: Physics of/at Advanced Pulsed Neutron Sources", June 14-17, 1994, Dubna, Russia
2. Shabalin E.P., On power oscillations and stability limitation of a pulsed reactor, Atomnaja Energija, v.61, Issue 6, pp. 401-406, 1986
3. Shabalin E.P., Antsupov N.P., et al., Pulsed characteristics of the feedback in the IBR-2 reactor, Atomnaja Energija, v.70, issue 5, pp.326-329, 1991.

ICANS-XIV
14th Meeting of the International Collaboration on
Advanced Neutron Sources
June 14-19, 1998
Utica, IL USA

SAMPLE ENVIRONMENTS AT THE INTENSE PULSED NEUTRON SOURCE (IPNS)

D. E. Bohringer and K. J. Volin
Argonne National Laboratory, Argonne, IL 60439 USA

ABSTRACT

Neutron diffraction is a powerful tool for structural studies of samples in special sample environments because of the high penetrating power of neutrons compared to x-rays. The Intense Pulsed Neutron Source (IPNS) at Argonne National Laboratory (ANL) offers its users a variety of sample environments for pulsed neutron scattering and diffraction experiments. At the present time over 80% of all experiments performed at the IPNS involve some type of ancillary equipment to control the sample environment[1]. These include closed-cycle refrigerators, cryostats, furnaces, magnets, and pressure cells. There are also devices for automatic sample changing, positioning, and orientating. Most instruments have at a minimum, a dedicated closed cycle refrigerator (10K to RT) configured for the instrument's typical sample dimensions and scattering angles. Standardization in instrument sample well dimensions, process control equipment, and control software has made multi-instrument use of many of the furnaces and cryostats possible. General use, multi-instrument equipment is maintained by the facility's technical staff. Instrument dedicated equipment is maintained by the respective instrument scientist with help from the ancillary equipment group. The design and upgrading of equipment is done by the ancillary equipment engineer with the oversight and input of instrument scientists, instrument engineer, and technical staff. Ancillary equipment conception and design is science driven, with the instrument scientists and even users providing the initial input for design criteria.

1. Introduction

Special sample environments have become one of the neutron scatterer's primary tools in the study of the structure and dynamics of materials. While many sample environments have been developed for general use, others have been developed to investigate certain specific properties of a particular material or class of materials. Often these are then modified to accommodate other types and sizes of samples. Over the past 17 years, ancillary equipment that provides a special sample environment for the neuron scatterer have been purchased, developed, invented and reinvented by our operations staff, instrument scientists, and users. Listed in Table 1 are the various pieces of ancillary equipment now in routine use on the neutron scattering instruments at the IPNS.

[1] IPNS Progress Report 1996.

Table 1. Ancillary Equipment at the IPNS		
Ancillary Equipment	**Parameter Range**	**Instruments**
High Temperature		
Block Heater	T = RT to 300°C	SAND
Coffee Can Furnace	T = RT to 350°C	GLAD, SEPD, GPPD
Heating Circulator	T = 30 to 100°C	QENS
Hot Stage Displex®	T = 20 to 800K(527°C)	QENS, GLAD, SEPD, LRMECS, GPPD
Howe Furnace	T = RT to 1100°C	QENS, GLAD, SEPD, LRMECS, GPPD
In-Situ Furnace	T = RT to 250°C	POSY II
Klipper Furnace	T = RT to 700°C	SAD
LUCYFE Furnace	T = RT to 1100°C	GLAD
Miller I & II Furnaces	T = RT to 1300°C in a static air, flowing inert, oxidizing, or reducing atmosphere, or vacuum.	SEPD, GPPD
SCD Furnace	T = RT to 700°C	SCD
Low Temperature		
Closed Cycle Helium Refrigerator	T = 10K to RT	HRMECS, QENS, GLAD, SCD, SEPD, LRMECS, SAND, SAD, HIPD, GPPD, CHEX
Heli-tran®	T = 2.5K to RT	SCD
Orange Cryostat	T = 1.5K to RT	HRMECS, QENS, GLAD, SEPD, LRMECS, HIPD, GPPD
Oxford Instruments Cryostat 5 kG Magnet	T = 1.5K to RT B = 0 to 5 kG	POSY
High Pressure		
4 kbar Liquid Pressure Cell	P = 0 to 4 kbar	SAD
2 kbar Pressure Cell 2W Displex®	P = 0 to 2 kbar T = 10K to RT	SCD
7 kbar Pressure Cell 12W Displex®	P = 0 to 7 kbar T = 20K to RT	SEPD
High Magnetic Field		
5 kG Magnet Oxford Instruments Cryostat	B = 0 to 5 kG T = 1.5K to RT	POSY
14 kG Magnet	B = 0 to 14 kG	SAD

Sample Changers		
Room Temperature Sample Changer	10 Positions	GLAD, SEPD, GPPD
Sample Changer	4 Positions	POSY II
Sample Positioners		
Sample Orienter	360° ϕ and 360°χ	GPPD
Sample Orienter	360° ϕ and 90°χ	SCD
Sample Rotator		SAD
X-Y-ϕ Translator	360° ϕ	SCD
X-Y-Z-ϕ Translator	360° ϕ	GPPD
Special Equipment		
Hydrogen Charging System		POSY II
Liquid Cell		POSY II
Residual Stress Analyzer		GPPD
Shear Cell		SAND

NOTE: It is best to contact the respective instrument personnel for specific instrument sample configuration and dimensions restrictions prior to submitting experiment proposal. The instrument acronyms are as follows:

Diffractometers

Special Environment Powder Diffractometer	SEPD
General Purpose Powder Diffractometer	GPPD
Glass, Liquid, & Amorphous Solid Diffractometer	GLAD
Single Crystal Diffractometer	SCD
High Intensity Diffractometer	HIPD
Small Angle Diffractometer	SAD
Small Angle Neutron Diffractometer	SAND

Spectrometers

High Resolution Medium Energy Chopper Spectrometer	HRMECS
Low Resolution Medium Energy Chopper Spectrometer	LRMECS
Quasi-Elastic Neutron Spectrometer	QENS
Chemical Excitation Spectrometer	CHEX

Reflectometers

POSY	POSY
POSY II	POSY II

Detailed information on specific individual ancillary equipment at the IPNS is available on the IPNS web site at http://www.pns.anl.gov.

2. General Rule of Standardization

In order to maximize the efforts of our operations staff, standardization has become the deciding factor in many of our instrument designs. This standardization has lead to a desired portability among instruments, non-duplication of effort, a centralized inventory of spare parts, and maximized the experience of staff with respect to operation and maintenance. Of course with any rule there are exceptions. We have tried to keep these to a minimum and they have almost always resulted from designs in which the IPNS technical staff was not involved, at least not until the equipment showed up at our door.

2.1 Instrument Geometry

From the beginning of IPNS[2], instrument geometry has been built around either a twelve inch diameter or twenty-four inch diameter sample well. The sample well flange o-ring surface to beam centerline dimension has been kept to a standard twelve inches for the small sample well and twenty-four inches for the larger well. This has allowed the ancillary equipment to move from instrument to instrument as required and also for out dated retired equipment to be refurbished or cannibalized for use on newer instruments.

2.2 Temperature Control

We have tried to standardize our temperature controllers so that our staff and users can become familiar with the manual operation, over remote computer control, if required. It also minimizes the effort in writing software drivers for each individual brand or model of controller.

For our low temperature cryostats and closed-cycle refrigerators, we have installed Lake Shore Cryotronics Model 330 Temperature Controllers. These can be field configured to read either silicon diodes or platinum resistors. They can also be factory ordered to read a thermocouple on one or both of their two sensor inputs, such as a Fe/Au thermocouple for low temperature applications. The output of the controller is 0-1 A to a maximum 50 W heater. The Lake Shore controller is a full PID controller with an autotune feature.

For our high temperature furnaces we have, after many false starts, decided on Eurotherm Controls' Model 905D Temperature Controllers. These must be factory ordered to read specific thermocouple type or RTD inputs. The output of the controller is 0-10 V to a voltage controlled DC power supply. The Eurotherm controller is also a full PID controller with an autotune feature. In addition to the Eurotherm controller we have installed Newport Model 81 Temperature Alarms in the control circuit. These are manually set by our operations staff when completing a Furnace Check List procedure for each experiment before power is allowed to be applied to the furnace itself.

---

[2] Sample-related Peripheral equipment At IPNS, D.E. Bohringer and R. K. Crawford, Proceedings of the Eighth Meeting of the International Collaboration on Advanced Neutron Sources (ICANS VIII), July 2-12, 1985, Rutherford Appleton Laboratory, UK, Rutherford Appleton Laboratory Report RAL-85-110.

Both the Eurotherm and Lake Shore controllers are configured for RS232 communications. Setpoints, PID values, ramp rates, and autotuning can be set or be toggled on/off from the instrument computer terminal.

2.3 Motion Control

Position, both linear and rotary, has been performed using Superior Electric Slo-Syn synchronous stepping motors controlled with Bi-Ra stepping motor controllers. These units have been used to orient samples on Huber goniometers, sample changers, and bar calibrators for linear position sensitive detectors.

2.4 Control Software

It has been a long-standing dictum at the IPNS that the runfile control software be standardized among the instruments. With minor differences, to account for choppers and such, the software interface is the same for the diffractometers, spectrometers, and reflectometers. So with the sample environment control software. From a single menu, accessed during the setup of a run, a user can install ancillary equipment control to change temperature, position, or orientation, into the run file. The user can also control the available ancillary equipment outside the run file setup by accessing the individual control software.

2.5 Exceptions to the General Rule of Standardization

There are always exceptions to any rule and these have almost always been either a user provided piece of ancillary equipment or one with a very narrow and specific use. We have learned over the years to adapt and accommodate these exceptions. And when it is warranted, we have taken on some exceptions as our standard because they have worked and worked well.

3. Instrument Dedicated Ancillary Equipment

Most instruments at the IPNS have at the minimum a dedicated closed-cycle helium refrigerator. These are dedicated full time to the instrument since they are in almost constant use and are configured for the respective instrument's specific beam dimensions and scattering angles. Some instrument dedicated ancillary equipment have been developed by the instrument scientists to exploit some particular feature of their respective instruments such as the 5 kG magnet on the POSY reflectometer or the 7 kbar High Pressure Cell on the SEPD powder diffractometer. Other ancillary equipment have been developed to address specific needs of our users. A good example of this would be the Residual Stress Analyzer developed and used on the GPPD powder diffractometer. The instrument dedicated ancillary equipment are developed and maintained by the respective instrument scientists with assistance from the NGS Operations staff.

4. General Use Ancillary Equipment

Many of the high temperature furnaces are shared among several instruments, as is our low temperature cryostat. The IPNS Ancillary Equipment engineer develops and maintains these pieces of ancillary equipment with the assistance from the NGS Operations staff and the oversight of the instrument scientists. This is a relatively new position in the IPNS organization and

recognition of the importance of safe, reliable, and well-characterized ancillary equipment. We are increasing our effort to perform more routine testing, profiling, and maintenance of the furnaces during our scheduled shutdown periods rather that during the course of an experiment. The ancillary equipment that falls under the general use/maintained category are as follows:

4.1 Howe Furnace

The Howe is a vanadium resistive-element type furnace used for sample heating to 1000°C. Incident and scattered neutrons pass through two vanadium heat shields, a vanadium heating element, an inner vanadium sample housing, and a sample container during experimentation. The sample environment is kept separate from the instrument chamber by a sample housing which enables sample exchange-gas purging and quick sample changes without the need to remove the entire furnace from the instrument. The furnace utilizes the instrument vacuum to protect the vanadium heating element from oxidation. A Balzers dual vacuum controller provides vacuum interlocks for the sample volume and the instrument chamber. The furnace is controlled using an Eurotherm controller and has remote computer interface capabilities. A Newport temperature alarm unit provides an independent temperature interlock. An Electronic Measurements 20V, 250A DC power supply is used to heat the furnace. A portable Edwards roughing pump and Balzers turbo pump are used to evacuate the sample volume. All control and interlock equipment are supplied in a mobile cabinet rack. The furnace uses one sheathed type K thermocouple positioned within the instrument vacuum in the center of the heating element for furnace control. A dual probe type K thermocouple is used for sample temperature monitoring and police interlocking, and is used as the sample container mount within the sample vacuum volume. This furnace is used primarily on the SEPD, GPPD, and GLAD instruments, but could be used on the following instruments as well but with a smaller sample than normally used: HRMECS and LRMECS. The Howe furnace can also be outfitted with a tantalum element and heat shields for use on QENS.

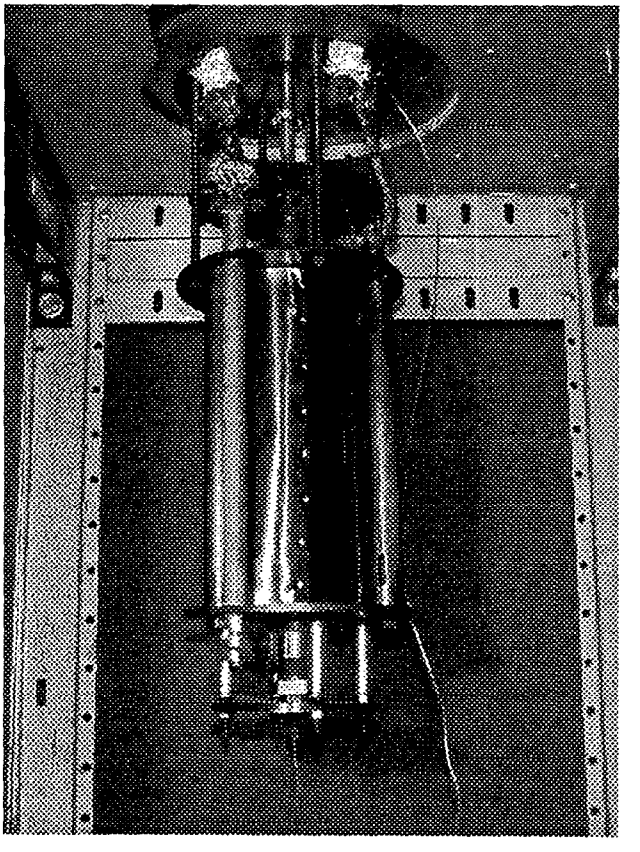

4.2 LUCYFE Furnace

The LUCYFE is a vanadium resistive-element type furnace used for sample heating to 1000°C, and is very similar to the Howe furnace. Differences between these two furnaces primarily involve the sample volume. The Howe has a separate sample volume from the instrument chamber, and can be used in conjunction with a purge gas during experimentation. The LUCYFE

sample shares its volume with the instrument, so is therefore not purge compatible. The LUCYFE does, however have a sample stick which enables quick sample changes without having to break instrument volume. The furnace utilizes the instrument vacuum to protect the vanadium heating element from oxidation. A Balzers dual vacuum controller provides vacuum interlocks for the sample volume and the instrument chamber. The furnace is controlled using an Eurotherm controller and has remote computer interface capabilities. A Newport temperature alarm unit provides an independent temperature interlock. An Electronic Measurements 10V, 250A DC power supply is used to heat the furnace. A portable Edwards roughing pump and Balzers turbo pump are used to evacuate the sample volume. All control and interlock equipment are supplied in a mobile cabinet rack. The furnace uses one sheathed type K thermocouple positioned within the instrument vacuum in the center of the heating element for furnace control. A dual sheathed type K thermocouple mounted to the sample centering stick is used for sample temperature monitoring and police interlocking. This furnace is intended primarily for use on the GLAD instrument.

4.3 Miller Furnaces

The Miller furnaces are tantalum ribbon resistive-element type furnaces used for heating samples to 1450°C. Alumina is the primary material used in construction of these furnaces. The sample volume is separate from the instrument volume, so the samples can be used with a static air, purge gas, or vacuum, and sample changes can be done without breaking instrument vacuum. Typically, powder samples are pressed into pellets for use in the Millers, but other sample container type arrangements can also be used upon request. The instrument vacuum protects the tantalum ribbon and heat shields from oxidation, and is interlocked using a Teledyne Hastings analog vacuum gauge. The furnaces are controlled using Eurotherm controllers and have remote computer interface capabilities. A Newport temperature alarm unit provides an independent temperature interlock. Electronic Measurements 250V, 20A DC power supplies are used to heat the furnaces. All control and interlock equipment are supplied in mobile cabinet racks. Each furnace uses tow sheathed type S thermocouples for control and police interlocking. The sample temperature is monitored using a bare-wire type S thermocouple located inside the sample volume and typically in contact with the sample. Due to the scattering geometry, only 90° scattering angles are available with the Miller furnaces; therefore, the only compatible instruments are the GPPD and SEPD.

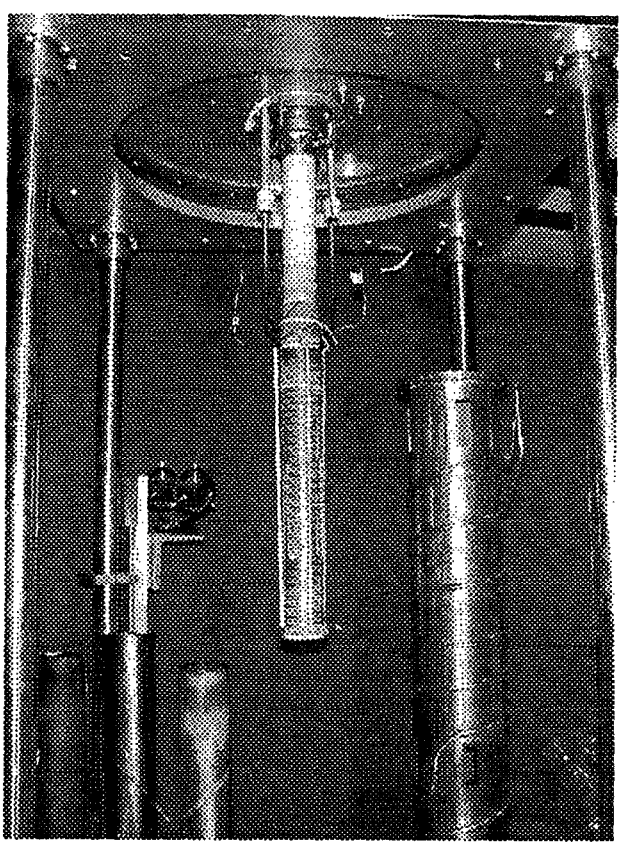

4.4 Coffee Can Furnace

The Coffee Can furnace is intended for experiments ranging from room temperature to 400°C. Four Watlow cartridge heaters heat this furnace. Two of these heaters are positioned above the sample embedded in the top aluminum plate: The other two are located in the bottom aluminum plate. The sample is heated primarily through radiation heat transfer to help ensure sample temperature homogeneity. A 7.16" diameter vanadium flanged tube 2.5" in length is typically used as the sample container, but other containers can be used upon request. The furnace operates within the vacuum volume of the instrument, and sample changes require complete furnace removal from the instrument well. The furnace is controlled using an Eurotherm controller and has remote computer interface capabilities. An independent Newport alarm unit provides additional defense in prohibiting furnace run-away. A 100V Kepco DC power supply is used to heat the furnace. All electronic components are located inside a mobile furnace control cabinet. The furnace utilizes three independent thermocouples for furnace control and sample monitoring. These three K thermocouples are physically located as follows: thermocouple #1 measures the temperature used to control the furnace, and is positioned directly on top of the top aluminum plate that houses the top heater cartridges; thermocouple #2 measures sample temperature, and can be positioned as necessary by the user, but is usually wrapped amount the thread that connects the sample container to the top plate; thermocouple #3 is the police thermocouple, and is located on the bottom aluminum plate that houses the two lower heater cartridges. This furnace is used primarily on the GLAD, SEPD, and GPPD instruments.

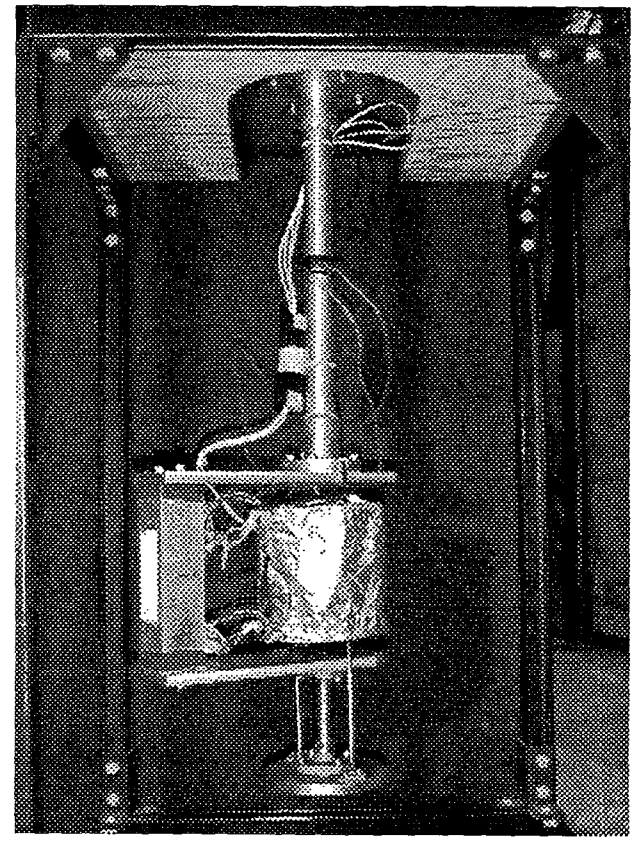

4.5 Hot Stage Displex®[3]

A "Hot Stage" Displex® has been implemented at the Intense Pulsed Neutron Source (IPNS) for performing neutron diffraction experiments in the temperature range 20K to 800K. The new piece of ancillary equipment allows for extended temperature range studies through room temperature without having to change sample containers or environments. The hot stage was designed for and installed on a refurbished closed-cycle helium refrigerator cold head. The unit

[3] A "Hot Stage" Displex®: 20-300K In A Neutron Scattering Environment, K. J. Volin and D. E. Bohringer, These proceedings.

employs four (4) single crystal sapphire stand off rods to provide a thermal conduction path to the sample at low temperatures, where sapphire is a conductor, and to isolate the sample and heater at high temperatures, where sapphire is an insulator. As with a standard closed cycle refrigerator, the first stage heat shield is held at about 20K throughout the temperature range. The second stage heat shield, along with the cold finger holding the sample container, is heated to the desired temperature with a resistance heater. A silicon diode located in the second stage and a platinum resistor mounted in the hot stage monitor temperature. The temperature is controlled by a Lake Shore Cryotronics Model 330 Temperature Controller with a RS-232 communications link to the neutron scattering instrument's data acquisition computer, allowing for run file temperature control. To ensure thermal equilibrium throughout the sample, the sample container is typically filled with one ATM. of helium. A new flange design for the standard closed-one-end vanadium sample cans has been incorporated to contain the helium atmosphere throughout the extended temperature range. Preliminary tests on a standard sample have shown a thermal gradient of <1 K/cm at 10K and at 800K over the length of the sample container. Cool-down times to 10K are on the order of 90 minutes, slightly longer than a standard Displex®. The neutron scattering background compares favorably with a standard closed-cycle refrigerator or mid-range furnace currently in use at the IPNS. This refrigerator/furnace is used primarily on the QENS, GLAD, SEPD, and GPPD instruments.

4.6 Orange Cryostat

The standard ILL "Orange" Cryostat was developed by the ILL cryogenics department to meet the needs of experimental scientists. The main requirements were for a robust and simple to use yet high performance cryostat suitable for neutron scattering. The main features of the Orange Cryostat include large sample top loading capability (50mm ϕ), isolated sample area with static exchange gas, low helium consumption and fast sample cycling times. The temperature of the Orange Cryostat is controlled between 4.2 and 300K with a Lake Shore Cryotronics Model 330 Temperature Controller. Temperature is monitored by two 100Ω platinum resistors located on the sample holder and on the variable temperature heat exchanger. The heat exchanger is fitted with a 50Ω heater. Several sample holders are available to accommodate the different sample configurations of the individual neutron scattering instruments. A Kinney pump is available to achieve temperatures below 4.2K. This cryostat is used primarily on the QENS, HIPD, GLAD, SEPD, and GPPD instruments.

5. Future Directions

Two things drive our ancillary equipment development; One is science driven, that is, to expand the limits of phase space that our current equipment is capable of accessing, enabling our users to perform experiments previously not realizable. The other is a desire to make the most efficient use of the scheduled beam time. As our source and moderators become more efficient and our neutron flux increases, run times are decreasing and there is the desire to shorten the sample turn around time to make the best use of beam time. We have done this in the past with sample changers, which allow the user to switch samples without breaking instrument vacuum. The directions in which we are developing ancillary equipment, at least in the near term, are as follows:

5.1 Low Temperature

- Purchase larger cooling capacity closed cycle refrigerators to decrease cool down.
- Develop a Low Temperature Sample Changer utilizing a stepping motor to move an entire closed-cycle helium refrigerator up or down through a double o-ring piston seal in a evacuated sample well. This unit is already constructed and its operation is being debugged.

5.2 High Temperature

- Construct a second Hot Stage Displex® to accommodate the scheduling conflicts among the instruments due to its over-subscription.
- Develop a larger bore furnace, on the order of 50 to 100 mm, to accommodate the larger sample configurations of the inelastic spectrometers.

5.3 High Pressure

- Interface pressure sensors to monitor and log the sample pressure during the run.
- Assemble a high pressure cell test facility. As the interest in high pressure continues to increase we have a real need to pressure test cells that a user might bring to perform an experiment and those of our own design.

6. Summary

IPNS has a wide range of ancillary equipment that provides special sample environments for the neutron scatterer. Standardization of instrument geometry, process control equipment, and control software has maximized the reliability, interchangeability, and efficiency of the equipment. Current equipment is constantly being upgraded and new equipment developed to meet the ever-expanding requirements of our user community.

7. Acknowledgements

We would like to acknowledge the assistance of L. Jirik, D. Leach, C. Piatak, M. Schleuter, R. Tafoya, J. Toeller, and T. Walsh of the IPNS NGS Operations staff, in the operation and support of the ancillary equipment program at the IPNS. The work reported in this paper was supported by the U.S. Department of Energy, BES-Materials Sciences, under contract W-31-109-ENG-38.

ICANS-XIV
14th Meeting of the International Collaboration on
Advanced Neutron Sources
June 14-19, 1998
Utica, IL USA

A "HOT STAGE" DISPLEX®: 20 - 800K IN A NEUTRON SCATTERING ENVIRONMENT

K. J. Volin and D. E. Bohringer
Argonne National Laboratory, USA

ABSTRACT

A "Hot Stage" Displex® has been implemented at the Intense Pulsed Neutron Source (IPNS) for performing neutron diffraction experiments in the temperature range 20K to 800K. The new piece of ancillary equipment allows for extended temperature range studies through room temperature without having to change sample containers or environments. The hot stage was designed for and installed on a refurbished closed-cycle helium refrigerator cold head. The unit employs four (4) single crystal sapphire stand off rods to provide a thermal conduction path to the sample at low temperatures, where sapphire is a conductor, and to isolate the sample and heater at high temperatures, where sapphire is an insulator. As with a standard closed cycle refrigerator, the first stage heat shield is held at about 20K throughout the temperature range. The second stage heat shield, along with the cold finger holding the sample container, is heated to the desired temperature with a resistance heater. Temperature is monitored by a silicon diode located in the second stage and a platinum resistor mounted in the hot stage. The temperature is controlled by a microprocessor-based controller with an RS-232 communications link to the neutron scattering instrument's data acquisition computer, allowing for run file temperature control. To ensure thermal equilibrium throughout the sample, the sample container is typically filled with one atm. of helium. A new flange design for the standard closed-one-end vanadium sample cans has been incorporated to contain the helium atmosphere throughout the extended temperature range. Preliminary tests on a standard sample have shown a thermal gradient of <1 K/cm at 10K and at 800K over the length of the sample container. Cool-down times to 10K are on the order of 90 minutes, slightly longer than a standard Displex®. The neutron scattering background compares favorably with a standard closed-cycle refrigerator or mid-range furnace currently in use at the IPNS.

1. Introduction

Since the inception of the IPNS there has been a need to measure the structural characteristics of materials at elevated temperatures. For many years, a resistance heater furnace, the Coffee Can Furnace (so named for it's visible appearance rather than it's actual construction material,) has served the neutron diffraction instruments well. A main fault of the Coffee Can Furnace was the lack of a cooling load that the resistive heaters could work against. This lead to a large thermal time constant in the system with an accompanying slow response to set point changes. Once heated above ambient, the return to room temperature followed an exponential tail. With the increased usage of furnace based experiments at the IPNS in recent years a real need was identified for a room temperature to 500°C furnace that was more responsive to set point changes. With the increased interest in polymers, a below ambient, i.e. -25°C, capability was also thought advantageous.

changes. With the increased interest in polymers, a below ambient, i.e. -25°C, capability was also thought advantageous.

2. Design and Construction

The design of the Hot Stage[1] is that of APD Cryogenics, Inc. in response to an inquiry from the IPNS about the possibility of operating a Displex®[2] at above room temperature. Users at IPNS have repeatedly asked how high in temperature could they run the closed-cycle helium refrigerators. A limit of 350K was typically given, this figure based on a number of factors concerned with the construction materials of the expander module cold head. APD Cryogenics engineers came back with an 800K Interface that could be mounted on their Model DE108 Expander Module. Figure 1 is a photo showing the Hot Stage Interface mounted on a refrigerator cold head. The temperature range of 10K to 800K is achieved by utilizing the unique thermal properties of single crystal sapphire. Figure 2 shows the thermal conductivity of sapphire plotted along with that of several materials used in the construction of furnaces for neutron scattering. At low temperatures, <100K, sapphire is a thermal conductor on the order of copper, aluminum, or even silver. The sapphire provides a thermally conductive path for sample cooling by the expander module cold head. At higher temperatures, sapphire becomes a thermal insulator on the order of stainless steel or vanadium. This thermally isolates the Hot Stage and sample from the cold head and allows the resistance heater to heat the sample above ambient. Figure 3 shows the temperature of the cold head and Hot Stage as a function of the Hot Stage set point. Heating from a base temperature of 20K, the temperature of the cold head and Hot Stage coincide until about 100K where the thermal properties of the sapphire begin to isolate the Hot Stage from the cold head. This transition is seen clearly in the plot of the percent power output to the heater. The cold head never heats up above 200K while the Hot Stage is heated to 800K.

3. Operation

The Hot Stage Displex® is operated similar to a standard closed-cycle refrigerator. The sample is loaded under an atmosphere of helium into an aluminum gasket sealed vanadium. The sample can is then screwed onto the Hot Stage. Care must be taken in attaching the sample to the Hot Stage due to the fragility of the four sapphire rods. The second stage and first stage heat shields are then attached and the unit installed into the sample well of the neutron instrument. A high vacuum of better than 10-5 vacuum is desired to avoid cryopumping air and moisture onto the heat shields. Initial cool-down times to 20K are on the order of 90 minutes, slightly longer than a standard Displex®. The temperature is controlled by a microprocessor-based controller[3] with an RS-232 communications link to the neutron scattering instrument's data acquisition computer[4], allowing for run file temperature control[5]. Temperature stability is ±0.1K throughout the temperature range. Preliminary tests on a standard sample[6] have shown a thermal gradient of <1

[1] 800K Interface, APD Cryogenics, Inc, Allentown, PA.
[2] Displex® is a registered trademark of APD Cryogenics, Inc, Allentown, PA.
[3] Lake Shore Cryotronics, Inc, Model 330.
[4] Typically a DEC VAXStation.
[5] TEMtur temperature control program, R. K. Crawford, IPNS, ANL, 1996.
[6] Helium filled 7/16"(1.1 cm) diameter x 5 cm vanadium sample can.

K/cm at 10K and at 800K over the length of the sample container. Control parameters, proportional band (gain), integral (rate), and derivative (reset), can be autotuned by the controller at each set point change, although in practice this is not usually deemed necessary.

4. Results

Beyond the thermal characteristics of the furnace, the crucial test of any piece of ancillary equipment is the neutron scattering data obtained. Already the Hot Stage Displex® has been used for experiments on the QENS spectrometer and on the SEPD and GLAD powder diffractometers. Figure 4 shows a comparison of raw TOF data taken on QENS with a sample in the Hot Stage Displex® at 350K and with a different sample in a standard Displex® at 50K. though the samples are different, the backgrounds of the two plots in the 1500 – 15000 μsec range are comparable if not identical and quite good for the measurement.

5. Future Improvements

With the first experiments completed, we have already identified several desired improvements to the Hot Stage Displex®. The list is not all inclusive but will include the following:

- Additional thermometry to monitor the sample temperature directly.
- Cadmium or gadolinium oxide shielding on the second stage cold finger to reduce the multiple scattering background.
- The addition of a high temperature alarm and other protective measures in the control circuitry.
- Instrument specific heat shields incorporating cadmium or gadolinium oxide masks tailored to the instruments neutron beam dimensions to reduce the stray scattering background.
- Improvements to the standard sample container to maintain a helium leak tight seal over the wide temperature range of the Hot Stage.

And if the scheduling of the Hot Stage Displex®, which has been a heavily requested item, continues as it has in its first several run cycles, we will certainly consider adding a second unit to our suite of ancillary equipment.

6. Summary

A "Hot Stage" Displex®[7] has been implemented at the Intense Pulsed Neutron Source (IPNS) for performing neutron diffraction experiments in the temperature range 20K to 800K. This new piece of ancillary equipment allows for extended temperature range studies through room temperature without having to change sample containers or environments. Preliminary tests on a standard sample[8] have shown a thermal gradient of <1 K/cm at 10K and at 800K over the length

[7] Displex® is a registered trademark of APD Cryogenics, Inc, Allentown, PA.

[8] Helium filled 7/16"(1.1 cm) diameter x 5 cm vanadium sample can.

of the sample container. Cool-down times to 10K are on the order of 90 minutes, slightly longer than a standard Displex®. The neutron scattering background compares favorably with a standard closed cycle refrigerator[9] or mid-range furnace[10] currently in use at the IPNS.

More information on the new "Hot Stage" Displex® and other ancillary equipment available at the IPNS is accessible at the IPNS Web site: http://www.pns.anl.gov.

7. Acknowledgements

In addition to the help and guidance of the design engineers at APD Cryogenics, we would like to acknowledge the assistance of J. Kowalski[11], D. Leach, J. Toeller, and C. Piatak, of the IPNS NGS Operations staff, in the design, construction, and assembly of the Hot Stage Displex®. We would also like to acknowledge the assistance of S. Short and J. Jorgensen, of the Materials Science Division, in the testing of the Hot Stage Displex® and R. Connatser of IPNS for providing the raw data plots of Figure 4. The work reported in this paper was supported by the U.S. Department of Energy, BES-Materials Sciences, under contract W-31-109-ENG-38.

[9] i.e. Standard DE-202 Displex®, 10K - RT.
[10] i.e. Coffee Can Furnace, RT - 350°C.
[11] Currently with ComEd, LaSalle, IL.

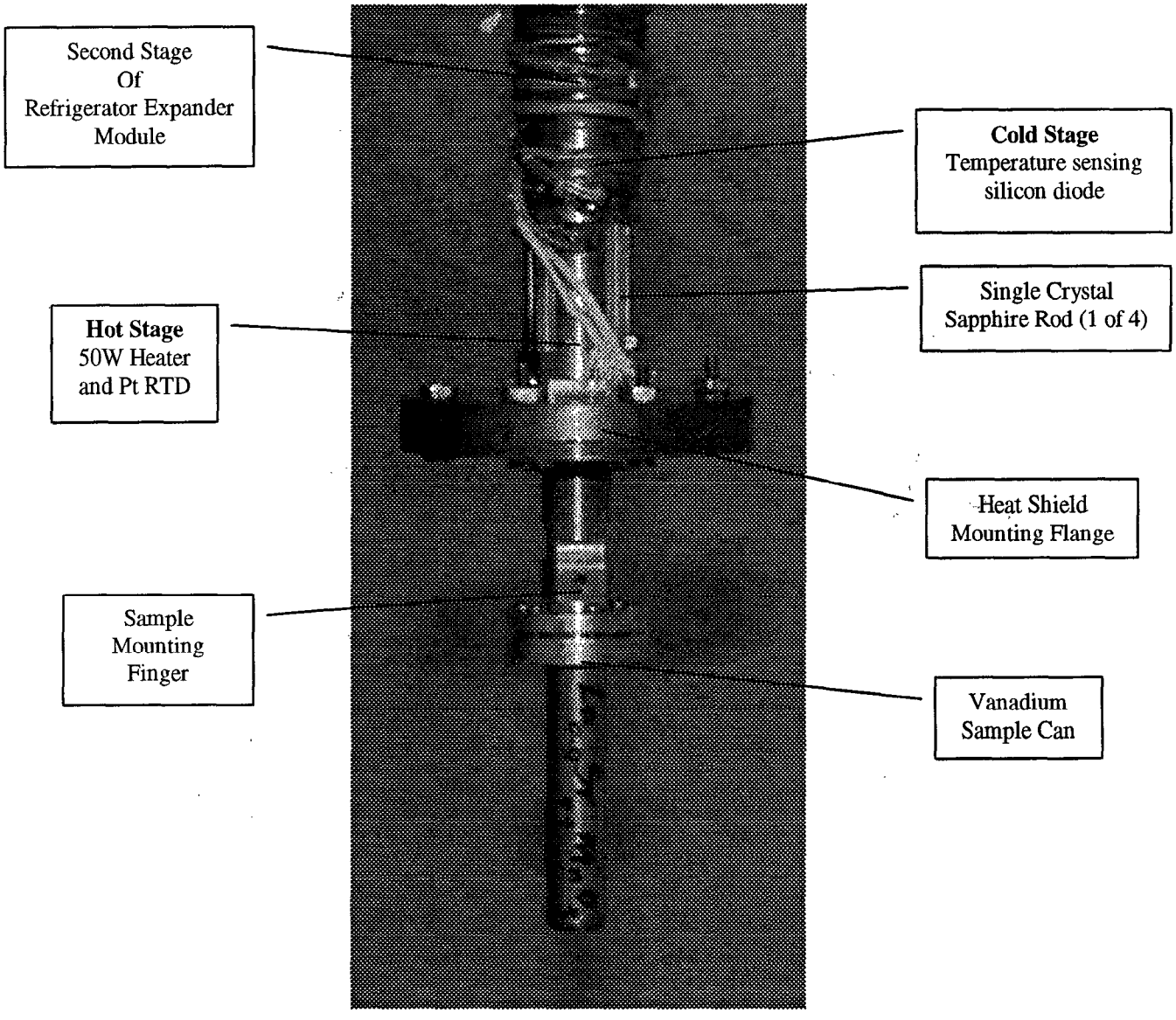

Figure 1. The Hot Stage Displex®. The sample can show is a low temperature indium o-ring sealed vanadium sample can of the type that is usually used in low temperature measurements on the powder diffractometers. A similar sample container with a flange capable retaining a helium leak tight seal throughout the temperature range of the Hot Stage is being developed.

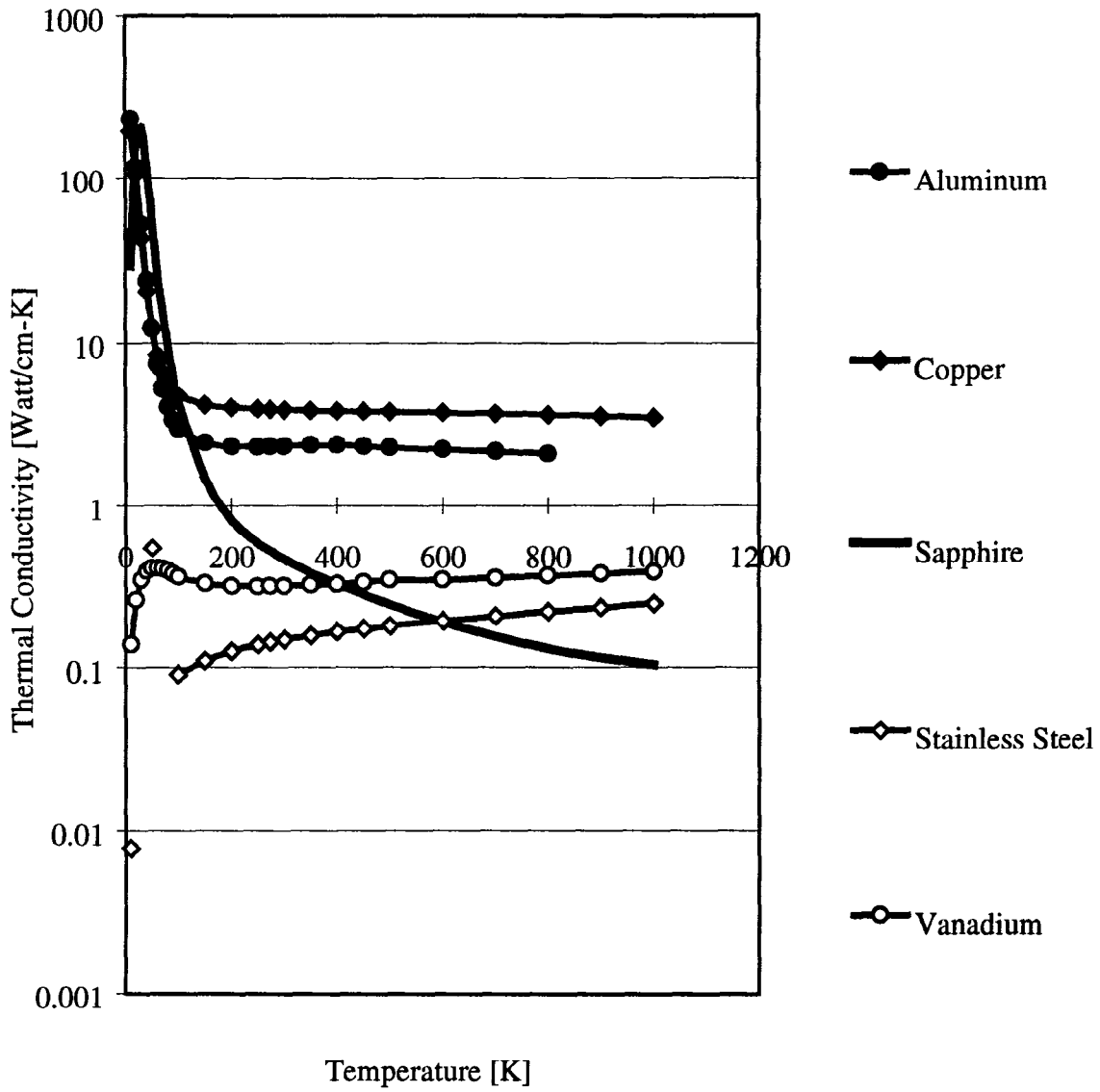

Figure 2. Thermal conductivity[12] of single crystal sapphire plotted along with that of aluminum, copper, 304 stainless steel, and vanadium.

[12] In Watts/cm-K from Thermophysical Properties of Materials, The TPRC Data Series Vol 1, 2, & 3, Y. S. Touloukian and C. Y. Ho, Eds., IFI/Plenum Data Corp, NY (1970).

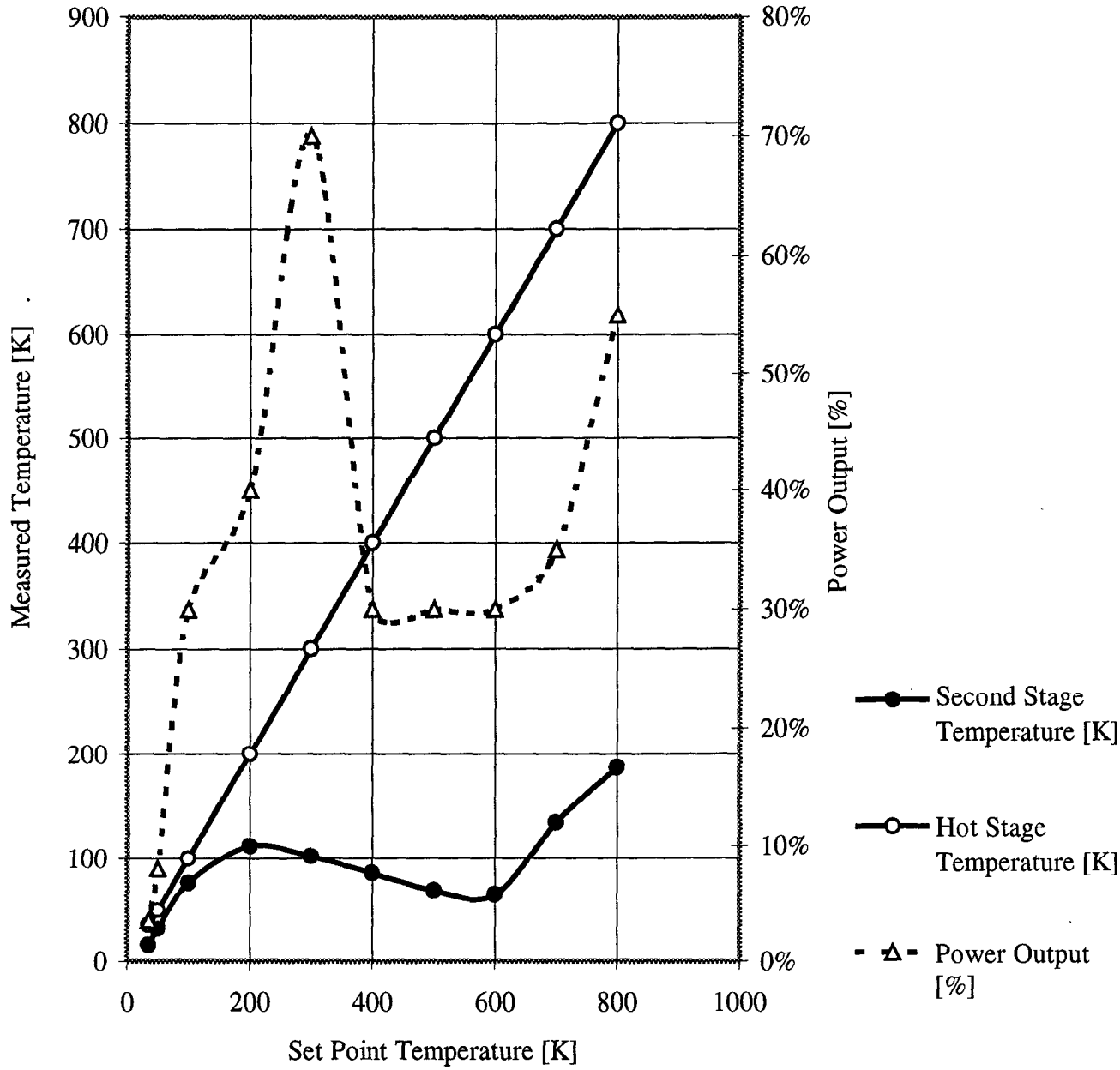

Figure 3. Heating plot of second stage temperature, Hot Stage temperature, and percent power output to heater as a function of Hot Stage set point.

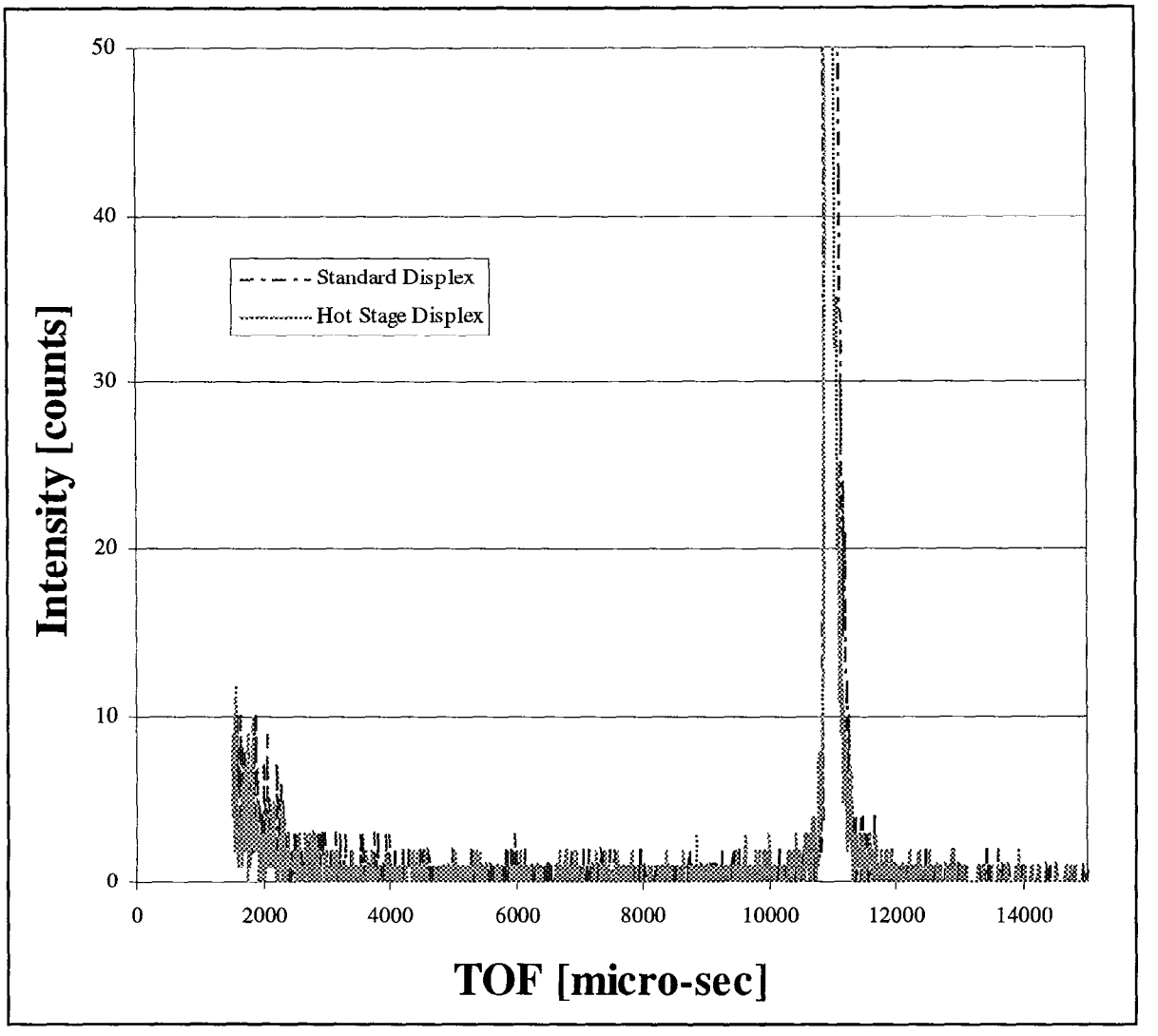

Figure 4. Comparison of raw TOF data taken on QENS with the Hot Stage Displex® and with a standard Displex®. Though the two plots are of different samples, the backgrounds of the two plots in the 1500 – 15000 μsec range are comparable and quite good.

The New Drive System for ISIS Disc Choppers

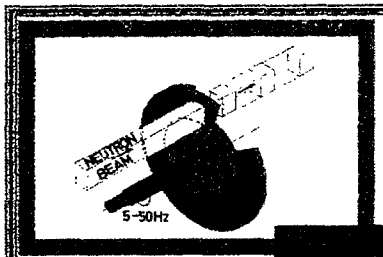

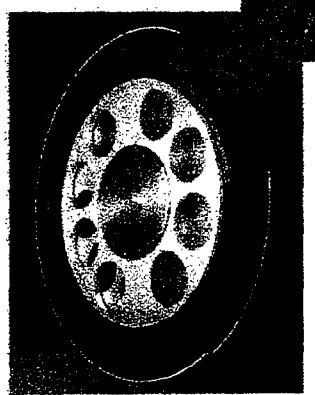

Disc Choppers at ISIS

Disc Chopper Technical Specification	
Frequency	5-50Hz
Absorbing Material	Boron Carbide in Epoxy resin
Power Supply controller	4kw DC servo motor
Accuracy	30 us
Instruments	MARI, HRPD, IRIS, LOQ CRISP, SURF, OSIRIS
New installations	GEM

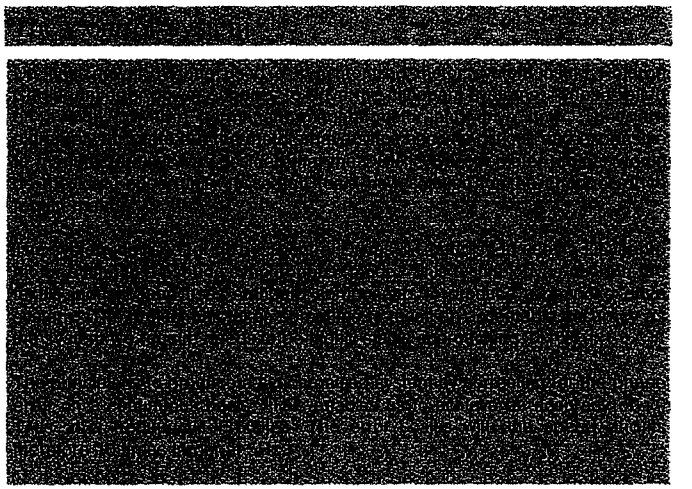

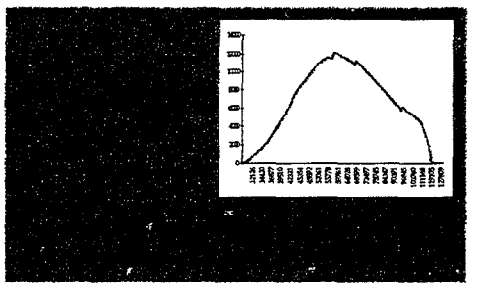

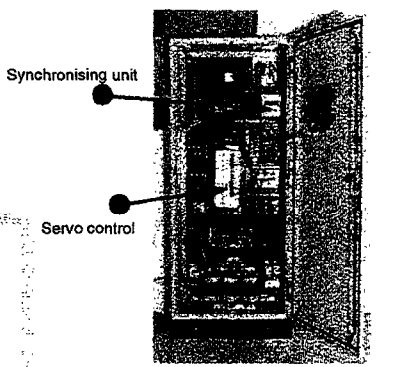

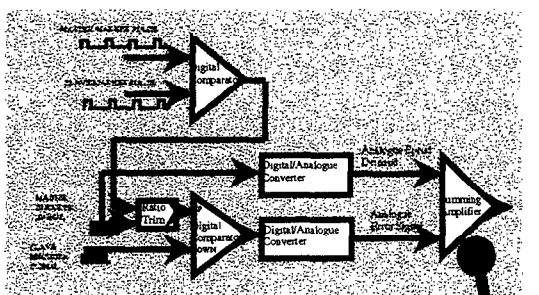

Basic Control Philosophy

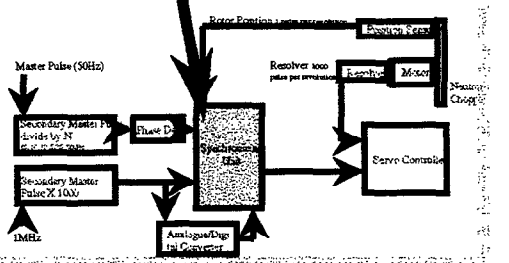

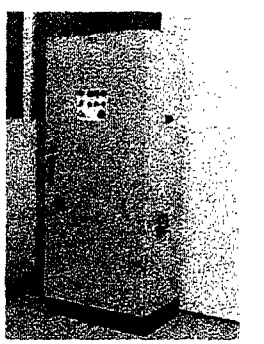

Z A Bowden, M L Fisher, P A Chorley, RAL,UK, B Halls, *Spectral Drives & Controls Ltd.*, Lowestoft Suffolk UK

CLRC

ISIS

A New Scintillator for Neutron Scattering Instruments

Dr. J. Bart Czirr
Mission Support Incorporated/Photogenics

We have developed an efficient new scintillator material that contains lithium, gadolinium and boron, all three of which possess large neutron capture cross sections for highly exothermic reactions. In addition, all three materials have low cross section isotopes that can be utilized to select the reactions of interest. The new material, $Li_6Gd(BO_3)_3$ activated with trivalent cerium, can be grown as clear single crystals suitable for large area neutron detectors. The outstanding characteristic of these materials is the high scintillation efficiency—as much as six times that of Li-glass scintillators. This increase in light output permits the practical use of the exothermic ^{10}B (n, alpha) reaction for low energy neutron detection. This reaction provides a four-fold increase in capture cross section relative to the ^6Li (n, alpha) reaction plus the intriguing possibility of demanding a charged-particle/gamma-ray coincidence to reduce background rates. These new materials will be useful in the thermal and epithermal energy ranges at reactors and pulsed neutron sources.

Four exothermic neutron capture reactions dominate the low-energy neutron detector field: ^3He (n,p)T, ^6Li (n,$\propto$) T, ^{10}B (n,$\propto$) ^7Li, and Gd(n,gamma). The ^3He reaction utilized in gaseous proportional counters has been the most popular system for several decades, but Li based scintillators have begun to supplant these detectors at both reactors and pulsed sources. Aside from BF_3 proportional counters, no practical ^{10}B-based detectors have been available. This is unfortunate, because the ^{10}B (n,$\propto$) reaction possesses several advantages over the other reactions, namely:

The capture cross section of ^{10}B is 4.1 times that of ^6Li.

The maximum range of the ^{10}B charged reaction products is 4 microns vs 40 microns for ^6Li. This permits the use of thinner detectors and could also result in superior spatial resolution in some situations.

The 478 keV gamma ray that is emitted in 94% of the capture reactions in ^{10}B can be utilized as a coincidence signal to greatly reduce the effects of ambient gamma background.

A condensed state ^{10}B detector will be much more efficient in thin layers that gaseous detectors.

Edge effects are greatly reduced in solid detectors.

In scintillator form, the ^{10}B detector recovery time can be much shorter than that of proportional counters.

The primary characteristic that has inhibited the use of ^{10}B-based scintillators is the low scintillation efficiency of B-loaded organic scintillators. The high energy-loss rate of the heavy charged reaction products is particularly detrimental to the efficient production of scintillation light in organic scintillator solvents. For example, in BC-454 plastic the light output per unit energy for the combined $\propto$, ^7Li signal from ^{10}B capture is only 4% that of electrons of the same energy. Another measure of the seriousness of this problem is that the light output for the ^{10}B reaction (2.31 MeV) is only 10% of that for the ^6Li reaction (4.79MeV), for liquid organic scintillators.

In light of the significant advantages attached to the ^{10}B reaction, it seemed useful to search for a B-based scintillator with greatly improved scintillation efficiency. The lithium lanthanide borates have been reported in the literature as a class of stoichiometric laser materials which can incorporate three of the popular neutron absorbing nuclei: B, Li and Gd(1). When activated with Ce^{3+}, these materials achieve a remarkably high scintillation efficiency compared to organic scintillators. Table I lists the measured signal size of $Li_6Gd(BO_3)_3(Ce)$ compared to the three most efficient competing materials. In addition, the estimated absolute number of detected photoelectrons in a typical PM tube is shown for the three reactions of interest. These latter numbers are based upon a measured value of 1025 photoelectrons per captured neutron in GS-20 glass scintillator. The observed factor of six improvement (over GS-20) in scintillation efficiency compensates for the factor of five decrease in light output from ^6Li to ^{10}B in the borate scintillator. The result is that the signal size from the present sample of $Li_6Gd(BO_3)_3(Ce)$ upon ^{10}B capture exceeds that of GS-20 for ^6Li capture. This result should provide a practical, good-pulse-height-resolution signal for many applications. Another material, with similar chemical and crystal-structure properties is $Li_6Y(BO_3)_3(Ce)$. The

advantage in substituting Y for Gd arises from the much lower neutron capture cross section for naturally occurring Y, thereby removing the strong competition for neutrons below 150 meV.

For applications requiring large-area detectors, it is advisable to use the borate crystals in powdered form incorporated within a transparent binder. Fortunately, the index of refraction of the crystals is within the range of transparent organic polymers. In particular, the measured index at 405 nm is 1.670, and a new polymer is available with an index at that wavelength of approximately 1.68. Therefore, at the average emission wavelength of 400 nm for the scintillator, the index of the plastic is slightly larger than that of the crystals. If necessary, the polymer can be diluted with a low index copolymer to match the crystals. (When polymerized within the new polymer, the crystals are invisible in white light.) Since the emission spectrum is only 90 nm wide, differences in dispersion between crystal and plastic should not introduce harmful light scattering problems, at least in thin layers.

Table II shows the various materials available for neutron detection and the energy ranges of applicability.

Table III lists the calculated and observed parameters for several materials.

Table IV lists the calculated efficiencies for four materials of interest. The effect of replacing natural gadolinium with low cross section yttrium or depleted gadolinium is significant at these energies.

Figure 1 shows the emission spectrum of $Li_6Gd(BO_3)_3(Ce)$ and Li_6 Y $(BO_3)_3(Ce)$ when excited by 340 nm UV light. The emission spectrum is well matched to the response functions of inexpensive PM tubes. The emission spectrum for charged-particle excitation is essentially identical.

Figure 2 is a plot of the pulse-height spectrum from a 1-mm thick single crystal of LiGdB. The peak near channel 380 is due to ^{6}LI capture, and the peak near channel 80 is due to ^{10}B capture. The crystal was grown with B enriched to 95% in B-10.

Figure 3 is a plot of the spectrum for the same material in microcrystalline form incorporated in casting resin.

Figure 4 is a plot of the pulse-height spectrum for a 1-mm thick sheet of GS-20 Li glass scintillator irradiated with thermal neutrons.

Figure 5 is a plot of ground GS-20 incorporated in an index-matching plastic polymer.

APPENDIX

The gamma-background sensitivity of several neutron detector materials was measured at the ISIS facility. The collimated neutron beam inpinged upon a cylinder of Cd, with the various detectors placed approximately 30 cm out of the beam and shielded from scattered neutrons. The relative response of the detectors was calculated from the observed number of background counts in a window centered at the position of the neutron capture peak, of width 2 x FWHM. The listed background sensitivity is the number of background counts per incident neutron per gm of ^{6}Li in the detector.

Table I
SCINTILLATOR COMPARISON
RELATIVE PULSE HEIGHT

Material	^{10}B(n, alpha)	^{6}Li(n,alpha)	Gd(n,gamma)
$Li_6Gd(BO_3)_3$	1.0	1.0	1.0
BC-454 (plastic)	0.09	—	—
GS-20 (glass)	—	0.165	—
GSO (crystal)	—	—	0.52
	PE/neutron*	**PE/neutron**	**PE/MeV**
Li_6 Gd $(BO_3)_3$	1290	6200	2780

*PE = Detected photoelectrons in PM tube.

Table II
DETECTOR OVERVIEW

COLD	10meV	THERMAL	150meV	EPITHERMAL
		^{7}Li Ln ^{10}B		^{7}Li Ln ^{10}B
^{3}He		^{6}Li Ln ^{11}B		^{6}Li Ln ^{11}B
Zn S (^{6}Li)		^{3}He		Zn S (^{6}Li)
		Zn S (^{6}Li)		^{6}Li glass
		^{7}Li Ln ^{11}B		

Li Ln B = Li_6 Ln $(B0_3)_3$ (Ce)

Ln = natural Gd, depleted Gd, Y

Table III
MATERIAL CHARACTERISTICS

	^{6}Li-Glass	$Li_6Gd(BO_3)_3$ (Li capture)	$Li_6Gd(BO_3)_3$ (B capture)
Atomic Density ($\times 10^{22}$ atoms cm^{-3})	1.72 (Li)	3.30 (Li)	1.65 (B)
Macroscopic Capture Cross Section (cm^{-1}) (at thermal)	16.1	30.9	63.3
Density (gm cm^{-3})	2.5	3.5	3.5
Relative Signal Amplitude for Alpha Particles	1.0	5.8	5.8
Relative Signal Amplitude for Neutron Capture	1.0	6.0	1.3
Neutron Capture, Peak Electron Energy Equivalent (MeV)	1.48	2.22	0.46
Alpha-to-Beta Ratio	0.23	0.30	0.30
Scintillation Decay time	60 ns	200 ns 700 ns (small)	200 ns 700 ns (small)
Index of refraction	1.55	1.66	1.66
Melting Point	1200°c	860°c	860°c

Table IV
DETECTION EFFICIENCY COMPARISON

Neutron Energy	0.25 mm Li YB (B-10 Capture)	0.25 mm Li Gd B (B-10 Capture)	0.25 mm Li Gd B (Li-6 Capture)	BC704 (Li-6 Capture)
0.025eV	80%	63%	43%	29%
0.10eV	56%	52%	30%	13%
0.20eV	44%	43%	23%	11%

Li Gd B with available Gd, depleted in odd isotopes.

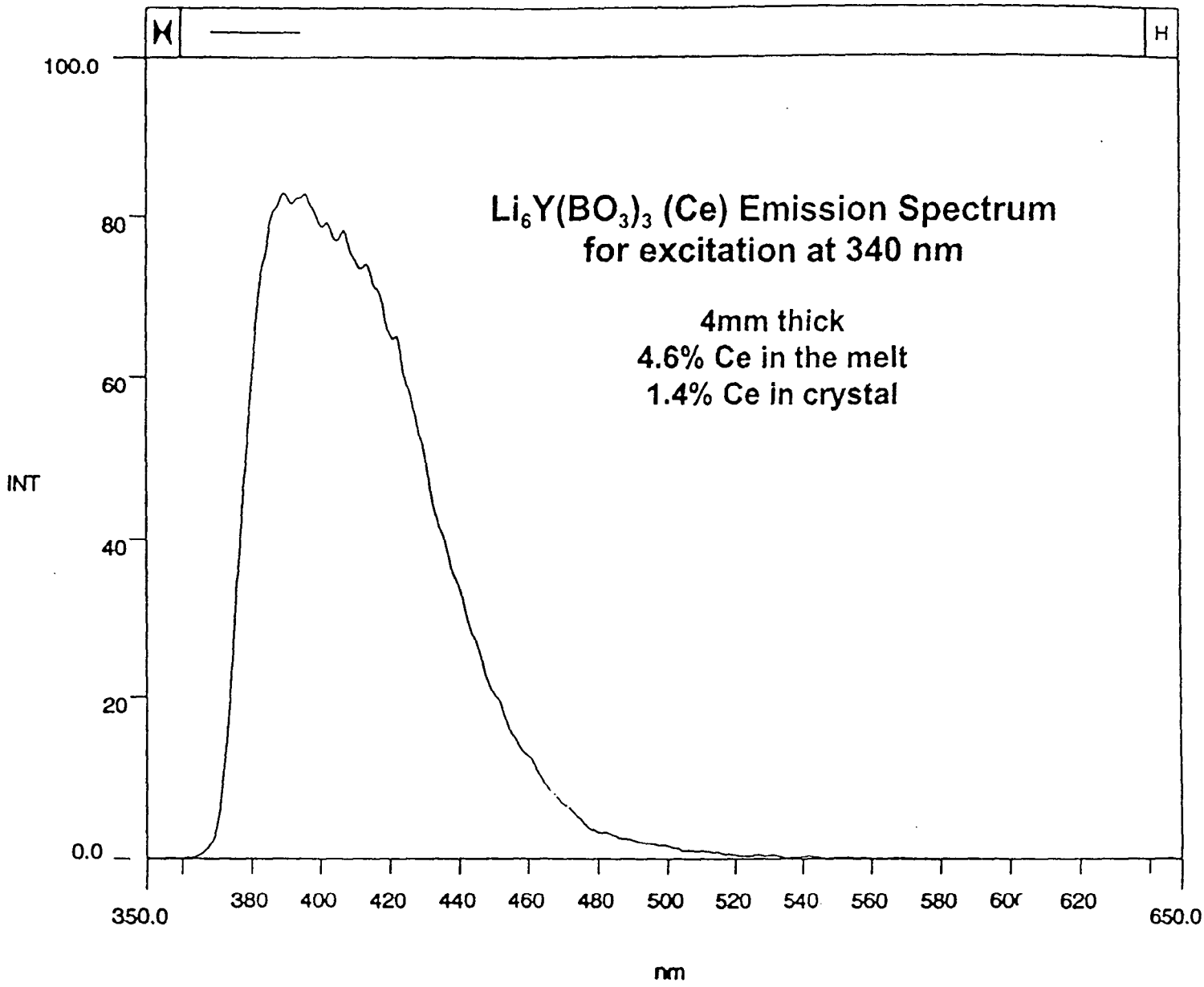
$Li_6Y(BO_3)_3$ (Ce) Emission Spectrum
for excitation at 340 nm
4mm thick
4.6% Ce in the melt
1.4% Ce in crystal
INT
100.0
80
60
40
20
0.0
350.0
380
400
420
440
460
480
500
520
540
560
580
620
650.0
nm

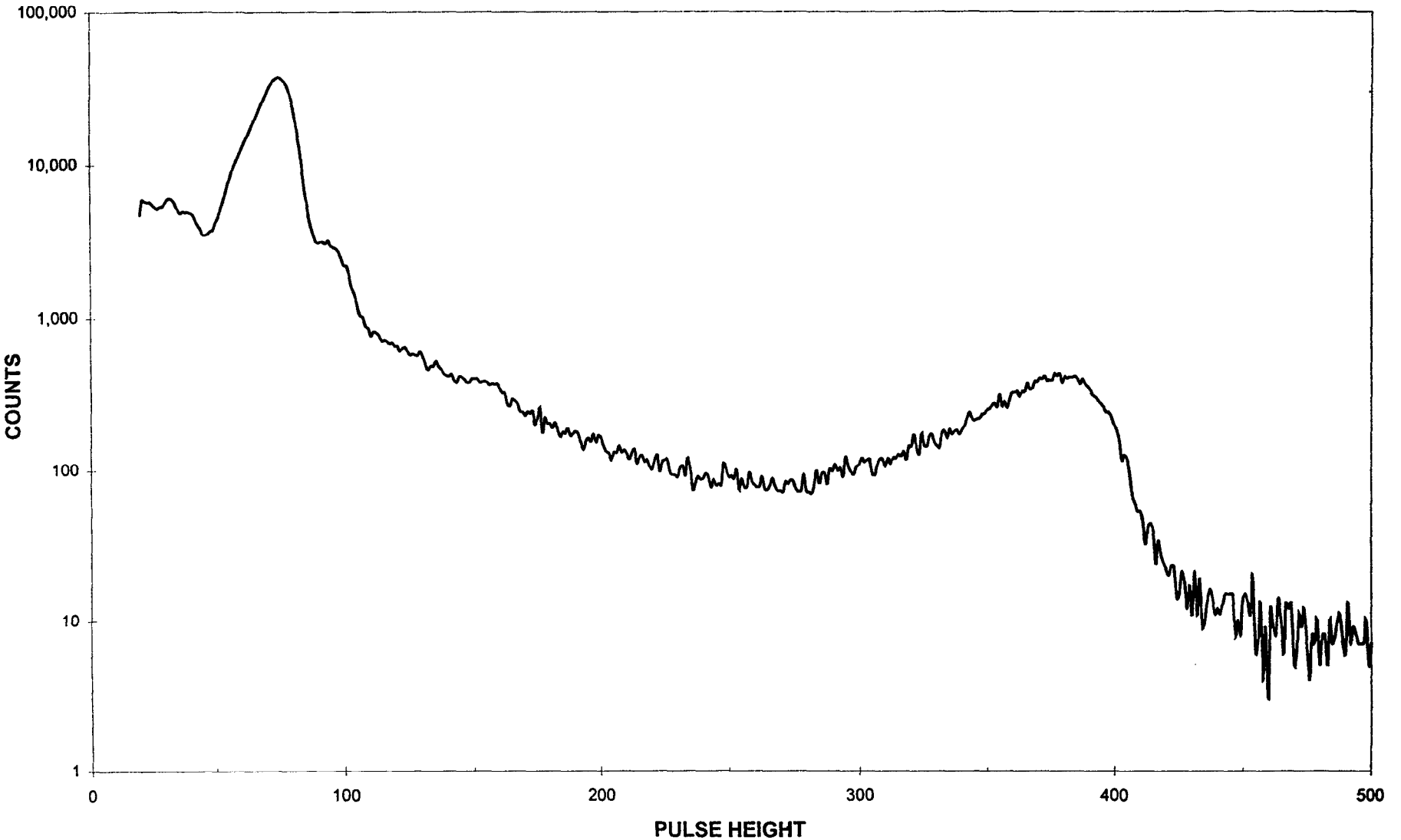
100,000
10,000
1,000
100
10
1
COUNTS
0
100
200
300
400
500
PULSE HEIGHT

FIGURE 2

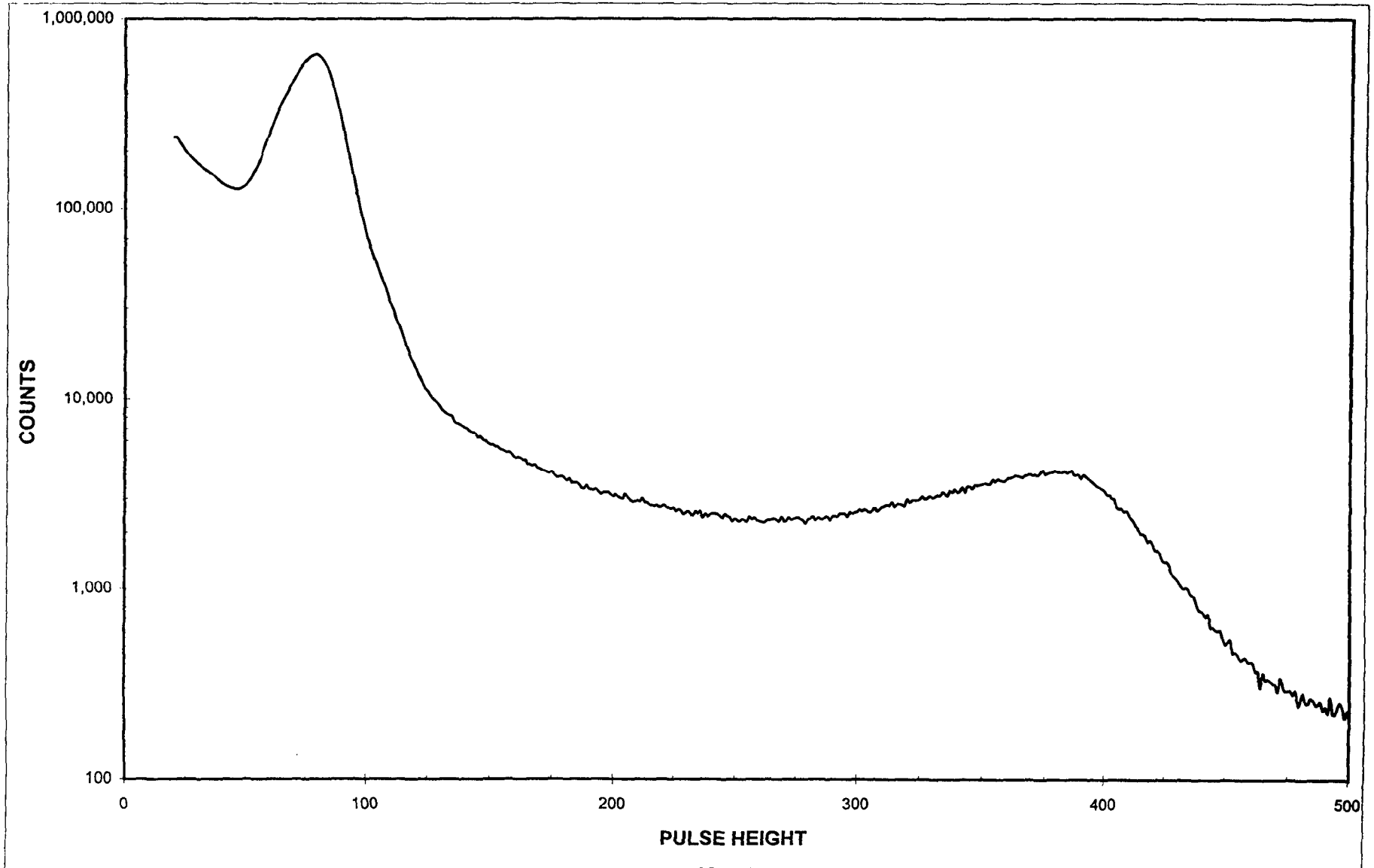
1,000,000
100,000
10,000
1,000
100
COUNTS
0
100
200
300
400
500
PULSE HEIGHT

FIGURE 3

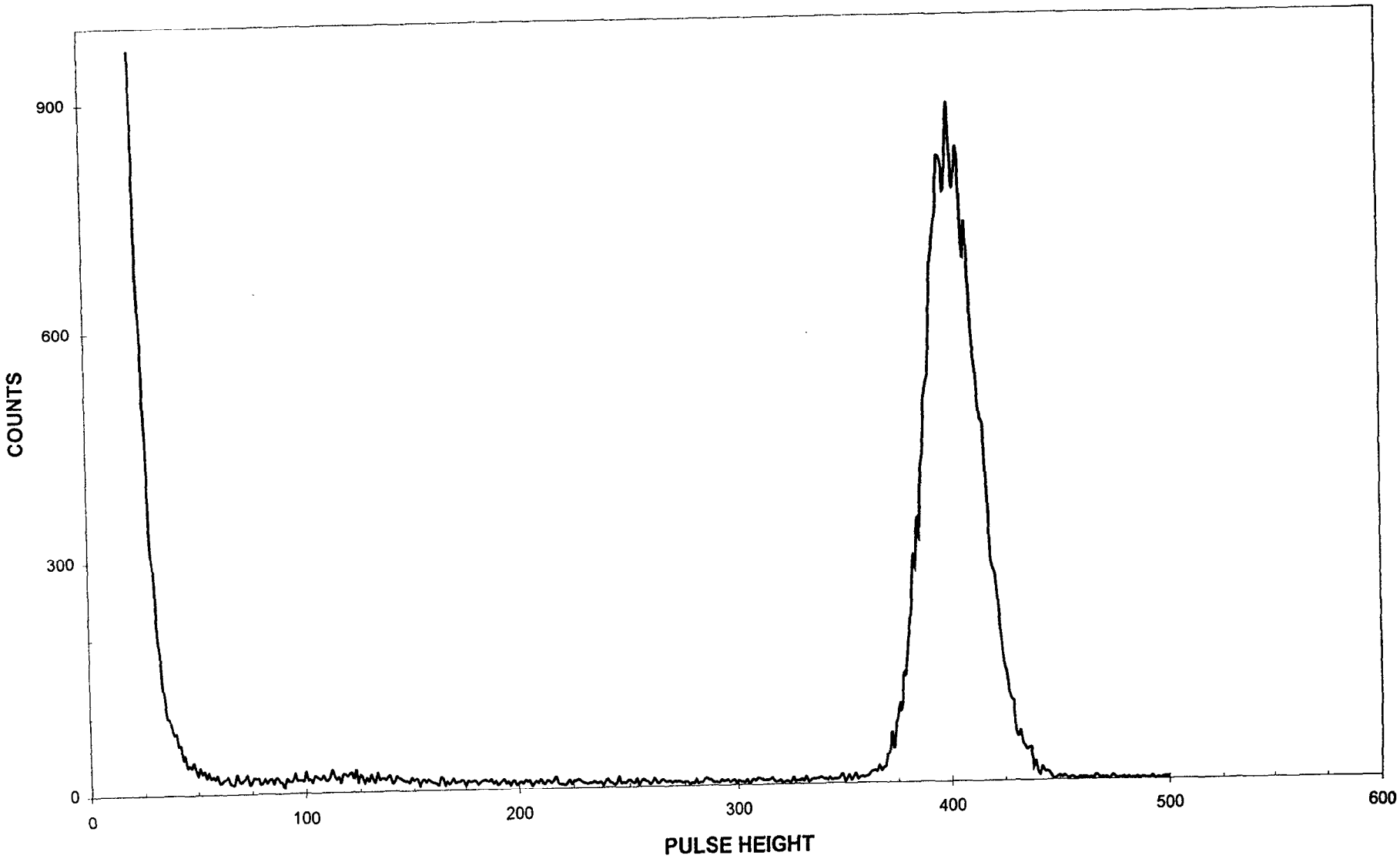

FIGURE 4

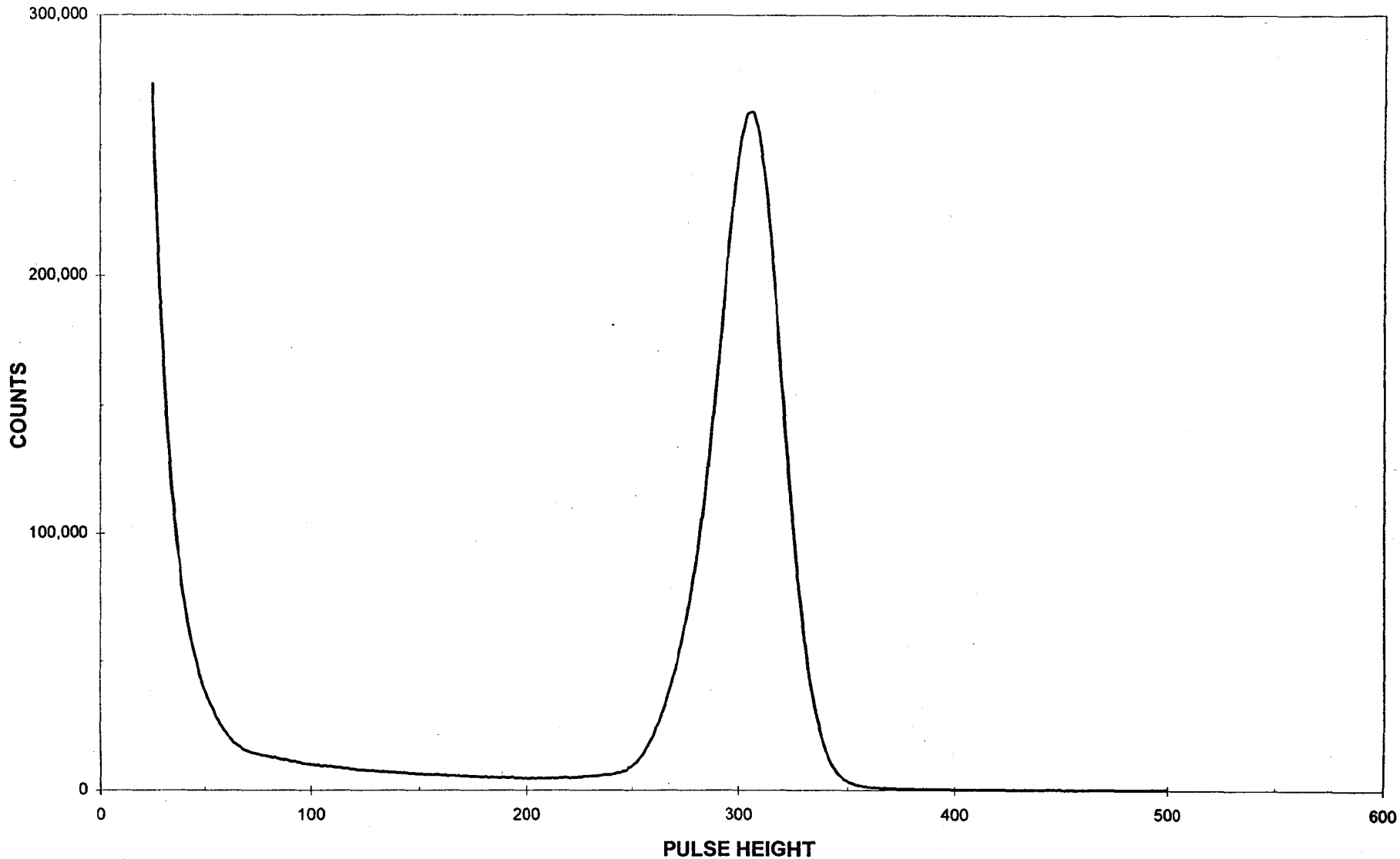
300,000
200,000
100,000
0
COUNTS
0
100
200
300
400
500
600
PULSE HEIGHT

FIGURE 5

Appendix Table I
Relative Detector Background Sensitivity

Material	Thickness $\frac{mg\ ^6Li}{cm^2}$	$\frac{\text{Background Counts}}{\text{Neutron} \bullet g\ ^6Li}$
GS-20 (glass)	31.4	1.0
GS-20 (glass)	23.5	0.91
GS-20 (glass)	15.7	0.54
GS-20 (glass)	7.9	0.20
LiGd Borate (single crystal)	22.6	0.16
GS-20+Polymer	3.8	0.74

ICANS-XIV
14th Meeting of the International Collaboration
on Advanced Neutron Sources
June 14-19, 1998
Starved Rock Lodge, Utica, Illinois, USA

Structural and Hydraulic Study on Cold Source Moderator

Tomokazu ASO, Shuichi ISHIKURA, Atsuhiko TERADA,
Tetsuya KAI, Makoto TESHIGAWARA, Masanori KAMINAGA,
Ryutaro HINO and Noboru WATANABE

Center for Neutron Science (CENS)
Japan Atomic Energy Research Institute (JAERI)
Tokai, Ibaraki, 319-1195, Japan

ABSTRUCT

In this paper, a concept of thin-walled structure for a cold source moderator applicable to a MW-scale target system is outlined, and stress and hydraulic analyses as well as flow visualization experiments carried out to improve the concept are introduced.

1. INTRODUCTION

In the Neutron Science Project of the Japan Atomic Energy Research Institute (JAERI), a 5MW neutron scattering facility is planed to be constructed first, where high intensity neutrons are generated at a target by spallation reaction between target materials and the proton beam. Since technology of a MW-scale target system has not been established yet, development of the 5 MW target system is one of the most difficult technical challenges in this project.

One of the key components consisting of the target system is a cold source moderator using supercritical hydrogen, which affects directly a neutron yield. Representative structure of the cold source moderator is that used at the ISIS [1]. **Figure 1** shows a first concept of the cold source moderator based on the ISIS moderator. Supercritical hydrogen flows into the inner vessel through the inlet pipe inserted in the vessel, and flows out through the outlet channel between the inlet pipe and the outer pipe which is welded at the top of the vessel. To investigate feasibility of this concept, structural and hydraulic analyses as well as flow visualization experiments using a water loop were carried out. This paper introduces analytical and experimental results, and outlines the vessel structure of the cold source moderator.

2. ANALYSIS ON STRUCTURAL STRENGTH

Thickness of the vessel is required to be as thin as possible in order to keep high neutron transmission rates relating to a high neutron yield. One of the major technical issues in the design of the cold source moderator is to keep structural strength of the moderator vessel under a supercritical condition of hydrogen, 1.5MPa and 20K. Forging aluminum alloys are usually used for vessel materials of the cold source moderator. To get a prospect of the allowable thickness of forging aluminum alloys, stress analyses were carried out under following conditions:

Inner vessel size	:	120mm wide, 120mm high, 50 mm long and 3 mm thick 180mm in curvature radius of curved surfaces
Temperature	:	20K
Internal pressure	:	1.5MPa
Vessel material	:	Forging aluminum alloy - A6061, A5083 and A2014

A multi-purpose structural analysis code, ABAQUS-Standerd Vr.57, was used to analyze stress distributions. Then, the simulation model was divided into 4800 elements using the 3-D quardrilateral shell element.

Figure 2 shows one of analysis results of stress distributions on the inner and the outer vessel surfaces. As seen in the figure, the maximum value of the Mises stress which indicates the sum of membrane and bending stresses is 93MPa on the outer surface and 112MPa on the inner surface, respectively. The maximum displacement is only 0.5mm, which occurs at the center of the curved surface.

Figure 3 illustrates stress-strain curves of forging aluminum alloys proposed for the vessel materials. A6061 (Al-Mg-Si-Cu-Cr) and A5083 (Al-Mg-Mn-Cr) are used widely for cryogenic vessels. A2014 (Al-Cu-Mg-Mn-Si) is used as a structure material of liquid hydrogen/oxygen fuel tanks of rockets. It can be seen that the design stress of A2014 alone exceeds the maximum Mises stress shown in Fig.2. However, the maximum Mises stress decreases as the vessel thickness increases. In the case of 5mm of the vessel thickness, the maximum Mises stress decreases to a value less than the design values of A6061 and A5083.

Figure 4 shows the neutron transmission rate as a function of wavelength for above candidate materials. As seen in the figure, the neutron transmission ratio of A2014 of 3mm thick is better than A6014 and A5083 of 5mm thick by 2%. It might be deduced that a main factor affecting the transmission rate is the thickness of the moderator vessel.

3. HYDRAULIC ANALYSIS AND FLOW VISUALIZATION

Hydrogen temperature rise affects the neutron yield, and moreover, has the potential to change the supercritical state into the liquid state. In the liquid state of hydrogen, there is some possibility that an excessive pressure fluctuation caused by local

boiling gives serious damages to the thin-walled moderator vessel. From these viewpoints, it is desirable to control the temperature rise less than 3K. Since the temperature rise depends on the flow pattern in the vessel, hydraulic analysis and flow visualization experiments were carried out to clarify the flow patterns.

The hydraulic analysis was carried out with a computational fluid dynamics code, STAR-CD, under the water flow conditions to learn a typical flow pattern. A simulation model was the simplified two-dimensional model whose dimensions were 25mm of the inlet pipe diameter, 60mm of the outer pipe diameter and 10mm of distance from the nozzle of inlet pipe to the bottom plate. **Figure 5** shows one of analysis results obtained under low inlet water velocity of 2m/s, where the Reynolds number (Re) is 56,000; Re is around 10^6 under the supercritical hydrogen condition. It can be seen that the recirculation flow caused by the jet blowing out from the inlet pipe nozzle is generated around the inlet pipe. More intensive recirculation flow will occur at higher Re. Since the intensive recirculation flow has a potential to cause vibrations of the inlet pipe and the vessels, the flow-induced vibrations will be necessary to taking into accounts in the moderator design for keeping the structural strength.

To verify analysis results, flow patterns were visualized with a particle image velocimeter using a laser pulse sheet (PIV system) under the water flow conditions. **Figure 6** shows a flow diagram and an outer view of the test apparatus. The moderator is simulated with two acrylic cylinders whose dimensions are the same as those of the simulation model. In the experiments, small amounts of fluorescence micro particles (10 μm) were mixed with water as the tracer. **Figure 7** shows one of pictures taken at around 70ms intervals using the PIV system. Processing a series of 50 pictures, a velocity distribution in the vessel was visualized. **Figure 8** shows a vector and contour maps of velocity distribution in the bottom region of the vessel. The measured flow pattern agrees very well with the analysis result. Also, from the measured result, a low velocity region can be clearly seen on the bottom surface below the nozzle of the inlet pipe. This low velocity region will be possible to affect the temperature rise of hydrogen.

On the basis of stress analysis and flow visualization results, the moderator vessel was modified as shown in **Fig.9**. The vessel is a thin-walled structure supported with thin frames and inner plates to keep the vessel strength. The vessel materials is the aluminum alloy such as A2014. Dimensions of the vessel are 120mm wide, 120mm high, 50mm long and 3mm thick. A twisted tape is installed inside the inlet pipe so as to suppress the low velocity region by the swirl flow caused by the twisted tape. Then, most of supercritical hydrogen flows through the inlet pipe towards the bottom of the vessel, but small amounts of flow bypass through small holes located at the bottom half of the inlet pipe to suppress recirculation flow. It is necessary to verify this concept through R&Ds on thermal hydraulics and structural strength.

4. CONCLUDING REMARKS

From stress analyses and neutronic calculations, forging aluminum alloy A2021 was found to be a most likely candidate material for a cold source moderator vessel, which can make a vessel thickness thin down to 3mm under a supercritical hydrogen condition of 1.5MPa and 20K so as to allow high neutron transmission rate. It is necessary to optimize a thin-walled structure for the cold source moderator vessel through R&Ds on neutronics, thermal-hydraulics, and mechanical structure.

Acknowlegement

We are grateful to A. T. Lucas (ORNL) for helpful advice on the cold source moderator.

References

[1] T. A. Broome, Proceedings of International Worlshop on Cold Source Moderators for Pulsed Neutron Sources, Argonne National Laboratory(1997).

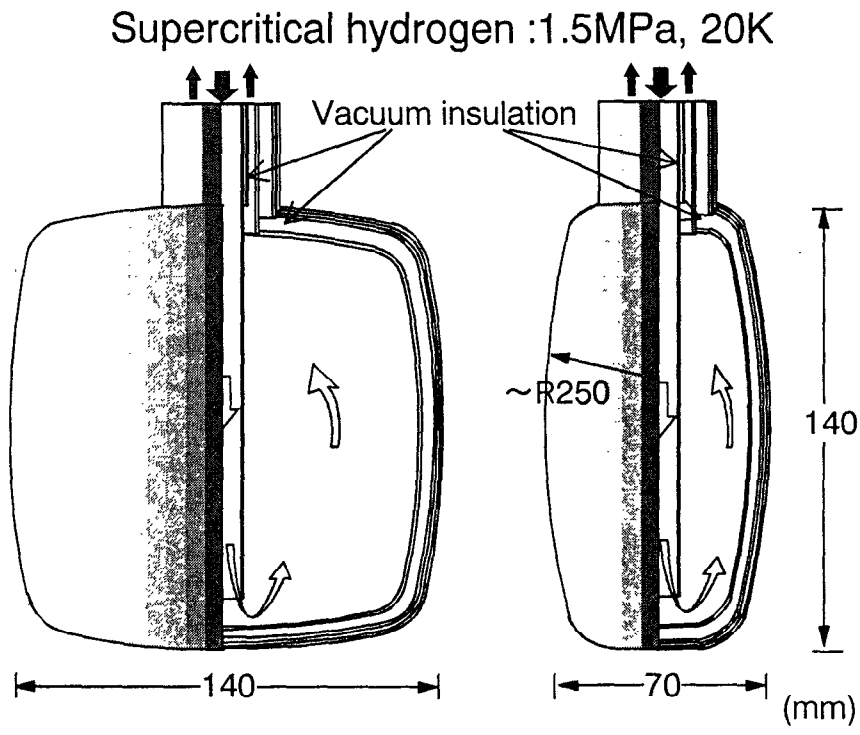

Figure 1 First concept of the cold source moderator

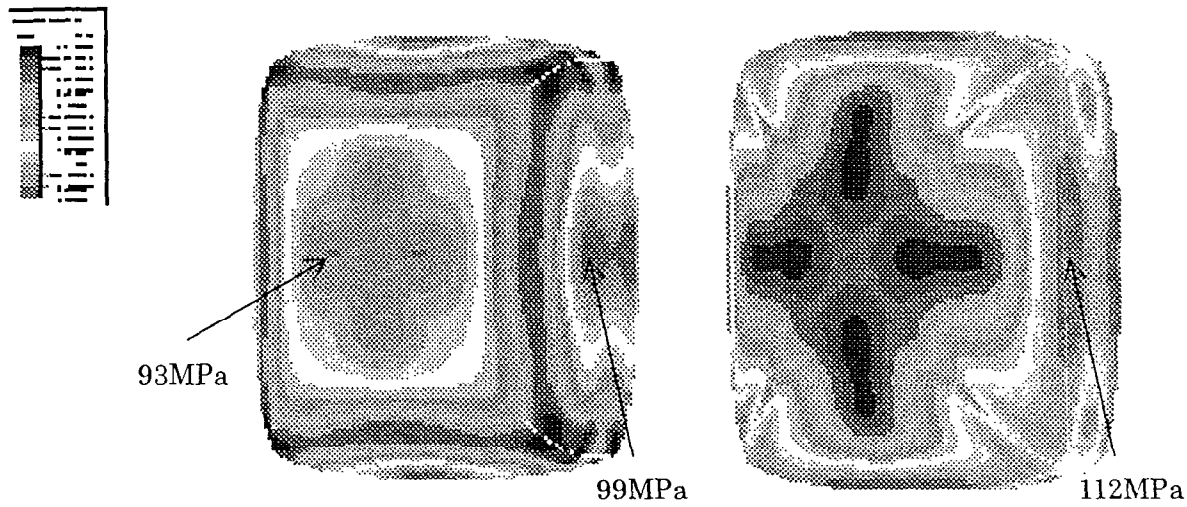

(a) Outer surface (b) Inner surface

Figure 2 Stress distributions on inner and outer vessel surfaces
(Vessel thickness : 3mm, Inlet pressure : 1.5Mpa, Material : aluminum alloy)

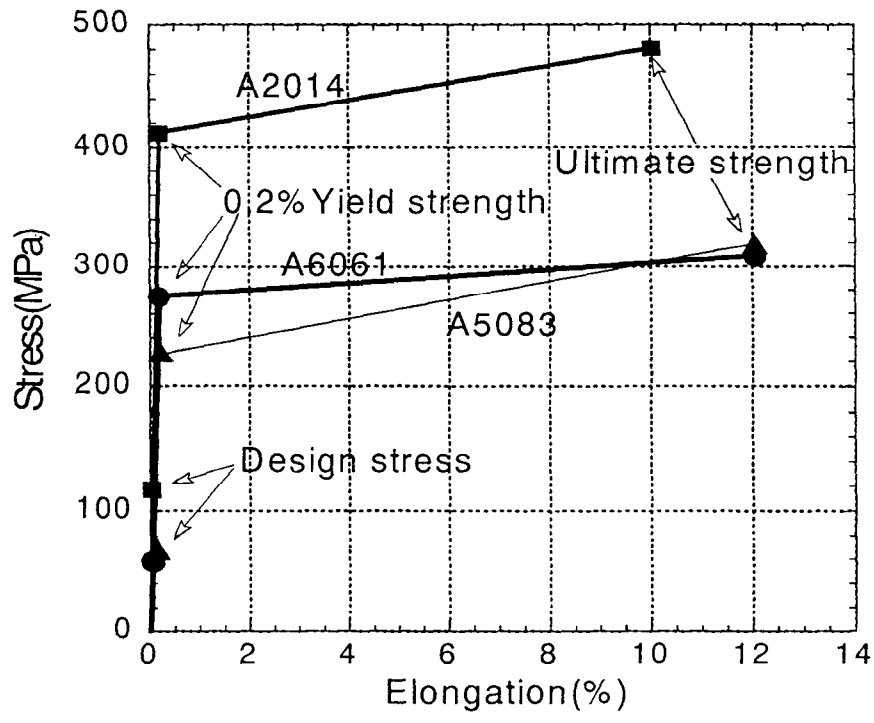

Figure 3 Design stresses and stress-strain curves of candidate aluminum alloys

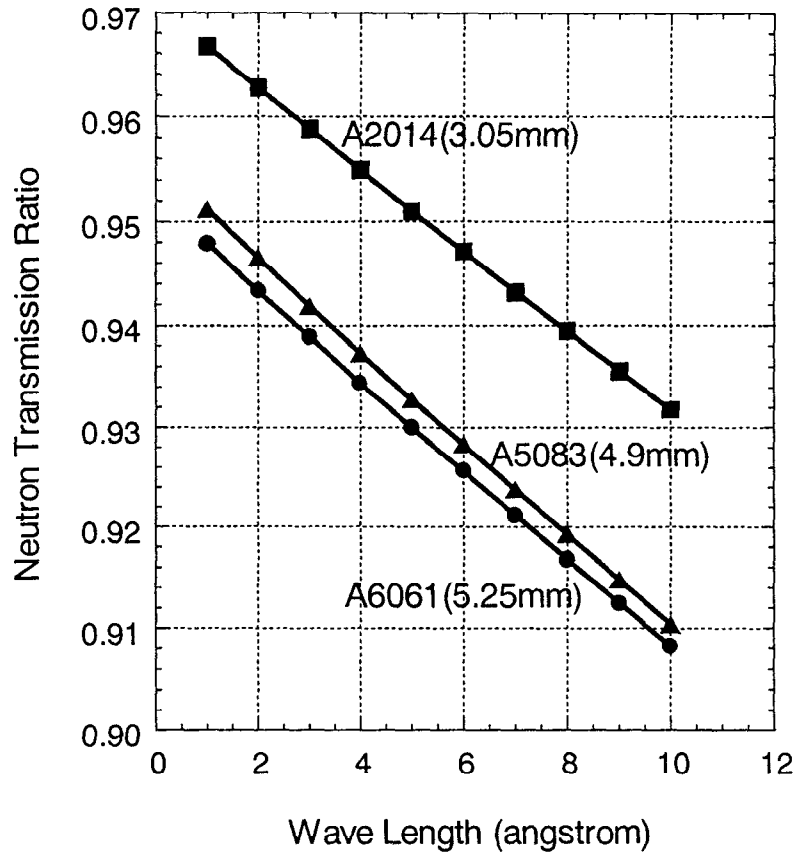

Figure 4 Neutron transmission ratio for candidate materials as the function of wave length

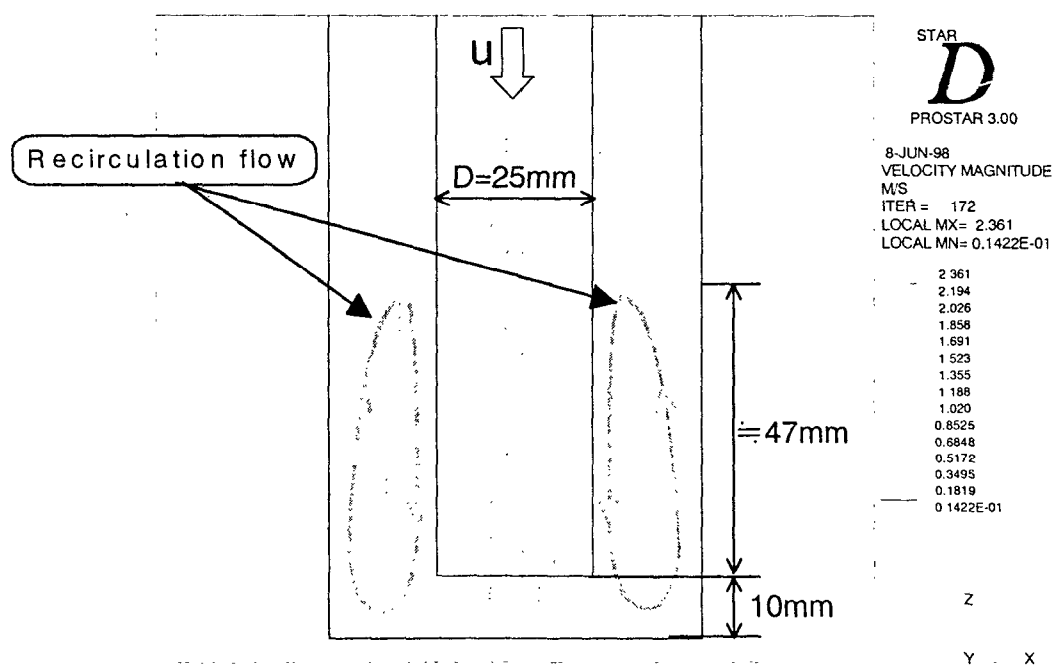

Figure 5 Analysis result obtained under low inlet velocity of 2m/s
(Fluid : water, Re = Du/ ν = 56,000)

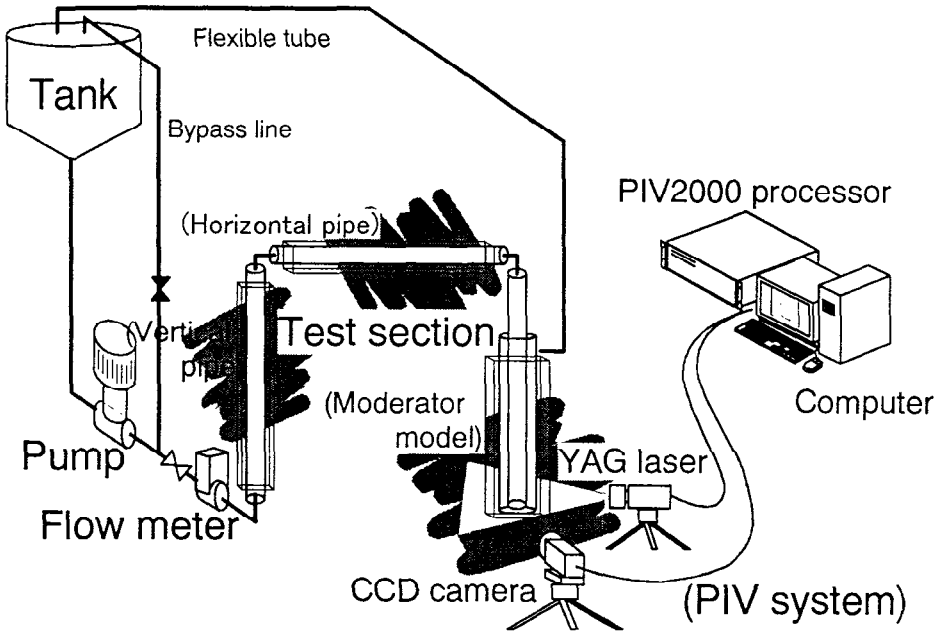

(a) Flow diagram of flow apparatus
(Water flow rate = ~500 l/min)

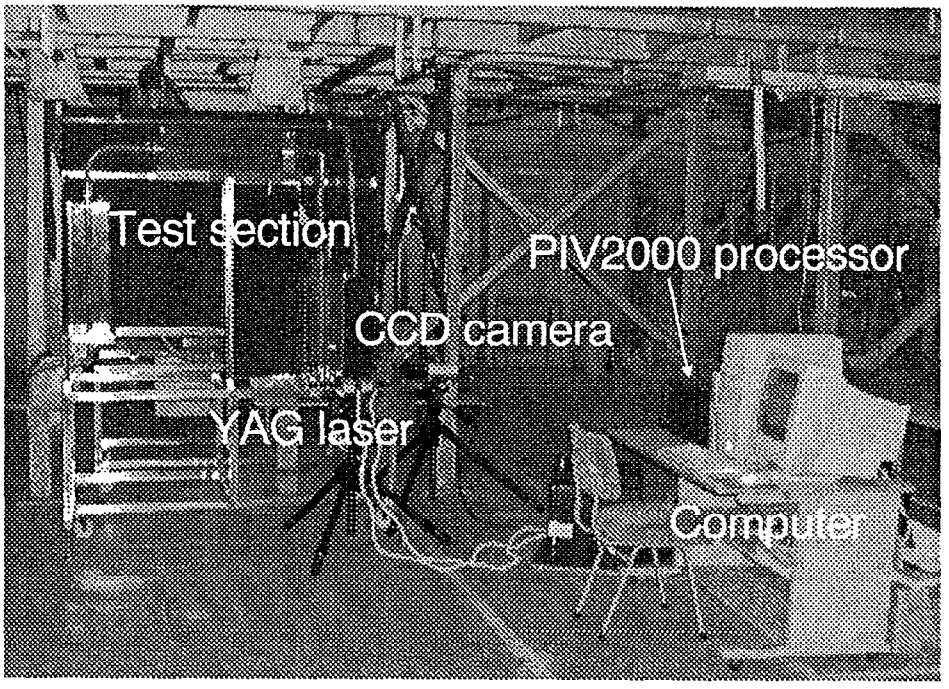

(b) Outer view

Figure 6 Experimental apparatus for flow pattern measurement

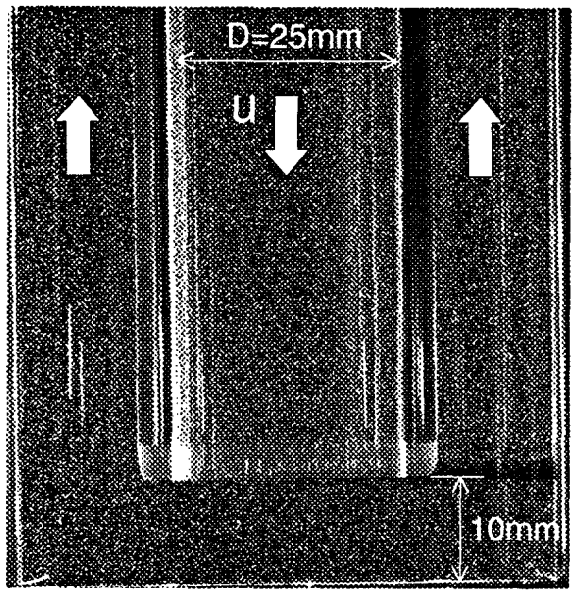

Figure 7 One of pictures taken at around 70ms intervals using PIV

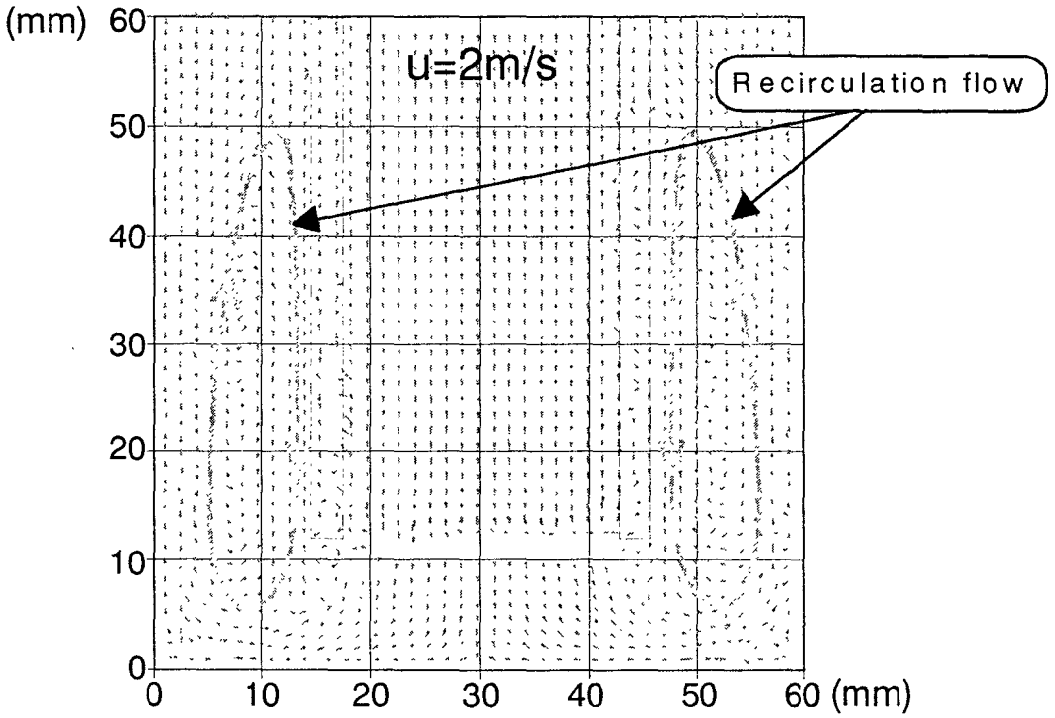

Figure 8(a) Vector map of water velocity measured by PIV

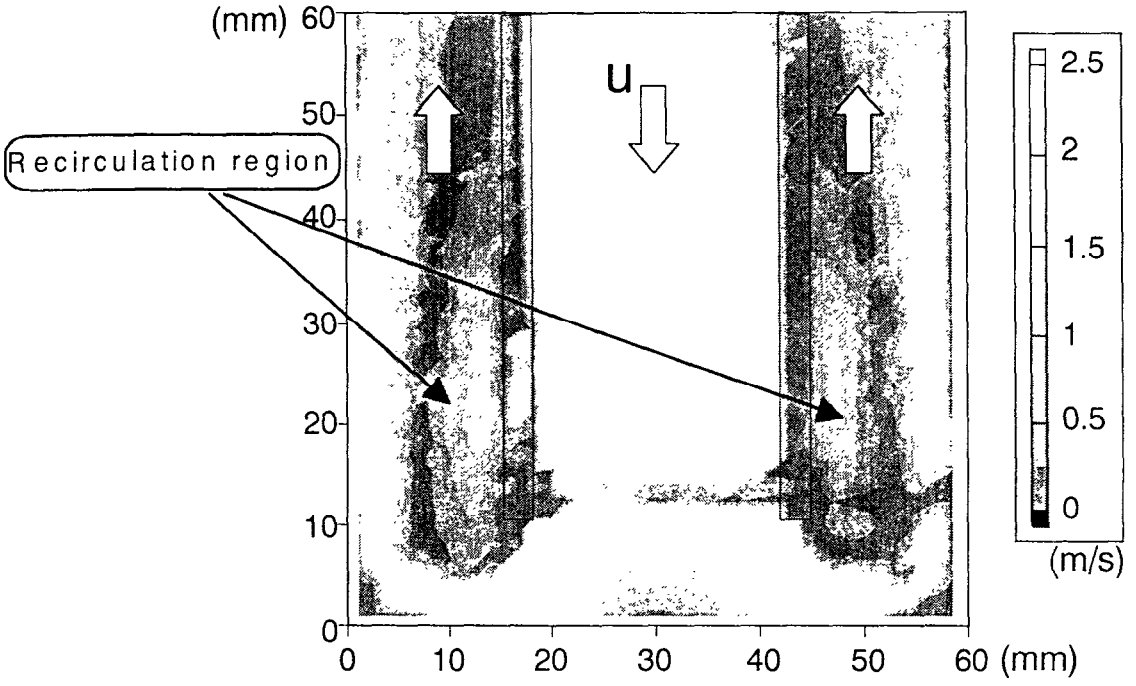

Figure 8(b) Contour map of measured velocity

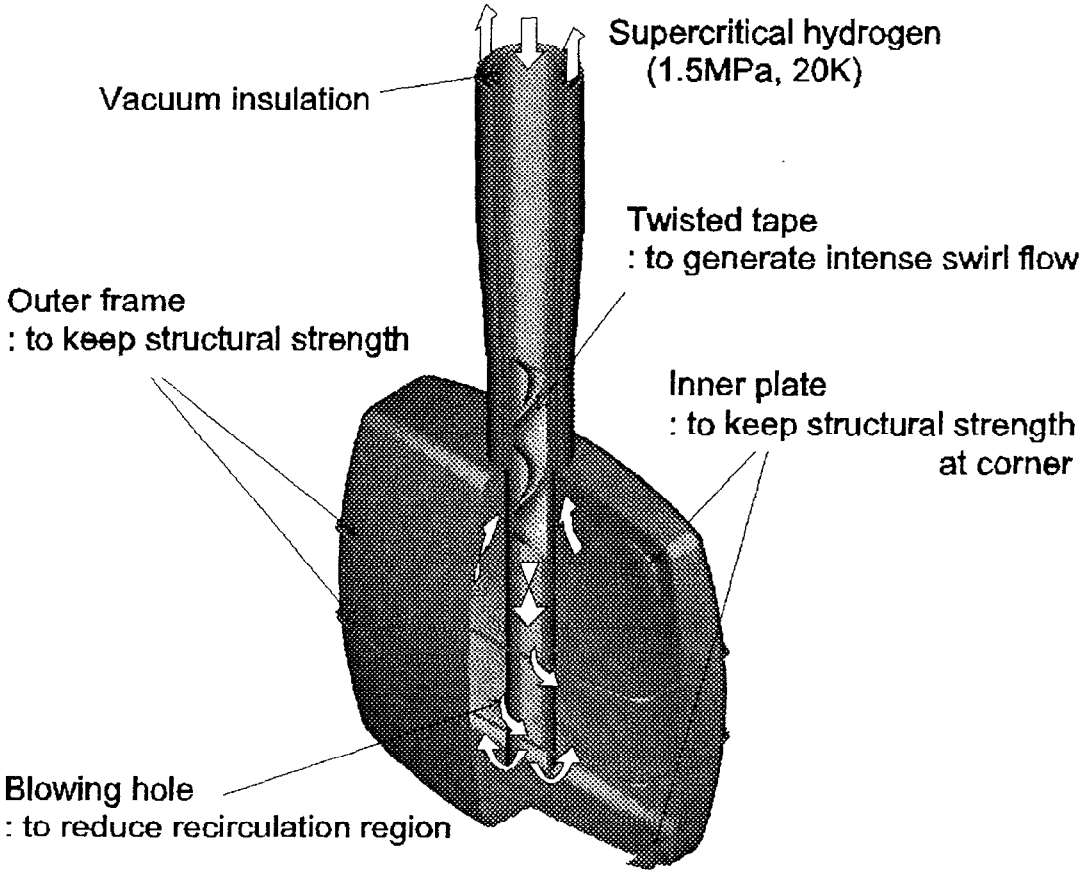

Figure 9 Modified concept of the cold source moderator

ICANS-XIV
14th Meeting of the International Collaboration on
Advanced Neutron Sources
June 14-19, 1998
Starved Rock Lodge, Utica, IL, USA

Incident Spectrum Determination for Time-of-Flight Neutron Powder Diffraction Data Analysis

J. P. Hodges, J. D. Jorgensen, S. Short and D. N. Argyriou
Materials Science Division, Argonne National Laboratory, Argonne, IL 60439.

J.W. Richardson, Jr.
Intense Pulsed Neutron Source, Argonne National Laboratory, Argonne, IL 60439.

Abstract

Accurate characterization of the incident neutron spectrum is an important requirement for precise Rietveld analysis of time-of-flight powder neutron diffraction data. Without an accurate incident spectrum the calculated model for the measured relative intensities of individual Bragg reflections will possess systematic errors. We describe a method for obtaining an accurate numerical incident spectrum using data from a transmitted beam monitor.

1. Introduction

With a multidetector diffractometer, which can be either electronically or geometrically focused, a focused diffraction data set is constructed by summing a number of histograms.[1,2] Each of these histograms is generated by one element of an extended array of detectors. The summing operation is made possible by time-focusing the individual histograms to a desired pseudo-time corresponding to a reference detector position, such that data for the same *d*-spacing are summed into the same data channel regardless of the neutron wavelength. Normally, the reference detector position is taken as the average scattering angle of the extended detector array.

2. Incident Spectrum Measurement

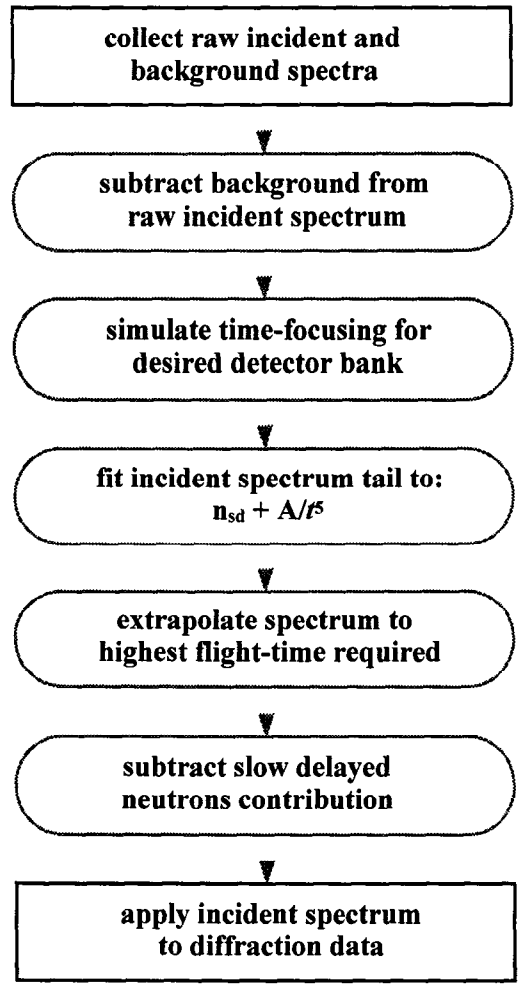

Fig. 1. A method for the construction of an effective incident spectrum.

An incident spectrum is a distribution of neutron flux versus a wavelength scale. However, for a focused time-of-flight diffractometer, the effective incident spectrum needed to model the data is a spectrum which, for any focused time (or *d*-spacing) channel, has been averaged over a range neutron wavelengths defined by the focusing operation. Features which are sharp in the actual incident spectrum, *e.g.* Bragg cutoffs due to window materials, are smoothed in the effective incident spectrum by the focusing operation. The determination of an effective incident spectrum for a particular diffraction data set is non-trivial because many aspects of the diffraction experiment can have an effect on the incident spectrum, *e.g.* sample environment, moderator temperature which can change with time, *etc.*.

The flow-chart presented in Fig. 1 displays a method for the construction of an effective incident spectrum that has proven to work well for the Special Environment Powder Diffractometer (SEPD) at IPNS. It should be possible to readily adapt this method to other time-of-flight neutron diffractometers.

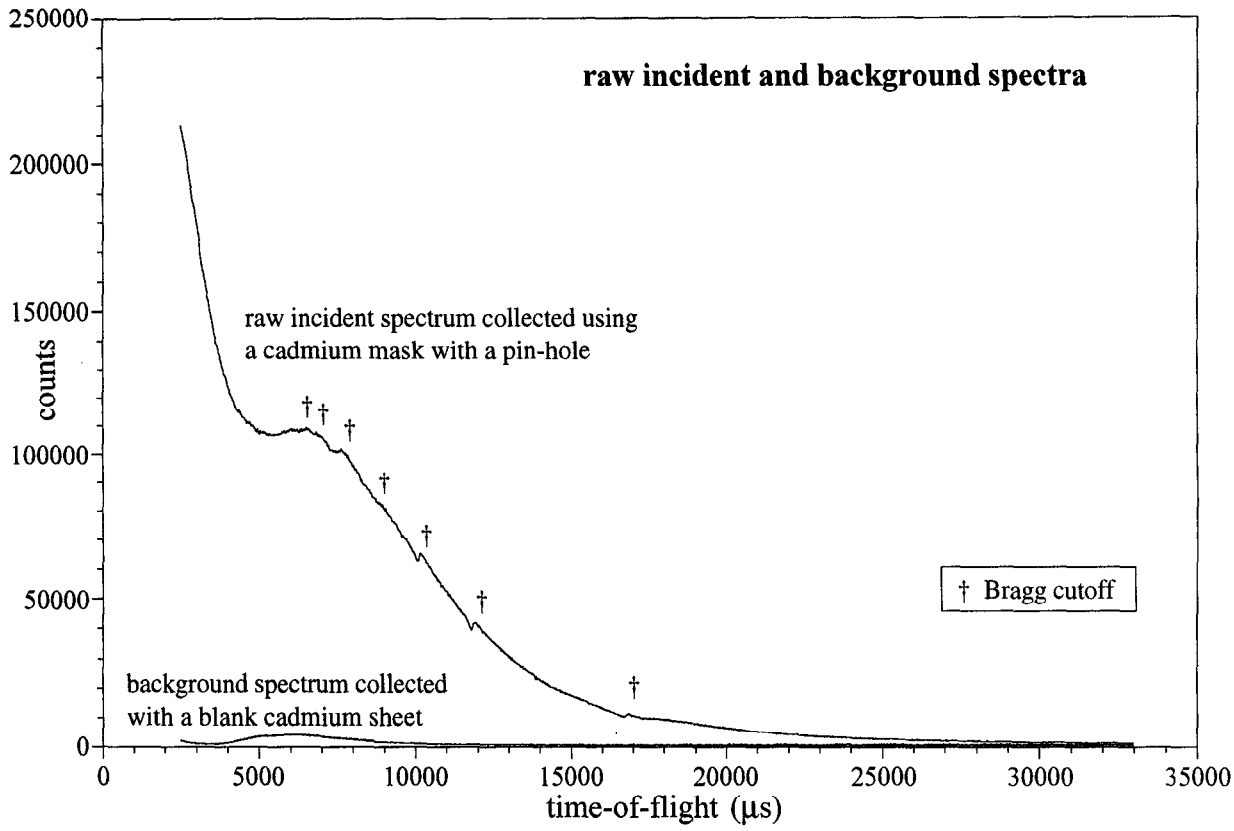

Fig. 2. Raw incident and background spectra collected on the SEPD.

Raw incident and background spectra, see Fig. 2, are collected in the transmitted neutron beam, downstream of the sample position, using a 10 atm He^3 proportional detector. A detector identical to those in the scattered detector banks is used so that minimal detector efficiency corrections (to be discussed later) are needed. The detector is shielded with B_4C except for a small hole for the transmitted beam. In order to prevent dead-time errors from saturation of the detector and/or associated electronics, a cadmium mask with a pin-hole (diameter ≈ 2 mm) is placed in front of the detector. To measure an incident spectrum applicable to normal data, no sample is placed in the sample position. The transmitted incident spectrum is first measured with the pin-hole in place. A background spectrum is also collected with a solid cadmium sheet of the same thickness in place of the pin-hole mask. The background spectrum is subtracted from the raw incident spectrum using the integrated counts in a low-efficiency upstream beam monitor to provide normalization. This yields an incident spectrum corrected for electronic, room background, and delayed neutrons with energies above the cadmium cutoff energy.

One clear advantage of measuring the incident spectrum using a transmitted beam detector, rather than the common approach of measuring the elastic incoherent scattering from vanadium in the sample position, is that the transmitted beam method will yield meaningful results for the normalization of data taken in special sample environments. In this case, the transmitted beam measurement is performed with the sample environment apparatus, *e.g.* pressure cell, furnace, *etc.*, in position. This yields an incident spectrum that includes the

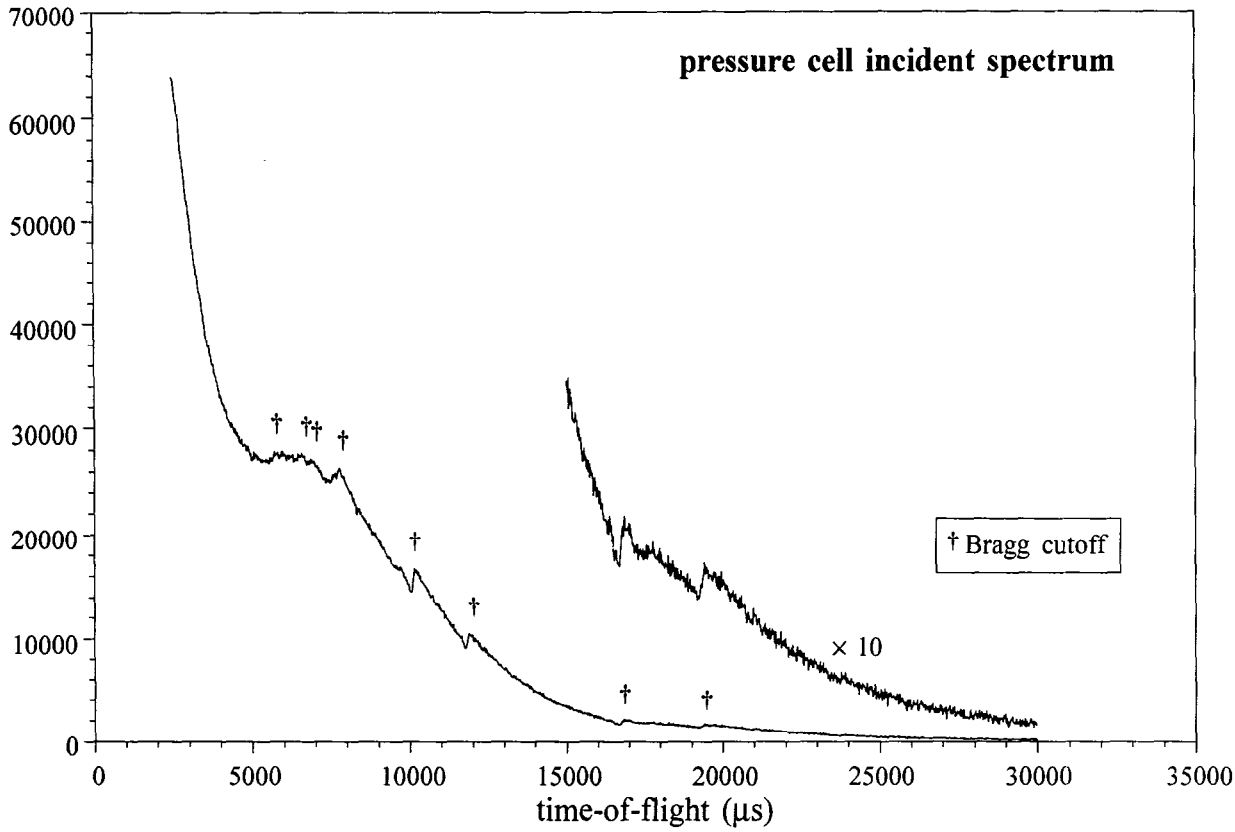

Fig. 3. Incident spectrum collected on the SEPD with a pressure cell in position.

attenuation of the neutron flux due to the presence of the apparatus in the incident and scattered beam. The attenuations are accurately measured if the transmitted and scattered paths through the apparatus are identical in composition and thickness. This is often the case, or very nearly so. Moreover, this can be used as a criteria in the design of special environment apparatus for use on a pulsed-source diffractometer. In Fig. 3 an incident spectrum that was measured with a high pressure cell in the sample position is shown. Large Bragg cutoffs due to the aluminum alloy pressure cell (adding to those from aluminum alloy windows along the flight path) appear as sharp features in the raw incident spectrum.

For special sample environments, the method of measuring the incident spectrum using a vanadium sample is not tractable because of multiple scattering. When the vanadium sample is placed inside the special environment apparatus, part of the detected neutrons result from multiple scattering involving the vanadium sample and the cell. This multiple scattering, which contaminates the measurement of the incident spectrum, cannot be directly measured because it disappears when the sample is removed; and methods for estimating its intensity and wavelength dependence are not sufficiently accurate to achieve the desired precision.

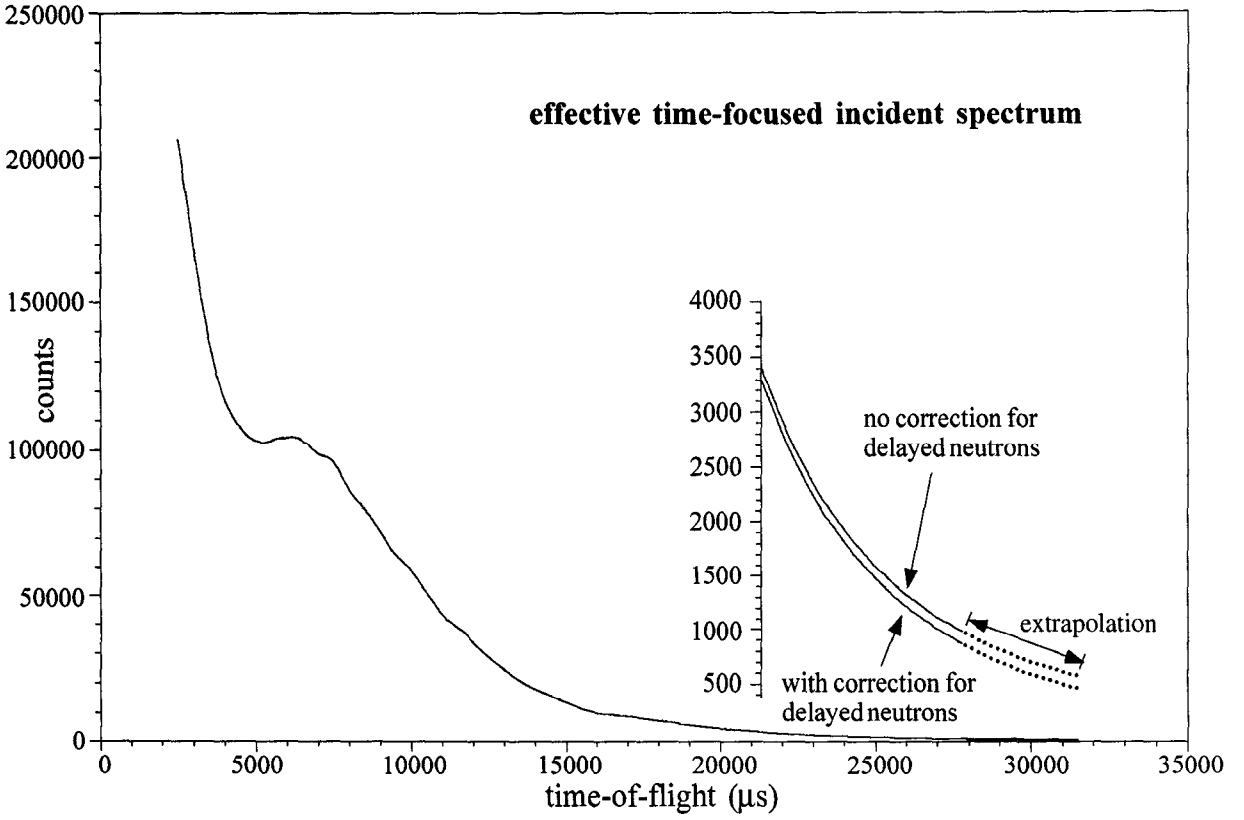

Fig. 4. An effective incident spectrum, that has been corrected for delayed neutrons and extrapolated to 31500 μs.

A second method we have used for estimating the slow delayed neutrons is based on trial-and-error methods to obtain the lowest R value in a Rietveld refinement. An estimate of the slow delayed neutrons is subtracted from the incident spectrum and a Rietveld refinement is performed using data from a standard material (such as Al_2O_3). This is repeated for different estimates of the slow delayed neutron contribution and the resulting R values from the refinements are plotted as a function of the assumed values for the slow delayed neutron flux expressed as a fraction of the total incident flux integrated over the usable time frame (typically 2500 to 30000 μs on the SEPD). A clear minimum in the R value indicates the correct slow delayed neutron fraction.

These two methods for determining the slow delayed neutron flux have yielded the same result. When expressed as a fraction of the total incident neutron flux over the time range 2500-30000 μs on the SEPD, the slow delayed neutron fraction is 0.0030. This value is consistent with what one would expect for the IPNS target, for which the total (slow + fast) delayed neutron fraction is estimated to be 0.0042.

Because of the physical arrangement of detectors on the SEPD, with the transmitted beam detector at a longer path length than the scattered detectors, the incident spectrum data do not extend to long enough times to correspond to the longest times measured in the scattered detector banks. The time window for the "focused" incident spectrum is further shorted because the

3. Simulating Time-Focusing

In order to generate an effective incident spectrum that can be applied to a time-focused diffraction data set collected from an extended detector array, a smoothing operation that corresponds to the time-focusing is applied to the measured incident spectrum. The parameters for the smoothing are determined by the geometrical layout of the diffractometer (defined by the incident and scattered neutron flight paths, and the positions of the various detectors plus sample). The ith channel of the effective incident spectrum, I_i^{eff} , constructed to be used with data from a particular detector array, for the case $i = 0$ at zero time-of-flight, is given by

$$I_i^{eff} = \frac{1}{j_{max} - j_{min}} \sum_{j_{min}}^{j_{max}} I_j^{inc} \tag{1}$$

where I_j^{inc} is the jth channel of the incident spectrum. The limits of the sum are given by

$$j_{min} = i \, \frac{\Delta t_{eff}}{\Delta t_{inc}} \cdot \frac{\ell_s}{\ell_t} \cdot \frac{\sin\theta_{min}}{\sin\theta_{ref}} \tag{2}$$

and

$$j_{max} = i \, \frac{\Delta t_{eff}}{\Delta t_{inc}} \cdot \frac{\ell_s}{\ell_t} \cdot \frac{\sin\theta_{max}}{\sin\theta_{ref}} \tag{3}$$

where Δt_{inc} is the channel width (in time) for the data collected at the transmitted beam detector, ℓ_t is the path length from the moderator to the transmitted beam detector, Δt_{eff} is the channel width for the effective incident spectrum (which is chosen to be equal to the channel width for the scattered data to be analyzed), ℓ_s is the path length from the moderator to the reference detector position, $\sin\theta_{ref}$ is the scattering angle for the reference detector, $\sin\theta_{min}$ is the minimum angle for the extended detector array, and $\sin\theta_{max}$ is the maximum angle for the extended detector array. The code that performs this smoothing also includes a small correction for detector efficiency. Although identical detectors are used in the transmitted and scattered positions, the pin-hole restricts the transmitted beam to passing through a full diameter of the detector, while the scattered neutrons can pass through any chord of the detectors. The correction for this small difference in efficiency is readily calculated.

Upon completion of these steps a "pseudo-time-focused" incident spectrum that corresponds to the time-focusing used in a particular detector array has been constructed. This spectrum has the general shape of the original incident spectrum but the sharp Bragg cutoffs have been smoothed into broad shallow steps and the statistical scatter has been greatly reduced. However, before this incident spectrum can be used to normalize scattered intensities it must be corrected for delayed neutrons.

4. Delayed Neutron Correction

When a uranium target is used at a pulsed neutron source (as is the case at IPNS), fission reactions produce a background of delayed neutrons that are moderated and emitted over a time scale that is very long compared to the pulsed time frame (1/30 s at IPNS). These delayed neutrons possess an energy spectrum almost identical to that of the prompt neutrons. However, their flux distribution is essentially time-independent over the time of a data frame. This results in a constant background of neutrons in both the measured sample diffraction data and incident spectrum. In the case of diffraction data that are analyzed by the Rietveld technique, this additional background in the scattered data is readily fit (along with the other contributions to the background which vary slowly in time) if there is a time-of-flight (*d*-spacing) independent term in the background function. However, the delayed neutrons can lead to significant errors in the incident spectrum. An incident spectrum containing only the prompt neutrons is needed to normalize Bragg intensities. Thus, the delayed neutrons must be accurately subtracted from the measured incident spectrum before it can be used for analysis.

The method we have described for measuring the incident spectrum results in a measurement that contains only slow delayed neutrons (i.e., those with energies below the cadmium cutoff energy). Fast delayed neutrons pass through both the cadmium with the pin-hole and the solid sheet of cadmium, and are thus subtracted out with the other contributions to background. The fast delayed neutrons appear as a constant neutron flux in the background spectrum (counted through the cadmium sheet) for long times-of-flight where the cadmium absorbs prompt neutrons (see Fig. 2).

We have used two methods for determining the contribution of slow delayed neutrons. The first assumes that the moderation is essentially complete at long wavelengths. Thus, we fit the "tail" of the spectrum (*e.g.* above 25000 μs) with the asymptotic form of a Maxwellian plus a constant term for the delayed neutrons:

$$I_t = n_{sd} + A/t^5 \qquad (4)$$

where n_{sd} is the background count of slow delayed neutrons and A/t^5 describes the time-dependent neutron flux as a function of time-of-flight, t. The slow delayed neutrons are then subtracted to obtained an incident spectrum suitable for use in Rietveld refinement. If this correction for slow delayed neutrons were not applied, the final spectrum would possess an error of approximately 1% at 15000 μs rising to greater than 15% at 30000 μs.

When the transmitted beam incident spectrum has been collected with a special environment apparatus, *e.g.* a pressure or furnace, in place, attenuation of the neutron beam occurs and must be included in the fitting procedure, yielding the equation:

$$I_t = n_{sd} + Ae^{-Bt}/t^5 \qquad (5)$$

here the e^{-Bt} term accounts for absorption.

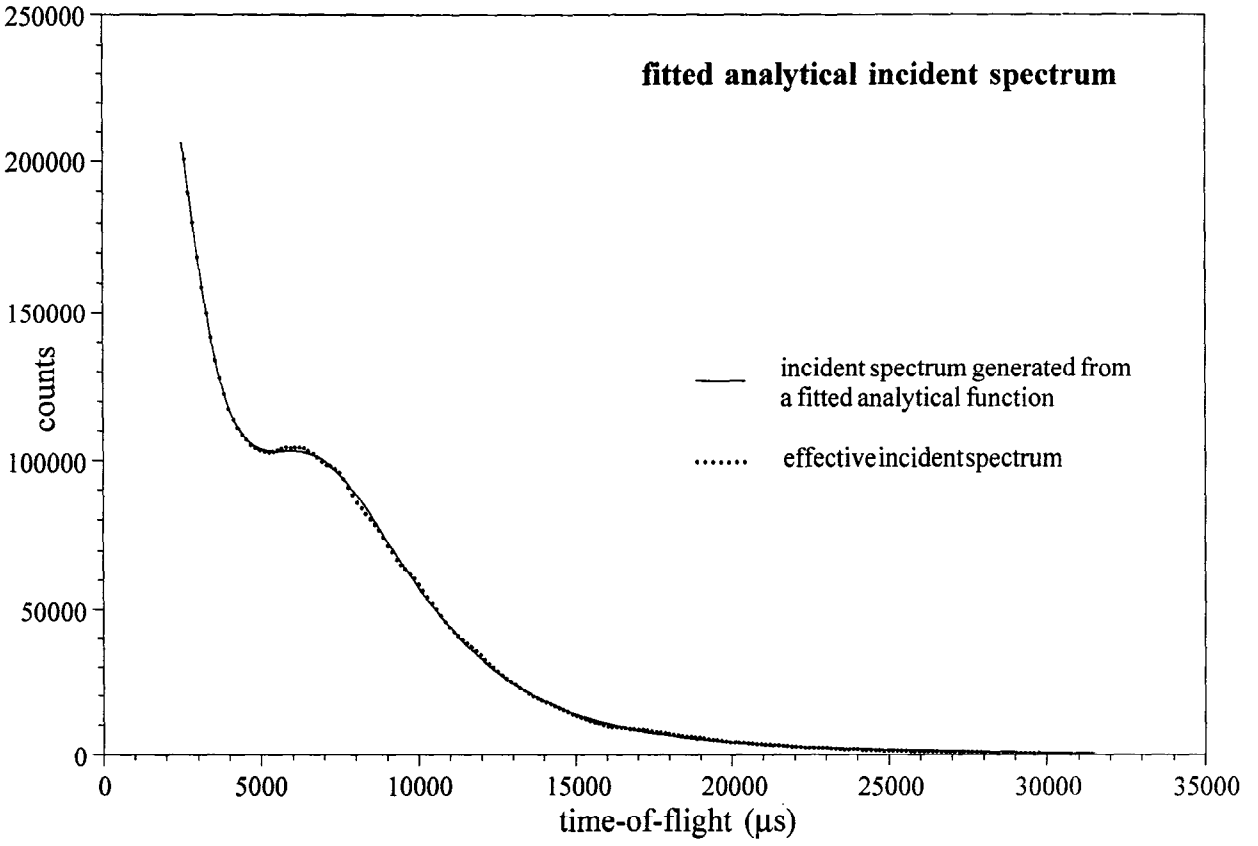

Fig. 5. An analytical incident spectrum that has not accounted for Bragg cutoffs and slow delayed neutrons plotted against the previously constructed effective incident spectrum.

conditions for the upper limit (j_{max}) of the summing operation, eq. 3, can not be met at long times. Fortunately, the shape of the incident spectrum at long times is well defined by eq. 4 or 5 and this can be used to extrapolate the effective incident spectrum to times that correspond to the data frame, as shown in Fig. 4.

5. Results

In order to illustrate the magnitude of error that arises from not accounting for Bragg cutoffs and delayed neutrons in the incident spectrum, it is interesting to compare the effective incident spectrum with an incident spectrum defined by a smooth analytical function as is often used in Rietveld refinement codes [3,4]:

$$I_t = P_1 + P_2 e^{-(P_3/t^2)}/t^5 + P_4 e^{-(P_5 t^2)} + P_6 e^{-(P_7 t^3)} + P_8 e^{-(P_9 t^4)} \qquad (6)$$

In Fig. 5, an analytical incident spectrum derived from fitting the time-focused incident spectrum before correction for delayed neutrons is plotted against the effective incident spectrum. Clearly, the analytical incident spectrum has the general shape of the effective spectrum, and it may

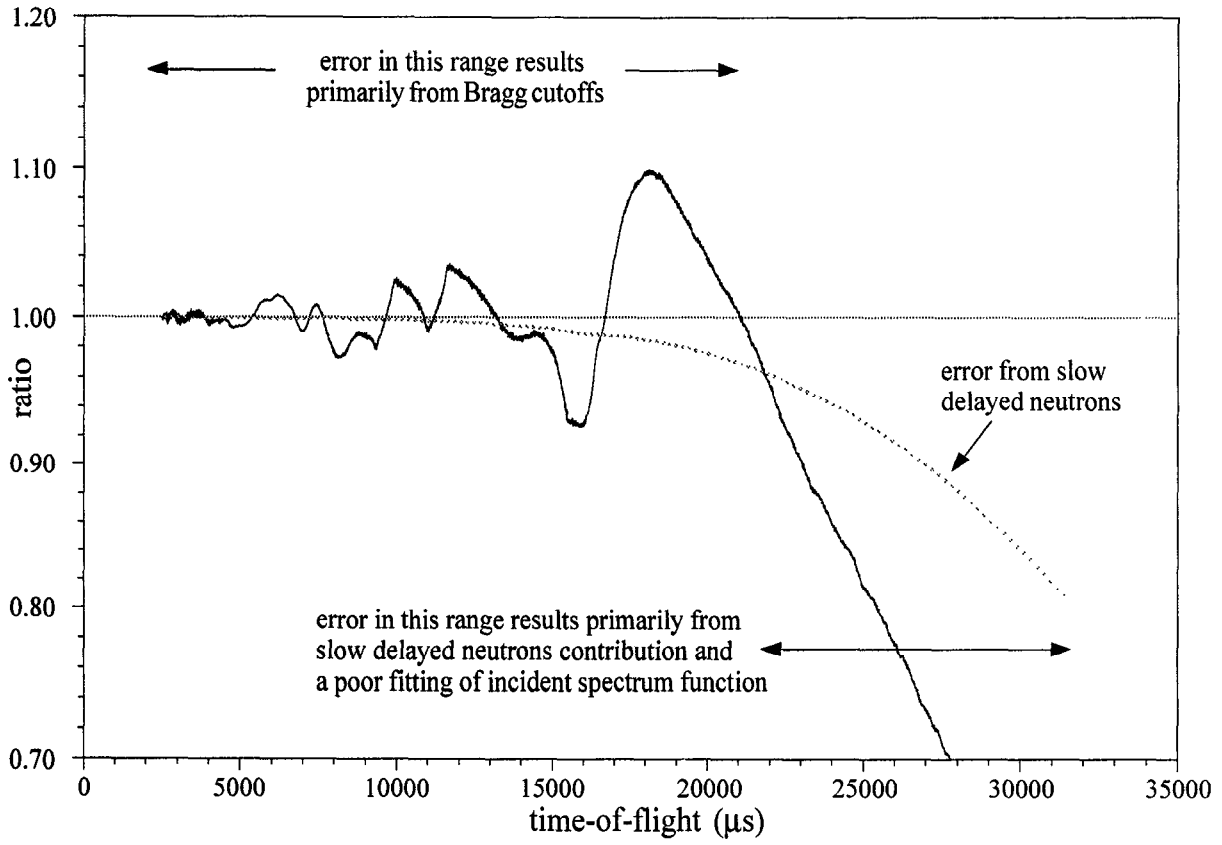

Fig. 6. The ratio of the effective incident spectrum to the analytical incident spectrum function, which illustrates the significant differences between them.

therefore appear that the differences between the two spectra are of minor significance. However, when one considers the ratio of these two spectra, as plotted in Fig. 6, the error that would be introduced in the estimates of relative peak intensities in a Rietveld refinement is evident. This error, deviance from unity in Fig. 6, results from excluding the effects of Bragg cutoffs and slow delayed neutrons, and is then compounded by a poor fitting of the analytical function to the tail of the incident spectrum. Clearly, the magnitude of error is very significant with regard to intended precise analysis of diffraction data.

6. Conclusion

To conclude, it is evident that in order to construct an effective incident spectrum, one must include the effects of Bragg cutoffs from window material, and the time independent background of delayed neutrons. The method outlined above achieves these aims by adopting a numerical, rather than analytical, approach for the construction of an effective incident spectrum. A particular advantage of this method, is its ability to easily accommodate different sample environments, *i.e.* the use of a pressure cell, a furnace *etc.*.

Acknowledgment

Work at Argonne National Laboratory is supported by the U.S. D.O.E., Basic Energy Sciences - Materials Sciences, under contract W-31-109-Eng-38.

References

1. J. D. Jorgensen and F. J. Rotella, High-Resolution Time-of-Flight Powder Diffractometer at the ZING-P' Pulsed Neutron Source, *J. Appl. Crystallogr.* 15, 27 (1982).
2. J. D. Jorgensen, J. Faber, Jr., J. M. Carpenter, R. K. Crawford, J. R. Haumann, R. L. Hitterman, R. Kleb, G. E. Ostrowski, F. J. Rotella, T. G. Worlton, Electronically Focused Time-of-Flight Powder Diffractometers at the Intense Pulsed Neutron Source, *J. Appl. Crystallogr.* 22, 321 (1989).
3. R. B. Von Dreele, J. D. Jorgensen, C. G. Windsor, Rietveld Refinement with Spallation Neutron Powder Diffraction Data, *J. Appl. Crystallogr.* 15, 581 (1982).
4. It should be noted that several alternative functions are available in recent Rietveld codes, such as GSAS, but none of them can fit the sharp features resulting from Bragg cutoffs.

ICANS-XIV
14th Meeting of the International Collaboration on
Advanced Neutron Sources
June 14-19, 1998
Starved Rock Lodge, Utica, Illinois

Behavior of ^{7}Be in the Moderator Cooling System at the Pulsed Neutron Source, KENS

S. Itoh, T. Miura, M. Furusaka, S. Yasui*, Y. Ogawa*, Y. Kiyanagi*, S. Sasaki and K. Iijima

High Energy Accelerator Research Organization, Tsukuba 305-0801, Japan
*Graduate School of Engineering, Hokkaido University, Sapporo 060-8628, Japan

ABSTRACT

We measured the radioactivity of ^{7}Be and ^{3}H in the cooling system of the ambient water moderator at KENS in order to obtain some knowledge about the behavior of ^{7}Be in the cooling water.

1. Introduction

At high-power pulsed-neutron facilities, some difficult operational problems arise in water cooling systems: ^{7}Be produced by the spallation reaction of oxygen nuclei in water with high-energy hadrons tends to coat the inside of the piping of the cooling systems. This leads to quite high radiation levels around the piping. The dose rate around the piping can be as high as 500 μSv/h at the ISIS Facility at Rutherford Appleton Laboratory, for instance [1]. At a higher-power neutron source, the dose rates will be much higher, and, therefore, the cooling system must be designed based on the radiation safety from ^{7}Be. It has been reported that the coating rate of ^{7}Be onto the container depends on the hydrogen exponent (pH) of water as well as the materials of the containers [2]. In the design of cooling systems in high-power facilities, it is important to have some knowledge about such behavior of ^{7}Be in cooling systems. The moderator cooling system at the pulsed spallation neutron source, KENS, at High Energy Accelerator Research Organization (KEK) is ideal for such investigations, because it is a simple cooling system where the flux of neutrons can be easily estimated. We have investigated the radioactivity of ^{7}Be and ^{3}H in the moderator cooling system to obtain some knowledge about the behavior of ^{7}Be.

2. Experimental

Figure 1 shows the target-moderator-reflector assembly at KENS. The proton beam with 500 MeV

Key words: ^{7}Be, activation of cooling water, ambient water moderator

hits the target with a cross section of 7.7×5.6 cm^2 and a length of 12 cm. The target consists of four tantalum blocks, and there are cooling water channels between the blocks perpendicular to the proton beam. The moderator of ambient water (H_2O) with 10×10×5 cm^3 is located under the target, and a neutron beam is provided from the moderator surface with the cross section of 10×10 cm^2 to the spectrometers. The water is supplied from its cooling circuit to the moderator (Fig.1). The cooling circuit consists of a pump, a surge tank, an ion-exchanger, a filter and a radiator. The pumping rate of the pump is 50 cm^3/s, and the water is supplied with a flow rate of 5 cm^3/s and 45 cm^3/s to the moderator and the radiator, respectively. The cooling water from the moderator and that from the radiator merge at the surge tank. The total volume of the water in the circuit is 2.5×10^4 cm^3. During the KENS machine cycle, Cycle 97-8 (9:00 13 Feb. 1998 - 9:00 23 Feb. 1998), the target was hit by 2.4×10^{19} protons. After the cycle, sampling of water in the moderator cooling system was performed from the sampling port located at the bottom of the surge tank, at t=0, 10, 20, 30 minutes, 1,2,3,6,9 hours, 1,2,3 and 7 days, where t is the time from the end of the cycle (9:00 23 Feb. 1998). The radioactivity and pH of each sample water were measured. The background radioactivity was also measured before the Cycle 97-8.

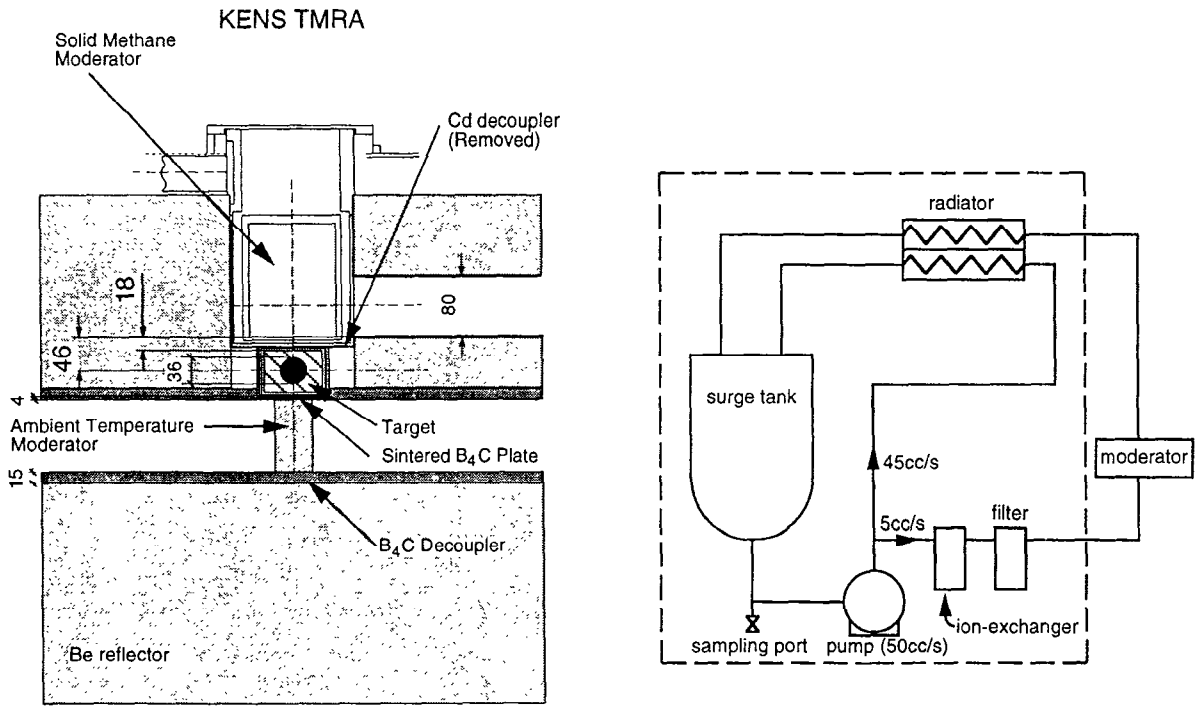

Fig.1 Target-moderator-reflector assembly at KENS (left) and schematic diagram of the cooling circuit of the water moderator (right).

3. Neutronics calculation and production rate

A neutronics calculation was performed by using LCS, in order to obtain the neutron flux in the moderator with the geometrical configuration shown in Fig.1. The flux is the averaged value over the moderator volume. Since the averaged proton current during the cycle was 4.5 μA, the neutron

flux with high energies greater than 20MeV was calculated to be $\phi_{HE}=2.0\times10^{10}$ cm^{-2}s^{-1}. From the energy spectrum of the neutron flux ($\phi(E)$) and the excitation functions ($\sigma(E)$) [3-5], the averaged production cross section for neutron energies greater than 20MeV was calculated as follows:

$$<\sigma>=\int_{20MeV}^{500MeV}\sigma(E)\phi(E)dE \Big/ \int_{20MeV}^{500MeV}\phi(E)dE \qquad (1)$$

and was obtained to be 12.2 mb and 7.6 mb for ^{3}H and ^{7}Be, respectively. The calculated flux of the thermal neutrons was well fitted to a Maxwellian centered at 27 meV, and the Maxwellian integral was obtained to be $\phi_{th}=6.7\times10^{10}$ cm^{-2}s^{-1} for 4.5 μA.

4. Detected activity in water samples

First, the detected activities of ^{3}H and ^{7}Be before and just after the cycle are summarized in Table I. The detected activities (A_{det}) in the moderator are the values at the end of the cycles, where the decay of the background activity is corrected. The activity (A_o) produced in the moderator during the cycle can be estimated from the neutron flux and the averaged production cross section described above. The detected activity of ^{3}H almost follows the estimation; however, that of ^{7}Be is only about 0.1% of the estimation. Next, the t-dependence of the detected activity ($A_D(t)$) of ^{7}Be and ^{3}H in the moderator are plotted in Fig.2. $A_D(t)$ is the detected activity at t, the sampling time from the beam stop, where the decay of the nucleus is corrected to the value at t=0, but the background activity measured before the cycle is not corrected. Although $A_D(t)$ of ^{3}H is independent of t, that of ^{7}Be decreases with increasing t as well fitted to the following formula:

$$A_D(t) = A_D(0)\ \{a\exp(-t/\tau_1)+(1-a)\exp(-t/\tau_2)\}. \qquad (2)$$

The following parameters were obtained by the fitting: $\tau_1=2.1\times10^4$s, $\tau_2=5.1\times10^5$s and a=0.53. $A_D(0)$ was detected to be 24.0 Bq/cm^3. Although the measured the pH were scattered (this may have depended on the condition of measuring pH: pH decreases when CO_2 in the air is dissolved in water), pH was roughly 7.5.

Table I. The detected activities of ^{3}H and ^{7}Be before and after the cycle. The detected activities (A_{det}) in the moderator are the values at the end of the cycles, where the decay of the background activity is corrected. The activity (A_o) produced in the moderator during the cycle can be estimated from the neutron flux and the averaged production cross section.

RI	activity (Bq/cm^3)		A_{det} (Bq/cm^3)	A_o (Bq/cm^3)	A_{det}/A_o
	before cycle	after cycle			
^{3}H	1580	1860	280	248	1.13
^{7}Be	11.8	24.0	13.7	1.23×10^4	0.0011

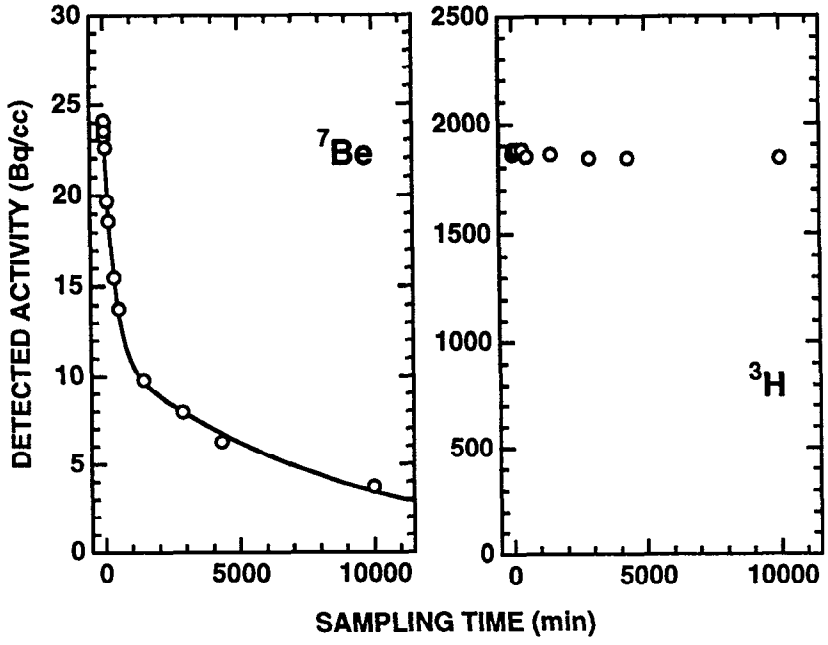

Fig.2 Sampling-time dependence of detected activity of ^{3}H and ^{7}Be. The solid line is a fitted curve (see text).

In the moderator, A_{det} of ^{3}H almost follows the estimation, and $A_D(t)$ of ^{3}H is independent of t. This indicates that the produced ^{3}H homogeneously exists in water of the circuit. On the other hand, A_{det} of ^{7}Be is about 0.1% of the estimation, and $A_D(t)$ depends on t. This suggests that the produced ^{7}Be is trapped inside of the circuit. It is noted that the measured pH was greater than 7, and therefore, the condition for coating of ^{7}Be onto the inside walls of the circuit was realized [2]. We try here to evaluate the detected activity of ^{7}Be by using the time constants obtained above. Since the obtained time constants are much less than the duration of the cycle (irradiation time), the background activity measured before the cycle need not be considered. At t=0, the ratio of the detected activity to A_0 is presented by

$$A_D(0)/A_0 = (1-c)A/A_0 + cA'/A_0, \tag{3}$$

where A is the activity estimated from the obtained time constants and A' is the activity due to a process other than that detected at present. A/A_0 is given by

$$A/A_0=\{\Sigma_i a_i(\lambda_0/\lambda_i)(1-\exp(-\lambda_i T))\}/(1-\exp(-\lambda_0 T)), \tag{4}$$

with the duration of the cycle (T), the decay constant of ^{7}Be ($\lambda_0=1.5\times10^{-7}s^{-1}$), $\lambda_i=\lambda_0+\tau_i^{-1}$ (i=1,2), $a_1=a$ and $a_2=1-a$. A/A_0 was calculated to be 0.26 and $A_D(0)/A_0$ 0.002. A' is negligibly small, because no other process described by eq. (2) was detected; eventually, c was obtained to be 0.99. The trapped activity is given by $(1-c)(1-A/A_0)$ and $c(1-A'/A_0)$ due to the presently-detected process and processes other than the present detection, and was estimated to be 0.006 and 0.992, respectively. This indicates that an overwhelming amount of ^{7}Be due to processes other than the

present detection is trapped in the cooling water circuit. Assuming that A' has a similar functional form to eq. (4) with the time constant τ', the upper limit of τ' can be estimated from $A_D(0)/A_0 > cA'/A_0$, and is obtained to be $\tau' < 1.6\times10^3$s ($\tau' < 10$s, if $A_D(0)$ in the inequality is replaced by its experimental error). This result suggests that almost all of the produced ^{7}Be is trapped with a very short time constant.

5. Distribution of ^{7}Be in the cooling circuit

In order to detect the activity due to processes other than the present detection, which should be almost A_0, the activity of a part of the piping was directly measured. A_0 was calculated to be 12 kBq/cm^3, *i.e.*, the total activity in all the circuit was 300 MBq. The sample of the piping was 6 cm of length and 0.8 cm of inside diameter, and the activity due to ^{7}Be inside the sample piping was measured to be 1.5 kBq 133 days after stopping the beam. The activity was estimated to be 8.5 kBq at the beam stop by correcting the decay of ^{7}Be. This activity is an integrated one for operation over about ten years. It is estimated that 60% of the detected activity is the production during the cycle of 10 days. Therefore, the activity of 5.1 kBq is the contribution to the cycle. In the following we discuss the contribution to the cycle. Since the surface area of the inside of all parts in the cooling circuit (except for the elements of the ion-exchanger and the filter) is 4.3×10^4 cm^2, the total activity and the averaged activity over the cooling circuit can be estimated to be 15 MBq and 0.6 kBq/cm^3, respectively, if ^{7}Be uniformly coats the inside of the cooling circuit. In order to know the distribution of ^{7}Be in the cooling circuit, the intensity of γ-ray was measured from outside parts of the circuit, except for the moderator, as listed in Table II. The measurement was performed by using a NaI detector, and the intensity is of the integrated energy spectrum including the peak of 477 keV of γ-ray from ^{7}Be. From the result, assuming the concentration of ^{7}Be in the ion-exchanger to be 10 times as large as that in the other parts, the total activity and the averaged activity over the cooling circuit can be estimated to be 41 MBq and 1.6 kBq/cm^3, respectively; this

Table II. The intensity of γ-ray at the outside parts of the cooling circuit measured by a NaI detector. The intensity (γ-ray counts) is of the integrated energy spectrum including the peak of 477 keV of γ-ray from ^{7}Be.

part of cooling circuit		γ-ray counts (10^4min^{-1})
ion-exchanger	upper part	213
	middle part	119
	lower part	62
filter	upper part	44
	lower part	44
surge tank	upper part	24
	middle part	37
	lower part	30
radiator		13
piping near surge tank		16
piping	circuit shielding outside	2
outside wall	circuit shielding outside	1

is still less than A_0. Since the activity from the ion-exchanger is very huge, the background for the other parts increases. If the concentration in the ion-exchanger is 100 times as large as that in the other parts, the total activity and the averaged activity can be estimated to be 300 MBq and 12 kBq/cm^3, respectively; this reproduces A_0. Although a quantitative discussion cannot be made further based on this γ-ray measurement on the outside parts of the circuit, this indicates the detection of a part of the activity due to the process other than the present detection in the sampling of water. Considering the short time constant of processes other than the present detection, it is also possible that a large amount of the produced ^{7}Be is trapped in the moderator, or near there. To elucidate the distribution of ^{7}Be in the circuit, a direct measurement of the activity from ^{7}Be in the inside moderator is also required, for instance. It is noted that ^{7}Be has a very large absorption cross section (σ_a=3.9×10^4 b) for thermal neutrons [6]; however, $\phi_{th}\sigma_a$ (=2.5×10^{-9}s^{-1}) is expected to be smaller than λ_0, τ_i^{-1} and τ'^{-1}. Therefore, the disappearance due to absorption is not significant compared with the trapping process.

6. Summary

In summary, we performed measurements of the activity of ^{7}Be and ^{3}H in the moderator cooling system at KENS in order to obtain some knowledge about the behavior of ^{7}Be in the cooling water. The detected activity of ^{3}H almost follows the estimated production, and the activity of ^{3}H in the sampling is independent of the sampling time. This indicates that the produced ^{3}H homogeneously exists in the water of the circuit. On the other hand, the detected activity of ^{7}Be is about 0.1% of the estimated production, and the activity in the sampling depends on the sampling time. This suggests that the produced ^{7}Be is trapped inside of the circuit. The sampling-time dependence of the activity shows two time constants with 5.1×10^{5}s and 2.1×10^{4}s shorter than the decay of ^{7}Be, and also suggests that almost all of the produced ^{7}Be is trapped due to processes other than the present detection with a time constant shorter than ~10^{3}s. To elucidate the distribution of ^{7}Be in the cooling circuit, further investigations are required.

Acknowledgement

We would like to thank Prof. Y. Nagai and Dr. M. Numajiri for discussing the cross sections, and S. Ishihama and T. Kunifuda for technical assistance for measuring radioactivity of the samples.

References

[1] T. Broome, Proc. ICANS-XII (Rutherford Appleton Laboratory, RAL94-025, 1994) T-20.
[2] K. Katoh et al., KEK Internal 81-12 (1982), in Japanese. The coating rate of ^{7}Be onto the container increases with increasing pH at a basic side, and the coating rate onto glass is larger than that onto acrylic acid resin.
[3] A. Yu. Konobeyev and Yu. A. Korovin, Nucl. Instr. Meth. Phys. Res. B 82 (1993) 103, and references therein.
[4] S. Shibata et al., Radiochimica Acta 75 (1996) 1.
[5] S. M. Read and V. E. Viola, Jr., Atomic Data and Nuclear Data Tables 31 (1984) 359, and references therein.
[6] P. E. Koehler et al., Phys. Rev. C 37 (1988) 917.

ICANS XIV
14th Meeting of the International Collaboration on Advanced Neutron Sources
June 14–19, 1998
Starved Rock Lodge, Utica, Illinois, USA

The High-Resolution Medium-Energy Chopper Spectrometer (HRMECS): Instrumentation Upgrade and Future Scientific Opportunities

C.-K. Loong, J. P. Hammonds, D. Yocum, J. C. Nipko, K. Takeuchi, D. Chen, L. I. Donley, G. E. Ostrowski, R. K. Crawford, H. Belch and R. Kleb

Intense Pulsed Neutron Source Division, Argonne National Laboratory
Argonne IL 60429-4814 USA

HRMECS is a first-generation pulsed-source chopper spectrometer designed and built at IPNS during the 1980's. It features a 4-m sample-to-detector flight path with detectors covering scattering angles from -20° to 140°, quite similar to the design of MARI which is a third-generation chopper spectrometer at ISIS. However, apart from having a much lower flux level than MARI has at ISIS, HRMECS has three major drawbacks: i) it has detectors covering only ~40% of the slots; ii) at low scattering angles there is no position-sensitive detectors to provide good Q-resolution; and iii) the Fermi choppers which employ mechanical bearings cannot be rotated at angular speeds exceeding 270 Hz thereby providing limited energy-resolution ($\Delta E/E_0$ ~2-4%).

Over the years, incremental improvements have been made to enhance the capabilities of HRMECS. Recently, HRMECS undergoes an extensive upgrade that addresses the above problems. Since the process is currently underway, we refer the reader to the HRMECS Web Site at http://www.pns.anl.gov/HRMECS/HRMECS_frameset.html where detailed, updated information can be found.

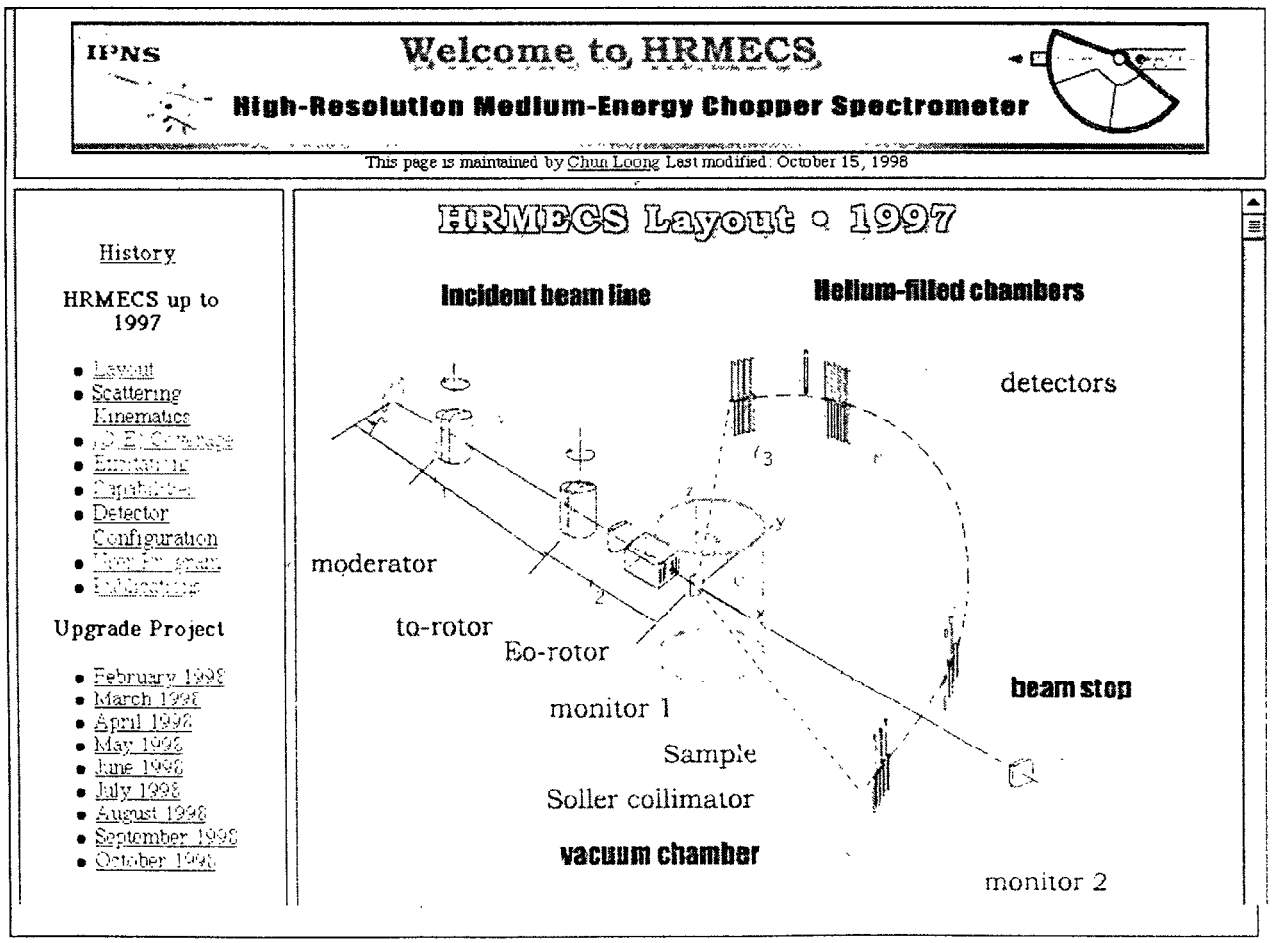

ICANS-XIV
14th Meeting of the International Collaboration
on Advanced Neutron Sources
June 14-19, 1998
Starved Rock Lodge, Utica, Illinois, USA

Material Development for Spallation Target at JAERI

K. Kikuchi, H. Kogawa, M. Futakawa, I. Ioka and R. Hino

Japan Atomic Energy Research Institute
Tokai-mura, Naka-gun, Ibaraki-ken, 319-1195, Japan

1. Introduction

The development of spallation target system for the Neutron Science Project is proceeding at Japan Atomic Energy Research Institute (JAERI). The materials subjected to pulsed pressure waves, intensive radiation damage, corrosion/erosion and mechanical strength are to be evaluated in order to assess the applicability of the target assembly[1].

- Thermal shock tests have been performed to evaluate the integrity of the container. In the ASTE (AGS Spallation Target Experiment) collaboration programme pressure wave has been measured.

- Radiation damage and irradiation data at high dose have been accumulated at HFIR through JAERI/ORNL collaboration for fusion project[2]. Furthermore a high dose, high He/dpa and high H/dpa will be necessary in order to know the effect of irradiation on the mechanical properties of the container material under spallation condition. SINQ in PSI will provide the useful irradiation data for the candidate materials. JAERI will participate post-irradiation tests.

Other irradiation tests have been done by using triple beams at TIARA (Takasaki Ion Accelerator for Advanced Radiation Application)[3] in JAERI.

- The factors of the corrosion/erosion for materials in the mercury environment have not been clear and only allows engineering works tentatively as a case study. Mechanical tests; tensile, fatigue and fracture toughness tests, are to be conducted under the mercury environment.

2. Stress wave in the solid disk

The thermal shock test has been done in order to know the stress waves in the solid. Fig.1 illustrates the test apparatus. The test equipment consists of the laser source, specimen disk, a dynamic strain amplifier and a wave memory. The laser source is ruby at a wave length of 694.3nm. The maximum energy emitted from this source is 1.0 J per pulse and the pulse duration is about 50ns. The beam profile is roughly rectangular distribution with a circle projectile at the beam diameter of 10mm. The one surface of disk specimen will be heated up and the dynamic response of the specimen will be measured by means of strain gage and/or the laser Doppler probe at the back surface of the disk.

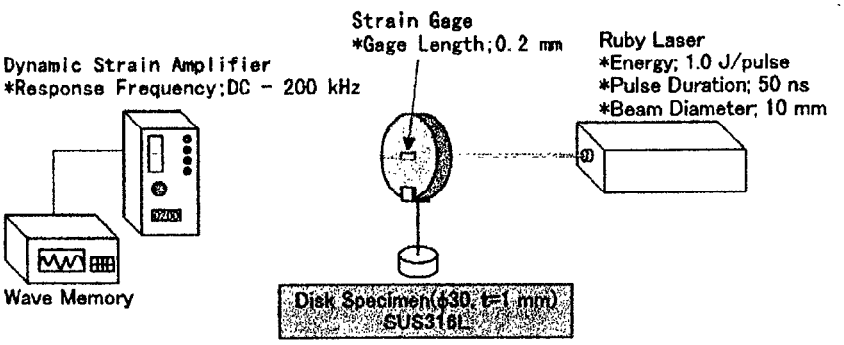

Fig. 1 Schematic drawing of test apparatus.

Fig. 2 shows the results of stress wave measurement for the type 316L stainless steel. After 2 μs from the laser exposure the maximum strain was induced to the centre of the disk. The calculation was done by using the structural analyses code ABAQUS under the input condition: the absorption ratio of the ruby laser to the material is 40 %, the heat deposition depth is 50 μm. The calculation results possibly follow the experimental results. Fig.3 shows the calculation of the thermal conduction to the depth direction in unsteady state. The maximum temperature is estimated to be 50.5°C at a time of 50 ns and then the temperature change is quite small until 20 μs in the figure.

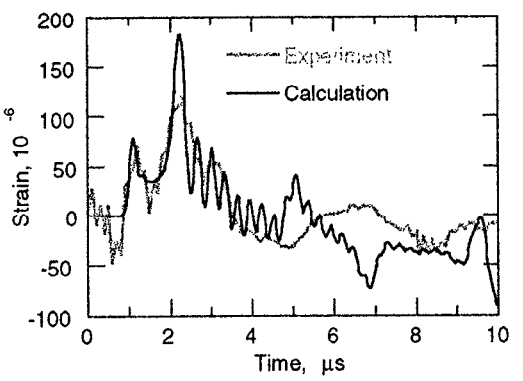

Fig.2 Thermal shock wave induced by the laser beam.

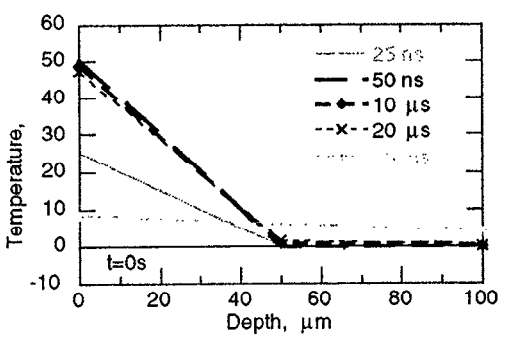

Fig.3 Thermal conduction to the depth direction of the disk.

3. Radiation damage

The radiation damage of the materials will be evaluated as shown in Fig.4. The irradiation data of fission

reactors were accumulated in order to get irradiation data. The data were also obtained from JAERI and ORNL collaboration for International Thermonuclear Experimental Reactor(ITER). The irradiation parameters under spallation for 316 austenitic stainless steel. is characterized by He production, H production and irradiation temperatures. These values are higher than irradiation parameter of fission condition except irradiation temperature. High dose and He/dpa and H/dpa irradiation data must be obtained for the spallation environment. HFIR (High Flux Isotope Reactor) irradiation are planed for high dose data. HFIR is a mixed spectrum fission reactor at ORNL.

TIARA test facilities as shown in Fig.5 is used to obtain high He/dpa and H/dpa data. TIARA, Takasaki Ion Accelerator for Advanced Radiation Application, has a triple ion beam facility. Moreover, JAERI participates an International collaboration, SINQ. Swiss neutron spallation source, irradiation program, to obtain spallation irradiation data of the structural materials. SINQ collaboration program is proceeding for accumulating the irradiation data. Irradiation of Phase 1 by SINQ will be started July 1998. JAERI will intend to participate post-irradiation tests. Table 1 shows an irradiation matrix of Phase 1. Main materials are 316 austenitic stainless steel, ferritic/martensitic stainless steel and Al alloys. Specimen for these test are irradiated at SINQ and then post-irradiation tests will be conducted at PSI.

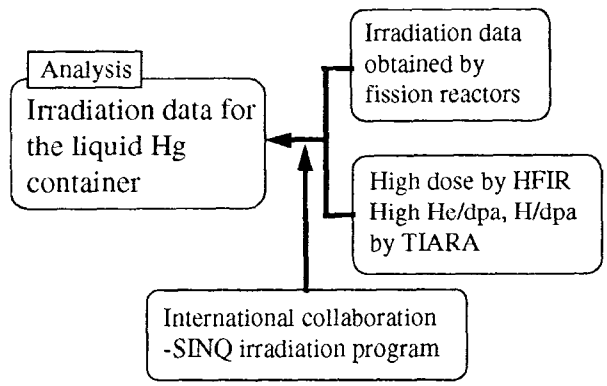

Fig.4 Materials evaluation for radiation damage.

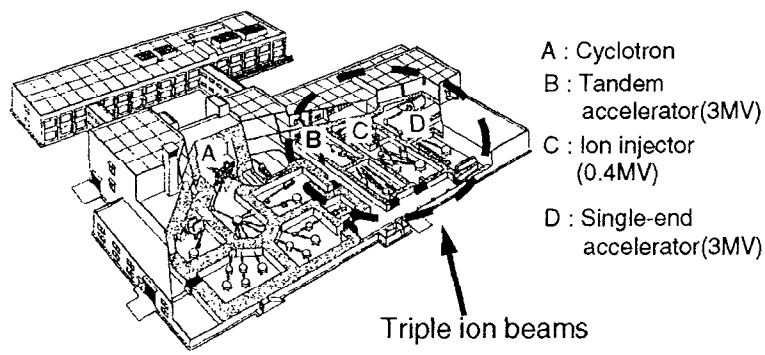

Fig.5 Takasaki Ion Accelerator for Advanced Radiation Application(TIARA)

Table 1 Irradiation matrix of Phase 1 by SINQ international collaboration.

Test Type	316SA, CW, WJ	Ferritic/Martensitic	Al	Ti-Zr, W, Mo
Tensile	X	X	X	X
Bend fatigue	X	X	X	
Tesrtest	X	X		
Bend	X	X		
Charpy		X		
Small punch	X	X		X
TEM	X	X	X	X

The materials used in HFIR are type 316 austenitic stainless steels. A chemical composition of the materials is shown in Table 2. Fig.6 shows, for example, engineering stress-elongation curves of irradiated J316 stainless steel[2]. He/dpa level is almost 10 (nearly fusion environment). Irradiation and test temperature range is 60 to 400°C. Dose levels are 7 and 18 dpa. The elongation of J316 decreased with dose, the strength increased with dose. Irradiation caused reduction of ductility at all temperatures.

Table 2 Chemical composition of Type 316 austenitic stainless steels

Alloy	Fe	C	Si	Mn	P	S	Ni	Cr	Mo	Ti	B	N
JPCA	bal.	0.06	0.50	1.77	0.027	0.005	15.6	14.22	2.28	0.24	0.003	0.0039
J316	bal.	0.058	0.61	1.80	0.028	0.003	13.5	16.75	2.46	0.005	-	-
316F	bal.	0.038	0.04	0.23	0.003	0.002	14.0	16.80	2.30	-	-	0.0011
ERH	bal.	0.061	0.67	1.7	-	-	12.4	17.3	2.1	0.21	-	0.003
EC316L	bal.	0.024	0.46	1.8	-	-	12.3	17.4	2.3	-	-	0.06

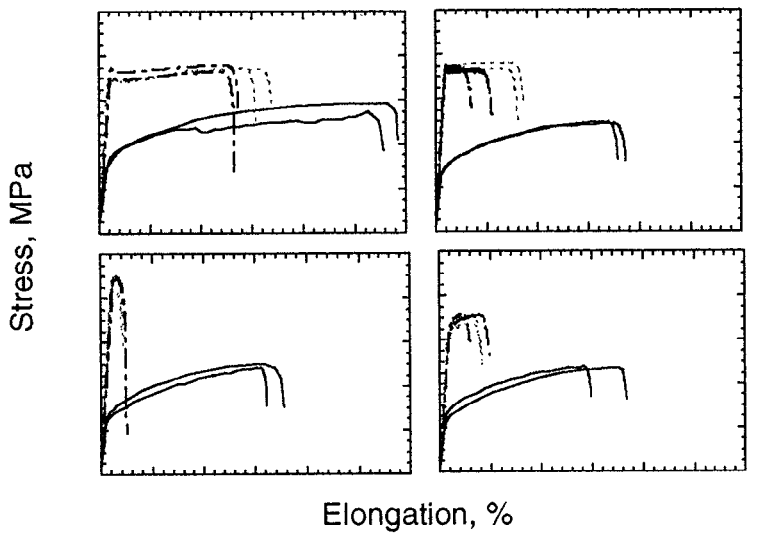

Fig.6 Engineering stress-elongation curves of J316 stainless steel at 7 and 18 dpa.

Fig.7 shows a preliminary result[3] from the TIARA facility. This figure shows load/depth-depth curves of the ion irradiated material obtained from the microhardness tests. This includes the results of the unirradiated, the ion irradiated and the ion irradiated after annealing. The materials tested were a Japan Primary Candidate Alloy (JPCA) in the solution-annealed(SA). The JPCA was modified from type 316 stainless steel to improve the swelling properties under the neutron irradiation. The specimens were in the form of TEM disks. in 3mm diameter by 0.2mm thickness. The TEM disks were irradiated in the JAERI triple ion facility(TIARA) using 12 MeV Ni ions with an irradiation rate of 1×10^{-3} dpa/s at a temperature of 200•. The TRIM85 code was used to compute the required ion fluences and the displacement dose as a function of depth beneath the specimen surface.

The results of the TRIM calculation for the specified irradiation conditions are shown in Fig. 8. The solid line goes with the left axis and shows the damage in dpa as a function of depth in the specimen. The peak dose is about 30 dpa around 2μm. The dashed line goes with the right axis and shows the injected Ni ions as a function of depth. The peak (0.7 at%) occurs about 2 μm. Both the displacement dose and Ni content in the ion irradiated TEM disk are varying as shown in Fig. 8. The effect of injected Ni ions on the microhardness of the TEM disk is neglected in this experiment because Ni is one of main elements of the JPCA. After the ion irradiation, some of the TEM disks were annealed at 500• for 8 hours in a vacuum. Microhardness tests were carried out on the surface of the TEM disk at room temperature. A microhardness testing machine, DUH-200 (Shimadzu Co.), was used for the hardness testing. A load was applied with a loading speed of 2.6×10^{-3} N/s, held 1 second and then removed. The load was continuously monitored along with the displacement with a resolution of 20 mN(2 mgf) and 0.01 μm, respectively.

The relationship between load and depth from the surface under loading in the microhardness test was given by $L/d=A+Bd$, where d is a depth(μm) from the surface, L is the load(N) at that depth, and A and B are constant. In particular, the value of B is in direct proportion to the microhardness of the material. The initial s age in each curve is neglected because this part of the curve includes a surface effect of the specimen. In Fig.7, the slope of the unirradiated line, which corresponds to B in the equation, is about 3. The slope of the ion irradiated curve is about three times as high as that of the unirradiated curve up to a depth of 0.4 μm and then decreases to 3. It means that the microhardness of the ion irradiated is as low as that of the unirradiated over 0.4 μm depth.

The ion injected layer (about 2 μm) affects the microhardness of the ion irradiated up to 0.4 μm depth. This tendency was observed in another study using the same technique. The slope of the ion irradiated specimen decreases to 4 up to 0.8 μm depth by annealing. It is considered that the change is attributed to thermal diffusion of defects induced by ion irradiation. It is well known that a hardness can be related to a yield strength. It seems that the change in yield strength of the irradiated material can be predicted by the change in microhardness of the ion irradiated TEM disk. Moreover, the effect of helium and hydrogen on mechanical properties of the irradiated materials can be estimated using the TIARA.

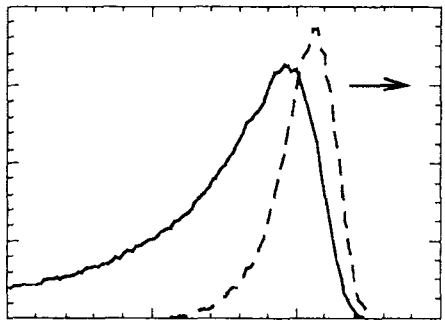

Fig.7 Load/depth-depth curves of the ion irradiated materials[3].

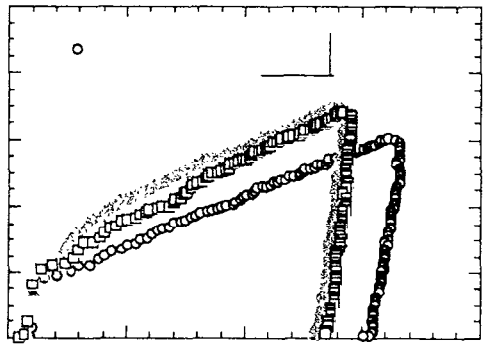

Fig.8 Displacement dose and Ni content in the ion irradiated TEM disk[3].

4. Corrosion/erosion test in mercury

Mechanical tests of the structural materials are scheduled to do in JAERI laboratories. These tests will show the effects of corrosion and/or erosion on the mechanical properties. In order to understand the combined effects of the corrosion/erosion with the irradiation effect the irradiation data under spallation environment should be obtain in the

mercury target system. A real target material which is used in the target will be the best material to evaluate those dual effects. In-beam tests of the materials will show useful data under the condition of proton exposure in the mercury environment. PSI will be one of the promising test facilities for the in-beam tests in the 72MeV proton line.

5. Summary

The thermal shock test was done to assess the damage of pulsed shock wave. The stress wave was measured by strain gauge and a computing work was done in order to simulate the stress history. Radiation damage test was done at TIARA. Through the micro-hardness test of the TEM disk specimen, the effect of ion irradiation on the hardness was was investigated.

References

[1] I Ioka, K.Kikuchi, M.Futakawa,H.Kogawa, R.Hino, "Target material and Damag" , presented at the 3rd Workshop of Neutron Science Research Program, JAERI,1998(to be published).
[2] J.E.Pawel et al.:"Effects of low temperature netron irradiation on deformation behavior of austenitic stainless steel", J. Nucl. Mater. 233-237, pp.202-206(1996).
[3] I. Ioka, A. Naito, K Shiba, J.P.Robertson, S.Jitsukawa, A.Hishinum,"Effects of Annealing on the Tensile Properties of Irradiated Austenitic Stainless Steel",(to be published).

ICANS-XIV
14th Meeting of the International Collaboration on
Advanced Neutron Sources
June 14-19, 1998
Starved Rock Lodge, Utica, Illinois, USA.

PRELIMINARY DESIGN STUDIES FOR AN IRIDIUM ROD TARGET AT THE BNL-AGS

H. Ludewig, J. Hastings, P. Montanez and M. Todosow
Brookhaven National Laboratory, Upton, New York. 11973.

Abstract

The BNL-AGS is an intense source of 24 GeV protons. It is proposed to explore the potential to use these protons as the driver for a Pulsed Spallation Neutron Source target. The proposed target design is based on an edge cooled iridium rod concept - similar to the anti-proton production target which operated reliably at CERN under similar conditions. Lead, lead fluoride, and beryllium are investigated as possible reflector materials, and ambient temperature light water and 80 K light water ice are proposed as initial moderator materials. Both moderators are decoupled by cadmium containing moderator chamber walls. The small size of the target has the advantage that the moderators can be placed close to the target (resulting in a bright source), and since a large fraction of the radioactive inventory is contained in the iridium rod, removal and disposition of this inventory should be relatively simple and inexpensive.

INTRODUCTION

This paper outlines a pre-conceptual design study carried out on a solid iridium, Pulsed Spallation Neutron Source (PSNS) target for the BNL-AGS. The BNL-AGS accelerates protons to energies ranging from 1.5 GeV - 24 GeV in pulses, at a frequency of 0.556 Hz. Each pulse has 1.0(14) protons and consists of six bunches of 40 ns duration separated by 400 ns. Thus, each pulse is approximately 2μs long. At 24 GeV each pulse has an energy of 384 kJ and thus the energy per bunch is 64 kJ. It is possible to deliver the bunches to a target at a frequency of 30 Hz. The proton energy to be assumed in this study is 24 GeV, and the spot size on the target will be 0.5 cm in diameter. The conceptual target design is based on an operating target at CERN [1] used for the production of anti-protons. Briefly, this target consists of a solid iridium rod, surrounded by a graphite sleeve, which in turn is clad by a thin layer of titanium. The titanium clad is surrounded by a coolant passage filled with flowing light water. The outer containment of the CERN target is a titanium structure, designed to maximize the production of anti-protons. In the design considered for the AGS, it is assumed that the inner layers of the target remain the same as the CERN target (iridium rod, graphite layer, titanium clad, and cooling water), beyond this point the target design reflects its primary purpose - being a neutron source. Thus, the cooling channel is contained in an aluminum tube, a thick reflector surrounds the aluminum tube. Finally, a light water moderator is embedded in the reflector and a neutron beam tube is included in the design analysis in order to evaluate the potential performance of the source. Thus the material choices are based on the following:

1. Iridium has a high density (22.46 gm/cc), atomic number, and thermal conductivity, and is mechanically strong.

2. Graphite and titanium were chosen, based on the positive CERN target experience.

3. Light water cooling is efficient for the current application, and also can act as a pre-moderator of the neutrons leaving the target.

4. Aluminum is selected as the outer containment since it will minimize parasitic neutron capture and activation during operation.

Lead is chosen as the primary reflector material and light water as the moderator respectively, primarily because they are being proposed at advanced pulsed neutron sources [2,3]. The possibility of using other reflecting materials (beryllium, fluoride compounds ,and layered structures) and cryogenic moderators (liquid hydrogen, light water ice, and liquid or solid methane) will be investigated in subsequent studies. The assembly as described above is shown in Figures 1 - 3. Figures 1 and 2 show the overall configuration and Figure 3 shows a detail of the iridium target and surrounding structures. Dimensions of the most important target assembly features are given in Table 1.

Table 1 - Dimensions of target features.

Iridium rod	1.0 (OD) x 15.0 (L)
Graphite sleeve	0.7 (Thick) x 15.0 (L)
Titanium clad	0.2 (Thick) x 15.0 (L)
Cooling water channel	0.5 (Thick) x 15.0 (L)
Aluminum containment	0.2 (Thick) x 15.0 (L)
Front drift tube (void)	1.0 (OD) x 45.0 (L)
Back drift tube (void)	1.0 (OD) x 40.0 (L)
Moderator volume	12. X 5.0 x 12.0
Neutron beam tube (void)	8.0 (OD)

The parameters of primary concern in this paper are the energy deposition in the target (iridium rod), reflector and moderator (TRAM). In addition, the activation of the TRAM assembly will be estimated following operation for a specified time period. The neutron flux in the moderator will be estimated as a result of the above calculations. The above calculations will be carried out using the Monte Carlo codes LAHET version 2.83[4] and MCNP4B[5]. The activation estimates will be made using a modified version of the ORIGEN code[6] and the spallation product cross section library created for the CINDER-90 code[7].

ENERGY DEPOSITION

The energy deposition in the various volumes of the TRAM assembly is required to complete its mechanical design. This determination takes account of the coulomb losses due to interaction of the primary protons and secondary charged particles, nuclear recoil and gamma rays due to π° decay and

de-excitation of residual nuclei. The gamma rays resulting from the last two mechanisms are transported from their point of creation in the MCNP calculation. In addition, energy deposition due to neutron slowing down and thermalization are included in the MCNP calculation. The latter component is particularly important in the moderator and cooling water volumes. The energy deposition calculated by the above method will be expressed as MeV/p, and is averaged over the volume of interest (reflector, moderator etc.), only the iridium rod is sub-divided into smaller volumes in order to improve the spatial description of the energy deposition. Each sub-division in the iridium rod is 3 cm long. Results of the above calculation are shown in Table 2.

Table 2 - Energy deposition in volumes of interest

Volume	Energy deposition	
	MeV/p	Watts*
Iridium vol. 1	954.0	3975.0
Iridium vol. 2	1140.0	4750.0
Iridium vol. 3	868.0	3617.0
Iridium vol. 4	715.0	2979.0
Iridium vol. 5	504.0	2100.0
Graphite sleeve	250.0	1042.0
Titanium clad	87.0	363.0
Cooling water	57.0	24.0
Aluminum containment	40.0	167.0
Moderator	71.0	296.0
Lead reflector (radial)	1226.0	5108.0
Lead reflector (back)	4325.0	18021.0

* Note: Current = 1.0(5)/24(9) x 6.21504(18) = 2.5896(13) p/s ; also 1 MeV/s = 1.60206(-13) W
Watts = MeV/p x 2.5896(13) x 1.60206(-13) = MeV/p x 4.1487

It is seen that the total TRAM assembly absorbs approximately 43.25 % of the primary proton energy. The iridium rod absorbs approximately 18 % and the lead reflector 23 %. In the case of the reflector the volumes are relatively large and the specific energy deposition is low, thus cooling should not be difficult. In the case of the iridium rod, estimates of the cooling requirements at an average beam power of 100 kW indicate a maximum temperature (~ 680°C) well below the melting point of iridium (due to the short conduction path and good thermal conductivity) for reasonable values of the heat transfer coefficient (5000 W/m^2-K) between the water and the titanium clad. However, due to the short proton pulse width (~ 2μs) and the relatively small volume of the target, enhancement of the thermal stresses due to thermo-mechanical shocks may be limiting in the above design, even though the CERN target operated satisfactorily under similar conditions.

TARGET ACTIVATION

The generation of radioactive nuclides (spallation products) and their decay following machine shutdown was estimated for the above TRAM configuration. It was assumed that the machine operates continuously for 10 days at an average beam power of 100 kW. The radioactivity in the TRAM following this period of operation was estimated, and subsequently allowed to decay for 1 day, 7 days, and 30 days following shutdown.

The spallation product mass distribution was estimated using the LAHET Code System. This is similar to the fission product mass distribution following a fission process. The neutron energy spectrum was estimated using the MCNP4B code. A one-group cross section library was created for each spallation product nuclide by collapsing an appropriate multi-group cross section library using the neutron spectrum determined by MCNP4B. The multi-group library used for this purpose was the 63-group compilation used with the CINDER-90 code. This library contains the nuclear data for 3400 nuclides. The one-group data and the nuclear decay data for the spallation products of interest are then used in an appropriately modified version of the ORIGEN code to track the creation, destruction, and decay of the spallation products in the neutron flux while the machine is running, and following shutdown. The original ORIGEN code is routinely used to calculate the activity in nuclear reactor cores due to fission products; the present version was developed at BNL for application to spallation systems.

By sub-dividing the TRAM into its components, and further sub-dividing the iridium target rod, it is possible to determine a space dependent radioactive inventory using the above approach based on the spatially varying neutron energy spectrum. The results of this analysis are shown in Table 3.

Table 3 - TRAM component activation
(Curies)
(Following 10 days of operation at a power of 100 kW)

Component	0 days	1 day	7 days	30 days
Iridium cell 1*	970	346	104	51
Iridium cell 2	1762	563	155	64
Iridium cell 3	1677	533	144	60
Iridium cell 4	1015	366	98	45
Iridium cell 5	800	305	75	35
Graphite	130	4	4	3
Titanium	84	42	13	3
Cooling water	37	0.5	0.3	0.2
Aluminum	80	3	--	--
Moderator (water)	25	0.2	0.2	0.1
Reflector (radial)	8086	2756	510	62
Reflector (back)	19830	6351	1200	167

* cell 1 closest to proton entry point - all cells 3 cm long.

The above calculations indicate that the bulk of the activity is confined to the iridium target and the lead reflector. Only the cooling water will pass out of the TRAM assembly to an intermediate heat exchanger. In the event of an accident only the activity associated with the cooling water should contribute to the source term, since the remaining activity should be confined to the TRAM assembly. The following are the major contributors to the radioactive inventory, by volume:

1. Iridium rod - Immediately following shutdown of the machine the major radioactive nuclides are a selection of isotopes of the elements from Tc to Pt, Br to Zr, and Ga to As; the primary contributor being Ir-194. After 30 days of decay/cooling the activity is primarily due to Ir-192, Ir-190, Ir-189, Os-191, Os-185, Re-183, W-181, and W-178.

2. Lead reflectors - Following shutdown the radioactivity in the lead reflectors is due to isotopes of Mn to Bi; with the primary contributors being Tl-195 to Tl-206.After 30 days of decay/cooling the primary activity is due to Bi-205, Tl-204, Tl-202, Hg-203, Au-195, Pt-188, Ir-189, Ir-188, Os-185, Re-183, W-181, W-178, and Ta-178.

The decay gamma-rays from these two volumes have a similar distribution in energy. In both cases the distribution has two peaks, and a monotonic decrease as the energy either increases or decreases. In the case of lead these two peaks occur at 0.1 MeV and 0.35 MeV, and in the case of iridium they occur at 0.06 MeV and 0.8 MeV. In order to determine the gamma-ray flux leaking from the surface of these volumes a transport calculation will have to be carried out in which these distributions are treated explicitly as sources. Since these materials have high values of "Z", they are self-shielding and thus only a fraction of the activity would leak out. Furthermore, the leakage spectrum will be biased in the high energy direction.

MODERATOR NEUTRON FLUX

The neutron flux averaged over the moderator volume was calculated for a number of candidate reflector types. In addition to the lead reflector, lead fluoride, and beryllium were considered as reflecting materials. Fluorine compounds are of potential interest as reflectors because the inelastic scattering cross section for fluorine has a relatively low threshold (~ 100 keV), compared to that for heavier nuclides (~ 1 MeV) [8]. This low threshold will efficiently slow source neutrons down to the threshold energy before they enter the moderator. The disadvantage of lighter nuclides in the reflector is the reduced neutron production due to a lower number of spallation reactions, and the lower (n,2n) cross section (except for beryllium and heavy water). A comparison of the neutron flux (ϕ (n/cm^2-s-p-eV)) in an ambient temperature water moderator in the thermal range (up to 1.0 eV) is shown in Figure 4 for the reflectors mentioned above. It is seen that the beryllium reflected system has the highest peak flux while lead has the lowest. The peaks for all the reflector types occur at the same energy (~ 0.025 eV).

The neutron pulse shape for a representative energy was determined for an ambient temperature moderator (room temperature light water), and a cold moderator (80 K light water using a proton free gas scattering kernel). These two determinations were carried out for both lead and lead fluoride reflectors. The neutron pulse is shown in Figures 5 and 6 for the energy ranges 0.02 eV - 0.025 eV

for the ambient temperature moderator, and for the energy range 0.005 eV - 0.01 eV for the cold moderators respectively. It is seen that in both cases the configuration with a lead fluoride reflector has a more intense neutron pulse (~ 15 % increase). The above result may be due to the relatively rapid slowing down due to inelastic processes (one or two collisions rather than many) to a lower energy (~ 100 keV) rather than the higher energy customarily associated with lead (~ 1 MeV).

The total flux averaged over the moderator volume was found to be highest for the lead reflected case (~ 20% higher than for the beryllium reflected case). However, in the thermal range the beryllium reflected configuration exhibits a higher flux. Furthermore, it has been found [2,3] that beryllium reflected pulsed neutron sources have pulse decay time constants which are approximately twice as large as those using lead reflectors for coupled moderators. In the case of decoupled moderators the decay constants will be closer in magnitude. In addition, the heat deposited in the moderator for a lead reflected configuration has been found [3] to be approximately double that for a similar configuration using beryllium as a reflector. In order to increase the source performance due to the enhanced neutron production of a heavy nuclide reflector and the potential advantage of efficient slowing down of fluorine, a compound containing both components, or a layered structure will have to be designed.

ESTIMATES OF THE OPERATING STRESSES

The operating stresses in a PSNS target will be due to the cyclic heating of heavy metal, and may be enhanced by thermal-mechanical shock waves. A steady state thermal stress was estimated based on the thermal analysis presented above. Assuming that the elastic modulus of iridium is 517 (9) N/m^2, the thermal expansion coefficient is 6.8 (-6) /K, and the temperature rise across the rod target is determined to be 110°C, an average thermal stress of 4.0(8) N/m^2 results. This value is approximately two thirds of the ultimate strength of iridium (6.0(8) N/m^2). According to a study carried out by P. Sievers [9] the thermal-mechanical shock enhancement of the average thermal stress can be estimated, and for rods is given by:

$$\sigma_\phi/\sigma_a = \sigma_r/\sigma_a \leq 6r/ct$$

where

c = velocity of sound (5.3(3) m/s for iridium)
r = radius of rod (0.005 m)
t = pulse duration (2.0(-6) s)
σ_ϕ and σ_r are the maximum azimuthal and radial stresses respectively
σ_a = average thermal stress

For the proposed target the value of 6r/ct is seen to be approximately 3.0. This implies the maximum stress in either the radial or azimuthal directions will be approximately twice the ultimate strength of iridium. A sectioned (either axially, azimuthally or both) rod structure will have to be designed to partially relieve the stress build up. A sectioned target design has been proposed for the solid metal target to be used in the AUSTRON project [10].

CONCLUSIONS

The following conclusions can be drawn from this study:

1. The BNL-AGS with an edge cooled solid iridium target is potentially a bright neutron source.

2. A similarly designed target has operated reliably at CERN under comparable conditions, indicating that a design based on a solid iridium rod encased in a graphite sleeve and clad by titanium should contain any shock induced failure of the iridium rod. The same mechanism will allow the target to potentially survive the thermal-mechanical shocks expected in the above application.

3. Both lead and lead fluoride are suitable reflectors - with lead fluoride yielding more intense neutron pulses.

4. Residual radioactivity is confined primarily to the iridium rod and lead reflector - cooling water will be the only pathway out of the TRAM area.

   - Iridium activity reduces by approximately a factor of 30 after one month.
   - Lead activity reduces by approximately a factor of 100 after one month.

5. Due to the small size of the target, its eventual disposal is potentially simple compared to larger target designs.

ACKNOWLEDGMENTS

This work was supported by the US Department of Energy under Contract DE-AC02-98-CH10886 with Brookhaven Science Associates. The authors are indebted to C.D. Johnson of CERN for sharing details of the iridium rod anti-proton target design with them, and Bill Wilson of Los Alamos National Laboratory for use of the CINDER-90 Libraries.

REFERENCES

1. T.W. Eaton, C.D. Johnson, and E. Jones,"Recent work on the Production of Anti-Protons from Pulsed-Current Targets" European Organization for Nuclear Research, Geneva, Switzerland. CERN/PS/86-15(AA) (July 1994).

2. "The ESS Technical Study Vol. 3", J. Kjems ed. Risø National Laboratory, P O Box 49,DK-4000 Roskilde, Denmark, ESS-96-53-M (November 1996).

3. N. Watanabe, "Neutronic Performance of Cold Moderators in JAERI 5MW Pulsed Spallation Source", International Workshop on Cold Moderators for Pulsed Neutron Sources, Argonne National Laboratory, IL (September 1997).

4. R.E. Prael, "Revised User Guide to LCS: The LAHET Code System with LAHET2.8". Los Alamos National Laboratory, Los Alamos, NM (1997).

5. MCNP4B2; Monte Carlo N-Particle Transport Code System, ed. J.F. Breismeister, Los Alamos National Laboratory, Los Alamos, NM. LA-12625-m (1997).

6. A.G. Croff, "ORIGEN2 - A Revised and Updated Version of the Oak Ridge Isotope Generation and Depletion Code", Oak Ridge National Laboratory, Oak Ridge, TN (1977).

7. W.B. Wilson, "Accelerator Transmutation Studies at Los Alamos with LAHET, MCNP, and CINDER-90", Los Alamos National Laboratory, Los Alamos, NM. LA-UR- 93-3080 (1993).

8. H. Ludewig, et al., "Status of Pulsed Spallation Neutron Source Target work at Brookhaven National Laboratory", 13th International Collaboration on Advanced Neutron Sources - ICANS XIII, Paul Scherrer Institute, Villigen, Switzerland (1995).

9. P. Sievers, "Elastic Stress Waves in Matter Due to Rapid Heating by an Intense High-Energy Particle Beam", CERN-Lab.II/BT/74-2 (1974).

10. P. Bryant, M. Regler, and M. Schuster, "The AUSTRON Feasibility Study", Bundesministerium für Wissenschaft und Forschung, Wien, Österreich (1994).

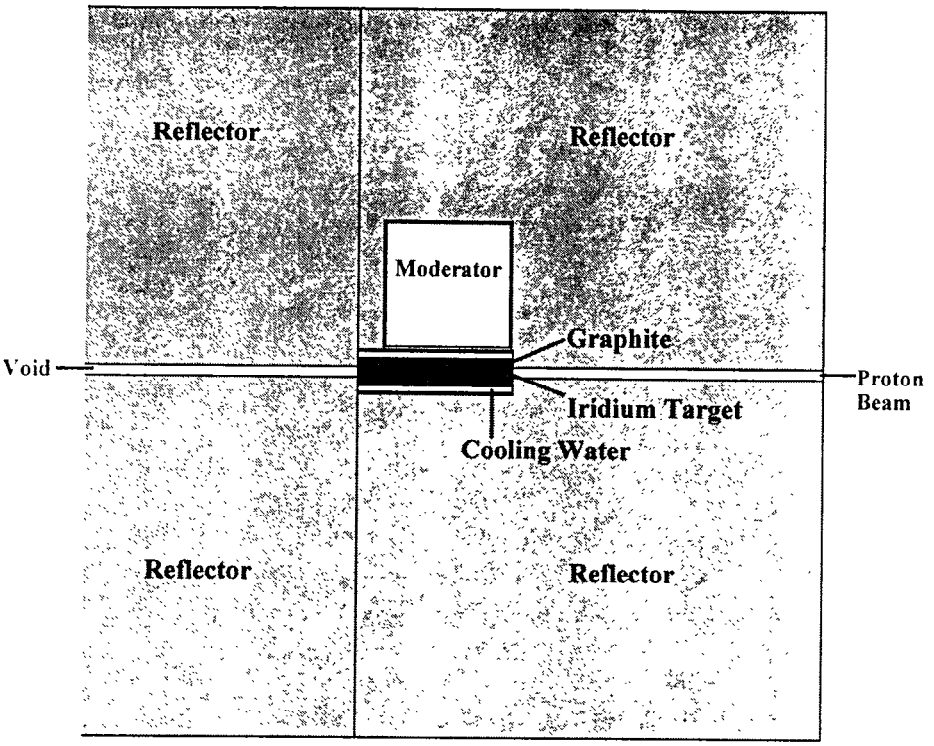

Figure 1 - TRAM Assembly
(Iridium Solid Target Configuration)

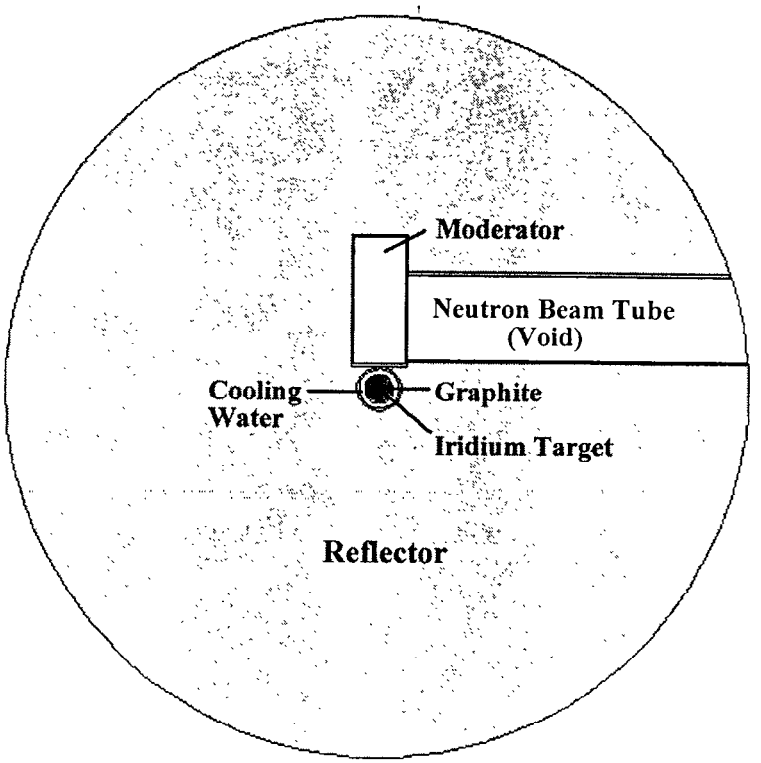

Figure 2 - TRAM Assembly
(Iridium Solid Target Configuration)

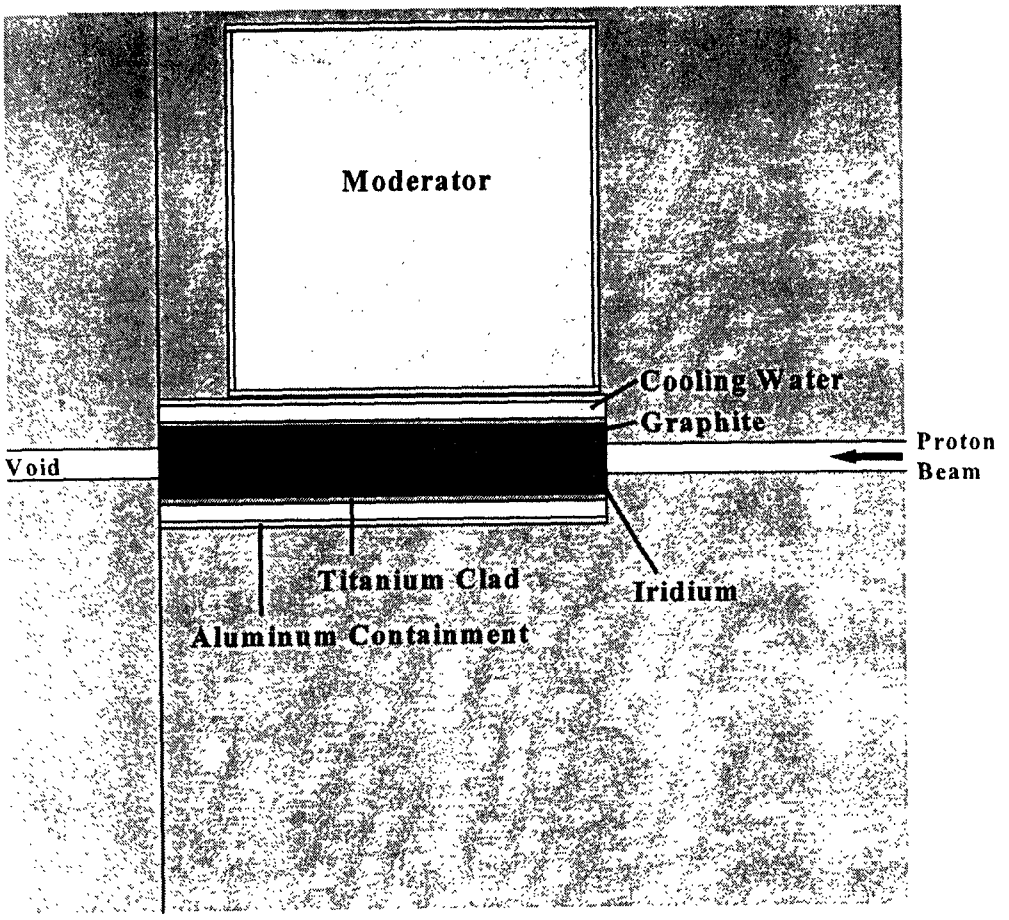

Figure 3 - Detail of Target

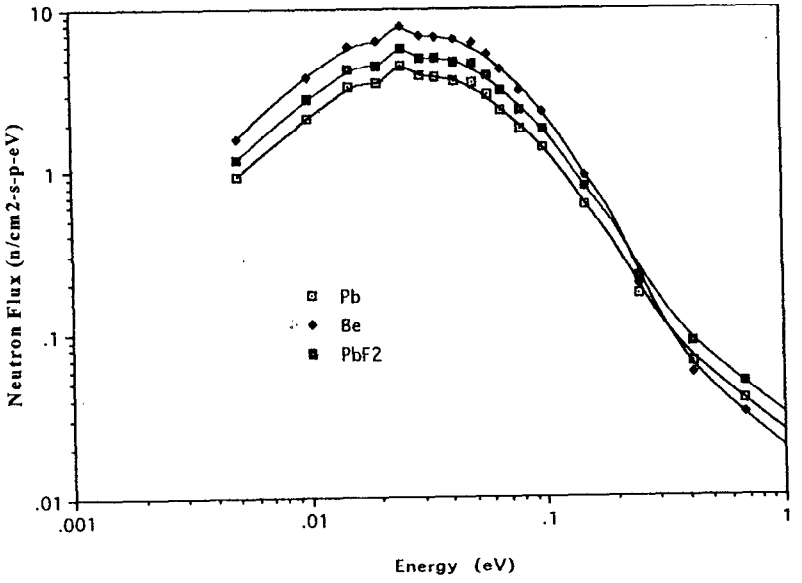

Figure 4 - Neutron Spectra Averaged Over Moderator Volume
(Ambient Temperature Light Water)

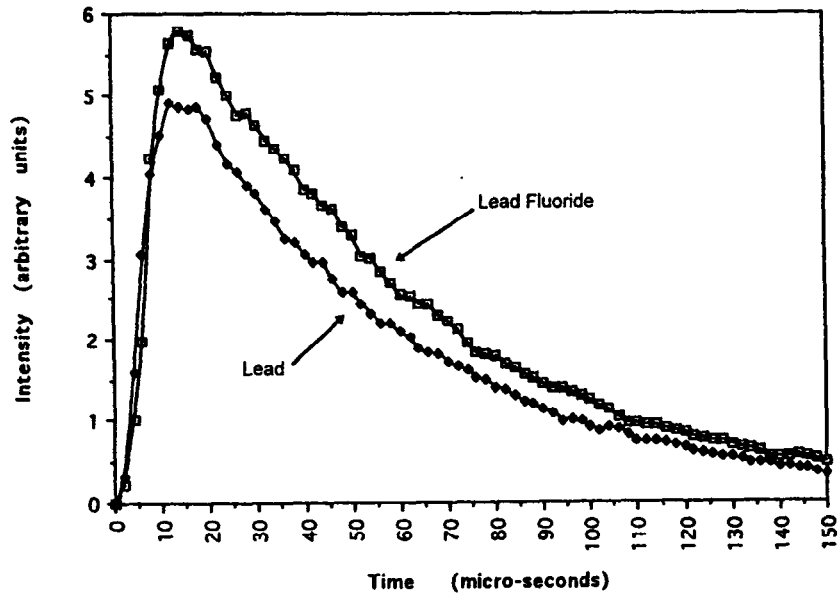

Figure 5 - Neutron Pulse in Moderator (.02 eV - .025 eV)
(Ambient Temperature Light Water)

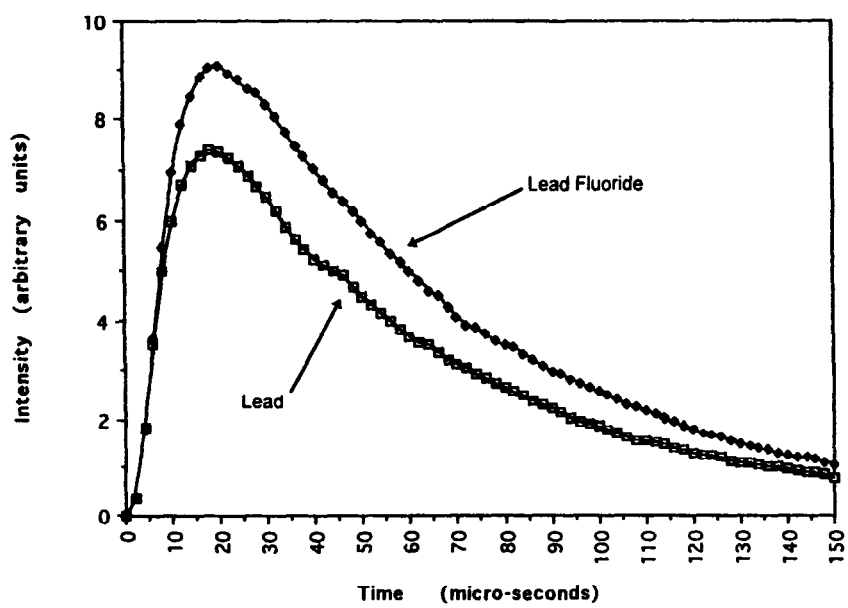

Figure 6 - Neutron Pulse in Moderator (.005 eV - .01 eV)
(80 K Proton Gas Model)

ICANS-XIV
14th Meeting of the International Collaboration
on Advanced Neutron Sources
June 14-19, 1998
Starved Rock Lodge, Utica, Illinois, USA

A Foil-less Charge Exchange Injection (LUCE) for the Intense Proton Storage Ring

Yasuo SUZUKI
Center for Neutron Science
Japan Atomic Energy Research Institute
Tokai-mura, Naka-gun, Ibaraki-ken 319-11, Japan

ABSTRACT

A new scheme of the charge exchange injection is reported for the next-generation neutron sources of 5 MW-class. Periodical magnetic field (undulators) and photon beam (a powerful laser) can ionize hydrogen beams efficiently in stead of stripping foils.

1. Introduction

LUCE is an abbreviation of 'Laser and Undulator Charge Exchange'. This injection system is composed of a neutralizer and an ionizer, which are placed along a straight section of the ring. The neutralizer strips the electron of H^- beam into H^0 with the magnetic field of a tapered undulator. The H^0 beam is excited to H^{0*} (n=3p) in the ionizer with laser light and the H^{0*} is ionized to H^- with the moderate magnetic field of a long tapered undulator as shown in Fig. 1.
(The parameters in this paper are calculated for a JAERI-NSP2: 1.587 GeV H^- injection)

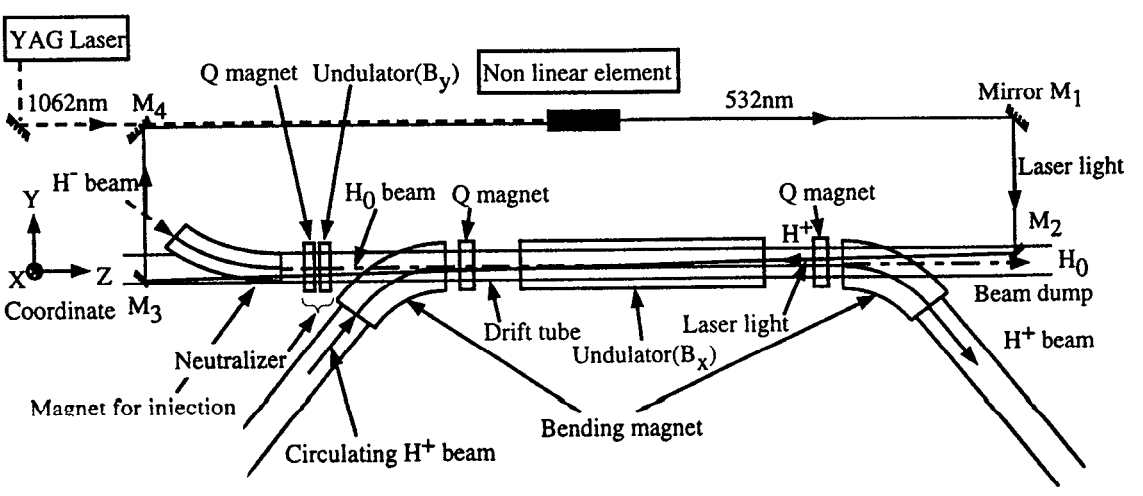

Fig. 1 A new scheme of injection

2. Magnetic field strength versus charge exchange probabilities

The Lorentz electric field generated by the interaction between the relativistic velocity of particle beam and the magnetic field, deforms the atomic potential and lets the electrons free from the

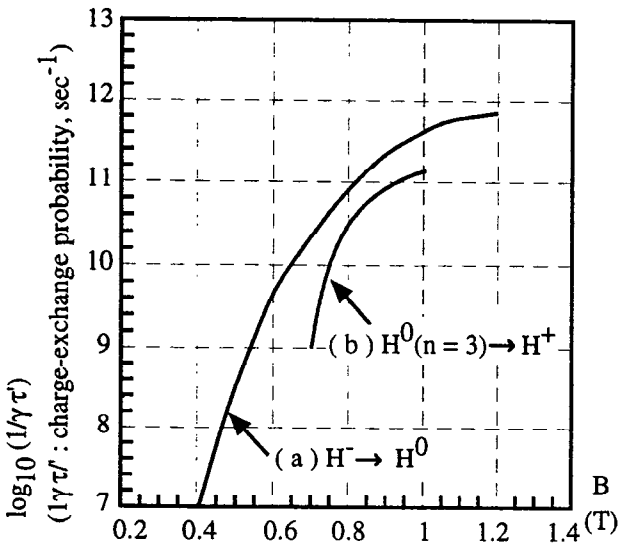

(a) caluculated from the paper of A. J. Jason et al. [1)]
approximate eq. (~1T)
$1/\gamma\tau' = 2.8 \times 10^{11} B^9$

(b) caluculated from the paper of D. S. Bailey et al. [2)]
approximate eq. (~0.8T)
$1/\gamma\tau' = 3.1 \times 10^{11} B^{11}$

Fig. 2 Magnetic field strength vs. charge-exchange probabilities.

atom (neutralization and ionization). The charge exchange probabilities versus the magnetic field for H^- and H^0 are obtained from the quantum theory[1,2)] for 1.587 GeV beam as shown in Fig. 2.

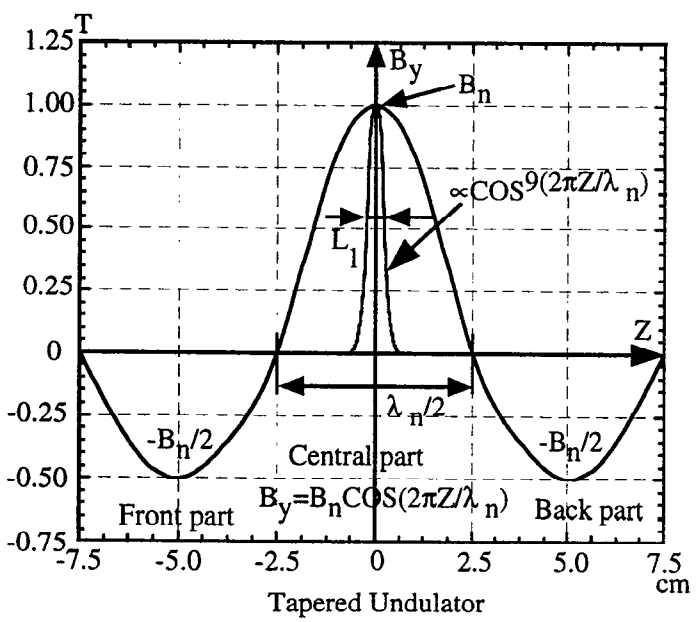

Tapered Undulator

(λ_n=10cm, B_n=1T, 1/2 wave length)

Fig. 3 Undulator magnetic field

3. The tapered undulator for the neutralize

A half period tapered undulator is applied for the neutralizer. The length of period is 10 cm and the maximum field strength is 1 T as shown in Fig. 3. Tapered magnets are facilitated to strip the electron of the H^- beam mainly around the peak position of the magnetic field strength and to let the H^0 beam go straightforwardly into the ring. The deflection angle of H^- beam can be analyzed from the equation of motion and the half width of the deflection angle$\Delta\Psi$ is expressed as:

$$\Delta\Psi = -(em_p\gamma\beta c)\, B_n L_1/2,$$

where L_1 is the effective length of neutralization zone. The deflection angle

become ~0 owing to adjustment of the tapered section of the undulator, and its width is minimized (.≤0.8 mrad)[3].

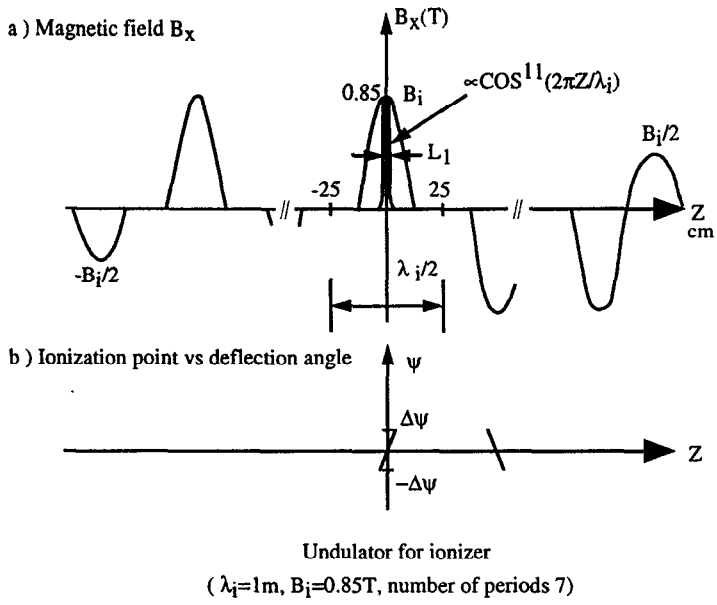

Fig. 4 Undulator magnetic field for the ionizer

4. The tapered undulator for the ionizer

A 7 periods tapered undulator is applied for the ionizer. The maximum strength of the magnetic field is 0.85 T. The length of period is 1 m but the free space of 25 cm is inserted between every half wave-form. The free spaces are used as the excitation region of H^0 beam by the laser light. Total length of the undulator is 7.75 m including the tapered magnets. The width of the deflection angle is estimated to 3 mrad after similar caluculations described in preceding section.

5. The optical system for the excitation of the H^0 beam

By relativistic Doppler shift, the 2nd harmonics wave (532 nm) of the Nd:YAg laser can be applied to excite H^0 beam resonantly as a Lyman series line L_β(102.5 nm).The optical resonator (a ring resonator in this case) is used to store the laser light and to interact

$$\frac{dN_1}{dt} = \gamma_1 N_3 + (N_3 - N_1)\Gamma,$$

$$\frac{dN_3}{dt} = -(\gamma_1 + \gamma_+)N_3 - (N_3 - N_1)\Gamma,$$

$$\frac{dN_+}{dt} = \gamma_+ N_3$$

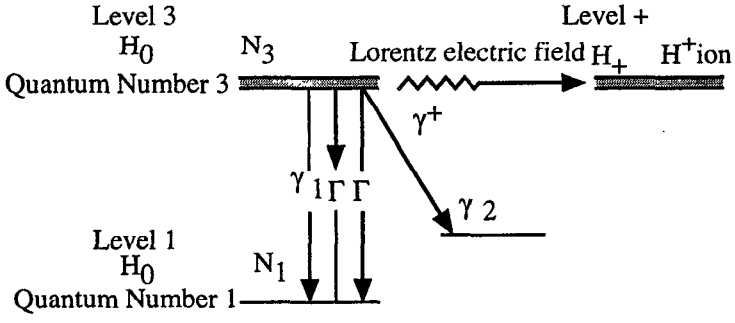

Fig. 5 Four level and the rate equations

multi-fold times with the H^0 beam. The ring resonator is estimated to amplify the photon density up to 100 times of the laser's. The wave-lengths of lasers to be applicable to the high power neutron sources are listed in Table 1, where the wave-length λ' in the frame of reference moving with H^0 beam, becomes shorter as $\lambda' = \lambda/\gamma(1+\beta)$ in the laboratory frame of reference by the relativistic

Doppler shift.

From calculation of the rate equation of excitation (see, Fig. 5 and 6), the excitation ratio to the injected H^0 is obtained by N_1^2 / N_1^0 and the charge exchange ratio R after passing 14 halves periods of the undulator is expressed as follows:

$$R = 1 - \cosh^{14}(\Gamma T_1)\exp(-14\Gamma T_1),$$

Region I

$N_1^1 = N_1^0 (1+e^{-2\Gamma T1})/2,$

$N_3^1 = N_1^0 (1-e^{-2\Gamma T1})/2,$

$N_+^1 = 0,$

Region II

$N_1^2 = N_1^1 \exp(-\lambda_2 T_2) = (N_1^0/2)(1+e^{-2\Gamma T1})$

$N_3^2 = 0,$

$N_+^2 = N_1^0 - N_1^1 \exp(-\lambda_2 T_2) = N_1^0 - (N_1^0/2)$

$(1+e^{-2\Gamma T1})$

Non-charge-exchange ratio during passing a half period of the undulator is as follows :

$N_1^2/N_1^0 = (1+e^{-2\Gamma T_1})/2$

$= \cosh(\Gamma T_1)\exp(-\Gamma T_1)$

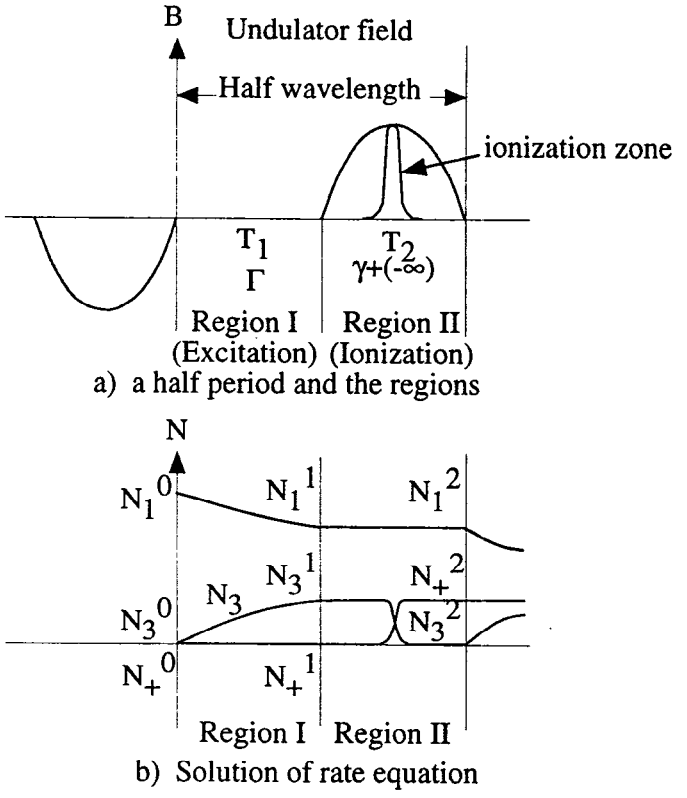

Fig. 6 Ionization process

where Γ is the induced transition probability and T_1 is the traveling time of particles in the free space (Lorentz shrinked) of the undulator. The required laser power is obtained 400W in average, 2.2 kW in peak. This power is within the practical level of development.

The momentum dispersion of H^0 beam is estimated to be 0.2 %. The resonant frequency of the beam absorption depends upon the momentum. The resonant condition, however, can be kept because the absorption frequency shifts by the Stark effect due to the Lorentz electric field which is generated by the interaction between the beam velocity and the weak magnetic field (≤15 Gauss) in the free space of the undulator. The shifted frequency of absorption of particles coincides with the line of laser light at a certain point in the free space. So, the line profile of laser light may be narrow as it is.

Beam nergy(GeV)	γ	β	$\gamma(1+\beta)$	Wave-length λ_α corresponds to L_α(121.52nm)	Wave-length λ_β corresponds to L_β(102.2 nm)	Wave-length λ_γ corresponds to L_γ(97.215nm)
σ / $\Delta\upsilon'$ $cm^2 s^{-1}$				0.0105	0.00208	0.000771
1.587 JAERI-NSP2	2.691	0.9284	5.189	630.6	531.9 YAG-2nd	504.4
1,5 JAERI-NSP	2.599	0.9234	4.999	607.5	512.4 Cu-Vapour(511)	486.0
1.334 ESS	2.422	0.9108	4.628	562.4	474.4	450.0
1,00 SNS	2.066	0.875	3,874	470.8	397.1	376.6
0.816 LANSCE1	1.870	0.845	3.45	419.2	353.6 YAG-3rd	335.4
0.797 LANSCE2	1.849	0.841	3.404	413.7	348.9 YLF-3rd	330.9

Table 1 Beam Energy & Laser Wave-length

6. Conclusion

Even if unionized neutral hydrogen beams may remain through the ionizer, they go to the beam dump straightforwardly. No uncontrollable scattering will occur and, the production of radioactives around the ring will minimized. Moreover, this device has no effect on the trajectory of the circulating proton beam in the ring.

We can expect a high performance of the charge exchange efficiency, a beam spill-less , a lower beam loss (1/1000 loss to beam dump), and a smaller growth of beam emittance owing to the width of deflection angle in this method. This scheme will be one of the optimal charge exchange methods for the next-generation neutron source.

Acknowledgments

The author would like to thank Drs. M.Kinsho, F. Noda, M, Mizumoto and I. Yamane for their helpful discussions and Drs. Y. Oyama, T. Mukaiyama and N. Watanabe for their encouragements.

References

1. A. Jason et al : IEEE Transactions on Nuclear Science, NS-28, No. 3, (1981).
2. D.S.Bailey et al : Nuclear Fusion, 51, 41 (1965).
3. Y.Suzuki et al : Proc. of the 1st APAC '98, Tsukuba, May 1998, to be published.

ICANS-XIV
14th Meeting of the International Collaboration on
Advanced Neutron Sources
June 14-19, 1998
Starved Rock Lodge, Utica, IL, USA

ADJUSTABLE COLLIMATION FOR THE GENERAL MATERIALS DIFFRACTOMETER (GEM)

L C Perrott, S A Temple, G Thomas
ISIS Facility, Rutherford Appleton Laboratory, CCLRC, Chilton, Didcot, UK

ABSTRACT

GEM is to be the new structured materials diffractometer for ISIS. This paper reviews its need for adjustable beam collimation to allow the incident beam to be matched to the sample size. The final solution for the adjustable collimation is also discussed.

1. Introduction

From the initial specification of GEM, adjustable collimation was a requirement. This instrument will serve a wide scientific community and it is predicted that sample sizes ranging from 20 x 40 mm (width x height) down to 3 x 3 mm will be investigated. With new materials often being supplied in small quantities the ability to accurately study them will be of great importance.

If very small samples are investigated with a much larger beam, the excess could scatter from sample holding equipment and increase the noise to signal ratio. As one of GEM's proposed advantages will be the range of sample sizes that it can study, it was decided that the beam profile should be adjustable. With adjustable collimation, the GEM user will be able to change the beam profile to match that of their sample whatever its size or aspect.

Most other beamlines on ISIS have fixed collimation. This consists of fixed rings of B_4C stacked along the beam tube and collimate the beam to the maximum size and cross section required. GEM has been designed with 5 adjustable apertures. These replace the fixed ring design and give GEM its flexibility.

2. Collimation Layout.

The apertures on GEM were to be located at various points down the beamline. Ideally to minimise the beam penumbra at the sample, a slit close to the moderator with another close to the sample would be required. There were two factors limiting the proximity of the second to the sample,

- Scatter from the aperture into the detectors (increasing the background signal).
- The Geometry of the back scattering detectors (physical fit of the detector around the aperture).

Similarly the aperture nearest the moderator could not be closer than 6.3 meters (the target station wall) as placing it within the shutter or insert shielding was not possible.

After analysis a further 3 apertures were required. These are placed at suitable points along the beam line. The collimation tubes between the apertures are lined with B_4C. The B_4C will

be installed to give ≈3 mm clearance to the maximum beam size. The surface is serrated creating multiple faces normal to the neutron beam. This will ensure that any stray neutrons which are not collimated by the apertures and reach the tube wall will be absorbed and not scattered into the sample. (*see figure 1 below.*)

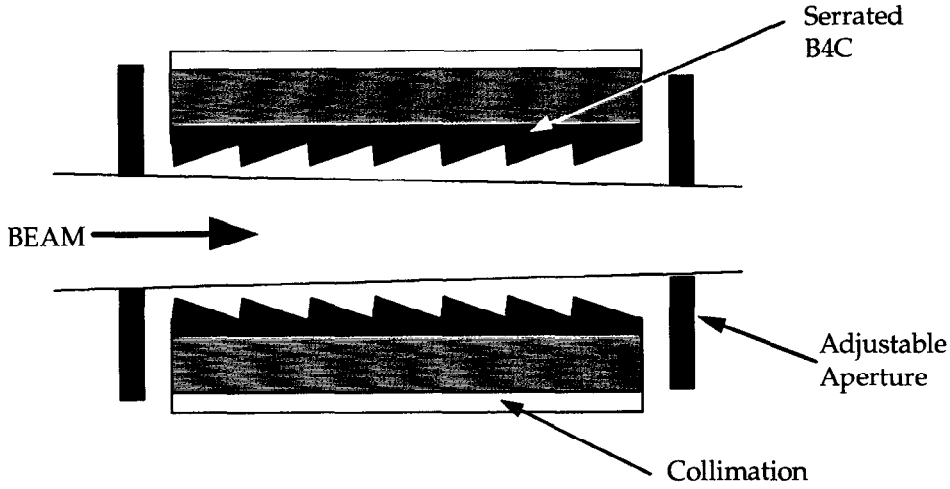

Figure 1.
Schematic of GEM beam tube design.

3. Aperture Design.

The GEM beam is rectangular, therefore two axis of collimation were required (vertical and horizontal). One axis of the prototype aperture can be seen below in *Plate 1.*

The system consists of a Stepper motor driven rack. This rack drives a pair of opposing B4C blades (see *plate 2* below). The design ensures that the opposing blades are always centred around the beam axis. The 5 apertures are set using a Programmable Logic Controller (PLC) to a positional accuracy of ±0.05mm. A micro switch is incorporated for pre-run zeroing. A rotary encoder prevents the motor skipping steps and an incorrect beam profile being created.

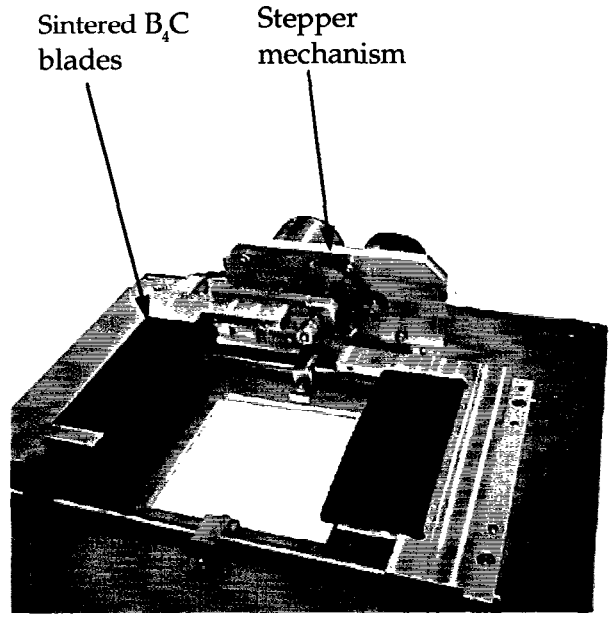

Plate 1.
GEM aperture (only one axis shown).

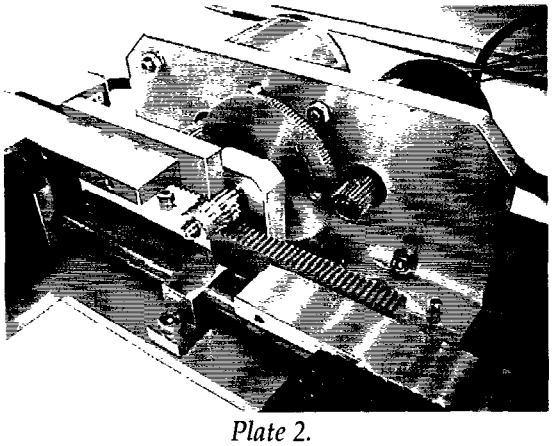

Plate 2.
GEM aperture mechanism

The blades are manufactured from 20mm thick sintered B_4C. The blade is stepped to minimise scatter. The beam is collimated by the leading face (moderator side). The step in the trailing face (sample side) then trims the beam to the required profile and absorbs scatter from the front edge (see *figure* 2. Below).

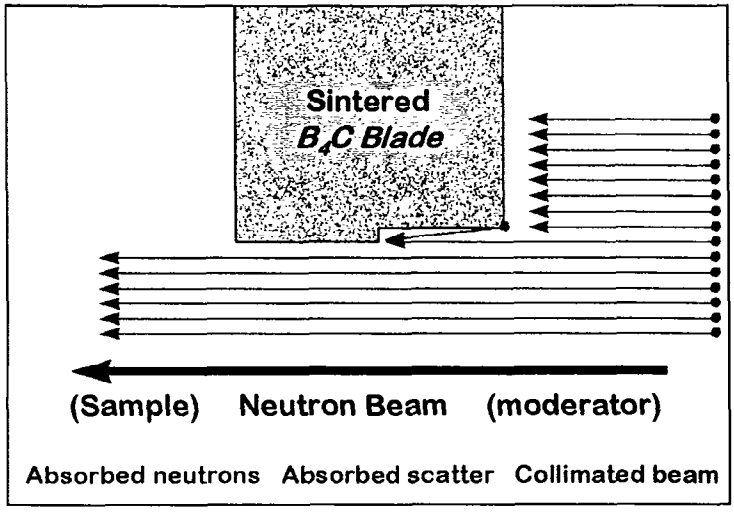

Figure 2
Aperture blade design

To reduce the number of vacuum windows the beam must pass through, several of the slits will be placed in vacuum. Components have been selected and tested to ensure reliability in vacuum and low out gassing rates. This will ensure that pump down times for the collimation tubes are low and a good vacuum can be maintained.

4. Conclusion

The first Aperture for GEM has been manufactured and is currently under bench test at ISIS. The test have shown that the required accuracy is achievable. The prototype aperture required some modification in the early phase of testing but we are now pleased with the performance of both the mechanism and drive system. We are now at a stage to procure the remaining units required for GEM.

ICANS XIV
14th Meeting of the International Collaboration on
Advanced Neutron Sources
June 14-19, 1998
Starved Rock Lodge Utica, Illinois

A New Polarized Neutron Reflectometer at KENS

M. Takeda, N. Toyoshima and Y. Endoh

Physics Department, Graduate School of Science, Tohoku University, Sendai, 980-8578 Japan

Abstract

A new polarized neutron reflectometer has been installed at KENS (Neutron Science Laboratory in High Energy Accelerator Research Organization) in Tsukuba. The reflectometer is designed for investigation of surface or interfacial magnetisms of thin films and multilayers. It has an analyzer for polarization analysis and an optional detector bank for off-specular reflectivity measurements which consists of ^{3}He squashed detectors. The overview and the status of the reflectometer are reported.

1. Introduction

The TOP spectrometer at KENS had been built to study mesoscopic magnetism, and was a multipurpose spectrometer which used cold polarized pulsed neutrons [1]. Various experiments, depolarization, polarized neutron reflection and small angle scattering had been done on TOP. During 1996 - 1997 the cold neutron experimental hall at KENS has been rebuilt, and the C1 cold neutron beam port was newly assigned to TOP [2]. However, the C1 port has to be shared with a Small/Wide-angle neutron diffractometer, SWAN, so that TOP could have no room for a detector bank for small angle scattering measurements. Polarized neutron reflection is a powerful tool for the investigation of magnetic thin films and multilayers because using polarized neutrons we can detect weak magnetic moments very accurately [3]. Thus, instead of TOP, a new polarized neutron reflectometer, PORE, has been designed and constructed on the basis of a lot of experience of polarized neutron experiments on TOP.

Neutron reflectivity measurements generally give the information about the depth profile of layer structure including magnetism. In addition to this, off-specular reflection, whose importance

many researchers begin to recognize recently, gives the information on surface and interface roughness in thin films and multilayers [4]. The plan of construction of the reflectometer has two stages, Phase 1 (standard measurements of specular reflectivities) and Phase II (optional measurements of off - specular reflectivities). The Phase I has been almost completed. On the other hand the preliminary experiments of phase II is now progressing.

2. Overview

The principal specifications of the reflectometer, PORE, are listed below and the plan view is shown in Fig.1.

Specification

• Beam port	C1 - 1 (50 Hz)
• Moderator	Solid Methane
• L1 (Moderator - Sample)	9.5 (m)
• L2 (Sample - Detector)	1.5 (m)
• Incident Polarized Neutron wavelength	$3 < \lambda < 16$ Å
• Scattering angle	$2° < 2\theta < 22.5°$
• $Q_{//}$ normal to the surface	$0.015 < Q_{//} < 0.7$ ($Å^{-1}$)
(specular reflection) Resolution	$(\Delta Q_{//}) / Q_{//\,min} > 0.03$
• Q_n parallel to the surface	$0 < Q_n < 0.05$ ($Å^{-1}$)
(off - specular reflection) Resolution	$(\Delta Q_n) / Q_n < 0.02$
• Beam size	30 mm (H) × 0.1 to 10 mm (V)
• Detector	Single ^{3}He gas detector for specular reflection
and	35 squashed ^{3}He gas detectors for off - specular reflection
• External magnetic fields	$\mu_0 H < 1$ (T)
• Temperature	$10 < T < 350$ (K)

The reflectometer utilizes cold neutron wavelength band of 3 - 16 Å from the solid methane cryogenic moderator. The wide band of incident neutrons makes it possible to cover wide range of momentum transfer value, Q, at the fixed incident angle. This is a typical advantage of reflectivity measurement using white beam. Incident unpolarized white neutrons are polarized by a optical device which consists of Fe/Si polarizing supermirrors (OSMIC) [5]. The polarizer also works as the frame overlap mirror. The beam polarizations are slightly changed by the collimation of

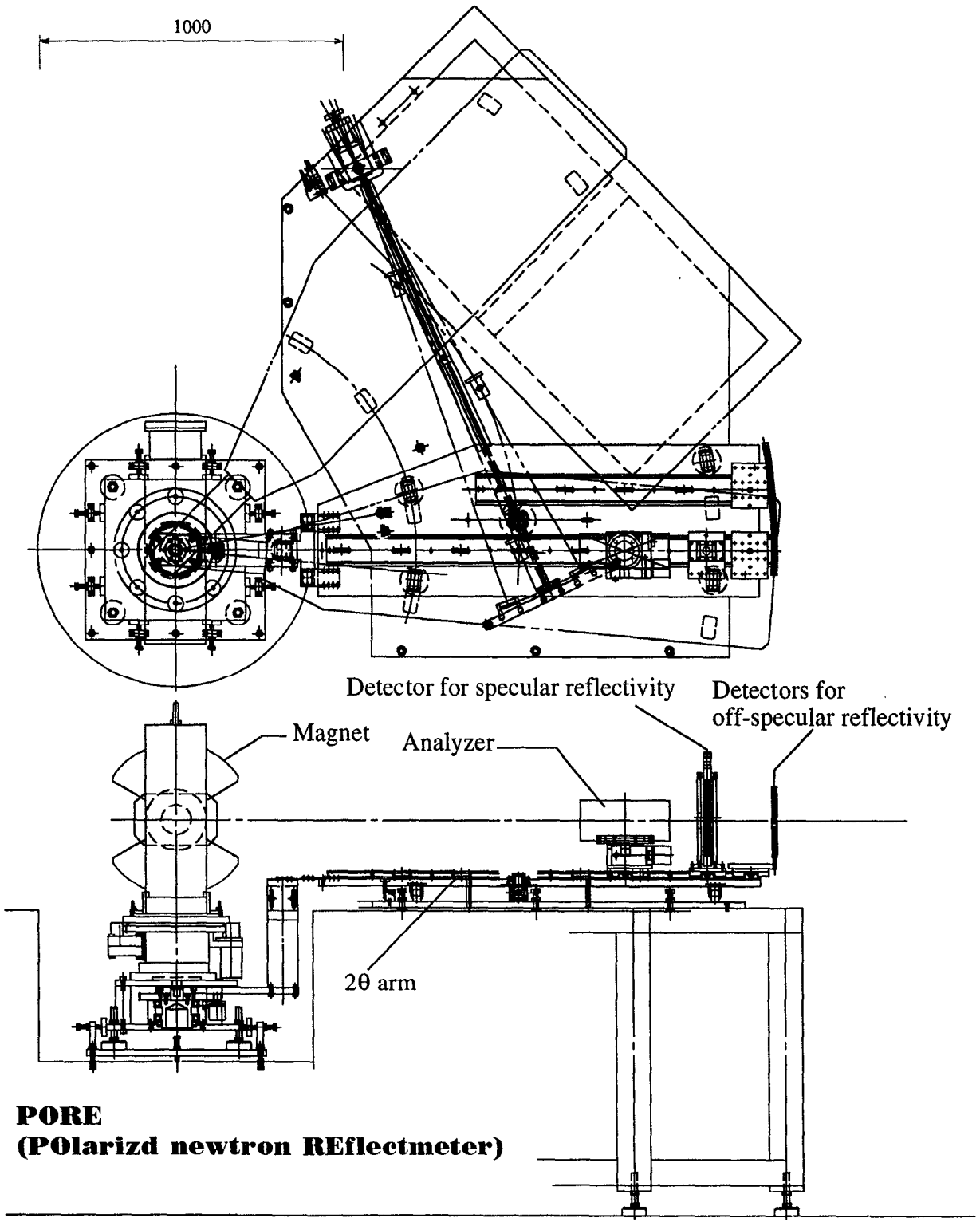

Figure 1 A plan view of the new reflectometer, PORE at KENS.
A polarizer, a flipper and a detector bank for off-specular measurements are not shown in this figure.

incident beam, however, keep constant value (> 92 %) for neutrons within the band. The direction of polarization can be reversed by a two coil flipper with almost perfect flipping efficiency before samples. In the normal operation neutron spins are flipped every 4 seconds. The polarized neutrons are collimated by two pairs of horizontal slits and collimator assembled by SUS306, B4C and Cd. At the sample position, beam is horizontally separated into two beams for PORE and SWAN, respectively, whose separation is only 40mm. Samples are vertically set to the sample position on a θ gonio stage from the geometry of beam sharing with SWAN. Therefore the scattering plane is always in the horizontal plane.

The reflection angle can be changed from -5 to 45 (deg.) by moving a 2θ arm driven by a stepping motor. The reflected neutrons from the samples are detected by a time analyzer and single 1"-^{3}He detector for the specular reflection measurements, and by 35 squashed ^{3}He detectors for the off-specular ones. Deficient 15 detectors are going to be added to the bank in the near future. The data are stored by a hard disk on a personal computer (Power Macintosh 7600/200, Apple) which controls the slits, polarizer, analyzer, incident angle and reflection angle by GPIB. The computer also controls the data taking system using a package software, LabVIEW, sold by NATIONAL INSTRUMENTS [6]. During measurements intensities of incident neutrons are monitored by a fission neutron monitor.

3. Examples

3.1 Phase I (Specular reflectivity)

Figure 2 shows the unpolarized neutron specular reflectivities of 2 - vinylpyridine-styrene-d8-2-vinylpyridine triblock copolymer (PDP) [7] measured by PORE. In the same figure data of the same sample taken by the CRISP spectrometer are plotted by open circle. CRISP is a neutron reflectometer which uses a wavelength band, from 0.5 to 6.5 Å, at Rutherford Appleton Laboratory pulsed neutron source ISIS in UK. ISIS is the world's brightest spallation neutron source, and the power of injected proton beam to neutron target is 160 kW . On the other hand, the power of KENS is only 3 kW. Although the power is not directly proportional to luminosity of neutron beam, intensity ratio is estimated to be at least 20.

In both measurements, the wide Q range was covered by changing the incident angle, ie. 0.6 and 1.5 (deg.), however, the covered Q ranges were not the same between these two spectrometers because of the difference of utilized wavelength band. Incident angle of 5 (deg.) was also used on PORE to cover higher Q region. In order to compare the data with the same instrumental resolution, ($\Delta\theta/\theta$) was kept the same value, 0.07 between two spectrometers. It took 1.5 hours to collect the data on CRISP and 5 hours on PORE typically. Reflectivities in the Qregion higher than 0.3 Å^{-1} have been buried under background noise on PORE. The figure shows that PORE is capable of measuring reflectivities down to values at least in the region of

10^{-5} with the same accuracy of CRISP.

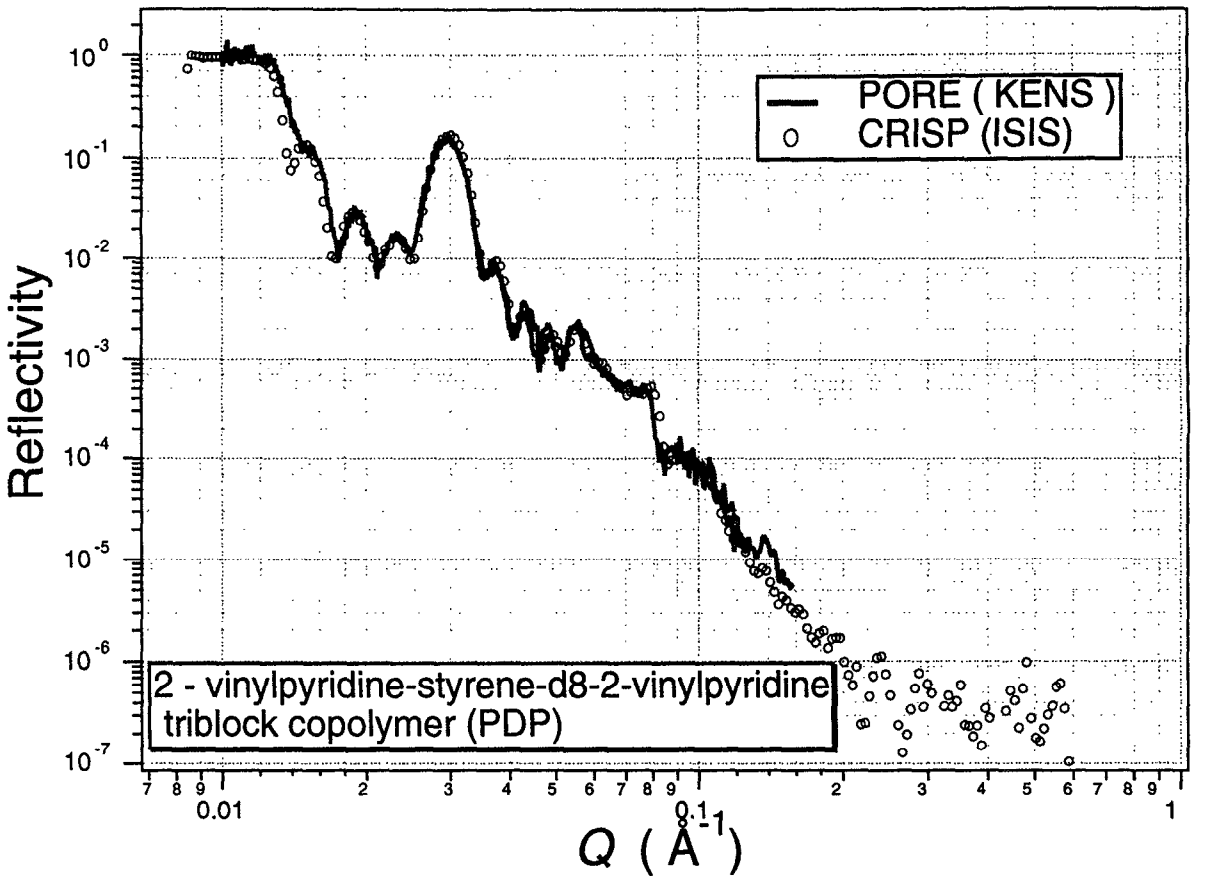

Figure 2 Reflectivities of a PDP triblock copolymer film on Si.

Polarized neutron specular reflectivity curves of natural Ni mirror with thickness of 2000 Å are displayed in Fig. 3 (a) and (b) with error bars. An external magnetic field of 40 Oe was applied in the mirror to maintain the polarization of neutrons. The total reflection of neutrons appeared in the lower Q region and clear fringes can be seen in the vicinity of the total reflection. In Fig. 3 (a), "Spin Flipper Off" means that spins of incident polarized neutrons are parallel to the magnetization of Ni mirror, and "On" in Fig. 3 (b) corresponds to antiparallel. The weak magnetic moments of Ni make the difference between these two data. The difference can be more clearly seen by flipping ratio, I_{off} / I_{on} (Fig. 4). Here I_{on} is the intensity in the case of flipper "ON" and I_{off} is that in the case of "Off". This figure shows the flipping ratio is very sensitive to weak magnetic moments.

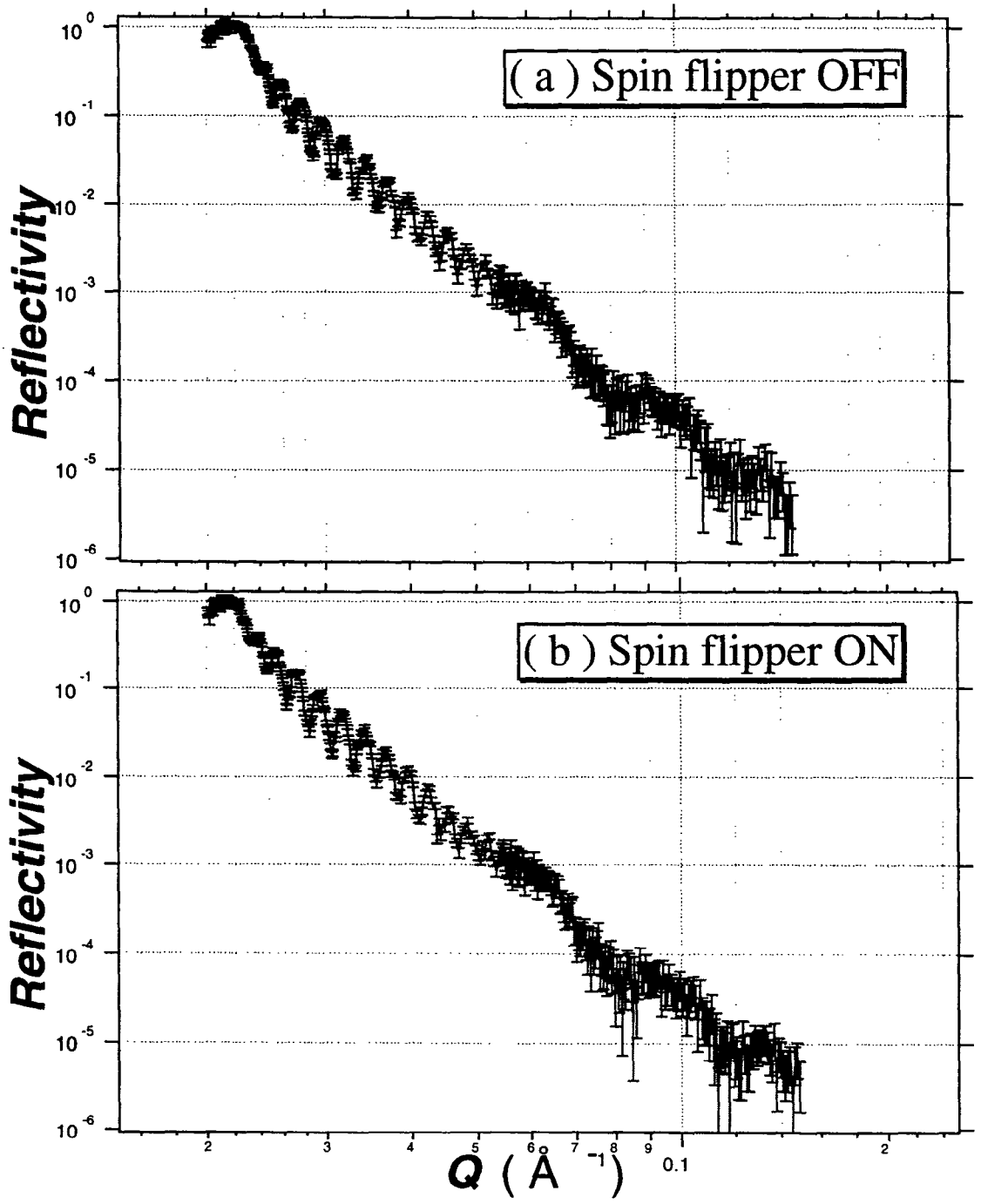

Figure 3: Polarized neutron reflectivities of a Ni mirror with thickness of 2000 Å, (a) spin flipper OFF and (b) ON

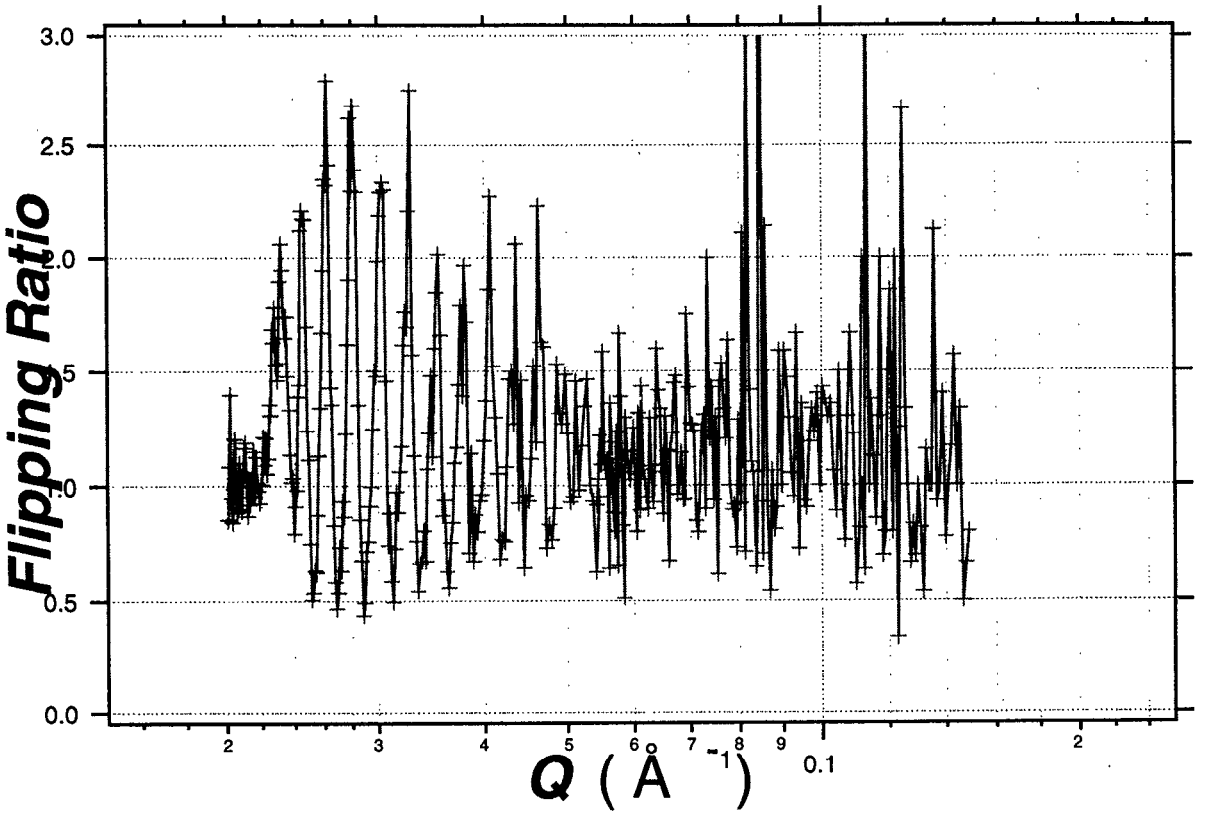

Figure 4: Flipping ratio deduced from Fig. 3

3.2 Phase II (Off - specular reflectivity)

Setup for the off-specular reflectivity measurements is now final stage. Almost all components have been installed and we started in doing preliminary measurements. Figure 5 shows one of the results of off-specular reflection of a Ni/Ti multilayer [Ni(55Å)/Ti(44Å)] × 15 on MgO [8] with flipper bing on (a) and off (b) under the field of 40 Oe. This contour map of intensities of reflected neutrons was collected by the optional detector bank for off-specular reflection measurement in which the 35 squashed detector with 4 mm in width by 100 mm in hight are lined up on arc.

In the contour map the horizontal axis is the number of TOF channel corresponding to wavelength of neutrons, and the vertical axis is the number of detectors corresponding to reflection angle. In this case the detector 0 corresponds to specular condition, ie. the incident angle of 1.5 (deg.) is equal to the reflection angle, and the reflection angle increases with increasing the detector number. Intensities under the condition that incident angles are different from reflection angles are that of off-specular reflection. Bragg peak from Ni/Ti bilayer with thickness of 99 Å

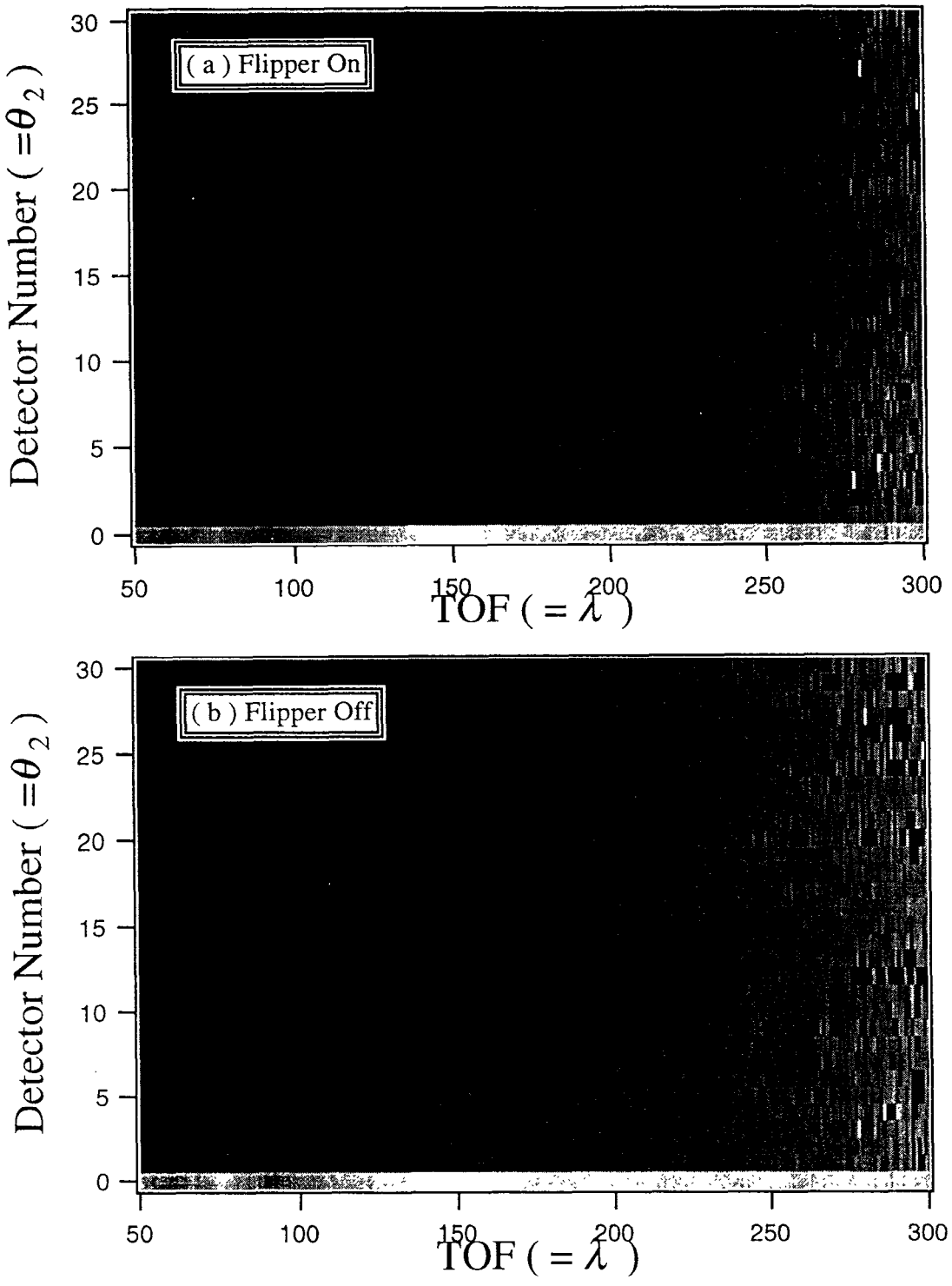

Figure 5 Contour map of intensities in gray scale. The vertical axis corresponds to reflection angle and the horizontal one to wavelength of neutrons. Detector 0 holds specular condition.

appears at around position (150, 0) both in Fig. 5 (a) and (b). Clear two streaks starting at point (150, 0) are observed in these two figures in the different way although a weak magnetic field was applied. One of the streaks which is not parallel to the vertical axis expresses the correlated interfacial roughness from the bottom to the topmost layer [4]. This indicates that the PORE reflectometer is very promising tools for the investigation of surface and interface roughness with magnetic origin with appropriate theory.

4. Concluding Remarks

The new polarized neutron reflectometer, PORE, at KENS works excellently for the specular reflection measurements and is ready to accept user proposals. However, the background in reflectivity is not well below 10^{-6}. If reflectivities down to 10^{-6} have to be measured, it is necessary to reduce the background noise by much better way. The off-specular reflection measurement is expected to be open to users within this year.

Acknowledgements

The authors would like to express their thanks to Dr. M. Frusaka, Dr. T. Otomo, Dr. T. Adachi and Mr. S. Satoh in KEK for many fruitful discussion and technical support. We also thank Mr. M. Onodera in Tohoku University for valuable technical assistance. Prof. Matsushita in ISSP and Dr. Torikai in KEK kindly allow us to use the sample and unpublished data of PDP. This work was supported by Grants-in-Aid for Scientific Research (No. 09236201 and (A)(2) 10130201 on Priority Area No. 281) from the Ministry of Education, Science, Sports and Culture .

References

[1] S. Itoh, T. Watanabe and Y. Endoh, Proc. of ICANS-XI ,Tsukuba (1990) 792.

[2] KENS REPORT - XI (1997) .

[3] H. Zabel and A. Schreyer, Neutron News **9** Issue 2 (1998) 18.

[4] S. K. Sinha, Physica B **173** (1991) 25.

[5] M. Takeda, K. Kurahashi, Y. Endoh and S. Itoh, Supplement A to J. Phys. Soc. Jpn. **65** (1996) 234.

[6] S.Satoh and M.Furusaka, Proc of DANEF'97, Kubuna (1997) 92.

[7] Y. Matsushita, J. Suzuki, N. Takabayashi, N. Torikai, M. Nomura and I. Noda, Macromolecules **31** (1998) 2378.

[8] P Böni, I. S. Anderson, R. Hauert, P. Ruterana, K. Solt, B. Farnoux, G. J. Herdman, J. Penfold and O. Schärpf, Proc. of ICANS-XI ,Tsukuba (1990) 910.

ICANS-XIV
14th Meeting of the International Collaboration on
Advanced Neutron Sources
June 14-19, 1998
Starved Rock Lodge
Utica, Illinois

Performance of the Small-Angle Diffractometer SAND at IPNS#

P. Thiyagarajan, V. Urban, K. Littrell, C. Ku, D.G. Wozniak, H. Belch, R. Vitt,
J. Toeller, D. Leach, J.R. Haumann, G.E. Ostrowski, L.I. Donley, J. Hammonds,
J.M. Carpenter and R. K. Crawford
Argonne National Laboratory, Argonne, IL 60439, USA.

ABSTRACT

The time-of-flight small-angle diffractometer SAND has been serving the scientific user community since 1996. One notable feature of SAND is its capability to measure the scattered intensity in a wide Q ($4\pi\sin\theta/\lambda$, where 2θ is the scattering angle and λ is the wavelength of the neutrons) range of 0.0035 to 0.5 $Å^{-1}$ in a single measurement. The optical alignment system makes it easy to set up the instrument and the sample. The cryogenically cooled MgO filter reduces the fast neutrons over two orders of magnitude, while still transmitting over 70% of the cold neutrons. A drum chopper running at 15 Hz suppresses the delayed neutron background. SAND has a variety of ancillary equipment to control the sample environment. In this paper we describe the features of the SAND instrument, compare its data on a few standard samples with those measured at well established centers in the world, and display two scientific examples which take advantage of measuring data in a wide Q-range in a single measurement. With a new set of tight collimators the Q_{min} can be lowered to 0.002 $Å^{-1}$ and the presently installed high-angle bank of detectors will extend the Q_{max} to 2 $Å^{-1}$.

1. Introduction

Small angle neutron scattering (SANS) is a general purpose nondestructive technique that enables the structural study of systems in nanometer to submicron length scale. When dealing with systems that undergo changes such as aggregation, phase transition or gelation as a function of time, it is essential to obtain the scattering data in a wide Q-range all at once. At reactor-based SANS instruments the range is spanned by making repetitive measurements in different instrument configurations and wavelengths. This

Work supported by U.S. Department of Energy, BES, Contract No. W-31-109-ENG-38.
Keywords: Small-angle, Instrument, performance.

becomes cumbersome and at times a great challenge to the scientists dealing with systems which may be either very delicate or very difficult for exact reproduction of both the sample and its environment in order to repeat the experiments. TOF-SANS instruments at pulsed sources are more effective for the study of such systems as they produce data in a wide Q-range in a single measurement.

The SAND instrument was designed based on over 10 years experience of running the SAD instrument [1] at IPNS for the scientific user community. The main objectives were to extend the Q-range of SAND beyond that of SAD (0.005 to 0.25 $Å^{-1}$), increase ΔQ resolution and intensity, and improve ease of operation. The design aspects of SAND have been already published [2]. We have published the physics assessment of cryogenically cooled MgO crystals as a neutron filter [3] and a theoretical discussion of the design and use of a drum chopper for reducing the delayed neutron background and extending the usable wavelength range by the elimination of alternate frames [4]. The data reduction procedure used at SAND is exactly the same as that for the SAD instrument [1].

2. Overview

Here we give an overview of the present features of SAND and its performance. The SAND instrument was designed to measure data in a Q-range of 0.002 to 2 $Å^{-1}$ in a single measurement. In the present configuration SAND enables measurements in a Q region of 0.0035 to 0.5 A^{-1} and we anticipate that it will reach its design goal in the near future. The minimum and maximum Q values to be reached are

$$Q_{min}=2\pi\phi_{min}/\lambda_{max} \qquad (1)$$

$$Q_{max}=2\pi\phi_{max}/\lambda_{min} \qquad (2)$$

In order to reach the smallest Q_{min} the SANS has to be measured at the lowest angle (ϕ_{min}) using neutrons with longest wavelength (λ_{max}). Similarly, the largest Q_{max} is accomplished by measuring data at the largest angle (ϕ_{max}) using the shortest wavelength (λ_{min}).

Fig.1 depicts the SAND instrument schematic and Table I presents the relevant instrument parameters. SAND has the same length as SAD and views the same cold source. However, it has a larger sample-to-detector distance, an optical alignment system, a larger area detector, a high-angle detector bank, a chopper to reduce the delayed neutron background, a better cryogenic cooler for the MgO filter, and a number of upgrades to control the sample environment.

At IPNS neutrons in 30 Hz pulses are produced by spallation in a depleted uranium target by 450 MeV protons (0.3 μsec duration) with a time-averaged proton current of 15 μA. A solid methane moderator at 24 K in a 0.7 l aluminum container grooved on the viewed side to increase the cold neutron flux thermalises high-energy neutrons. This moderator has been designed to maximize the cold neutron flux while preserving a narrow pulse width at each wavelength. Graphite and beryllium reflectors decoupled by a 0.5 mm layer of cadmium surround the moderator. Significant fast neutrons and γ-rays exist in the

prompt beam spectrum, and if not attenuated cause detector recovery effects that can persist to long times-of-flight.

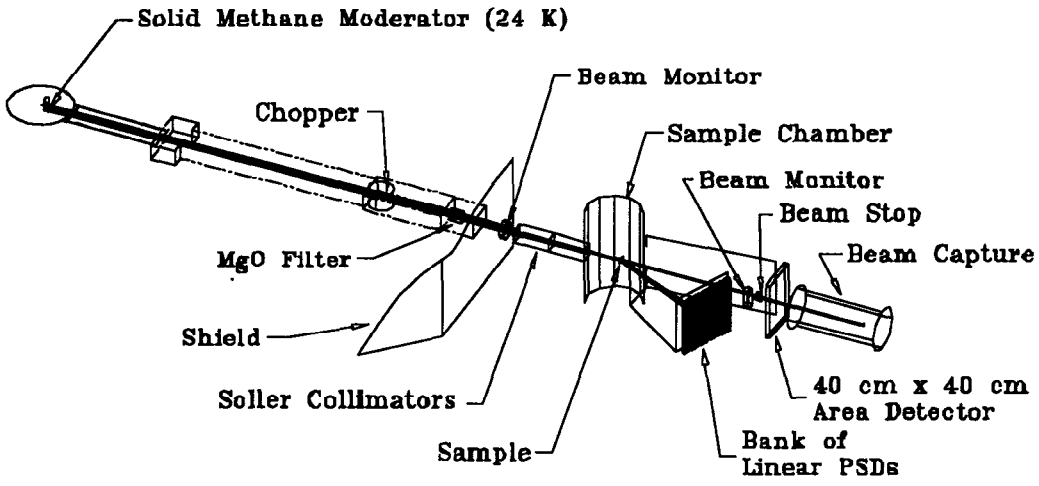

Figure 1. Schematic of TOF-SANS instrument, SAND at IPNS.

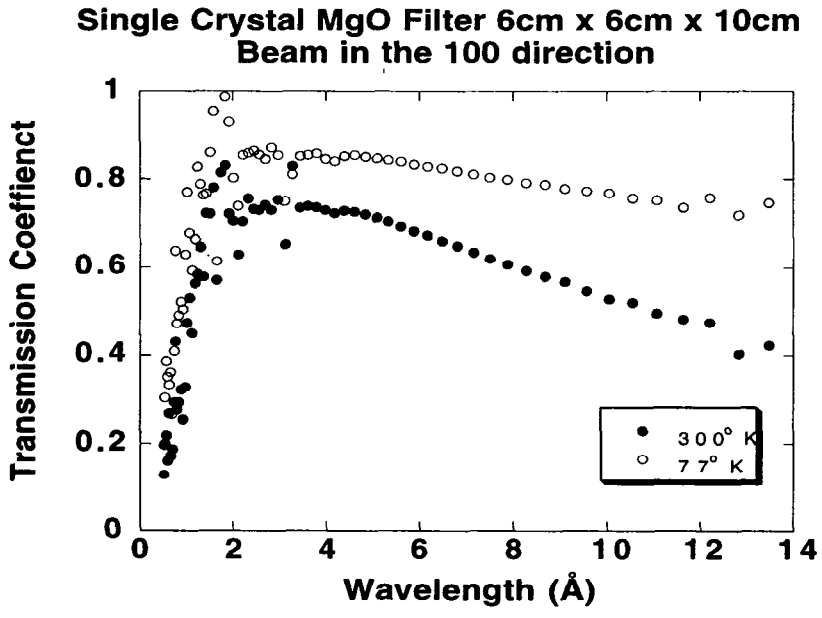

Figure 2. Measured Transmission coefficients of MgO filter.

Table 1. Instrument Parameters of SAND

Parameter	Value
Source frequency	30 Hz
Moderator	decoupled Solid CH_4 at 24 K
Source-to-sample distance	7.00 m
Source-to-beam monitor (M1)	5.65 m
Source-to-Transmitted beam monitor(M2)	8.65 m
Sample-to-area detector distance	2.00 m
Sample-to-LPSD distance	1.524 m
Focusing collimators	
Coarse	0.0034 radians fwhm
Fine	0.0014 radians fwhm
Vertical focusing collimator	
Entrance width / channel	0.1 cm
exit width / channel	0.0894 cm
Collimator exit-sample distance	77 cm
length	32.8 cm
Horizontal focusing collimator	
Entrance width / channel	0.0844 cm
exit width / channel	0.0767 cm
Collimator exit-sample distance	50 cm
length	25 cm
Beam diameter at moderator	9.0 cm
Maximum Beam diameter at sample	2.0 cm
Beam diameter at area detector	2.1 cm
Area detector	
active volume	40 x 40 cm^2, 2.5 cm thick
Fill gas	2.6 atm ^3He & 0.8 atm (95% Xe+5% CO_2)
Resolution	6-8 mm fwhm
Encoding	rise time, 128 x 128 pixels
max scattering angle	9°
LPSD	
active volume per detector	1.1 cm dia x 60 cm long
number of detectors	65
resolution	1-2 cm along detector
fill gas	~6 atm ^3He
encoding	charge division, 64 segments / detector
max scattering angle	36°
Wavelength range	0.5 - 14 Å (68 channels const $\Delta T/T=0.05$)
$\mathbf{Q_{max}}$	2 $Å^{-1}$

A cryogenically cooled (77 K) MgO filter arranged to have a cross section of 6 cm x 6 cm and a length of 10 cm is employed as a filter. This consists of 27 crystals of dimensions 2 cm x 2 cm x 2 cm and 32 crystals of dimensions 1.5 cm x 1.5 cm x 2 cm.

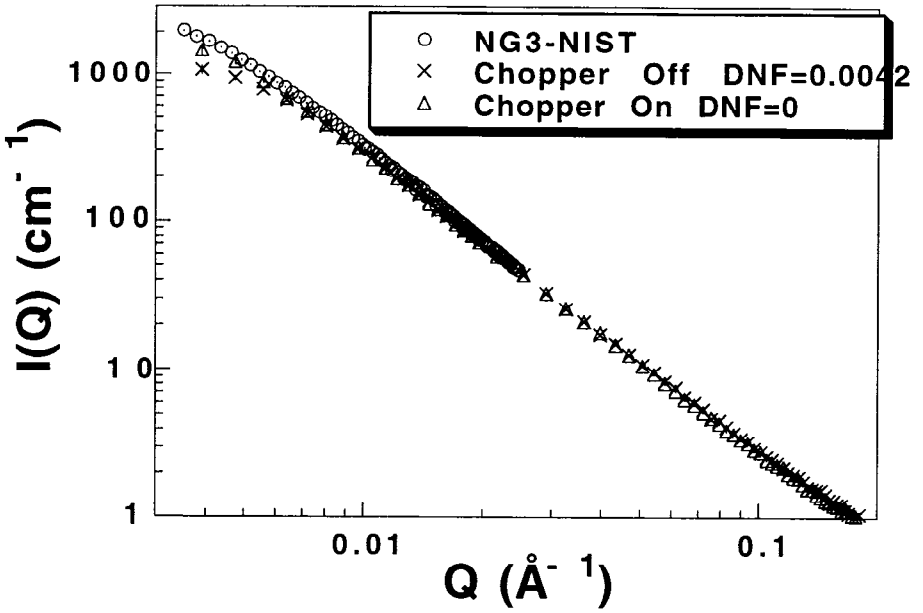

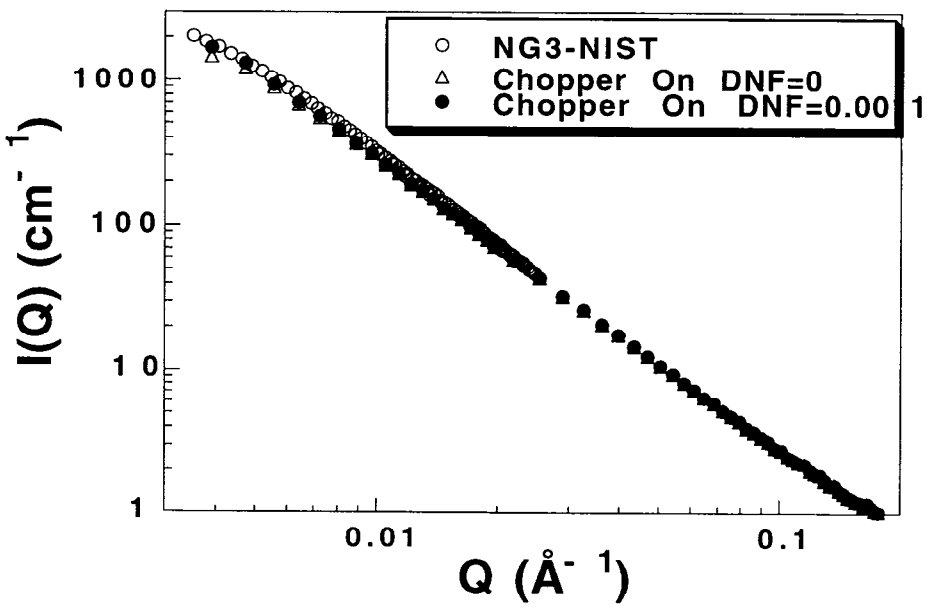

Figure 3. Comparison of the low Q data of Bates-poly with and without the Delayed Neutron Chopper.

We recently showed that MgO is the best choice for attenuating the fast neutrons while still achieving the best transmission of cold neutrons [3]. The measured transmission coefficients of this filter at ambient and 77 K are shown in Fig. 2. The use of the MgO filter, however, limits the usable λ_{min} to 1 Å.

The depleted uranium target produces delayed neutrons that arrive at the detector at all times. This produces a sample-dependent background that has to be corrected [5]. The effects due to delayed neutrons are very high for the samples rich in hydrogen. One can employ software techniques [1,5] to correct for the effects due to delayed neutrons. However, a chopper can nearly eliminate the background coming into the long wavelength channels that produce data in the low Q region. We have shown that a ~ 18.5 cm diameter drum chopper with a ~ 1 cm thick B_4C shell as the absorber, operated at 15 Hz (open twice per revolution) can serve this function [4]. Reducing the background by the chopper produces higher quality data in the low Q region than just the software correction. This is illustrated in Fig. 3 where we compare the data for the Bates-poly standard with the measured absolute differential scattering cross-section at the NG3-SANS at NIST. It is clearly seen that the SAND data measured with the chopper with no correction agrees better with the NIST data than that corrected by using just the software. Using software correction for the residual delayed neutrons further improves agreement.

The usable λ_{max} at SAND is restricted to 14 Å by the source frequency of 30 Hz at IPNS and the 9 m the source-to-detector distance. Currently, SAND produces data in the Q region of 0.0035 to 0.5 $Å^{-1}$. This already surpasses the Q-range and the quality of the data produced by SAD. The SANS data for the Bates-poly standard measured at SAD and SAND for 30 minutes are shown in Fig. 4. It is clearly seen that the data from SAND extends both ends of the Q-range of SAD. Furthermore, the statistical precision of the SAND data is higher than that of SAD in a Q region of 0.08 to 0.25 $Å^{-1}$.

The background in the low Q region is higher at SAND than that at SAD. Since this effectively limits the Q_{min} for the weak scatterers, systematic investigations are underway to determine the source of this background. Even though this background differs from the anisotropic background produced by the previously used Soller collimators at SAD [6], we cannot rule out Soller collimators at SAND as a source.

We plan to extend this lower Q_{min} value by increasing the λ_{max} of the neutrons and tightening the collimation. Since the solid methane moderator produces a significant flux of long wavelength neutrons, the chopper can be used as a frame-elimination chopper [4]

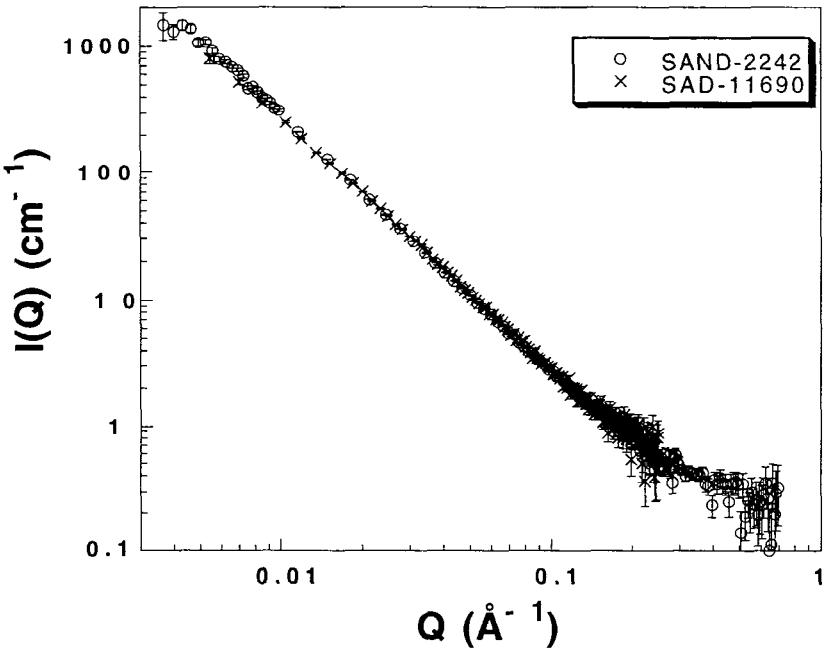

Figure 4. Comparison of SANS data for Bates-poly measured at SAD and SAND.

to extend the λ_{max} at SAND. As neutrons of different wavelengths travel with different velocities, the short-wavelength neutrons arising from one source pulse can arrive at the detector at the same time as the slower, long wavelength arising from a previous pulse. This overlap of neutron pulses in the detector, known as frame overlap, imposes an effective upper limit of 14 Å on the range of wavelengths that can be used, limiting the

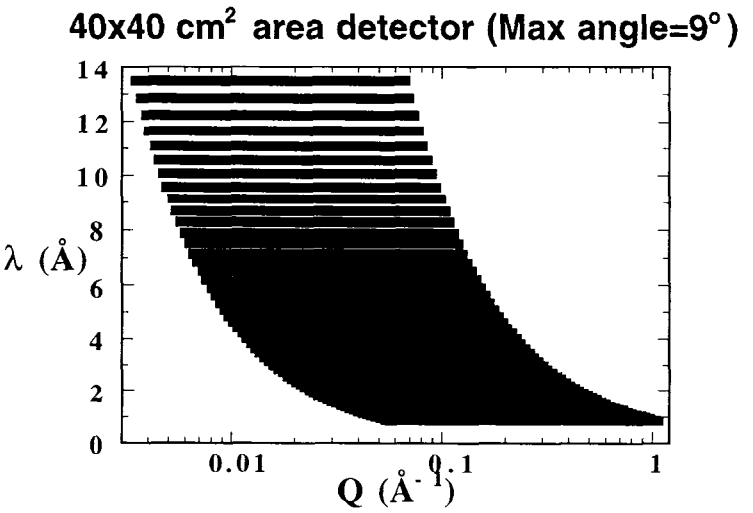

Figure 5. The Q-range at different wavelengths at SAND.

Q_{min} that can be reached. However, if the chopper revolves at 7.5 Hz so that the beam is opened at 15 Hz, the chopper blocks every second pulse. By increasing the separation in time between neutron pulses, the upper limit on the useable wavelength can be increased to 28 Å, and that will decrease the Q_{min} value by half. At the same time, the chopper continues to remove a substantial fraction of the delayed neutrons from the beam. At present we are working to stabilize the phasing between the chopper and the neutron pulses so that the chopper can run at 7.5 Hz as well as at the current 15 Hz. In addition we plan to employ high resolution Soller collimators and a high resolution 40 x 40 cm^2 area sensitive proportional counter to extend the Q_{min} to 0.002 $Å^{-1}$ using λ_{max} = 14 Å.

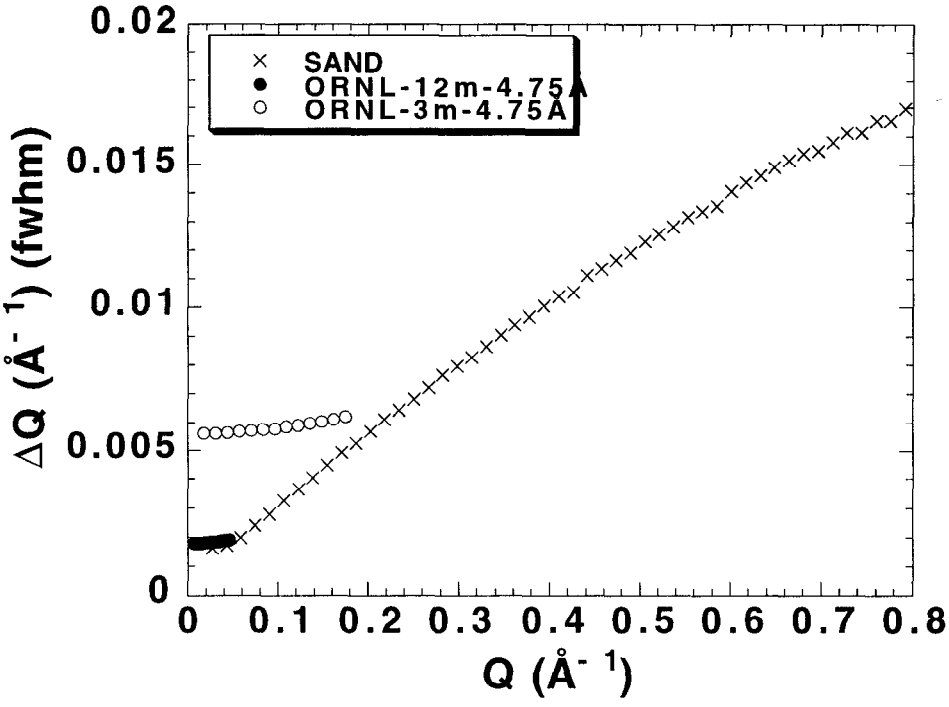

Figure 6. The Q resolution of SAND and the SANS instrument at ORNL.

To extend the Q_{max} to higher values we have already installed a bank of linear position sensitive detectors. Implementation to produce data in the higher Q region is in progress. We have shown the Q-range accessed by the 40 x 40 cm^2 area detector at different wavelengths in Fig. 5. The maximum scattering angle subtended by the high-angle bank of detectors will increase from 9° to 36°, not only extending the Q-range on the high Q side but also improving the quality of the data in the whole Q region. In the low Q region the ΔQ resolution of SAND is comparable to that at the reactor-based instruments, while at the higher Q region the resolution of SAND is superior (see Fig. 6).

SAND has a variety of ancillary equipment such as furnaces, a sample changer, a pressure cell, and a shear cell (Table II) for controlling the sample environment.

Table II. Ancillary Equipment Available at SAND

Equipment	Environment	Temperature Range
10 Position Sample Changer (circulating bath)	Ambient, Nitrogen Purge	10 – 90°C
Resistance Heater	Ambient, Coarse vacuum, Nitrogen Purge	30 - 250°C
1 - 60 rps Shear Cell	Ambient	10 - 90°C
Furnace (under development)	Vacuum	100 - 1700°C
Displex	High vacuum	5 - 300 K
Sample Stretcher (elastomer films)	Ambient	Ambient
Sample Rotator (slurry, suspensions)	Ambient, Nitrogen purge	Ambient
Pressure Cell (liquid samples)	1-2500 bars	0 – 80°C
Magnet	5 to 10 K Gauss	

3. Standard Samples

In our previous paper [1] we have shown that the quality of the SANS data from SAD is comparable to that from the reactor-based SANS instruments. When the data are measured in a wide Q region, the experiment times are comparable even with the high-power reactor-based instruments. SAND surpasses SAD in both the Q-range and in the statistical precision of the data. In order to show that the quality of the data from SAND is comparable to that from the reactor-based SANS instruments, we have shown data for the Bates-poly standard in Fig.4 and for the vycor glass sample in Fig. 7. As can be

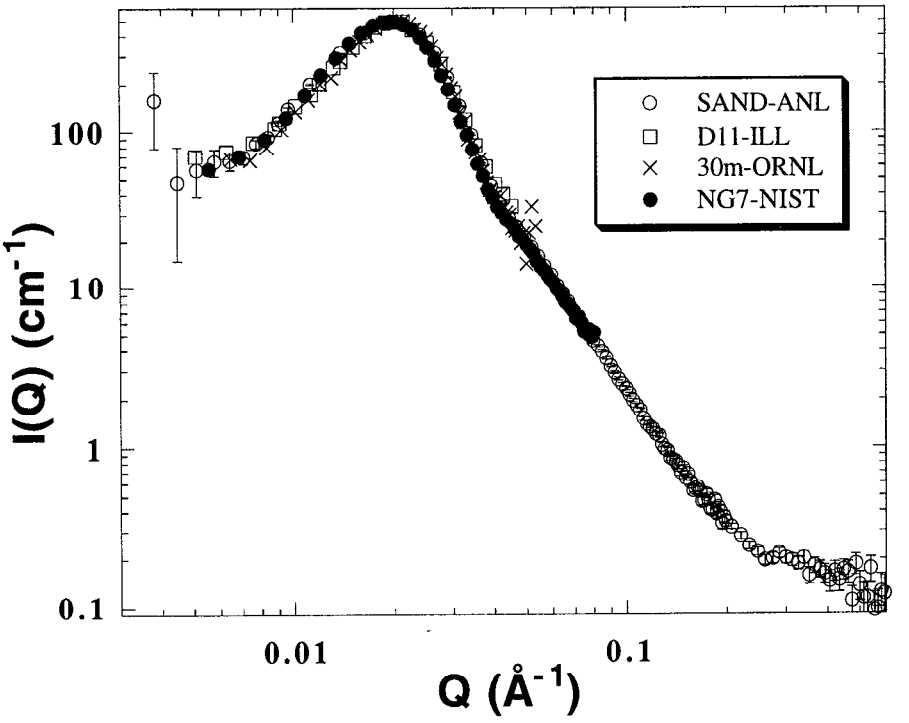

Figure 7. SANS data measured at various centers for Vycor glass.

seen from the figures, the data measured at reactor-based SANS instruments at two settings cover only approximately half of the Q-range covered by SAND in a single measurement. Moreover, scattering data in a wide Q region is required to properly characterize the nanostructure of the pores and their spatial correlation in this type of glass.

4. Scientific Examples

The wide Q region available at SAND in a single measurement is very important for a number of problems, especially for studies involving systems that may change as a function of time and other experimental conditions. This is especially true for studying samples at extreme conditions such as high temperature, pressure and shear. Here we give two examples that took advantage of the Q-range accessed by SAND.

4.1. Stability of Chaperonin from *S. shibatae*

The first system deals with the structure of a supramolecular protein complex of the major heat shock protein from *S. shibatae* [7] at different temperatures as a function of cofactors ATP and Mg. In this organism the chaperonin proteins, with MW of about 57

kD, self-assemble to form a 18-mer supramolecular complex which resembles a double-doughnut structure. SANS study of a similar system from *E. coli* has clearly shown that the double-doughnut structure produces peaks in the scattering data [8]. The self-assembled supramolecular protein structure from *S. shibatae* also produces several secondary peaks in the SANS pattern as in Fig. 8. If the protein monomers formed random aggregates, they would not produce such secondary peaks. The 18-mer complex is believed to provide protection to the organism's other proteins that may denature under stress such as high temperature. According to biochemical studies, the self-assembly process as well as the stability of the 18-mer complex depends on the presence of ATP and Mg. In the absence of ATP and Mg the complex aggregates at elevated temperatures. Elucidating the structural features that evolve at different temperatures as a function of cofactors will require data in a wide Q region. The low Q data is essential to determine the molecular weight of the complex as well as to determine whether any larger

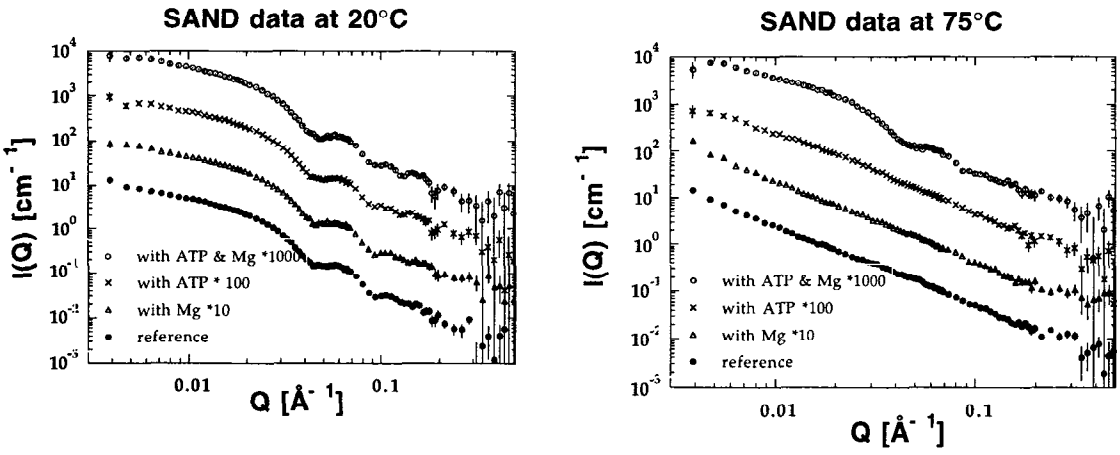

Figure 8. SANS of Chaperonin from *S. shibatae* in D_2O from SAND.

complexes are formed. The high Q data (secondary peaks) is required to infer the presence and stability of the 18-mer complex. This complex system thus requires data in a wide Q region, preferably measured in a single measurement as these are delicate and may slowly change with time even during storage. To elucidate the structural features in this system we measured the protein samples in D_2O solution at different temperatures at SAND. In Fig.8 we have shown the data at 20°C and 75°C. The presence of the18-mer complex is clearly seen at all conditions at 20°C. However, at 75°C the complex is stable only in the presence of both ATP and Mg. In the absence of either of those cofactors the proteins seem to form tubules through end-to-end association. Since Q_{min} at SAND is

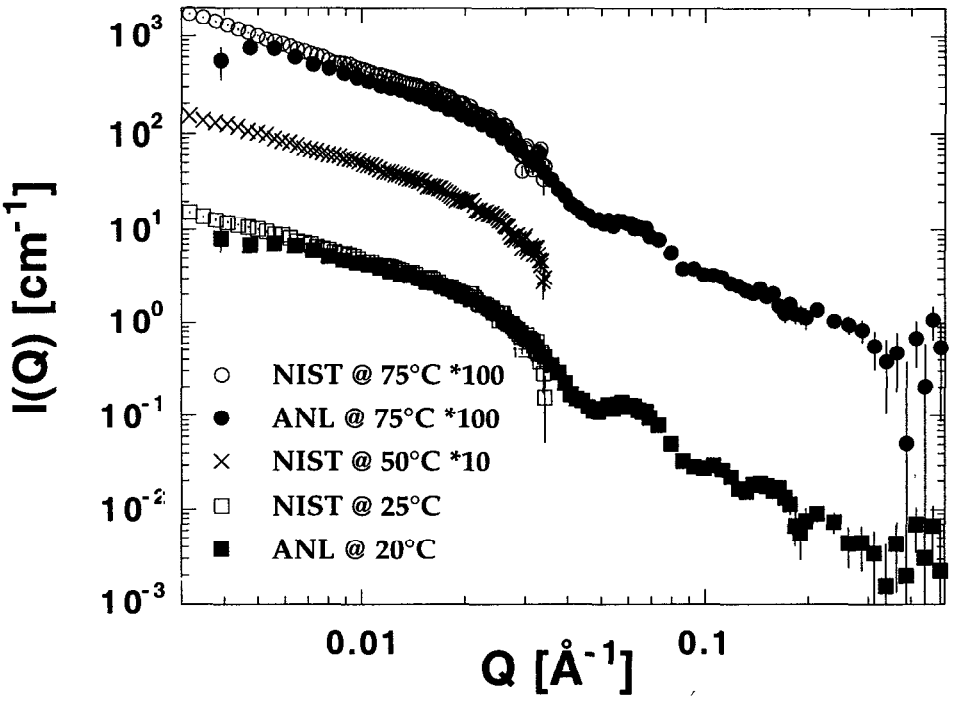

Figure 9. SANS of chaperonin from *S. shibatae*+ATP+Mg in solution at different temperatures from SAND at ANL and NG3 at NIST.

limited, we measured this system in the low Q region at the SANS instrument at NIST. In Fig. 9 we have compared the NIST data with that from SAND. The data sets agree well in regions where data overlap. The low Q data from NIST indicate that the particles are quite larger; however, the Q-range spanned in a single measurement at NG3-SANS is insufficient to determine whether the particles are indeed polymers of the 18-mer complex or precipitates. On the other hand, the Q_{min} at SAND is inadequate for the complete characterization of the system. The best situation would be to have a TOF-SANS instrument that can cover a wide Q region of 0.002 to 2 Å^{-1} in a single measurement. We plan to improve SAND to accomplish that.

4.2 Environmentally Responsive Gels

Our second example is environmentally responsive gel samples provided by Prof. S. Gehrke, University of Cincinnati. We measured hydrogels of hydroxypropyl cellulose (HPC) and poly(N-isopropylacrylamide) (PNIPAAm) in D_2O that undergo similar shrinking when heated above their respective transition temperatures, but exhibit quite different permeabilities [9]. This suggests that the internal structure of the collapsed state of HPC hydrogel is quite different from that of PNIPAAm gels. Understanding this highly unusual behavior is of significant practical and fundamental importance, as gels

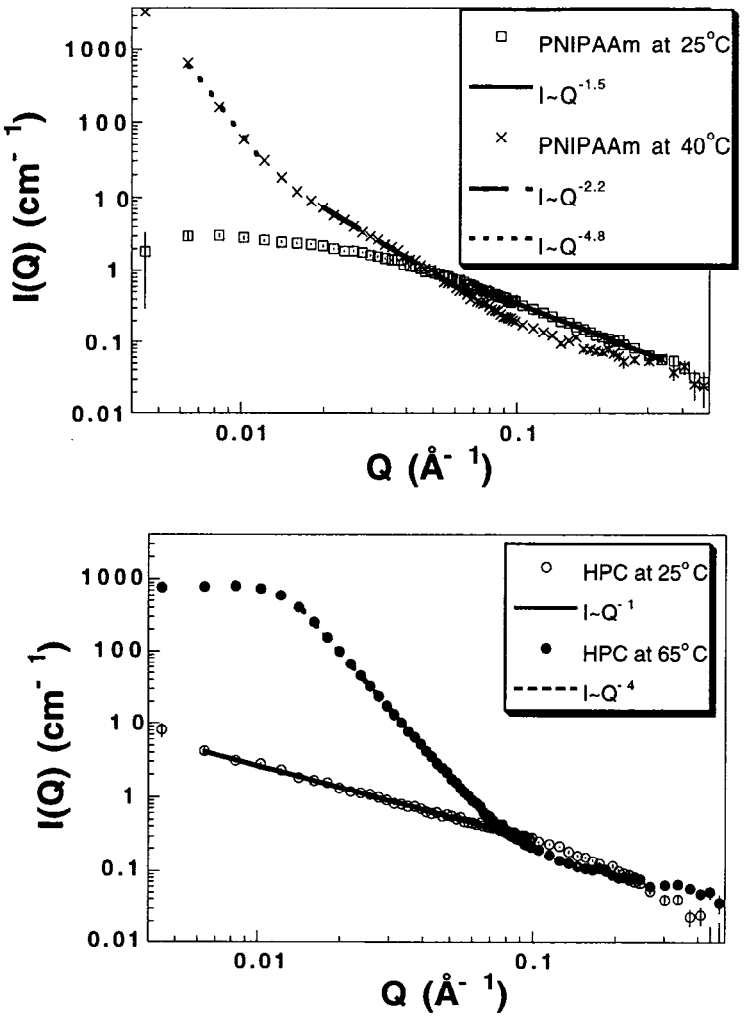

Figure 10. SANS data and suggested structure of PNIPAAm and HPC hydrogel at room temperature and above their respective transition temperatures.

are widely used in separation media and biomedical applications, e.g. chromatography, gel electrophoresis, artificial organs, and drug delivery. The wide Q-range monitored in a single experiment on SAND was very important for this study because the shrinking process follows complicated kinetics, and it was not clear from the beginning on what length scales the most dramatic structural differences would be observed. Our experimental data (Fig. 10) illustrate that this problem requires data in a wide Q-range in a single measurement.

The SANS from PNIPAAm at 25°C shows a power law scattering of $Q^{-1.5}$ and a plateau region at lower Q. We observe the scattering of network strands that are not fully stretched (Q^{-1}) but rather follow the self-avoiding path of linear polymers in a good solvent ($Q^{-5/3}$). At $Q < 0.05$ Å^{-1} the network strand correlation vanishes, as the observed length scale exceeds the network mesh size and the gel appears homogenous. Upon

heating above its transition temperature, PNIPAAm reveals a gradual change of structure in the high Q data. The observed exponent close to -2 suggests a random coil structure of network strands. We believe that D_2O is trapped in the network, giving rise to the huge increase in scattering intensity at $Q < 0.01$ Å^{-1}. The large exponent of -4.8 in the power law scattering indicates a diffuse surface of the solvent filled cavities, which is very likely due to a swelling gradient across the D_2O/collapsed-gel interface. The scattering patterns of HPC are very different. At room temperature stretched network strands (Q^{-1}) are observed. Upon heating above its transition temperature, HPC forms 3-dimensional objects with smooth surface (Q^{-4}). Since the collapsed hydrogel contains comparable volumes of HPC and D_2O, it is difficult to conclude further on the nature of these objects, i.e. whether we see HPC agglomerates in D_2O or D_2O-filled pores in HPC matrix or a mix of both. A more thorough analysis is in progress.

5. Summary

The performance of the SAND instrument is comparable to that of reactor-based instruments over the full range of Q available. Measurements of scattering by standard samples at SAND have demonstrated that data measured at SAND is similar in quality to that measured in comparable times at instruments at the most powerful research reactors. Furthermore, the ΔQ resolution of the SAND instrument is the same or better than that of the reactor-based instruments. Work is currently underway to improve the versatility and ease of operation and the quality of the data measured with SAND. The new high-angle bank of linear position-sensitive detectors will increase the maximum Q accessible to 2 Å^{-1} and increase the quality of data in the high Q region. Similarly, the range and quality of the data measured at low Q will be improved through the installation of finer focussing soller collimators and a higher resolution area detector and through the implementation of a frame-elimination mode for the delayed-neutron chopper. The wide Q-range accessible in a single measurement allows for the simultaneous measurement of local structure, molecular weight, and aggregation of subunits from a single sample. This is a great advantage for parametric studies and measurements involving delicate systems or samples that are annealing, organizing, or otherwise evolving in time.

Acknowledgment

The authors acknowledge the valuable contributions of Dr. J. E. Epperson and R. Kleb in the design and building of SAND instrument. We also thank our collaborators Dr. Joachimiak, CMB Division, Argonne National Laboratory, and Dr. S. Gehrke, University of Cincinnati, for permitting us to use the data in the scientific examples.

References

[1] P. Thiyagarajan, J. E. Epperson, R. K. Crawford, J. M. Carpenter, T.E. Klippert and D. G. Wozniak, The Time-of-Flight Small Angle Neutron Diffractometer (SAD) at IPNS, Argonne National Laboratory, *J. Appl. Cryst*, , 30, 280-293, 1997.

[2] R. K. Crawford, P. Thiyagarajan, J. E. Epperson, F. Trouw, R. Kleb, D. Wozniak and D. Leach, The New Small-Angle Diffractometer SAND at IPNS. *Proc. 13th International Collaboration on Advanced Neutron Sources, Switzerland,* October 11-14, 1995, *PSI-Proc* 95-02, 99-117, 1996.

[3] P. Thiyagarajan, D. Mildner and R.K. Crawford, Neutron Transmission of a Single Crystal Mgo Filter J. Apply. Cryst, 1998 (In Press).

[4] R. K. Crawford, J. E. Epperson, P. Thiyagarajan and J. M. Carpenter, Analysis of a Drum Chopper for Use on a New Small Angle Diffractometer at IPNS. Proc. ICANS-XI 873-889, 1990.

[5] J. E. Epperson, J. M. Carpenter, P. Thiyagarajan, and B. Heuser, Measurement of the Delayed Neutron Fraction and Correction of Small Angle Scattering Data from a Pulsed Spallation Source for This Effect, Nuclear Instruments and Methods A289, 30-34, 1990.

[6] R.K. Crawford, J.E. Epperson and P. Thiyagarajan, Soller Collimators for Small-Angle Neutron Scattering, Inst. Phys. Ccof. Ser. (97) 419-426, 1989.

[7] B.M. Phipps et al., Structure of a molecular chaperone from a thermophiclic archaebacterium, Nature, 361, 475-477, 1993.

[8] P. Thiyagarajan, S.J. Henderson and A. Joachimiak, Solution structures of GroEL and its complex with rhodanese from small-angle neutron scattering, Structure 4, 79-88, 1996.

[9] S. Gehrke in Responsive Gels: Volume Transitions II, 81-144, Springer-Verlag, Berlin, New York, 1993.

WORKING GROUP REPORTS

ICANS XIV
June 14-19, 1998
Starved Rock Lodge
Utica, IL, USA

Working Group on Monte Carlo Simulation of Neutron Scattering Instruments

R. K. Crawford

This working group session can be regarded as the second in a series of meetings aimed at establishing an international collaboration to develop improved Monte Carlo neutron tracking software for neutron scattering instrument simulation. The first meeting in this series was a workshop held at Argonne National Laboratory November 13-14, 1997.[1]

Many of us have developed Monte Carlo software to solve specific problems in the past. However, now we are beginning to need much more sophisticated software, capable of realistically tracking neutrons through an instrument from moderator to detector while including the possibilities that a variety of low- to high-probability events will occur along the way. Uses envisioned for such software include instrument design and optimization, experiment design, data analysis, diagnosis of problems in experimental data or instrument performance, and training of users. A very large amount of effort is required to develop such broad software capabilities, and it no longer makes sense for any one laboratory to try to do it all by themselves. This realization is driving the current effort to establish a collaborative mode for the development of such software.

Issues addressed at this ICANS working group meeting included the setting of standards for such software, providing centralized support for software maintenance and for communications among the collaborators, validation of the software, and funding for this process. A particularly useful feature was the participation at this session of people involved in source calculations. This enabled exchange of information to help define the source calculations needed and the nature of the interface between the source calculations and the instrument simulations.

Standards

The first major set of issues that need to be addressed is the development of standards. Of highest priority is to define the architecture for this software, and to identify at what levels within this architecture collaboration is to occur. We can envision four different layers to this software:

- The physics modules that describe the neutron source or the interaction of the neutron with a given component on the instrument
- The geometry of the instrument including the position and orientation of the different components, surfaces, and regions, and the materials involved in each
- The actual Monte Carlo calculation engine that moves the neutron between components, handles statistics, enables the saving of histories to identify the sources for problems, etc.
- The user interface that allows definition of the instrument, control of the simulation, and visualization of the output.

Standards for each of these layers and for the interfaces between them will define the architecture. At the moment there is some disagreement concerning the architecture that is appropriate. Resolution of this disagreement and definition of the architecture standards is required before most other collaboration activities can proceed, and is of the highest priority. The goal is to define a preliminary set of standards, at least for the architecture, by September 30, 1998. This is addressed in the action items below.

It is envisioned that a primary role of this collaboration will be to develop the physics modules for the components. This lends itself well to a division of labor according to the components of greatest interest at each of the different laboratories. Development of these modules at several different laboratories requires the establishment of standards and standard templates for such modules and for how the geometry and coordinate systems will be handled. Such modules should include documentation, and should be self-describing so they can be properly

integrated with the other layers of the software. Standards for the calculational and visualization layers will enable different versions of these to be developed at different laboratories as the need arises. These standards should make it possible for any new visualization or calculational software to work with previously created physics modules.

Maintenance

An immediate need is for an improved means of sharing information among the persons interested in collaborating on this project. ANL agreed to set up a web page for this purpose, and the meeting also generated a mailing list of additional persons interested in being kept informed. The complete mailing list will be posted on the web page. A centralized repository for validated code and for the currently approved standards will need to be established. Centralized tracking of the status of development and validation will be important. Management of the process for code and standards approval requires some central authority. In some of the proposed architectures, one or more layers of the software will be maintained and run on a central web server rather than on the users' client systems. All of these activities require the definition of a process and the identification of some group to assume the responsibility.

A model that was suggested for this centralized operation was that of a "journal", with an individual code module corresponding to an article being submitted by a particular author. The central organization would serve as "editorial board" to send each submitted module to "reviewers" for testing. When the module was accepted, it would then be added to the centralized repository. This model seemed to the group to make sense, but it needs wider circulation and discussion before being adopted. Groups to assume each of these activities for the collaborative project have not yet been identified. LANL is currently providing some of these services for the Monte Carlo software they have been developing.

Validation

Most of the existing Monte Carlo codes have not been benchmarked against existing data. There is a need to perform and document such validation both for existing codes and for newly developed modules. Both the individual modules and the integrated software packages need to be validated. To assist in this process measured data needs to be assembled for several "standard" instruments. This information should include a complete description of the geometry and materials comprising an existing instrument, similar information for one or more samples measured on this instrument, and files of data resulting from these measurements for each sample.

Resources and Funding

In the U.S. there are at present three groups funded for development of Monte Carlo instrumentation simulation software. These are groups at LANL, ORNL, and ORNL scientists working at ANL on the SNS project. Other U.S. laboratories also work on Monte Carlo codes, mostly on an ad hoc basis, and any such development in the future could probably be designed to conform to the collaborative standards with little difficulty. In Europe, the ESS project will provide some activity in this area, and other laboratories continue to develop their own codes as the need arises. In Japan both KEK and JAERI are interested in the development of such codes, but have not yet started any serious activity on this. The potential exists to funnel significant resources into this collaboration if the necessary standards and procedures can be put in place. In particular, the SNS project has expressed the intent to devote a significant amount of effort over the next six years to develop Monte Carlo software and the ESS project also expects increased levels of effort in this area.

A means must still be found to fund the central maintenance activities discussed above. Charging a subscription fee to the collaborating laboratories was discussed as one possible mechanism. The submission of a proposal to external funding agencies was also suggested. When the level of centralized activity that must be supported becomes better defined, it may also be possible that this activity could be sustained by funds available within one or more of the collaborating laboratories and projects. All of these routes should be explored.

Status

At the Monte Carlo workshop last Fall an international advisory committee was established to set up the framework for the collaboration and to guide collaboration activities. Members of this committee were Kent

Crawford (ANL, chair), Ulrich Wildgruber (BNL), Luke Daemen (LANL), Lee Robertson (ORNL), Ian Anderson (ILL), and Mark Hagen (ISIS). At that time the absence of a committee member from Japan was noted, and it was agreed to add a representative from Japan as soon as practical. One concrete accomplishment of this working group session was to add Masatoshi Arai (KEK) to this advisory committee.

A second concrete accomplishment of this meeting was the agreement of ANL to set up a web page for the continued dissemination of information about this Monte Carlo collaboration. Participants in this working group session who wanted to be kept informed about the Monte Carlo project added their names to the Monte Carlo e-mail list, which also currently includes names of the attendees at last Fall's workshop. This mailing list will be used to notify people when the web page is operational.

A third concrete accomplishment was to agree to the set of action items outlined below.

Action Items

1. A meeting of representatives from ANL, ORNL, and LANL will be set up as soon as possible, preferably in July 1998, to resolve the philosophical differences concerning the architecture to be adopted for this collaboration and to define a preliminary standard for this architecture. Luke Daemen will take the lead in organizing this meeting.
2. A Monte Carlo web page will be set up at ANL. The Monte Carlo mailing list will be posted on this web page. Ken Herwig will take the lead on this.
3. A list of proposed standards for "non-controversial" items requiring standardization, such as format to be used for documentation (the working group recommended PDF), order of parameters used in subroutines, etc., will be circulated to those on the Monte Carlo e-mail list for approval. Luke Daemen will take the lead on this.
4. Additional meetings will be scheduled as needed to continue the development of other necessary standards and of the centralized management process. This awaits the outcome of item 1.

References

[1] "Report on the Workshop on Monte Carlo Simulation of Neutron Scattering Instrumentation", Argonne National Laboratory, November 13-14, 1997. SNS Technical Report ANL/SNS/97-2.

ICANS XIV
14th Meeting of the International Collaboration on
Advanced Neutron Sources
June 14-19, 1998
Starved Rock Lodge, Utica, IL

Report on the Workshop Group Meeting on: Next Generation Powder Diffractometers

Paolo G. Radaelli

ISIS Facility, Rutherford Appleton Laboratory, Chilton Didcot, Oxfordshire, OX11 0QX, UK

I. OUTLINE OF THE WORKSHOP

The workshop was held on Thursday, June 18 1998, and was attended by a small group of people (~8), representing US, European, Russian and Japanese facilities. The attendees were asked to work on the following list of questions:

- What are the most promising future scientific opportunities for neutron powder diffraction (NPD)?
- How can we extend the present, most successful NPD techniques, into the next century? Are there new techniques, or methods that were not very successful in the past and should be revisited?
- How can we link instrument types with scientific requirements? How have the present instruments designs come about?
- Can we come up with a short list of truly "novel" instruments?
- What technology do we need to make our ideas into real instruments?

II. SCIENTIFIC OPPORTUNITIES

A short discussion was held on the future scientific opportunities for NPD. It was agreed that a lengthy debate was not appropriate, since plenty of publications already exist on the subject. However, most of the participant felt that "physical" diffraction, "chemical" crystallography (including catalysis and in-situ reactions), materials science and engineering science will still represent the core applications of NPD. The issue of whether more "routine" industrial measurement capabilities (like drug structure determination and testing of real engineering components) should be offered was debated, but the reaction of the participants on this subject was rather negative. As far as the interaction between neutrons and other radiation sources (namely X-ray synchrotron) and techniques is concerned, the general opinion was that complementarity should be stressed over competition.

III. TECHNIQUES

In our opinion, structural refinement is by far the most successful NPD technique. There was general consensus on the fact that the primary direction to extend refinement techniques should be in the direction of greater speed. This will allow complex phase diagrams to be mapped in detail. Also, kinetic studies, including both stroboscopic studies of reversible phenomena and "single-pulse" measurements of irreversible processes, should become routine. Another extension of the technique should be in the direction of studying smaller samples, both for novel materials and for demanding special environments (e.g., diamond anvil cells). The Q-domain of the data should be extended: low-Q data are needed for magnetic diffraction and host-guest problems, areas in which pulsed sources should progressively become competitive with reactors. High-Q data are needed to study subtle defects, lattice anharmonicity and to study disorder. In this respect, it was remarked that reciprocal space and real-space data (Fourier-transformed) should become more complementary, not only for liquid and amorphous materials, but also for studying disorder and local effects in crystalline materials. Some of the "traditional" strengths of NPD, like isotopic substitutions, should be carried into the next century. Also, combined x-ray and neutron refinements should become more widespread.

The possibility of solving unknown small-molecule crystal structures on a routine basis was debated at length. Since pharmaceutical companies are among the potential users of this technique, this issue has a potentially large financial impact on neutron scattering in general. The majority of the participant felt that, as things stand, the likelihood of

successfully competing with or offering a useful complement to synchrotron-based techniques in this field is small. However, the scenario may change as new instruments are developed. On the contrary, there was general consensus on the fact that the majority of new instruments should incorporate some structural solution capabilities, especially to study new phases which can only be created "in-situ" and, in particular, metastable phases. The connection between this and the levitating sample techniques was underlined.

Among the other desirable extensions of NPD, the following were mentioned: i. Diffraction imaging; ii. Establishing a continuous link between powder and single-crystal diffraction (for textured samples, fibres, twinned crystals etc.); iii. Tackle inelasticity correction by measuring $S(Q_{elastic})$ as a function of wavelength; iv. Exploiting polarised neutrons and polarisation analysis; v. Develop extended Real-Space representations of the data (spherical harmonics, etc.).

The general consensus was that neutrons should not be used to test real industrial components before they are marketed, but should rather the efforts should be concentrated on engineering science (strain modelling, etc.). Also, ultra-high-resolution applications were not believed to be of particular interest.

IV. INSTRUMENT DESIGNS

The participants were asked to take a fresh look at the present instrument designs and their historical development. Most of the present designs were developed in the eighties, under a strict set of technological constraints. In particular, the lack of computing powder and disk storage space required a significant amount of electronic pre-processing (focusing) to be performed. Also, linear position-sensitive detectors were not as widely available as in the present days. Alternative instrument concepts were already envisaged in the eighties, but were not implemented. Clearly, the technological limitations have now changed, and this could have an impact of future instrument designs. Also, it was clearly indicated that the data produced by the new instruments should be easier to analyse even by the casual user. Therefore, the pulse-shape and geometrical aberrations should be minimised, even at the expense of some flux or of an increased detector cost.

The wisdom of maintaining a segmented detector structure, divided in several banks, was questioned by various speakers. A continuous detector design, with fine pixillation also along the polar coordinate, would allow the full three-dimensional structure of the data to be exploited. In this scenario, the user would be free to use all the data (e.g., for single-crystal or texture applications) or to chose the one-dimensional projection that best suits his/her needs (e.g., angle-dispersive data for magnetic structure determination and large structure refinements). The benefit of this approach to determine the most appropriate inelasticity corrections for disordered systems was also discussed. The difficulties connected with building such instruments were also debated. Having an appropriate collimation to reduce backgrounds was seen as a potential problem. Also, such concept would require the development of "expert" software codes that would help the user to visualise the data and make informed and timely choices.

The panellists were asked to propose one or more truly "novel" instrument concepts. It was agreed that many of the present-day instruments will still be valid in the future, but no need was felt to discuss them. The following "innovative" designs were suggested:

- Small-Sample Powder & Single crystal diffractometer. This instrument will have a 40-80m flight-path and could benefit from a high repetition rate from a cool or cold moderator. It would have a compact design and will be highly pixillated in all three dimensions. Its software should have very good visualisation, slicing and projection capabilities. Such and instrument would be suitable for powder and single crystals, crystallographic and magnetic structural solution, host-guest problems, texture and microstructural analysis.
- "Fast Neutron" diffractometer. This instrument will have a 20-30m flight-path, and should be designed for combination Real/Reciprocal space techniques applied to disordered materials, very high-Q Rietveld, Pair Distribution Functions, inelasticity corrections and anharmonicity studies.
- Polarised-neutron TOF diffractometer. It will benefit from a ^{3}He polarising filter for single-crystal studies. The development of fast spin nutators, in conjunction with a narrow wavelength bandwidth and polarisation analysis, will allow it to separate structural from magnetic scattering in powders.
- Time-Resolved Diffractometer. A dedicated instrument should be developed for time-resolved studies, with the aim of reaching single-pulse diffraction. This instrument will have a rather short flight-path, or, alternatively, focusing optics, and will work at high repetition rates.

A particular emphasis was placed on dedicated special-environment diffractometers, built around a single piece of equipment (e.g., high-pressure cells, pulsed magnets etc.). Also, it was agreed that the flexibility of all instruments should be enhanced by means of add-on focusing "snouts" or capillary devices. The possibility of building "combination" instruments (elastic + inelastic) was also discussed.

V. TECHNOLOGICAL REQUIREMENTS

The workshop was concluded with an extended discussion on the technological requirements of future NPD instruments.

- Targets. The distribution of NPD instruments between low- and high-repetition rate targets should be revised, since many of the proposed instruments would benefit from a high repetition rate.
- Moderators. There was unanimous consensus on the fact that a "good" pulse shape should be pursued, even at the expense of some flux. For example, this makes cold coupled moderators rather unattractive for NPD applications.
- Optics. The issue of vertical focusing versus polar angle detector coverage was briefly touched. A vertically-focused beam effectively saves on detector cost, and is more efficient for small samples where extreme resolution is not required, and at the other extreme, for very tall samples. However, it was felt that the possibility of having a "clean" unfocused beam should be preserved, and focusing should be an "add-on" option. Also, it was agreed that future guides for long-flight-path instruments should be straight, in order to preserve at least a fraction of the epithermal neutrons. The past concerns about fast and delayed neutron background have been overcome by the development of efficient T_0 (nimonic) choppers.
- Choppers. High-speed choppers should be developed, in order to allow efficient bandwidth tailoring at high-repetition-rates. Flexible and efficient chopper control systems should be developed, to allow ramping and "sliding" of the chopper phases.
- Electronics. It should be possible to de-couple the chopper time frame from the data time frame, for extended-Q data collection on a single data set.
- Detectors. The emphasis is on pixillation, mechanical flexibility, efficiency and stability.
- Polarisers. The present ^{3}He filters are perceived as not yet adequate for an efficient polarised-beam diffractometer, especially if the correlation technique is employed (see paper by G. Williams in these proceedings). In particular, the relaxation times should be extended beyond the present ~80 hrs. Also, fast spin flippers and nutators should be developed.
- General Software. Highly-pixillated instruments require powerful visualisation and data reduction codes, capable of helping the user to make timely decisions. This is even more crucial if the instrument is used to explore complex, multi-dimensional phase diagrams. The development of these codes should be given high priority and adequate funding. It was proposed that some of the expertise in the field on Monte Carlo instrument simulation should be transferred to this domain. The new codes should be interfaced with existing databases to allow, for example, fast phase identification.
- Rietveld Software. This obviously represents a crucial component in the NPD data analysis. It should be possible to routinely perform on-line Rietveld fits, as it is already the case for constant-wavelength data. The Rietveld method is being and should be further extended to more than one dimensions, for instance to analyse texture data, single-crystals and phase diagrams. The possibility of an international collaboration on the matter was suggested. Also, it was proposed that complex data could become "public" after a certain period of time, following the model of astronomical data.
- Measuring Strategies. The presently implemented single-user, multi-environment approach is still to be the main operation mode for powder instruments. The benefits of this approach, especially in terms of educational value for young researchers, were perceived to outweigh the potential gains in instrument performance obtainable form a multi-user, single environment mode, which could nevertheless be employed for some routine measurements. Also, the possibility of remote instrument operation ("Virtual Lab.") was briefly discussed, but it was felt that this technology is, at present, still ahead of its time.

ICANS-XIV
14th Meeting of the International Collaboration on
Advanced Neutron Sources
June 14–19, 1998
Starved Rock Lodge, Utica, Illinois, U.S.A.

REPORT OF THE WORKSHOP ON SMALL-ANGLE AND REFLECTOMETRY INSTRUMENTS ON FUTURE SPALLATION SOURCES

P.A. Seeger

This workshop was well attended, with 16 people participating. Most were more involved with small-angle scattering rather than with reflectometry, with the result that most of the discussions emphasized the need for a variety of small-angle capabilities. Furthermore, the discussions frequently assumed the scenario that we were specifying requirements for the initial suite and add-on instruments for SNS. This led to rather conservative requests, with some consideration of practicalities. The consensus was that the initial instruments on one of the new high-power sources should take full advantage of the increased flux, but with minimal technological risk and with only modest improvements of the design specifications compared to current instruments.

GENERAL statements relevant to both Reflectometry and Small-Angle

1. Backgrounds must be kept low, so that the increased count rate will also be an improvement in the signal-to-noise ratio. The use of T_0 choppers was assumed to keep the high-energy pulse away from the sample and detector areas, and the T_0 choppers themselves will have to be heavily shielded. This in itself will preclude the use of "short" flight paths.

2. Detector R&D is essential. We will not be able to handle the anticipated count rates with the detectors we are now using. High speed, low noise, and time stamping are essential. Reflectometers should plan to use 2D position-sensitive detectors for off specular and in-plane scattering. Future designs will require higher resolution (1 mm) than is now being used.

3. Sample areas must be large enough to accommodate a large variety of environment and ancillary equipment. At a minimum, there should be a space of 1 m along the beam direction, a width of 2 m transverse to the beam, and free height from floor to ceiling. It must be possible to work in this area with the neighboring beams on (shutter closed). This requirement and the shielding push the moderator-to-sample distance to at least 10 m.

4. Pulse rate should be 10 Hz. "Conventional" instrument designs that use the entire wavelength band in each pulse require a low repetition rate. This is especially true for the length of instrument (15–20 m) dictated by shielding at the high-power sources. If the pulse rate is any faster, then choppers will have to be used to limit the wavelength band, and the beam power will *not* be fully used.

REFLECTOMETER

1. Minimum reflectivity down to 10^{-7} or better, essentially equal to the best current instruments, must be guaranteed. This requires low background.

2. Horizontal surface geometry is required for the first reflectometer. In addition to liquid interfaces at one or a few fixed angles, a solid sample can be tilted to access higher or lower angles. No one present was aware of any requirements or advantages of vertical surfaces. If the pulse rate is faster than 30 Hz or so, then a "reactor" style instrument with variable beam angle should be considered.

3. Scanning with programmable slits becomes practical at the higher flux rates of the new sources. This is most useful if the entire pattern is measured at once, hence wants low pulse repetition rate.

4. Off-specular and in-plane scattering should be included. These measurements also require that backgrounds be kept low.

5. Today's Clever Idea from Jack: When doing reflectometry at a reactor with variable incident angles, the collimation slits may be adjusted at each setting. At a pulsed source, that can be accomplished by using dynamic slits with actuators driven in synchronization with the pulse in a preprogrammed pattern to optimize at each wavelength.

SMALL-ANGLE SCATTERING

A "utility" machine with $Q_{min} = 0.001$ Å^{-1} should be specified as the first instrument. The majority of users can be served with this minimum Q. With a moderator-to-sample distance of 10 m, pinhole collimation can be used. The collimation should begin inside the bulk shield. (This may require some R&D on radiation damage. The engineering and shielding people must become involved in the project early.)

Wide Q range, $Q_{max} = 10$ Å^{-1}, should be available on the same machine, for simultaneous measurements of phenomena at different length scales. There was considerable discussion about this, and the conclusion was that this feature must be exploited to take full advantage of pulsed sources. In particular, measuring reaction kinetics requires that the entire Q range is determined in a single setting. Several problems must be considered. Low backgrounds are essential, and the method will work best for samples with low incoherent scattering. A moveable detector provides a selection of dynamic ranges (not the full range at once), but covers the situation of the interesting region falling between two detector banks. If wide-angle detector banks are used, the optimum sample geometry is cylindrical instead of flat samples. If the wavelength band is used to extend the Q range, then the sample thickness appropriate for short wavelengths produces too much multiple scattering at long wavelengths. Dynamic slits should be investigated here also.

VLQD. Very-Low-Q Diffractometers should be considered for the second tiers of instruments at the new sources. Perhaps because several in the group are involved with designing an instrument with an ellipsoidal mirror, or perhaps because that is the best idea now available for a VLQD, such an instrument was proposed (see article by Hjelm *et al.* in these proceedings). The time scale allows for the considerable R&D effort needed to learn how to fabricate the mirror.

ICANS XIV
14th Meeting of the International Collaboration on
Advanced Neutron Sources
June 14-19, 1998
Starved Rock Lodge, Utica, IL

ICANS-XIV : Working Group Report

Critical Heat Flux : Limitation to Solid Target ?

Organiser : Y. Takeda / PSI

Scope and aims :
Heat transfer limit is one of the key issues which limit the use of solid target in high power beam neutron source. It has been often spoken about and considered in setting up a concept of liquid metal target. It has however never been discussed about this limitation in scientific and technological manner based on experimental data. The aim of this session is to collect the results of the recent experimental efforts in the world which investigate a critical heat flux (CHF) of a thin plate with a very narrow gap of cooling channel, and to discuss and find a limitation of solid target from heat transfer view point.

Presentations :
Takeda (PSI) gave an introductory remark on the various boiling regime and its relevance to the heat transfer in terms of boiling curve. He explained the definitions of critical heat transfer (CHF), departure from nucleate boiling (DNB) and burn-out point. He emphasised that the pattern of boiling curve is strongly dependent on geometry, flow condition, system pressure etc. and one has to be careful in using the data from other sources.

Mishima (KUR) presented the experimental data on the CHF for the thin plate with a 2 mm gap for cooling water with respect to flow rate. The data on CHF was compared with existing correlation curves by Burgles and Dittus-Boelter. He estimated target temperature vs. beam power.

Hino (JAERI) introduced their experimental data of the rectangular channel for plate target configuration with a bypass to simulate multiple channel flow. He showed the CHF against mass velocity, gap distance, influence of inlet temperature and heated length. The Influence of flow excursion, which may arise by being affected from other channels in parallel, was also reported.

Pitcher (LANL) read a paper about the work done for the APT target, where the target geometry is rod bundle and the inlet flow is two-phase. They investigated CHF with respect to inlet flow mass flux and beam power. It showed that a flow instability is quite important which occurs prior to DNB. The onset of flow instability (OFI) depends strongly on the liquid quality (dissolved gas) and on a bypass flow once it happens.

Conclusion :
All of these studies made a comparison with the existing correlation curves and confirmed that those correlation curves can be used for evaluating a heat removal of the solid target. They raised the numbers for the maximum beam power to be limited as roughly 1 to 5 MW/m^2. But these values are strongly based on the system parameters, which are yet unjustified.

Following note would be a useful conclusion as a guideline for design concept :

ONB : Onset of Nucleate Boiling limits a beam power for a normal operation.
OFI : Onset of Flow Instability is a limit of normal operation for two-phase flow cooling.
CHF : Critical Heat Flux is a real limiting factor but under a certain accident scenario.

$$Q_{ONB} \leq Q_{CHF}/n \quad \text{where } n=1 \ldots 10$$

Important note is that the CHF (Q_{CHF}) is a limit value and cannot be adopted as a design value. The design value should be based on the Q_{ONB}, which is far smaller than these values.

ICANS-XIV
14th Meeting of the International Collaboration on Advanced Neutron Sources
June 14-19, 1998
Starved Rock Lodge, Utica, Illinois

Summary of the Objective Discussion of Solid and Liquid Targets for High-Power Sources

Noboru Watanabe[1] and Phillip Ferguson[2]

[1]Japan Atomic Energy Research Institute, Tokai-mura, Naka-gun, 319-1195, Japan
[2]Manuel Lujan, Jr., Neutron Scattering Center, Los Alamos National Laboratory, USA

The discussion of advantages and disadvantages of solid and liquid targets for 'high-power' sources started with the definition of 'high-power.' For 5 MW systems, there was a general agreement that a liquid target is necessary. Only when considering proton beam powers in an intermediate range is a choice between solid and liquid targets necessary. For this reason, the discussion was limited to beam powers between 0.6 MW and 1.5 MW, which includes many of the next-generation sources (the first stage of SNS and JAERI, as well as JHF, LPSS, etc.).

The two types of target systems were compared in six different areas: neutronic performance, thermo-hydraulics, structural aspects, materials considerations, radiation damage/target lifetime, and operational issues. From a neutronics point of view, fully engineered target systems should be compared. To date, comparisons have focused on changing target materials without regard to the peak proton current density for which the targets were designed. With no definitive calculations completed to date, the present state of knowledge would not select one target system over another solely on the basis of neutronic performance. From a thermo-hydraulics standpoint, both systems present some challenges that can probably be overcome with some effort. The issue of mercury wetting does not seem to be a problem as evidenced by data presented at this conference.

Structural issues are similar for the two types of target systems. When considering materials issues, fatigue tests are indispensable for evaluating solid clad target systems. For a liquid target system, study of Hg corrosion in a prototypic radiation field is necessary. Initial estimates indicate that, at 2 MW, a liquid Hg target may last twice as long as a solid target system (3 months vs. 6 months). However these estimates are just 'best guesses.' Materials irradiation studies should continue to build confidence in target lifetime estimates.

From an operations standpoint, the waste stream from a solid target system will be high due to the short target lifetime (roughly 3 months at 2 MW). In addition, a method of filtering Be-7 before it deposits in the target cooling loops is important for both target system, but particularly for a solid target system. R&D costs for a liquid target system are likely to be higher than for a solid target system, although the R&D cost for a solid target system will not be negligible (cladding materials and methods, verification of heat transfer coefficients for rod systems, etc.).

The conclusion of this discussion was a general agreement that solid and liquid target systems both have strengths and weaknesses for beam powers between 0.6 MW and 1.5 MW. Neither target system has a clear advantage over the other in this power range.

ICANS-XIV
14th meeting of the International Collaboration on Advanced Neutron Sources
June 14-19, 1998
Starved Rock Lodge and Conference Center
Utica, IL, USA

Summary Report for the Working Group "Needs for Target Systems and Instrument Materials, Beamline Components, Detectors, and Beamline Technology"

M. Furusaka
Neutron Science Laboratory (KENS),
High Energy Accelerator Research Organization (KEK), Tsukuba-shi 305, Japan

Abstract
A discussion is given of about the needs for components and systems which are critical for future spallation neutron sources, from the target systems down to the neutron detectors and data analysis software. We first describe the data logging requirements for the neutron generation system, which are crucial for the diagnosis of the system. For the moderator system, the role of the intensity distribution at the surface of the moderator is discussed. By properly designing a neutron flight path, with or without an appropriate optical device, which takes into account the moderator intensity distribution, we will be able to optimize the whole system more efficiently. Normally, a neutron flight-path will have several windows along it, which are one of the sources of background. Some of the many ways of improving this situation are discussed. Also a discussion about chopper systems is given, particularly the phasing problems. Detector development is a key issue to the success of the future spallation neutron sources. There have been continuing efforts to develop new kind of detector systems, other than He-gas based detector systems, which are widely used at current sources.

1. Data logging for neutron generation for the diagnostic purposes

The diagnostic information pertaining to a proton beamline, such as, the proton beam-current, profile, and position, are usually recorded by an accelerator control and monitoring system, while the target and moderator temperatures are normally recorded by a separate target-control system, because of safety requirements. The monitoring of a target-moderator system based on the measurement of neutron spectra in an absolute manner by using a fission detector would be a very powerful technique from a maintenance and diagnostic point of view. Unfortunately, few facilities currently have a dedicated and reliable monitoring system for the target-moderator assembly. Very often they are maintained by a neutron-scattering instrument group and may be modified by the user's needs. An online measurement of the ortho/para ratio of a liquid hydrogen moderator would be an interesting option, although we do not know how to accomplish this.

For the logging system, we should use the same scheme for both the accelerator control and target/moderator control systems, and we should be able to record the data in and retrieve the data from a common database.

2. Moderator

Information about the intensity distribution over the surface of a moderator is useful in the design of a neutron spectrometer. With this information we would be able to take advantage of the distribution, and could design the spectrometer so that it looks at the brightest spot on the moderator. Despite of this obvious usefulness, we have little information about the distribution. It is known that there is an intensity variation in the vertical direction, but far less is known about the two dimensional variation. There are some efforts being made to measure it, but it is not yet satisfactory.

In order to make full use of the a knowledge of the intensity distribution, we could employ a single or multiple-grooved moderator concept. A single-grooved moderator combined with one of the optical devices would be a very promising option.

3. Neutron optical devices

The technology for fabricating super mirror material is still evolving. Nowadays, it is easy to get a super-mirror guide which has a critical-angle which is two to tree-times that of a Ni mirror (2-3 Q_c). However, there is a supply problem for this type of mirror material. As a consequence guide tubes with applications for thermal or even epithermal neutrons rather than solely for cold neutrons can be envisaged. For these applications, a mirror which has higher Qc is indispensable. While the development of 4 Q_c super mirror is underway we should however push this limit even further.

There are irradiation problems for a guide tube which is very close to a target-moderator-reflector (TMRA). For a such environment, super mirror material deposited on a metal plate is indispensable. The surface polishing technique for the deposition of super mirror onto metal has been available for a while, but it is a rather expensive procedure.

The combination or optimization of the moderator-optical devices should be exploited and in this aspect, the knowledge of the intensity variation over the moderator surface would be crucial for the optimization of the spectrometer.

Focusing devices, such as a toroidal or ellipsoidal-mirror will also be important. Mirrors which have a surface-irregularity in the order of the mrad range have been developed for the X-ray astronomy field. These mirrors can be used for the focusing device for neutrons. There are actually several examples of this kind of device and there are many future possibilities in this field.

One of the promising fields for a high-power spallation neutron sources is to be able to make everyday use of a neutron-polarization technique. A white-beam neutron polarization and analysis technique which would work for potentially any beam-line is a welcome option. A magnetic mirror method is one way of getting such polarized neutrons, but a dynamical polarization filter method using proton-polarizations is another. Nowadays, proton-polarization can be done at around liquid-nitrogen temperatures, and room temperature proton polarization is not a dream. A He-3 neutron-polarization filter technique has been developed at several laboratories around the world. Although this technique is almost at a practical level, one of the current limitations is its polarization-decay time problem. The development of He-3 polarized-neutron detector would be a very nice option.

4. Windows

Any neutron flight-path will have several windows along it, which are sources of neutron background, and thus we would like to avoid these windows if possible. For example, Al-windows have Bragg cut-off edges, and although it should be theoretically straight forward to correct for this effect, in reality, it is a tedious problem.

The window materials for a small-angle diffractometer should have a very low small-angle scattering background. Single-crystals of Si or sapphire are the candidate materials to reduce such effects.

While it is rarely mentioned it is the case that prompt-γ's are produced by Al-windows, and thus produce a background. This effect is especially serious for scintillation detectors and Zr-windows could be an alternative to Al-windows in such situations.

If the material used in a window cannot be changed, we could reduce the thickness of such windows. Nowadays, by means of finite element methods (FEM), we can design very thin membrane windows. For example, the chopper spectrometer MAPS at ISIS has very thin detector windows of 0.5 mm thickness, which can withstand a vacuum/atmosphere interface. Note that the size of the windows are 1 m by 1.8 m. Another example is the small-angle diffractometer SAD at IPNS. It has a membrane window for the scattering chamber for the small-angle detectors, in which the get-lost pipe is welded onto the membrane window so that there is no window at the main neutron beam exit position.

We could push this concept to the limit. It is obvious that no window is the best available solution and we could realize this by employing a plasma window together with fast acting shutter for safety if needed.

5. Chopper

Choppers are important components for future spallation sources and we need to develop a t_0 chopper system which has very fast opening time to cope with high-energy neutrons up to multi-eV neutrons. An alternative approach would be to use a filter such as single crystals of sapphire to avoid high energy neutrons, which would help in reducing the background produced by such high-energy neutrons.

For the fast chopper, the phasing of more than two such devices could be a problem. If we could have a master clock for an accelerator system, this problem becomes less important, but it is not clear whether this is a strict requirement or not.
Flame-overlap choppers or a mirror system are also indispensable.

6. Detector

Detector development is key to the success of the future pulsed-spallation neutron sources, but we did not go into detail for the detector part, because a "Detector workshop" was to be held shortly afterwards at BNL on 24-26 September 1998.
Our goal is to develop a detector system which will have, i) high-spatial resolution, ii) high-counting rate, iii) high-stability, and which is iv) low cost. The last item is important, since we have to cover a very wide area with position sensitive detectors (PSD). For example, in the case of MAPS, 16 m^2 is covered by He-3 gas linear PSDs, which cost $2M.
Although a few new breeds of detector systems have been developed during the last few decades, it seems that gas detectors are still the most widely used. There are several ways to improve this type of detector. Multi-wire gas chambers and micro-strip He-3 gas detectors are two of them. These have been developed and installed at several sites. There are also new kinds of detector under development, such as, (Li, ZnS) scintillation counter + CCD, a two-dimensional position-sensitive solid-state detector system, an amorphous Si + converter system and so on. A neutron image-plate detector which has a time-resolving capability of the order of a msec is also proposed and under development.
While the detector system itself is a key development issue, we can not forget about the software system. With the increasing spatial-resolution, together with a huge number of detectors, we are faced with a huge number of pixels but which contain dilute information. We have to develop a properly designed software system, or more generally an architecture, to handle this kind of huge data-set. Some sort of data compression mechanism should be built into the upstream of the data acquisition system. The human interface should also be properly incorporated into this architecture. For example, a real-time display-feedback should be built into such a system. For this kind of display device, high-energy physics and NMR-tomography groups have a lot of experiences and we should learn from them.

ICANS-XIV
14th Meeting of the International Collaboration on
Advanced Neutron Sources
June 14-19, 1998
Utica, IL USA

Working Group: Spectroscopy in Future Neutron Sources

C.-K. Loong

I. Direct Geometry: Chopper Spectrometers
   1. A scattering flight-path built "around" the key components such as:
      polarizers for incident and scattered beams
      high magnetic field for samples
      high pressure cells
      high temperature furnaces
   2. Full flexibility in detector configuration, consider movable detector module
   3. Employment of large solid-angle position sensitive detector arrays

II. Inverse Geometry: Crystal-Analyzer Spectrometers
   1. Exploration of the transmitted beams after the analyzers (stacked multiple analyzers)
   2. Concurrent diffraction and inelastic scattering measurements
   3. Useful for high-pressure and high-temperature sample environment

III. Pulsed-Source Spin Echo Spectrometers
   Advantages: wide-Q overage, manipulation of pulsed magnetic fields
   Need to develop a user-friendly machine

ICANS-XIV
14th Meeting of the International Collaboration on Advanced Neutron Sources
June 14-19, 1998
Starved Rock Lodge, Utica, IL, USA

WORKSHOP GROUP On MODERATOR PERFORMANCE ENHANCEMENT AND DEVELOPMENT ACTIVITIES (Progress and Needs)

Gary J. Russell, Chairman and Eric J. Pitcher, Co-Chairman

Summary

The workshop group broke into several subgroups for detailed discussions. However, in order to focus the efforts of the workshop group(s) and to develop topics for discussion, the group adopted the following charter:

> *Review the moderators in use at the present operating spallation neutron sources, and give an overview of improvements being made to enhance the neutronic performance of these moderators. Characterize the present thinking on "moderator types" for the next-generation, high-power (0.6-5 MW) pulsed spallation sources. Review ideas for improving the neutronic performance of moderators. Survey development activities underway and being contemplated for new moderator types, and facilities for measuring the neutronic performance of moderators. Look at activities aimed at providing new scattering kernels and improving existing ones. Discuss engineering issues that must be faced in practical moderator design.*

Moderators Used in Existing Spallation Sources and Planned Improvements

At low-power (< 20 kW) pulsed spallation sources (KENS and IPNS), H_2O at ambient temperature, liquid CH_4 at 100 K, solid CH_4 at 20 K, and liquid H_2 at 20 K are used as moderators. For intermediate-power (100-200 kW) pulsed sources (Lujan Center and ISIS), solid CH_4 at 20 K is not a practical moderator material, and the moderators in use are H_2O at ambient temperature, liquid CH_4 at 100 K, and liquid H_2 at 20 K. At the quasi-continuous high-power (~1 MW) spallation source at PSI, D_2O at ambient temperature and liquid D_2 at 20 K are used as moderator materials. Planned moderator improvements at these existing sources include:

- partially coupled moderators (Lujan Center);
- upstream/back-scattering moderators (Lujan Center);
- reorientation of grooved moderator (IPNS); and
- conversion of liquid CH_4 at 100 K to solid CH_4 at 20 K (IPNS).

Conventional Moderator Performance Enhancement Techniques

There is a general trend toward increased intensity at the cost of resolution at spallation sources. Significant gains (e.g., up to ~70% for changing from B decoupler/liners to Cd decoupler/liners) can be realized by matching moderator time resolution to scientific instrument requirements.

Partially coupled moderators and poisoned reflectors can result in important gains (factors of 2 to 4) for instruments that can stand a broader neutron pulse width. The intensity from a liquid H_2 moderator at 20 K can be enhanced by the use of an optimized premoderator or cold Be reflector/filter. Matching the neutronic performance of a moderator to the instrument requirements is a key concept in all moderator designs.

Moderators for New High-Power Pulsed Spallation Sources (0.6-5 MW)

For high-power pulsed spallation sources, the first plans generally call for the same moderator materials (e.g., H_2O and liquid H_2) as for the intermediate-power spallation sources, with the same moderator performance enhancement techniques. Problems associated with either liquid or solid CH_4 are generally regarded as precluding their use in high-power spallation sources. However, the Japanese Hadron Facility (JHF) project is considering using a liquid CH_4 moderator at 0.6 MW spallation source due to the comparatively low-power operation and by placing the moderator in an upstream location with sufficient premoderation to reduce energy deposition (and damage) in the moderator. The Spallation Neutron Source (SNS) project may use a composite moderator of H_2O and liquid H_2 due to the small extrapolation of this approach from existing technology. The ESS project is considering using a flowing moderator of solid CH_4 pellets in liquid H_2. The SNS project may consider such a moderator for its second target station. The European Spallation Source (ESS) project is able to use present and future moderator developments because of the longer planning period for the ESS project. The Japanese Atomic Energy Research Institute (JAERI) is considering neutronically optimized liquid H_2 and H_2O moderators in their initial moderator suite for their 5-MW pulsed spallation source.

Advanced Cold Moderator Development

There is an international effort to develop Advanced Cold Moderators (ACoM). The goals of the ACoM effort are as follows:

- ✓ Develop a moderator that exceeds the neutronic performance of liquid H_2 by at least a factor of 2 for energies less than 5 meV.
- ✓ Advance a moderator with better slowing-down properties than liquid H_2.
- ✓ The moderator should be capable of operating in the temperature range 15-350 K.
- ✓ Have workable concept in 3-4 years.

Improved (and New) Scattering Kernels

The availability of well-validated scattering kernels for premoderator, moderator, reflector, and structural materials is a crucial aspect in the design and optimization stages of new target/moderator/reflector assemblies. In addition to the existing ENDFB-VI.2 data, the Synthetic Scattering Function (SSF) developed by Dr. Granada's group offers the possibility of generating scattering kernels for other potential cold moderator materials. The SSF has been recently integrated into the NJOY code, thus allowing for the preparation of cross sections in a standard format for neutronic calculations. New measurements at ANL have been made on the density-of-states of solid CH_4, which will lead to a new scattering kernel for this material. The LRMECS instrument at ANL is particularly useful in this regard, and continued measurements of this type on a variety of cold moderator materials would be extremely useful and are strongly

encouraged. Work continues at LANL to prepare a quality-checked set of scattering kernels for distribution to the ICANS community and others by the end of 1998.

Experimental Facilities for Target/moderator/Reflector Neutronic Studies

The following table is a compilation (by Y. Kiyanagi) of experimental facilities where neutronic measurements of target/moderator/reflector configurations are possible. The table summarizes the characteristics of these facilities.

Table I. Experimental Facilities Worldwide

Facility	Particle Type Energy	Current Rep Rate Pulse Width	Comments
Hokkaido Linac (Japan)	electrons < 0.045 GeV	< 20 μA < 100 pps 0.01-3 μs	Two cold sources (permanent and portable); beam size and distribution of produced neutrons are adjustable; TOF
AGS (USA)	protons 1.5-24 GeV	10 μA @ 24 GeV 1 μA @ 2.4 GeV 0.5 pps 0.04-2 μs	Power deposition study (target, moderator, reflector); physics parameters (spatial and temporal); TOF
JESSICA (Germany)	protons 0.1-2.5 GeV	1.6×10^{-6} μA 0.1 pps 1 μs	Cold source test facility; power deposition measurements; geometric optimization; easy test of various moderator and reflector materials; TOF
KENS Beam Dump (Japan)	Protons 0.5 GeV	6 μA maximum 20 pps ~0.05 μs	Need to drill the shield door to have a neutron flight path; safety assessments will be required before use; TOF
Bariloche Linac (Argentina)	Electrons <0.03 GeV	< 2.5 μA < 100 pps 1.4 μs	Lead target; ambient or liquid-nitrogen cooled moderator; total cross section measurements; TOF

Moderator Engineering Issues

Curved moderator viewed surfaces are preferable from a structural viewpoint when constructing moderator canisters. Moderator field-of-view and "effective thickness" are important design considerations. Safety criteria for spallation cold sources generally employ triple containment. Bellows at cryogenic temperatures are not only useful, but in many cases are essential in the design of a cold moderator cooling circuit. Cold source cooling system design should employ good sound engineering practices.

General Issues

Cooling of neutron decouplers at high-power pulsed spallation neutron sources deserves further attention, as well as the materials (and perhaps development of materials) for this application. It is important to keep in mind the need to be able to measure the ortho/para-hydrogen concentration in an operating liquid H_2 moderator at a pulsed spallation source. The communication channels(s) between moderator designers and scientific instrument designers needs to be kept up (and improved). It is vital to get moderator performance criteria from the instrument designers as soon as possible in a spallation source project so that the proper moderators can be designed to meet their needs.

More Detailed Discussion

Below are some more detailed thoughts expressed by some of the sub-groups. We have made no attempt to alter their comments in any substantive way. We have acknowledged the contributors as they were given to us (the leader of the sub-group is listed first).

Conventional Moderator Performance Enhancement Techniques
(P. Ferguson, J. Carpenter, E. Iverson, M. Teshigawara, and N. Watanabe)

There is a general trend toward increased neutron intensity at the cost of resolution at the existing spallation sources. For example,

- ✓ ZING-P, E_d >100 eV
- ✓ KENS, E_d 97 eV for H_2O moderator
- ✓ ISIS, E_d 1-3 eV
- ✓ IPNS, E_d ~0.3-0.5 eV
- ✓ Lujan Center, E_d ~0.3-0.5 eV,

where, E_d is the decoupling energy of the decoupler material, which is generally Cd or B.

For the Lujan Center, a 70% intensity gain (E< 100 eV) is seen when changing E_d from ~ 3 eV to 0.5 eV (i.e., from B to Cd). Additional gains may be obtained in changing from Cd to Gd decoupling by using an AlGd alloy with which IPNS has some experience. Matching moderator time-resolution to the instrument requirements is very important and intensity is lost when the pulse resolution is much better than that which the instrument requires.

Neutronic gains up to a factor of 6-7 can be obtained when moving from a fully decoupled system to a fully coupled system at the expense of neutron pulse width. Gains in intensity up to a factor of ~4 can be seen in a poisoned reflector system being installed at the Lujan Center. There is a significant amount of work that can be done to gain intensity at existing spallation sources by matching the neutron pulse width to the scientific instrument requirements.

Present moderator studies at JAERI indicate substantial neutronic gains on the order of 30-40% for optimized extended premoderator designs. In addition, cold Be reflector/filter calculations at Los Alamos show possible gains of 50-50% in long wavelength neutrons without much increase in the neutron pulse width.

IPNS is planning to move from a horizontal-grooved to a vertical-grooved moderator. The net moderator performance will probably be the same; however, the performance of the vertical reflectometers which view the moderator may increase substantially (~70%). This further highlights the importance of moderator/instrument matching.

Finally, a ring moderator concept was presented which shows some promise and deserves further study.

Moderators for New High-Power Pulsed Spallation Sources (0.6-5 MW)

(L. Charlton, D. Picton, and M. Teshigawara)

The first plans for moderators at high-power sources generally call for the same moderator materials (liquid H_2O, liquid D_2O, liquid H_2, and liquid D_2) as moderators at low-power sources, with the same moderator performance-enhancement techniques as used for the lower-powered spallation target systems. The SNS project may use a composite moderator due to the small extrapolation from existing technology. (Note: the new Los Alamos spallation target system recently installed and ready for commissioning in the summer of 1998 employs both a composite Be/H_2O moderator and Be/liquid H_2 moderator in their upstream/back-scattering moderator positions).

Radiation damage problems associated with liquid and solid CH_4 moderators are generally regarded as precluding their use in the same manner as they are used in low-power spallation sources. The ESS program is considering using a pelletized CH_4 moderator and the SNS may consider such a moderator for a second target station. The JHF program is considering using a liquid CH_4 moderator due to the comparatively low-power (0.6 MW) of the source by combining upstream placement of the moderator with premoderators to reduce energy deposition and radiation damage in the CH_4 moderator.

The ESS program is able to use both present and more advanced moderator concepts in their planning due to the longer timetable being considered for the effort.

New High-Power Pulsed Sources (0.6-5 MW)

There are several projects/programs under consideration that extend the power of spallation source significantly. These new sources are summarized below.

JHF – The JHF project initially calls for a Neutron Arena with a pulsed spallation source operating at 0.6 MW (200 μA of 3-GeV protons at 25 Hz), with possible operation at 50 Hz and 1.2 MW.

SNS - The SNS project will have two liquid H_2 moderators on the top of the target system, and two liquid H_2O moderators on the bottom. The two ambient-temperature liquid H_2O moderators will produce neutrons with an energy spectrum with a peak at ~30 meV. Both of the liquid H_2O moderators will be decoupled and poisoned, with the neutron decoupling done by surrounding all sides of the moderator (except for the viewed surface) with 1-mm of Cd. The poisoning will be done by using 50 μm of Gd placed parallel to the viewed surfaces of the moderator. The exact depth of the poison layer will be determined later by instrument requirements.

The upstream liquid H_2 moderator will be decoupled and poisoned in the same manner as the upstream liquid H_2O moderator. The downstream liquid H_2 moderator will be fully coupled to maximize the neutron output. This selection of moderators was made to be as consistent as possible with the 10 instruments chosen as an initial set.

Preliminary optimization of the moderators (as well as some of the other SNS target station components) was done using a "figure-of-merit" given by the moderator intensity divided by the square of the neutron pulse width. This was done only for the initial stages of the design. Later optimization will be done using a full interaction with the instrument designers and with the

input provided by their state-of-the-art computer codes used in instrument design. It was felt that a simple figure-of-merit provided a valuable tool for early studies, particularly when the set of instruments is not finally determined and when time constraints preclude a lengthy consideration of the requirements of the 10 initial instruments.

ESS - The ESS reference design incorporates two target stations: a) the "H" station (high-repetition rate) which will probably operate at ~50 Hz, taking 4 out of 5 pulses, and the "L" station (low-repetition rate), which will probably operate at ~10 Hz, taking 1 out of 5 pulses.

The "H" station will be similar to the present ISIS configuration and will probably incorporate two 300 K H_2O moderators and two 20 K liquid H_2 moderators. The "L" station will be used exclusively for cold neutron production, and will incorporate two or more liquid H_2 moderators.

The main issues for further moderator studies are associated with the cold moderators. On the "H" station, at least one of the liquid H_2 moderators will take the place of a 100 K liquid CH_4 moderator in the expectation that the lifetime of a liquid CH_4 would be too short on the ESS due to radiation damage problems. A study will need to be carried out to identify an optimum moderator configuration, e.g., a 20 K liquid H_2 moderator with a 300 K H_2O premoderator. Other concepts, e.g., a pelletized solid CH_4 moderator in liquid H_2 should also be considered.

In the case of the "L" station, it is likely that at least one of the moderators will be wholly or partially coupled with the reflector to optimize neutron intensity as opposed to pulse width. A detailed study will be required in order to fully optimize the target-moderator-reflector configuration. A similar study is envisaged for the proposed second target station for ISIS.

JAERI – The JAERI Neutron Science Project has a vision to be the "neutron supplier" for Japan into the next century. The present thinking is to provide a 5 MW pulsed spallation source supplying cold, thermal, and epithermal neutrons. At present, the target is assumed to be a liquid metal target (presumably mercury), employing horizontal proton beam insertion. Since about one third of the total available angles around the JAERI spallation source is allocated to each field of experiments utilizing cold, thermal, or epithermal neutrons, the required angular coverage for each kind of moderator(s) becomes about 100 degrees. This angular coverage cannot be covered by one viewed surface, and two viewed surfaces become indispensable. For a moderator having only one viewed surface, two such moderators are required.

For a cold neutron source, a coupled moderator composed of liquid H_2 or supercritical H_2 plus a hydrogenous premoderator (e.g., H_2O at ambient temperature). This particular moderator configuration is sometimes called a coupled liquid H_2 moderator with a premoderator. This moderator has been developed to provide higher time-integrated and peak cold neutron intensities than a conventional decoupled liquid H_2 moderator or solid CH_4 moderator does. This moderator can satisfy high-intensity experiments such as SANS, reflectrometry, etc. in which the time-integrated intensity is important, together with high-resolution experiments in which the peak intensity is essential. Two such moderators are envisioned since this moderator has only one viewed surface.

For high-resolution thermal neutron experiments, a decoupled liquid H_2 moderator with a interleaved poison sheet is being considered, since a decoupled solid or liquid CH_4 moderator probably cannot as yet be effectively used at MW-level spallation sources. R&D of a mixed moderator for this purpose will require a long period. Optimization studies on a decoupled

/poisoned liquid H_2 moderator is under progress. At the present stage of the design work, a high-intensity thermal neutron moderator is not being considered since high-resolution thermal neutron experiments are much more promising than high-intensity ones at an SPSS.

For a high-resolution epithermal neutron moderator, a H_2O moderator of an appropriate thickness (tentatively ~3 cm) is being considered. The optimal thickness will be determined after extensive discussions by users on the most interesting energy range in future science.

Advanced Cold Moderator Development
(G. Bauer, E. Iverson, and E. Shabalin)

The term advanced cold moderators is meant to apply to such systems which have a potential to enhance the performance of cold moderators over what is currently achievable on any particular type of source but cannot be realized without developed technologies.

Two recent studies for next generation neutron sources (ESS, Europe, and the SNS, USA) clearly establish the overwhelming need for cryogenic moderators: 36 out of 45 instruments proposed for the ESS; and 33 out of 37 for the SNS requested cryogenic moderators to supply them with neutrons. Currently the only cryogenic moderator systems that can be operated reliably on a high-flux neutron source are based on liquid hydrogen. Development is desirable in two ways:

- It was shown by calculations as well as by experience on low-power spallation sources that a factor of three or more could be gained in useful intensity, if a neutronically optimal moderator substance could be used.

- For every neutron energy, there exists a moderator temperature at which the intensity output is maximum. Therefore, a system that could be operated in a wide temperature range would provide unparalleled flexibility to adjust to evolving needs.

If realized, this would be a more efficient way of improving source performance than any potential increase in source power.

According to current thinking, the system would be based on heterogeneously cooled pellets of methane or a clathrate (e.g., methane clathrate) that would be thermally annealed at appropriate intervals to release stored energy. Pellets would also be replaced continuously or batchwise at a rate required by the accumulation of non-annealable radiation damage, which would degrade performance. Data on the excitation frequency spectrum of methane clathrate have recently become available, which clearly show the presence of intense low energy peaks at 1 meV and higher as well as the full frequency spectrum of water. The hope that methane clathrate might make a good moderator is largely based on this finding.

In order to ultimately realize such a system, a large body of work has to be carried out:

- ✓ Other promising candidate moderator materials should be identified and their suitability for the present purpose should be examined, based on their physical and chemical properties. Where such information is not available in the literature, suitable experiments must be carried out.
- ✓ Quantitative information on the neutronic properties (cross sections, density of states) must be collected or provided through suitable experiments.

- ✓ Scattering kernels that allow one to predict the performance as a moderator and its optimization by computational methods must be evaluated.
- ✓ Radiation effects must be studied to predict the allowable residence time in the high radiation field near the primary neutron source.
- ✓ Methods of fabrication of the moderator material in a suitable form and of cooling must be developed.
- ✓ In the case of solids, the problem of transportation to and from the moderator vessel must be solved.
- ✓ Ways to anneal radiation damage and to recycle the material, respectively to identify and sort out irreparably damaged parts must be developed.
- ✓ Prototypic setups must be constructed to test the practicality and reliability of the concepts developed.
- ✓ Full load tests must be carried out to make sure that no rate dependent effects exist which falsify the results obtained at low loads.

In an attempt to accomplish these tasks, an international collaboration is in formation, for which 12 laboratories have expressed interest so far. A working plan has been established with the following milestones:

- ➢ 01/1999 - Room temperature pellet transport: working model
- ➢ 06/1999 - Moderator materials: neutronic performance examined
- ➢ 03/2000 - Moderator materials: radiation effects; pellet production methods developed
- ➢ 01/2003 - Integrated Test Assembly ready

Five papers on the subject in question have been presented at the ICANS-XIV meeting.

Moderator Engineering Issues
(T. Lucas, M. Furusaka, H. Jeyck, Y. Ichoro, K. Clauson, H. Barnert-Weimer, and T. Scott)

As with any equipment, the design of a cold source system relies on a solidly based and constructively thought out specification that should be supportable and should represent an optimization of the true physics requirements and engineering feasibility. This subgroup discussed some typical topics as outlined below.

How Important Are Flat Moderator Viewing Surfaces? - Clauson (RISO) took the view that reliability is the key factor and that the added thickness required by flat surfaces at internal pressures up to 15 bar abs would largely negate the advantage. Furthermore, no problems of asymmetry had been observed from their curved moderator vessels. This is a problem that frequently arises in practical moderator design.

Moderator Viewing Surface Size and Thickness - As a general rule, the moderator should be close to the sizes of the beam viewing area. However, Furusaka indicated that an optimization method exists that can be applied as a general rule. The optimum thickness of a moderator should be applied to the meridian plane, as this is most representative of neutron thickness.

Accepted Safety Criteria for Cold Sources - The generally accepted requirements for a cold source system, with particular reference to those installed in a reactor, is the provision of a

secondary inert barrier around cold source components. This includes vacuum insulated components (representing triple containment).

Use of Bellows at Cryogenic Temperatures - Bellows can suffer from having their own problems especially at cryogenic temperatures. However, it was generally agreed that used intelligently, they are not only useful, but, in many cases, essential. Clausson reported that bellows used in their cold moderator system have given no problems throughout the life of the system.

General Engineering Practices - The wisdom of allowing manufacturers of specialist equipment an opportunity to comment on a design was expressed. This can result in the best possible compromise between physics, engineering, and manufacturing limitations.

Liquid Methane as a Moderator - Polymerization of liquid CH_4 is a well-known phenomenon in a radiation field. However, the resulting gains over liquid H_2 has prompted Furusaka to reconsider its possible use up to 1 MW. Experience with the ISIS system indicates that at a power level of 0.2 MW, the methane inventory requires to changing every one to two days, and the moderator vessel blocks up in about half an operational year. However, Lucas believes that a major part of the problem is an inability to adequately remove hydrogen gas produced as a by-product during irradiation. Also, better flow through the moderator would lower the transport time through the moderator and help reduce buildup of solid materials in the vessel. Provided a cryogenic vessel assembly could be made easier to replace (in say 3-4 days), an annual replacement program would probably be acceptable. With design improvements, this just might make liquid CH_4 a more practical moderator for higher-power spallation sources.

Poison Layers in Moderator Vessels - The warning was voiced that poison layers in a moderator can represent a significant heat load that can easily be neglected. It is essential that this be calculated as a heat generator, and be factored in with the other heat loads.

Acknowledgements

The chairman and co-chairman of this Workshop Group would like to acknowledge the help and thoughtful discussions made by the Group and their contributions to this report.

VENDOR PAPER

ICANS XIV
14th Meeting of the International Collaboration on
Advanced Neutron Sources
June 14-19, 1998
Starved Rock Lodge, Utica, IL

Daimler-Benz Aerospace
Dornier
88039 Friedrichshafen, Germany

Hugo Betzold

Tel +49-7545-82596 Fax +49-7545-82693
E-mail Hugo.Betzold@dss.dornier.dasa.de

EQUIPMENT AND SOFTWARE FOR RESEARCH WITH NEUTRONS

Incorporated in the Daimler-Benz Aerospace, Dornier is one of the leading high-tech companies in Germany.

In the field of advanced technologies Dornier developed neutron velocity selectors which reach the utmost limit of what is technically feasible today.
The unique feature of this SANS neutron velocity selector is the use of carbon fibre epoxy material for the very thin, helically twisted rotor lamellae which are coated with ^{10}B or Gd_2O_3 as absorbing material.
This novel design allows rotor speeds of up to 28,300 rpm (= 430 m/s peripheral velocity).

Based on this technology Dornier is a partner for:

- neutron velocity selectors (monochromotors)
- higher-order neutron filters (harmonic filters)
- disk choppers
- FERMI choppers
- components for choppers (slats, multi-slit disks etc.)

as well as for software and peripheric instrumentation, e.g. as:

- control systems (PC based)
- monitoring systems for choppers and selectors
- interface to a host.

The successful use in many laboratories world-wide reflects the fact that Dornier's neutron research related instruments and components meet high experimental requirements and allows a broad versatility of applications.

References:

BNL, Upton, NY; **GKSS**, Geesthacht; **HMI**, Berlin; **IFE**, Kjeller; **ILL**, Grenoble; **ISSP**, Tokyo; **KAERI**, Seoul; **KFA**, Jülich; **LANL**, Los Alamos, NM; **MPI**, Mainz; **NIST**, Gaithersburg, MD; **NPMR**, Chalk River, ON; **PSI**, Villigen; **PTB**, Braunschweig; **RISO**, Roskilde; **SERC**, Didcot; **TUM**, Munich

GROUP PHOTO

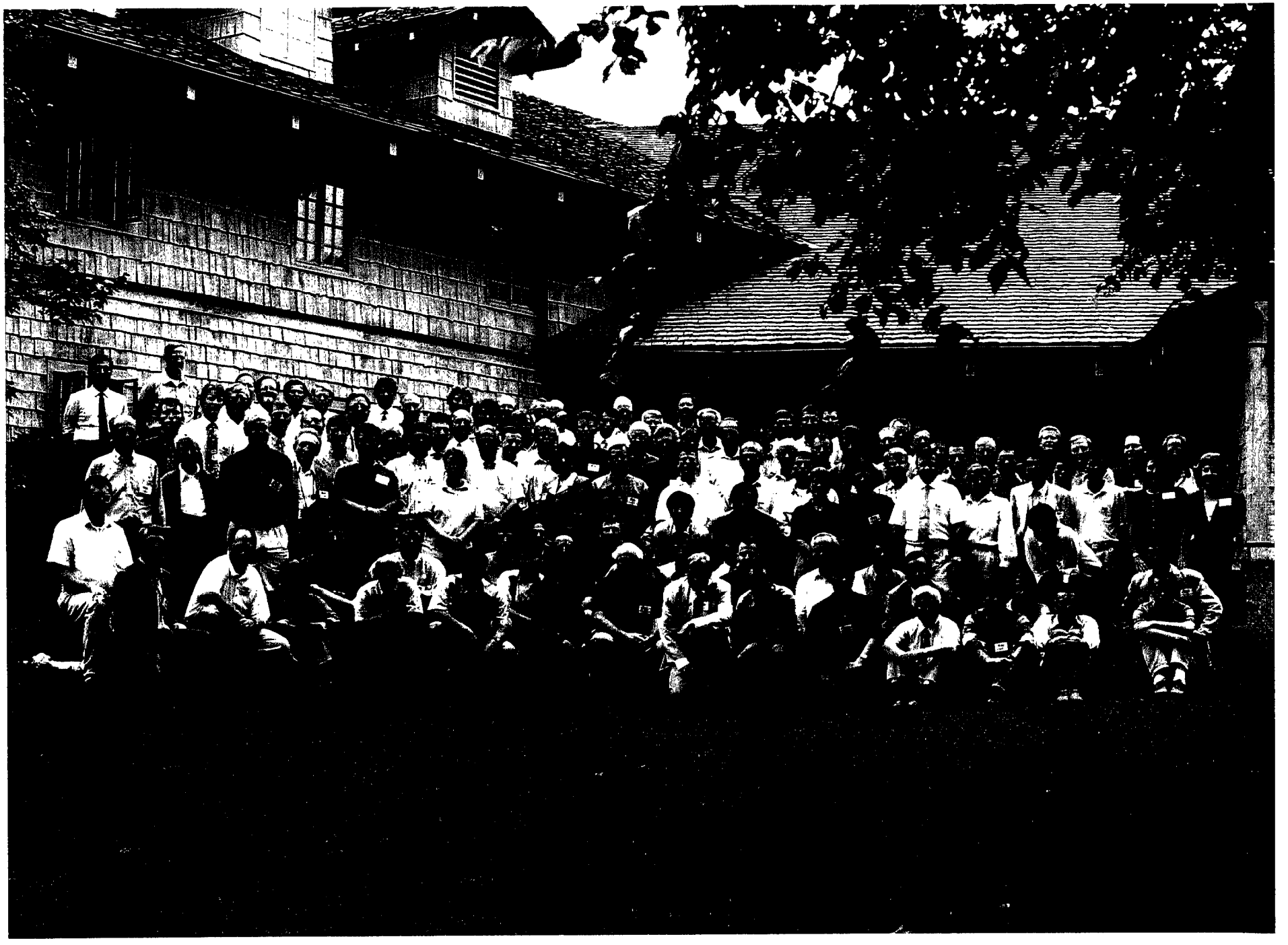

LIST OF ATTENDEES

ICANS-XIV Conference
June 14-19, 1998
Starved Rock Lodge and Conference Center
Utica, IL

Jose Alonso
Oak Ridge National Laboratory
P.O. Box 2009, 104 Union Valley Road
Oak Ridge TN 37831-8218
US
Phone: 423-576-2874
FAX: 423-576-3041
E-Mail: alonsojr@ornl.gov

John Ankner
University of Missouri
526 Research Reactor
Columbia MO 65211
US
Phone: 573-882-5344
FAX: 573-882-3443
E-Mail: ankner@reactor.murr.missouri.edu

Bill Appleton
Oak Ridge National Laboratory
P.O. Box 2008
Oak Ridge TN 37831-6240
US
Phone: 423-574-4321
FAX: 423-574-0323
E-Mail: appletonbr@ornl.gov

Masatoshi Arai
High Enery Acc. Res. Org. (KEK)
1-1 Oho,
Tsukuba Ibaraki-ken 305-0801
JAPAN
Phone: +81-0298-64-5613
FAX: +81-0298-64-3202
E-Mail: arai@kekvax.kek.jp

Anatoli Balagurov
Joint Institute for Nuclear Research
Frank Lab. of Neutron Physics
Dubna Moscow Region 141980
RUSSIA
Phone: +7-09621-65803
FAX: +7-09621-65882
E-Mail: bala@nf.jinr.ru

Jeremy Balchin
ISIS Facility
Rutherford Appleton Laboratory
Chilton, Didcot Oxon OX11 0QX
UNITED KINGDOM
Phone: 44-1235-44-6654
FAX: 44-1235-44-6660
E-Mail: J.Balchin@rl.ac.uk

Heidrun Barnert-Wiemer
Forschungszentrum Jülich
D-52425 Jülich
Jülich
GERMANY
Phone: +49-2461-61-6475
FAX: +49-2461-61-6816
E-Mail: H.Barnert-Wiemer@FZ-Juelich.de

Gunter Bauer
Paul Scherrer Institut
WHGA/244
CH-5232 Villigen PSI
SWITZERLAND
Phone: +41-56-310-2524
FAX: +41-56-310-3131
E-Mail: bauer@psi.ch

Henry Belch
Argonne National Laboratory
9700 S. Cass Ave.; Bldg. 360
Argonne IL 60439
US
Phone: +1-630-252-6061
FAX: +1-630-252-4163
E-Mail: hbelch@anl.gov

Alexandre V. Belushkin
Joint Institute for Nuclear Research
Frank Laboratory of Neutron Physics
Dubna Moscow Region 141980
RUSSIA
Phone: +7-09621-65657
FAX: +7-09621-65429
E-Mail: belushk@nf.jinr.ru

Hugo Betzold
Dornier Satellitensysteme GmbH
88039 Friedrichshafen

GERMANY
Phone: +49-7545-82596
FAX: +49-7545-82693
E-Mail: Hugo.Betzold@dss.dornier.dasa.de

Roger Blackman
Argonne National Laboratory
9700 S. Cass Ave., Bldg. 360
Argonne IL 60439
US
Phone: 630-252-6570
FAX: 630-252-1485
E-Mail: rrblackman@anl.gov

Donald Bohringer
Argonne National Laboratory
9700 S. Cass Ave.; Bldg. 360
Argonne IL 60439
US
Phone: 630-252-8799
FAX: 630-252-4163
E-Mail: debohringer@anl.gov

Zoe Bowden
ISIS Facility
Rutherford Appleton Laboratory
Chilton, Didcot Oxon OX11 0QX
UNITED KINGDOM
Phone: 44-1235-44-6145
FAX: 44-1235-44-5720
E-Mail: zab@horus.nd.rl.ac.uk

Ira H. Bresof
Argonne National Laboratory
9700 S. Cass Ave.; Bldg. 360
Argonne IL 60439
US
Phone: +1-630-252-8705
FAX: +1-630-252-4163
E-Mail: ihbresof@anl.gov

Paul Brod
Argonne National Laboratory
9700 S. Cass Ave.; Bldg. 360
Argonne IL 60439
US
Phone: 630-252-5418
FAX: 630-252-4163
E-Mail: pbrod@anl.gov

Bruce S. Brown
Argonne National Laboratory
9700 S. Cass Ave.; Bldg. 360
Argonne IL 60439
US
Phone: +1-630-252-4999
FAX: +1-630-252-4163
E-Mail: bsbrown@anl.gov

Franklin Brumwell
Argonne National Laboratory
9700 S. Cass Ave., Bldg. 360
Argonne IL 60439
US
Phone: 630-252-6558
FAX: 630-252-9987
E-Mail: fbrumwell@anl.gov

Martyn Bull
ISIS Facility
Rutherford Appleton Laboratory
Chilton, Didcot Oxon OX11 0QX
UNITED KINGDOM
Phone: 44-1235-44-5805
FAX: 44-1235-44-5720
E-Mail: mjb01@isise.rl.ac.uk

Nathan Bultman
Los Alamos National Laboratory
MS P946; PO Box 1663
Los Alamos NM 87544
US
Phone: +1-505-667-0298
FAX: +1-505-667-2068
E-Mail: nbultman@lanl.gov

John M. Carpenter
Argonne National Laboratory
9700 S. Cass Ave.; Bldg. 360
Argonne IL 60439
US
Phone: +1-630-252-5519
FAX: +1-630-252-4163
E-Mail: jmcarpenter@anl.gov

Lowell A. Charlton
Oak Ridge National Laboratory
P.O. Box 2008 MS 6363
Oak Ridge TN 37931
US
Phone: 423-574-0628
FAX: 423-574-0323
E-Mail: lac@ornl.gov

Dong Feng Chen
Argonne National Laboratory
9700 S. Cass Ave.; Bldg. 360
Argonne IL 60439
US
Phone: 630-252-3555
FAX: 630-252-4163
E-Mail: dfchen@anl.gov

Wang Chun Chen
Univ. Illinois
103 S. Goodwin Ave.
Urbana IL 61801
US
Phone: 217-333-1568
FAX: 217-333-2295
E-Mail: wchen@students.uiuc.edu

Omar Chmaissem
Argonne National Laboratory
9700 S. Cass Ave.; Bldg. 223
Argonne IL 60439
US
Phone: 630-252-5541
FAX: 630-252-7777
E-Mail: omar_chmaissem@qmgate.anl.gov

Kurt N. Clausen
Risø National Laboratory
Frederiksborgvej 399; Postbox 49
DK-4000 Roskilde
DENMARK
Phone: +45-4677-4704
FAX: +45-4677-4790
E-Mail: kurt.clausen@risoe.dk

R. Kent Crawford
Argonne National Laboratory
9700 S. Cass Ave.; Bldg. 360
Argonne IL 60439
US
Phone: +1-630-252-7769
FAX: +1-630-252-4163
E-Mail: rkcrawford@anl.gov

Bart J. Czirr
Mission Support Inc. Photogenics
455 North University Ave., Suite 206
Provo UT 84106
US
Phone: 801-374-6722
FAX: 801-374-6652
E-Mail: MSIZ15@AOL.COM

Luke L. Daemen
Los Alamos National Laboratory
MLNSC MS-H805
Los ALamos NM 87545
US
Phone: +1-505-667-9695
FAX: +1-505-665-2676
E-Mail: LLD@lanl.gov

Joey Donahue
Los Alamos National Laboratory
LANSCE-7;H840
Los Alamos NM 87454
US
Phone: +1-505-667-2856
FAX: +1-505-665-4049
E-Mail: jdonahue@lanl.gov

Lawrence Donley
Argonne National Laboratory
9700 S. Cass Ave., Bldg. 360
Argonne IL 60439
US
Phone: 630-252-6582
FAX: 630-252-9987
E-Mail: ldonley@anl.gov

Jeffrey Dooling
Argonne National Laboratory
9700 S. Cass Ave., Bldg. 360
Argonne IL 60439
US
Phone: 630-252-1196
FAX: 630-252-9987
E-Mail: jcdooling@anl.gov

Roger Eccleston
ISIS Facility
Rutherford Appleton Laboratory
Chilton, Didcot Oxon OX10 OQX
UNITED KINGDOM
Phone: 44-1235-495409
FAX: 44-1235-445720
E-Mail: R.S.Eccleston@rl.ac.uk

Eric Empey
Argonne National Laboratory
9700 S. Cass Ave., Bldg. 360
Argonne IL 60439
US
Phone: 630-252-1181
FAX: 630-252-4163
E-Mail: eempey@pns.anl.gov

Phil Ferguson
Los Alamos National Laboratory
LANSCE, MS H805, P.O. Box 1663
Los ALamos NM 87545
US
Phone: +1-505-667-2072
FAX: +1-505-665-2676
E-Mail: ferguson@lanl.gov

Tom Fornek
Argonne National Laboratory
9700 S. Cass Ave.; Bldg. 360
Argonne IL 60439
US
Phone: +1-630-252-8601
FAX: +1-630-252-3344
E-Mail: fornek@anl.gov

Christopher D. Frost
ISIS Facility
Rutherford Appleton Laboratory
Chilton, Didcot Oxon OX11 0QX
UNITED KINGDOM
Phone: 44-1235-44-5683
FAX: 44-1235-44-5270
E-Mail: cdf@isise.rl.ac.uk

Michihiro Furusaka
High Energy Acc. Res. Org. (KEK)
1-1 Oho
Tsukuba Ibaraki-ken 305-0801
JAPAN
Phone: +81-298-64-5618
FAX: +81-298-64-3202
E-Mail: michihiro.furusaka@kek.jp

Tony Gabriel
Oak Ridge National Laboratory
P.O. Box 2008
Oak Ridge TN 37831-6364
US
Phone: 423-574-6082
FAX: 423-574-9619
E-Mail: tag@ornl.gov

Abdul Ganni
Kurt J. Lesker Company
1515 Worthington Ave.
Clairton PA 15025-2700
US
Phone: 412-233-4200
FAX: 412-233-4275
E-Mail: abdulg@lesker.com

Jose Rolando Granada
Argentine AEC
8400 S.C. De Bariloche (RN)
ARGENTINA
Phone: +54-944-45250
FAX: +54-944-45299
E-Mail: granada@cab.cnea.edu.ar

John R. Haines
Oak Ridge National Laboratory
P.O. Box 2009; Bldg. 9201-2, MS 8071
Oak Ridge TN 37831
US
Phone: 423-574-0966
FAX: 423-574-7926
E-Mail: hainesjr@ornl.gov

John Hammonds
Argonne National Laboratory
9700 S. Cass Ave.; Bldg. 360
Argonne IL 60439
US
Phone: +1-630-252-5317
FAX: +1-630-252-4163
E-Mail: jphammonds@anl.gov

Iwao Harada
Hitachi, Ltd.
7-2-1 Omika-cho
Hitachi-shi Ibaraki-ken 319-1221
JAPAN
Phone: +81-0294-53-3111
FAX: +81-0294-53-2830
E-Mail:

Jerome Hastings
Brookhaven National Laboratory
Bldg. 725
Upton NY 11973
US
Phone: 516-344-3930
FAX: 516-344-3238
E-Mail: hastings@bnl.gov

Robert (Rob) Henning
Argonne National Laboratory
9700 S. Cass Ave.; Bldg. 360
Argonne IL 60439
US
Phone: 630-252-5346
FAX: 630-252-4163
E-Mail: rhenning@anl.gov

Ken Herwig
Argonne National Laboratory
9700 S. Cass Ave.; Bldg. 360
Argonne IL 60439
US
Phone: +1-630-252-5371
FAX: +1-630-252-4163
E-Mail: kherwig@anl.gov

Hajo Heyck
Paul Scherrer Institut
WHGA/244, CH-5232
Villigen PSI
SWITZERLAND
Phone: +-41-56-310-2315
FAX: +-41-56-310-3131
E-Mail: hajo.heyck@psi.ch

Ryutaro Hino
Center for Neutron Science, JAERI
Tokai-mura
Naka-gun Ibaraki-ken 319-11
JAPAN
Phone: +81-29-282-6424
FAX: +81-29-282-6496
E-Mail: hino@cat.tokai.jaeri.go.jp

Rex P. Hjelm
Los Alamos National Laboratory
LANSCE-12, MS-H805
Los Alamos NM 87545
US
Phone: +1-505-665-2372
FAX: +1-505-665-2676
E-Mail: Hjelm@lanl.gov

Jason Hodges
Argonne National Laboratory
9700 S. Cass Ave.; Bldg. 223
Argonne IL 60439
US
Phone: 630-252-3289
FAX: 630-252-9595
E-Mail: jason_hodges@qmgate.anl.gov

Takashi Ino
High Enery Acc. Res. Org. (KEK)
1-1 Oho
Tsukuba Ibaraki-ken 305-0801
JAPAN
Phone: +81-298-64-5614
FAX: +81-298-64-3202
E-Mail: takashi.ino@kek.jp

Shinichi Itoh
High Enery Acc. Res. Org. (KEK)
1-1 Oho,
Tsukuba Ibaraki-ken 305-0801
JAPAN
Phone: +81-298-64-5616
FAX: +81-298-64-3202
E-Mail: shinichi.itoh@kek.jp

Eric Iverson
Argonne National Laboratory
9700 S. Cass Ave.; Bldg. 360
Argonne IL 60439
US
Phone: +1-630-252-1181
FAX: +1-630-252-4163
E-Mail: eiverson@anl.gov

Michael James
Los Alamos National Laboratory
APT-TPO MS H809
Los Alamos NM 87545
US
Phone: 505-665-6521
FAX: 505-667-2787
E-Mail: mrjames@lanl.gov

James Jorgensen
Argonne National Laboratory
9700 S. Cass Ave.; Bldg. 223
Argonne IL 60439
US
Phone: 630-252-5513
FAX: 630-252-7777
E-Mail: jjorgensen@anl.gov

Masayoshi Kawai
High Enery Acc. Res. Org. (KEK)
1-1 Oho,
Tsukuba Ibaraki-ken 305-0801
JAPAN
Phone: +81-0298-64-5637
FAX: +81-0298-64-3202
E-Mail: masayoshi.kawai@kek.jp

Kenji Kikuchi
Materials Strength Lab, JAERI
Shirakata-Shirane 2-4
Tokai-Mura Ibaraki-ken 319-1195
JAPAN
Phone: +81-29-282-5058
FAX: +81-29-282-6489
E-Mail: kikuchi@popsvr.tokai.jaeri.go.jp

Yoshiako Kiyanagi
Hokkaido University
Kita-13, Nishi-8,Kita-ku
Sapporo 060-8628
JAPAN
Phone: 81-11-706-6650
FAX: 81-11-706-7896
E-Mail: kiyanagi@qe.eng.hokudai.ac.jp

Jyotsana Lal
Argonne National Laboratory
9700 S. Cass Ave.; Bldg. 360
Argonne IL 60439
US
Phone: 630-252-6042
FAX: 630-252-4163
E-Mail: Lal@anl.gov

Paul Lewis
Los Alamos National Laboratory
LANSCE-DO H848
Los Alamos NM 87545
US
Phone: 505-665-0932
FAX: 505-665-1302
E-Mail: lewis@lanl.gov

Tiejun Li
Univ. Illinois
103 S. Goodwin Ave.
Urbana IL 61801
US
Phone: 217-333-1862
FAX: 217-333-2295
E-Mail: t-li7@uiuc.edu

Xiaohe Li
Argonne National Laboratory
9700 S. Cass Ave., Bldg. 360
Argonne IL 60439
US
Phone: 630-252-3555
FAX: 630-252-4163
E-Mail: xli@anl.gov

Ken Littrell
Argonne National Laboratory
9700 S. Cass Ave., Bldg. 360
Argonne IL 60439
US
Phone: 630-252-5396
FAX: 630-252-4163
E-Mail: klittrell@anl.gov

Valeri L. Lomidze
Joint Institute for Nuclear Research
Frank Lab. of Neutron Physics
Dubna Moscow Region 141980
RUSSIA
Phone: +7-09621-63387
FAX: +7-09621-65-119
E-Mail: lomidze@nf.jinr.ru

Chun Loong
Argonne National Laboratory
9700 S. Cass Ave.; Bldg. 360
Argonne IL 60439
US
Phone: 630-252-5596
FAX: 630-252-4163
E-Mail: ckloong@anl.gov

Trevor Lucas
Oak Ridge National Laboratory
P.O. Box 2008; Bldg. 6025, MS 6363
Oak Ridge TN 37831
US
Phone: 423-574-8998
FAX: 423-574-9619
E-Mail: A9T@ornl.gov

Hans Ludewig
Brookhaven National Laboratory
Bldg. 701
Upton NY 11973
US
Phone: +1-516-344-2624
FAX: +1-516-344-7650
E-Mail: ludewig@necs01.dne.bnl.gov

Robert Macek
Los Alamos National Laboratory
LANSCE-DO, MS H848, P.O. Box 1663
Los ALamos NM 87545
US
Phone: +1-505-667-8877
FAX: +1-505-665-1302
E-Mail: macek@lanl.gov

Alexander Malik
Paul Scherrer Institut
OFLB - C001,
CH-5232, Villigen PSI
SWITZERLAND
Phone: +-41-56-310-4491
FAX: +-41-56-310-4435
E-Mail: malik@psi.ch

Thom Mason
Oak Ridge National Laboratory
P.O. Box 2008
Oak Ridge TN 37831
US
Phone: +1-423-241-1499
FAX: +1-423-576-3041
E-Mail: masont@ornl.gov

T. J. McManamy
Oak Ridge National Laboratory
P.O. Box 2009
Oak Ridge TN 37831-8218
US
Phone: 423-576-0039
FAX: 423-576-3041
E-Mail: mcmanamytj@ornl.gov

Gerald McMichael
Argonne National Laboratory
9700 S. Cass Ave., Bldg. 360
Argonne IL 60439
US
Phone: 630-252-9231
FAX: 630-252-9987
E-Mail:

Dennis McWhan
Brookhaven National Laboratory
P.O. Box 5000, Bldg. 460
Upton NY 11973-5000
US
Phone: 516-344-3927
FAX: 516-344-5584
E-Mail: mcwhan@bnl.gov

Valeri Melikhov
Joint Institute for Nuclear Research
Frank Lab. of Neutron Physics
Dubna Moscow Region 141980
RUSSIA
Phone: +7-095-926-22-31
FAX: +7-09621-65-119
E-Mail: woolf@nf.jinr.ru

Ferenc Mezei
Los Alamos National Laboratory
LANSCE-DO H850
Los Alamos NM 87454
US
Phone: 505-667-7633
FAX: 505-665-2767
E-Mail: mezei@lanl.gov

Mark Middendorf
Argonne National Laboratory
9700 S. Cass Ave., Bldg. 360
Argonne IL 60439
US
Phone: 630-252-1683
FAX: 630-252-9987
E-Mail: mmiddendorf@anl.gov

Laura Miller
Argonne National Laboratory
9700 S. Cass Ave.; Bldg. 360
Argonne IL 60439
US
Phone: +1-630-252-6485
FAX: +1-630-252-4163
E-Mail: ljmiller@anl.gov

Kaichiro Mishima
Kyoto University
Research Reactor Inst.; Kumatori-cho
Sennan-gun Osaka 590-0494
JAPAN
Phone: +-81-724-51-2449
FAX: +-81-724-51-2637
E-Mail: mishima@rri.kyoto-u.ac.jp

Brian Mitchell
Argonne National Laboratory
9700 S. Cass Ave.; Bldg. 360
Argonne IL 60439
US
Phone: 630-252-5346
FAX: 630-252-4163
E-Mail: bmitchell@anl.gov

Paul Montanez
Brookhaven National Laboratory
Bldg. 725D
Upton NY 11973
US
Phone: +1-516-344-2785
FAX: +1-516-344-3238
E-Mail: p-montanez@bnl.gov

Ralf Neef
Inst. für Kern Physik
Forschungszentrum Jülich
D-52425 Jülich
GERMANY
Phone: 49-2461-616224
FAX: 49-2461-613930
E-Mail: R.D.NEEF@FZ-JULICH.DE

Tosiya Otomo
High Enery Acc. Res. Org. (KEK)
1-1 Oho,
Tsukuba Ibaraki-ken 305-0801
JAPAN
Phone: +81-298-64-6515
FAX: +81-298-64-3202
E-Mail: toshiya.otomo@kek.jp

Yukio Oyama
JAERI
Tokai-mura
Naka-gun Ibaraki-ken 319-11
JAPAN
Phone: +81-029-282-6936
FAX: +81-029-282-5996
E-Mail: oyama@fnshp.tokai.jaeri.go.jp

Leigh Perrott
ISIS Facility
Rutherford Appleton Laboratory
Chilton, Didcot Oxon OX11 0QX
UNITED KINGDOM
Phone: 44-1235-44-6160
FAX: 44-1235-44-6660
E-Mail: lcp@sci.rl.ac.uk

David J. Picton
The University of Birmingham
School of Physics and Astronomy
Birmingham B15 2TT
UNITED KINGDOM
Phone: 44-121-414-4696
FAX: 44-121-414-4725
E-Mail: dave@aps5.ph.bham.ac.uk

Eric Pitcher
Los Alamos National Laboratory
P. O. Box 1663, MS H816
Los Alamos NM 87545
US
Phone: 505-667-0651
FAX: 505-667-7443
E-Mail: pitcher@lanl.gov

Paolo G. Radaelli
ISIS Facility
Rutherford Appleton Laboratory
Chilton, Didcot Oxon OX11 0QX
UNITED KINGDOM
Phone: 44-1235-44-6290
FAX: 44-1235-44-5692
E-Mail: P.G.Radaelli@.rl.ac.uk

James Richardson
Argonne National Laboratory
9700 S. Cass Ave.; Bldg. 360
Argonne IL 60439
US
Phone: +1-630-252-3554
FAX: +1-630-252-4163
E-Mail: jwrichardson@anl.gov

Garrett Rinehart
Argonne National Laboratory
9700 S. Cass Ave., Bldg. 360
Argonne IL 60439
US
Phone: 630-252-6561
FAX: 630-252-9987
E-Mail: grinehart@pns.anl.gov

Joyce Roberts
Los Alamos National Laboratory
LANSCE-12, MS H805; PO Box 1663
Los Alamos NM 87545
US
Phone: +1-505-667-3629
FAX: +1-505-665-2676
E-Mail: joycer@lanl.gov

Robert Robinson
Los Alamos National Laboratory
LANSCE-12, MS-H805
Los Alamos NM 87545
US
Phone: +1-505-667-3626
FAX: +1-505-665-2676
E-Mail: rrobinson@lanl.gov

Gary J. Russell
Los Alamos National Laboratory
Lujan Center MS H805, P.O. Box 1663
Los ALamos NM 87545
US
Phone: +1-505-667-2937
FAX: +1-505-665-2676
E-Mail: russell@lanl.gov

William Ruzicka
Argonne National Laboratory
9700 S. Cass Ave.; Bldg. 360
Argonne IL 60439
US
Phone: 630-252-6834
FAX: 630-252-4163
E-Mail: ruzicka@anl.gov

Motoaki Sakashita
Hitachi, Ltd.
3-2-1, Saiwai-cho
Hitachi-shi Ibaraki-ken 317-0073
JAPAN
Phone: 0294-23-5437
FAX: 0294-23-6662
E-Mail:

Arthur Schultz
Argonne National Laboratory
9700 S. Cass Ave.; Bldg. 360
Argonne IL 60439
US
Phone: 630-252-3465
FAX: 630-252-4163
E-Mail: ajschultz@anl.gov

Terry Scott
Argonne National Laboratory
9700 S. Cass Ave.; Bldg. 360
Argonne IL 60439
US
Phone: +1-630-252-6092
FAX: +1-630-252-4163
E-Mail: tlscott@anl.gov

Philip A. Seeger
Los Alamos National Laboratory
239 Loma del Escolar
Los Alamos NM 87544
US
Phone: +1-505-662-7163
FAX: +1-505-662-0956
E-Mail: PASeeger@aol.com

Eugene Shabalin
Joint Institute for Nuclear Research
Frank Lab. of Neutron Physics
Dubna Moscow Region 141980
RUSSIA
Phone: +7-09621-65253
FAX: +7-09621-65119
E-Mail: shab36@nf.jinr.ru

Stanislav F. Sidorkin
Institute for Nuclear Research RAS
60th October Anniversary Prospect 7a
117312 Moscow
RUSSIA
Phone: +7-095-334-0712
FAX: +7-095-135-2268
E-Mail: sidorkin@al20.inr.troitsk.ru

Kazuhiko Soyama
JAERI
Tokai-mura,
Naka-gun Ibaraki-ken 319-11
JAPAN
Phone: +81-029-282-6936
FAX: +81-029-282-5996
E-Mail: soyama@jrr3fep2.tokai.jaeri.go.jp

Jennifer Stapleton
Argonne National Laboratory
9700 S. Cass Ave., Bldg. 360
Argonne IL 60439
US
Phone: 630-252-6221
FAX: 630-252-9987
E-Mail: jstapleton@pns.anl.gov

Uschi Steigenberger
ISIS Facility
Rutherford Appleton Laboratory
Chilton, Didcot OXON OX11 OQX
UNITED KINGDOM
Phone: 44-1235-445145
FAX: 44-1235-445383
E-Mail: usm@isise.rl.ac.uk

Vernon Stipp
Argonne National Laboratory
9700 S. Cass Ave., Bldg. 360
Argonne IL 60439
US
Phone: 630-252-6604
FAX: 630-252-9987
E-Mail: vstipp@anl.gov

Dianne M. Swart
Kurt J. Lesker Company
1515 Worthington Ave.
Clairton PA 15025-2700
US
Phone: 412-233-4200
FAX: 412-233-4275
E-Mail: diannes@lesker.com

Hiroshi Takada
Center for Neutron Science, JAERI
Tokai-mura
Naka-gun Ibaraki-ken 319-11
JAPAN
Phone: +81-29-282-5336
FAX: +81-29-282-5663
E-Mail: takada@omega.tokai.jaeri.go.jp

Masayasu Takeda
Tohoku University
Physics Dept. , Graduate School of Science
Aramaki, Aoba-ku Sendai 980-77
JAPAN
Phone: +81-22-217-6487
FAX: +81--22-217-6489
E-Mail: takeda@iiyo.phys.tohoku.ac.jp

Yasushi Takeda
Paul Scherrer Institut
CH-5232
Villigen PSI
SWITZERLAND
Phone: +-41-56-310-3568
FAX: +-41-56-310-3717
E-Mail: takeda@psi.ch

Nobuyuki Takenaka
Kobe University
Dept. Mech. Eng., 1-1 Rokkoda
Nada Kobe 657
JAPAN
Phone: +81-78-803-1106
FAX: +81-78-803-1108
E-Mail: takenaka@mech.kobe-u.ac.jp

Ken Takeuchi
Argonne National Laboratory
9700 S. Cass Ave., Bldg. 360
Argonne IL 60439
US
Phone: 630-252-3555
FAX: 630-252-4163
E-Mail: ktakeuchi@anl.gov

Andrew Taylor
ISIS Facility
Rutherford Appleton Laboratory
Chilton, Didcot Oxon OX11 0QX
UNITED KINGDOM
Phone: +44-1235-44-6681
FAX: +44-1235-44-5383
E-Mail: Andrew.Taylor@rl.ac.uk

Makoto Teshigawara
JAERI
Tokai-mura
Naka-gun Ibaraki-ken 319-11
JAPAN
Phone: +81-29-282-6217
FAX: +81-29-282-5663
E-Mail: teshi@linac.tokai.jaeri.go.jp

Thierry Thelliez
Los Alamos National Laboratory
P. O. Box 1663, MS M310
Los Alamos NM 87545
US
Phone: 505-665-8631
FAX: 505-665-5725
E-Mail: tgt@lanl.gov

P. Thiyagarajan
Argonne National Laboratory
9700 S. Cass Ave.; Bldg. 360
Argonne IL 60439
US
Phone: 630-252-3593
FAX: 630-252-4163
E-Mail: thiyaga@anl.gov

Ian M. Thorson
TRIUMF
4004 Wesbrook Mall
Vancouver British Columbia V6T 2A3
CANADA
Phone: 604-222-1047 or 7420
FAX: 604-222-1074
E-Mail: THORSON@Triumf_CA

Holger Tietze-Jaensch
F/Z-Juelich
IFF/ESS
D-52425 Juelich
GERMANY
Phone: +49-2461-61-4688
FAX: +49-2461-61-2410
E-Mail: H.TIETZE@fz-juelich.de

Michael Todosow
Brookhaven National Laboratory
Bldg. 701; PO Box 5000
Upton NY 11973-5000
US
Phone: +1-516-344-2445
FAX: +1-516-344-7650
E-Mail: todosowm@bnl.gov

Frans Trouw
Argonne National Laboratory
9700 S. Cass Ave., Bldg. 360
Argonne IL 60439
US
Phone: 630-252-7665
FAX: 630-252-4163
E-Mail: trouw@anl.gov

Colin Uden
ISIS Facility
Rutherford Appleton Laboratory
Chilton, Didcot Oxon OX11 0QX
UNITED KINGDOM
Phone: 44-1235-44-6681
FAX: 44-1235-44-5383
E-Mail: a.d.taylor@rl.ac.uk

Volker Urban
Argonne National Laboratory
9700 S. Cass Ave.; Bldg. 360
Argonne IL 60439
US
Phone: 630-252-5396
FAX: 630-252-4163
E-Mail: vurban@anl.gov

Ken Volin
Argonne National Laboratory
9700 S. Cass Ave.; Bldg. 360
Argonne IL 60439
US
Phone: +1-630-252-6092
FAX: +1-630-252-4163
E-Mail: kvolin@anl.gov

Noboru Watanabe
Center for Neutron Science, JAERI
Shirakata Shirane, Tokai-mura
Naka-gun Ibaraki-ken 319-1195
JAPAN
Phone: +81-29-282-5640
FAX: +81-29-282-5996
E-Mail: watanabe@linac.tokai.jaeri.go.jp

John White
Australian National University
Research School of Chemistry
Canberra
AUSTRALIA
Phone: +-61-26-2493578
FAX: +-61-26-2494903
E-Mail: jww@rsc.anu.edu

W. Gavin Williams
ISIS Facility
Rutherford Appleton Laboratory
Chilton, Didcot Oxon OX11 OQX
UNITED KINGDOM
Phone: +44-1235-445599
FAX: +44-1235-445642
E-Mail: wgw@isise.rl.ac.uk

Thomas Worlton
Argonne National Laboratory
9700 S. Cass Ave.; Bldg. 360
Argonne IL 60439
US
Phone: 630-252-8755
FAX: 630-252-4163
E-Mail: tworlton@pns.anl.gov

Denis Wozniak
Argonne National Laboratory
9700 S. Cass Ave., Bldg. 360
Argonne IL 60439
US
Phone: 630-252-3592
FAX: 630-252-4163
E-Mail: dwozniak@pns.anl.gov

Ichiro Yanagisawa
Mitsubishi Heave Industries, Ltd.
1-1-1 Wadamisaki, Hyogo-ku
Kobe City Hyogo-ken
JAPAN
Phone: 81-078-672-2998
FAX: 81-078-672-3435
E-Mail:
ichirou_yanagisawa@kind.kobe.mhi.cu.jp

Robert Zolecki
Argonne National Laboratory
9700 S. Cass Ave., Bldg. 360
Argonne IL 60439
US
Phone: 630-252-3215
FAX: 630-252-9987
E-Mail: razolecki@anl.gov

VENDOR LIST

Displays at ICANS XIV:

Daimler-Benz Aerospace
Dornier Satellitensysteme GmbH
Germany
Product: Equipment and Software for Research with Neutrons
Representative: Dr. Hugo Betzold

Kurt J. Lesker Company
Clairton, PA
Product: Neutron Components
Representatives: Abdul Ganni and Dianna Swart

Financial contributions were received from the following companies who were unable to display at ICANS XIV:

Euro Collimators Limited
H. H. Martyn Works
England
Products: Design and Manufacture of All Types of Collimators
Representative: George Harrison

NTK
Neutronentechische Komponenten GmbH
Germany
Product: Neutron Guides
Representative: Erich Steichele

AUTHOR INDEX

Author	Page Number
Adams, M.A.	761
Aeppli, G.	598
Aksenov, V.L.	41
Alonso, J.	71
Amrein, B.	374
Ananiev, V.D.	41
Appleton, B.R.	32
Arai, M.	468
Argyriou, D.N.	813
Aso, T.	252, 804
Assoufid, L.	628
ASTE Collaboration	244, 457, 468
Balagurov, A.M.	650
Balchin, J.J.P.	761
Barnert-Wiemer, H.	557
Barnes, J.M.	678
Bauer, G.S.	10, 101, 229, 301, 321, 329, 361, 374, 382, 396, 703, 717
Belch, H.A.	764, 829, 864
Belushkin, A.V.	41, 768
Bertolini, L.R.	628
Betzold, H.	907
Bewley, R.I.	581
Beynon, T.D.	669
Bohringer, D.E.	773, 783
Bowden, Z.	791
Broholm, C.	598
Broome, T.A.	669, 761
Brown, B.S.	3
Brun, T.O.	586
Bull, M.	642
Bultman, N.K.	345
Carlile, C.J.	761
Carpenter, J.M.	3, 98, 144, 507, 751, 764, 864
Charlton, L.	678
Chen, D.	829
Conrad, H.	244
Cragg, D.A.	761
Crawford, R.K.	3, 201, 221, 764, 829, 864, 881
Czirr, J.B.	792
Daemen, L.L.	202, 586
Dai, Y.	301, 717
Dementyev, A.	703, 717
Donley, L.I.	829, 864
Döring, K.	557
Eccleston, R.S.	184, 581
Eckert, J.	586

Endoh, Y. 855
Ferguson, P.D. 489, 524, 890
Fornek, T. 221
Foster, S. 581
Frost, C.D. 184
Fujii, T. 424
Fult, B. 598
Furusaka, M. 56, 569, 823, 891
Futakawa, M. 244, 830
Gabriel, T.A. 678
Geissmann, K. 374
Gillette, V.H. 533
Grachev, M.I. 301
Granada, J.R. 533
Guttek, B. 329
Haga, K. 252, 329
Hagen, M. 642
Hammonds, J. 829, 864
Harada, I. 288
Harris, M. 642
Hastings, J.B. 57, 229, 836
Hata, N. 424
Haumann, J.R. 864
Hayashida, Y. 424
Heidenreich, G. 361
Herwig, K.W. 221
Heuser, B. 628
Heyck, H. 374
Hibiki, T. 411
Hino, R. 22, 252, 269, 278, 288, 804, 830
Hjelm, R.P. 202, 628
Hodges, J.P. 813
Iijima, K. 823
Ikeda, H. 46, 56
Ikeda, K. 278
Ikeda, Y. 457, 468, 728
Ino, T. 320
Ioka, I. 830
Ishikura, S. 252, 278, 288, 804
Ishiyama, W. 132
Itoh, S. 823
Iverson, E.B. 507, 751
Iwasa, H. 125, 569
Jericha, E. 61
Johnson, J.O. 678
Jorgensen, J.D. 813
Kai, T. 728, 743, 804
Kamba, K. 288
Kaminaga, M. 252, 269, 278, 288, 804

Kamiyama, T. 125, 569
Kasugai, Y. 457, 468
Kato, H. 125
Keimer, B. 598
Kern, S. 598
Kikuchi, K. 244, 830
Kikura, H. 321
Kinoshita, H. 252
Kiyanagi, Y. 125, 424, 468, 478, 569, 823
Kleb, R. 764, 829
Kogawa, H. 252, 830
Konno, M. 569
Kosako, K. 728, 743
Kravchuk, L.V. 301
Ku, C. 864
Kurosawa, K. 278
Larese, J.Z. 57, 586
Leach, D. 864
Lehmann, E. 703, 717
Lielausis, O. 382
Littrell, K. 864
Loong, C.-K. 829, 894
Lucas, A.T. 687
Ludewig, H. 57, 836
Macek, R. 84
Malik, A. 361
Mason, T.E. 598
McEwen, K. 642
McMichael, G.E. 3
Meigo, S. 448, 457
Mezei, F. 113, 119
Miller, M.E. 751
Mishima, K. 411
Miura, T. 823
Mizumoto, M. 22
Montanez, P. 57, 836
Mook, H.A. 598
Mukaiyama, T. 22
Murakami, K. 132
Nagao, T. 728, 743
Nagler, S.E. 598
Nakagawa, H. 125
Nakamura, F. 269
Nakashima, H. 457, 468, 728, 743
Neef, R. 441
Ni, L. 229, 396
Nipko, J.C. 829
Norris, J. 184
Ogawa, Y. 125, 424, 569, 823

Oku, T. 125
Orlov, Y.I. 301
Osborn, R. 598
Ostrowski, G.E. 829, 864
Oyama, Y. 22, 457, 468, 728, 743
Pepe, M.E. 533
Pepyolyshev, Y.N. 768
Perrott, L.C. 852
Peters, L.D. 751
Petrillo, C. 642
Picton, D.J. 669
Pitcher, E. 489, 524, 895
Platnieks, I. 382
Radaelli, P.G. 159, 884
Rauch, H. 61
Regler, M. 61
Rhodes, N.J. 184
Richardson, Jr., J.W. 813
Robinson, R.A. 598, 657
Russell, G.J. 489, 524, 895
Ruzicka, W. 3
Sacchetti, F. 642
Saito, Y. 411
Sakakibara, J. 320
Sakashita, M. 269, 288
Sasa, T. 448
Sasaki, S. 823
Sbaffoni, M.M. 533
Schlueter, M.W. 751

Takenaka, N. 424
Takeuchi, K. 829
Taylor, A.D. 51
Temple, S.A. 852
Terada, A. 252, 804
Teshigawara, M. 728, 743, 804
Thelliez, T.G. 202
Thiyagarajan, P. 628, 864
Thomas, G. 852
Todosow, M. 57, 836
Toeller, J. 864
Tomkinson, J. 761
Toyoshima, N. 855
Tsujimoto, K. 448
Uchida, S. 278
Uden, C.N. 761
Urban, V. 864
Uzawa, M. 278
Vinogradov, A.V. 41, 768
Vitt, R. 864
Volin, K. J. 773, 783
von Holzen, G. 229
Wakabayashi, T. 125
Watanabe, N. 22, 457, 468, 569, 728, 743, 804, 890
Weber, H. 61
White, D.J. 184
Williams, W.G. 51, 169
Worlton, T.G. 195
Wozniak, D.G. 864
Yanagisawa, I. 278
Yasui, S. 823
Yasumura, R. 424
Yocum, D. 829
Zsigmond, G. 113